PROCEEDINGS
ELEVENTH WORKSHOP
GEOTHERMAL RESERVOIR ENGINEERING

January 21-23, 1986

Henry J. Ramey, Jr., Paul Kruger, Frank G. Miller,
Roland N. Horne, William E. Brigham,
and John R. Counsil
Stanford Geothermal Program
Workshop Report SGP-TR-84*

*Sponsored by the Geothermal and Hydropower Technologies Division of the U.S. Department of Energy, Stanford-DOE Contract No. DE-AS03-80SF11459 and Contract No. DE-AS07-84ID12529

Library of Congress Catalog Card Number 86-061508

TABLE OF CONTENTS

Page

Preface . . . . . -vii-

Introduction

Noi'i o Puna: Geothermal Research in Hawaii - A. Seki et al 1

Well Testing

Preliminary Studies of Two-Phase Effects on Pressure Transient Data - B.L. Cox and G.S. Bodvarsson 7

The Significance of Early Time Data in Interference Testing for Linear Boundary Detection - A. Sageev et al 15

Injectivity and Productivity Estimation in Multiple Feed Geothermal Wells - J.D. Leaver 23

Customized Well Test Methods for a Non-Customary Geothermal Well M. Burr 29

Fractures

Reservoir Behaviour in a Stimulated Hot Dry Rock System A.S. Batchelor 35

Reservoir Fracturing in The Geysers Hydrothermal System: Fact or Fallacy? - J.J. Hebein 43

Initial Measurements of Petrophysical Properties on Rocks from the Los Azufres, Mexico, Geothermal Field - E. Contreras et al 51

Pressure Testing of a High Temperature, Naturally Fractured Reservoir - S. Kelkar et al 59

Fracture Detection and Mapping - N.E. Goldstein and J.L. Iovinitti 65

Representative Element Modeling of Fracture Systems Based on Stochastic Analysis - T.M. Clemo 71

Dual Permeability Modeling of Flow in a Fractured Geothermal Reservoir - J.D. Miller 77

Reinjection

Reinjection Model Studies in Fractured and Homogeneous Geothermal Systems - H. Hosca and E. Okandan 85

Breakthrough Time for the Source-Sink Well Doublet W. Menninger and A. Sageev 93

Tracer Developments: Results of Experimental Studies M.C. Adams et al 97

Thermal Stability of Chelated Indium Activable Tracers C. Chrysikopoulos and P. Kruger 103

Modeling

Natural State Model of the Nesjavellir Geothermal Field, Iceland
G.S. Bodvarsson et al 109

The Evolution and Natural State of Large-Scale Vapor-Dominated Zones - S.E. Ingebritsen 117

Quantitative Model of the Cerro Prieto Field - S.E. Halfman et al 127

Geosciences

The Effect of Temperature and Permeability on Hydrothermal Sericite Compositions in the Coso Hot Springs Geothermal System
B. Bishop and D. Bird . . . . . *

The Influence of Groundwater Flow on Thermal Regimes in Mountaineous Terrain - C.B. Forster and L. Smith 135

Hot Springs Monitoring at Lassen Volcanic National Park, California 1983-1985 - Michael L. Sorey 141

Inert and Reacting Tracers for Reservoir Sizing in Fractured, Hot Dry Rock System - J.W. Tester et al 149

Discussion on Maturing Geothermal Fields

Modeling Studies of Cold Water Injection into Fluid-Depleted, Vapor-Dominated Geothermal Reservoirs - C. Calore et al 161

Cooling of the Wairakei Reservoir During Production - P. Bixley 169

Field Studies

The Coupling of the Numerical Heat Transfer Model of the Pauzhetka Hydrothermal System (Kamchatka, USSR) with Hydroisotopic Data
A.V. Kiryukhin et al 175

Pressure Profiles in Two-Phase Geothermal Wells: Comparison of Field Data and Model Calculations - A. Ambastha and J.S. Gudmundsson 183

A Field Study of Tracer and Geochemistry Behavior During Hydraulic Fracturing of a Hot Dry Rock Geothermal Reservoir
B.A. Robinson 189

Logging

Pressure-Temperature-Spinner Survey in a Well at The Geysers
A. Drenick 197

Fracture Detection: Interpretation of Well Logs to Select Packer Seats and Locate Injection Intervals - D. Dreesen et al 207

* This work is available as a Stanford University, Department of Geology Master's Report, "Solution Mineral Equilibria in the Coso Geothermal System," B. Bishop, 1983.

Single Borehole Geothermal Energy Extraction System for Electrical Power Generation - G.E. Lockett 215

Reservoir Physics

Deliverability and Its Effect on Geothermal Power Costs
J.A. Marcou and J.S. Gudmundsson 217

Enhancement of Steam Phase Relative Permeability Due to Phase Transformation Effects in Porous Media
A. Verma and K. Pruess 223

The Streaming Potential Generated by Flow of Wet Steam in Capillary Tubes
S.S. Marsden, Jr. and C.K. Tyran 225

A Tool and a Method for Obtaining Hydrologic Flow Velocity Measurements in Geothermal Reservoirs
C.R. Carrigan et at 231

Natural Vertical Flow in the Los Azufres, Mexico, Geothermal Reservoir - E.R. Iglesias et al 237

Permeability Enhancement Using High Energy Gas Fracturing
T.Y. Chu et al 245

Not Presented

Conceptual Schematic Geologic Cross-Sections of the Geysers Steam Field - J.J. Hebein 251

Significant Silica Solubility in Geothermal Steam
R. James 259

Power Potential of Geothermal Wells Related to Reservoir Temperature
R. James 267

The Response to Exploitation of Rotorua Geothermal Field
Malcolm A. Grant 271

Geothermal Two-Phase Wellbore Flow: Pressure Drop Correlations and Flow Pattern Transitions
A.K. Ambastha and J.S. Gudmundsson 277

Evaluation of Porous Medium Permeability by Acoustic Logging Finds Geothermal Applications - B. Conche et al 283

List of Participants 291

PREFACE

The Eleventh Workshop on Geothermal Reservoir Engineering was held at Stanford University on January 21-23, 1986. The attendance was up compared to previous years, with 144 registered participants. Ten foreign countries were represented: Canada, England, France, Iceland, Indonesia, Italy, Japan, Mexico, New Zealand and Turkey.

There were 38 technical presentations at the Workshop which are published as papers in this Proceedings volume. Six technical papers not presented at the Workshop are also published and one presentation is not published. In addition to these 45 technical presentations or papers, the introductory address was given by J. E. Mock from the Department of Energy.

The Workshop Banquet speaker was Jim Combs of Geothermal Resources International, Inc. We thank him for his presentation on GEO geothermal developments at The Geysers.

The chairmen of the technical sessions made an important contribution to the Workshop. Other than Stanford faculty members they included: M. Gulati, E. Iglesias, A. Moench, S. Prestwich, and K. Pruess.

The Workshop was organized by the Stanford Geothermal Program faculty, staff, and students. We would like to thank J.W. Cook, J.R. Hartford, M.C. King, A.E. Osugi, P. Pettit, J. Arroyo, J. Thorne, and T.A. Ramey for their valued help with the meeting arrangements and preparing the Proceedings. We also owe great thanks to our students who arranged and operated the audio-visual equipment.

The Eleventh Workshop was supported by the Geothermal Technology Division of the U.S. Department of Energy through Contract DE-AS03-80SF11459. We deeply appreciate this continued support.

January 1986
H.J. Ramey, Jr.
P. Kruger
R.N. Horne
W.E. Brigham
F.G. Miller
J.R. Counsil

PROCEEDINGS, Eleventh Workshop on Geothermal Reservoir Engineering
Stanford University, Stanford, California, January 21-23, 1986
SGP-TR-93

NOI'I O PUNA: GEOTHERMAL RESEARCH IN HAWAII

Arthur Seki, Bill Chen*, Patrick Takahashi, and Jim Woodruff

Hawaii Natural Energy Institute
University of Hawaii at Manoa
Honolulu, Hawaii 96822

ABSTRACT

Noi'i O Puna - The Puna Research Center (PRC), located on the grounds of the HGP-A power plant site in Puna, Hawaii, was dedicated on August 24, 1985. Research projects, supported by the U.S. Department of Energy (USDOE), State, County, utility, and the private sector have been initiated in the areas of geothermal reservoir engineering, silica utilization, and corrosion of materials.

An international geothermal applications workshop was held in Hilo, Hawaii the day before the dedication to discuss common problems and methods of solution by cooperative research. The three main categories addressed were process chemistry design, reservoir engineering, and agriculture/aquaculture applications. The workshop identified how PRC might be used for these research purposes.

The advantages provided by PRC include the availability of non-proprietary information, an operational power plant with adjacent laboratory, proximity of private wells, the Fellows in Renewable Energy Engineering program, and strong support from the State, County, and utility. A second workshop is in the planning stages to follow through on the recommendations and will be held in the Orient next year.

The Community Geothermal Technology Program, featuring projects conducted by individuals and companies in the local community, has been funded and will actively initiate projects this month. This program received matching funds from the USDOE, County of Hawaii and the private sector.

INTRODUCTION

The research test facility, Noi'i O Puna - the Puna Research Center (PRC), was dedicated in August 1985. The facility is located on the grounds of the HGP-A power plant on the Big Island of Hawaii (see Figures 1, 2, 3, and 4). PRC will provide heat and high pressure brine (186°C, 11.25 kg/cm^2) for research on direct use applications and by-product recovery. A number of research projects and a special community program of direct heat use have been initiated through support from the U.S. Department of Energy (DOE), State and County governments, utility, and industry.

RESEARCH EFFORTS

Research projects being conducted at PRC largely relate to reservoir engineering, silica recovery, and corrosion. An international series of geothermal applications workshops, and the Community Geothermal Technology Program are also affiliated with PRC.

Reservoir Engineering

The reservoir engineering project is re-examining all engineering data collected in light of recent findings from the HGP-A well. The original results were calculated utilizing the theory developed for oil and gas fields. However, caution is needed in using these methods for several reasons, including the fact that the theory is basically for single-phase flow, and HGP-A produces two-phase flow.

These early pressure drawdown and buildup tests revealed the following results [1, 2]:

1. The HGP-A reservoir is tight (low permeability of perhaps less than 1 milli darcy), and the well suffers from significant skin damage, resulting in a discharge rate of only 38-60 percent of the full potential;
2. There appears to be at least two production layers with permeability-thickness (kh) values. While the theory does not permit a calculation of the two kh values, there is indication that the effective kh ranges between 1000-1500 milli darcy-feet. Evidence of the two-production-zone theory is also reflected in the temperature/pressure profiles measured downhole in HGP-A well (see Figures 5 and 6), where three distinct slopes are seen in the pressure plots.

Recent geochemistry data have provided more evidence to the theory that two production layers do exist - one layer producing mostly

* University of Hawaii at Hilo; Hilo, Hawaii

steam and the other mostly water. Thus, with this new information calculations will be completed to verify this two-production-zone model [3, 4].

Silica Recovery [3, 5]

The objectives of this research program are to determine whether: a marketable form of silica can be recovered from the geothermal fluids at HGP-A; the silica precipitation process can be controlled using chemical additives; and markers or tracers exist in the cuttings from the geothermal wells already drilled that will differentiate between steam and water production aquifers.

The first of these entail an analysis of the charcteristics of silica precipitated under a variety of pH, temperature, and chemical conditions. Recovery rate and particle size determinations will be made for each condition in order to check whether marketable particle sizes (> 100 m^2/gm) can be obtained. Currently, a method has been identified on a laboratory scale that removes silica quite effectively and at a particle size having market potential. If optimal particle sizes can be obtained on a batch scale, a continuous recovery pilot process will be developed to determine whether product quality can be maintained.

The recovered material will be analyzed for purity, including trace metal concentrations. Specialty products of high purity such as special doped silica products might be fabricated from this material.

By using a variety of additives to the geothermal brine, chemical reactions which could inhibit or polymerize the silica will be examined. An accelerated reaction in a settling chamber before it reaches the valves and heat exchangers is desired. Initial experiments will be conducted at boiling and atmospheric pressure and, if a control agent is found, a pressurized reaction vessel will be used.

An additional study will search for chemical or physical markers in the cuttings and drilling logs to help differentiate between liquid producing aquifers with silica and dry steam producing aquifers without silica. The identification of such markers would permit a drilling engineer to exclude the silica producing aquifers and thereby reduce the scaling problems associated with water production, or conversely, tap only the shallower silica saturated fluid for commercial purposes.

Corrosion of Materials

Investigations on the corrosive properties of the geothermal fluid on various materials have been on-going at the HGP-A site. The goal is to develop criteria for selection of materials to be used in equipment (pipes, valves, heat exchangers, etc) that will transport and extract heat from the fluid. Exposure tests of the relevant metallic and polymeric materials are being performed to classify the corrosiveness of the fluid on a global reference scale, which would allow comparison with data developed elsewhere [6].

The tests at HGP-A have shown that relative to geothermal sites world-wide, the Hawaiian geothermal fluid is moderately aggressive. Of the three environments tested, the aerated flashed steam caused the most corrosion, followed by the liquid after flashing. The non-aerated flashed steam was the least aggressive. Aluminum alloys suffered severe pitting in all three environments, while the high alloy stainless steels were fully resistant. Carbon steel and copper alloys suffered severe general corrosion in the aerated steam, moderate damage in the non-aerated steam, and considerable general or crevice corrosion damage in the liquid. Nickel, zinc, and Monel 400 were severely pitted, especially in the aerated steam and in the liquid [7].

Preliminary tests in the silica settling pond on several types of plastics indicated that most plastics which survived the temperature were relatively resistant to chemical attack. At the present time testing in the hot end of the silica settling pond is being carried out to select plastics for engineering applications. While the evaluation is not complete, results indicate that a number of common plastics were embrittled in the fluid during the two-month exposure period [6].

International Workshop [8, 9]

An invitational workshop on geothermal technology for the Pacific Basin was held in August 1985 at the University of Hawaii Hilo Campus to bring together researchers, scientists, and technologists from Pacific countries to discuss common problems and means of resolution. The three specific areas of interest were process chemistry design, reservoir engineering, and aquaculture/agriculture applications.

The most critical problem identified by the process chemistry group was scaling. Two separate approaches were discussed: a field-oriented research program to investigate the various methods of inhibiting or accelerating scale formation; and a theoretical modeling of the geothermal fluid chemistry to determine the critical parameters associated with scale formation and solid species saturation in the fluid. The chief recommendation for future research was to pursue both avenues interactively using the laboratory and field results to guide the theoretical models of fluid saturation and to use the theoretical results to suggest potentially fruitful laboratory or field methods. Another problem discussed that required research was mineral recovery.

The reservoir testing session considered an

inventory of benefits offered by the Puna Research Center for cooperative research. The advantages included: an existing steam field containing a single well feeding a 3 MW power plant; two-phase reservoir fluid of extremely high temperature (186°C at the wellhead, and 358°C at bottomhole); direct communication with the University of Hawaii; an interested and supportive utility in Hawaiian Electric Company; adjacent commercial geothermal development; a geographic location in relatively close proximity to the ocean; and possible recharge by seawater. Experiments can be conducted involving either the power plant or the HGP-A well. An adjacent well drilled by Thermal Power may offer possibilities for inter-well experiments. As the reservoir is in an existing fractured rift zone typical of other circum-Pacific systems, this situation appears especially appropriate for cooperative research.

The following recommendations were made by the group: drill a second well in the Puna geothermal field; conduct multi-well interference testing; develop and test new downhole instruments; and identify the source and nature of the fluids at HGP-A. In order to permit multi-well testing, and to provide backup steam production capability, the group labeled drilling and completion of a new well as the highest priority. Multi-well testing between the Thermal Power, HGP-A, and the experimental well would then more accurately enable estimation of the size of the reservoir. Interference testing between the Thermal Power and HGP-A wells was also suggested.

The agri-aquaculture group felt that non-electrical use of geothermal energy is already state-of-the-art, and therefore, small scale demonstrations should be initiated to prove commercial feasibility in Hawaii. Recommended were the following applications which show promise in the Puna district: food processing (human food, animal feed); food technology; refrigeration (ice-making and cold storage); greenhouse operations; dehydration; aquaculture; and balneology.

The second international workshop will be held late in 1986 or early 1987 in the Orient. A steering committee has been formed and is tentatively planning to hold the meeting in Japan with re-convened sessions in Taiwan, Philippines, China, and/or Indonesia.

Community Geothermal Technology Program (CGTP)

The CGTP is similar to an earlier U.S. Department of Energy appropriate technology program and provides the opportunity for small businesses and individuals to use the discarded geothermal fluids for non-electric purposes. The topics that show promise for funding include soil heating and greenhouse use; green papaya drying; refrigeration; glass making; lumber drying; and cloth dyeing [8].

OTHER DEVELOPMENTS

The College of Engineering and the Hawaii Natural Energy Institute at the University of Hawaii are completing a search for a geothermal researcher for the Fellows in Renewable Energy Engineering (FREE) program. This program involves corporate and foundation endowment of teaching and research positions to advance the development of renewable energy technologies. The Hawaiian Electric Industries has provided $250,000 specifically to support a FREE researcher in geothermal energy. A selection will be announced soon.

The entire geothermal facility, which includes the visitor center, Puna Research Center, and HGP-A power plant, has been transferred to State ownership and placed under the authority of the Natural Energy Laboratory of Hawaii Board. This board is composed of officials from the State, County, and University of Hawaii and currently oversees the work at the Seacoast Test Facility located at the western tip of the Big Island, where ocean energy and related aquaculture research have been on-going since 1981 [10].

Private developers have drilled several geothermal wells in the vicinity of the HGP-A site. Recently, the consortium of Thermal Power, AMFAC, and Hawaiian Dredging completed its third well, Kapoho State 1A (see Figure 1). Preliminary flow tests have indicated good steam production. A proposal has been submitted to the State to provide steam and brine for the HGP-A power plant and PRC [11].

CONCLUSION

Since 1976 six wells have been completed and tested in Hawaii. A 3 MW powerplant has provided reliable electricity for four years. The activities at PRC should further increase interest and stimulate geothermal development in Hawaii.

ACKNOWLEDGEMENTS

Funding from the Federal, State, and County governments, utility, and private industry have supported geothermal research and development at HGP-A and PRC. The U.S. Department of Energy provided grants through two contracts: DE-FG03-85-SF-15798 and DE-FG03-85-SF-15799.

REFERENCES

[1] Yuen, P., Chen, B., Kihara, D., Seki, A., and Takahashi, P., "HGP-A Reservoir Engineering," Hawaii Geothermal Project, University of Hawaii, September, 1978.

[2] Chen, B., Kihara, D., Seki, A., and Yuen, P., "Well Test Analysis of HGP-A," Proceedings of the 1979 SPE-AIME California Regional Meeting, Ventura, California, April 18-20, 1979.

[3] Chen, B., "Research Proposal on the Puna High Tech Facility," U.S. Department of Energy Grant No. DE-FG03-85-SF-15799, August, 1984.

[4] Thomas, D., "A Geochemical Model of the Kilauea East Rift Zone," Draft Report, Hawaii Institute of Geophysics, University of Hawaii, November 1985.

[5] DeCarlo, E., Hawaii Institute of Geophysics, University of Hawaii, Personal communication, September, 1985.

[6] Larsen-Basse, J., "Continued Study of Some Geothermal Material Problems," Proposal to Hawaii Natural Energy Institute, University of Hawaii, July 1985.

[7] Larsen-Basse, J. and Lam, Kam-Fai, "Corrosion Tests in Hawaiian Geothermal Fluids," Proceedings of the International Congress on Metallic Corrosion, Toronto, Canada, June 3-7, 1984, Vol. 3, 641-648.

[8] Takahashi, P., "Community and International Geothermal Technology Transfer Program," U.S. Department of Energy Grant No. DE-FG03-85-SF-15798, December, 1984.

[9] Takahashi, P., "Proceedings of the Invitational Workshop on Geothermal Technology for the Pacific Basin," held at the University of Hawaii at Hilo campus, on August 23, 1985, Hawaii Natural Energy Institute, December, 1985.

[10] Huizingh, J., Executive Director, Natural Energy Laboratory of Hawaii, Personal communication, November 1985.

[11] "Thermal Power Company Proposal to Supply Fluids to the HGP-A Power Plant," Department of Planning and Economic Development, November, 1985.

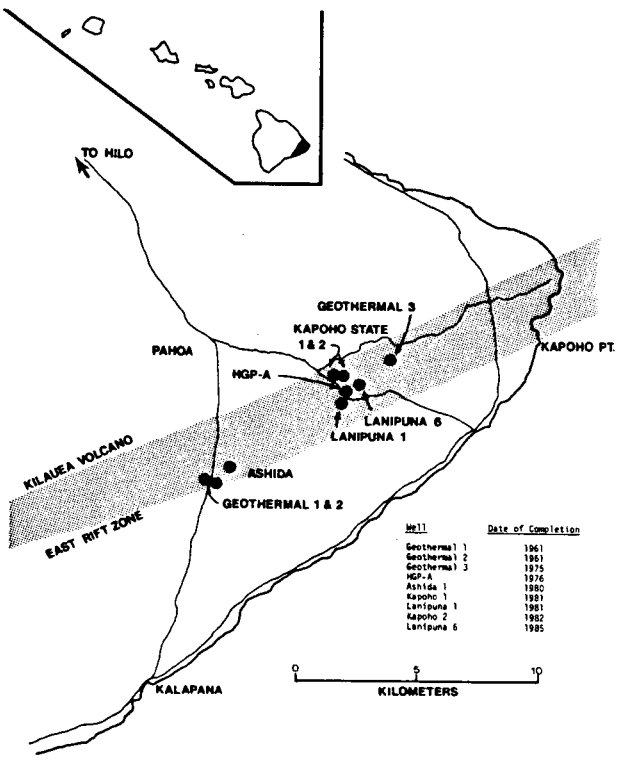

Figure 1. Map of Geothermal Wells in Hawaii

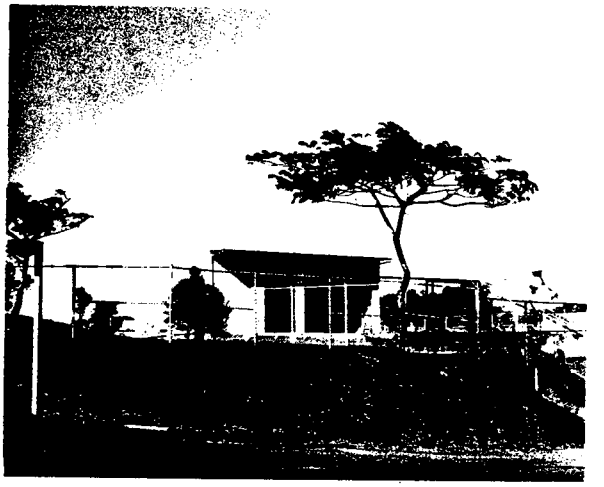

Figure 2. Noi'i O Puna - Puna Research Center

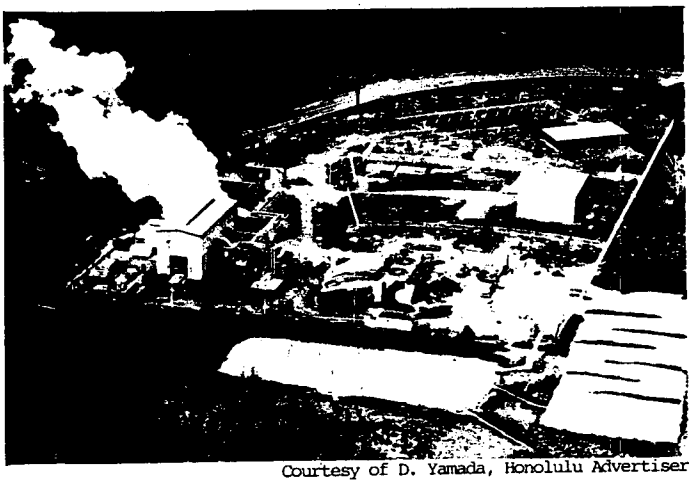

Courtesy of D. Yamada, Honolulu Advertiser

Figure 3. HGP-A Site

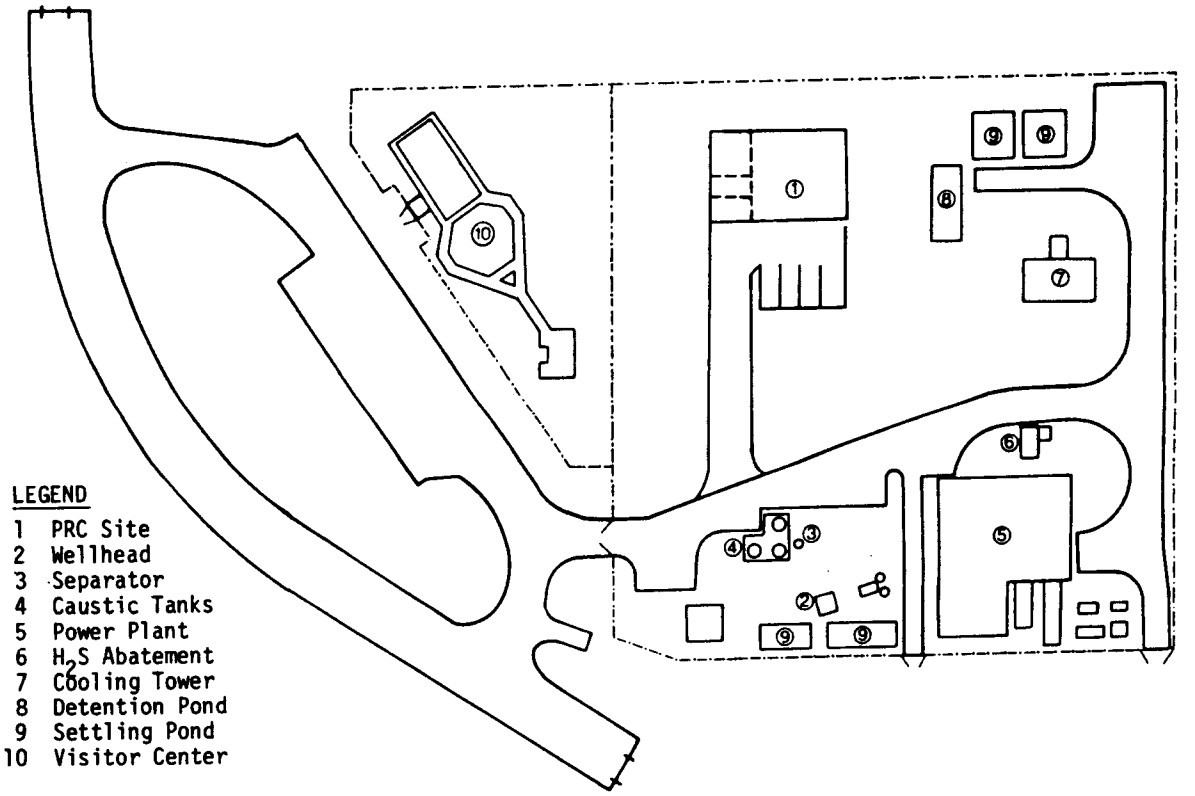

Figure 4. Schematic of HGP-A Site

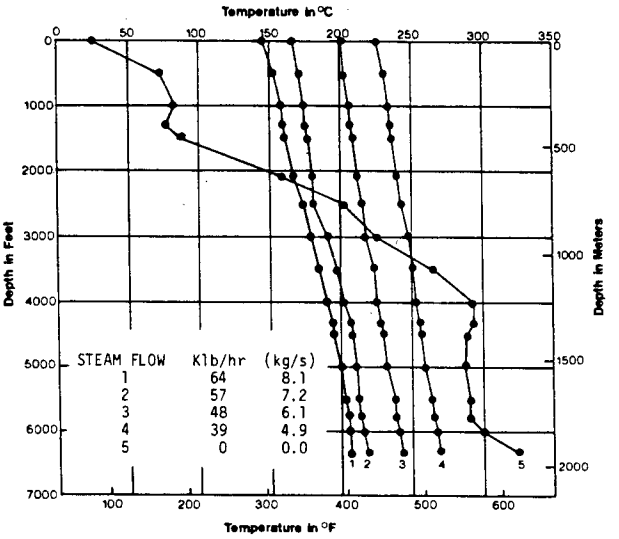

Figure 5. Temperature Profiles in HGP-A [1,2]

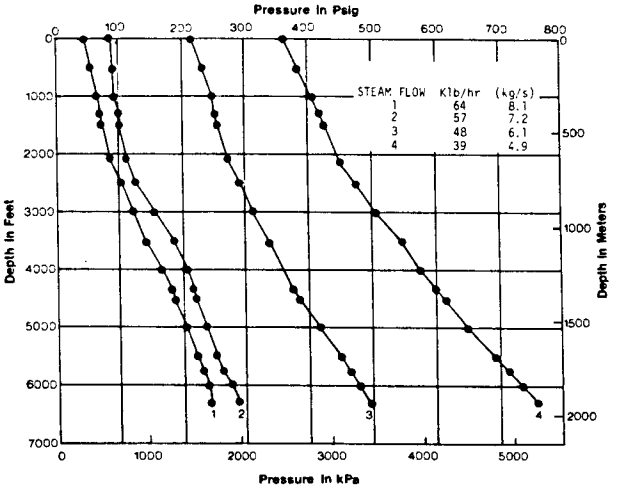

Figure 6. Pressure Profiles in HGP-A [1,2]

PROCEEDINGS, Eleventh Workshop on Geothermal Reservoir Engineering
Stanford University, Stanford, California, January 21-23, 1986
SGP-TR-93

PRELIMINARY STUDIES OF TWO-PHASE EFFECTS ON PRESSURE TRANSIENT DATA

B. Lea Cox and Gudmundur S. Bodvarsson

Earth Sciences Division, Lawrence Berkeley Laboratory
University of California, Berkeley, California 94720

INTRODUCTION

Presently, there are few methods available for analyzing pressure transient data from two-phase reservoirs. Methods published in the oil and gas literature (Earlougher, 1977) have been adapted for analyzing data from geothermal reservoirs, assuming a uniform initial steam saturation. However, it is well known that two-phase conditions often prevail only in parts of the reservoir, primarily in the top portion, and that vapor saturations are not uniform. Thus, there is a need to examine the pressure behavior during well tests considering more realistic conditions.

Two-phase effects are important in pressure transient analysis because the mobility of two-phase mixtures can differ significantly from that of single-phase fluids. Also, the compressibility of two-phase mixtures is orders of magnitude higher than for single-phase liquid and vapor (Grant and Sorey, 1979).

In this paper we perform scoping calculations on the effects of two-phase zones on well pressure transients. Three different cases are considered (Figure 1). The first is that of a fully two-phase system (e.g. Krafla, Iceland; Stefansson, 1981). This problem has been studied by various authors, including Moench and Atkinson (1977, 1978), Grant (1978), Garg (1978, 1980), Grant and Sorey (1979), and Aydelotte (1980). Some of the complexities of this type of system are discussed. The second problem is that of a single-phase liquid reservoir with a localized two-phase zone. Possible field examples include Cerro Prieto, Mexico and Baca, New Mexico, USA. This problem was studied by Sageev and Horne (1983a,b) and Sageev (1985); they used a constant pressure approximation for the two-phase zone. In this paper we investigate the pressure transients in a well located near an isolated two-phase zone in a single-phase liquid reservoir, and compare them to type curves based upon the constant pressure approximation. The third problem considered is that of a two-phase layer overlying a single-phase liquid layer. One example of such a reservoir is the Svartsengi geothermal field in Iceland (Gudmundsson et al., 1985). Little research has been done on pressure transients in such systems. The numerical code MULKOM (Pruess, 1983) is used to simulate the three cases.

FULLY TWO-PHASE RESERVOIR

The fully two-phase system (Figure 1, case A) is modeled with a radial, single-layer mesh with fine uniform grid spacing near the well, and logarithmically increasing grid size farther away. The grid extends sufficiently far from the well so that no boundary effects occur. The well fully penetrates the reservoir, and produces at a constant flow rate. The parameters assumed in the simulation are shown in Table 1. The accuracy of the numerical grid was verified by running a single-phase liquid case and the results compared to the conventional Theis solution (Theis, 1935). In this case the calculated transmissivity and storativity agreed with the input values to within 5%.

Various simulations were carried out using uniform two-phase initial conditions. Figure 2 shows the resulting pressure transients for an initial vapor saturation of 5%; results are given for the production well and several observation wells. The shape of the pressure transient curves is similar to the conventional Theis curve for single-phase liquids. Using the methods of Grant and Sorey (1979) and Garg (1978, 1980), these curves were matched to the Theis curve, and the total kinematic viscosity corrected to account for the two-phase effects. The total kinematic viscosity (ν_t) can be calculated with the following equation:

$$\nu_t = \left(\frac{k_{rl}\ \rho_l}{\mu_l} + \frac{k_{rv}\ \rho_v}{\mu_v} \right)^{-1} \qquad (1)$$

where μ and ρ are the viscosity and density of the different phases (l for liquid, v for vapor), and k_r is the relative permeability. The transmissivity (kH) and storativity (ϕCH) can then be calculated using conventional equations (Earlougher, 1977). Complications arise because the total kinematic viscosity depends on relative permeabilities,

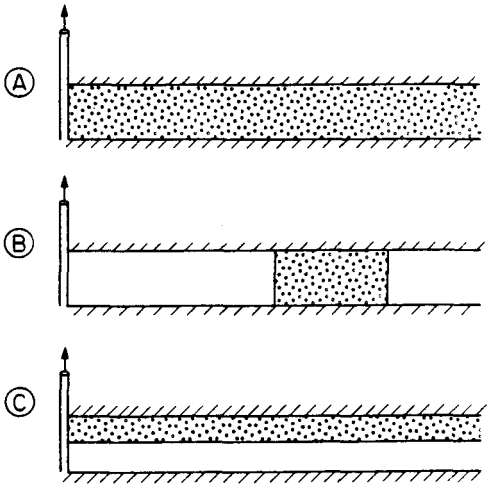

Figure 1. Problems considered: A) fully two-phase reservoir; B) isolated two-phase zone in a single-phase liquid reservoir; C) layered system.

Table 1. Parameters used in simulations.

Rock Properties	
absolute permeability	$5 \times 10^{-15} m^2$
thermal conductivity	2 J/m/s/°C
heat capacity	1000 J/kg°C
porosity	0.05
density	2650 kg/m^3
Well Parameters	
well radius	0.1 m*, 5.0 m**
production rate	25 m^3/s
distance from well to two-phase zone	500 m
Reservoir Parameters	
thickness of reservoir	500 m
size of two-phase zone	100 m^2, 1500 m^2

which presently are not well known. The sensitivity of (ν_t) to variations in the relative permeability function was investigated by Bodvarsson et al. (1980) and O'Sullivan (1981). Further studies, not described here, indicate that if one assumes different relative permeability curves from those used in the simulation, calculated values of kH and ϕCH could be off by an order of magnitude. Therefore, because of uncertainties regarding relative permeabilities, the values of kH and ϕCH for two-phase systems should only be considered as first-order estimates.

A further complication arises because the total kinematic viscosity also depends on pressure and enthalpy, which change with time. The pressure transients from both the production well and several observation wells were analyzed, assuming either initial or final pressures to investigate which value would give most accurate results. For all cases tested, the final pressures and enthalpies gave the best results, and calculated values of kH and ϕCH were within 10 to 15% of the actual values used in the simulations.

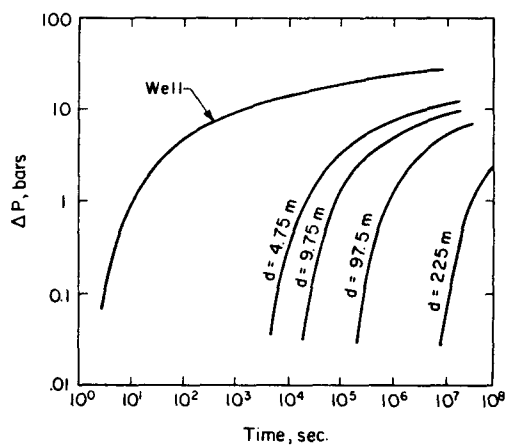

Figure 2. Pressure transients for a production well and several observation wells in a fully two-phase reservoir, where d is the distance from the production well to the observation well.

LOCALIZED TWO-PHASE ZONES

In many geothermal systems, the main single-phase liquid reservoir contains isolated two-phase zones. Field examples are Baca, New Mexico (Grant, 1979) and Cerro Prieto, Mexico (Lippmann and Bodvarsson, 1983). Analytical methods for studying pressure transient data from such systems were developed by Sageev and Horne (1983a,b) and Sageev (1985), who treated the two-phase zone as a constant pressure circular subregion (Figure 3). They justified this approximation by the high compressibility of two-phase fluids compared to that of single-phase fluids. Using this approach, Sageev and Horne (1983a,b) developed type curves for estimating the size of the circular subregion and distance from the well. In this paper we simulate the problem of an isolated two-phase subregion surrounded by a single-phase liquid region. Our primary interest is to investigate the effects of the two-phase zone on the pressure transients of a well located in the single-phase region. We also investigate the applicability of the constant pressure approximations to two-phase zones.

In order to calibrate the grid, simulations were run for the case of an actual constant pressure zone using a single layer two-dimensional mesh (Figure 4). To simplify the numerical model we use a rectangular rather than a circular subregion. Two cases are simulated, one with a large subregion (1500 m^2), and the other with a small subregion (100 m^2). Figure 5 shows the comparison of our results with those of Sageev and Horne (1983a,b) for the large constant pressure zone. The match is reasonably good at all times and enabled the calculation of the correct kH and ϕCH from the early time data. From the later time data we were able to obtain the correct distance between the well and the zone, as well as the correct size of the constant pressure zone.

The grid used to simulate the isolated two-phase zone is identical to that used for the constant pressure zone except that the internal subregion is discretized to allow for throughflow to the well. A uniform initial pressure of 100 bars is assigned to all the elements in the mesh. The

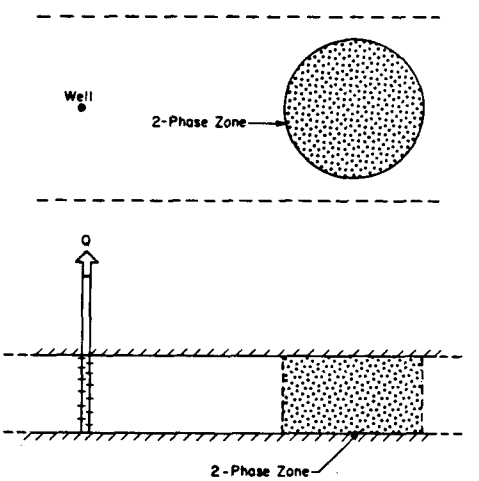

Figure 3. Top and side view of a well producing in a single-phase liquid reservoir with an isolated two-phase zone.

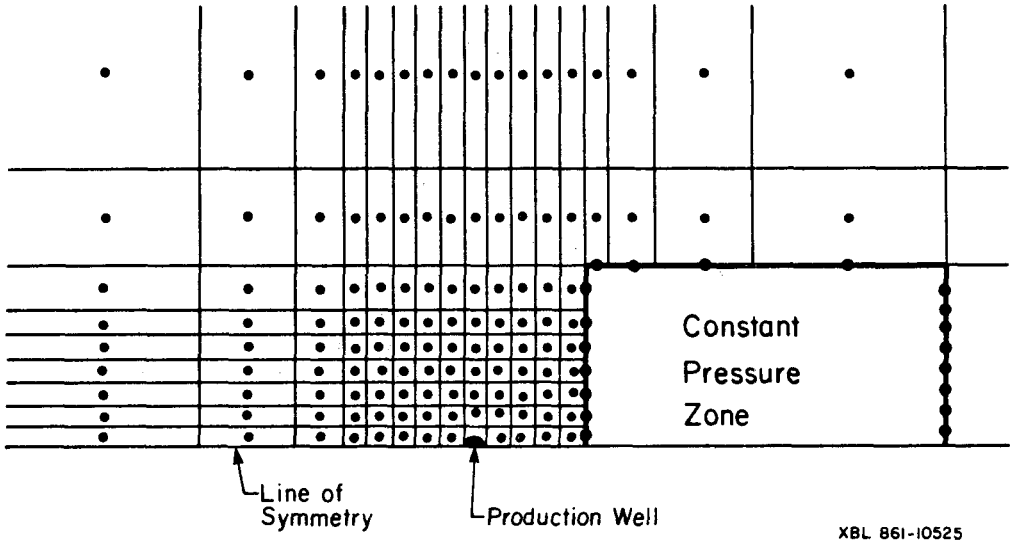

Figure 4. Two-dimensional grid used to simulate a constant pressure zone in a single-phase liquid reservoir.

single-phase outer region is assigned a uniform initial temperature of 250 °C. A uniform initial vapor saturation is assumed for the two-phase subregion. The temperature of the two-phase zone corresponding to the initial pressure is 310 °C.

Although the initial pressure distribution is stable, the initial temperature distribution is not; the temperature of the two-phase zone is about 61 °C higher than that of the outer region. Hence, conductive heat transfer will tend to equilibrate the temperatures. The effects of thermal conduction were tested by running a simulation with no production from the well. The results indicate that the effects of thermal conduction for the time periods considered in this study are minimal. After 3 years, the areal extent of the two-phase zone is reduced by about 5%, but the vapor saturation distribution is only slightly affected. However, most importantly, there is no pressure change at the well.

After confirming the stability of the initial conditions, the simulations were carried out for a period of 3 years, assuming a constant production rate. The computed pressure transients for the cases of small and large two-phase subregions are shown in Figures 6 and 7, respectively. For both cases the pressure transients differ significantly from those obtained when the constant pressure approximation is used. This is because of the higher total kinematic viscosity (and therefore lower mobility) of two-phase fluids as compared to the single-phase fluids. For times up to about 2 months, the pressure transients for the case with a large two-phase zone are similar to those of the constant

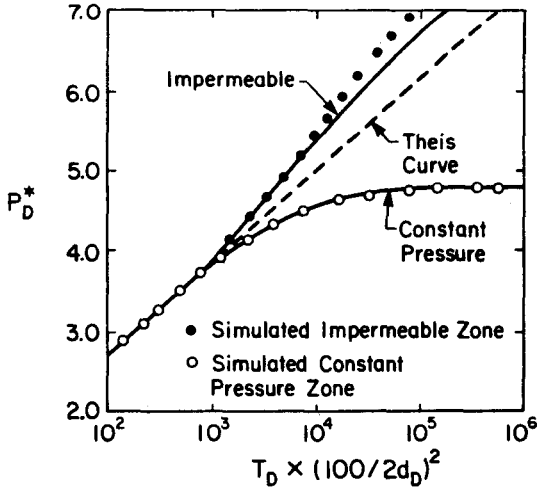

Figure 5. Comparison of the analytical (solid lines; Sageev and Horne, 1983a,b) and computer generated pressure transients for large constant pressure and impermeable zones in a liquid reservoir. XBL 862-10630

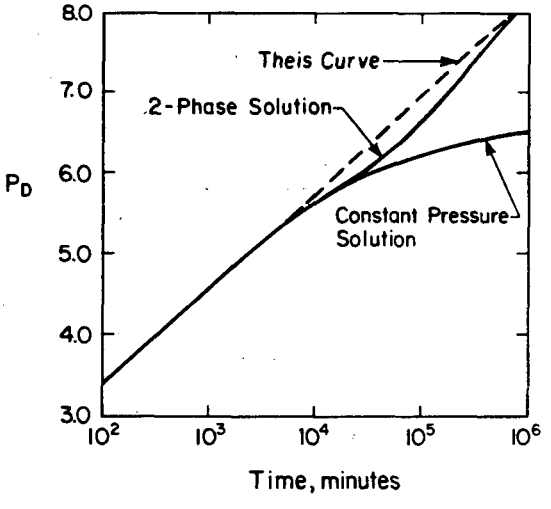

Figure 6. Computed pressure transients from a well producing in a single-phase liquid reservoir with a small two-phase zone and with a constant pressure zone. XBL 861-10508

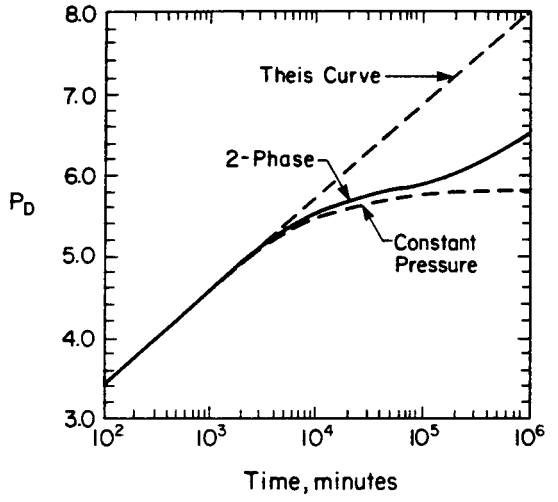

Figure 7. Computed pressure transients from a well producing in a single-phase liquid reservoir with a large two-phase zone and with a constant pressure zone. XBL 861-10507

pressure approximation. This suggests that if the two-phase zone is very large or the well is very close to it, for certain periods of time, the pressure transients will be similar to those using constant pressure approximations. The presence of the two-phase zone will cause a deviation from the Theis solution, similar to that observed for the case with a constant pressure zone. However, at later times, the relatively low fluid mobility in the two-phase zone causes much more rapid pressure changes, in some cases even resulting in a steeper slope than that given by the Theis solution.

Sensitivity Studies

From the sensitivity studies we found that the presence of the two-phase zone affects the pressure transients at the well for two primary reasons. First, the high compressibility contrast will cause a plateau in the pressure response, and second, the fluid mobility in the two-phase zone will control the late-time pressure behavior. The higher the initial vapor saturation, the higher the total kinematic viscosity of two-phase mixtures, and the lower the fluid mobility. Thus, high initial vapor saturations shorten the duration of the plateau region and cause a steepening in the late-time pressure response. Consequently, the constant pressure approximation will be significantly in error for high initial vapor saturations.

Similar effects were found using different relative permeability curves. For most of the simulations we use linear relative permeability curves (X-curves), with immobile liquid and steam cutoffs of 0.40 and 0.05, respectively. When the Corey (1954) relative permeability curves were used (with the same cutoffs), a smaller plateau and a steeper late-time slope were obtained. This is because the Corey curves give lower liquid mobilities than the X-curves. Porosity effects shift the curves along the time axis, because the total fluid storage is affected. However, for this problem porosity effects are practically negligible.

The effects of varying the distance between the well and the two-phase zone are shown in Figure 8. All of the slopes follow the Theis curve at early time, then flatten out due to the high compressibility of the two-phase zone. Finally the slopes steepen due to the low mobility of the two-phase zone. The shorter the distance between the well and the two-phase zone, the sooner the divergence from the Theis curve. Also, for a well near the two-phase zone, the flattening of the curve is more extreme, and the late-time slope is steeper. It is possible to estimate the distance from the well to the two-phase zone by analyzing the deviation time, and using a constant pressure type approximation. Data from several observation wells can be used to estimate the size of the two-phase zone.

The effects of an isolated two-phase zone on the pressure transient curve are summarized on Figure 9. The early-time slope follows the Theis curve, as the well sees only the single-phase fluids. The effect of storage in the two-phase zone is seen next; as the curve bends, its shape ressembles that of the constant pressure solution. Next, the slope steepens due to the lower mobility of the two-phase fluids. The curve eventually parallels the Theis curve, as the two-phase zone acts as a positive skin around the producing well.

LAYERED SYSTEM

The final problem considered is that of an infinite two-phase layer overlying a single-phase liquid zone. A two-layer radial grid (Figure 10) was used in the simulations. By using only two layers, we cannot accurately resolve the early time interaction between the two-phase zone and the underlying liquid region. For initial conditions we use a stable hydrostatic pressure distribution. All of the elements in the top layer have the same initial conditions ($P \approx 40$bars; $S_v = 0.10$; $T \approx 250\,^\circ$C). The bottom liquid layer initially has a temperature of 250 °C and a pressure of 60 bars. Two cases are considered, one with production from the overlying two-phase layer and the other with production from the underlying single-phase liquid layer.

The pressure transients resulting from producing fluids from the liquid zone are shown in Figure 11, for the production well and several observation wells. In all cases, the slopes of the early-time pressure transient data reflect

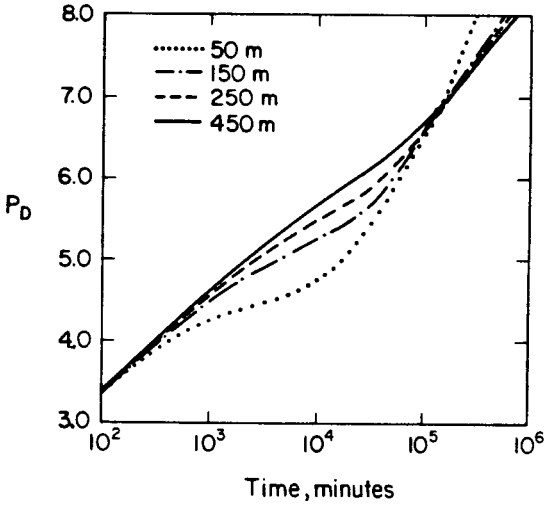

Figure 8. Simulated pressure transients from a well producing in a single-phase liquid reservoir with a two-phase zone, with varying distance between the well and the two-phase zone. XBL 861-10509

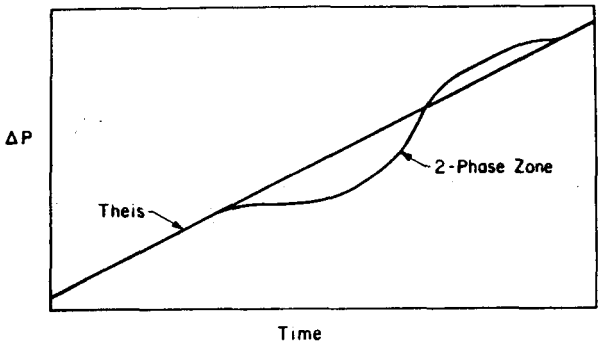

XBL 861-10523

Figure 9. Hypothetical pressure transient from a well producing in a single-phase liquid reservoir with an isolated two-phase zone.

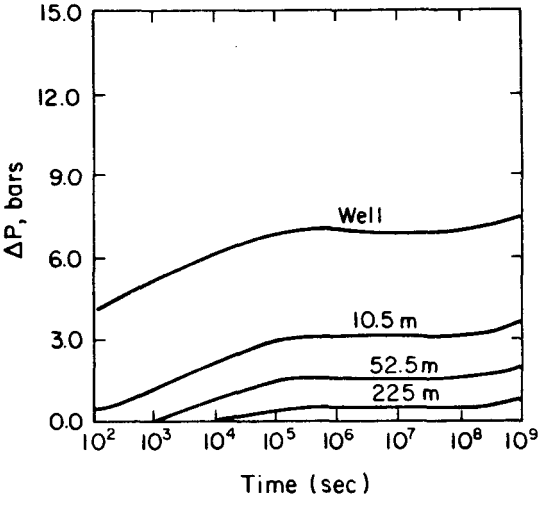

Figure 11. Computed pressure transients from a well producing from a single-phase liquid layer beneath a two-phase layer and from several observation wells at varying distances from the production well. XBL 861-10520

the liquid portion of the reservoir, and yield the correct kH and ϕCH of that layer. However, at later times the slope decreases and the pressure levels off, resembling the pressure transients for a system with a constant pressure boundary.

The cause of this behavior can be explained by the physics of the problem. Production from the liquid zone results in a pressure decrease in that zone, and fluid drainage from the overlying two-phase layer. This causes boiling and increases the vapor saturation in the two-phase zone because gravity forces will cause only the liquid and not the steam to drain downwards. The drainage and boiling in the two-phase zone causes a slight pressure drop, which in turn activates horizontal steam and liquid flow in the two-phase zone. Although this helps to maintain the downward drainage of liquid water, the steam inflow also stabilizes the pressure in the two-phase zone. The steam condenses, increasing the temperature and pressure. Thus, this steam flow tends to stabilize the pressure, so that the pressure transient curve looks similar to that resulting from a constant pressure zone. Figure 12 shows the pressure drop in the liquid zone after about 6 months of production, but no pressure changes in the two-phase zone.

The plateau in the pressure-log time plot (Figure 11) only lasts for a limited time (a few years); after that the slope increases again. This late-time increase in the slope is due to the development in the upper layer of an expanding zone with immobile liquid water. If the initial vapor saturation is large enough that the liquid is immobile everywhere in the two-phase zone, there is no drainage of liquid water, and the two-phase zone does not at all affect the pressure transients (Figure 13).

For the case of production from the two-phase zone (Figure 14), the initial slope is steeper than in the previous case, because of the lower mobility of the two-phase fluids relative to the single-phase liquid. Again, the correct kH and ϕCH can be estimated from this early-time data. At later time the two-phase zone is recharged from the liquid layer, causing a drop in enthalpy. This in turn causes pressures to stabilize and eventually increase.

The pressure increase resulting from the enthalpy decline is an interesting effect. During production, most wells produce at a constant bottom-hole pressure and not at a constant flow rate. In such tests, the recharge from the liquid layer into the two-phase layer would result in a flow rate increase. This has been observed in several two-phase geothermal fields (e.g., Krafla and Namafjall, Iceland; Stefansson and Steingrimsson, 1980).

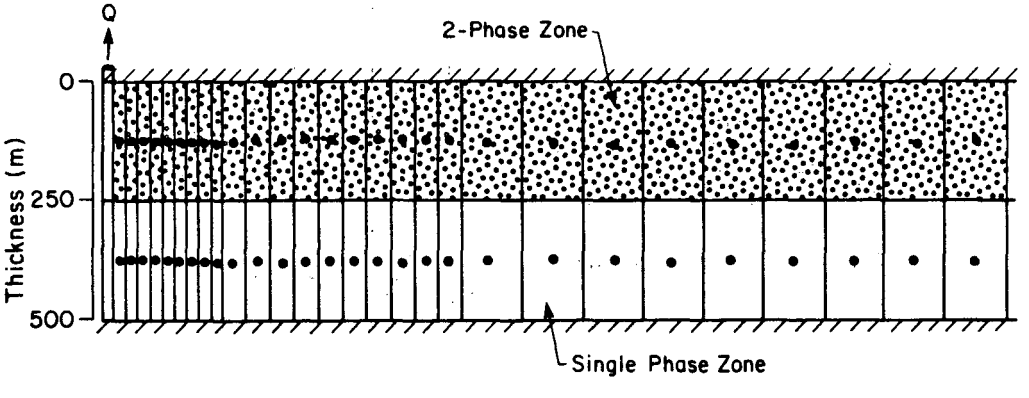

Figure 10. Radial grid used to simulate a system with a two-phase layer overlying a single-phase layer. XBL 861-10526

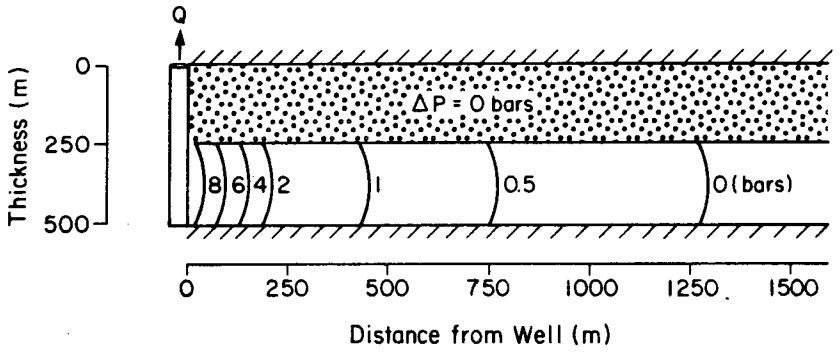

Figure 12. Pressure drawdown in a layered system after 2 years production from the underlying single-phase liquid layer. XBL 861-10513

CONCLUSIONS

We have carried out scoping calculations for several well test problems involving two-phase zones. For the fully two-phase reservoir, wrong assumptions regarding relative permeability curves can yield order-of-magnitude errors in kH and ϕCH. Therefore, pressure transient analysis methods should be used with caution. Late-time pressure and enthalpy values, yield the best estimates of kH and ϕCH.

In single-phase liquid reservoirs with an isolated two-phase zone, the constant pressure approximation generally appears not to be valid. The high storage of two-phase zones causes a bend in the semi-log pressure transient curve, followed by a steeper slope due to the relatively lower mobility of two-phase fluids. The time of deviation from the line source (Theis) solution could be used to estimate the distance between the producing well and the two-phase zone. Furthermore, data from several observation wells can be used to estimate the size of the two-phase zone.

In geothermal reservoirs with a two-phase zone overlying a single-phase liquid layer, drastically different pressure responses are obtained when feed zones are assumed to be in the liquid zone rather than in the two-phase zone. Production from the liquid zone results in pressure transients that resemble constant pressure effects. Pressure in the overlying two-phase zone remains practically constant because the 'steam phase' is trapped. If only vapor is mobile in the two-phase zone (steam cap), effects on the pressure transients in the liquid layer are negligible. Production from the overlying two-phase layer causes initially a high pressure response due to the low mobility of the two-phase mixture. Later on, recharge from the underlying liquid layer causes an enthalpy decline in the steam cap and an associated leveling (or increase) in fluid pressure. This agrees with data obtained from several two-phase geothermal fields, where flowrate increases occur at late-time.

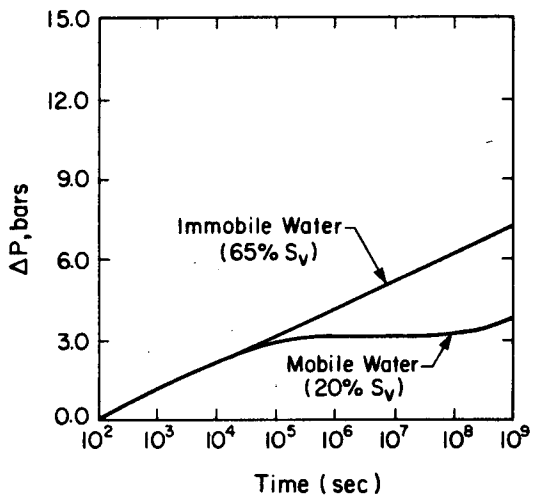

Figure 13. Computed pressure transients resulting from fluid production from the underlying liquid layer, assuming different initial vapor saturations in the overlying two-phase layer. XBL 861-10518

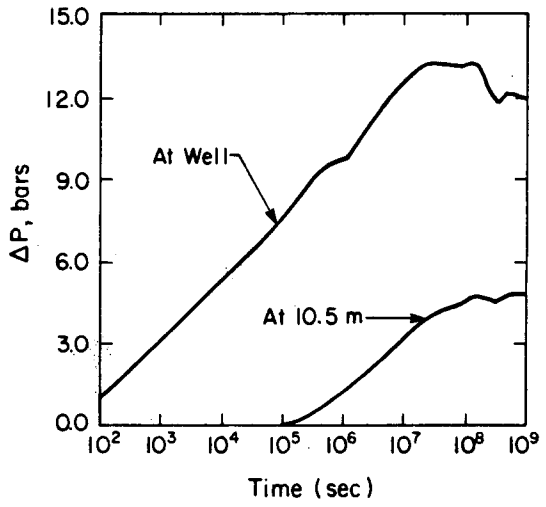

Figure 14. Computed pressure transients resulting from fluid production from the upper two-phase layer. Pressure transients shown are for a producing well and a nearby observation well. XBL 861-10519

ACKNOWLEDGEMENTS

Helpful discussions with S.M. Benson during the course of this work are appreciated. The authors also acknowledge valuable technical review by M.J. Lippmann. This work was supported through U.S. Department of Energy Contract No. DE-AC03-76SF00098 by the Assistant Secretary for Conservation and Renewable Energy, Office of Renewable Technology, Division of Geothermal Technology.

REFERENCES

Aydelotte, S.R., 1980. Transient well testing in two-phase geothermal reservoirs, Lawrence Berkeley Laboratory Report LBL-10562.

Bodvarsson, G.S., O'Sullivan, M.J. and C.F. Tsang, 1980. The sensitivity of geothermal reservoir behavior to relative permeability parameters, Proceedings of the Sixth Workshop on Geothermal Reservoir Engineering, Stanford University, Stanford, CA, SGP-TR-50, pp. 224-237.

Corey, A.T., 1954. The interrelation between gas and oil relative permeabilities, *Prod. Mon.*, 19, pp. 38-41.

Earlougher, R.C., 1977. Advances in well test analysis, Society of Petroleum Engineers of AIME, Monograph 5, Dallas, Texas.

Garg, S.K., 1978. Pressure transient analysis for two-phase geothermal reservoirs, *Geothermal Resources Council Transactions,* Vol 2., pp. 203-206.

Garg, S.K., 1980. Pressure transient analysis for two-phase (liquid water/steam) geothermal reservoirs, paper presented at 53rd Annual Fall Conference, Soc. Petrol. Eng. of AIME, Houston, Texas, Oct. 1-3, Vol. 20, No. 3, pp. 206-214.

Grant, M.A., 1978. Two-phase linear geothermal pressure transients: a comparison with single-phase transients, *N.Z. J. Sci.*, 21, pp. 355-364.

Grant, M.A., 1979. Interpretation of downhole measurements at Baca, Proceedings of the Fifth Workshop on Geothermal Reservoir Engineering, Stanford University, Stanford, CA, SGP-TR-40, pp. 261-268.

Grant, M.A. and M.L. Sorey, 1979. The compressibility and hydraulic diffusivity of a water-steam flow, *Water Resources Research,* Vol. 15, No. 3, pp. 684-686.

Gudmundsson, J.S., Olsen, G., and S. Thorhallsson,1985. Svartsengi field production data and depletion analysis, Proceedings of the Tenth Workshop on Geothermal Reservoir Engineering, Stanford University, Stanford, CA, SGP-TR-84, pp. 45-52.

Lippmann, M.J. and Bodvarsson, G.S ., 1983. Numerical studies of the heat and mass transport in the Cerro Prieto geothermal field, *Waters Resources Research,* Vol. 19, No. 3, pp. 753-767, LBL-15509.

Moench, A.F. and P.G. Atkinson, 1977. Proceedings of the Third Workshop on Geothermal Reservoir Engineering, Stanford University, Stanford, CA, pp. 64-69.

Moench, A.F. and P.G. Atkinson, 1978. Transient pressure analysis in geothermal steam reservoirs with an immobile vaporising liquid phase, *Geothermics,* Vol. 7, pp. 253-264.

O'Sullivan, M.J., 1981. A similarity method for geothermal well test analysis, *Water Resources Research,* Vol. 17, No. 2, pp. 390-398.

Pruess, K., 1983. Development of the general purpose simulator MULKOM, Annual Report 1982, Earth Sciences Division, Lawrence Berkeley Laboratory, Berkeley, CA.

Sageev, A., 1985. Interference testing near a steam cap, Geothermal Resources Council Transactions, Vol. 9, Part II, pp. 569-572.

Sageev, A. and R.N. Horne, 1983a. Drawdown pressure transient analysis of a well near a steam cap, Geothermal Resources Council Transactions, Vol. 7, pp 473-476.

Sageev, A. and N.H. Horne, 1983b. Pressure transient analysis in a reservoir with a compressible or impermeable circular subregion: Gas cap or EOR-induced, SPE 12076, presented at the SPE Annual Fall Meeting, San Francisco, Ca.

Stefansson, V., 1981. The Krafla geothermal field, northeast Iceland, in *Geothermal Systems,* edited by L. Rybach and L.J.P. Muffler, pp. 273-294, John Wiley, New York.

Stefansson, V., and B. Steingrimsson, 1980. Production characteristics of wells tapping two-phase reservoirs at Krafla and Namafjalll, in Proceedings of the 6th Workshop on Geothermal Reservoir Engineering, Stanford Univ., Stanford, CA, SGP-TR-50, pp. 49-59.

Theis, Charles V., 1935. The relation between the lowering of the piezometric surface and the rate and duration of discharge of a well using ground-water storage, *Trans. Amer. Geophys. Union,* 2, pp. 519-524.

PROCEEDINGS, Eleventh Workshop on Geothermal Reservoir Engineering
Stanford University, Stanford, California, January 21-23, 1986
SGP-TR-93

THE SIGNIFICANCE OF EARLY TIME DATA IN INTERFERENCE TESTING FOR LINEAR BOUNDARY DETECTION

Abraham Sageev[1], *Jonathan D. Leaver*,[1,2] *and Henry J. Ramey, Jr.*[1]

[1] *Department of Petroleum Engineering, Stanford University*
[2] *Ministry of Works and Development, New Zealand*

ABSTRACT

This paper considers the significance of early time data for detecting linear boundaries using interference testing. When the ratio r_2/r_1 is greater than 5, existing methods of analysis may be used. For ratios of r_2/r_1 smaller than 5, special considerations are needed. When the ratio of r_2/r_1 is smaller than 2, there is no significant indication of the presence of a linear boundary in the pressure response. The effects of missing pressure data during the early time flow period, and earth tides on the linear boundary analysis are described and demonstrated with a flow test in the Ohaaki geothermal field in New Zealand.

INTRODUCTION

The detection of impermeable linear boundaries of reservoirs is of great importance in predicting the behavior of these reservoirs under exploitation. These linear boundaries may be detected and located by the analysis of their effect on nearby wells, both observation and source wells. *Stallman* [1952] presented log-log type curves for a constant rate line source producing near a linear boundary. *Stallman* extended the line source solution presented by *Theis* [1935], using the method of images to generate the linear boundaries. The pressure-time response can be matched to the *Stallman* [1952] curves, and the ratio r_2/r_1 may be estimated.

The estimation of the ratio r_2/r_1 using the log-log match is difficult. The curves are closely spaced and interpolating between the curves can lead to a great deal of uncertainty. *Davis and Hawkins* [1963], *Witherspoon et. al.* [1967], and *Earlougher* [1977] developed the semi-log double straight line analysis method. This method is based on the observation that the infinite acting early time data produce a semi-log straight line after a dimensionless time of ten, and the late time data cause the slope of this straight line to double. *Davis and Hawkins* [1963] and *Witherspoon et. al.* [1967] discussed the several limitations of the double straight line analysis method. If either of the semi-log straight lines has not developed, the method cannot be used. Interference responses typically display boundary effects prior to a dimensionless time of ten, hence, may not produce the first infinite acting semi-log straight line.

Sageev et. al. [1985] presented a dimensionless semi-log analysis method for detecting the distance between the image and the observation wells. In the case of analyzing pressure data from the source well, this method yields the distance between the source well and the linear boundary. *Sageev et. al.* [1985] presented a method that requires either the two straight line development or one of the straight lines and the transition between them. Their semi-log type curve is applicable for ratios of r_2/r_1 greater than 5. *Leaver et. al.* [1985] presented applications of this semi-log type curve matching method for the drawdown or injection flow periods for detecting a linear boundary in the Ohaaki geothermal field in New Zealand. *Leaver et. al.* [1985] also presented applications of two buildup analysis methods for detecting linear boundaries developed by *Fox* [1984] and *Eipper* [1985].

This paper concentrates on the detection of impermeable linear boundaries from interference tests with small values of the ratio r_2/r_1. First, the theoretical effects of a linear boundary are described in view of the log-log and semi-log pressure-time responses, and the semi-log pressure derivative responses. Then, the effects of missing pressure data during the early time flow period are described. Finally, the potential effects of earth tides and barometric pressure on the early time pressure response of an observation well are discussed. Pressure-time data from the Ohaaki geothermal field in New Zealand are used to demonstrate the effects of missing data and earth tides.

THEORY

The method of images of line sources is used to generate the effects of an impermeable linear boundary (*Carslaw and Jaeger* 1960, *Kruseman and De Ridder* 1970, and *Ramey et. al.* 1973). A schematic diagram of a semi-infinite system bounded by an impermeable linear boundary is presented in Figure 1. The dimensionless pressure solution for this system is:

$$P_D = -\frac{1}{2}\left[E_i(-X_1) + E_i(-X_2)\right] \tag{1}$$

where the dimensionless terms are defined as:

$$X_i = \frac{r_{Di}^2}{4t_D} \tag{2}$$

$$p_D = \frac{2\pi kh(p_i - p)}{q\mu} \tag{3}$$

$$t_D = \frac{kt}{\phi\mu c r_w^2} \tag{4}$$

$$r_D = \frac{r}{r_w} \tag{5}$$

The dimensionless pressure responses of semi-infinite systems bounded by an impermeable linear boundary are

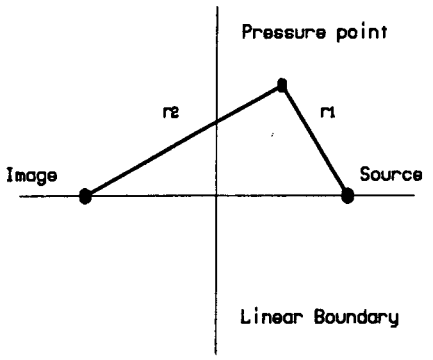

FIGURE 1: A schematic diagram of semi-infinite system.

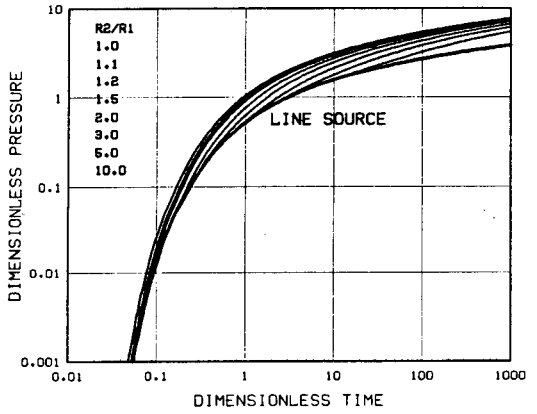

FIGURE 2: Log-log type curve for a semi-infinite system. (After *Stallman*, 1952).

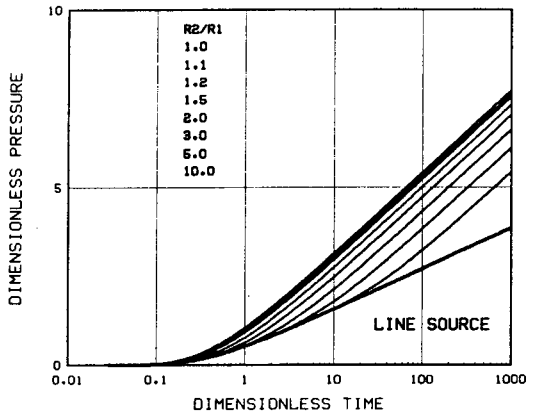

FIGURE 3: Semi-log type curve for a semi-infinite system.

presented in Figures 2 and 3. Figure 2 is similar to the log-log *Stallman* [1952] type curve. The ratio r_2/r_1 varies between 1 and 10. The lowermost curve in Figure 2 represents the *Theis* line source solution. The uppermost curve represents a semi-infinite system where the observation point is adjacent to the boundary, yielding an r_2/r_1 of unity. In view of Equation 1, this curve is a sum of two identical exponential integrals, and is shifted by a factor of 2 in the vertical direction form the line source curve. As the value of the ratio r_2/r_1 increases, the dimensionless pressure response departs from the line source solution at later times, as the effects of the impermeable boundary become significant at the observation point.

Figure 3 is a semi-log presentation of the same data as in Figure 2. *Sageev et. al.* [1985] showed how all the semi-log curves for r_2/r_1 ratios greater than 5 may be collapsed to a single curve. The curves having r_2/r_1 ratios smaller than 5 depart form the line source curve before the first semi-log straight line develops, and are not similar to each other in early times. Hence, these curves may not be collapsed to a single curve. The curves having r_2/r_1 ratios between 1 and 1.5 are closely spaced in both Figures 2 and 3, making log-log and semi-log type curve matching difficult.

The similarity of the curves for small values of the distance ratio is presented in Figure 4. In this figure, the line source curve is translated along the time and pressure axes by factors of 1.075 and 1.96 respectively, to match the curve for an r_2/r_1 of 1.1. The two curves match well. The square of the difference between these two curves is presented in the lower thin curve in Figure 4. The two minima in the error curve represent the fact that the two matched curves cross each other twice. The difference between the two curves is smaller than the resolution expected even from very sensitive pressure recording devices. Hence, transient pressure data from wells near an impermeable linear boundary with an r_2/r_1 ratio of 1.1 can be matched successfully to the line source solution. Based on the translation of the line source curve, this match would yield almost the correct storativity but a transmissivity which is a factor of 2 lower. No indication of the presence of an impermeable boundary would be present.

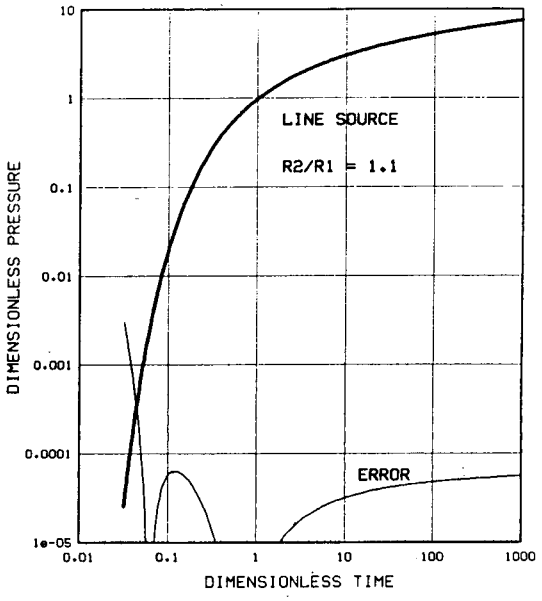

FIGURE 4: A log-log match of the line source curve to the curve for $r_2/r_1 = 1.1$.

A standard procedure in analyzing interference pressure data that match the line source solution is to evaluate the minimum reservoir area that is free of any boundaries. In the case of a linear boundary, this area is elliptical in shape, as described by *Vela* [1977]. This analysis with interference data coming from a configuration with a distance ratio less than 2 will over estimate the reservoir area free of boundaries. The magnitude of this over estimation depends on the duration of the test. For example, if a pressure response with a distance ratio of 1.1 matches the line source up to a dimensionless time of 20, the minimum distance ratio determined from this match would be 10. This match would locate the linear boundary at a distance ten times further than the actual boundary location.

The results from an interference test with a distance ratio smaller than 2 should be compared with results from other responses in observation wells or the source well. In the case of the source well, the distance ratio is large and the distance ratio and transmissivity may be estimated. The difference between the transmissivities of the source well and the observation well may indicate the correct match of the interference data.

Although the curves for r_2/r_1 ratios of 1.1 and 1.5 are very similar to the line source, the curve for an r_2/r_1 ratio of 2 is unique, and cannot be matched to the line source curve. Figure 5 presents the two curves without any translation. This yields an early time match to the infinite acting line source response, but after a dimensionless time of 1, the two curves are different. This can also be seen in the error curve. The error is small at early time, and increases rapidly with time. Figure 6 presents a late time match of the line source to the curve for an r_2/r_1 ratio of 2. Here, the early time line source behavior is not matched, as described by the error curve. The minimum in the error curve is caused by the two curve crossing one another. Hence, the line source curve cannot match simultaneously the early time and the late time responses of an observation well with a r_2/r_1 ratio of 2, and the detection of a linear boundary is possible.

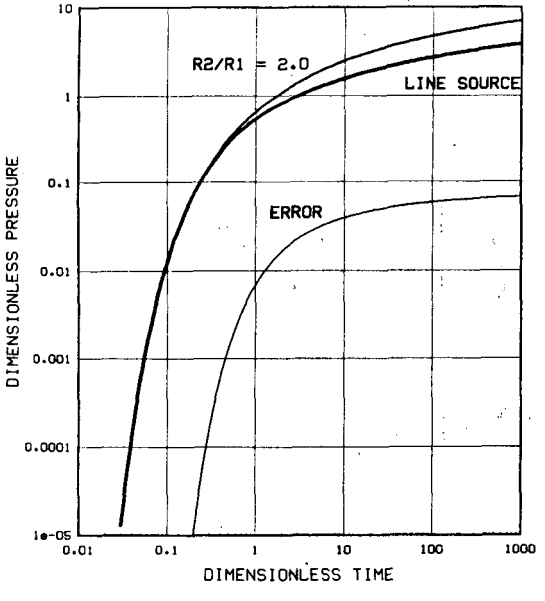

FIGURE 5: A log-log response of the line source and a semi-infinite system with $r_2/r_1 = 2.0$.

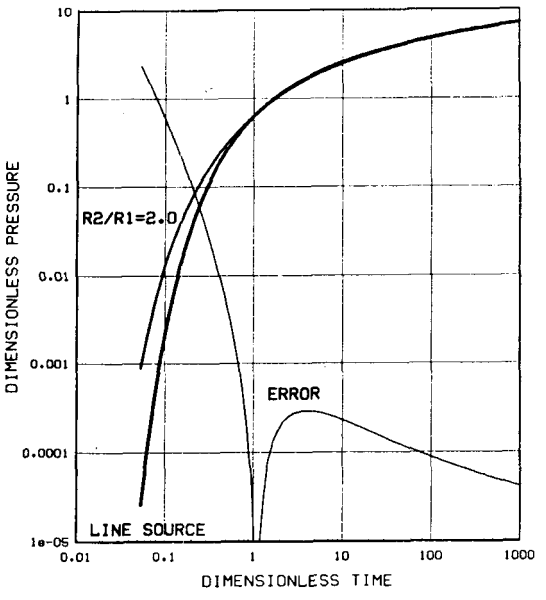

FIGURE 6: A log-log response match of the line source curve to the curve for $r_2/r_1 = 2.0$.

The log-log and the semi-log responses are summarized in Figure 7. The upper family of curves represents the log-log pressure responses, as presented in Figure 2. The lower family of curves, translated by a factor of 5 for display purposes, represents the semi-log pressure derivatives. From the pressure derivative curves, it is clear that for r_2/r_1 ratios greater than 5 the semi-log type curve matching technique is applicable because there is a distinct transition between the infinite and the semi-infinite behaviors. Pressure responses from cases with r_2/r_1 ratios between 2 and 5 can be analyzed using the type curves presented here, since these responses are significantly different from the line source. Also, pressure responses with r_2/r_1 ratios smaller than 2 can be matched to the line source curve, and may lead to erroneous estimations of some reservoir parameters.

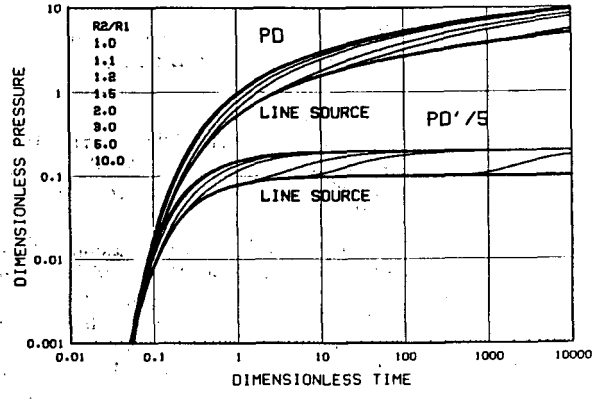

FIGURE 7: Log-log type curve for dimensionless pressures and semi-log dimensionless derivatives for a semi-infinite system.

MISSING DATA

The detection of linear boundaries from transient pressure tests is based upon the transition between the infinite acting and semi-infinite acting pressure responses. If this transition is not present little can be done to detect the linear boundary. Some tests may have the required time span for the detection of a linear boundary, but, for human or mechanical reasons, some of the pressure data are missing. Local sampling problems that arise from discretizing the time and pressure domains are not considered. Local sampling is assumed adequate. Concern is with a time period of missing pressure data that is significantly longer than the sampling intervals required for transient pressure analysis.

Figure 8 presents an example of missing pressure data form a drawdown buildup test in the Ohaaki geothermal field in New Zealand. Test C3 was started on May 1, 1984 and the drawdown portion of it lasted for 339 hours. The active well, BR20, produced at a constant rate of 84 *l/s*, and pressures were measured with a quartz crystal gauge at the observation well, BR34. The distance between the two wells was 1145 meters. The pressure scale in Figure 8 is normalized by the flowrate measured during the test. Pressures were not recorded from the 12th to the 54th hour of the test. The early time data of this test, prior to 10 hours, are affected by earth tides and barometric pressure changes, and will be discussed in the next section.

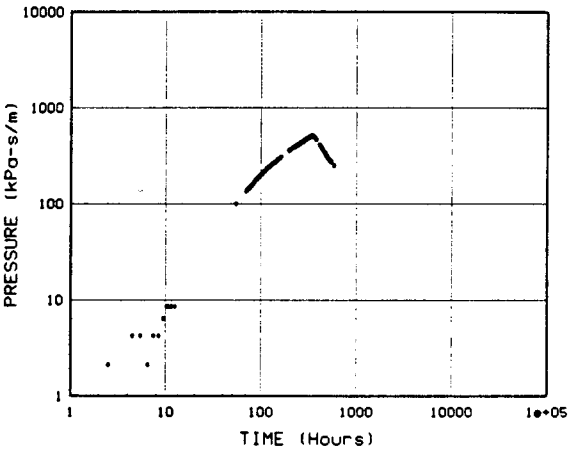

FIGURE 8: Pressure data from Test C3 in the Ohaaki geothermal field, New Zealand.

How does the fact that some of the pressure data are missing affect the analysis of the test? We will consider a hypothetical case and then present the attempts to analyze the test from Ohaaki.

Consider the interference pressure response from a semi-infinite reservoir with a distance ratio of 2. Figure 9 presents four cases of pressure responses, three of which have missing pressure data. Figure 9A is the complete response that spans the transition flow period, and can be successfully analyzed for the detection of the linear boundary. In Figure 9B, a log cycle of the data during the transition is missing. Yet, the early time infinite acting response and the late time semi-infinite response are well defined. The two portions of the pressure data cannot be

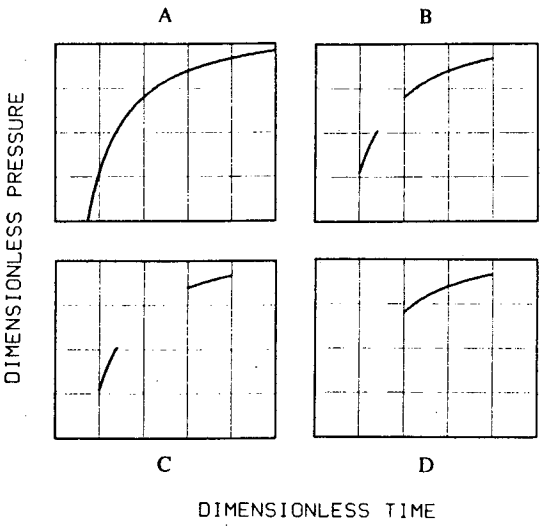

FIGURE 9: Hypothetical cases for missing pressure data, $r_2/r_1 = 2.0$.

matched to the line source simultaneously, and the data can still be successfully analyzed for detecting the linear boundary.

The pressure response presented if Figure 9C has a longer period of missing data than the response of Figure 9B. Yet, this pressure response can be successfully analyzed since the infinite and the semi-infinite responses are well defined. In the pressure response presented in Figure 9D, all the infinite acting pressure response is missing. The late time semi-infinite response can erroneously be matched to the line source curve, hence, yielding incorrect reservoir parameters, and providing no indication of the presence of a linear boundary.

The first ten hours of the test from Ohaaki are influenced by earth tides and barometric pressures, making the condition of data in this test similar to the response presented in Figure 9D. Various matches of the drawdown data of this test are presented in Figure 10. The distance ratio varies between 1.2 and infinity (for the line source).

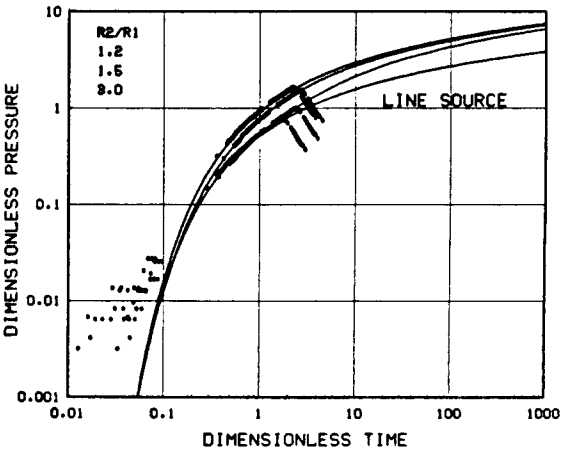

FIGURE 10: Four possible log-log matches of Test C3 data to the *Stallman* type curves.

The storativities derived from the log-log match vary by a factor of less than 2, but the transmissivities vary within an order of magnitude. Without information from other flow tests, the analysis of the pressure data is ambiguous. In this case, the pressure data are missing in the time period that is required to establish the infinite acting response of the reservoir, and the late time data represent the semi-infinite behavior. Hence, a unique analysis of this tests is not possible.

EARTH TIDES AND BAROMETRIC PRESSURE

Some pressure recording techniques require adjustments and corrections that account for pressure changes caused by earth tides and barometric pressure. The data from the test in the Ohaaki field were obtained by a quartz crystal gauge and corrections were applied. In this section, we describe the effects of the combined earth tides and barometric pressure and present an attempt to reconstruct the background atmospheric pressures. Then, some simulated interference responses are described along with some practical aspects of processing the early time data. A generalized analysis method for earth tides and barometric pressures is not presented.

Figure 11 presents a record of the barometric pressure at the Ohaaki field during the the time that the flow test was carried out. Daily oscillations are detectable on this large scale figure, and major trends of the barometric pressure over periods of days and weeks can be established. The first ten days of this record are presented in Figure 12. We concentrate on a five day period between 24 and 144 hours of this record. In this period, a linear overall decline of the barometric pressure is evident. In addition, the daily oscillations are distinct, and are a combination of two sine waves with different amplitudes.

The first sine wave has a daily cycle, and the second sine wave has two cycles per day. This second sine wave with the higher frequency is responsible for the small depressions at the top of each pressure cycle that occurs at noon time in each of the five days. Hence, there is one linear overall pressure decline that represents the regional barometric trend, and two oscillatory pressure functions, superimposed on the linear pressure trend, caused by the sun and the moon.

Figure 13 presents a simulated pressure response of these three pressure functions. The thick oscillating curve that displays similar characteristics to the Ohaaki barometric record, is the sum of the three other curves on the figure. The amplitude of the high frequency wave is 0.7 the amplitude of the low frequency wave. Also, there is a phase shift of 0.6π assigned to the high frequency wave.

Figure 14 presents a match of the simulated barometric pressure of Figure 13 to the five day record presented in Figure 12. The match is quite good. The intention is to demonstrate that knowing the barometric pressure during the flow test, and matching it to simulated responses may help in the future to filter out their effects from reservoir pressure data. Also, it may be possible after deconvolving the barometric pressure into its components, to evaluate reservoir properties such as storativity and transmissivity.

The effects of earth tides may be significant during the early time response of an observation well. On a dimensionless match to the line source, there are three parameters that determine the importance of earth tides: the amplitude, the phase with respect to the start of the test,

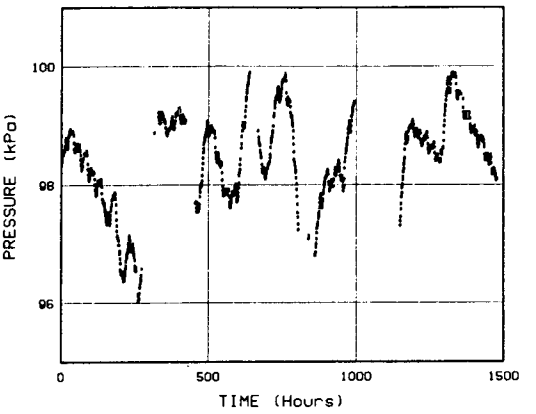

FIGURE 11: Barometric record during Test C3.

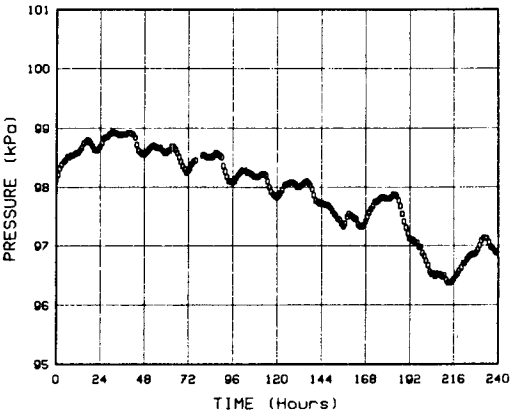

FIGURE 12: The first 240 hour of the barometric record presented in Figure 11.

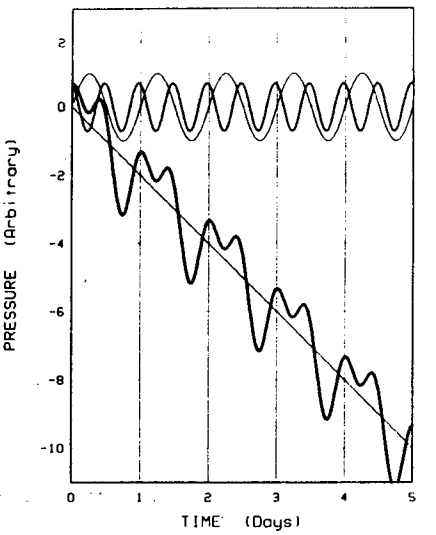

FIGURE 13: A superposition of two earth tide related sine wave functions and one linear barometric pressure function.

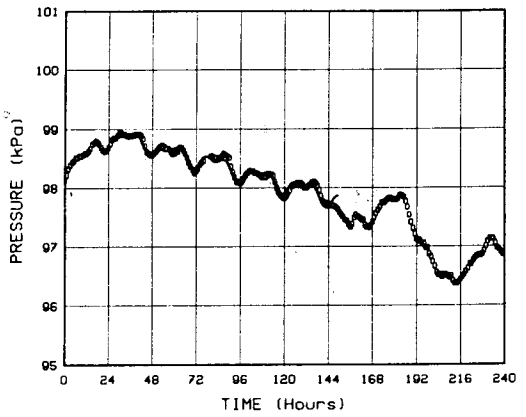

FIGURE 14: A match of five days of the barometric pressure record by a response composed of two sine waves and one linear pressure function.

and the frequency. Figure 15 presents three hypothetical earth tide effects superimposed on the line source curve. The curve denoted by **A** has a dimensionless pressure (p_D) amplitude of 0.05, a zero phase, and a dimensionless time (t_D) frequency of 0.2. The large amplitude causes the oscillations of the pressure to extend up to a dimensionless time of 1. The other two curves denoted with **B** and **C** have a dimensionless pressure amplitude of 0.01, and there are no oscillations present. Both these curves have a zero phase, but have different frequencies. Curve **B** has double the frequency of curves **A** and **C**. With combinations of different phases and frequencies it is possible to get oscillations at early time even with low amplitudes.

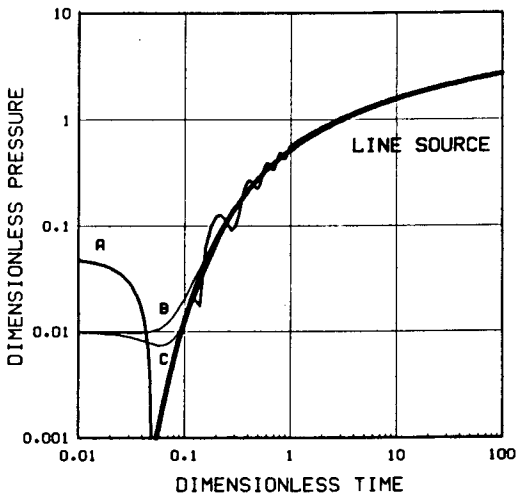

FIGURE 15: Superposition of the line source with a single sine wave.

The data from the Ohaaki test matched to the various curves in Figure 10 indicate a dimensionless pressure amplitude of 0.01, and a dimensionless time frequency of 0.2. This is one of the reasons for the deviation of the early time data prior to 10 hours, that cannot be matched to the line source. The linear barometric pressure decline was not considered since it had a smaller effect than the earth tide effects. Some processing methods may call for smoothing of pressure data or clipping of anomalies where the pressure declines unexpectedly. The magnitude of interference pressure changes in the early time flow period may be of the same order of magnitude as the earth tide and barometric pressure changes. Under such conditions, smoothing or clipping may lead to loss of information.

DISCUSSION

The main advantage of interference testing over source well testing for detecting reservoir limits is the increased characteristic length scale. When analyzing source well pressure data, the characteristic length scale is the diameter of the wellbore, that is typically on the order of a few inches. In interference testing, the characteristic length scale is the distance between the observation well and the source well, that is on the order of tens or hundreds of feet. Also, some near wellbore effects are not significant in interference testing, for example, wellbore skin in the source well in a constant rate test.

The main disadvantage of interference testing is the decreased amplitudes of the pressure changes. As the observation well is located further form the source well, the space resolution increases but the magnitude of the pressure changes decreases. These are competing effects that have to be addressed during the design stages of a test. When the early time pressure changes are small, the effects of earth tides and barometric pressure may be significant, and might lead to large uncertainties in the estimation of reservoir parameters.

In the case of interference testing for linear boundary detection, there is an added problem that is purely geometrical. As we have shown in the Theory section, for distance ratios smaller than 2, it is practically impossible to detect the presence of an impermeable linear boundary, regardless of the actual distance between the observation well and the source well.

CONCLUSIONS

1. Interference tests with a distance ratio greater than 5 may be analyzed for the detection of impermeable linear boundary using the current log-log and semi-log dimensionless type curve matching techniques.
2. Interference tests with a distance ratio between 2 and 5 may be analyzed for the detection of a linear boundary using type curves presented in this paper.
3. Interference tests with a distance ratio less than about 2 have a response similar to the line source, making linear boundary detection impossible.
4. Interference test data with distance ratios smaller than 2 matched to the line source yield an over estimation of the minimum distance between the observation well and the image well.
5. Analysis of interference pressure data for the detection of an impermeable linear boundary require two out of the three flow periods: the infinite acting response, the transition response between the infinite and the semi-infinite flow periods, and the semi-infinite response.
6. When missing pressure data leave only one distinct flow period, a unique analysis is not possible, as demonstrated by test C3 in the Ohaaki geothermal field.

7. Early time interference pressure changes may be of the same magnitude AS earth tide and barometric pressure changes. In such cases, significant deviations from the line source response are expected.
8. Clipping or smoothing of the early time pressure data may cause loss of information. Atmospheric pressures should be recorded, and if necessary, filtered out of the interference data.
9. Five days of the atmospheric pressure record from Ohaaki were matched with a combination of two earth tide related sine waves and a linear barometric function.

ACKNOWLEDGEMENTS

J. D. Leaver acknowledges the permission of the Commissioner of Works, Ministry of Works and Development, New Zealand to publish this paper. Test data collected by M.W.D., Wairakei, was filtered and supplied by Mark McGuinness, Applied Math. Division, DSIR, Wellington. Financial support was provided by M.W.D., New Zealand, N.Z.E., New Zealand, Stanford Geothermal Program, DOE Contract No. DE-AT02-80SF11459, and by Stanford University.

NOMENCLATURE

c_t	compressibility
h	formation thickness
k	permeability
p	pressure
p_D	dimensionless pressure, $2\pi kh(p_i-p)/q\mu$
q	flowrate
r	radius from source well
r_D	dimensionless radius, r/r_w
r_w	wellbore radius
r_1	distance between observation and source wells
r_2	distance between observation and image wells
t	time
t_D	dimensionless time, $kt/\phi\mu c_t r_w^2$
ϕ	porosity
μ	dynamic viscosity

REFERENCES

Carslaw, H. S. and Jaeger, J. C.: *Conduction of Heat in Solids*, 2nd ed. Oxford University Press, 1960.

Davis G. E. and Hawkins M. F.: "Linear Fluid-Barrier Detection by Well Pressure Measurements." *J. Pet. Tech.*, (Oct. 1963) 1077-1079.

Earlougher R. C.: *Advances in Well Test Analysis*. Society of Petroleum Engineers of the American Institute of Mining and Engineering, Dallas, Texas, Vol. 5, (1977) 123-126.

Eipper M. E.: Computer Generation of Type Curves. *M.S. thesis, Stanford Geothermal Programme Report SGP-TR-86*, Stanford University, (1985).

Fox G.: Linear Boundary Detection using Pressure Buildup Tests. *M.S. thesis, Stanford Geothermal Programme Report SGP-TR-83*, Stanford University, (1984).

Kruseman, G. P., and De Ridder, N. A.: "Analysis and Evaluation of Pumping Test Data," International Institute of Land Reclamation and Improvement, Wageningen, The Netherlands (1970).

Leaver, J. D., Sageev, A., and Ramey, H. J., Jr.: "Linear Boundary Detection In A Single Interference Test," Proceedings of the 7th New Zealand Geothermal Workshop, (Nov. 1985) 65-68.

Ramey, H. J., Jr., Kumar, A. and Gulati, M. S., "*Gas Well Test Analysis Under Water Drive Conditions*", American Gas Association, Arlington, VA, (1973).

Sageev A., Horne R. N., Ramey H. J., Jr.: "Detection of Linear Boundaries by Drawdown Tests: A Semilog Curve Matching Approach," *Water Resources Research. vol. 21, no.3*, 305-310.

Stallman, R. W.: "Nonequilibrium Type Curves Modified for Two-Well Systems", U.S. Geol. Surv., Groundwater Note 3, (1952).

Theis, C. V.: "The Relationship between the Lowering of Piezometric Surface and Rate and Duration of Discharge of Wells using Groundwater Storage," *Trans.*, AGU, **2** (519), (1935).

Vela, S.: "Effect of a Linear Boundary on Interference and Pulse tests - The Elliptical Inference Area," *J. Pet. Tech.*, Aug., (1977) 947-950.

Witherspoon P. A., Javandel I., Neuman S. P., and Freeze R. A.: *Interpretation of Aquifer Gas Storage Conditions from Water Pumping Tests*, Monograph on Project NS-38, American Gas Association, New York (1967), 93-128.

PROCEEDINGS, Eleventh Workshop on Geothermal Reservoir Engineering
Stanford University, Stanford, California, January 21-23, 1986
SGP-TR-93

INJECTIVITY AND PRODUCTIVITY ESTIMATION IN MULTIPLE FEED GEOTHERMAL WELLS

Jonathan D. Leaver

Department of Petroleum Engineering, Stanford University
Ministry of Works and Development, New Zealand

ABSTRACT

A method is presented which allows individual zone injectivity/productivity to be determined without downhole flow measurements. Mass balance in conjunction with the specific pressure change measured at selected points in the the well is related to the individual zone injectivity/productivity which can then be used to estimate productive capacity. A sample staged completion test programme is presented to obtain the maximum information from a completed well without discharge or use of the downhole flow meter.

INTRODUCTION

Wells drilled in liquid-dominated geothermal fields may have large mass flow rates, high temperatures, and large amounts of dissolved solids. Discharge testing of some geothermal wells involving the disposal or reinjection of up to 50,000 m^3 of geothermal brine may have to await the installation of a complex array of surface equipment before testing can proceed. Even a brief vertical discharge of the well may be precluded due to thermal, noise or chemical pollution. In the Mokai field, New Zealand, a vertical discharge of well Mk5, at a mass flow rate of 200 kg/s and enthalpy about 1290 kJ/kg produced noise levels of over 120dBA near the wellhead. In order to obtain some measure of the productive or injective well capacity it is useful to determine individual permeable zone injectivity/productivity from injection tests which are not normally subject to the same environmental constraints as production tests.

BACKGROUND

Analysis of wellbore temperature and pressure profiles has taken on new significance with the development of downhole flow meters. These devices are able to provide the information required to confirm or refute previously held theories on the significance of specific profiles. Ironically this enabled the development of methods to determine permeable zone flow characteristics without using the flow meter.

Development of wellbore profile interpretation has proceeded rapidly since 1979. *Grant* (1979) showed how various pressure and temperature profiles could be produced in the wellbore depending on the phases present and flow occurring in the wellbore. *Stefansson and Steingrimsson* (1981) covered the application of various tools in geothermal well logging and interpretation techniques. *Dench* (1980) used measurements from the Olkaria geothermal field to show that pressures in the wellbore equalled the formation pressure only under specific constraints. *Horne* and *Castanada* (1981) used various temperature and pressure profiles to determine the existence of flows in the wellbore and locate selected permeable zones. *Bixley* and *Grant* (1981) presented a method to use pressure and temperature profiles to calculate individual permeable zone injectivity/productivity for a well with two dominant zones of permeability. The use of enthalpy balances and downhole chemistry in similar analyses is also discussed. *Grant et al.* (1982) presented data from a number of New Zealand geothermal fields showing linearity of formation pressure profiles in those that were liquid-dominated. *Grant et al.* (1983) discuss the identification of internal flows in the wellbore and the effect of these on pressure transients. *Gudmundsson* (1984) used a well with a single feed zone to demonstrate the use of the pressure pivot along with a wellbore simulator to predict the output curve.

The current study evolved from the need to determine individual permeable zone characteristics in Mokai well, Mk6, which contains six main permeable zones (*Leaver*, 1984). Staged completion testing had been undertaken in order to test temperature buildup techniques. During final completion testing the downhole flowmeter became inoperable necessitating the use of alternative techniques to calculate the required flow parameters.

CONCEPTUAL DEVELOPMENT

Instantaneous flow in a well is principally controlled by the location of permeable zones and the difference between the formation pressure profile and the flowing pressure profile. The difference between the two profiles determines both the magnitude and direction of the flow. Inherent assumptions are that the transmissivity (kh) and the viscosity (μ) are constant and that skin damage if present is the same at all permeable zones.

For *Darcy* flow in the formation:

$$q = -\frac{2\pi rkh}{\mu}\frac{\partial p}{\partial r} \tag{1}$$

For steady state horizontal flow, integrating Equation 1 between reference points 0 and 1 and assuming zero skin gives:

$$q = \frac{2\pi kh(p_1-p_0)}{\mu\, ln(r_1/r_0)} \tag{2}$$

or

$$q \propto K(p_1-p_0) \tag{3}$$

where

$$K = \frac{2\pi kh}{\mu\, ln(r_1/r_0)} \tag{4}$$

K may represent either the injectivity or productivity index depending on the direction of flow.

Figure 1 shows a schematic layout of typical pressure profiles during injection.

The *pivot point* is defined as the point at which the well pressure equals the formation pressure. From *Darcy's* Law for a single permeable zone of high transmissivity (kh) and low absolute flow rate (q), the pivot point will be located at the permeable zone as the difference between the well and formation pressures is small. For more than one feed zone the depth of the pivot point in the well will be determined by the permeability of each zone and the characteristics of the well and formation pressure profiles.

In Zone A of Figure 1 permeable zones above the pivot point will produce brine into the well during surface injection. Conversely injected fluid will flow into the formation in those permeable zones below the pivot point.

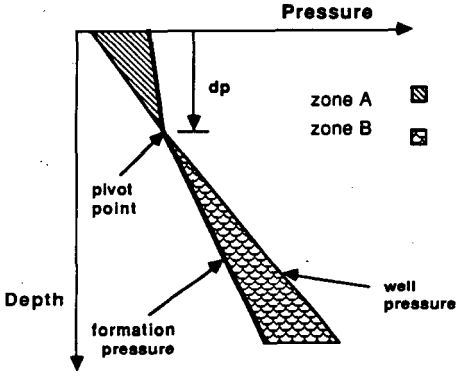

FIGURE 1: Schematic of typical pressure profiles.

MATHEMATICAL DEVELOPMENT

Principal assumptions used are:

(i) Radial *Darcy* flow in a homogeneous isotropic medium.

(ii) Incompressible fluid and formation.

(iii) Negligible thermal interaction effects such as condensation of vapour and contraction of the formation during injection.

Three cases are considered in the development of a general formula:

Case I---Single Permeable Zone

Consider a well with a permeable zone at location 1 in Figure 2. If the pressure gauge is located at the same depth as the permeable zone the injectivity is determined from the relation:

$$I_1 = \frac{\Delta q_s}{\Delta p_{w1}} \tag{5}$$

where

$$\Delta p_{w1} = p_{w1} - p_{f1} \tag{6}$$

If the pressure change is measured at some arbitrary depth, d_g, then a different overall injectivity will be measured.

$$I_0 = \frac{\Delta q_s}{\Delta p_{wg}} \tag{7}$$

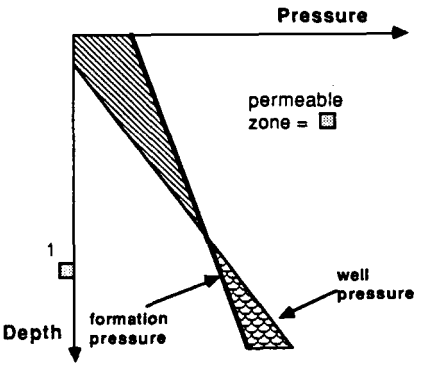

FIGURE 2: Single permeable zone in a geothermal well.

Substituting for Δq_s from Equation 5 gives:

$$I_1 = I_0 \frac{\Delta p_{wg}}{\Delta p_{w1}} \tag{8}$$

Case II---Double Permeable Zone Well

Consider a well with permeable zones at locations 1 and 2 in Figure 3. For this case the individual zone permeabilities cannot be directly calculated as the pressure profile in the well is determined by the equilibrium between the two permeable zones.

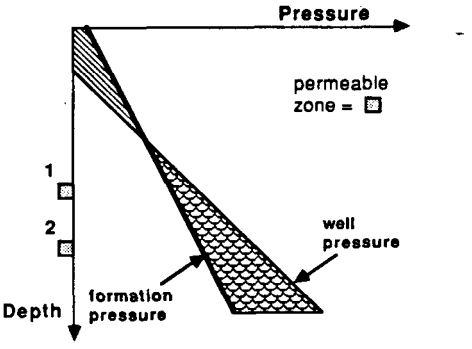

FIGURE 3: Double permeable zone configuration in a geothermal well.

The overall injectivity can be measured as for case I.

$$I_0 = \frac{\Delta q_s}{\Delta p_{wg}} \tag{9}$$

The individual zone injectivities are:

$$I_1 = \frac{\Delta q_1}{\Delta p_{w1}} \quad \text{and} \quad I_2 = \frac{\Delta q_2}{\Delta p_{w2}} \tag{10}$$

From conservation of mass

$$\Delta w_s = \Delta w_1 + \Delta w_2 \tag{11}$$

or

$$\frac{\Delta q_s}{v_s} = \frac{\Delta q_1}{v_1} + \frac{\Delta q_2}{v_2} \tag{12}$$

Eliminating flow terms using Equations 9, 10 in 12 gives:

$$\frac{I_0\,\Delta p_{wg}}{v_s} = \frac{I_1\,\Delta p_{w1}}{v_1} + \frac{I_2\,\Delta p_{w2}}{v_2} \tag{13}$$

Rearranging:

$$I_0 = \frac{\dfrac{I_1\,\Delta p_{w1}}{v_1} + \dfrac{I_2\,\Delta p_{w2}}{v_2}}{\dfrac{\Delta p_{wg}}{v_s}} \tag{14}$$

Since this equation has two unknowns I_1 and I_2 a second equation is required which is obtained by measuring the well pressure for a second step in flow rate. This equation will be identical in form to Equation 14.

Case III---General Case

Consider the case of a well with $n + m$ permeable zones with productivities, J_i , and injectivities, I_j , where there are n permeable zones above the *pivot point* and m permeable zones below the *pivot point* (Figure 4). Using induction from the previous two cases gives:

$$I_0 = \frac{\sum_{j=1}^{m} \dfrac{I_j \Delta p_{wj}}{v_j} - \sum_{i=1}^{n} \dfrac{J_i \Delta p_{wi}}{v_i}}{\dfrac{\Delta p_{wg}}{v_s}} \tag{15}$$

$n + m$ flow rate steps are required to uniquely determine the individual zone productivities (J_i) and injectivities (I_j). Furthermore pressure differences (Δp_w) must be calculated opposite each permeable zone in order to solve Equation 15.

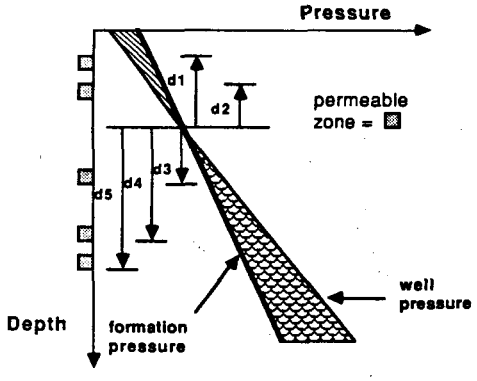

FIGURE 4: Multiple permeable zone configuration in a geothermal well.

In liquid dominated geothermal fields the number of pressure measurements required can be reduced by using the characteristic of these systems that the formation pressure profiles are linear with depth (*Grant et al.*, 1982). During water injection the well pressures below the water surface are also near linear with depth. This necessarily assumes:

(i) Flows from the formation into the well during injection do not significantly affect the overall density of the fluid column in the well.

(ii) Frictional flow effects in the wellbore are small.

(iii) Heat transfer from the formation to the wellbore fluid is small.

Once linearity of the pressure profiles has been established the geometry of the profiles can be used to modify Equation 15 so that only the permeable zone depths need be known along with two pressure measurements in order to establish the pressure change at each permeable zone.

By similar triangles from Figure 2:

$$\left[\frac{\Delta p_{wi}}{|d_p - d_i|}\right]_{i=1,n} = \left[\frac{\Delta p_{wj}}{|d_p - d_j|}\right]_{j=1,m} = \frac{\Delta p_{wg}}{|d_p - d_g|} \tag{16}$$

substituting from Equation 16 in 15 for Δp_{wi}, Δp_{wj} gives:

$$I_0 = \frac{\sum_{j=1}^{m} \dfrac{I_j\,|d_p - d_j|}{v_j} - \sum_{i=1}^{n} \dfrac{J_i\,|d_p - d_i|}{v_i}}{\dfrac{|d_p - d_g|}{v_s}} \tag{17}$$

DISCUSSION

Equations 16 and 17 require $n + m$ step changes in flow rate for each permeable zone injectivity/productivity to be uniquely determined. The number of flow rate step changes required is reduced by one for each permeable zone whose injectivity/productivity can be determined independently. If the upper permeable zones are producing brine into the well during injection, enthalpy balance techniques in conjunction with the temperature and pressure profiles can be used to independently determine the injectivity/productivity of these zones.

The use of pressure profiles to determine permeable zone injectivity/productivity requires a knowledge of the depth of the permeable zones, the specific volume of the formation fluid at each permeable level, and the stabilised pressure profiles at the required number of injection flow rates. The accurate location of feed zones and the effect of injected fluid on individual permeable zone characteristics are the principal limitations in application of the technique. An important feature is that no downhole flow measurements in the wellbore are required.

APPLICATION

Staged completion testing of a well enables the characteristics of some permeable zones to be determined during the drilling operation. Staged testing may cause delays during drilling of the well but this can be offset by the additional information obtained and by eliminating the need for extended testing on completion of the well at target depth.

The extent and type of testing undertaken will reflect the amount of information required from any single well. A flow chart is presented in Figure 5 to show how the following information could be obtained:

(i) Transmissivity, skin and under certain conditions productivity of the uppermost permeable zone.

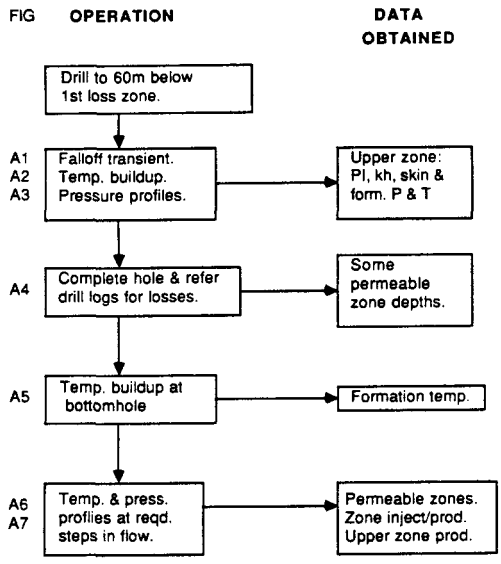

FIGURE 5: Flow chart for staged completion well testing

(ii) Formation pressures and temperatures.

(iii) Individual permeable zone injectivities.

A more detailed explanation of the techniques used to determine individual permeable zone flow characteristics from staged completion tests is given in Appendix A.

CONCLUSIONS

(1) Individual zone injectivity/productivity can be determined without the use of downhole flow measurements.

(2) Fewer pressure profile measurements are required where the formation and well pressure profiles are known to be linear with depth.

(3) Staged completion testing should be considered if in addition to the injectivity of each permeable zone, information on productivity, transmissivity and skin factor are required.

ACKNOWLEDGEMENTS

Comments on the draft of this paper made by Dr. Jon Gudmundsson and Dr. Abraham Sageev of Stanford University were much appreciated. The author acknowledges the permission of the Commissioner of Works, Ministry of Works and Development, New Zealand to publish this paper. Financial support was provided by M.W.D., New Zealand, N.Z.E., New Zealand, Stanford Geothermal Program, DOE Contract No. DE-AT02-80SF11459, and Stanford University.

NOTATION

d_g	depth of gauge below surface
d_p	depth of pivot point below surface
h	formation thickness
I	injectivity
I_0	overall injectivity calculated at d_g
J	productivity
J_0	overall productivity calculated at d_g
k	permeability
K	proportionality constant in *Darcy's* Law
m	number of permeable zones below the pivot point
n	number of permeable zones above the pivot point
p	pressure
p_f	formation pressure
p_w	well pressure
p_{wg}	well pressure measured at gauge depth
q	volumetric flow rate
q_s	surface volumetric flow rate
r	distance between source well and pressure point
t	time
w_s	surface mass flow rate
v	specific volume
v_s	surface specific volume
μ	dynamic viscosity

REFERENCES

Bixley P. F. and Grant, M. A.: "Evaluation of Pressure-Temperature Profiles in Wells with Multiple Feed Points," *Proc., 3rd N.Z. Geothermal Workshop* (1981), 121-124.

Dench N.: "Interpretation of Fluid Measurements in Geothermal Wells," *Proc., 2nd N.Z. Geothermal Workshop* (1980), 55-59.

Grant M. A.: "Interpretation of Downhole Measurements in Geothermal Wells," *Applied Mathematics Division, D.S.I.R.*, Wellington, New Zealand. Report AMD-88, (1979).

Grant M. A., Bixley P. F., Donaldson I. G.: "Internal Flows in Geothermal Wells: Their Identification and Effect on the Wellbore Temperature and Pressure Profiles," *Soc. Pet. Eng.*, Annual Conference, (Oct. 1981), paper SPE-10317.

Grant M. A., Donaldson I. G., Bixley P. F.: *Geothermal Reservoir Engineering*, Academic Press Inc., New York, (1982).

Gudmundsson J. S.: "Discharge Analysis for Two-Phase Geothermal Wells," *Trans., Geothermal Resources Council*, Vol. 8 (Aug. 1984), 295-299.

Horne R. H. and Castanada M.: "Location of Production Zones with Pressure Gradient Logging," *Proc., 3rd N.Z. Geothermal Workshop* (1981), 115-119.

Leaver J. D.: "Well Mk6: Report on Completion Test, Heating and First Discharge," *Ministry of Works and Development*, Wairakei, file 34/6 (April 1984).

Roux B., Sanyal S. K., Brown S.: "An Improved Approach to Estimating True Reservoir Temperature from Transient Temperature Data," *Proc., 5th Stanford Geothermal Workshop* (1979), 373-384.

Stefansson V. and Steingrimsson B.: "Geothermal Logging," *Orkustofnun*, Report OS-80-017/JHD-09, Reykjavik, (1980).

APPENDIX A

TYPICAL DATA FOR UPPER ZONE TESTING

A pressure falloff transient performed in conjunction with shutting the well in for temperature buildup measurements can provide an estimate of the formation pressure, skin, and transmissivity. The transient data may need to be

constructed from a number of pressure profiles performed during buildup. Frequent linearity of pressure profiles during injection and warmup facilitate interpolating data to the permeable zone depth which may not be accurately known initially (Figure A1).

The method of *Roux et al.*(1979) can be used to obtain an estimate of the formation temperature (Figure A2).

For a single permeable zone pressure profiles measured at the start and end of the temperature buildup test may show a pivot which locates the permeable zone depth and provides an estimate of the formation pressure. Sudden inversions in the temperature profile due to cold drilling fluid in the formation can also indicate the permeable zone location. Depths over which the profile is constant may indicate internal flow in the wellbore (Figure A3).

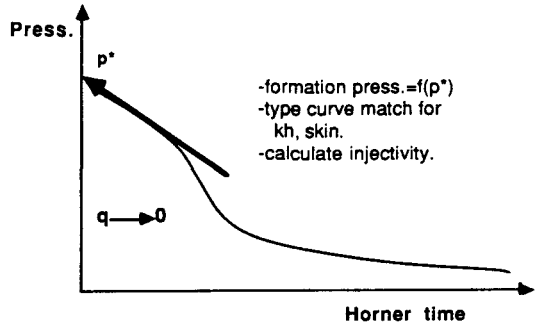

FIGURE A1: Pressure falloff transient.

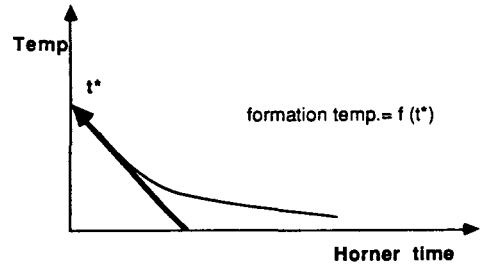

FIGURE A2: Temperature Buildup.

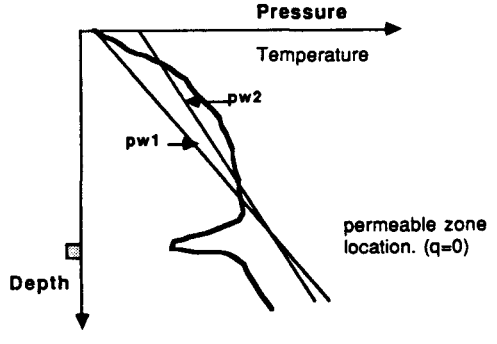

FIGURE A3: Pressure and temperature profiles during warmup.

TYPICAL DATA FOR COMPLETED WELL TESTING

Drilling logs can be used to determine permeable zone depths at which circulation losses occur (Figure A4).

A temperature buildup to determine bottomhole formation temperature is best performed immediately on well completion to reduce the time required to achieve acceptable results. Temperatures between the upper zone and bottomhole formation temperatures can be interpolated from a BPD or other applicable profile (Figure A5).

Injection into the well may cause upper zones to produce brine. By varying the flow rate, enthalpy balance techniques can be used to determine productivity at locations where temperature increases show the inflow of hot brine from permeable zones. Only the lowest of the permeable zones accepting injected fluid will be detectable using the bottomhole increase in temperature which reflects static bottomhole conditions below this lowest permeable zone (Figure A6).

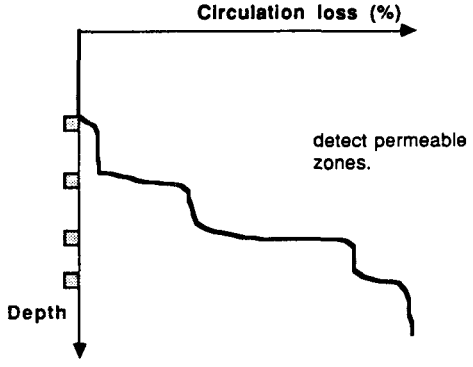

FIGURE A4: Permeable zone detection from circulation losses.

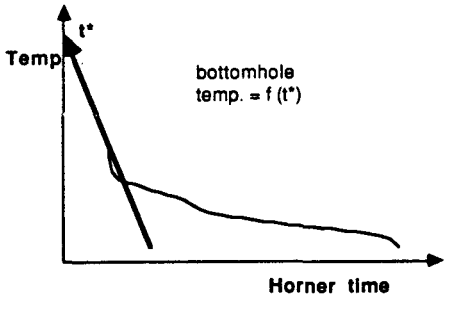

FIGURE A5: Bottomhole temperature buildup.

Individual zone injectivities can be determined by using step changes in the injected flow rate to produce the required number of different well pressure profiles (Figure A7).

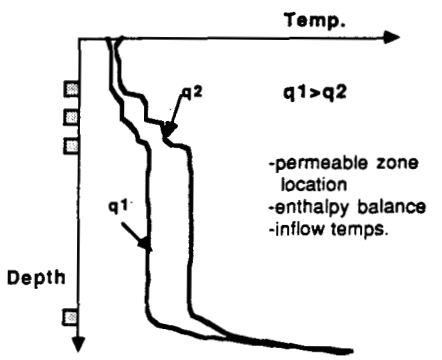

FIGURE A6: Temperature profile variation with flow rate.

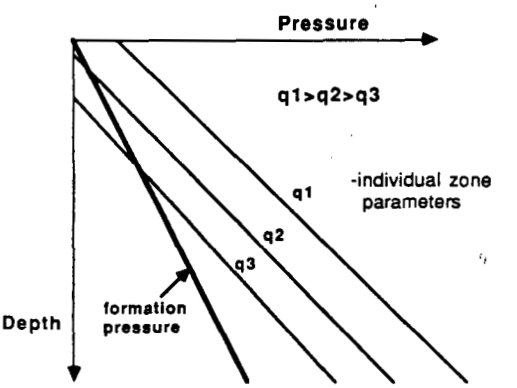

FIGURE A7: Pressure profile variation with flow rate.

PROCEEDINGS, Eleventh Workshop on Geothermal Reservoir Engineering
Stanford University, Stanford, California, January 21-23, 1986
SGP-TR-93

CUSTOMIZED WELL TEST METHODS FOR A NON-CUSTOMARY GEOTHERMAL WELL

Myron Burr

Unocal Geothermal Division

ABSTRACT

Recent testing of Thermal 4, The Geysers blowout well, has shown that the flow has two different components: a low enthalpy, mineral-laden flow from a well drilled within the existing wellhead and a high flowrate, high enthalpy annular flow. The commingled flows were mechanically separated and individually tested. The results of the test show that the flows are from two very different sources that are in weak hydraulic communication. Work is in progress to apply this information to bring Thermal 4 within compliance of the 1986 air quality regulations.

BACKGROUND

Original Blowout, P&A Attempts, and Redrill

Thermal 4 was drilled and blew out in 1957 during the initial commercial development of The Geysers, California, by the Magma-Thermal Power Project (Raasch 1985). Records of the blowout and of the attempts to control it were sketchy until the history was recently pieced together by Vantine (1984). Unknown at the time, the well was drilled into the Thermal Landslide, shown in Figure 1. The 11-3/4" casing was set at 132 ft, at or very near the base of the landslide. Drilling continued open-hole to 503 ft when steam was discovered discharging downslope from the rig. From this vent a large crater developed from which enormous quantities of rock debris were blown out by the steam. Boulders and large amounts of water were admitted to the crater to kill and plug it; but this proved unsuccessful. The blowout remained in this venting condition until 1959 when Magma-Thermal drilled Thermal 11 in an attempt to kill Thermal 4.

Thermal 11 was directionally drilled beneath the estimated bottomhole location of Thermal 4 as depicted in Figure 2. An estimated 2.5 to 4.5 million gallons of water were pumped into Thermal 11 which watered out the steam source. However, the water supply was depleted before cement could be pumped into the Thermal 4 wellbore. The water which had been pumped into the hole flashed to steam

FIGURE 1

SURFACE GEOLOGIC SETTING OF THERMAL 4 AND UNIT 2 WELLS

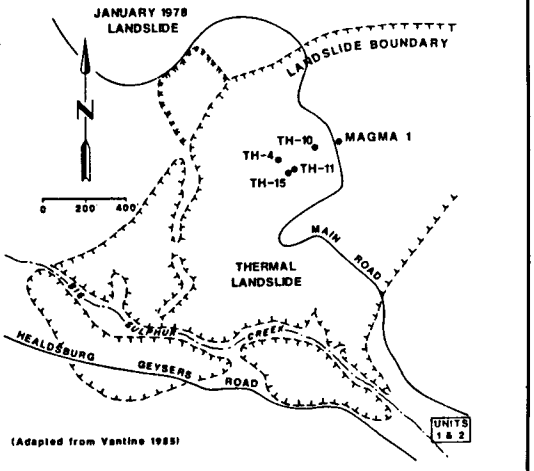

and caused a phreatic eruption in which large quantities of water, mud and rock were ejected from the blowout crater. Other phreatic eruptions followed during the next few days when additional water was pumped into the hole. The void created by these eruptions and those in 1957 caused the ground surface around the Thermal 4 wellhead to collapse shortly thereafter. The collapse crater grew to a maximum of 120 ft and was at least 60 ft deep. Additionally, it severed the Thermal 4 casing at 80 ft. A 65 ft length of 22" casing was positioned over the point of greatest steam flow in the bottom of the collapse crater as a control vent and the crater was backfilled.

In 1962, grout holes were drilled into the fill to stabilize the area. This precaution was followed by the redrill of Thermal 4 through the 22" casing. The 6-5/8" casing was set in bedrock at 358 ft and the well was drilled to 436 ft. An attempt to hydraulically and explosively fracture the formation through to the original Thermal 4 wellbore proved unsuccessful in establishing effective communication with the blowout. Further abandonment attempts were

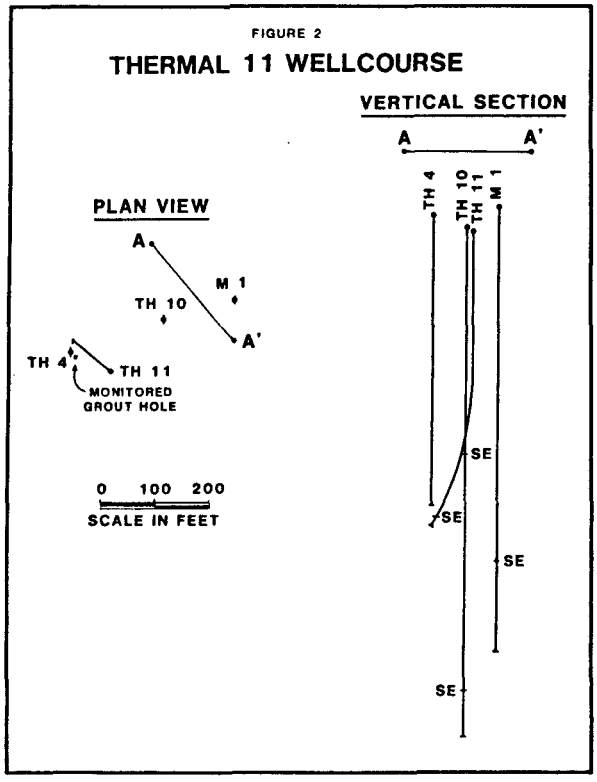

discontinued. Later additional fill was placed on the collapse crater area, the wellhead was raised to its present elevation by welding a short length of 24" casing on top of the 22" casing, and several more grout holes were drilled.

A landslide in January, 1978, adjacent to the Thermal Landslide caused changes in perched groundwater levels as evidenced by wellhead pressure increases and scale deposits at Thermal 4. The scale was found to be 93 percent water soluble NaCl and Na_2SO_4, indicative of a groundwater source.

Recent Efforts

More recently, efforts have been made to understand the characteristics of Thermal 4 in order to formulate plans to again attempt to control the well and its H_2S emissions. Vantine (1985) has described the Thermal Landslide as a large permeable deposit of locally hydrothermally altered serpentinite debris with a maximum thickness of about 150 ft near Thermal 4. The landslide debris overlies Franciscan formation bedrock which is composed mainly of graywacke in the Thermal area. Studies conducted after the January 1978 Landslide show the Thermal Landslide to be water bearing and the perched water levels within the landslide to be highly sensitive to seasonal and heavy rainfall.

In conjunction with Vantine, Mogen, et al (1985) and Mogen and Maney (1985) reported the findings of an extensive testing program for the Thermal Shallow Reservoir. They found that the Thermal 4 flowrate was dependent on production from the Unit 2 wells - Thermal 10, 11, 15 and Magma 1. They also found that variations in the producing enthalpy of Thermal 4 were apparently attributable to groundwater level fluctuations.

In October, 1984, this author removed the Thermal 4 wellhead to more closely examine the flow conduit. This examination revealed flows from the 6-5/8" x 24" annulus and the 6-5/8" casing. By February 1985 the two flows had been separated as shown in Figure 3 and a test program was begun. This paper discusses the results of that 1985 test program.

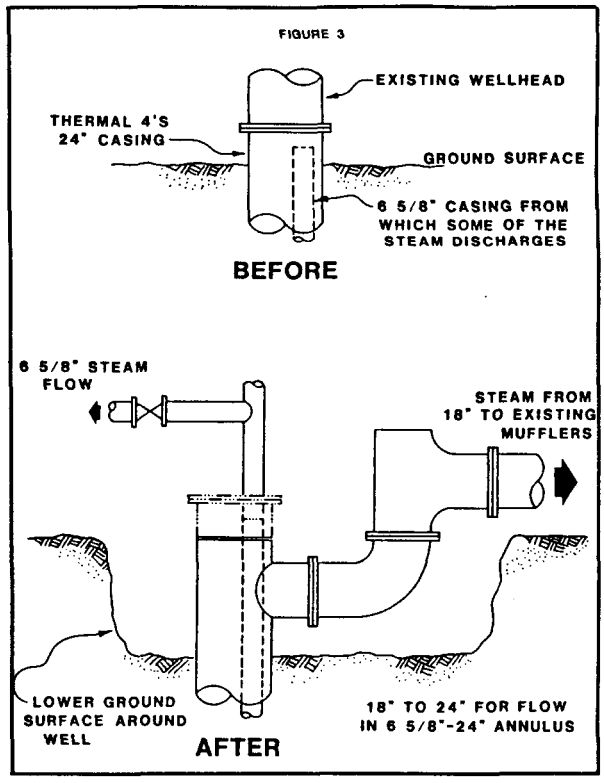

1985 THERMAL 4 TESTING RESULTS

Initial testing of both the 6-5/8" casing and 6-5/8" x 24" annular flowstreams revealed them to be distinctly different in flowrate, enthalpy and chemical composition. Table 1 summarizes these results. The 6-5/8" casing contributed only three percent of the total flowrate. However, it is believed to be the sole contributor to the enthalpy cycling (plus and minus as much as 25 Btu/lb every 2.5 to 8 hours) previously observed in Thermal 4 (Mogen et al (1985)). It is also believed to be the source of scaling minerals deposited in the Thermal 4 wellhead. The chemical compositions and enthalpy differences suggest that the fluid sources are primarily groundwater for the 6-5/8" casing flow and the Thermal Shallow Reservoir

TABLE 1

INITIAL 1985 THERMAL 4 TEST RESULTS

	6-5/8" FLOW	ANNULAR FLOW
Rate (1000 lb/hr)	3.3	95
Quality (%)	55	100
Enthalpy Cycling	YES	NO
Noncondensible Gas Concentration (ppm wt)	2040	2350
H_2S Concentration (ppm wt)	132	171
Isotopes (Probable Source)	Ground-water	Deep Reservoir
Condensate Chemistry	Ground-water Elements	Deep Reservoir Elements
Scale Chemistry	Ground-water Minerals	No Scale Observed

for the annular flow. Pressure, flowrate and wellbore survey data were analyzed to confirm this hypothesis.

Flowrate Characteristics of Thermal 4

The most obvious mechanism controlling the annular flowrate is production from the Thermal Shallow Reservoir to Pacific Gas and Electric Company's Unit 2 power plant. The Thermal 4 annular flowrate exhibits its greatest changes when the Unit 2 wells are shut in or during early-time production, as shown in Figure 4. During one shutin of the Unit 2 wells in April, 1985, the annular flowrate increased almost 8,000 lb/hr in one 24 hour period.

Figure 4 also indicates another mechanism which might be utilized to control the Thermal 4 annular flowrate. One day after the 6-5/8" casing shutin on February 20, 1985, the annular flowrate began to decline at approximately 1000 lb/hr per day over the next 32 days. At the same time, the annular flow enthalpy dropped from 1189 Btu/lb to 1161 Btu/lb amounting to a 50 F^{o} temperature drop. This precipitous flowrate decline is unprecedented in any previous observations of Thermal 4. Correlations with rainfall and groundwater levels have been

FIGURE 4

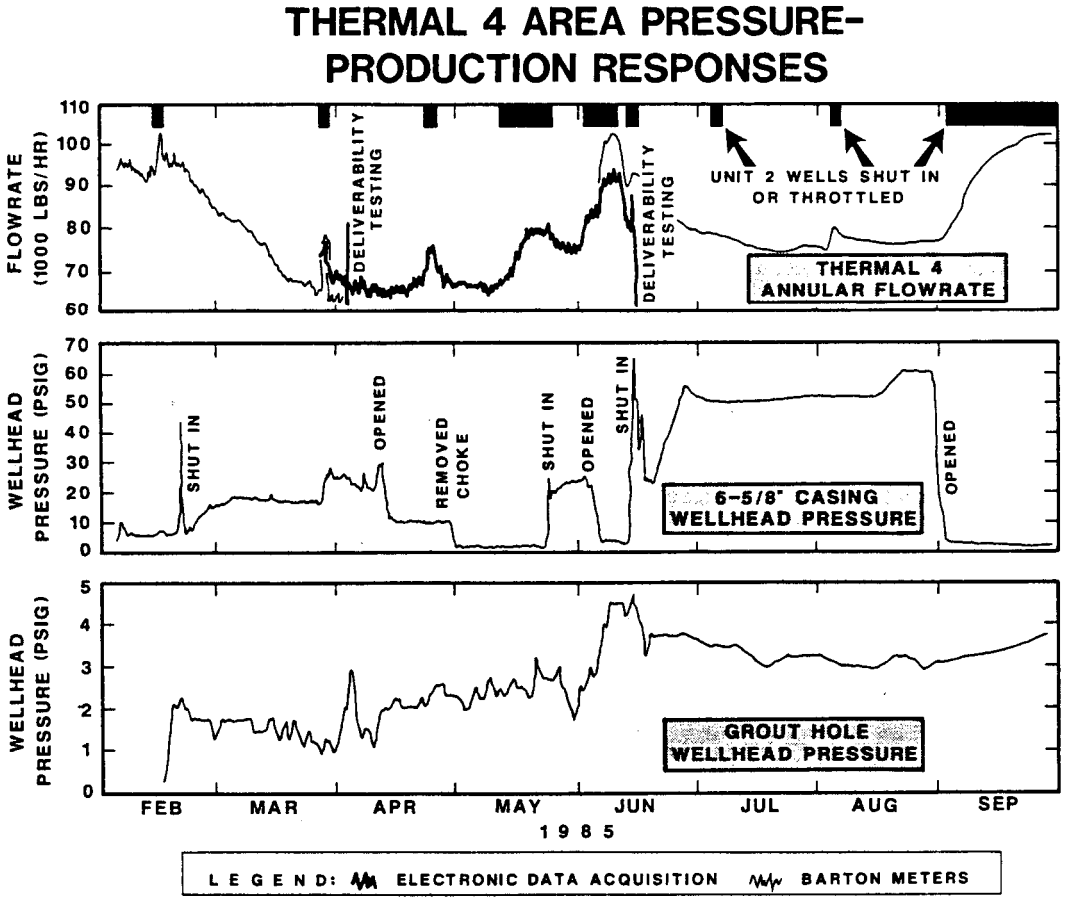

observed in the past but none has had such a dramatic effect. The maximum decline rates associated with seasonal rainfall have been about 500 lb/hr per day. Hence, shutting in the low enthalpy 6-5/8" flow appears to quench the high enthalpy annular flow. However, the mechanism by which this occurs is not fully understood.

Pressure Characteristics of Thermal 4

Pressures within the landslide were obtained by monitoring the wellhead pressure of a flowing grout hole located 27 ft from the Thermal 4 surface location and completed to 150± ft (Figure 2). While these pressure measurements are approximate, there is a good correlation between them and the annular flowrate and the 6-5/8" casing status. The landslide debris appears to be in limited communication with the 6-5/8" and annular flows.

Communication of the annular flow with the landslide debris was further demonstrated when the annular flow was throttled back, in the conventional flow-after-flow manner, to develop its deliverability curve. Figure 5 displays the data obtained and the curves drawn for the two initial flows of 67,500 and 85,000 lbs/hr. The shutin point of the first deliverability curve is an actual shutin. However, for safety reasons, the annular flow was shut in for only ten minutes. During this first test, following the long period of unprecedented decline mentioned above and with the 6 5/8" casing closed, ground vent activity picked up significantly. Ground vent activity was even greater during the second deliverability test, during which the maximum prudently attainable wellhead pressure was 14.5 psig. This second test was conducted after a long shutin period for wells supplying Unit 2 and with the 6 5/8" casing open. Thus, communication between the annular flow and the landslide debris was demonstrated but not quantified. The

FIGURE 5

THERMAL 4 ANNULUS DELIVERABILITY

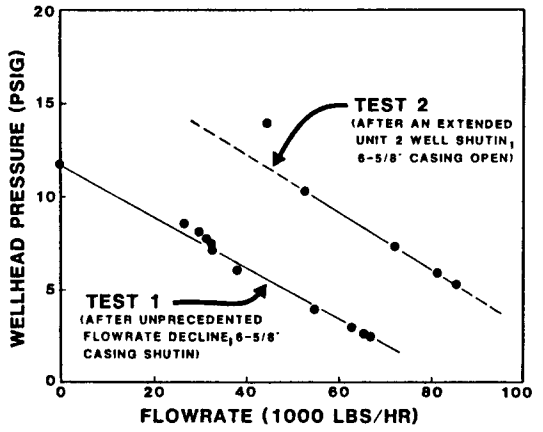

associated ground venting demonstrates that there is an upper limit to the amount of throttling that can safely be applied to Thermal 4.

Temperature/Pressure/Spinner Surveys

Flowing and static temperature, pressure and spinner surveys were run into the 6-5/8" casing from the surface to 360 ft. A caliper survey was also run to help analyze the spinner data. The enthalpy cycling of the 6-5/8" flow was found to be the result of geysering in the wellbore. All of the fluid was found to be entering the wellbore as liquid water at or just below the casing shoe. A static pressure survey found a bottomhole pressure of 77 psia which was within 20 psi of the Thermal Shallow Reservoir producing pressure at the time. This supports the previous conclusion that the 6-5/8" flow is in limited communication with the annular flow.

Thermal 4 Production Model

A model of the Thermal 4 production sources and controls consistent with the 1985 test results has been developed and is shown in Figure 6. The annular flowstream derives its

FIGURE 6

THERMAL 4 PRODUCTION MODEL*

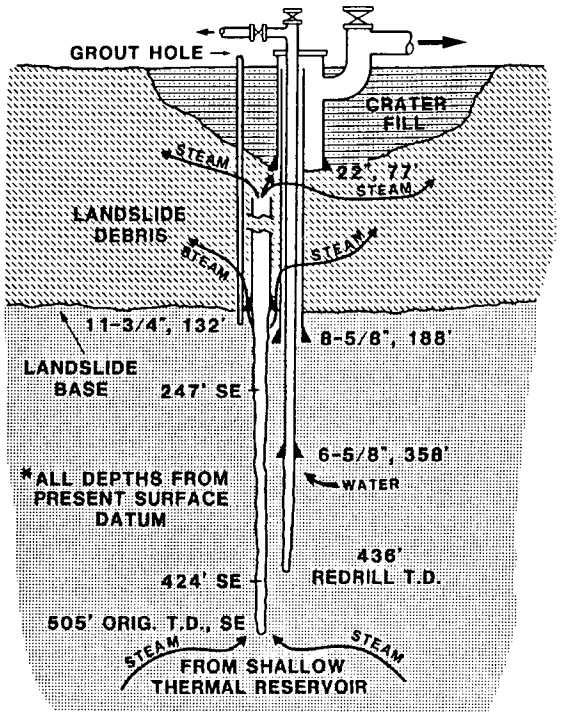

flow from the Thermal Shallow Reservoir via the original Thermal 4 wellbore. The 6-5/8" casing produces a low-enthalpy, two-phase mixture of groundwater from what appears to be the Thermal Shallow Reservoir caprock and is in limited communication with the annular

flow. The 6-5/8" and annular flows are also in limited communication with the landslide/fill material. In this model the controlling mechanisms for the the annular flow are Unit 2 well status (shut in or flowing), 6-5/8" flow condition, annular throttling, and rainfall in the form of groundwater.

CONCLUSIONS

The recent testing of Thermal 4 has determined the following:

1. The distinctly different flowrates, enthalpy states and chemical compositions of the annular and 6-5/8" flows show them to be from very different sources.

2. However, pressure and flowrate data show these two flows to be in weak hydraulic communication.

3. While the primary control of the annular flow is the Thermal Shallow Reservoir pressure, other partial controls are rainfall, 6-5/8" flow condition, and direct throttling of the annulus.

4. The ability to segregate the scale-laden, low-enthalpy flow from the major Thermal 4 flowstream combined with some ability to control its flowrate allows for several different options for Thermal 4 emissions compliance.

REFERENCES

Mogen, P. G. and Maney, J. (1985), "The Thermal 15 Relief Well and Production Performance of the Thermal Shallow Reservoir," Proceedings of the Tenth Workshop on Geothermal Reservoir Engineering, Stanford, January 22-24, 1985.

Mogen, P. G. (1985), Pittinger, L. F. and Magers, M. A., "1982 Thermal Shallow Reservoir Testing," Proceedings of the Tenth Workshop on Geothermal Reservoir Engineering, Stanford, January 22-24, 1985.

Raasch, G. D. (1985), "Development of the Thermal Shallow Reservoir," Proceedings of the Tenth Workshop on Geothermal Reservoir Engineering, Stanford, January 22-24, 1985.

Vantine, J. V. (1984), personal communication.

Vantine, J. V. (1985), "Hydrogeology of the Thermal Landslide," Proceedings of the Tenth Workshop on Geothermal Reservoir Engineering, Stanford, January 22-24, 1985.

PROCEEDINGS, Eleventh Workshop on Geothermal Reservoir Engineering
Stanford University, Stanford, California, January 21-23, 1986
SGP-TR-93

RESERVOIR BEHAVIOUR IN A STIMULATED HOT DRY ROCK SYSTEM

Anthony S Batchelor

Camborne School of Mines, Cornwall TR10 9DU, England

ABSTRACT

Research into the stimulation of hot dry rock (HDR) systems in crystalline rock has been underway in Cornwall, England for several years. Two deviated wells were drilled to a depth of 2100 m in 1981 with an interwell separation of 300 m. These wells were connected by massive hydraulic injections using water, but the interconnection was insufficient to permit long term circuation without excessive water losses. In 1985 a third well was drilled to a depth of 2600 m in a direction chosen from the analysis of the reservoir behaviour during the previous circulation. A massive stimulation (200 l/s, 75 bbl/min) of gel was used to connect the wells and circulation was re-established in August 1985.

Reservoir models have been developed from hydraulic analyses, thermal behaviour, microseismic mapping, tracer dispersion and chemical modelling.

The system behaves like an interconnected network of flow paths with a few dominant routes acting as flow conduits. The storage is associated with pressure dependent joint compliance, but it is isolated from the dominant flow paths.

No unique physical model has yet been derived but the various techniques have been used to establish constraints on the geometry and nature of the heat transfer regions. The experiments are still in progress.

INTRODUCTION

Research into the feasibility of extracting geothermal energy by the Hot Dry Rock (HDR) process is underway in several countries, Batchelor 1984. The work in England has been described at two previous Stanford Workshops (Batchelor 1982, Pine 1983) and these papers describe the general location and progress of the research programme up to 1983. The details are not repeated here.

The objective of the work in the UK is to determine whether or not it is feasible to interlink pairs of boreholes by massive hydraulic stimulation in a crystalline rock mass with a low intrinsic permeability in order to form a subterranean heat exchanger. The artificially enhanced flow paths must be associated with sufficient heat transfer area and a low resistance to flow to enable the heat to be extracted as a financially viable process.

The current experiments in the UK have not been directed towards producing a prototype working system; the work has concentrated on developing and understanding of the fundamental rock mechanics processes associated with the stimulation.

BRIEF RESUME OF EXPERIMENTAL PROGRESS

Two deviated wells were drilled in 1981 to a depth of 2100 m; the wells were aligned in the same plane with a vertical separation of 300 m. Fundamental measurements of the in-situ conditions were made at the end of drilling. These included:

i The in situ stress field and its variation with depth.

ii The orientation of the pre-existing jointing.

iii The petrology of the rock fabric.

iv The static and dynamic properties of the rock fabric.

v The in situ dynamic rock properties.

vi The undisturbed hydraulic properties of the rock in-situ.

vii The equilibrium temperature profiles for the wells.

These measurements enabled a conceptual model of the undisturbed conditions to be developed.

An extensive microseismic monitoring net was established (Batchelor et al 1983) and a series of stimulation and circulation experiments took place over a period of 18 months from November 1982.

Figure 1 shows an isometric view of the two wells and the microseismically active region. It can be seen that the active zone grew

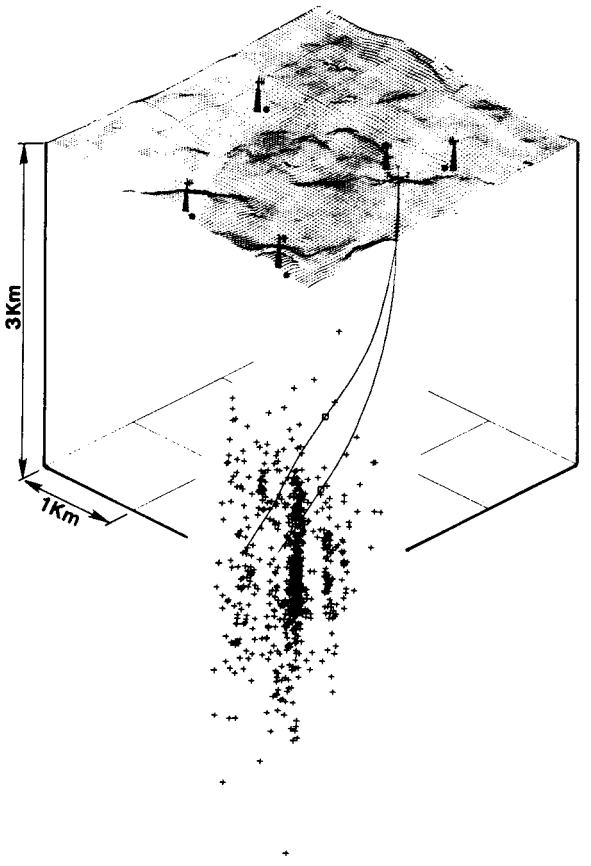

Figure 1 - The first two wells with the associated microseismicty

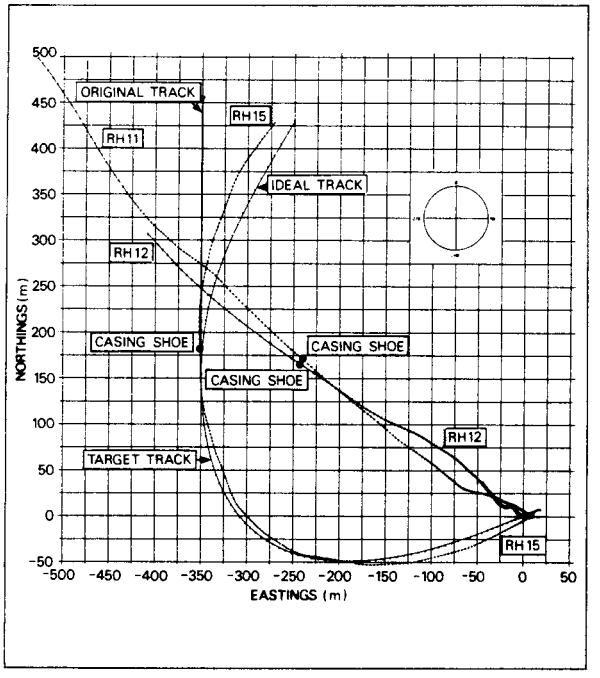

Figure 2 - A plan view of the track of the third well, RH15

downwards and subsequent analysis showed that this was due to the severely anisotropic stress field at the site (Pine and Batchelor 1984). During the circulation trials a total of 300 000 m^3 of water was injected into the system and only 100 000 m^3 recovered. The 'missing' 200 000 m^3 was consumed by the continuous growth of the microseismically active structure which caused large areas of rock to be exposed to moderate pressure and allowed diffusive losses to take place on a substantial scale despite the low initial permeability.

The geometry of the microseismic sensor network was not designed to locate microseismic events at substantial depths below the wells. When the results indicated significant downward growth, suggestions were made that the structure was an artefact of the sensor geometry (Anon 1984). Although definite field evidence was available showing that the bulk of the events were occurring below the wells (Baria 1985) there was no proof that the more permeable region had developed downwards.

It was decided to drill a third well that penetrated the microseismically active region approximately 300 m below the base of the earlier wells to explore this area.

This well had two objectives:

i To intersect any permeable zone of enhanced residual permeability.

ii To make a direct measurement of the relationship between microseismic events and stimulated flow paths.

THE THIRD WELL

Constraints on the surface location of the third well meant that the trajectory had to be drilled as part of a long spiral. A plan view is shown in Figure 2 in relation to the two previous wells. The drilling and completion of this well is reported in CSM 1985. The well was finished in December 1984 and a nitrogen lift production test was run immediately.

Simultaneous production logging took place during this test by running the tool through the drillpipe used for the gas injection. This enabled the flow zones to be identified and correlated with the microseismic cloud. Figure 3 shows the relationship of the flow zones to the microseismic activity and it can be seen that the only section of the well that produced fluid was the zone within the envelope of the microseismicity.

TESTING THE NEW WELL

After completion of the well, a series of low flow rate injection and production experiments took place to determine the nature of the interwell connection. The bases for each of these tests were similar; one well was used for production or injection and the other well for observation. These tests were modelled by

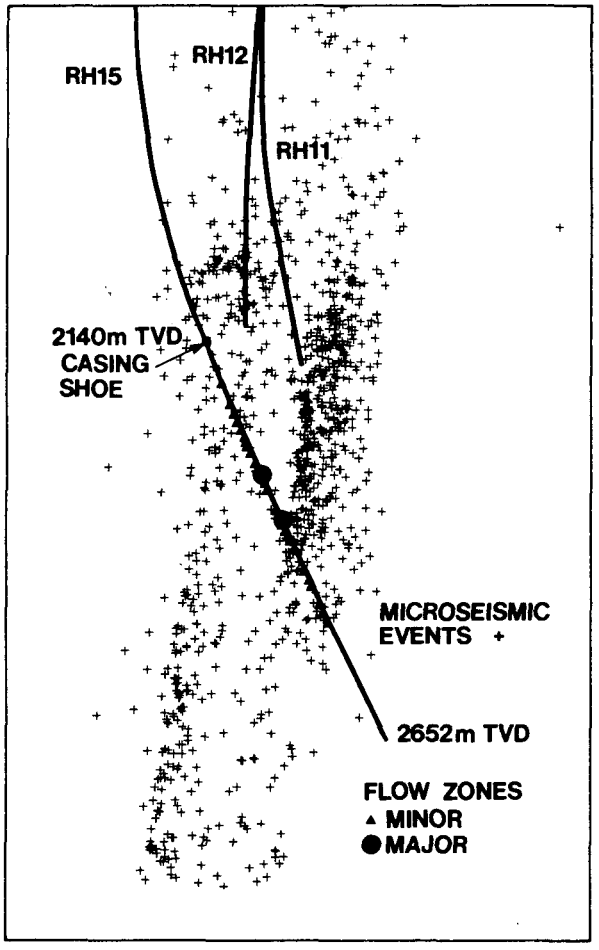

Figure 3 - The flow zones in RH15 with the original microseismicity

superposing two line source models in a uniformly permeable region. No boundaries were detected, Figure 4 shows the excellent match achieved with such a model for both the injection and observation wells. The derived parameters were:

$$\frac{kh}{\mu} = 4.875 \times 10^{-10}\ m^3/Pa.s$$

$$\frac{k}{\mu c \phi} = 0.975\ m^2/s$$

A porous media model fitted the data closely and it was possible to derive an impedance value based on superposition,

$$I = \frac{\mu}{4\pi kh}\left[\ln\left(\frac{r^2}{r_w^2 e^{-2s_2}}\right) + \frac{q_1}{q_2}\cdot\ln\left(\frac{r^2}{r_w^2 e^{-2s_1}}\right)\right]$$

(nomenclature at end)

This gives the impedance I in terms of the kh/μ and skin values at the wells; excellent agreement with the measured values was obtained.

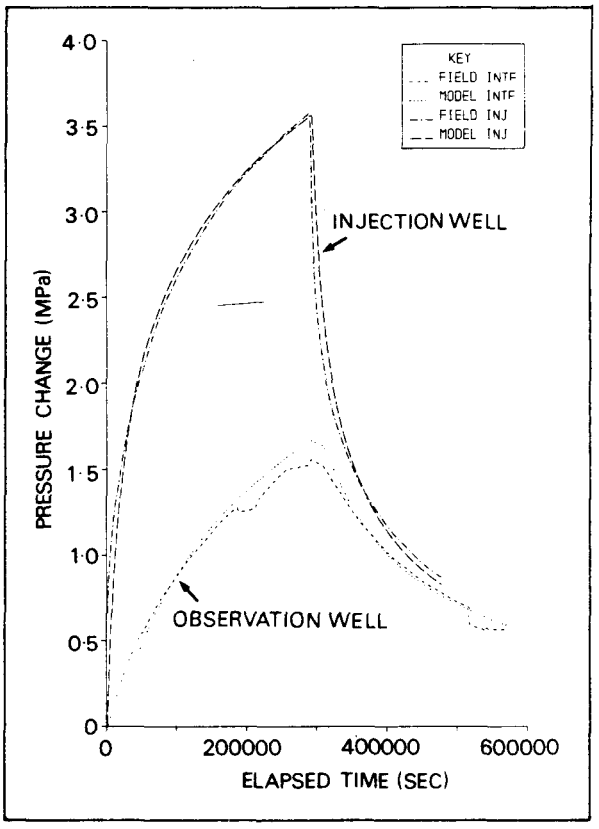

Figure 4 - Field and model results from an injection interference test

At the end of these tests it was concluded that the residual permeability between the wells had been enhanced by the previous massive injection of water but the residual apertures were insufficient to allow circulation to take place without further stimulation.

The design and execution of the stimulation is outside the scope of this paper and will be reported in detail elsewhere. It consisted of an injection of 5500 m^3 (1.2 million galls) of gel injected at flow rates of over 200 l/s (75 bbl/min) and reaching a maximum at 264 l/s (98 bbl/min). This was the largest gel stimulation undertaken in Europe and was run on 4 July 1985. On-line monitoring of the seismicity was able to track the location of the induced events caused by the stimulation during the eight hours of injection. Figure 5 shows a view of the seismicity in relation to the three wells. It can be seen that the active region is contained within the interwell zone. No further seismicity has taken place since that stimulation.

THE CIRCULATION TESTS (To 14 December 1985)

Figure 6 shows the injection flow and corresponding wellhead pressure since 7 August 1985. There have been three flow rates sustained for approximately 50 days each. During the second flow rate period a series of step pulses lasting one day can be seen in the centre of the figure. The corresponding plot of injection

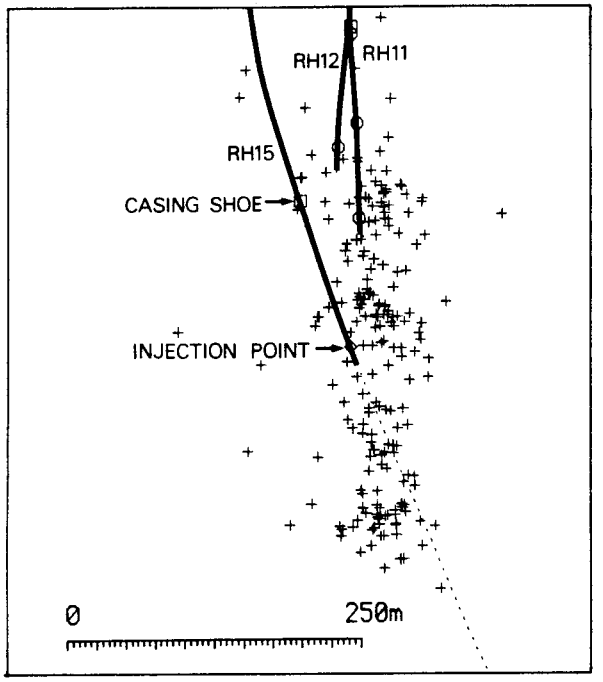

Figure 5 - The induced microseismicity during the massive stimulation with gel

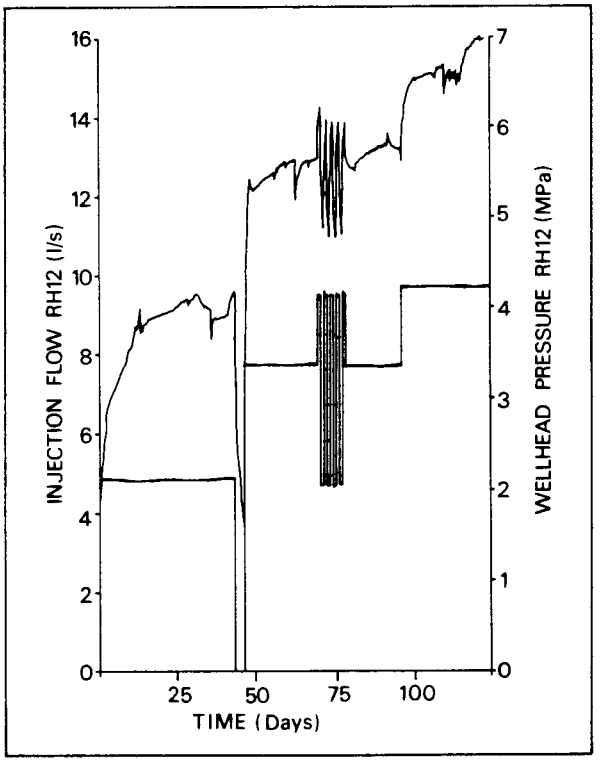

Figure 6 - The injection flow and pressure since August 1985

wellhead pressure versus production flow shows that the impedance in the system has been largely constant throughout that time, Figure 7. In addition, the water loss rate has been found to be reasonably steady, 1.3 l/s.

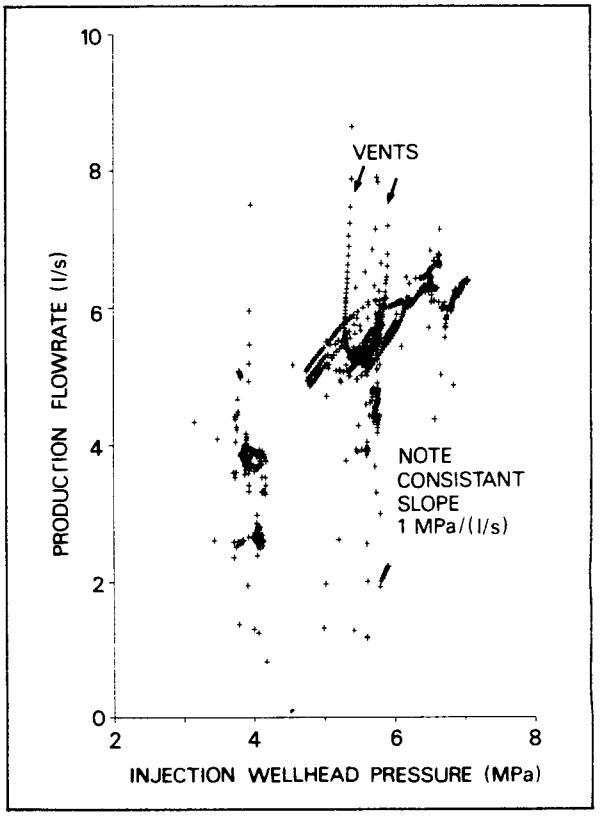

Figure 7 - Injection pressure v production flow since August 1985

HYDRAULIC MODELLING

The successful hydraulic modelling of the early data could not be continued after the fracturing operation. Individual sections of data could be matched to porous media models, but no composite solution could be found. Various finite differences and FRIP, see Pine et al 1985, models were run and none was able to get a match without invoking channeled flow and various constrained boundary conditions.

A finite difference model with the source and sink in a high permeability zone surrounded by a gradational change to low permeability was able to get a reasonable match to some of the behaviour, but there were discrepancies during step changes of either pressure or flow.

It was decided to attempt a simple resistance analogue model to identify the essential components of any physical model. The one that seemed to fit the data most accurately is shown in Figure 8, Lawton 1985. The essential feature of this model is that the flow path is associated with a very small storage term and the majority of the storage is isolated by resistances. In addition, there is a resistance between the heat exchange area and the production well, approximately 20-30% of the total resistance to flow. There is no significant storage after the outlet resistance. This means that when the production well

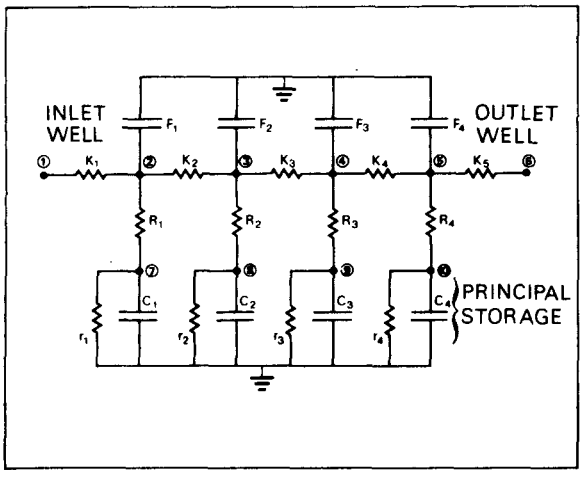

Figure 8 - Electrical analogue circuit to match system performance

is shut-in there is a rapid rise in pressure in the first few seconds. This model was able to match the entire flow history of the circulation since stimulation with reasonable accuracy. The work is now underway to translate the elements into the physical reality of the reservoir.

The overall impedance is approximately 1 MPa/l/s; less than one third of the value before the stimulation. This value has not changed throughout the circulation and is still too high for an economically viable operation.

TRACER TESTS

A tracer test has been run after each flow rate change. During the nominal 10 l/s injection, one non-reactive tracer test was run in late November followed by a combination of a non-reactive and reactive tracer experiment run from 9 December. The theory and some of the results from the reactive tracer test are given in another paper in this volume, Tester et al 1985. Figure 9 shows the superposed curves from the non-reactive tracer studies. It can be seen that there is no effect of the changing flow rate or pressure on the concentration v produced volume relationship, therefore, it may be concluded that the geometry of the flowing regime is similar under all three flow conditions.

The underlying principle of the reactive tracer test is that the tracer is a compound that reacts at a certain temperature and pH condition in the reservoir to form conservative reaction products. The concentration of original tracer and the corresponding concentration of product are measured in the production flow in order to determine the downhole conditions relating to that reaction. The experiment used Ethyl Acetate reacting with water to form Acetic Acid and Ethanol in the reservoir. Figure 10 shows the normalised non-reactive tracer plus the Ethanol and Ethyl Acetate production curves over the corresponding production.

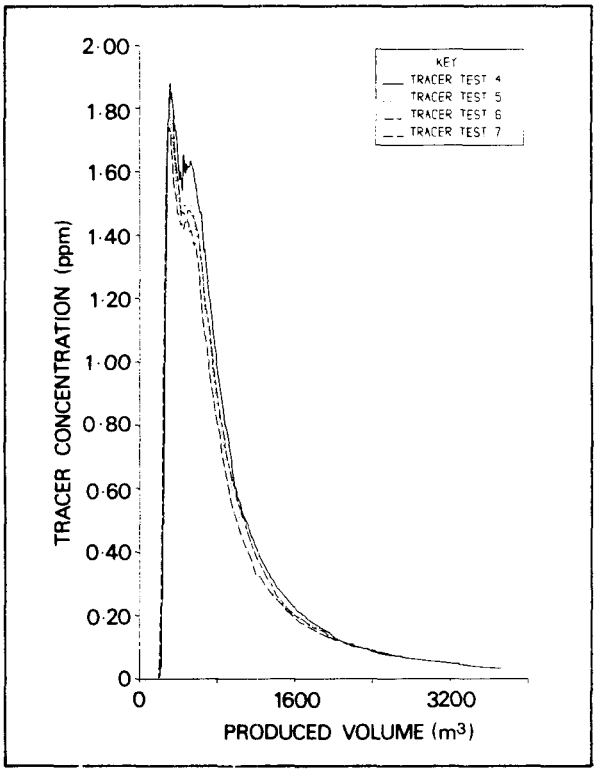

Figure 9 - Tracer distributions during the four tracer tests at various flow rates

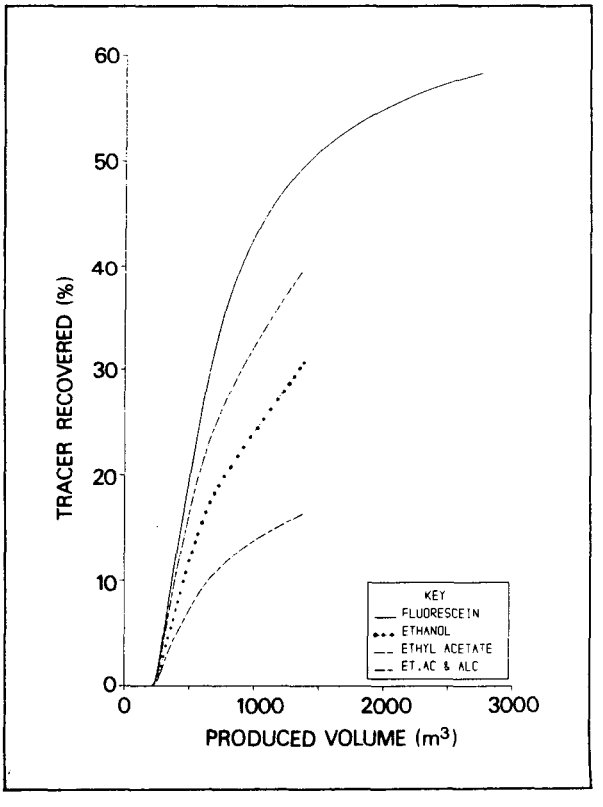

Figure 10 - Normalised tracer recovery during reactive tracer test

The preliminary conclusions from this test are that the longer residence flow paths are less reactive than the short flow paths. This is contrary to an intuitive solution based on porous media analysis. It means that the longer flow paths are either cooler, or have a lower pH, than the principal production flow path. One model that would fit this observation is that there is a system of dominant flow paths that penetrate rock at a higher temperature than the average production. Injection flows circulate below the production well and then cool as they rise to the wellbore. These are coupled with some flow paths that stay up at the top of the structure in a region cooled continuously by the injections and find their way into the production well without warming significantly.

The hydraulic modelling indicates that it is necessary to decouple the 'storage' from the flow system in order to match the data; these tracer results may imply that the bulk of the stored fluid is cooler than the equilibrium temperatures in the storage region.

It will be important to repeat the reactive tracer experiment during the continuing circulation to try and understand whether or not the average reservoir temperature is declining. There is no indication from temperature logging that thermal breakthrough has been detected in the wells.

CONCLUSIONS

Five techniques have been used to derive a working model of the reservoir:

- Thermal behaviour
- Active geochemistry
- Tracer dispersion
- Microseismic event mapping
- Hydraulic monitoring

Formation evaluation has shown that the granite is fractured pervasively by two orthogonal sets of joints containing a range of subvertical members. The joint geometry has created a pattern of interlocking prismoidal blocks of granite. The existing stress field is offset to one of the joint directions by approximately 25° and the anisotropy of the stresses has generated subcritical shear stress conditions on certain of the joints. Very small increases in fluid pressure within the joints has been sufficient to cause shear motion on an individual structure. When water was used as the injection fluid, the seismically active region grew uncontrollably downwards because of the severity of the anisotropy. A massive injection of gel was used to control the viscosity of the stimulating fluid and inhibit far field seismicity. This has been successful.

Despite the extensive stimulation, no new flowing connections have been observed in the production well. The flow has been significantly enhanced on the pre-existing natural joints. The principal flow zones occur on joints that are oriented within 20° of the maximum stress direction. However, not many joints in this direction produce fluid. It has been concluded that the principal limitation to the productivity of an individual structure is related to the connectivity of the joints between the wells.

The action of stimulation is to dilate the natural apertures by raising the pressure and causing both shear and normal motions on the joints.

The heat transfer region is associated with a characteristic flowthrough volume of approximately 200 m^3 of water. The implied apertures of the flow path are of the order of 0.1 mm. The inference from these results is that the heat transfer region is between 1 and 4 million m^2. The mean residence time of the system is approximately 40 hours. The system has been in continuous circulation for over 3100 hours and no thermal drawdown has been observed.

Hydraulic analysis shows that there is a direct channeled flow path associated with a minimum amount of storage capacity within the flow zone itself. However, there is significant fluid stored in the overall structure. This appears to be stored at less than equilibrium temperature of the surrounding rock.

The resistance to flow of the current system (1 MPa/l/s, 10 psi/gpm) is still too high for an economically viable HDR operation.

The experiments continue with the immediate target of achieving a sustained production of 25 l/s at 80°C which will be the equivalent of 75 l/s at 200°C because of the significant reduction in viscosity at high temperature. It is hoped this flow will be attained before April 1986.

ACKNOWLEDGEMENTS

Obviously the results of this paper are the synthesis of the work of the Project team and not just the author. The entire Project staff (60 people) has been involved with each of the experiments in one form or another and the credit should go to them.

The work has been supported by Contract E/5A/CON/125/960 by the UK Department of Energy and Contract EN3 G/E1/019/GB of the EEC whose support is gratefully acknowledged.

NOMENCLATURE

k = permeability (m^2)

h = formation heights (m)

μ = viscosity (Pa.s)

c = compressibility (Pa^{-1})

ϕ = porosity

I = impedance to flow ($Pa/m^3/s$)

r = interwell distance (m)

r_w = wellbore radius

s_2 = skin factor at production well

q_1 = injection flow

q_2 = production flow

s_1 = skin at injection well

REFERENCES

Anon. (1984) Review of Batchelor A S, Baria R, Hearn K: Monitoring the effects of hydraulic stimulation by microseismic event location: a case study, in SPE-AIME 58th annual technical conference, San Francisco, Oct 1983. (SPE 12109).

Baria R, Hearn K, Batchelor A S. (1985) Induced seismicity during the hydraulic stimulation of the potential hot dry rock geothermal reservoir. In Pennsylvania State University 4th conference on acoustic emission/microseismic activity in geologic structures and materials, University Park, Pennsylvania, Oct 1985.

Batchelor A S. (1984) An overview of hot dry rock technology. In 4th international conference on energy options: the role of alternatives in the world energy scene. Institution of Electrical Engineers, London, Apr 1984.

Batchelor A S. (1983) Stimulation of a hot dry rock geothermal reservoir in the Cornubian granite, England. In 8th workshop on geothermal reservoir engineering, Stanford University, California, Dec 1982.

Batchelor A S, Baria R, Hearn K. (1983) Monitoring the effects of hydraulic stimulation by microseismic event location: a case study. In Institution of Mining and Metallurgy conference on Rockbursts: prediction and control, London, Oct 1983.

Camborne School of Mines Geothermal Energy Project. (1986) Drilling operations 1984 Volume 3: drilling and casing well RH15. Phase 2B report, 2B-6.

Lawton R. (1986) An analytical model of the hot dry rock reservoir. Camborne School of Mines Geothermal Energy Project Phase 2B report.

Pine R J. (1984) Pressure transient analysis for large scale hydraulic injections in the Carnmenellis granite, England. In 9th workshop on geothermal reservoir engineering, Stanford University, California, Dec 1983.

Pine R J, Batchelor A S. (1984) Downward migration of shearing in jointed rock during hydraulic injections. International Journal of Rock Mechanics Mining Sciences & Geomechanical Abstracts. Vol 21, No 5, pp 249-263.

Pine R J, Cundall P A. (1985) Applications of the Fluid-Rock Interaction Program (FRIP) to the modelling of hot dry rock geothermal energy systems. In Swedish National Group of the ISRM international symposium on the fundamentals of rock joints, Bjorkliden, Lapland, Sweden, Sep 1985.

Tester et al. (1986) Inert and reacting tracers for reservoir sizing in fractured, hot rock systems. In 11th workshop on geothermal reservoir engineering, Stanford University, California, Jan 1986.

PROCEEDINGS, Eleventh Workshop on Geothermal Reservoir Engineering
Stanford University, Stanford, California, January 21-23, 1986
SGP-TR-93

RESERVOIR FRACTURING IN THE GEYSERS HYDROTHERMAL SYSTEM: FACT OR FALLACY?

Jeffrey J. Hebein

Diamond Shamrock Thermal Power Co.
3333 Mendocino Avenue, Suite 120
Santa Rosa, California 95401

ABSTRACT

Proper application of proven worldwide fracture determination analyses adequately aids in the detection and enhanced exploitation of reservoir fractures in The Geysers steam field. Obsolete, superficial ideas concerning fracturing in this resource have guided various malformed judgements of the actual elusive trends. Utilizing regional/local tectonics with theoretical rock mechanics and drilling statistics, offers the most favorable method of fracture comprehension. Exploitation philosophies should favor lateral drilling trends along local tensional components and under specific profound drainage/faulting manifestations to enhance high productivities. Drill core observations demonstrate various degrees of fracture filling, brecciation, strain responses, and rock fracture properties, giving the most favorable impression of subsurface reservoir conditions. Considerably more work utilizing current fracturing principles and geologic thought is required to adequately comprehend and economically exploit this huge complex resource.

INTRODUCTION

Reservoir fracturing in The Geysers field is often termed as debatable and elusive, yet need not be when appropriate current tectonic/hydrothermal studies are applied. Determination of reservoir fracture trends and location can be ascertained through application of methods by Stearns and Friedman (1972). Utilization of active regional and local stress fields, active fault and drainage trends, theoretical rock mechanics, drilling experiences, oriented drill cores, and borehole televiewer logging, definitely allow the geologist to determine and drill high permeability trends and zones. Many former and current interpretations of Geysers fracturing use obsolete, superficial geologic thought, which could be greatly enhanced through the utilization of correct tectonic principles that have proven to be very effective in defining reservoir fracturing in worldwide fluid energy systems for the last 35 years.

MEGATECTONICS

The Geysers regional tectonics are excellently portrayed by McLaughlin (1981, Figure 7), where the steam field lies within a wide shear zone bounded by the right lateral Maacama and Collayomi Fault zones (Figure 1). Former Franciscan imbricate thrust faults (McLaughlin, 1978, 1981) are assumed to be inactive and hydrothermally sealed for up to the last three million years (Hebein, 1985). The San Andreas system fault scheme of Moody and Hill (1956) and a regional strain ellipsoid (Wilcox, et al., 1973) can now be applied so as to comprehend the regional and local stress/strain patterns.

The drainage in Figure 1 represents segments of large, deep, near vertical faults and joints in the earth's crust. Regional/local shears probably traverse through the creeks. Enhanced tectonic strain induces profound erosion along active fault trends ("creekology").

LOCAL TECTONICS

The strain ellipsoid can be utilized to determine the local strains within the steam field (Figures 2 and 3). Refer to Thomas (1981, Plate V). Individual block rotations within the steam field allow for various positioning of the strain ellipsoid in different portions of the Geysers field. Figure 4 illustrates a typical shear model and how the Geysers drainage mimics potential fault trends.

Some steam field workers continue to profess the importance of old, imbricate thrust contacts (long inactive and sealed?) in reservoir permeability, yet the author downplays any importance and concentrates on current active tectonic stresses/strains. Numerous fluid injection tracer tests demonstrate reservoir radial flow out from the injection point with differing preferential pathlines over various times, suggesting a thoroughly fractured non-homogeneous reservoir.

SPECIFIC DRILLING PHILOSOPHIES

Directional drilling beneath creeks in many parts of the steam field has demonstrated that profoundly enhanced reservoir permeability exists under such drainage (faulting and jointing) trends. The author proposes (Figure 4) a drilling scheme of deep lateral penetration parallel to the fields variable tensional components which should intersect more tension joints and synthetic/antithetic shears of various orders. Drilling under drainage through the shear or tensional component is also stressed whenever possible. Compressional trend and vertical drilling (Hebein, 1985) should be avoided. If reservoir rock blocks are indeed fractured, this method will enhance penetration of a maximum number of permeable zones. Statistically, most reservoir fractures (main metagraywacke, felsic

intrusions, and sometimes the lithocap) should be near vertical and follow the three general directions on the regional strain ellipsoid.

OBSERVED DRILL CORE FRACTURING

Deep oriented drill cores from the Bottlerock area exhibit fresh vertical tension fractures in an en echelon fashion and correspond to surface drainage directional patterns immediately above the core point(s). Large rock fragments blown up from the Bottlerock reservoir (top) exhibit profound sericitic alteration (condensate sealing) with sheared slickensides cemented with realgar. Cores from the shallow Big Geysers area exhibit sub-vertical and vertical fractures filled with quartz-pyrite-epidote-chalcopyrite-sphalerite-galena veins, those in turn fractured and filled with quartz-adularia-argentite veins. Some sericitization exists in the rock matrix, suggesting a shallower hot spring chaotic fracturing environment. Ancient schistosity trends are sealed tight. Small fracture caverns are witnessed. Quartz flooding has enhanced the already highly brittle nature of the metagraywackes. Deep rock fragments blown up from the Bottlerock reservoir are very similar in nature to the aforementioned descriptions. Deeper Big Geysers cores exhibit vertical, enechelon, epidote-filled tension fractures, in turn shot through by crosscutting quartz-actinolite-chalcopyrite veins in systematic mega to mini-breccia fashion.

Cores from the Little Geysers exhibit profound quartz flooding and sealing of ancient schistosity trends. Fractures in three or more subvertical to vertical trends are flooded with quartz-actinolite-chalcopyrite veins. Sealing is profound. Felsic intrusive cores from the Little Geysers area are shot through by tourmaline veins (some small explosion breccia dikes), those in turn shot through by quartz veins, those in turn shot through with actinolite-quartz veins, those in turn shot through by sericitic alteration holes (perhaps due to steam cell sealing). High angle fracture trends run parallel to one another and also cut across some in a complex and chaotic fashion. Fracture caverns are witnessed.

CONCLUDING REMARKS

Considerably more work is required to adequately map fracture trends and enhancements in the Geysers steam field. The complexities of such a deep, large, completely faulted resource, coupled with varying personal interpretations of reservoir fracturing has lead to multi-lined avenues of geologic thought (some non-supportive) among the resource operators. Acceptance and use of appropriate tectonic fracturing principles aligned with wellfield observations and drilling experiences, offers the most favorable attitude for the exploitation of any fluid energy resource. Many obsolete and inadequate ideas concerning field fracturing must be dismissed in favor of new scientific approaches for the proper economic exploitation of steam permeability. The aforementioned discussion offers a realistic and incident-proven approach to solve the complexing problems of the Geysers reservoir(s).

REFERENCES

Harding, T. P., 1974, Petroleum traps associated with Wrench Faults: American Association of Petroleum Geologists Bulletin, Vol. 58, #7, pp 1290-1304.

Hebein, J. J., 1985, Historical Hydrothermal Evolutionary Facets Revealed Within the Exploited Geysers Steam Field: Geothermal Resources Council Bulletin, Vol. 14, #6, pg. 13-16.

McLaughlin, R. J., 1978, Preliminary Geologic Map and Structural Sections of the Central Mayacamas Mountains and The Geysers Steam Field, Sonoma, Lake and Mendocino Counties: U.S.G.S. Open File Report #78-389, 2 Plates

McLaughlin, R. J., 1981, Teconic Setting of Pre-Tertiary Rocks and its Relation to Geothermal Resources in The Geysers - Clear Lake Area, in Research in The Geysers-Clear Lake area, Northern California: U.S.G.S. Professional Paper 1141, pg. 3-23

Moody, J. D. and Hill, M. J., 1956, Wrench-Fault Tectonics: Geological Society of America Bulletin, Vol. 67, #9, pg. 1207-1246.

Stearns, D. W. and Friedman, Melvin, 1972, Reservoirs in Fractured Rock: American Association of Petroleum Geologists Memoir 16, pg. 82-106.

Thomas, G. E., 1974, Lineament - block tectonics: Williston-Blood Creek Basin: American Association of Petroleum Geologists Bulletin, Vol. 58, #7, pp 1305-1322.

Thomas, R. P., 1981, Subsurface Geology, in A Reservoir Assessment of The Geysers Geothermal Field, California Division of Oil and Gas, #TR27, pg. 9-20, with plates.

Wilcox, R. E., Harding, T. P., and Seely, D. R., 1973, Basic Wrench Tectonics: American Association of Petroleum Geologists Bulletin, Vol. 57, pg. 74-96.

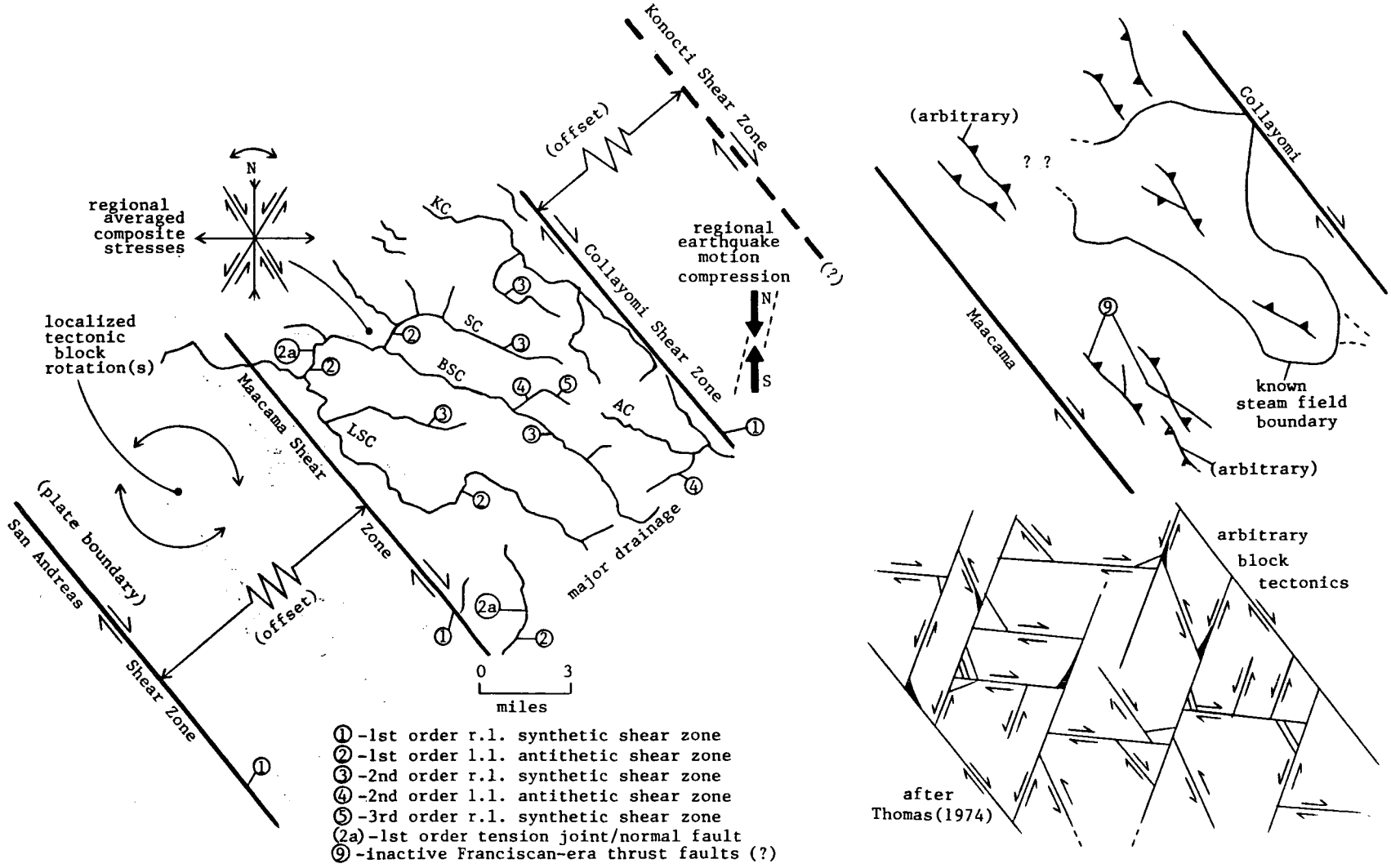

Figure 1. A conceptual illustration depicting the regional stresses and strains about the Geysers Steam Field, modified in part after McLaughlin(1981,figure 7). Specific drainage trends are probably localized prolifications of shears that traverse across the entire fieldwide drainage patterns. The fault type guide generally follows the nomenclature of Moody and Hill(1956). Here, most drainage segments appear to follow the San Andreas fault classification scheme. Tension jointing can occur as block boundaries or as interblock fractures. All trends follow the strains on the regional strain ellipsoid.

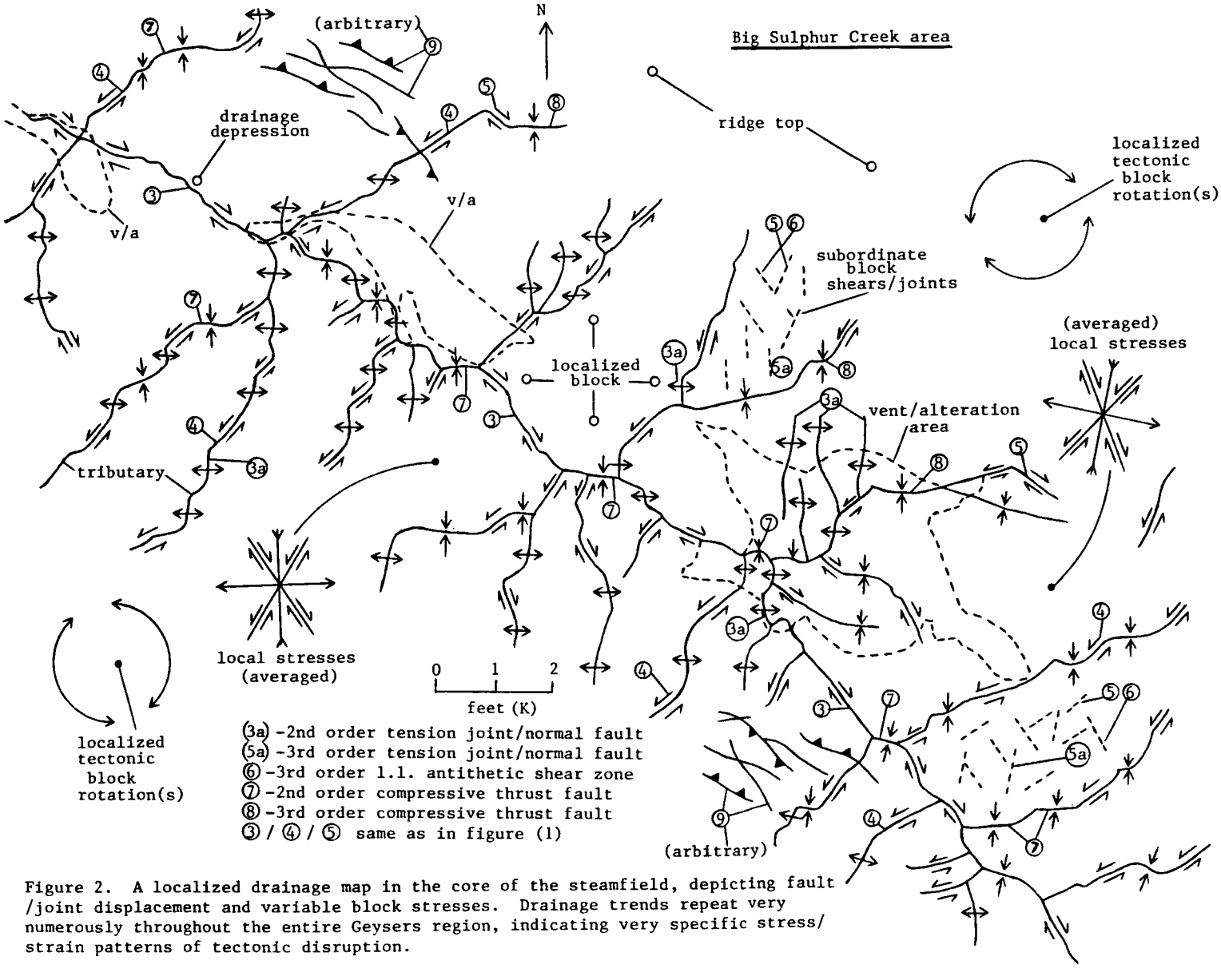

Figure 2. A localized drainage map in the core of the steamfield, depicting fault /joint displacement and variable block stresses. Drainage trends repeat very numerously throughout the entire Geysers region, indicating very specific stress/ strain patterns of tectonic disruption.

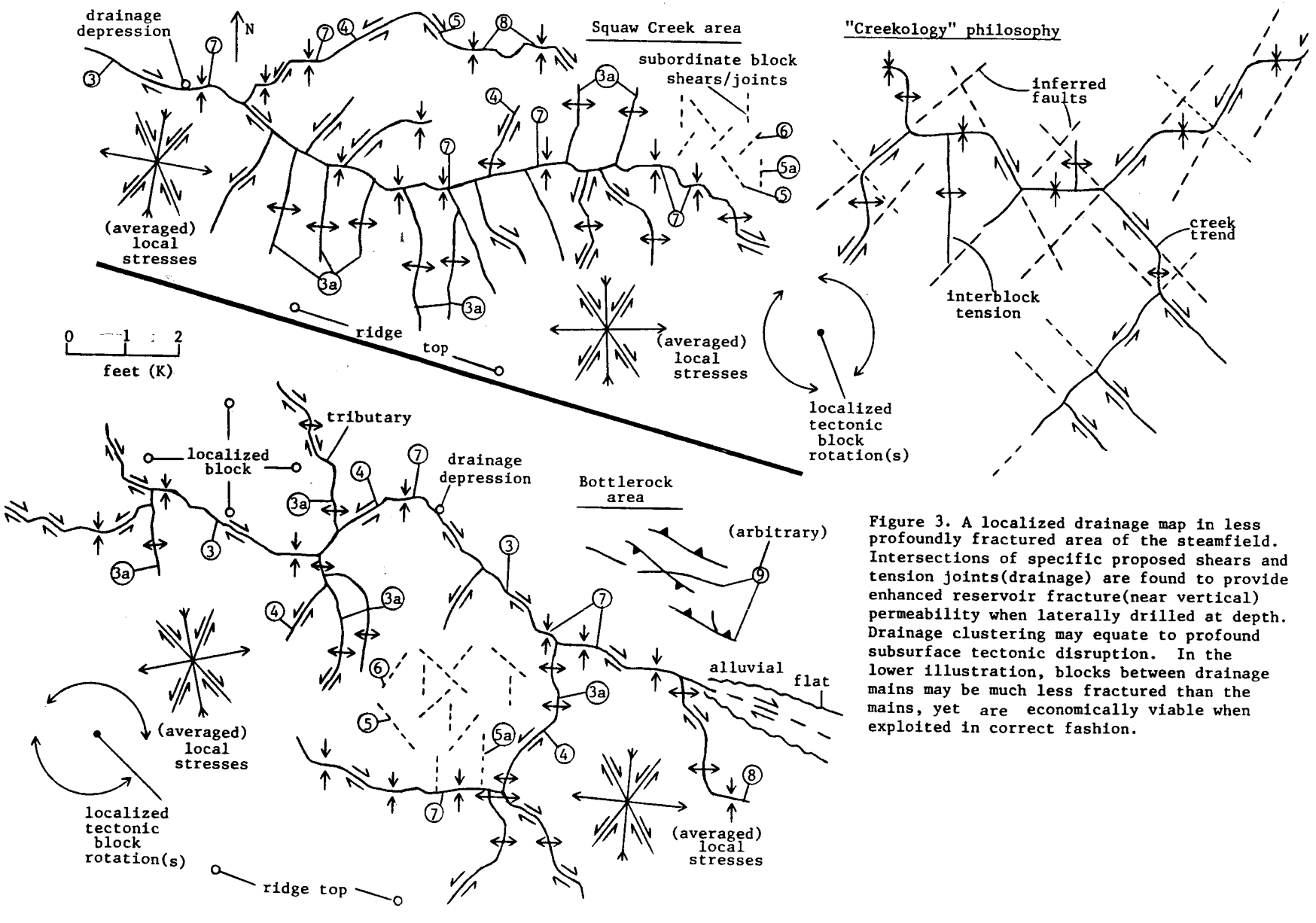

Figure 3. A localized drainage map in less profoundly fractured area of the steamfield. Intersections of specific proposed shears and tension joints(drainage) are found to provide enhanced reservoir fracture(near vertical) permeability when laterally drilled at depth. Drainage clustering may equate to profound subsurface tectonic disruption. In the lower illustration, blocks between drainage mains may be much less fractured than the mains, yet are economically viable when exploited in correct fashion.

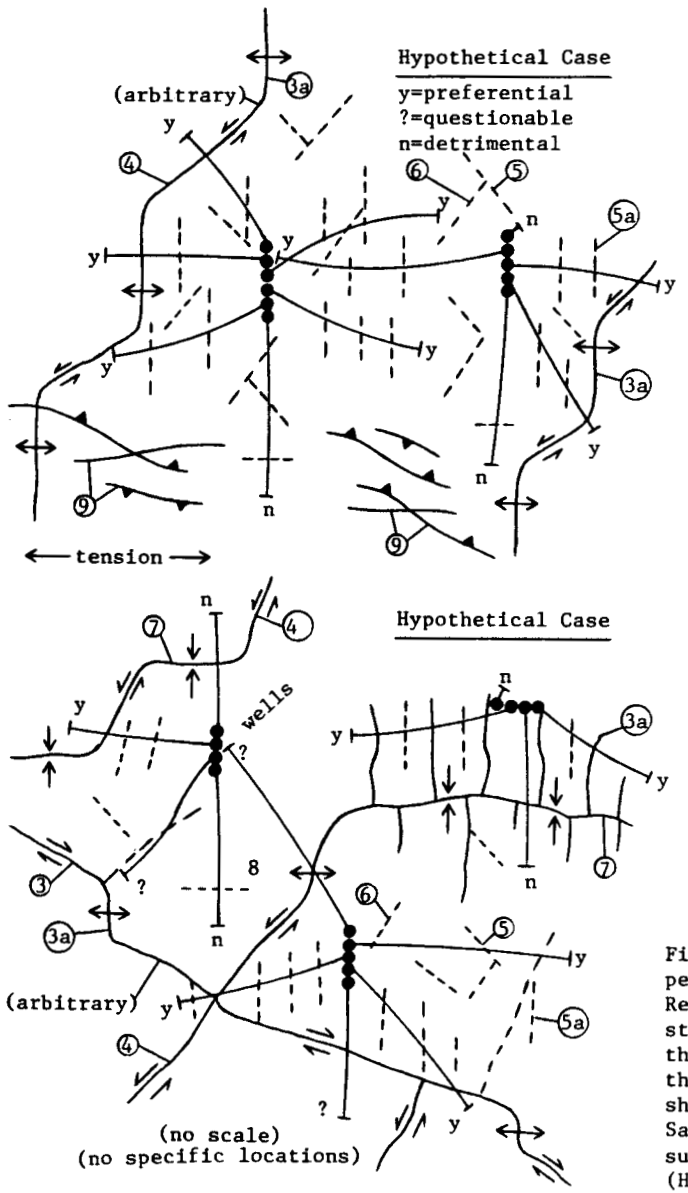

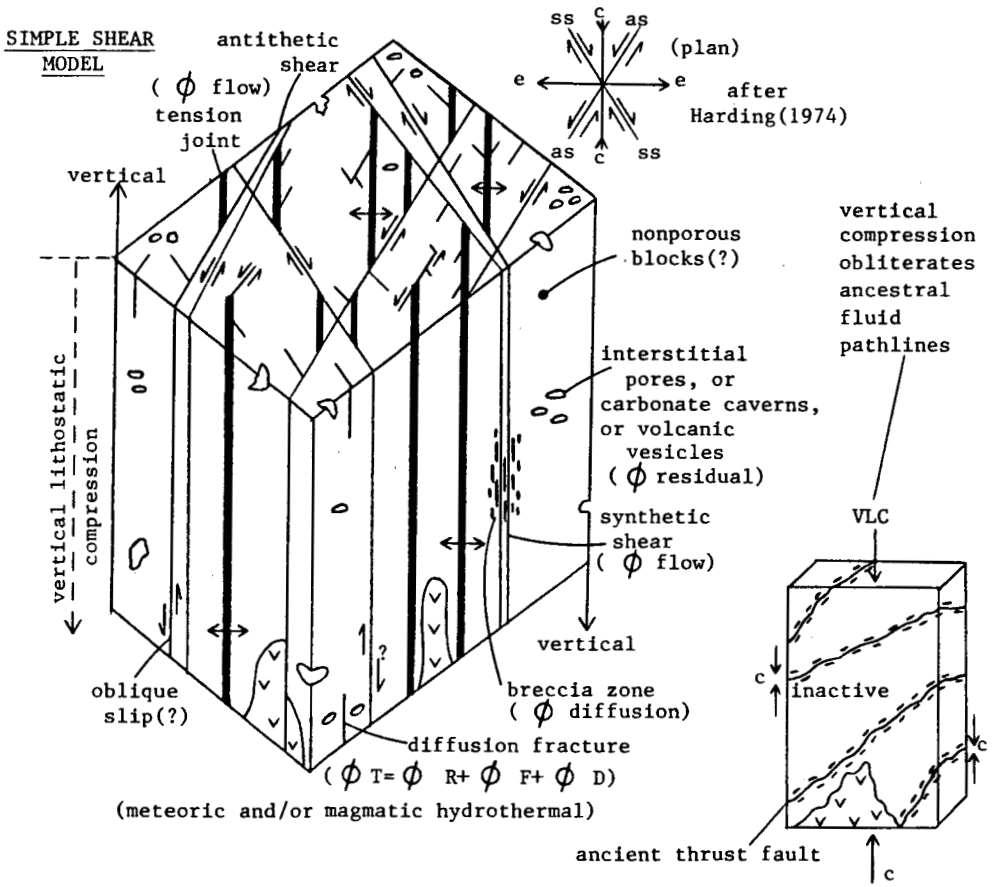

Figure 4. A proposed fieldwide drilling scheme, so as to enhance the number and permeability of near vertcal fractures penetrated by laterally deviated wellbores. Reservoir permeability will run in three general directions, determined by the local stresses and rock mechanics. The block model is applicable to the current state of the steamfield. Vertical lithostatic compression would obliterate ancient imbricate thrust faults(Franciscan stratigraphy) while ancestral hydrothermal mineralization should have sealed the compressed fault paths pervasively. The right-lateral San Andreas stresses/strains about the steamfield are incompatable with the relic subductive imbricate thrust fault fracturing that has long since ceased to exist. (Hebein, 1985).

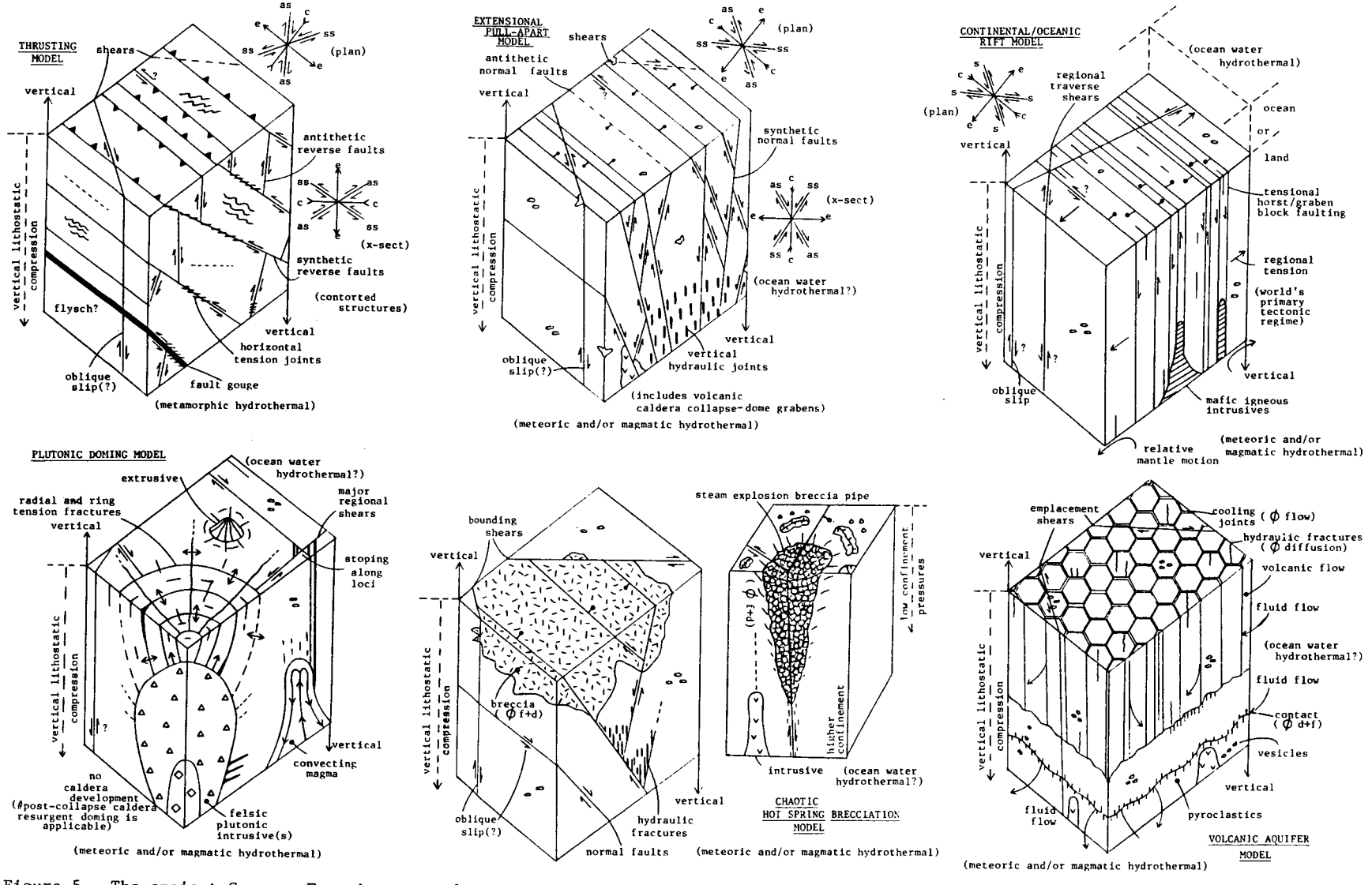

Figure 5. The ancient Geysers Franciscan complex was once a thrusting environment; presently inactive and hydrothermally sealed. This regime should not be confused with other types of tectonic regimes, applicable to other worldwide hydrothermal systems, active and fossil. An idealized collapsed and resurgent caldera model(Yellowstone?) could possess several of the above model tectonic systems. Geopressured environments(lithostatic confinement pressures) are not represented in any of the models. Other tectonic/fracture model(s) may exist.

PROCEEDINGS, Eleventh Workshop on Geothermal Reservoir Engineering
Stanford University, Stanford, California, January 21-23, 1986
SGP-TR-93

INITIAL MEASUREMENTS OF PETROPHYSICAL PROPERTIES ON ROCKS FROM THE LOS AZUFRES, MEXICO, GEOTHERMAL FIELD

E. Contreras and E. Iglesias

Instituto de Investigaciones Eléctricas
Apartado Postal 475
Cuernavaca, Morelos, México.

A. Razo

Comisión Federal de Electricidad
Av. Las Camelinas 3527, Piso 7
Morelia, Michoacán, México.

INTRODUCTION

Petrophysical properties of geothermal reservoir rocks are valuable information for many activities, including reservoir characterization, modelling, field test analysis and planning of exploitation techniques. Petrophysical data of rocks from geothermal reservoirs located in volcanic areas is in general very scarce. In particular, no petrophysical data of rocks from the Los Azufres geothermal field area has ever been published.

This work presents the results of initial petrophysical studies on outcrop rocks and drill core samples from the Los Azufres geothermal field. These studies are the first part of an ongoing experimental program intended to establish a data-base about physical properties of the Los Azufres rocks, in support of the many reservoir engineering activities which require of such information.

The experimental work carried out consisted of laboratory measurements of density, porosity, permeability, compressibility, thermal conductivity, thermal expansion, electrical resistivity and sonic wave velocities. Some of the experiments were aimed at investigation of the effects of temperature, pressure, saturation and other parameters on the physical properties of rocks.

DESCRIPTION OF SAMPLES

The specimens for this study were cut from outcrop rocks collected at eight sites in the Los Azufres area and drill core samples from the wells A1, A5, A9 and A19. Fig. 1 is a map showing the approximate location of the outcrop sampling sites, which are indicated by numbers 1 to 8, and the four wells.

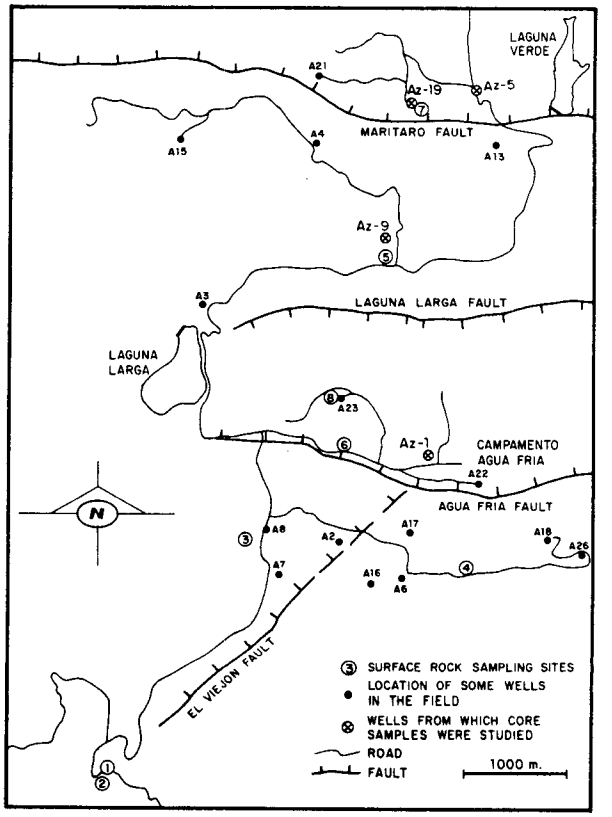

Fig. 1. Map of the Los Azufres Geothermal field area showing the approximate location of the outcrop sampling sites and wells.

Taking into account the geology of the area, the outcrop rocks were sampled from specific sites thought to be representative of the subsurface formations. Care was taken to avoid sampling outcrop rocks showing evidence of weathering processes. The drill core samples were provided by Comision Federal de Electricidad (CFE) from its valuable stock of cores retrieved during drilling operations.

The petrographic classification of the rocks and the depths from which drill core samples were cut are indicated in Table 1.

Table 1. Origin and Petrographyc classification of samples

Sample No.	Sampling Site	Depth (m)	Petrographyc Classification
1	1	----	Microlitic Andesite
2	2	----	Pyroxene Andesite
3	3	----	Microlite Andesite
4	4	----	Porfiritic Andesite
5	5	----	Ignimbrite
6	6	----	Riolite
7	7	----	Microlitic Andesite
8	8	----	Riolite
A1	Well A1	1825	Pyroxene Andesite
A5	Well A5	1160	Porfiritic Andesite
A9	Well A9	1705	Porfiritic Andesite
A19	Well A19	1000	Microlitic Andesite

EXTENT OF THE STUDIES AND EXPERIMENTAL PROCEDURES

Dry bulk density and effective porosity were determined on five specimens of each outcrop sample and each drill core sample. Measurements were accomplished using a set of techniques recommended by the International Society for Rock Mechanics as "Suggested Method for Porosity/Density Determinations Using Mercury Displacement and Boyle's Law Techniques", (ISRM, 1972). Density and porosity values obtained using these techniques are accurate to within ±1 kg/m³ and ±0.1 porosity percent, respectively.

Absolute permeability was measured on three specimens of the sample A5, five specimens of the sample A9 and five specimens of the sample A19. Measurements were carried out at room conditions using a Core Lab gas permeameter. Dry air and bottled nitrogen were used as permeating fluids. Gas permeability results were corrected to take into account the slippage Klinkenberg effect, thus obtaining equivalent liquid permeability values. Corrections were carried out using the charts recommended by Core Lab. It is estimated that permeability values are accurate to ±5% of the actual permeability.

Bulk compressibility was measured on two specimens of the sample from outcrop site number 1, one specimen of the sample A9 and two specimens of the sample A19. All the specimens were cylindrical, 2.5 cm diameter by 5 cm length, and were tested in dry condition. The specimens were jacketed with teflon tubing to prevent the confining fluid from entering the pore spaces. Hydrostatic stress was applied in the range from 0 to 420 bar and it was cycled at least three times to investigate hysteresis and repeatibility phenomena in the behavior of the rocks. The hydrostatic stress was varied at a uniform rate of about 40 bar/min. The linear compaction along the longitudinal axis of the specimens was continuosly measured as a function of the hydrostatic pressure. To investigate the effects of temperature on compressibility, measurements at 25°C and 250°C were carried out on some specimens.

Compressional and shear wave velocities were measured on a specimen from the sampling site number 7. The specimen, 5 cm diameter by 5 cm legth, was tested in dry and water-saturated conditions, and in both cases it was subjected to uniaxial compressive stress along its longitudinal axis. Starting at 25 bar, the stress was increased in 25 bar steps up to 150 bar. Wave-velocity measurements were carried out at every stress level in the direction of the longitudinal axis of the specimen. The testing temperature was 25°C. The velocities were measured with the pulse first-arrival technique, in which the time required for an elastic wave pulse to traverse a sample of known length is determined. The apparatus and the technique used have been described by King (1970). The accuracy of the velocity measurements is ±0.4%.

Electrical resistivity was measured on a specimen, 5 cm diameter by 5 cm length, from the sampling site number 7. The specimen was saturated using brines of two different concentrations. The testing temperature was 20°C. The specimen was subjected to four hydrostatic stress levels in the range from 7 bar to 100 bar. The electrical resistivity was measured at every stress level and for each of the saturating conditions as a function of frequency in the range 10 Hz to 100 KHz. The experimental method used is the two-electrode technique as it has been described by King (1977) and by Pandit and King (1979).

Thermal conductivity and diffusivity were measured on a specimen, 5 cm diameter by 10 cm length, of the drill core sample A19. Conductivity was measured at 25°C, 150°C and 250°C on the dry specimen subjected to 80 bar confining pressure. The technique used is the transient line heat source method as described by Woodside and Messmer (1961). Conductivity values determined with this technique are accurate to within ±5%. Diffusivity was only measured at 250°C. The technique used is based upon a classical heat transfer model presented by Carslaw and Jaeger (1959), which allows determinations to be carried out with an accuracy of ±5%.

Linear thermal expansion was measured on a specimen, 2.5 cm diameter by 5 cm length, from sampling site number 1. The specimen was subjected to a 50 bar confining pressure and was jacketed with teflon tubing to prevent the confining fluid from entering the pore spaces. Temperature was increased from 20°C to 280°C at a uniform rate of 1.5°C/min. The linear thermal expansion was continuosly measured along the longitudinal axis of the specimen as a function of temperature. The overall accuracy of the measurements is ±5%.

RESULTS AND DISCUSSION

Table 2 shows the density and porosity results. The reported figures are the mean values of the individual determinations carried out on five specimens of each sample. The standard deviation of the individual determinations is also indicated in Table 2.

Fig. 2 shows the relationship between the mean values of the porosity and density results, along with a density-porosity correlation for Cerro Prieto sandstones reported by Contreras (1983), which is presented here for comparison purposes. The Cerro Prieto rocks data shows an excellent linear correlation. On the basis of the conceptual relations between porosities and densities of rocks, this correlation can be interpreted as indicating that Cerro Prieto sandstones feature uniform grain density and non-isolated porosity. On the other hand, the Los Azufres rocks data disperses significantly from the linear correlation defined by its best fit line, although a general trend of correlation is observed. The deviations from the linear correlation probably are a cosequence of isolated porosity and variations in grain density in the Los Azufres rocks.

Table 2. Results of Dry Bulk Density and Effective Porosity Measurements

	Density (gr/cm^3)		Porosity (%)	
	Mean Value	Std. Dev	Mean Value	Std. Dev
1	2.67	0.03	1.8	0.3
2	2.46	0.02	9.3	1.0
3	2.83	0.03	2.6	0.4
4	2.25	0.01	8.0	0.9
5	1.53	0.02	20.5	1.5
6	2.05	0.01	8.7	1.1
7	2.65	0.02	1.7	0.3
8	2.25	0.03	3.5	0.4
A1	2.72	0.01	2.1	0.4
A5	2.40	0.02	12.0	1.2
A9	2.66	0.03	3.2	0.3
A19	2.31	0.03	16.8	1.2

Table 3 shows the results of the permeability measurements. Regardless of their medium to high porosities, the specimens of the samples A5 and A19 gave low permeability values. For most of the Cerro Prieto sandstones of comparable porosities, permeabilities are two to three orders of magnitude higher, which suggests poor pore conectivity in the Los Azufres rocks. The specimens of the low-porosity sample A9 also gave low permeabilities, excepting the specimen A9-3 for which the measured permeability was unexpectedly high. Close examination of this specimen shown a microfracture from one side to another along the direction of the applied flow, thus explaining the higher permeability and illustrating the relative importance that pores and fractures may have in the process of fluid conduction through a fractured rock mass.

Table 3. Permeability Results

Specimen	Porosity (%)	Permeability (microdarcy)
A5-1	9	94.0
A5-2	10.2	179.0
A5-3	10.1	181.0
A9-1	2.1	2.8
A9-2	---	< 1.9
A9-3	2.8	2224.0
A9-4	3.1	< 1.9
A9-5	1.0	< 1.9
A19-1	14.7	3.8
A19-2	15.1	41.0
A19-3	15.2	11.0
A19-4	15.2	4.2
A19-5	14.2	< 1.9

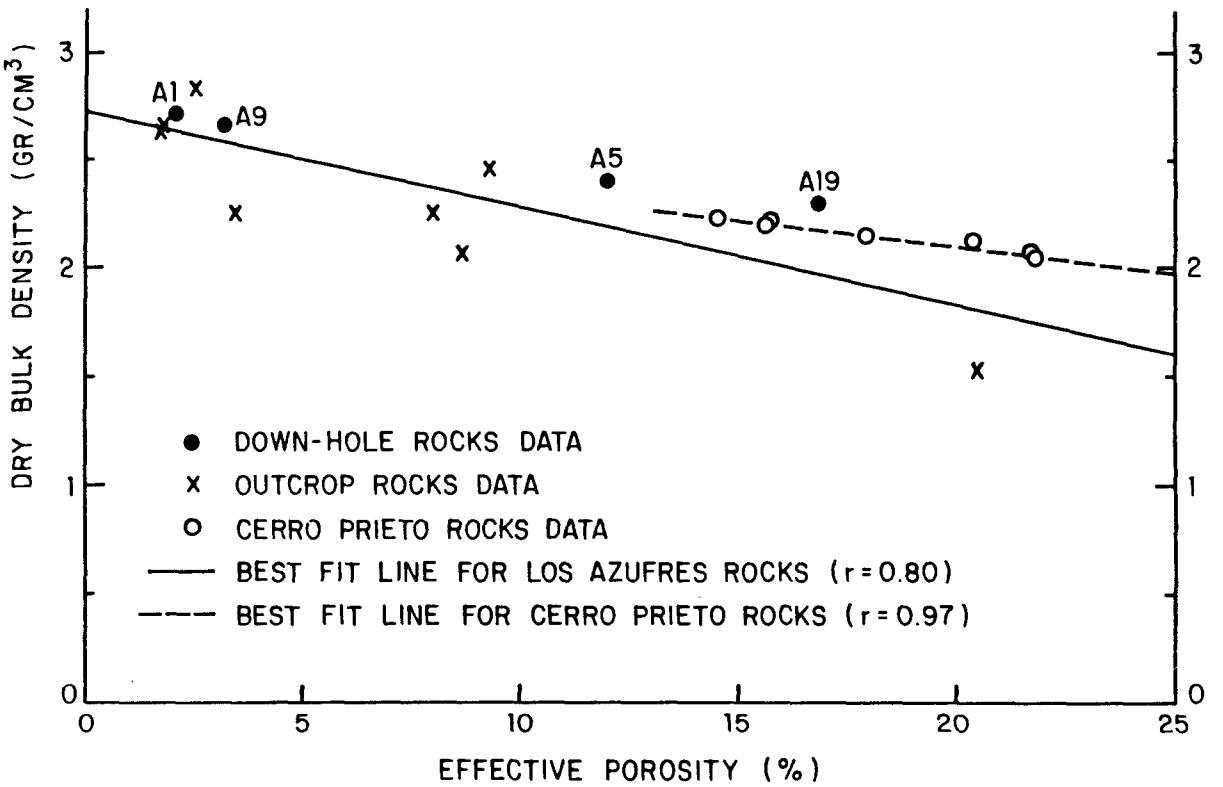

Fig. 2. Relationship between effective porosity and dry bulk density for Los Azufres and Cerro Prieto rocks.

The results of the acoustic velocities are shown in Fig. 3. Compressional and shear wave velocities were observed to increase slighty with increase in axial stress for both the dry rock and the saturated rock. Saturating the specimen resulted in slightly higher compressional-wave velocities and slightly lower shear-wave velocities. The slight effects of the axial stress and the saturation on the acoustic velocities were in agreement with the low porosity of the specimen tested (1.2%).

Compressibility results are shown in Fig. 4, wherein the volumetric bulk compressibility coefficients of the specimens tested are plotted as a function of hydrostatic pressure. The volumetric compressibility coefficients were calculated as three times the corresponding linear compressibility coefficients, which in turn were determined as the slopes of the linear compaction against hydrostatic stress plots. As it was expected, the more porous rocks were also the more compressible. Compressibility decreased with increasing pressure; this effect being more pronounced for the specimens with higher porosity.

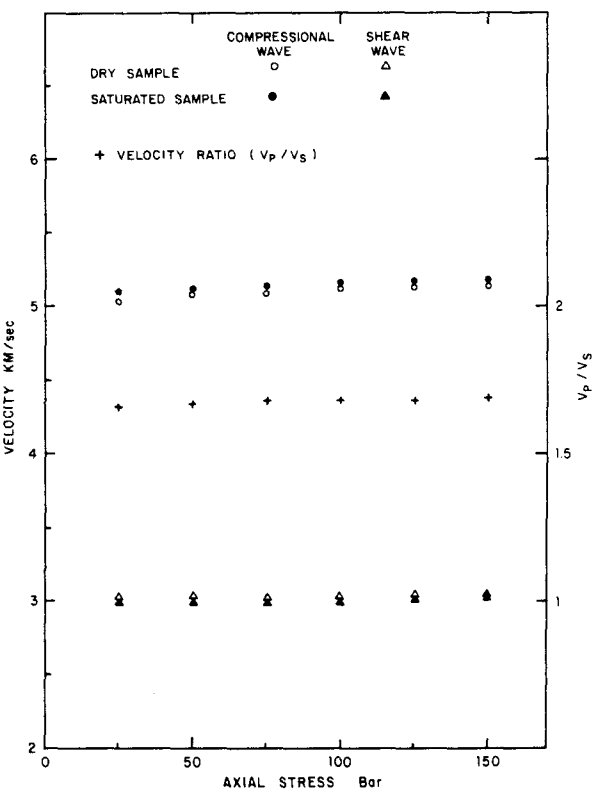

Fig. 3. Compressional and shear-wave velocities as functions of axial stress and saturation for a microlitic andesite specimen from sampling site number 7.

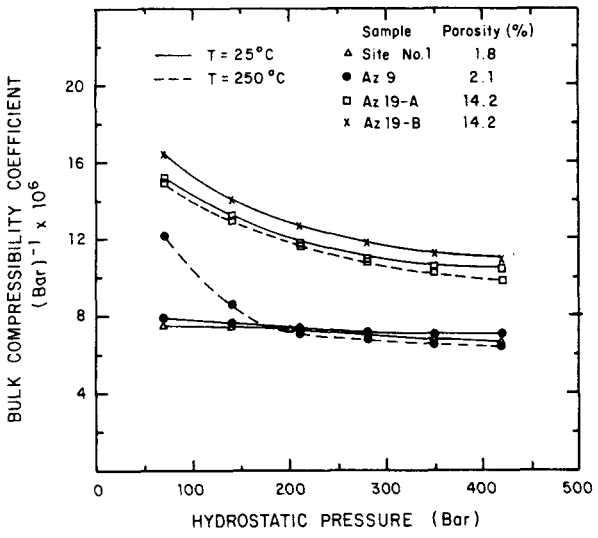

Fig. 4. Bulk compressibility coefficients of the Los Azufres rocks as functions of hydrostatic pressure.

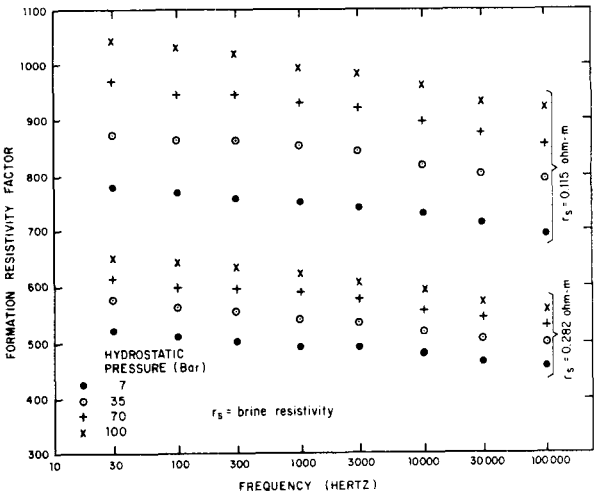

Fig. 5. Resistivity formation factor of a microlitic andesite specimen as function of frequency, hydrostatic pressure and saturating brine resistivity.

For the specimen of the sample A9, increasing the temperature from 25°C to 250°C resulted in higher compressibility only at low pressure values. No temperature effect was observed on a specimen of the sampling site number 1. Regarding the effects of hydrostatic stress cycling, for all of the specimens tested a very repeatable behavior was observed, with no compaction remaining upon completion of the loading-unloading cycles.

However, hysteresis loops were observed in all the cases, more pronouncedly for the more porous rocks.

The electrical resistivity results are shown in Fig. 5, wherein resistivity formation factors calculated from the resistivities measured are plotted as function of frequency. The formation factor exhibits an inverse frequency dependence, which can be interpreted as indicating the existence of a reactive resistivity component caused by either a ionic double layer at charged clay surfaces or mineral metallic components distributed in the rock. A consistent increase in the formation factor with increased hydrostatic pressure was also observed. This can be originated by alterations in the paths through which the electrolytic conduction takes place. Regardless of the low porosity of the specimen tested (1.2%), the effect of pressure on electrical resistivity is remarkable. This phenomenon suggests that even moderate stress variations on the rocks can significantly modify the pores and fractures and originate changes in other related properties such as permeability. The formation factor was also observed to depend upon brine saturant resistivity. This phenomenon is a separate evidence that suggests the ocurrence of electrical conduction through a way different to the electrolytic way. The increase in formation factor with brine resistivity is probably due to the lesser importance of the effect of mineral surface conductivity as the brine saturant resistivity decreased.

Table 4 shows the thermal conductivity and diffusivity results. Conductivity was observed to decrease moderately with increasing temperature. The conductivity values reported here are within the range of the conductivities at 20°C reported by Clark (1966) for a wide variety of igneous rocks (1.6 to 4.0 Watt/m-°C). The specific heat

Table 4. Thermal Properties

Temperature °C	Conductivity Watt/m-°C	Diffusivity cm^2/sec	Specific Heat cal/gr-°C
25	2.00	----	----
150	1.80	----	----
250	1.75	0.66	0.28

value reported in Table 4 was calculated from the conductivity and diffusivity data at 250°C and the dry bulk density at room conditions.

Fig. 6 shows the result of the thermal expansion test. The linear thermal strain measured along the longitudinal axis of the specimen is plotted against temperature. It was observed that the linear thermal expansion coefficient, as given by the slope of the strain against temperature plot, exhibits a significant dependence upon temperature.

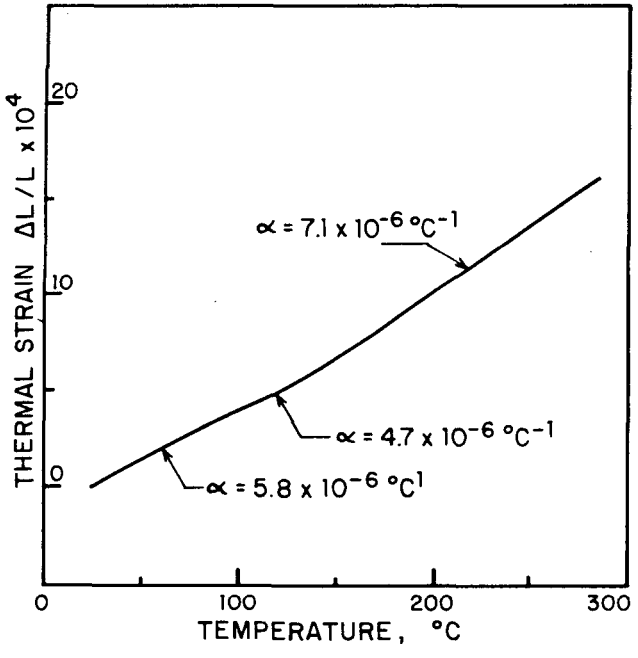

Fig. 6. Linear thermal expansion of a microlitic andesite specimen.

CONCLUSIONS

In this work, the first laboratory-determined data about physical properties of rocks from the Los Azufres geothermal field area has been presented. Due to the limited extent of some of the measurements carried out, no claim can be stated about the representativity of the values reported. However, these results can be useful, at least, as indicators of the orders of magnitude that can be expected for the values of the physical properties of the Los Azufres rocks.

The density, porosity, permeability and compressibility results indicate that the values of the physical properties of the Los Azufres rocks range between wide limits.

It was observed, corroborating similar observations already published elsewhere, that temperature, pressure, saturation as well as other parameters affect most of the physical properties of rocks. Thus, it must be emphasized that to obtain reliable results on specific applications such as interpretation of geophysical data, well logs and pressure tests, it is necessary that the required data about rock properties be obtained from tests on local rocks, and that measurements be carried out on samples subjected to in-situ conditions.

ACKNOWLEDGEMENTS

We thank Profs. W. H. Somerton and M. S. King, with the Department of Mechanical Engineering of the University of California at Berkeley, for allowing us to use some of their sophisticated equipment and for technical support in carrying out the electrical resistivity and acoustic wave velocity measurements.

REFERENCES

Carslaw, H. S. and Jaeger J. C. (1959), "Conduction of Heat in Solids". Second Edition; Clarendon Press, Oxford, England. pp 200-201.

Clark, S. P. (1966), in "Handbook of Physical Constants", Section 21. The Geological Society of America Memoir 97.

Contreras, E. (1983), "Estudio y Determinación de Propiedades Físicas de Rocas". Instituto de Investigaciones Eléctricas (México), Informe IIE/10/11/1663/FE-G29/I 03/P, pp. 83-89.

ISRM (1972), "Suggested Methods for Determining Water Content, Porosity, Density, Absorption and Other Related Properties". Commission on Standardization of Laboratory and Field Tests Document No. 2. Lisbon, Portugal.

King, M. S. (1970), "Static and Dynamic Elastic Moduli of Rocks Under Pressure". Proceedings, 11th Symposium on Rock Mechanics; Berkeley, Calif. pp. 329-351.

Pandit, B. I. and King, M. S. (1979). "A Study of the Effects of Pore-Water Salinity on Physical Properties of Sedimentary Rocks at Permafrost Temperatures". Canadian Journal of Earth Sciences, Vol 14, pp. 1566-1580.

Woodside, W. and Messmer, J. H. (1961), "Thermal Conductivity of Porous Media, I: Unconsolidated Sands; II: Consolidated Rocks". Journal of Applied Physics, Vol. 32, No. 9, pp. 1688-1699 and 1699-1706.

PROCEEDINGS, Eleventh Workshop on Geothermal Reservoir Engineering
Stanford University, Stanford, California, January 21-23, 1986
SGP-TR-93

PRESSURE TESTING OF A HIGH TEMPERATURE NATURALLY FRACTURED RESERVOIR

SHARAD KELKAR, GEORGE ZYVOLOSKI, ZORA DASH

Earth and Space Science Division
Los Alamos National Laboratory
Los Alamos, NM 87544

ABSTRACT

Los Alamos National Laboratory has conducted a number of pumping and flow-through tests at the Hot Dry Rock (HDR) test site at Fenton Hill, New Mexico. These tests consisted of injecting fresh water at controlled rates up to 12 BPM (32 ℓ/s) and surface pressures up to 7,000 psi (48 MPa) into the HDR formation at depths from 10,000 - 13,180 feet (3050 -4000 m). The formation is a naturally fractured granite at temperatures of about 250°C. The matrix porosity is <1% and permeability is on the order of 1 nD (10^{-21} m^2). Hence most of the injected fluid is believed to move through fractures. There has been no evidence of fracture breakdown phenomena, and hence it is believed that pre-existing joints in the formation are opened by fluid injection. Water losses during pumping are significant, most likely resulting from flow into secondary fractures intersecting the main fluid conducting paths.

The pressure-time response observed in these tests can be interpreted in terms of non-isothermal, fracture-dominated flow. As the fluid pressure increases from small values to those comparable to fracturing pressures, the formation response changes from linear fracture flow to the highly nonlinear situation where fracture lift off occurs. A numerical heat and mass flow model was used to match the observed pressure response. Good matches were obtained for pressure build up and shut-in data by assigning pressure dependent fracture and leak-off permeabilities.

Introduction: The response of a fracture dominated, non-isothermal system to high injection/falloff pressures is strikingly different from conventional petroleum or geothermal reservoirs. Petroleum reservoirs often behave like media with constant porosity and permeability and isothermal flow. In geothermal reservoirs, although the temperature dependence of fluid properties must be accounted for, the formation can still be treated as having constant porosity and permeability. Non-isothermal injection/ falloff tests at low pressures have been analyzed for geothermal reservoirs (Bodvarsson, Pruess, and O'Sullivan 1985; Cox and Bodvarsson, 1985; Miller, 1980). Isothermal pressure behavior during hydraulic fracturing treatments (Nolte, 1982; Nolte and Smith, 1981) and in-situ stress measurements (Hickman and Zoback, 1981) has also been discussed.

This behavior is in contrast to the case of hot dry rock (HDR) reservoirs at Fenton Hill, New Mexico, where cold water is injected into a hot rock mass at pressures approaching the earth stresses. The pressure behavior of this reservoir can be explained by considering the fluid flow through a small number of fractures. These fractures are inflated as fluid pressure increases, giving rise to a strongly pressure-dependent aperture and conductivity. As the fluid pressure in the fracture approaches the normal earth stress the fracture lifts off and any further fluid injection results in fracture volume increase, giving rise to a nearly constant wellbore pressure. If the well is shut-in after reaching the constant pressure range, a sudden drop in pressure is observed followed by a more gradual decay, resulting from the leak-off of the fluid stored in the wellbore to the formation through fractures.

The two most important formation parameters determined from pressure tests in the Fenton Hill reservoir are the near wellbore impedance and fracturing pressures. The near wellbore impedance at low pressures can be determined from the square-root time portion of the injection data. In a typical test this occurs during early pumping when the transient thermal effects in the wellbore are important. The pressure fall off from the shut-in data can be used to estimate impedance and leak-off permeabilities at higher pressures. Again thermal transient effects are important. Fracturing pressures are obtained from extrapolating the fracture extension pressures to zero flow rate. Although the fracture extension pressures, in principal, are insensitive to thermal transients, the time required to approach fracturing pressures depends on fracture impedance and temperature-dependent fluid properties. Hence, in practical situations

where the pumping times are limited, erroneous results can be obtained unless temperature effects are taken into account.

These considerations have motivated a detailed modeling study of the early time pressure buildup and fall-of data acquired from field tests. In this paper a numerical model of a pressure dependent joint is used for studying its pressure response. The data from a recent pumping test (Expt. 2061) is analyzed, providing a quantitative assessment of the effect of both the pressure-dependent aperture and temperature on reservoir properties.

Description of the Pumping Experiment: Experiment 2061 was carried out by injecting 1.38 million gallons (5.2 million ℓ)of fresh water into the well EE-3A at depths between 12,555' (3827 m) and 13,180' (4017 m). A "thief" zone accepts water at pressures significantly lower than those encountered in the tests, and hence the test interval was isolated using an inflatable packer (Dreesen et al, 1986). The injection rates ranged from 1 bpm (2.7 ℓ/s) to 12 bpm (32 ℓ/s). Water was also injected down the annulus into the thief zone to improve packer performance by lowering the pressure differential across the element. Pre-test and post-test temperature logs were used to identify the fluid outlets. Most of the fluid exited at 13,180' with minor flow exits through 6 other fractures.

The pressure vs time response of the system early in the test is shown by the solid line in Figure 1. This is the data used for history matching. At very early times the response is linear, indicating wellbore storage. At a pressure of about 800 psi (5.5 MPa), the curve deviates from the straight line and pressure increases at a slower rate, indicating flow out of the wellbore into a system with increasingly lower flow impedance. At about 4200 psi (29 MPa), further pumping produced practically no change in the pressure. The pumping was stopped after 45 min., resulting in a sudden drop of 145 psi (1 MPa), followed by a gradual decay.

Description of the Model: Calculations were performed using the 3-D finite element reservoir simulator FEHM (Zyvoloski, 1983). The reservoir was modeled in radial geometry as a wellbore intersecting a horizontal penny shaped fracture with radial flow bounded by a permeable strata. Heat and mass transfer was allowed between the fracture, the wellbore and these strata. The element grid is shown in Figure 2. All of the boundaries are "no flow." Also shown in the figure is a fracture near bottomhole representing the main fluid outlet, as well as an upper zone fracture connected only to the annulus. This upper zone fracture represents the low pressure thief zone, isolated from the test interval by the packer. Fluid flow through the fracture was modeled using the parallel plate law.

$$k = w^2/12 \qquad (1)$$

where k is the permeability, factor, and w is the aperture. The fracture aperture, w, was related to the local pressure using an empirical equation (Zyvoloski, 1985) given by

$$w = w_o \exp(B\Delta P) \qquad (2)$$

where w_o and B are constants determined such that w equals some predetermined value (see Eq. 3) at a fracturing pressure ΔP_f. The form of the aperture law was motivated by the work of Barton et. al. (Barton, 1984), whose data suggest an exponential rise in fracture conductivity with pressure. The exponential relation provides "pressure regulation" by allowing the aperture to open to large values once the pressure reaches a predetermined extension condition. The effect is illustrated in Figure 3, which shows the relationships of aperture and joint permeability with pressure. Since the pumping test is short, the pressure affects only a small region around the wellbore. Thus the formula of Geertsma and de Klerk (Geertsma, 1969) for maximum aperture is used:

$$w_{max} = 2\,(\mu Q R/G)^{.25} = w_o \exp(B\,\Delta P_f) \qquad (3)$$

where μ is the viscosity, Q is the flow rate, R is the fracture radius, and G is the rock shear modulus. Using values appropriate to Fenton Hill and Experiment 2061 ($Q = .00265\ m^3/S$, $R = 5$ m, $G = 2.65 \times 10^{10}$ Pa), we obtain a maximum aperture of 0.0002 m. In addition to the pressure dependence of the joints, it was also necessary to assume pressure dependent leak-off permeabilities in order to match shut-in data.

Results and Discussion: Figure 1 shows the computer model results of the simulation of Exp. 2061, along with the experimental data. The match is very good for both the build up and shut-in. The parameters used to fit the experimental data are shown in Table I. In obtaining the match several interesting facts were uncovered. First, it was impossible to match the sharp leveling off of pressure while pumping without a pressure-dependent aperture. Second, it was necessary to assume pressure-dependent permeabilities orthogonal to the main fracture. Without this assumption, the pressure dropped much faster than the experimental results, as shown in Figure 4. It was also encouraging to note that the same aperture law was needed for both the build-up and shut-in modeling. This means, in contrast to the commonly held belief, that at least for the low pressure

pumping in the new Phase II reservoir at Fenton Hill, it is not necessary to invoke "self propping" in order to explain the observed "soft" shut-in behavior.

Also shown in Figure 1 are the calculated pressures for the case of isothermal flow using the same parameters as those in Table I. Figure 5 shows a match obtained for the isothermal case by adjusting the formation parameters. The parameters needed for the match are given in Table II. Note that the match is not as good as that for the temparature-dependent simulation. While it was not necessary to change the aperture law the maximum permeabilities in the x and y directions were larger by almost an order of magnitude. The discrepency is due to the difference in viscosities of the surface and bottomhole fluids. Thus we have a result similar to that observed for non-isothermal pressure testing in homogeneous reservoirs. The apparent fracture extension pressure for the isothermal case is 10 percent higher than that for the non-isothermal case. Also the slope of the shut-in curve indicates a lower apparent fracture impedance for the non-isothermal case. Future work will be focused on further quantifying these effects and extending them to longer duration tests. The parameters obtained from these simulations will then be used for estimating longterm reservoir behavior.

CONCLUSION

1. The assumption of a pressure dependent aperture law in a reservoir simulator is an effective way to model pressure build-up tests in fractured reservoirs.

2. Pressure dependence of leak-off permeability was necessary to explain shut-in data in a recent Fenton Hill pumping test.

3. Apparent impedance values and ISIP pressures were lower for the non-isothermal analysis than for the isothermal case.

4. Pressure-dependent apertures are necessary to describe pressure behavior of the Fenton Hill reservoir. Simulations indicate that temperature dependent properties must be accounted for.

REFERENCES

1. Barton, N., S. Bandis, and K. Bakhtar, Aug. 1984, "Strength, Deformation, and Conductivity Coupling of Rock Joints," submitted to Int. J. Rock Mech. Min. Sci., August 1984.

2. Bodvarsson, G.S., K. Pruess and M.J. O'Sullivan, April 1985, "Injection and Energy Recovery in Fractured Geothermal Reservoirs," SPEJ.

3. Cox, B.L. and G.S. Bodvarsson, Jan. 1985, "Non-Isothermal Injection Tests in Fractured Reservoirs," 10th Annual Workshop on Geothermal Reservoir Engineering, Stanford University, Stanford, CA.

4. Dash,Z.V. and H.D. Murphy, Aug. 1985, "Estimating Fracture Apertures From Hydraulic Data and Comparison with Theory," Proceedings of the Geothermal Resources Council Annual Meeting, Kailua-Kona, Hawaii.

5. Dreesen, D.S., K.L. Burns, P. Chavez, Z.V. Dash, S. Kelkar, J. Kolar and S.S. Levy, Jan. 1986, "Fracture Detection: Interpretation of Well Logs to Select Packer Seats and Locate Injection Intervals," 11th workshop on Geothermal Reservoir Engineering at Stanford University, CA.

6. Geertsma, J., and F.J. de Klerk, Dec. 1969, "A Rapid Method of Predicting Width and Extent of Hydraulically Induced Fractures," JPT.

7. Hickman, S.H. and M.D. Zoback, Dec. 1981, "The Interpretation of Hydraulic Fracturing Pressure-Time Data for In-situ Stress Determination," Proceedings of a workshop on Hydraulic Fracturing Stress Measurements, National Academy Press, Washington, DC.

8. Miller, C., Dec. 1980, "Wellbore Storage Effects in Geothermal Wells," SPEJ.

9. Nolte, K.G., May 1982, "Fracture Design Considerations Based on Pressure Analysis," SPE 10911, SPE Cotton Valley Symposium, Tyler, TX.

10. Nolte, K.G. and M.S. Smith, Sept. 1981, "Interpretation of Fracturing Pressures," JPT.

11. Zyvoloski, G., 1983, "Finite Element Methods For Geothermal Reservoir Simulation," Int. J. Num. Analytical Methods in Geomech., V.7.

12. Zyvoloski, G., June 1985, "The Sizing of a Hot Dry Rock Reservoir From a Hydraulic Fracturing Experiment," 26th US Symposium on Rock Mech., Rapid City, S.D.

Table I

Parameters for Non-Isothermal Model

Parameter		Value
Permeability	r-direction	10^{-15} m^2 (max)
	y-direction	10^{-18} m^2 (max)
	joint	10^{-10} m^2 (max)
Porosity	Matrix	.01
	fracture	1.0
Rock Density		2500kg/m^3
Rock Specific Heat		1000J/kg°C
Joint Radius		300m (maximum)
		5m (nominal)
Fracture Width		.0002m (maximum)
Initial Pressure		0.MPa
Initial Temperature	0<y<750m	12.35 -.0956y °C
	750<y<4100m	72.29 + 0.00996y +0.0000105y^2
Injection rate	0<time<46 min	1BPM(2.65 l/s)
	46<time<56min	0.0
w_o		.001
B^o		32.7

Table II

Parameters for Isothermal Model

Parameter		Value
Permeability	r-direction	$5x10^{-15}$ m^2 (max)
	y-direction	$5x10^{-18}$ m^2 (max)
	joint	10^{-10} m^2 (max)
Porosity	Matrix	.01
	fracture	1.0
Rock Density		2500kg/m^3
Rock Specific Heat		1000J/kg°C
Joint Radius		300m (maximum)
		5m (nominal)
Fracture Width		.0002m (maximum)
Initial Pressure		0.MPa
Initial Temperature		12.35°C
Injection Rate	0<time<46 min	1BPM(2.65 l/s)
	46<time<56min	0.0
w_o		.001
B^o		32.7

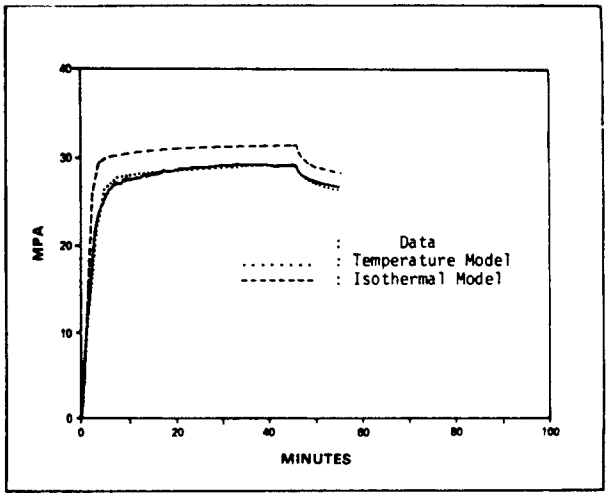

Figure 1. Observed and Model Pressure Response, Expt 2061

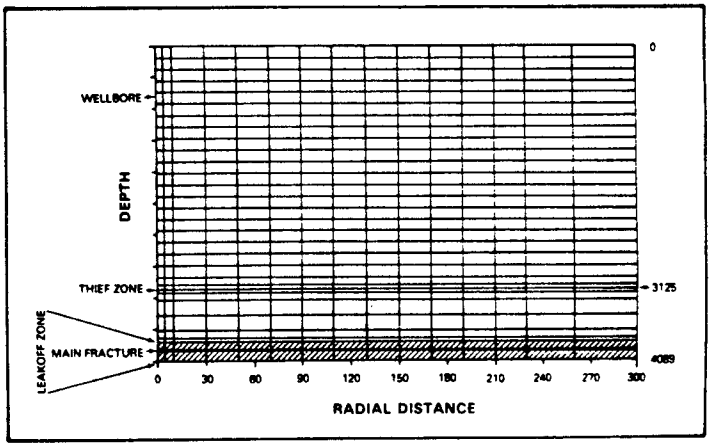

Figure 2. Schematics of the Model and Numerical Grid

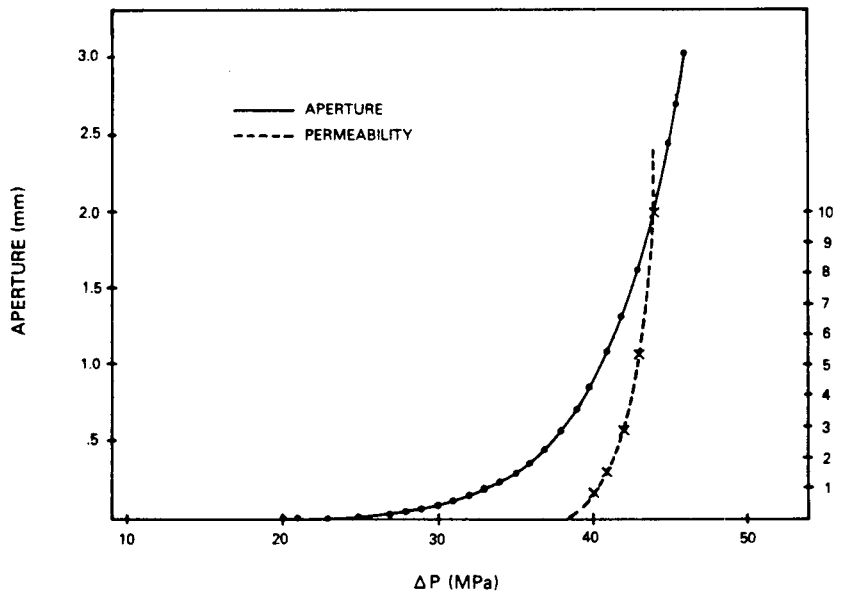

Figure 3. Fracture Apperture and Permeability vs. Pressure Used For Modeling

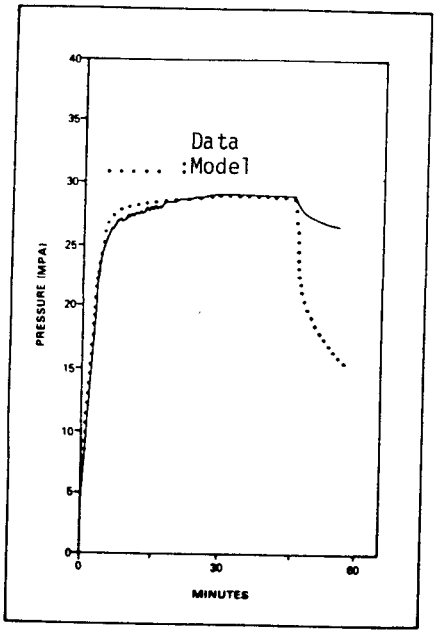

Figure 4. Model Results Using Constant Leakoff Permeability, Compared With Experimental Data.

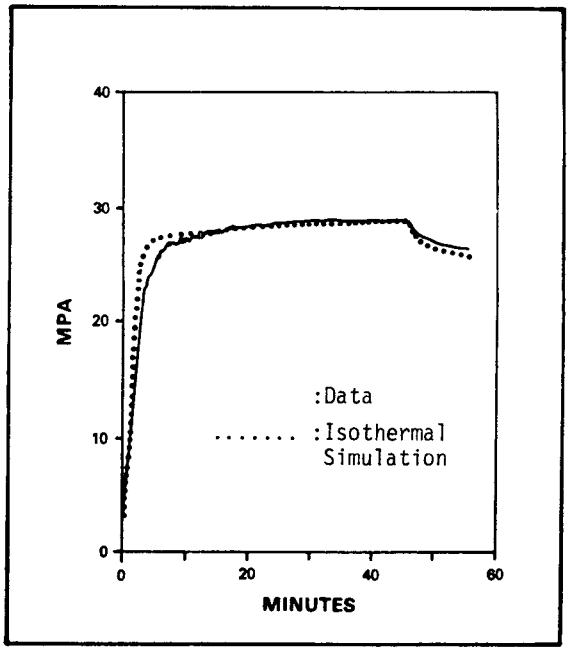

Figure 5. Isothermal Simulation of the Experimental data Using Values From Tabel 2.

PROCEEDINGS, Eleventh Workshop on Geothermal Reservoir Engineering
Stanford University, Stanford, California, January 21-23, 1986
SGP-TR-93

FRACTURE DETECTION AND MAPPING

Norman E. Goldstein and*
*Joseph L. Iovenitti***

*Earth Sciences Division
Lawrence Berkeley Laboratory
University of California
Berkeley, California 94720

**Thermal Power Company
3333 Mendocino Avenue
Santa Rosa, California 95401

Abstract

Because the costs of drilling, completing, and testing a well can be extremely high, it is important to develop better tools and methods for locating high permeability zones prior to drilling, and to develop better tools and methods for identifying and characterizing major fracture zones during the drilling and well testing stages. At the recommendation of the LBL Industry Review Panel on Geothermal Reservoir Technology, we organized and convened a one-day workshop this past July to discuss various aspects of DOE's current and planned activities in fracture detection, to review the geothermal industry's near-term and long-term research needs, to determine the priority of those needs, to disseminate to industry the status of research in progress, and to discuss the possibility of future joint research between industry and DOE. In this paper we present a brief overview of the workshop from the perspective of those who participated in it and provided us with written comments to a questionnaire that was distributed.

INTRODUCTION

In March 1985, the LBL Industry Review Panel on Geothermal Reservoir Technology, discussed last year by Gulati and Lippmann (1985), reconvened to review the status of the DOE Geothermal Technology Division's (DOE/GTD) Reservoir Technology Program. Among the Panel's recommendations was that DOE contractors and industry organize and hold a number of informal one-day workshops on specific topics as a timely way of transferring information on current research being sponsored by DOE/GTD. The authors were asked to organize and convene a workshop on fracture detection and mapping.

The informal workshop, held on 11 July 1985, was attended by around 30 invited scientists and engineers from geothermal companies, consulting and service organizations, DOE/GTD program managers, and DOE contractors (Table 1). Representatives from the different research groups gave brief reports on their work. As is usually the case, some of the invited speakers were unable to attend, and so we were unable to discuss the full range of topics being studied through the auspices of DOE and the USGS. Due to the limited time available, however, it would have been virtually impossible to cover everything properly had everyone attended. We also managed to bring to the workshop speakers whose work is not funded by DOE, but whose expertise is germane to the subject. The workshop agenda is shown in Table 2. Goldstein and Cox (1985) compiled an informal summary report that has been distributed only to the workshop participants, but copies are available through the Earth Sciences Division of LBL.

At the end of the workshop an hour was devoted to general discussions. One of us (JLI) distributed a prepared questionnaire asking the attendees to respond in writing to five questions:

(1) What do you consider the principal research areas? Please prioritize.

(2) What areas of current research should be expanded or contracted? Please explain.

(3) What additional areas of research, not currently being conducted, should be undertaken?

(4) What do you consider potentially viable areas for joint efforts by industry and DOE?

(5) Do you feel that a more in-depth workshop, lasting approximately two days, on selected topics is warranted? If so, what topics should be discussed?

Because only 11 written responses were returned we could not prioritize research needs. Nevertheless, we summarize here some of the key points made to the questionnaire and expressed during the workshop.

PRINCIPAL RESEARCH DIRECTIONS

Opinions expressed in answer to questions 1,2,and 3 usually reflected the individual's background and experiences. The remarks seemed to fall into three major areas of concern:

(1) locating fractures and zones of high permeability *prior* to drilling,

(2) identifying the major permeable zones *during* drilling, and

(3) developing better physical and conceptual models for fractured geothermal reservoirs.

Not mentioned in the questionnaire responses or brought up during the workshop is the topic dealing with the relationship between fracture permeability and large-scale or dominant fluid flow paths within the reservoir region. However, this topic is touched upon in the following discussions.

DISCUSSION

Locating Fractures and Zones of High Permeability Prior to Drilling

Where fluid flow is controlled primarily by fractures, it is vital to target wells to intersect fractures that are well connected and which drain a large volume of rock. This may require an understanding of the nature and controls of fracturing, and which fractures or fracture sets have the major control over fluid flow at reservoir depths.

a. Detailed geological mapping of faults, fracture and joint traces, and volcanogenic features on the ground, supported by air photos, LANDSAT and other airborne imagery, is considered basic to understanding the deformation history of a region. Brought out at the workshop was the point that major lineaments and arcuate traces seen on air photos are quite often related to permeable zones, some of which persist to depth. On the basis of historical water well records, the chances of encountering good aquifers are measurably better for wells sited on or near these features and their intersections. However, surface features may not always extrapolate to reservoir depths. For example, observable rocks may be allochthonous, and/or may have experienced a different cooling and tectonic stress history from those at depth. Some of the uncertainties might be worked out if one had a reasonably accurate model for the thermal/tectonic evolution of the area. In fact, clay-box analog models are still used to develop fracture concepts for structurally complex terranes where elastic theory alone does not suffice.

b. The workshop did not include discussions of geochemical techniques, but references were made to geochemistry in the written responses by several who favor more geochemical research. One area of study related to permeable zones involves the study of certain soil gases (H, ^{3}He, ^{222}Rn, and various noble gases) as indicators of migration paths. On the basis of the current literature a considerable amount of study is being directed to soil-gas anomalies, which the authors often associate with seismic activity, fractured rocks, and the storage and release of volatiles from crustal or mantle sources.

c. Further advances in the use of surface geophysical techniques for fracture mapping are possible. While it is still debated whether geothermal systems emit measurable seismic energy due to thermal stress cracking, many geothermal fields are reported to have higher levels of seismic noise. Most occur in tectonically active areas where the detailed study of the seismicity may provide information on the location and style of brittle deformation, including the deviatoric stress directions. Lew Katz discussed the correlation between seismic emission anomalies and several geothermal areas in Nevada, pointing out that emission anomalies often correlate with known cross faults (Katz, 1984). In contrast, The Geysers field shows unusual seismic behavior. Previously aseismic areas within the steam field have become active after production commences, failure occurring on randomly oriented and distributed faults that are uncorrelated to mapped faults (Oppenheimer, 1985).

High attenuation of seismic waves has also been noted at major fault intersections, and there is growing evidence that stress-aligned, water-filled microcracks are the cause of seismic anisotropy. This feature is observed as the splitting of shear waves into components with different polarizations and different group velocities (Crampin, 1978). Some of the best evidence for this effect has come from Vertical Seismic Profiling (VSP) in wells using a clamped 3-component borehole geophone and directional shear-wave sources at the surface. Majer et al.(1985) have used this approach to determine the dominant direction of fractures at The Geysers geothermal field with apparent success.

An alignment of water-filled fractures should also produce an electrical anisotropy. Where observed at geothermal fields, electrical anisotropy has been explained as the effect of stronger ionic conduction in the direction of the dominant open fractures (Stagalino et al., 1982). Interestingly, concurrent investigations of both electrical and seismic anisotropy have not yet been carried out in a fracture dominated environment to see how well both parameters agree, and whether they correctly indicate the principal flow direction.

One of the simpler and more interesting geophysical methods for detecting fluid flow in major fractures is self-potential. Several workshop attendees endorsed further studies related to the electrokinetic SP effect, including more SP surveys at thermal and non-thermal areas.

It was generally agreed that conventional surface geophysics (active seismic, gravity, and electrical-electromagnetic) is capable of resolving many major fault zones (macrofractures), but the same techniques would not resolve discrete fracture zones at reservoir depths due to the small target dimensions, and interference from surface and deeper sources of geologic noise. Individual, subhorizontal permeable zones such as cataclastic rocks (e.g.,tectonic breccias), rubbly flow tops, and well-jointed flows would be hard to detect unless the zones were thick, continuous, and shallow. Subvertical to vertical permeable zones such as breccia pipes and fractured zones at intersecting faults would also be undetectable unless they approach the surface or have a small depth-to-diameter ratio.

d. Detailed case studies of fractured geothermal systems, including fossil hydrothermal systems, are considered very important for characterizing the type(s) of fracture system(s) and for understanding the interrelationships between fracture parameters and hydraulic processes. Case study reports are appearing for studies made in the U.S., Canada, Sweden, and other countries that are evaluating sites for the geologic disposal of nuclear waste. Some of the information may be directly applicable to geothermal systems, but there are enough basic geologic differences that the waste-site studies will not supplant case studies of fractured geothermal hydrothermal systems. Presently, the only fractured reservoir for which there is adequate published information is the Redondo Creek area of the Valles Caldera, New Mexico, discussed by Dennis Nielson at the workshop.

Case studies must have complete geologic, geochemical and geophysical information, including the signatures of upflow and discharge zones. Geochemical studies of veins and fracture minerals may provide information on the time-temperature-pressure history of the flow system. Geologic studies are needed to determine the age of the fractures and their relation to the mechanical and thermal stress history of the area.

Identification and Location of Major Permeable Zones During Drilling

Under certain drilling situations identification of major permeable zones has not been straightforward. Properly locating such zones during drilling can be critical to, among other things, setting of production casing, avoiding wasteful and futile attempts to test production from the wrong zone, and deciding whether a hole should be completed. Because most holes are drilled vertically they are not optimally oriented to intersect open fractures, most of which are likely to be subvertical to vertical at reservoir depths. It would be desirable to have tools and methods to detect a nearby fracture zone so that a deviated wellbore leg can be drilled while the rig is still on the hole.

a. Only slight mention of well-logging techniques was made at the workshop. It is fairly common knowledge that these techniques have been evaluated for fracture detection under controlled test conditions at a number of crystalline rock sites (Paillet, 1981; Hearst and Nelson, 1985; Jones et al., 1985, among others). The multi-arm caliper, borehole televiewer (BHT) and other acoustic tools, the dipmeter and other resistivity tools, and the neutron (porosity) log are all effective for locating fractures. The BHT and dipmeter give fracture orientation. No log has been conclusively shown to be effective for aperture or hydraulic parameters, and only the BHT will resolve vertical fractures (Paillet, 1981). Because the most interesting fractures admit hot fluids into the wellbore, a combination of self-potential, temperature, and spinner logs (the latter if the well can be made to flow) are considered very valuable. To this list one might add natural γ-ray if the circulating groundwater picked up trace amounts of Rn.

The problems and practical limitations of borehole logging in geothermal environments have been discussed in the recent literature by several authors. One such case study, presented by Al Waibel at the workshop, dealt with a layered volcanic sequence for which there was very poor correlation between the various techniques that one uses to identify fractures and fluid entries. Lost circulation zones were encountered in lava flows, sills or dikes, and welded tuffs. However, none of these zones were indicated on temperature profiles or on other geophysical logs.

In spite of these problems, borehole logs are an important component of any field case study, and the development and testing of improved tools to withstand temperatures higher than 200 to 250 °C needs to be continued. Distinct from determining fracture location, density and orientation, the estimation of hydraulic parameters of individual fractures or fracture zones from well logs has also received serious attention. The results have usually been disappointing. However, in a field test at a non-thermal area a linear relation was found between neutron log response and the logarithm of hydraulic conductivity for the fractured granite (Jones et al.,1985).

b. An estimate of hydraulic conductivity or permeability of a specific interval in a hole is commonly done by means of pressure tests using a single-hole straddle-packer and/or drillstem device. The limitations with these methods are that the results pertain only to the immediate vicinity of the borehole, and in a direction more or less perpendicular to the hole (Hsieh et al., 1983). Moreover, conventional pressure transient methods suffer from problems of non-uniqueness of the pressure decay curves when multiple fractures with variable apertures and lengths intersect the hole and the need for high resolution of early time data. Discussions were held at the workshop on some novel approaches being studied. Sally Benson talked about nonisothermal well testing, thermal front tracking, and turbulent flow analysis. Paul Kasameyer described the tidal strain technique for obtaining the dominant direction of fractures intersecting the borehole (Hanson and Owen, 1982).

c. Surface-to-borehole geophysics has some promising aspects. The workshop attendees were particularly impressed by the VSP approach, and also thought that the tidal strain and electrical methods, as described by Craig Beasley (Beasley and Ward, 1985), might have application. Among the surface-to-borehole geophysical methods one might also include seismic monitoring during a large-volume hydrofracture. Leigh House described one such study conducted at Fenton Hill where the cloud of induced microearthquakes mapped the path of fluid invasion.

d. Although electromagnetic(EM) and acoustic borehole and crosshole techniques are being evaluated for their ability to detect a major proximal fracture not intersected by the hole, there remain a number of engineering problems regarding transmitter design and signal recognition. Pulsed acoustic and EM sources that are directional, steerable, and will work in the confines of a well have been designed and tested to a limited degree, but not to the extent of commercialization and not for use in geothermal environments.

e. A few replies mentioned the need for additional studies of geochemical, mineralogic, and physical property variations encountered in geothermal systems. This information is needed to calibrate and interpret information from surface and borehole investigations, and to understand the past and present temperatures, pressures, and water-rock reactions. The best studied geothermal systems exhibit zonation in major and trace element geochemistry, mineralogy, and physical properties that are mainly a function of temperature, hydrothermal circulation and chemical reactions, boiling, and the mixing of non-thermal waters. It should be possible to reconstruct from the zonation patterns a picture of the fluid circulation system, resolving zones of upflow, mixing, and discharge.

f. Although a discussion of geochemical tracers was not presented at the workshop, two respondents felt that multi-well tests, that include the use of tracers, was needed to study the dominant flow paths in deep (7,000 to 10,000 feet) fractured reservoirs. Tracers will be covered during the one-day workshop on "Chemical Aspects of Injection", scheduled for 24 January 1986 at Stanford University.

Development of Better Conceptual Models for Fractured Reservoir Rocks

Conceptual models for fractured systems were touched upon at the workshop, and the subject was again mentioned by two respondents. Rephrased as a question, a problem statement would go as follows. "Is it possible to characterize the fracture systems of geothermal reservoirs, and if so do the characteristics fall into specific types that would be useful in locating drilling targets and aiding in reservoir modeling"? For the purposes of history matching production data and estimating pressure declines, the reservoir engineer's conceptual model for the fracture system need not be geologically and hydraulically accurate. Such accuracy is not required by the physics because of the volume averaging effects and the diffusive nature of the processes. On the other hand, the geologist is required to develop as quickly as possible a physically realistic model of the fracture system based on woefully incomplete data. Even where good data are available, the best conceptual models are likely to be inadequate. There are several reasons for such a statement:

(1) Although many fracture zones are known to persist to depth, fracture orientations that one discerns at the surface will not necessarily be the same at reservoir depths.

(2) Stochastic and discrete models of a fractured region usually do not account for the rare feature with both large extent and large effective aperture that dominates the hydrology, the so-called "superconductor"

(3) Most real fractures do not behave as the idealized opening of fixed aperture between two parallel plates. Normal stresses and fracture fillings, among other factors, cause a tortuosity in the flow channel such that the flow system behaves more as a system of interconnected and braided pipes (Tsang, 1984). This model of fractures would appear to explain several paradoxes that have been reported: (a) why most of the fluid entering a borehole often comes from one (or at most a few) fractures, and not necessarily from the zone of highest fracture density; and (b) why the equivalent apertures derived from tracer migration and constant head permeability measurements on a single fracture differ by many orders of magnitude (Abelin et al., 1983). A combination of tortuosity and finite fracture lengths also explains why fluid entries of closely spaced wells often appear uncorrelated when plotted in cross-section, and show little communication when tested.

If we are to have better conceptual models they will have to evolve from many careful studies of fracture systems, active and fossil, thermal and non-thermal, and the development of physical models of bulk fractured rocks. The fracture systems would have to be related to the thermal-tectonic history of the region and to the water-rock geochemistry as well.

JOINT EFFORTS BY INDUSTRY AND DOE

Representatives of geothermal companies at the workshop expressed the thought that there could be more joint research efforts between their companies and DOE contractors. The fact that there have been few joint efforts is viewed as a matter of DOE and its contractors not taking the initiative. The following topics were suggested as possible ones for joint research:

- Sharing of efforts and results for integrated borehole, surface, and surface-to-borehole surveys.
- Closer collaboration on the application of geophysical methods (surface and drillhole), geochemistry and tracer studies.
- Collaboration on a major, multidisciplinary case history study of fractured systems.
- Joint research associated with existing DOE-Industry programs such as the Cascade Drilling Program.
- More active dialogue between DOE-sponsored groups and Industry to discuss and assess technological problems.

FUTURE WORKSHOPS AND SYMPOSIA

There was unanimity on the question of future workshops and symposia. All felt that one day was too little time to cover all that needed to be discussed, and that there should be another session at least two days in duration. Some of the special topics suggested for a future workshop are the following:

- nature of fracture permeability,
- geologic and geochemical studies for well placement,
- post-drilling borehole studies, and
- field case studies that include integrated approaches.

It was also expressed that an expanded workshop also include relevant material being gathered in other geotechnical studies, such as those related to the underground storage of nuclear waste. We are presently looking into the feasibility of holding an extended workshop or symposium.

SUMMARY AND CONCLUSIONS

An informal workshop on Fracture Detection and Mapping was held under the auspices of the LBL Advisory Panel on Geothermal Reservoir Technology and the Geothermal Technology Division of DOE. The main purpose of the workshop was to effect better technology transfer from DOE researchers to the geothermal industry. A questionnaire dealing with current and possible future DOE research and with potential areas for jointly sponsored DOE and industry projects was distributed to the participants. Although only about 25 percent of the participants responded with written comments, it was clear to us that the responses indicated three areas of concern: locating fractures and zones of high permeability prior to drilling; identifying

major permeable zones during drilling; and developing better physical and conceptual models of fractured geothermal reservoirs. The respondents agreed that an extended workshop or symposium is needed, and we are now looking into this suggestion.

ACKNOWLEDGMENTS

This work was supported by the Assistant Secretary for Conservation and Renewable Energy, Office of Renewable Technology, Geothermal Technology Division of the U.S. Department of Energy under Contract No. DE-AC03-76SF00098. The authors would like to thank Thomas Doe, Karsten Pruess, and Jane Long for discussions on fractured networks and fracture flow.

REFERENCES

Abelin, H., Gidlund and Neretnieks, I., 1983, Migration experiments in a single fracture in the Stripa granite: Preliminary results, in *Proceedings of the Workshop on Geological Disposal of Radioactive Waste in Situ Experiment in Granite, Stockholm, Sweden,* pp. 154-163, Organisation for Economic Co-Operation and Development, Paris, 1983.

Beasley, C.W. and Ward, S.H., 1985, Three-dimensional mise-á-la-masse modeling applied to mapping fracture zones: Earth Sci. Lab., Univ. Utah Res. Inst., DOE/SAN/12196-3, ESL-143, 108.

Crampin, S.S, 1978, Seismic wave propagation through a cracked solid: polarization as a possible dilatancy diagnostic: Geophys. J. Roy. Astron. Soc., 53, 467-496.

Goldstein, N.E. and Cox, L., 1985, Fracture detection and mapping workshop: Minutes of the informal workshop, Lawrence Berkeley Laboratory, Earth Sciences Division.

Gulati, M.S. and Lippmann, M.J., 1985, Recommendations of the Industry Advisory Panel on Geothermal Reservoir Definition: Proc., 10th Workshop on Geothermal Engineering, Stanford Univ., SGP-TR-84, 5-11.

Hanson, J.M. and Owen, L.B., 1982, Fracture orientation analysis by the solid earth tidal strain method: Soc. Petrol. Eng., Paper SPE-11070, presented at the 57th Annual Fall Technical Conference and Exhibition, New Orleans, 18 p.

Hearst, J.R. and Nelson, P.H., 1985, Well logging for physical properties: McGraw-Hill, New York, 571 p. (see chapter 14, 451-471).

Hsieh, P.A., Neuman, S.P. and Simpson, E.S., 1983, Pressure testing of fractured rocks -- a methodology employing three-dimensional cross-hole tests: Department of Hydrology and Water Resources, Univ. Ariz., Tucson, NUREG/CR-3213, 176 p.

Jones, J.W., Simpson, E.S., Neuman, S.P. and Keys, W.S., 1985, Field and theoretical investigations of fractured crystalline rock near Oracle, Arizona: Department of Hydrology and Water Resources, Univ. Arizona, Tucson, NUREG/CR-3736, 104p.

Katz, L.J., 1984, Seismic emissions surveys: Geoth. Resour. Counc., Trans., 8, 505-510.

Majer, E.L., McEvilly, T.V., Eastwood, F., and Myer, L., 1985, Fracture detection using P- and S-wave VSP's at The Geysers geothermal field: Lawrence Berkeley Laboratory, submitted to Geophysics.

Oppenheimer, D., 1985, Induced seismicity mechanism at The Geysers, California: Geotherm. Gesources Coun., Trans., 9, pt. 2, 41-44.

Paillet, F.L., 1981, A comparison of fracture characterization techniques applied to near-vertical fractures in a limestone reservoir, Proc. Soc. Prof. Well Log Analysts, 22nd Logging Symposium, paper xx.

Stagalino, G., Aumento, F., Al Marsi, A. and Noaman, T., 1982, The circular vertical soundings method applied to the exploration of the Dhamar-Rada'a (Y.A.R.) Geothermal area: Geotherm. Resour. Council, Trans., 6, 169-172. Tsang, Y.W., 1984, The effect of tortuosity on fluid flow through a single fracture: Water Resour. Res., 20, 1209-1215.

TABLE 1

ATTENDEE LIST
FRACTURE WORKSHOP
11 July 1985
Lawrence Berkeley Laboratory

Name	Affiliation
Craig Beasley	UURI
Sally Benson	LBL
Bill Berge	Grace Geothermal
John Henry Beyer	Consultant
Jim Combs	Geothermal Resources Intl., Inc.
Lea Cox	LBL
William Dailey	LLNL
Mel Erskine	Consultant
David D. Faulder	Chevron Geothermal Co. of Calif.
Norman Goldstein	LBL
Leigh House	LANL
Gerry Huttrer	Geothermal Systems
Joe Iovenitti	Thermal Power Co.
Paul Kasameyer	LLNL
Lewis Katz	Utah Geophysical
Art Lange	Albireo Ltd.
Ki Ha Lee	LBL
Marceló Lippmann	LBL
David Long	Grad. Student with Al Waibel
Ernie Majer	LBL
Glenn Melosh	Unocal-Geothermal
Larry Meyer	LBL
Marty Molloy	DOE/SAN
Malcolm Mossman	Santa Fe Geothermal
Robin Newmark	LLNL
Dennis Nielson	UURI
Richard Parizek	Penn State
Dean Pilkington	Steam Reserve
Marshall Reed	DOE/GTD
Susan Spencer	INEL
Al Waibel	Columbia Geoscience

TABLE 2

Agenda
Informal Workshop on
Fracture Detection and Mapping

11 July 1985
Bldg 50A, Fifth Floor Conference Rm
Lawrence Berkeley Laboratory

8:30 AM	
Opening Remarks	Norman Goldstein LBL
	Joe Iovenitti Thermal Power Co.
Fault and Fracture Studies Based on Aerial Photographs	Dick Parizek Penn State
Fault and Fracture Mapping Based on Enhanced LANDSAT Imagery	Mel Erskine Consultant
GEOLOGICAL STUDIES	
Permeability in the Cascade Range	Al Waibel Columbia Geoscience
Predictive Structural Models for the Development of Fracture Permeability in Geothermal Areas	Dennis Nielson UURI
11:00 AM	
SURFACE GEOPHYSICAL STUDIES	
Overview of Surface Geophysics	Norman Goldstein LBL
Seismic Emissions and Microearthquakes	Lewis Katz Utah Geophysical
1:15 PM	
BOREHOLE STUDIES	
Hydrofracture Experiments at Beowawe and Fenton Hill	Leigh House LANL
The Tidal Strain Technique	Paul Kasameyer LLNL
Pressure Transient Detection of Fracture	Sally Benson LBL
Application of Electrical Geophysics to the Detection and Delineation of Fracture Zones	Craig Beasley UURI
Low-Frequency EM Fracture Detection	Ki Ha Lee LBL
Vertical Seismic Profiling	Ernie Majer, Larry Myer LBL
4:30-5:30 PM	
General Discussions	

PROCEEDINGS, Eleventh Workshop on Geothermal Reservoir Engineering
Stanford University, Stanford, California, January 21-23, 1986
SGP-TR-93

REPRESENTATIVE ELEMENT MODELING OF FRACTURE SYSTEMS BASED ON STOCHASTIC ANALYSIS

T. M. Clemo.

Idaho National Engineering Laboratory
Idaho Falls, Idaho, 83415

ABSTRACT

An important task associated with reservoir simulation is the development of a technique to model a large number of fractures with a single description. Representative elements must be developed before reservoir scale simulations can adequately address the effects of intersecting fracture systems on fluid migration. An effective element model will sharply reduce the cost and complexity of large scale simulations to bring these to manageable levels. Stochastic analysis is a powerful tool which can determine the hydraulic and transport characteristics of intersecting sets of statistically defined fractures. Hydraulic and transport characteristics are required to develop representative elements.

Given an assumption of fully developed laminar flow, the net fracture conductivities and hence flow velocities can be determined from descriptive statistics of fracture spacing, orientation, aperture, and extent. The distribution of physical characteristics about their mean leads to a distribution of the associated conductivities. The variance of hydraulic conductivity induces dispersion into the transport process.

The simplest of fracture systems, a single set of parallel fractures, is treated to demonstrate the usefulness of stochastic analysis. Explicit equations for conductivity of an element are developed and the dispersion characteristics are shown. The analysis reveals the dependence of the representative element properties on the various parameters used to describe the fracture system.

NOTATION

a	depth of fracture into the plane of the element
b	fracture aperture
$\bar{b}$	average (expected) aperture
$c(z,t)$	solute concentration as a function of z and t
g	gravitational acceleration
k	hydraulic conductivity
ℓ	length of a fracture
λ_ℓ	expected length of l
λ_z	average spacing of fracture centers in the z direction
μ	absolute viscosity
λ_s	average spacing of fracture centers normal to the fracture faces
$< >$	expectation operator
ln	natural logarithm
$p( )$	probability density function

$$p_{ln}(x) = \frac{1}{(2\pi\sigma_X^2)^{1/2}} \quad \frac{e^{-[\ln(x/\bar{x})]^2/2\sigma_X^2}}{x}$$

where $\bar{x} = e^{(<\ln x>)}$;

σ_X^2 = variance of ln(x)

$$p_e(x) = 1/\lambda_x \quad ^{-x/\lambda_x}$$

where λ_x = mean of x

Q	flow rate
ρ	fluid density
ϕ	pressure
t	time
T	length of the element, in z direction
v	average velocity of fluid in a fracture
W	width of the element, normal to fracture faces
σ^2	variance of ln(b)
z	distance along a fracture

INTRODUCTION

This paper addresses an area of reservoir modeling that has not had significant exposure in the literature. Specifically, the development of representative element models to simulate a small portion of a fracture system. The main thrust of the paper is that, given a statistical description of a fracture system, a large number of fractures can be modeled with a single element. These elements can be combined with other elements and representations of individual fractures to form a reservoir scale simulation of manageable size and cost. A promising technique for deriving the properties of a representative element is the analytical reduction of statistical distributions into expected values. This technique is known as stochastic analysis.

The paper provides a brief background of current research in fractured reservoir modeling, followed by a discussion of what parameters may be needed to characterize a fracture system. The final portion of the paper is an example of using stochastic analysis to model a simple fracture geometry.

BACKGROUND

Modeling of fractured media has been based on two primary approaches, continuum and discrete. These two approaches are briefly discussed below and compared to a third approach which contains elements of both.

The continuum approach is based on a lumped parameter model of the fracture system, where the continuum is composed of representative elements. These elements model the hydraulic and transport behavior of a large number of fractures. For simulations of real fracture systems, the hydraulic and transport properties are determined from a statistical description of the fracture system. A requirement of the elements is that they represent a fracture system that is sufficiently large such that effects of individual fractures can not be distinguished in the response of the model. The scale must be large enough so that the fractured rock can be treated as if it were homogeneous. Consequently, reducing a large number of fractures to a single representation has become an active area of research (Dershowitz 1984).

A homogeneous porous media approximation is the most common method of representing a fracture network as a continuum. A major assumption of the porous media model is that transport dispersion can be modeled as a Gaussian random process using a dispersivity coefficient to determine the variance of transport about the mean movement. Recently a number of studies have called into question the validity of the porous media approximation (Simmons 1982, Dagan 1982, Schwartz et al. 1983).

The discrete approach represents the opposite end of the spectrum. All fractures which are considered relevant are modeled as individual entities. The fractures can be described from knowledge of the individual fractures in the system or be a stochastically generated realization based upon a statistical description of the fracture system. The discrete approach trades the difficulties of determining a representative element for a large amount of information processing required of the model. Presently these requirements limit discrete fracture simulations to reservoirs with few relevant fractures or small portions of a fracture system. Discrete fracture simulations are a promising approach to determining proprieties for representative elements (Dershowitz 1984, Long 1985, Schwartz et al. 1983).

At the Idaho National Engineering Laboratory, a slightly different approach to reservoir scale simulations of fracture systems is in development. The dual permeability approach is a compromise between discrete modeling and continuum modeling. Dual permeability treats the most important fractures in the system discretely and models the rest with representative elements. Furthermore, by incorporating most of the fractures into representative elements, the dual permeability approach can significantly reduce the processing requirement of the simulation. By treating the most important fractures discretely the complexity of the representative element is reduced. The complexity of the elements can be controlled by choosing the level of detail modeled discretely. In many cases the dual permeability approach will allow simulation of reservoirs that are too large for discrete simulation, yet are dominated by a few major fractures or faults making the continuum representation impossible. The fracture system found at the Raft River geothermal field is an example of a system that is highly dominated by a few flow channels and therefore not readily simulated as continuous media. Figure 1 was generated using statistical distributions of fracture spacing based on acoustic televeiwer log data from Raft River (Miller et al., 1984).

Figure 1 is the motivating example for this analysis. In Figure 1 a few large and widely spaced fractures comprise two dominant fracture sets. A third set of small closely spaced fractures completes the flow net. The first observation to be made from Figure 1 is the sparse nature of the large fractures. To model this system with a continuum model would require a much larger representative volume than depicted in the figure. The second observation to note is the large number of small fractures. A discrete

simulation of this system would have to ignore most of these fractures. Unfortunately, these lesser fractures may provide a significant hydraulic connection between the larger fractures.

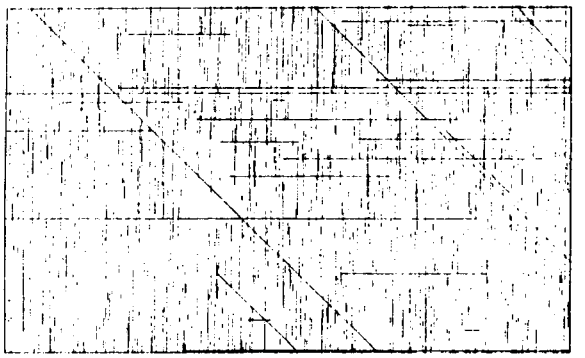

Figure 1: Two-dimensional Representation of a Fracture System. Spacing Acquired from Raft River Data.

The figure provides motivation to develop a two-dimensional representative element for a single set of parallel fractures, the closely spaced set in Figure 1. The representative element must simulate the hydraulic connection provided by this set. It must also simulate the transport dispersion characteristics of the fracture set. One option is to develop type curves based on discrete fracture simulations of various realizations of the fracture set. The geometry of a single parallel set of fractures makes stochastic analysis a viable tool to develop the element models.

Before proceeding with the model development, an aside on complexity is in order. This paper deals with the most simple case which can be studied analytically, a single set of parallel fractures. The next level of complexity involves two fracture sets which intersect. If these sets are such that few intersections occur, then the system is amenable to stochastic analysis. More complex is two fracture sets with frequent intersections. Whether these systems can be solved analytically or must be developed from dual permeability or discrete simulations is not clear. Intersections of multiple sets is probably beyond stochastic analysis. The power of the dual permeability approach will allow these more complex elements to be built up from simpler elements. This paper treats the simplest geometry, keeping a general approach for application to more complex systems.

FRACTURE SYSTEM CHARACTERIZATION

A statistical description of fracture sets comprising the system is required before a representative element model can be developed. This section identifies the parameters that may effect the element properties. A brief review of current statistical models is presented along with the statistical models chosen for this analysis.

Evans (1983) provides an excellent discussion of statistical distributions of fracture parameters. The fracture sets can be described by probability functions of location or spacing, extent or size, fracture aperture, shape, and orientation. Fracture surface characteristics and fracture tortuosity may also be important although these factors are not considered in this development. Fracture shape may be an important factor in developing a representative element. For this treatment however, fractures are assumed to be all of the same depth into the plane of the element.

Evans reports the spacing between fractures found from line samples have been described as lognormal or exponential. Exponential spacing results from a uniform random placement of fractures in space and is assumed for this study. A lognormal distribution would have only a minor impact on the development described below.

The length of fractures is assumed to be distributed as a negative exponential. Lognormal length distribution is also commonly used. The lognormal distribution was investigated but dropped due to the intractability of the resulting equations. Orientation is treated as fixed within the set.

The consequences of different assumptions about aperture characteristics were easily studied. The fracture aperture is assumed variously as a.)constant, b.)lognormal, c.)proportional to length, and d.)lognormally distributed about a mean proportional to length. In the latter assumption the variance of the logarithm of aperture is constant. A lognormal distribution is believed to result from the multiplicative effects of different distributions (Hahn 1967). In this light, given a proportionality of mean aperture and length, a constant variance of the logarithm seems the most appropriate assumption for the aperture.

ELEMENT DEVELOPMENT

As previously mentioned this paper treats a very simple class of representative elements. Specifically the element is a two-dimensional representation of a single set of parallel fractures. The elements are rectangles such that two sides are in the plane of the fracture faces and the other two sides are normal to the fracture faces (Figure 2). The normal sides are treated as constant head boundaries, with the other sides having a no flow condition.

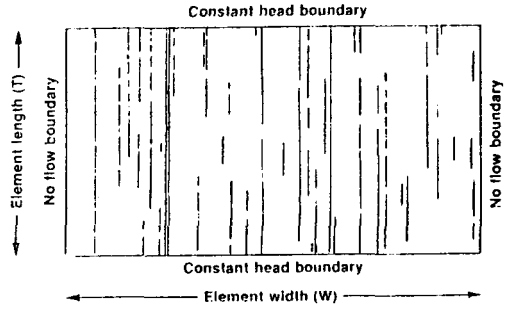

Figure 2: Example Representative Element.

The representative element considered here must simulate pressure response, bulk flow, and transport. Pressure and flow modeling require both a capacitive term to model the pressure response to fluid storage and a conductive term.

Storage is a bulk property determined for the reservoir as a whole. The storage of an individual element is determined by the reservoir storage multiplying the volume represented by the element.

Hydraulic conductivity and fluid transport require more complex analysis than the storage term. The development of these properties and their dependence on the statistical model assumptions are presented in the next two sections.

HYDRAULIC CONDUCTIVITY

Conductivity requires a calculation of the average flow through the element for a unit pressure differential. The parallel fracture system requires only a conductivity between the two fixed head sides. More complicated elements will require a conductivity tenser in two and three dimensions. All fractures that act as a flow path contribute to the conductivity. Limiting the model to laminar flow, the average velocity along a fracture is related to the pressure drop by (Lamb, 1945)

$$v = \frac{\rho g}{12\mu} \; b^2 \; \frac{d\phi}{dz} \qquad (1)$$

The flow is then the cross sectional area of the fracture times the average velocity. For constant depth fractures as is normally assumed in two dimensional models, the flow is proportional to the cube of the fracture aperture as;

$$Q = \frac{\rho g}{12\mu} \; b^3 a \; \frac{d\phi}{dz} \qquad (2)$$

The flow through a fracture connecting both sides of an element of length T is;

$$Q = \frac{\rho g}{12\mu} \; b^3 a \; \frac{\Delta\phi}{T} \qquad (3)$$

The conductivity of the fracture is defined as flow per unit pressure gradient or;

$$k = Q \div \frac{\Delta\phi}{T} = \frac{\rho g}{12\mu} \; b^3 a \qquad (4)$$

If the aperture is independent of all other factors and is lognormally distributed, then the expected conductivity of a fracture is;

$$\langle k \rangle = \int_0^\infty \frac{g}{12\mu} \; b^3 a \; P_{ln}(b) \; db \qquad (5)$$

$$\langle k \rangle = \frac{\rho g}{12\mu} \; \bar{b}^3 d \; e^{9\sigma^2/2} \qquad (6)$$

Equation 6 reveals a strong dependence of the average conductivity upon the variance of the logarithm of aperture.

The length distribution of fractures also affects the element conductivity. Only fractures which connect both sides of the element contribute to flow in this parallel system. Consider fractures with centers, Z, distributed uniformly along the z axis of the element. The fracture will connect the two sides only if the length, ℓ, is such that;

$\ell > 2Z$ if $Z > T/2$ or $\ell > 2(T-Z)$ if $Z < T/2$.

This criteria is symmetric about T/2.

For a negative exponential distribution of fracture length, the distribution function of connecting fractures becomes

$$P(\ell) = \frac{1}{\lambda_z} \; \frac{(\ell - T)}{\lambda_\ell} \; e^{-\ell/\lambda_\ell} \quad \text{for } \ell > T \qquad (7)$$

$$= 0 \quad \text{for } \ell \leq T$$

For fractures with aperture unrelated to length and expected fracture spacing, λ_s, the conductivity of the element is

$$\langle k \rangle = \frac{1}{\lambda_s} \; \frac{g}{12\mu} \; \bar{b}^3 e^{9\sigma^2/2} \; \frac{\lambda_\ell}{\lambda_z} \; e^{-T/\lambda_\ell} \qquad (8)$$

The expression for conductivity in Equation 8 has the units of a material property (i.e. conductivity per unit area normal to the direction of flow). The conductivity of the element is not a material property. It is a measure of the effective hydraulic conductance of a specific element. Equation 8 reveals that the effective conductivity of the element decreases exponentially with separation T due to the exponential length distribution of fractures.

The above assumption that aperture is independent of fracture size is not realistic. The following development assumes that the aperture is a direct function of the length as;

$$b = \alpha \ell \qquad (9)$$

The expected conductivity of an element is

$$\langle k \rangle = \frac{1}{\lambda_s} \; \frac{\rho g}{12\mu} \; \int_T^\infty \alpha^3 \ell^3 \rho(\ell) \; d\ell \qquad (10)$$

$$\langle k \rangle = \frac{1}{\lambda_s} \frac{\rho g}{12\mu} \alpha^3 \frac{\lambda_\ell}{z} [T^3+6T^2\lambda_\ell+18T\lambda_\ell+24\lambda_\ell]e^{-T/\lambda_\ell} \quad (11)$$

Figure 3 presents a comparison of the sensitivity of conductivity to element length, T, for apertures correlated and uncorrelated to fracture length. Figure 3 makes it clear that more attention needs to be payed to mean fracture length if apertures are assumed to be uncorrelated with length.

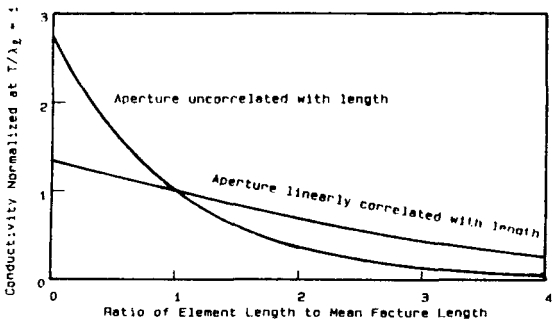

Figure 3: Sensitivity of Conductance to Element Length.

If aperture is related to fracture size by a lognormal distribution where $b = \beta\ell$ and σ^2 = constant

$$P(b:\ell) = \frac{1}{(2\pi\sigma^2)^{1/2}} \frac{e^{-[\ln(b/\beta\ell)]^2/2\sigma^2}}{b} \quad (12)$$

now

$$\langle k \rangle = \frac{1}{\lambda_s} \frac{\rho g}{12\mu} \int_T^\infty \int_o^\infty b^3 p(b:\ell) p(\ell)\, db\, d\ell \quad (13)$$

which is identical to the direct proportionality case with $\alpha = \beta e^{3\sigma^2/2}$

The conductivities developed above are the expected values for elements of width W. It is important to consider the effect of the width of the element on the variance of the conductivity. The variance of the conductivity of the fractures increases proportionately to the expected number of fractures, W/λ_s contained by the element. The variance in the number of fractures represented by the element is also W/λ_s for an exponential spacing of fractures (Parzen 1962). These variances of the element conductivity are independent and therefor additive. The conductivity of the elements also increase linearly with W/λ_s which means the relative variance deceases linearly with the element width.

As mentioned earlier, the conductivity determined in this analysis has the units of a material property but is a measure of the expected conductivity of a specific geometry. The representative element properties are strictly modeling tools and should not be construed as a measure of physical properties.

TRANSPORT

Once fluid enters a fracture in this system, it remains in the fracture until it reaches the end of the element. Consider a pulse of solute entering the element at time zero. Following the development presented by Simmons (1982), the distribution of the expected concentration as a function of time and the distance along the element is:

$$c(z,t) = \int_o^\infty \delta(t-z/v)p(v)dv = p\,(z/t) \quad (14)$$

The distribution (dispersion) of the pulse is simply a scaled version of the velocity profile. To model the element, the time distribution of breakthrough is needed. Replacing Z by T

$$c(T,t) = p(T/t) \quad (15)$$

Using Equation 1,

$$T/t = \frac{\rho g}{12\mu} b^2 \frac{\Delta\phi}{T} \quad (16)$$

$$t = \left(\frac{\rho g}{12\mu}\right)^{-1} \left(\frac{\Delta\phi}{T^2}\right)^{-1} b^{-2} \quad (17)$$

The transit time t is therefore directly related to aperture and

$$p(t)dt = p(b)db \quad (18)$$

From 17,

$$db = 1/2 \left(\frac{\rho g}{12\mu}\right)^{-1/2} \left(\frac{\Delta\phi}{T^2}\right)^{-1/2} t^{-1/2}\, dt \quad (19)$$

Given a lognormal aperture distribution as in the first of the three conductivity calculations.

$$p(t) = \frac{1}{(2\pi\sigma_t^2)^{1/2}} \frac{e^{-[\ln(t/\bar{t})]^2/2\sigma_t^2}}{t} \quad (20)$$

Where;

$$\bar{t} = \frac{\rho g}{12\mu} \frac{\Delta\phi}{T^2} \bar{b}^2 \text{ and } \sigma_t^2 = 4\sigma^2 \quad (21)$$

The transit time for a solute packet can be found using the Monte Carlo technique. The effect of the Poiseuille profiles can be incorporated into a Monte Carlo simulation by dividing the transit time by a generated velocity ratio from the Poiseuille velocity distribution. The distribution function is;

$$P(\gamma) = 1/3 \left(\frac{\gamma}{1-2\gamma/3}\right) \quad (22)$$

Where γ = the ratio of the velocity at a random position in the fracture to the mean velocity.

Equations 23 and 24 present the distribution function for transport given a linear

correlation of aperture and fracture length.

$$P(t) = \frac{1 - \frac{T\alpha}{\kappa t^{\frac{1}{2}}}}{2\alpha^2 \lambda_\ell^2} e^{-\kappa} e^{-t^{\frac{1}{2}}/\alpha\lambda_\ell} \quad (23)$$

Where,

$$\kappa = \left[\frac{\rho g}{12\mu} \frac{\Delta\phi}{T^2}\right]^{\frac{1}{3}} \quad (24)$$

When aperture is lognormally distributed about a fracture length dependent mean, Equation 25 defines the probability distribution of velocities. Equation 25 does not yield a closed form solution and must be evaluated numerically.

$$P(b) = \int_T^\infty P(b:\ell)P(\ell)\, d\ell \quad (25)$$

CONCLUSIONS

The Dual permeability approach to reservoir scale simulation has some important advantages over discrete fracture simulation or the continuum approach. These advantages are embodied in the ability to adjust the degree of complication treated discretely versus the complexity of the representative elements. Further, some reservoirs may be simulated by only a dual permeability model.

The dual permeability approach will provide a more robust simulation capacity because the technique does not require homogeneity of the elements. It will allow the modeler to treat highly important fractures discretely and yet retain full information of the influence of the minor fractures.

The primary research needed to be performed to develop dual permeability modeling, is the development of representative elements. This study involved the simplest of fracture systems to be modeled as a representative element. The study provided a complete description of the hydraulics and transport properties of this class of two dimensional elements. These elements can be used in a dual permeability model which simulates transport of solute as discrete particles.

Even these simple elements can provide a significant reduction in simulation cost. More complicated elements can also be created, although some tough problems need to be addressed. The first hurdle is the description of a fracture intersection, both hydraulically and in terms of transport. Fracture interactions will introduce transition probabilities into the transport equation. Once the simple elements have been described, more complicated elements may be amenable to analytic development. If not, a dual permeability model can be used to empirically find the element properties as is now done to develop continuum models.

ACKNOWLEDGEMENT

This work was performed by EG+G Idaho, Inc. for the U. S. Department of Energy under contract No. DE-AC07-76ID01570.

REFERENCES

Dagan G. (1982), Stochastic modeling of groundwater flow by unconditional and conditional probabilities, Water Resources Research, 18(4), 835-848, 1982.

Dershowitz W. S. (1984), Rock Joint Systems, Ph.D. thesis, MIT., 1984.

Evans D. D. (1983), Unsaturated Flow and Transport Through Fractured Rock - Related to High-Level Waste Repositories, NUREG/CR-3206, University of Arizona, 34-43, 1983

Hahn J.P. (1967), Statistical Models in Engineering, Whiley, 1967.

Lamb H. (1945), Hydrodynamics, Dover, New York, 1945.

Long J. C. S. (1985), Verification and Characterization of Continuum Behavior of Fractured Rock at AECL Underground Research Laboratory. BMI/OCRD-17, LBL-14975. University of California. February, 1984.

Miller J. D., D. W. Allman, D. Wulf, (1984), Raft River Fracture Characterization and Reservoir Simulation, SE-PB-84-58, Idaho National Engineering Laboratory, 1984.

Parzen E. (1962), Stochastic Processes, Holden-Day, Pg. 30, 1962,

Schwartz, F. W., L. Smith, A. S. Crowe (1983). A stochastic analysis of macroscopic dispersion in fractured media. Water Resources Research, 19(5), 1253-1265, 1983

Simmons C. S. (1982). A stochastic-convective transport representation of dispersion in one-dimensional porous media systems, Water Resources Research, 18(4), 1193-1214, 1982.

PROCEEDINGS, Eleventh Workshop on Geothermal Reservoir Engineering
Stanford University, Stanford, California, January 21-23, 1986
SGP-TR-93

DUAL PERMEABILITY MODELING OF FLOW IN A FRACTURED GEOTHERMAL RESERVOIR

John D. Miller and David W. Allman

Idaho National Engineering Laboratory
Idaho Falls, ID 83415

ABSTRACT

A three dimensional fracture system synthesis and flow simulation has been developed to correlate drawdown characteristics measured in a geothermal well and to provide the basis for an analysis of tracer tests. A new dual permeability approach was developed which incorporates simulations at two levels to better represent a discrete fracture system within computer limitations. The first incorporates a discrete simulation of the largest fractures in the system plus distributed or representative element simulation of the smaller fractures. The second determines the representative element properties by discrete simulation of the smaller fractures. The fracture system was synthesized from acoustic televiewer data on the orientation and separation of three distinct fracture sets, together with additional data from the literature. Lognormal and exponential distributions of fracture spacing and radius were studied with the exponential distribution providing more reasonable results. Hydraulic apertures were estimated as a function of distance from the model boundary to a constant head boundary. Mean values of 6.7, 101 and 46 μm were chosen as the most representative values for the three fracture sets. Recommendations are given for the additional fracture characterization needed to reduce the uncertainties in the model.

INTRODUCTION

The objective of the work presented in this paper is to model the flow system in the vicinity of a geothermal well as the basis for a subsequent correlation of measured tracer responses. Data from Raft River Well RRGP-5B was used as the basis for the study. This well was tested in September through November, 1982 as part of a Department of Energy research program on the injection of spent geothermal fluids. A series of drawdown tests were conducted along with a number of injection-backflow tracer tests. This analysis is part of an ongoing effort, incorporating field studies and analytic, physical model and computer simulation, which is directed towards an understanding of the processes controlling the movement of fluids in a geothermal reservoir. The following sections provide a summary of the modeling approach and its computer implementation, the RRGP-5B borehole characterization, fracture system synthesis and flow correlation, and recommendations for further fracture characterization.

MODELING APPROACH

The fluid transport system in a fractured geothermal reservoir is composed of interconnected conduits ranging in scale from major fault zones through large fractures down to microcracks with a minimum aperture for flow of 0.2 μm (Romm, 1966). The challenge presented to the flow modeler is the necessity of explicitly simulating the upper portion of this range within computer memory and run cost limitations. Solute and heat transport present an even larger challenge since the majority of the rock surface for heat transfer and sorption occurs in the smaller end of this flow range. In addition the microcracks smaller than 0.2 μm must be included as the host for the "matrix" diffusion process.

The approach in this work is an extension of earlier work on two-dimensional models by Miller (1983), Clemo (1985), and Hull (1985). The analytic basis for the approach is given by Clemo (1986). Fractures are addressed in three different ranges of size, termed faults, global fractures, and distributed fractures. Faults are classified as those conduits sufficiently large as to provide a trivial head gradient for substantial flows. These elements are represented as constant head boundaries. They may either be deterministically identified from drilling, flow testing or geophysical methods or may be the largest elements of a complete probability distribution, if one could be defined. The global fractures are the next smaller set and are discretely described with properties chosen from probability distributions since they cannot, at this scale, be distributed and they cannot be specifically described. The distributed fractures are the remainder. They are incorporated in a representative element bounded by the global fractures. The properties of this representative element are found from a sub-scale model in which the smaller fractures are described

discretely. To summarize, the complete flow simulation incorporates two models: a large scale model which incorporates the well and the faults as its flow or head boundaries, the large fractures as discrete elements and the smaller fractures as representative or distributed elements. The second model describes the representative element with global fractures omitted and with the next smaller set of fractures modeled discretely. Each of these models is as detailed as possible within computer memory and cost limitations.

The model, of necessity, incorporates a number of approximations. As is common in the discrete fracture analysis and simulation literature, fractures are idealized as circular, parallel sided, planar discs. Real fractures are rough, curved or laterally stepped and are probably not circular due to interference with other fractures. Indeed, some fractures terminate on other fractures (Dershowitz et al., 1985). The model, in addition, neglects the variation of fracture orientation from the mean of each orientation set. The remainder of the geometric approximations have to do with the probability density distributions of spacing, radius and aperture which are discussed in a subsequent section.

Based on the subsequently described acoustic televiewer survey, the RRGP-5B fracture system model consists of a hydrofracture and three differently oriented probabilistic sets of parallel fractures. Each fracture is represented as a circular disc. Figure 1 shows the approach given by Huang and Evans (1985) and adopted for this study: a given fracture intersects another fracture (or the boundary of the model) in a line. The head is assumed constant over the length of the line and is located, for reference, at a node at its midpoint. A flow path exists in a fracture between two lines of intersection. Laminar flow is computed in this path using the cubic law (Lamb, 1945) in which flow varies as the cube of the aperture. The length of the path is the distance between nodes and the width is approximated as the average of the two intersection lengths, without consideration of their orientation. As shown in Figure 1, in a fracture with more than two intersections or nodes, a flow is computed independently between each node and every other node. Consideration of a more sophisticated model is deferred to future studies.

This analysis departs from the Huang and Evans approach in the inclusion of the distributed fracture flow paths. As described previously, the conductivities of these paths are determined from representative element simulations with fractures of global size excluded. Separate representative element simulations are conducted to determine

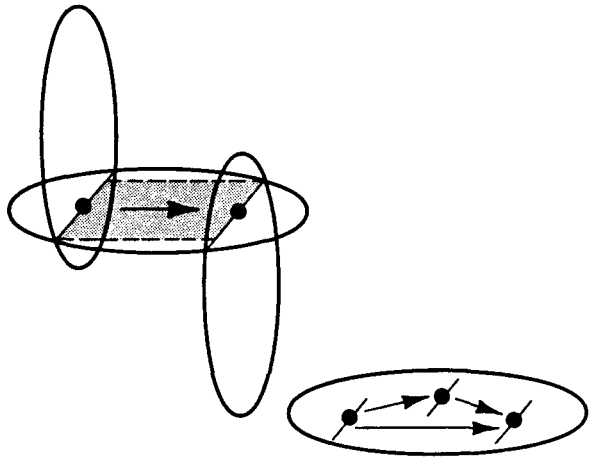

6 0290

Figure 1. Discrete Fracture Flow Paths

the conductivity normal to each of the three fracture sets. A hydraulic gradient is imposed normal to the set being evaluated. The thickness of the representative element model is an important parameter. As shown by Clemo (1986), the conductivity between two planes decreases with increasing separation between those planes because of the reduction in number of cross fractures large enough to directly span them. Thicknesses were chosen equal to the mean separation of the corresponding fracture set in the global model.

Figure 2 shows the computational process. Consider a fracture somewhat smaller than those included in the global model, which bridges two global fractures of a common

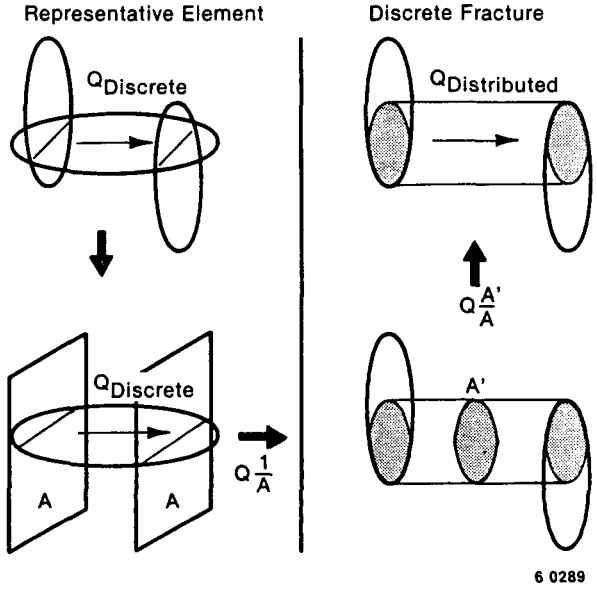

6 0289

Figure 2. Distributed Fracture Flow Paths

set. The contribution of this fracture to the conductivity between the two global fractures is computed discretely and is averaged, in the representative element, over the cross-sectional area of that model. Applying the resultant conductivity over the shadow or overlap area between the two global fractures in the discrete simulation then introduces the requirement that the distributed fracture lie in a region which intercepts both global fractures. The discrete pathway due to the small fracture has been replaced by the conditions that a fracture be long enough to bridge the gap and that it occurs in a suitable lateral position.

The determination of the distributed fracture paths to the hydrofracture is more complex since it is not parallel to any of the fracture sets. A probabilistic fracture is assigned a distributed fracture path to the hydrofracture if it shadows it without shadowing a fracture nearer to the hydrofracture. These calculations are made assuming all fractures parallel the hydrofracture. The path crossection is the area of the entire fracture as projected onto the plane of the hydrofracture and its length and conductivity are computed as before.

In all cases, distributed fracture flow is computed between the average heads for each of the two fractures. It should be noted that this calculation identifies the entire fracture as a pressurized body which receives or provides flow to the number of smaller fractures which intercept it.

COMPUTER IMPLEMENTATION

The conceptual model described above is implemented in a sequence of two codes which are together called FRACSL3D (FRactured media flow and transport - Advanced Continuous Simulation Language, 3D). The first code is initiated with a synthesis of fracture location, orientation and radius. Fracture centers are located, in directions parallel to the fracture plane, randomly throughout the model. As discussed subsequently, two different approaches were used to locate the fracture centers in the third (normal) direction.

After describing the hydrofracture and synthesizing the three probabilistic sets, the distributed fracture paths were found as described in the preceding section. The fracture-to-fracture and fracture-to-boundary intersections were then found using subroutines developed by Huang and Evans (1984). The fracture, distributed fracture path, and intersection information was then output to a data file.

The second code reads the data file and additional data, calculates the fracture paths and solves for the head and flow distributions. This program was developed at the Idaho National Engineering Laboratory as a series of subroutines with supporting routines from the ACSL (Advanced Continuous Simulation Language) problem solver code (Mitchell and Gauthier, 1981).

Apertures, widths, lengths, and conductivities are computed for the various fracture paths. Apertures are assumed to vary linearly with fracture radius with proportionality constants chosen as discussed subsequently. Fixed head or flux boundary conditions may be applied at any node. Alternatively, connection to a remote constant head boundary may be made by specifying the distance to that boundary. The path conductivity is assumed to be equal to the mean for the global fractures within the model.

A first order differential equation is written for the conservation of mass at each node and the steady state flow and head distribution is found by iterating to drive the head derivatives to zero. Both codes are implemented on a CDC CYBER 176 computer with 130,368 decimal words of small core available to the user. The flow code is limited to several hundred nodes while the synthesis code can analyze much larger systems. The total cost of the 13 computer runs providing the reported data was approximately $75. These costs are low enough to permit the multiple realizations necessary for some studies.

RRGP-5B BOREHOLE CHARACTERIZATION

Raft River Well RRGP-5B was completed in metasedimentary quartzite and schist at a depth of 4911 ft. An acoustic televiewer survey was made by the United States Geological Survey for a 495 foot borehole interval prior to well completion. A second survey of the production interval, made after the liner was installed and the well was hydrofractured, showed no new fractures other than the hydrofracture itself. A total of 142 discontinuities were found in the 495 foot pre-completion interval. Figure 3 shows a plot of the cumulative frequency of occurrence vs. separation distance for the region between 4445 and 4695 ft. This region was selected because it is homogeneous in fracture distribution and includes the observed portion of the hydrofracture below the liner and the postulated portion above the bottom of the liner. The data, shown for three orientation sets, are fitted by lognormal distributions. Table 1 summarizes the characteristics of the three fracture sets.

FRACTURE SYSTEM SYNTHESIS

As shown schematically in Figure 4, the model is established by describing the hydrofracture, a model space, and the probabilistic fractures within that space. Based on acoustic televiewer observations

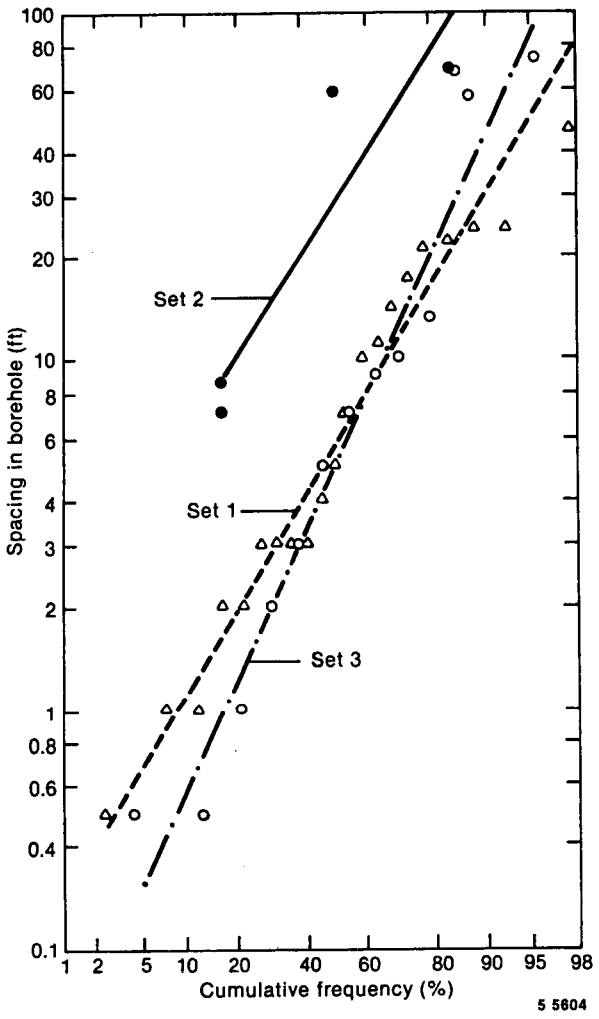

Figure 3. Fracture Spacing

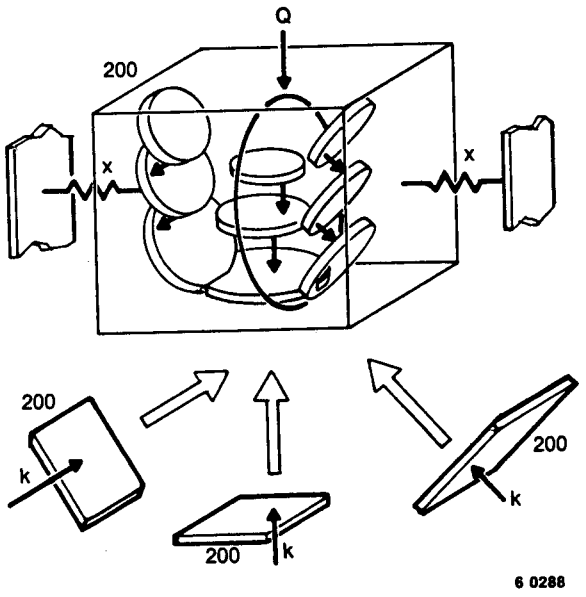

Figure 4. RRGP-5B Model

of the portion of the wellbore below the well liner, the hydrofracture was described as a 100 ft radius circle, centered on the bottom of the liner and oriented in a vertical plane with strike to the north. A cubic model space 200 ft on a side was chosen to surround the hydrofracture and thereby model the distribution of flow from the well through the hydrofracture and into the formation. This volume was centered on the bottom of the wellbore liner and oriented with vertical faces running N-S and E-W.

In the initial synthesis of probabilistic fractures, the spacing between successive members of the same set was based on the lognormal distribution shown in Figure 3 and Table 1. Since this distribution is that of a scanline (borehole) sampling, the spacing between fractures which are located laterally throughout the model region must be considerably smaller. The model separations were adjusted until scanline samplings equalled the measured mean separations.

These results are sensitive to the fracture radius distribution. Since radius distributions are not known for the Raft River fracture system, data on radius-to-spacing ratio from the literature was used. Mahtab et al. (1973) reported trace length, separation and physical apertures for a copper mine in a granite batholith. Three nearly orthogonal fracture sets were found in quartz monzonite and in monzonite porphyry. While the distributions were not fitted by the author, the means were given. The Mahtab et al. trace length means were first multiplied by .635 to provide the expected value of radius. The ratio of mean-radius-to-mean-spacing was found to be 3.16 when averaged over the 6 fracture set-rock type combinations. Gale et al. (1985) reported mean-radius-to-mean-separation values for the Stripa ventilation drift which average 1.15 for the four fracture sets. A value of 2.15 was assumed for the Raft River analysis as the mean of the values from the literature. The distribution, for the first analysis, was assumed to be lognormal.

Fractures were synthesized within a 300 ft. cube centered on and parallel to the model cube. The additional space was provided to extend fractures into the model from centers located outside it. Synthesis and scanline studies were conducted separately for each of the three fracture sets.

In order to reduce the number of nodes to the capability of the flow code, it was necessary to limit the fractures to those larger than 250 ft. radius. Two observations can be made from this result. The first is that the resulting model is unsatisfactory since the extra fracture generating space outside the model only provides for fractures

TABLE 1

WELL RRGP-5B FRACTURE SET CHARACTERISTICS
DEPTHS 4445-4695 ft

Set	Number of Separations	Strike	Dip	Borehole Spacing: Mean of $\log_{10}$ ft	Borehole Spacing: std dev of $\log_{10}$ ft	Mean Normal[1] Spacing ft
1	21	N12W	79E	.753	.539	2.036
2	3	N34E	46E	1.480	.551	30.77
3	12	N18W	20E	.701	.708	14.17

(1) normal spacing = (borehole spacing) (cos dip)

with radii less than 50 feet. The more significant observation is that the synthesized fracture system is dominated, probably excessively so, by large fractures. Reduction of the mean-radius-to-mean-spacing ratio of 2.15 would probably not affect the results significantly since a larger number of fractures would then be required to provide the required scanline spacing.

While the acoustic televiewer spacing data is obviously well fitted by the lognormal characteristic shown in Figure 3 it should be noted that the smaller fractures may not be detected. In the literature as reviewed by Evans (1983), scanline length distributions were best fitted by a lognormal distribution by some researchers while an exponential distribution provided the best fit to data for others. In addition, a power law distribution with probability varying with trace length to an exponent varying between -1.3 and -1.8 was found best by Segall and Pollard (1983). The analysis of fracture permeability at the Stripa ventilation draft by Gale et al. (1985) utilized both lognormal and exponential distributions.

As an alternative, a second analysis was performed for exponential distributions of spacing and radius, again differing by a factor of 2.15. The exponential spacing was provided by randomly locating the fracture centers in the normal direction (Priest and Hudson, 1981). The single parameter in the exponential distribution of the spacing, the mean value, was chosen as the arithmetic mean of the measured spacings. Fractures are located randomly in the three directions until a scanline has accumulated the number of interceptions which provide the required mean spacing. This procedure was modified analytically to avoid treating the very large number of small fractures which would not intercept the scanline. The distribution of radii was limited to the larger values and the mean spacing for the scanline was increased accordingly. After providing for the correct scanline sampling rate, the fractures simulated discretely in the global analysis were limited to those greater than 100 ft radius to provide a manageable global flow model. The three representative elements shown schematically in Figure 4 were then developed using the same distributions. Fracture radii were limited to 100 ft at the maximum and minimums of 27 to 32 ft. Table 2 summarizes the four geometric models. While these calculations would normally be made on the basis of the mean of a number of fracture system realizations, the fracture system statistics are not sufficiently well defined to warrant the refinement.

FLOW CORRELATION

Drawdown tests were conducted at well RRGP-5B at flow rates ranging from 75 to 300 gpm. Steady-state conditions were reached in an average of 235 seconds after the start of drawdown and the well recovered to the initial condition in an average of 130 seconds after the end of production. Figure 5 shows the variation with flow rate of drawdown and recovery heads at steady-state. The drawdown and recovery heads are essentially identical and the mean values rise with increasing flow at a rate greater than linear. The formation characteristics, found by subtracting a calculated wellbore loss, also rises at a greater than linear rate, showing the presence of non-linear or turbulent flow in the formation. A linear formation drawdown was estimated by drawing a tangent to the initial portion of the formation curve.

Predicted drawdowns were found by solving for the flow distributions in the four geometric models previously described. The individual representative element models were used to evalute the conductivity normal to the hydrofracture and fracture sets 2 and 3. Distributed flow between global

TABLE 2

GLOBAL AND REPRESENTATIVE ELEMENT MODELS
EXPONENTIAL DISTRIBUTION OF SPACING AND RADIUS

Model	Fracture[1] Generating Region - ft	Model[1][2] Region - ft	Fracture Radius-ft	# Fractures	# Internal Nodes	# Boundary Nodes	# Discrete Fracture Paths	# Distributed Fracture Paths	Representative Element[4] Conductivity ft/day
Global	600/600/600	200/200/200	above 100	31	64	102	765	14	---
Element[3] 1	400/250/400	200/50/200	32 to 100	33	32	114	294	--	.0472
Element 2	238/400/400	38/200/200	27 to 100	23	20	98	131	--	.0209
Element 3	239/400/400	39/200/200	27 to 100	26	41	98	310	--	.2520

(1) x by y by z

(2) model region centered in fracture generating region

(3) representative element for conductivity normal to hydrofracture

(4) through smallest model dimension; at aperture-to-radius ratio = .5E-5

fractures in set 1 was neglected since these fractures are widely separated. Flow solutions for the three representative element models yielded conductivities for a particular aperture-to-radius value. These conductivities were then incorporated in the global model where a single value of aperture-to-radius ratio was used to adjust the apertures and the conductivity of both representative element fractures and global fractures. The selection of a distance from the model boundary to a remote, fixed-head boundary completes the input set and a flow solution is obtained. Since all component head rises are dependent on the cube of the aperture, system head rises for other values of aperture-to-radius ratio are obtained by a simple ratio.

The contribution of the representative element to the computed drawdown was found by zeroing the representative element conductivities used in the global flow simulation. The drawdown head increased by 9.0%, corresponding to the cube of the ratio of the dominant apertures in the representative element models to those in the global model.

Flow calculations, for both global and representative element models, were based on linear flow between smooth parallel plates. However, the existence of non-linear flow in some of the fracture paths is shown by the non-linear drawdown characteristic given in Figure 5. As summarized by Gale et al. (1985), the onset of non-linear flow has been observed at a Reynolds number of 80 at a relative roughness of 1.0 and at about 100 at a relative roughness of 0.862. The average Reynolds number over the 534 discrete fracture paths in the global model is 10.5, based on a hydraulic diameter equal to twice the aperture. This value is independent of the aperture values for a system otherwise fixed in flow and geometry. True Reynolds numbers, however, range to considerably

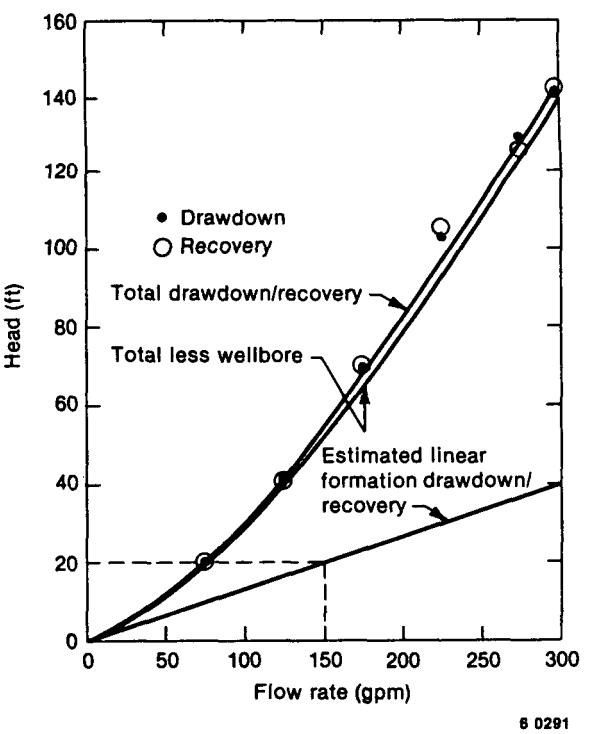

Figure 5. Measured and Linear Drawdown Characteristics

numbers, however, range to considerably higher values because the model may have multiple fracture paths in a given portion of a fracture. Indeed, 120 fracture paths occur in the largest fracture in the system (273 ft radius) and 66 fracture paths occur in the 100 ft radius hydrofracture. Since these tend to be the longest paths in the system, a substantial portion of the flow path may have effective Reynolds numbers greater than one hundred. In the absence of information on fracture roughness, the

analysis was completed by matching values predicted by linear flow relationships to the estimated linear formation drawdown shown in Figure 5.

Figure 6 shows the variation of predicted drawdown head with remote boundary distance and aperture-to-radius ratio for a 150 gpm flow rate. A 100 ft distance was chosen as the best estimate, based partially on the detection, during drilling, of a high transmissivity aquifer at a point near the top of the modeled region. While this does not define the distances to a constant head boundary from the other five faces of the model, the previously discussed 235 second (drawdown) and 130 second (recovery) times tend to confirm the existence of relatively close constant head boundaries. A more precise definition will be provided by work in progress on a fully transient solution. The mean set apertures at the 100 ft remote boundary distance and a 20 ft linear drawdown head are 6.7, 101, and 46 μm for sets 1, 2, and 3, respectively. These values are subject to considerable uncertainty, as to the shape of the spacing and radius distributions, the mean of the radius distribution and the non-linear flow term and may only be accurate to within a factor of three. They may be compared to hydraulic apertures of 6 μm at Stripa (Gale et al., 1985) and 11.8 μm at Chalk River (Raven et al., 1985). In addition to the difference in natural fracture systems, it should be noted that the Raft River fractures may have been opened by the hydraulic stimulation treatment.

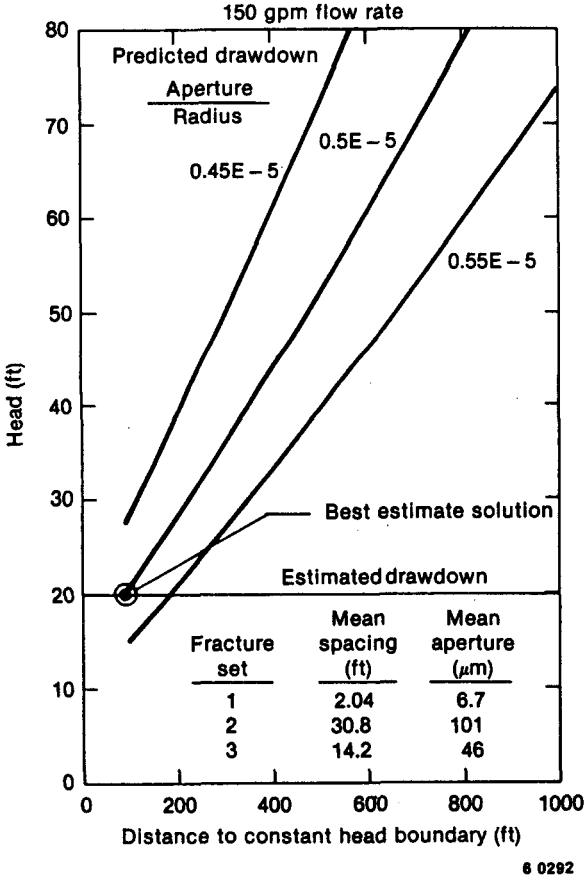

Figure 6. Linear Drawdown Correlation

RECOMMENDED FRACTURE CHARACTERIZATION

A substantial body of work on fracture mapping and characterization has been reported in the interim since this well was completed and tested. Acoustic televiewer data has been complemented by the use of the tube wave device (Paillet and Keys, 1984) which shows the presence of water in a fracture intersecting the wellbore as a discontinuity in an acoustic wave propagated down the borehole. The same authors discuss the use of the heat-pulse flow meter which measures extremely low velocities in the wellbore as a means of detecting fluid bearing fractures. Neutron logging correlated well with conductivity measurements at the Oracle test site in Arizona (Jones et al., 1985) and additional fracture characterization was provided by oriented cores. Doe and Osnes (1985) present methods for determining fracture characteristics from packer testing of individual fractures. The determination of fracture extent, however, may ultimately require other geophysical techniques, such as radar, or the drilling of offset boreholes. Another avenue of approach which may be of benefit in determining fracture extent and fracture distribution in space is the application of existing technology to the description of the structural and hydrothermal processes which created the fracture system. Approaches such as those by Segall and Pollard (1983) and Knapp and Norton (1981) may be developed to correlate borehole characterization data and, in so doing, provide a quantitative description of fracture characteristics not easily obtained from borehole studies.

SUMMARY

A new, dual permeability simulation of fracture system flow has been developed as an effective means of simulating the range of fracture size in a 3D discrete fracture model within the limitations of computer cost and core size. A global model incorporates discrete representations of the larger fractures and a representative element representation of the smaller fractures. The conductivity of the representative element is found by a separate discrete simulation of the smaller fractures. The combined simulation incorporated fractures with radii down to 13.5 to 16 percent of the size of the model. The level of detail and the cost of the simulation are such as to permit, with suitable model extensions, accurate studies of solute transport in fractured geothermal systems.

Definition of the fracture system in this study depended on the form of the distribution of spacing in three-dimensional space and on assumptions as to fracture size distribution. In addition, smaller uncertainties were introduced by the absence of a defined pressure boundary condition and by the presence of non-linear fracture flow. Further information on fracture characteristics will be provided by transient flow simulation and by the addition of a transport model and correlation with measured tracer responses. The uncertainties in these studies can be reduced by more extensive fracture characterization data obtained on the basis of recent advances in packer testing, flow measurement, tube wave and neutron logging and other geophysical methods, and from oriented cores. Further data may ultimately be provided by correlating sampled data with a structural-hydrothermal rationale for the evolution of the fracture system.

This work was funded by the U. S. Department of Energy under Contract No. DE-AC07-76ID01570.

REFERENCES

Clemo, T. M., (1986), Representative Element Modeling of Fracture Systems Based on Stochastic Analysis, Proceedings, Eleventh Workshop on Geothermal Engineering, Stanford University, December 1983, pp 373-379.

Clemo, T. M., (1985), FRACSL Code Development and Correlation of East Mesa Test Results, Proceedings, 10th Workshop on Geothermal Reservoir Engineering, Stanford University, January 1985, pp 287-292.

Dershowitz, W. S., Gordon, B. M. and Kafritsas, J. C., (1985), A New Three-Dimensional Model for Flow in Fractured Rock, Proceedings IAH Symposium on Hydrogeology of Rocks of Low Permeability, Tucson, January 1985, pp 441-448.

Doe, T. W. and Osnes, J. D., (1985), Interpretation of Fracture Geometry from Well Tests, Proceedings, International Symposium on Fundamentals of Rock Joints, Bjorkliden, Sweden, September 15-20, 1985.

Evans, D. D., (1983), Unsaturated Flow and Transport Through Fractured Rock - Related to High-Level Waste Repositories, NUREG/CR-3206, March 1983.

Gale, J. E., Rouleau, A., and Atkinson, L. C., (1985), Hydraulic Properties of Fractures, Proceedings IAH Symposium on Hydrogeology of Rocks of Low Permeability, Tucson, January 1985, pp 1-16.

Huang, C. and Evans, D. D., (1985), A 3-Dimensional Computer Model to Simulate Fluid Flow and Contaminant Transport Through a Rock Fracture System, NUREG/CR-4042, January 1985.

Hull, L. C., (1985), Laboratory Validation of a Dual-Permeability Reservoir Code, Proceedings, Tenth Workshop on Geothermal Reservoir Engineering, Stanford University, January 1985, pp 293-296.

Jones, J. W., Simpson, E. S., Neuman, S. P., and Keys, W. S., (1985), Field and Theoretical Investigations of Fractured Crystalline Rock Near Oracle, Arizona, NUREG/CR-3736, August, 1985.

Knapp, R. B. and Norton, D., (1981), Preliminary Numerical Analysis of Processes Related to Magma Crystallization and Stress Evolution in Cooling Pluton Environments, American Journal of Science, 281, January, 1981, pp. 35-68.

Lamb, H., (1945), Hydrodynamics, Dover Publications, New York.

Mahtab, M. A., Bolstad, D. D., and Kendorski, F. S. (1973), Analysis of the Geometry of Fractures in San Manuel Copper Mine, Arizona, Bureau of Mines RI 7715, January 1973.

Miller, J. D., (1983), A Fundamental Approach to the Simulation of Flow and Dispersion in Fractured Media, Proceedings, 9th Workshop on Geothermal Reservoir Engineering, Stanford University, December 1983, pp 373-379.

Mitchell and Gauthier, Assoc., Inc., (1981), Advanced Continuous Simulation Language (ACSL), User Guide/Reference Manual, Box 685, Concord, Mass. 01742.

Paillet, F. L. and Keys, W. S., Applications of Borehole Geophysics in Characterizing the Hydrology of Fractured Rocks, Proceedings, National Water Well Association Subsurface Investigations Conference, San Antonio, February, 1984.

Priest, S. D. and Hudson, J. A. (1981), Estimation of Discontinuity Spacing and Trace Length Using Scanline Surveys, International Journal of Rock Mechanics and Mining Science and Geomechanics, 18, pp 183-197.

Raven, K. G., Smedley, J. A., Sweezey, R. A. and Novakowski, K. S., (1985), Field Investigations of a Small Groundwater Flow System in Fractured Monzonitic Gneiss, Proceedings IAH Symposium on Hydrogeology of Rocks of Low Permeability, Tucson, January 1985, pp 72-86.

Romm, E. S., (1966), Flow Characteristics of Fractured Rocks, (in Russian). Nedra, Moscow, 283 pp.

Segall, P. and Pollard, D. D., (1983), Joint Formation in Granitic Rock of the Sierra Nevada, Geological Society of America Bulletin, 94, May 1983, pp 563-575.

PROCEEDINGS, Eleventh Workshop on Geothermal Reservoir Engineering
Stanford University, Stanford, California, January 21-23, 1986
SGP-TR-93

REINJECTION MODEL STUDIES IN FRACTURED AND HOMOGENEOUS GEOTHERMAL SYSTEMS

H.Hosca, E.Okandan

Middle East Technical University
Ankara, Turkey

INTRODUCTION

Reinjection of geothermal waste waters has become an important topic of interest for industry as well as for research. The environmental concerns due to chemical composition of geothermal waste waters had urged the industry to dispose it underground.

In several field applications no interference due to thermal front breakthrough was observed on the other hand some cases are reported where reinjection had caused severe declines in energy production due to unexpected breakthrough of injected water.(1,2)

Several analytical and numerical studies are available (3,4) where the effect of fractures on the movement of thermal front are discussed. It was shown that when the conduction heat transfer from matrix to fracture dominates, retardation of the thermal front movement will be observed (3). Bodvarsson and Pruess (5) considered the above problem in a five-spot well pattern. They observed as the amount of fluid injected reaches the amount produced, the long-term energy output of the system increases. Pruess (4) in his study compares the behavior of porous medium and fractured medium in terms of pressure decline due to production. Temperature and pressure profiles are presented between an injector and a producer where heating of the injected water in porous medium and in fractured medium with small fracture spacing was high compared to a larger fracture spacing. Such observations from the numerical studies were checked against some limited field examples (5,6). However understanding of the injection effects in fractured reservoirs is limited.

This work presents the results of laboratory experiments where effects of reinjection on temperature and pressure behavior of a porous medium and a fractured medium were investigated. The porous medium was a crushed limestone pack, with 10 mm average particle size, packed in a 3-D box model where injection and production ports are located on the diagonal ends simulating a five-spot pattern. The fractured medium was made from unifromly cut marble blocks packed in such a way to permit uniform fracture geometry.

The pressure and temperature response of both models are analyzed as a function of

i) depth of injection and production
ii) injection rate

where $20^{o}C$ injection water is injected into $110^{o}C$ reservoir.

EXPERIMENTAL SET UP AND PROCEDURE

The model of the porous medium is the same as reported in the previous study by Parlaktuna and Okandan (8). The fractured medium was made from marble blocks which were cut in cubes and parallelipipeds and packed in a way to produce the desired fracture network and to allow a longer path of travel for the injected water. Marble cubes were 10x10x10 cm where as paralellipipeds were 10x10x20 cm in dimension. The packing model is given in figure 1. Blocks are in close contact as much as the smooth machining of the surfaces allow. The stainless steel box which contains the blocks has plane marble plates at the bottom and sides where heaters were installed. This configuration allowed even heat input into the model which was not much affected by the heater location.

The thermocouples were installed in the fracture by placing them in slots machined on the marble surfaces. There are total of 44 thermocouples placed at four different depths in the model (Fig.1). Two thermocouples were placed in matrix blocks at the injection side to see the cooling effect in marble, and another two were used in the producing ports. The injection water reservoir,pressurized with a high pressure source was used to inject a constant mass of fluid per unit time. The produced fluids were collected after cooling at the out flow end. The injection and production ports are located across the fractures which cut the well bore axis perpendicularly. Different injection production depth combinations are possible during the experiments.

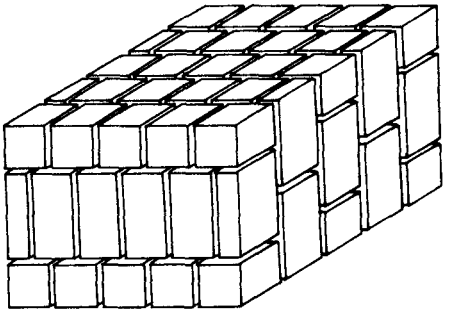

Figure 1. Packing of marble blocks

In both models the pore volume was filled completely with water. Then with the heaters the system temperature was raised to 110°C and pressure to 310 kPa in porous model and to 265 kPa in fractured model creating a hot water system. Initially in fractured medium the marble blocks had a higher temperature than fluid contained in the fractures and it was recorded as 115°C.

The production from both models continued until pressure declined to about 210 kPa. Then injection of 20°C water was started with the desired rate. Temperatures, pressure, injected and produced volumes were recorded continuously. The test data for both models are given on Table 1.

TABLE 1. EXPERIMENTAL DATA

POROUS MEDIUM		h: 20 cm		Porosity : 40%			
	Run No.	Prod.depth h_p/h_t	Initial Press (kPa)	Press.before inj.(kPa)	Total mass Prod.before inj. (gr)	Injection rate gr/min	Prod.rate gr/min
H_i/H_t=0.15	P-1	0.85	310	203	2800	50	43
	P-2	0.85	310	202	2780	100	57
	P-3	0.3	307	204	1820	50	46
	P-4	0.3	310	198.5	2440	100	63
H_i/H_t=0.8	P-5	0.85	310	209.6	3430	50	51
	P-6	0.85	310	213	3285	100	65
	P-7	0.3	310	221	4455	100	92
	P-8	0.3	310	224.7	4130	50	75
FRACTURED MEDIUM		h: 40 cm		Porosity: 4.03%			
H_i/H_t=0.25	F-1	0.25	267	206.8	2420	100	36
	F-2	0.25	258.5	210.3	1650	50	43
	F-3	0.75	265	206.8	1830	100	36
	F-4	0.75	265	208.6	1430	50	38
H_i/H_t=0.75	F-5	0.25	262	203.4	1700	100	44
	F-6	0.25	262	203.4	1560	50	37
	F-7	0.75	265	203	1750	100	42
	F-8	0.75	267	208.6	1980	50	35

RESULTS AND DISCUSSION

The pressure and temperature behavior of both models will be discussed in terms of depth of injecton and production and mass input rate.

Pressure Behavior During Depletion:

Models behaved differently during this period. The pressure behavior in each model was not affected much by the positioning of production ports provided rates were similar. When comparison between fractured and porous medium is made (Fig.2), the initial pressure decline rate was high in porous medium then it decreased to a constant value reflecting the finite volume of the system. For fractured medium initial decline rate was less and it reached a higher constant rate decline compared to porous model.

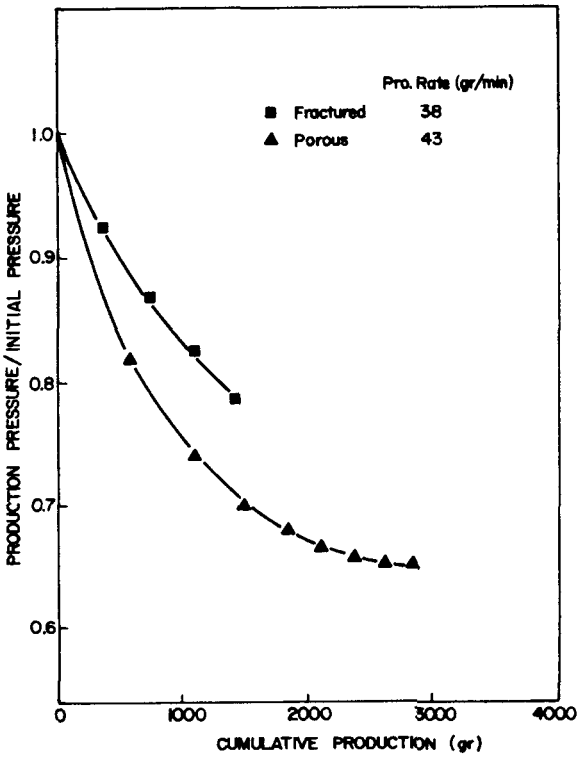

Figure 2. Comparison of production pressure decline for fractured and porous media.

The mass production totalled 14% of initial mass during 35% decline in pressure for porous model. For the fractured medium 24% of initial mass was produced while pressure drop was 22% of its original value. (Run P1 and F4)

Pressure Behavior During Injection:

This phase of the operation was strongly affected by relative positioning of injection and production ports in both models. The pressure increase was dependent on the ratio of injected and produced water. The pressure increase in both models during injection occured for both mass input rates.
For both models these rates resulted in P/I ratios (prod.rate /inj.rate) less than one, and indicated larger mass input than output caused higher pressure maintenance (Figure 3). Similar results were reported by Bodvarsson et'al(5) from the numerical model studies.

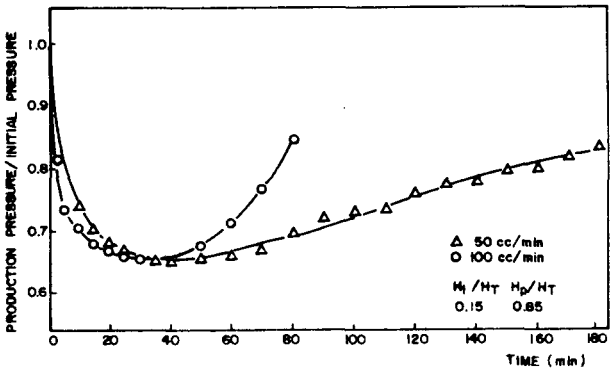

Figure 3.a. Effect of Injection Rate on Production Pressure

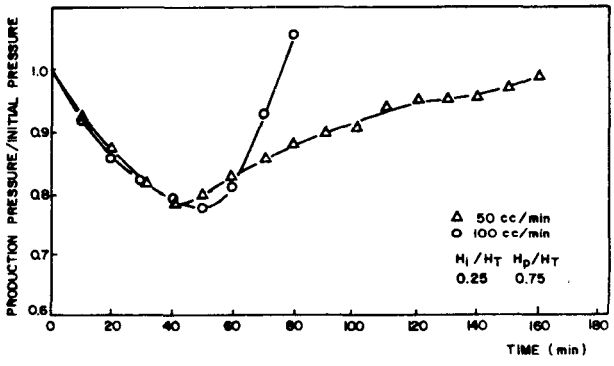

Figure 3.b. Effect of Injection Rate on Production Pressure

However the degree of pressure increase was affected by the location of injection and production levels. The highest pressure increase was observed when fluid was forced to travel a longer path (Fig.4) which also benefitted from thermal sweep effects. The usual practice of injecting at a deeper level which makes use of the fluid head in well bores

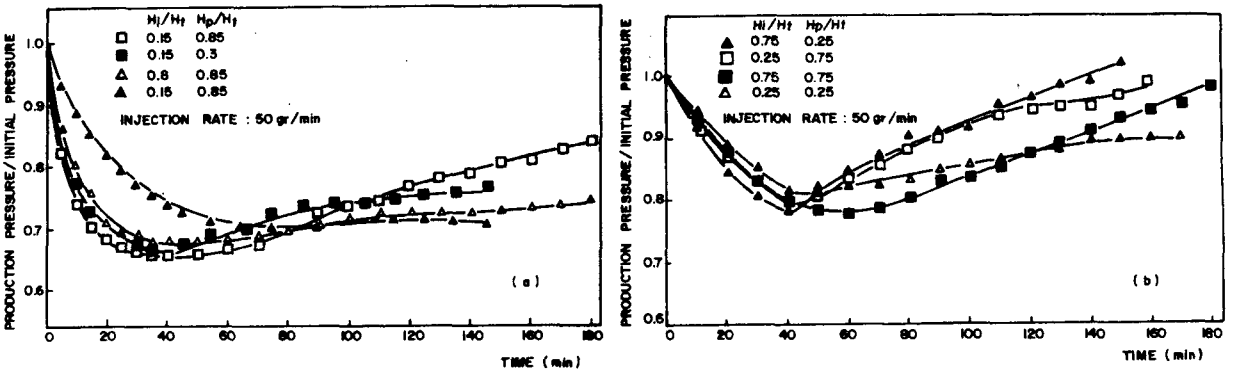

Figure 4. Effect of Injection and Production Depth on Pressure Behavior of a) Porous model b) Fractured model

and producing at a shallower depth must also be advantageous from the point of view of pressure and temperature behavior of the geothermal systems.

Considering this favorable condition for injection and production depth, 100% pressure maintenance after reinjection was achieved at a shorter period when P/I was 0.38 in fractured medium. However for a similar time period when P/I was 0.43, porous medium reached 85% of its original pressure.

A general difference between both types of media was the response of the models after reinjection started. Fractured medium showed a quicker response to injection by exhibiting a steeper increase in pressure while for porous medium longer period had to elapse before pressure started to increase at the producing end. (Fig.3,4).

Temperature Distributions:

The analysis of results are presented in terms of temperature change along the diagonal of the models between injection and production ends. In both models during production no temperature change was observed.

In fractured medium as injection starts, movement of cold water immediately cools the first fracture and the movement of this thermal front can be followed through the fracture network of the reservoir. (Figure 5) However this drop in temperature after a certain distance of travel in the fractures approaches zero and then the increasing temperature indicates heat conduction is dominant from matrix to fracture fluid. This phenomenon also decreased the thermal front rate which can be observed by following $\Delta T=0$ along the diagonal at different times (Figure 5). Similar behavior was observed in porous model as shown on figure 6.

Figure 7 and 8 present the same data along the diagonal plane between the injector and the producer. The contours are drawn using discrete temperature readings from thermocouples to visualize how the front was moving.

The higher rate of injection caused a faster cooling at the vicinity of the injection point. Still the effect of heat conduction was obvious from the temperature profiles (Fig.9).

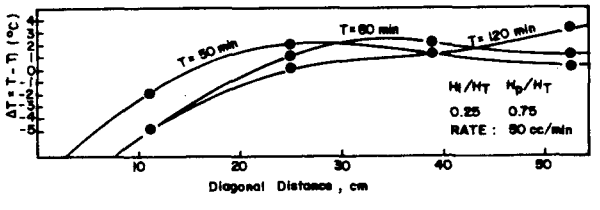

Figure 5. Movement of Thermal front in fractured model

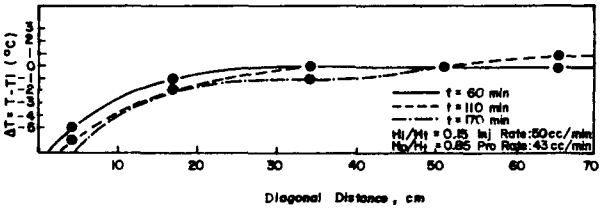

Figure 6. Movement of Thermal front in porous model

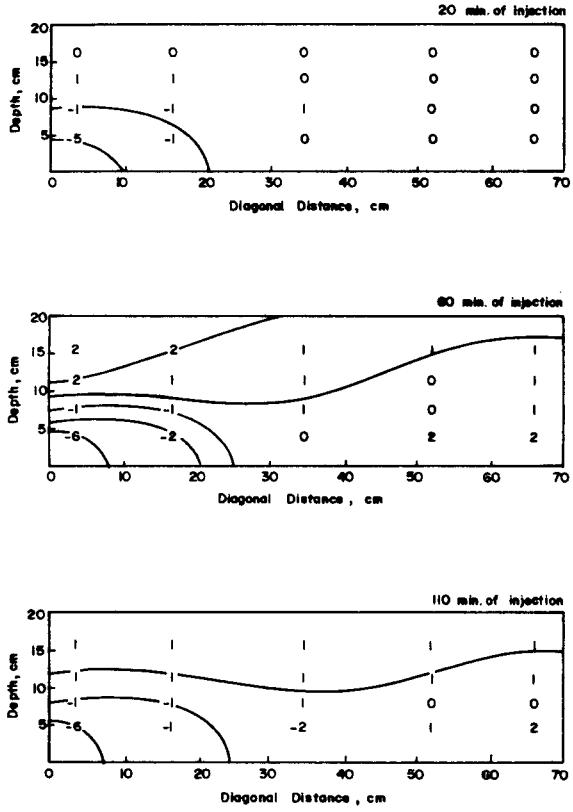

Figure 7. Temperature profile along the diagonal plane of porous model

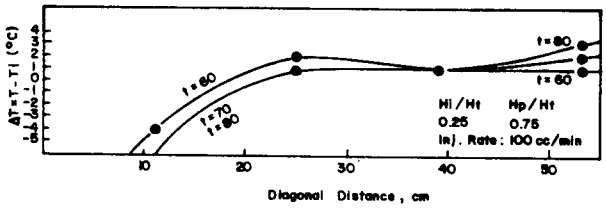

Figure 9. Effect of injection rate on the improvement of thermal front

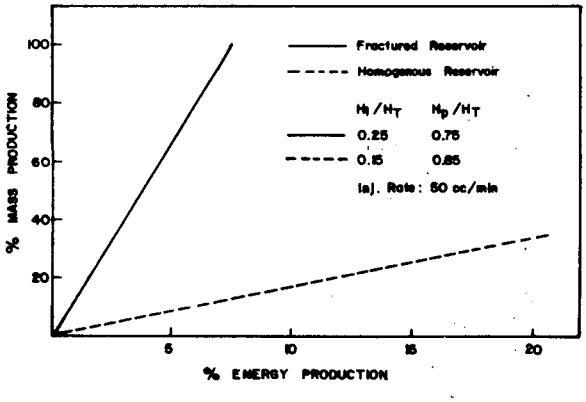

Figure 10. Energy recovery from porous and fractured models

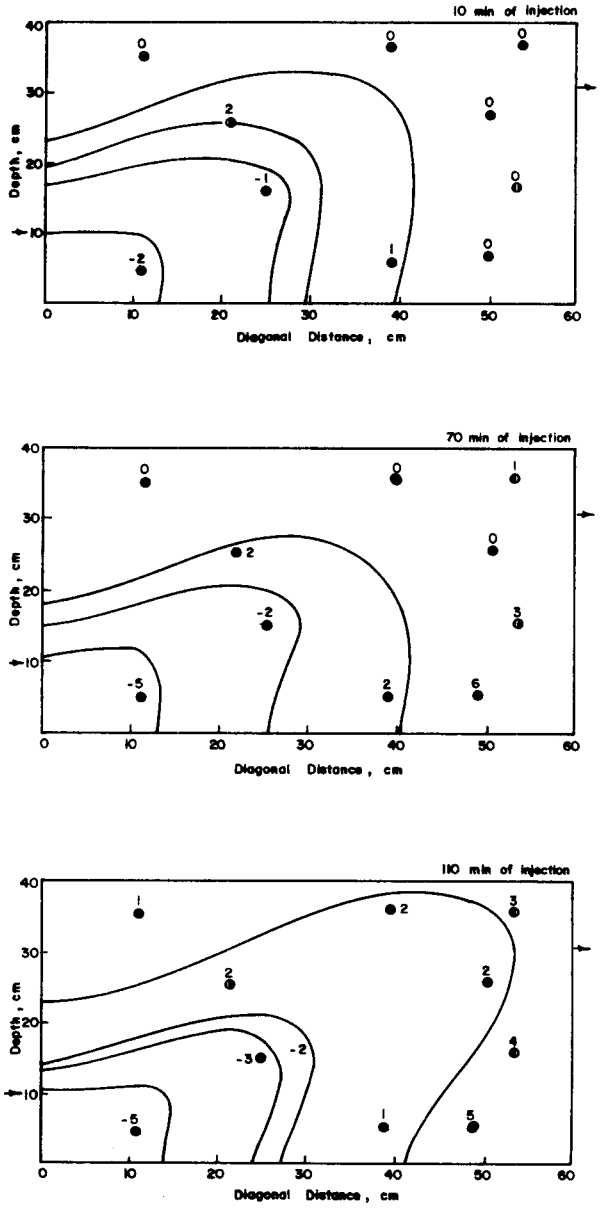

Figure 8. Temperature profile along the diagonal plane of fractured model

TABLE 2. ESTIMATES OF kh. FROM PI VALUES

H_p/H_t	Run.No.	PI cc/sec/atm	k, darcy	kh, darcy-cm
FRACTURED MEDIUM				
0.25	1,2,5,6	0.31 - 0.65	0.0012-0.0025	0.048 - 0.1
0.75	3,4,7,8	0.3 - 0.4	0.0012-0.0017	0.044 - 0.068
POROUS MEDIUM				
0.3	3,7,8	1.16 - 0.78	0.0059-0.0039	0.118 - 0.078
0.8	1	4	0.0202	0.404

Estimation of Permeabilities of Models :

Productivity index values are determined for both models using pressure decline data during depletion (Table 2). The differences in PI for each model where production depths were different, indicate different flow patterns where different fractures were contributing to flow, which may also in itself contain the effect of production through a perforation especially in the case of porous medium.

Kh-values for the fractured medium were used to estimate fracture size (b) and block size (a) using the fracture flow model given on figure 11.

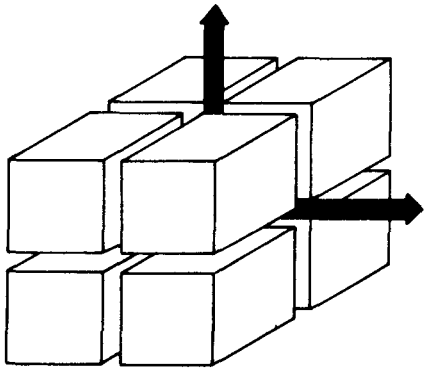

Figure 11. Flow model in fracture network

For such a model (9),

$$k_f = 0.62\, a^2 \phi_f^3$$

$$k_f = 5.55 \times 10^{-4} b^2 \phi_f$$

where a, (cm), k_f(darcy), b (microns) are used.

The block size calculated was 7.9 cm compared to 10 cm real size and fracture opening was 0.001 mm. The porosity of fractures ϕ_f, when calculated using

$$\phi_f = 3b/100a$$

is 3.1% compared to 4.03% from experimental data.

CONCLUSION

Mechanism of injection and production from a single phase geothermal source was studied on physical laboratory models which simulated porous medium and fractured medium.

1- Pressure maintenance in both models was possible by injecting cold water after some production was obtained. The increase in pressure was dependent on the mass input and output ratios, and also on the model type.Porous medium responded slowly to this operation where as fractured model showed a sharp increase.

2- A favorable injection-production depth relation was obtained when injected water was made to travel longer distance in the system. Therefore an efficient application is injection at a lower depth than production.

3- Injection was also beneficial in terms of energy extraction from matrix. This heat conduction from matrix retards the movement of thermal front and also enhances the energy sweep in the fractured model. In porous medium similar behavior was observed but heat conduction was not as affective.

4- The block size and fracture opening of the fractured model was estimated using PI values. The flow model behavior approached to two dimensional, vertical and horizontal flow around cubical blocks.

5- Energy recovery from fractured medium was 7.5% after 1 PV of water was injected, indicating most of the original energy is still available. For porous medium these figures were 26% recovery in energy when 39% PV of water was injected (Fig.10).

REFERENCES

1- Horne, R.N. "Geothermal Reinjection experience in Japan" J.P.T. June 1982, 34,495-503.

2- Horne, R.N. "Reservoir Engineering Aspects of Reinjection", United Nations Seminar on Utilization of Geothermal Energy for Electric Power Production and Space Heating" Florance, Italy, 14-17 May 1984.

3- Bodvarsson G.S. and Tsang, C.F., "Injection and Thermal Breakthrough in Fractured Geothermal Reservoirs" *Journal of Geophysical Research*, 1980, 82(B2) 1031-1048.

4- Pruess, K. "Heat Transfer in Fractured Geothermal Reservoirs with Boiling", Water Resources Research (Feb.1983) vol.19.pg.201-208.

5- Bodvarsson, G.S., Pruess, K., O'Sullivan, M.J., "Injection and Energy Recovery in Fractured Geothermal Reservoirs", SPE paper No.11689, presented in California Regional Meeting, March 23-25, 1985, Ventura, California

6- Morris, C.M., Campbell, D.A., "Geothermal Reservoir Energy Recovery - A three Dimensional Simulation Study" SPE paper no.8229, presented at 54th. Annual Fall Technical Conference, Las Vegas, Sept. 1979.

7- Bodvarsson, G.S., Haar, S.V., Wildt,M., Tsang,C.F., "Preliminary Studies of the Reservoir Capacity and Generating Potential of the Baca Geothermal Field, New Mexico", Water Resources Research (Dec.1982) vol 18. p.1713.

8-Parlaktuna, M.,Okandan, E. "Laboratory Physical Model for Pattern Injection in Geothermal Systems", Proceedings, Ninth Workshop, Geothermal Reservoir Engineering, Stanford Calif. Dec.1983, pg.339.

9- Van Golf Racht, T.D. "Fundamentals of Fractured Reservoir Engineering", Elsevier Publishing Co, 1982, pg.180.

PROCEEDINGS, Eleventh Workshop on Geothermal Reservoir Engineering
Stanford University, Stanford, California, January 21-23, 1986
SGP-TR-93

BREAKTHROUGH TIME FOR THE SOURCE-SINK WELL DOUBLET

Will Menninger and Abraham Sageev

Stanford University

Stanford CA 94305

ABSTRACT

A pressure transient analysis method is presented for interpreting breakthrough time between two constant rate wells. The wells are modeled as two line source wells in an infinite reservoir. The first well injects at a constant rate and the second well produces at a constant rate. We studied the effects of transient pressure conditions on breakthrough time. The first arrival of injected fluid at the production well may be significantly longer under transient condition than under steady state condition. A correlation of the deviation of the breakthrough time for transient pressure conditions from the steady state condition is presented.

INTRODUCTION

Pressure transient analysis methods are used to estimate reservoir properties so that exploitation schemes may be evaluated. The method presented in this paper permits the interpretation and design of a special case, which will be referred to as the rate-rate doublet. In this two-well system, one well produces at a constant rate and the other well injects at the same constant rate. The two time dependent parameters in the rate-pressure doublet model are the pressure responses of each well. These parameters and ensuing equations will be described further in the Theory section. We have assumed a unit mobility ratio and that the injected fluid completely displaces the inplace fluid (piston-like displacement).

A constant rate well is approximated as a line source, since the the well-to-well length scale is much larger than the finite radius of the well. The constant rate line source well has been used as a building block for calculating the responses of various reservoir systems. *Theis* (1935) presented the line source pressure solution in an infinite domain. *Carslaw and Jaeger* (1960) and *Van Everdingen and Hurst* (1949) presented the pressure solution for a finite radius well in an infinite system. *Mueller and Witherspoon* (1965) showed the geometrical and time conditions under which the line source and the finite radius solutions are practically identical. They concluded that for observation wells located at a distance twenty times the wellbore radius the line source approximation is applicable. Also, this approximation is applicable for any observation well after a dimensionless time of ten.

Since the diffusivity equation describing the flow in the system is linear, superposition in space of constant rate line sources may be used. *Stallman* (1952) presented the superposition of two constant rate line sources replicating the effects of constant pressure or impermeable linear boundaries. In the same way, superposition of arrays of rate sources (*Kruseman and De Ridder* 1970, and *Ramey et al* 1973) were used to generate the effects of combinations of rectangular boundaries around a well. Using superposition, the line source approximation, and fluid flow particle tracking, transient breakthrough times for a tracer flowing from an injecting well to a producing well are calculated. This paper presents the effects of the transient flow period on the breakthrough time for the rate-rate doublet, and compares the transient and the steady state breakthrough times.

The transient breakthrough time is computed using a fluid flow front tracking technique that is essentially the physical representation of the Euler method for solving differential equations. As initial conditions, we have a particle at the injecting well at a time t_i after both wells were activated. From these initial conditions, equations (6) and (9) give us the instantaneous velocity of the particle at that point. We allow the particle to move a small, finite distance, dx, in a given time, dt, at the calculated velocity. After this move, the velocity is recalculated at the new point in space and time, and the process repeats until the particle arrives at the producing well. As the length of the discrete time increments reduces, the transient numerical solution becomes accurate, and is the basis for a comparison to the steady state solution.

THEORY

Transient Breakthrough Time

The source-sink doublet model uses an imaging method to generate a constant pressure linear boundary (*Carslaw and Jaeger* 1960, *Kruseman and De Ridder* 1970, and *Ramey et al* 1973). Figure 1 presents a schematic diagram of the rate-rate doublet configuration. The dimensionless pressure solution for this model is:

$$P_D = -\frac{1}{2}\left[E_i(-X_1) - E_i(-X_2)\right] \tag{1}$$

where

$$X_i = \frac{r_{Di}^2}{4t_D} \tag{2}$$

and the dimensionless terms are defined as:

$$p_D = \frac{2\pi kh(p_i - p)}{q\mu} \tag{3}$$

$$t_D = \frac{kt}{\phi\mu c_t r_w^2} \tag{4}$$

and

$$r_D = \frac{r}{r_w} \tag{5}$$

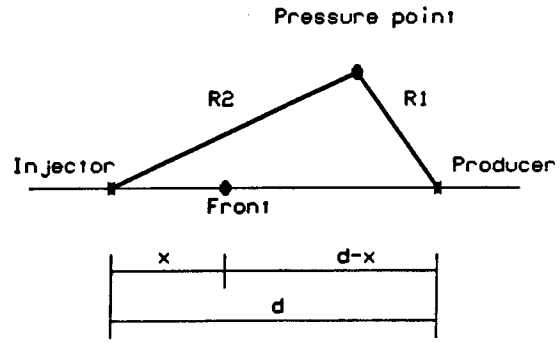

FIGURE 1: A schematic diagram of the rate-rate doublet system.

Since we are only concerned with breakthrough time, the problem can be treated in one dimension. The injecting well is placed at the origin, and the producing well is placed at a distance d away along the x-axis in the positive direction. The breakthrough time is found by tracking fluid flow along the x-axis. The distance between the injecting well and the observation point is r_{D1}, thus, $r_{D1} = x$. The distance between the observation point and the producing well is r_{D2}, thus, $r_{D2} = d - x$ (See Figure 1). The velocity of the fluid is related to the change in pressure with respect to change in distance:

$$V_x = -\frac{k}{\mu}\frac{\partial P}{\partial x} = -\frac{k}{\mu}\frac{q\mu}{2\pi khr_w}\frac{\partial P_D}{\partial x_D} = \frac{-q}{2\pi hr_w}\frac{\partial P_D}{\partial x_D} \quad (6)$$

The calculation of $\frac{\partial P_D}{\partial x_D}$ is based upon the formula for the derivative of the Exponential Integral:

$$\frac{dE_i(u)}{du} = \frac{1}{u}e^u\,du \quad (7)$$

If Equation (1) is fitted to our one dimensional problem stated above, we obtain the following result:

$$P_D = -\frac{1}{2}\left\{E_i\left[-\frac{\left(\frac{x}{r_w}\right)^2}{4t_D}\right] - E_i\left[-\frac{\left(\frac{d-x}{r_w}\right)^2}{4t_D}\right]\right\} \quad (8)$$

Differentiating Equation (8) yields:

$$\frac{\partial P_D}{\partial x_D} = -\left[\frac{1}{\frac{x}{r_w}}\right]e^{-\frac{\left(\frac{x}{r_w}\right)^2}{4t_D}} - \left[\frac{1}{\frac{d-x}{r_w}}\right]e^{-\frac{\left(\frac{d-x}{r_w}\right)^2}{4t_D}} \quad (9)$$

The particle velocity, V_x, is calculated using Equations (6) and (9).

Steady State Breakthrough Time

Calculation of steady state breakthrough time is achieved by letting time go to infinity. In that case, the exponentials in Equation (9) go to unity, and a steady state condition is achieved:

$$\frac{\partial P_D}{\partial x_D} = -\frac{1}{\frac{d-x}{r_w}} - \frac{1}{\frac{x}{r_w}} \quad (10)$$

Equation (10) implies that the velocity domain is only a function of space, hence an analytical steady state breakthrough time solution may be derived. From mechanics,

$$V_x = \frac{dx}{dt} \quad (11)$$

which implies

$$t_{bt} = \int_0^d \frac{dx}{V_x} \quad (12)$$

Substituting Equation (6) and Equation (10) into Equation (12) yields:

$$t_{bt} = \frac{2\pi h}{q}\int_0^d \left[\frac{1}{\frac{1}{d-x}+\frac{1}{x}}\right]dx \quad (13)$$

which simplifies to:

$$t_{bt} = \frac{2\pi h}{qd}\int_0^d \left[xd - x^2\right]dx \quad (14)$$

Finally, the steady state breakthrough time is (*Brigham* 1979):

$$t_{bt} = \frac{2\pi hd^2}{6q} \quad (15)$$

This resulting breakthrough time for steady state is compared to the transient value.

RESULTS

An algorithm was developed to calculate transient breakthrough time based on three parameters: initial tracer injection time, t_i ; rate of injection, q ; and distance between wells, d. The algorithm sets $x = r_w$ and $t = t_i$ as the starting condition for particle tracking. The velocity is then calculated from x and t using equations (6) and (9). The increment of time, dt, is calculated from the velocity so that $dx = V_x dt$ will be a constant throughout the algorithm. The increment of time, dt, is then added to t and dx is added to x and the process repeats until x is greater than $d - r_w$.

Figure 2 presents a graph where initial injection time is graphed along the x-axis, and q varies for each curve. As expected, each curve asymptotically approaches a constant breakthrough time, the steady state value. The higher curves appear flatter than the bottom curves because of the logarithmic scale.

The difference between steady state and transient breakthrough times depends on various input parameters when the tracer is injected at the same time the two wells are activated. Figure 3 shows graphs of errors between steady state and transient breakthrough times. In this figure, d is graphed along the x-axis to show that the error does not depend on d. All of the curves are very flat. The error does depend on q, though, since there is a distinct curve for each different value of q.

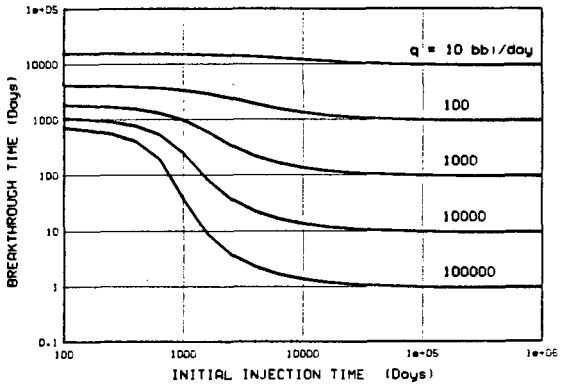

FIGURE 2: Graph of transient breakthrough time with t_i graphed along the x-axis and q varying from 10 to 100000 bbl/day. d is constant at 100 feet.

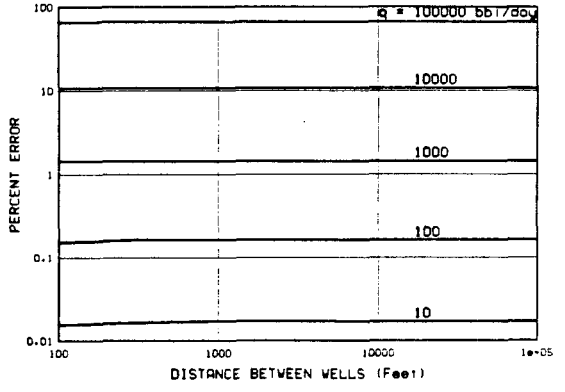

FIGURE 3: Graph of error between steady state and transient breakthrough time. d is graphed along the x-axis, and q varies 10 from 100000 to bbls/day. t_i is constant at 0.0001 days (practically zero).

In Figure 4, we put q along the x-axis, since it is obviously a key parameter that the error depends on. For each different curve, the value of $\mu c_t/hk$ is different. Changing the value of $\mu c_t/hk$ results in four (almost) straight lines that may be translated horizontally. In Figure 5, these four lines have been merged into one line by graphing the value $q\mu c_t/hk$ (10^{-7}) along the x-axis, which achieves a horizontal translation of each curve on a log-log scale. Thus, the error between the transient and the steady state breakthrough time depends on one parameter, $q\mu c_t/hk$.

Figure 5 may be used for designing and interpreting tracer tests when the tracer is injected at the same time the wells are activated. The onset of steady state (for example, when the pressures are less than 1% of the steady state pressures) is not a function of the flow rate. The particle of tracer is less attracted to to the production well during the transient flow period in comparison to the steady state period. Hence, the higher the flow rate the larger the deviation of the transient breakthrough time form the steady state breakthrough time.

Finally, in Figure 6, the distance of the front from the injecting well is graphed vs. the time from tracer injection. This graph shows a different curves for different injection

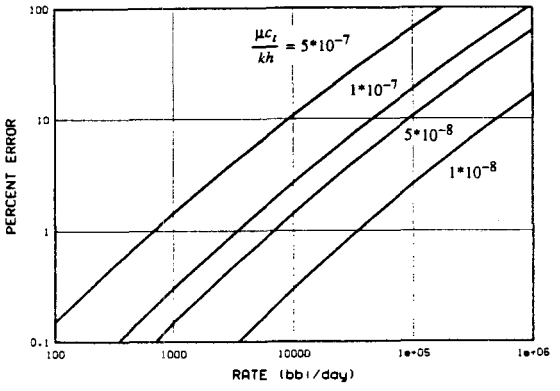

FIGURE 4: Graph of error between steady state and transient breakthrough time. q is graphed along the x-axis. The different curves represent different values of the quantity $\frac{\mu c_t}{hk}$.

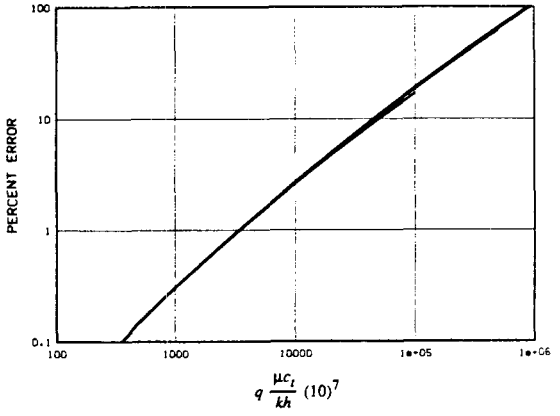

FIGURE 5: The same four curves as in Figure 4, except with $q\frac{\mu c_t}{hk}$ (10^7) graphed along the x-axis.

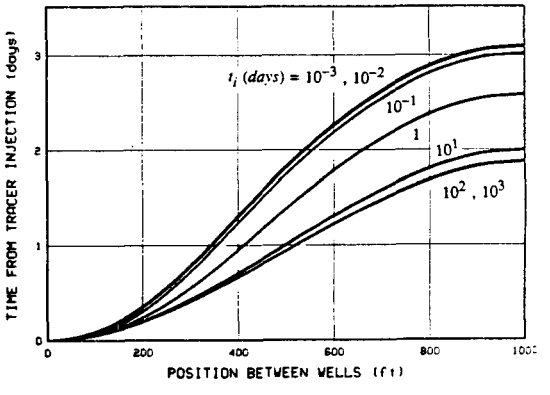

FIGURE 6: The position of the front vs. time from injection for an error parameter set to 50%. The seven different curves represent different initial injection times, from completely transient to steady state.

times. We set the error parameter to give a 50% error when initial injection time is zero. The uppermost curves are the zero injection time curves, with a breakthrough time nearly 50% longer than that of the lowermost curves, which approach steady state. Note that the error is even larger before breakthrough because conditions approach steady state as the particle approaches to the producing well. At half the distance to breakthrough, the error is nearly 100%.

CONCLUSION

1. A single correlating parameter, $q\mu c_t/hk$, describes the effects of the transient flow period on tracer breakthrough time.
2. For systems with high values of $q\mu c_t/hk$, transient breakthrough times will be markedly longer than steady state breakthrough times at early initial injection of the tracer.
3. For all systems, the transient breakthrough times approach the steady state breakthrough times when the tracer is injected after the wells were activated and the system allowed to approach steady state conditions.

ACKNOWLEDGEMENTS

Financial support was provided by the Stanford Geothermal Program, DOE Contract No. DE-AT02-80SF11459, and by Stanford University.

NOMENCLATURE

c_t = compressibility
d = distance between wells
h = formation thickness
k = permeability
p = pressure
p_D = dimensionless pressure, $2\pi kh(p_i-p)/q\mu$
q = rate of injection/production
r = radius
r_d = dimensionless radius, r/r_w
r_w = wellbore radius
t = time
t_{bt} = breakthrough time
t_D = dimensionless time, $kt/\phi\mu c_t r_w^2$
V = velocity
x = distance along x-axis
ϕ = porosity
μ = viscosity

REFERENCES

Brigham, W.E.: Stanford University Advanced Reservoir Engineering Class, Stanford University, 1979.

Carslaw, H.S. and Jaeger, J.C.:*Conduction of Heat in Solids*, 2nd ed. Oxford University Press, 1960.

Kruseman, G.P., and De Ridder, N.A.: "Analysis and Evaluation of Pumping Test Data," International Institute of Land Reclamation and Improvement, Wageningen, The Netherlands (1970).

Mueller, T.D., and Witherspoon, P.A.: "Interference Effects Within Reservoirs and Aquifers," *J. Pet. Tech.* (Oct. 1965) 1803-1812.

Ramey, H.J., Jr., Kumar, A. and Gulati, M.S., "*Gas Well Test Analysis Under Water Drive Conditions*", American Gas Association, Arlington, VA, (1973).

Sageev, A., and Horne, R.N.: "Pressure Transient Analysis of Reservoirs with Linear or Internal Linear Boundaries," SPE 12076, Presented at the 58th Annual Technical Conference and Exhibition, San Francisco, California (Oct. 1983).

Sageev, A., and Horne, R.N.: "Interference Between Constant Rate and Constant Pressure Reservoirs Sharing a Common Aquifer," *SPEJ* (June, 1985) 419-426.

Stallman, R.W., "Nonequilibrium Type Curves Modified for Two-Well Systems", U.S. Geol. Surv., Groundwater Note 3, (1952).

Stehfest, H.: "Algorithm 368, Numerical Inversion of Laplace Transforms," *Communications of the ACM*, D-5 (Jan. 1970) 13, No. 1, 47-49.

Theis, C.V., "The Relationship between the Lowering of Piezometric Surface and Rate and Duration of Discharge of Wells using Groundwater Storage," Trans., AGU, 2, 519, (1935).

Van Everdingen, A.F. and Hurst, W.: "The application of the Laplace Transformation Flow Problems in Reservoirs," *Trans.*, AIME (Dec. 1949) 186, 305-324.

PROCEEDINGS, Eleventh Workshop on Geothermal Reservoir Engineering
Stanford University, Stanford, California, January 21-23, 1986
SGP-TR-93

TRACER DEVELOPMENTS: RESULTS OF EXPERIMENTAL STUDIES

M. C. Adams[1], J. H. Ahn[1], H. Bentley[2], J. N. Moore[1], and S. Veggeberg[2]

[1]University of Utah Research Institute
Salt Lake City, Utah 84108

[2]Hydro Geo Chem, Inc.
Tucson, Arizona 85705

INTRODUCTION

Tracers can be used to monitor the movement of groundwaters and geothermal fluids and they can be used as a reference to quantify changes in fluid chemistry as a result of injection. Despite their potential importance to the geothermal operator, very few tracers are presently available and of those that are, little is known about their stability or behavior at the elevated temperatures that typify resources capable of electric power generation. During the past two years the University of Utah Research Institute has been involved in tracer research and testing, largely through the DOE Injection Research Program. The purpose of this paper is to summarize the results of these laboratory and field investigations.

TRACER DEVELOPMENT

The ideal tracer should be detectable in small quantities, inexpensive, environmentally safe, and be absent from natural geothermal fluids and groundwaters. The tracers currently in use in high-temperature environments fall into three major categories: 1) radioactive isotopes; 2) salts of iodide, bromide, and chloride; and 3) organic dyes. Each of these classes of tracers has significant limitations. Radioactive isotope tracers must be limited to those not used as natural process tracers, such as ^{3}H and ^{36}Cl. In addition, the half-life of the tracer must be chosen such that errors from decay corrections are not large. Another problem with radioactive tracers is their toxicity. For example, the tracer used during injection tests at the Wairakei and Broadlands geothermal fields, ^{131}I, is one of the more toxic radionuclides (McCabe et al., 1983). The salts, while relatively stable and inexpensive, are limited by the high halide background in many geothermal systems, requiring large quantities of salt for adequate tracer detection. An additional drawback to the use of salts is that the cation of the salts will interfere with cation geothermometry of the injected fluid (Adams, 1985).

Relatively little is known about the commonly used organic dyes, fluorescein and rhodamine WT. Adsorption at geothermal temperatures has not been demonstrated for these compounds. Although fluorescein is light sensitive, it has been used successfully during injection tests at East Mesa, California (Adams, 1985). Rhodamine WT has been used with limited success at Klamath Falls, Oregon, and Svartsengi, Iceland (Gudmundsson et al., 1984).

One drawback of all the commonly used tracers is their lack of diversity, which restricts the number of wells that can be individually monitored in a producing field at one time. Thus, in geothermal fields where many injection wells are in use, it is not yet possible to independently trace the movement of fluids injected into each of them. A new class of tracers is now being tested that will meet the requirement of diversity. These are the fluorinated, methylated, and sulfonated hydrocarbons.

The tracers being tested can be divided into six substitutional groups. These are ring fluorinated, methyl perfluorinated, sulfonated, ring perfluorinated, methylated, and carboxylated. The substrates for the substitutions are benzene, benzoic acid, and phenylacetic acid.

The salts of substituted benzoic acids were originally selected as groundwater tracers (Bentley, 1982) because they possess many of the characteristics of ideal tracers (Davis et al., 1980; Davis et al., 1985). These compounds are negative ions at the pHs observed in natural groundwaters and are therefore non-sorbing. They are low in toxicity, especially at the tracer concentrations used, chemically stable, exotic to the environment, detectable at trace concentrations and are available as a large suite of similar species. The addition of fluorine to the benzene ring lends greater resistance to microbial degradation, with stability increasing in direct relationship to the degree of substitution (Bentley, 1983). Selected fluorinated benzoic acids, particularly pentafluorobenzoic acid, p-fluorobenzoic acid, and m-trifluorobenzoic acid have been used extensively in numerous groundwater studies over the past few years (for example, see Hydro Geo Chem, 1985a,b).

One of the objectives of our tracer program

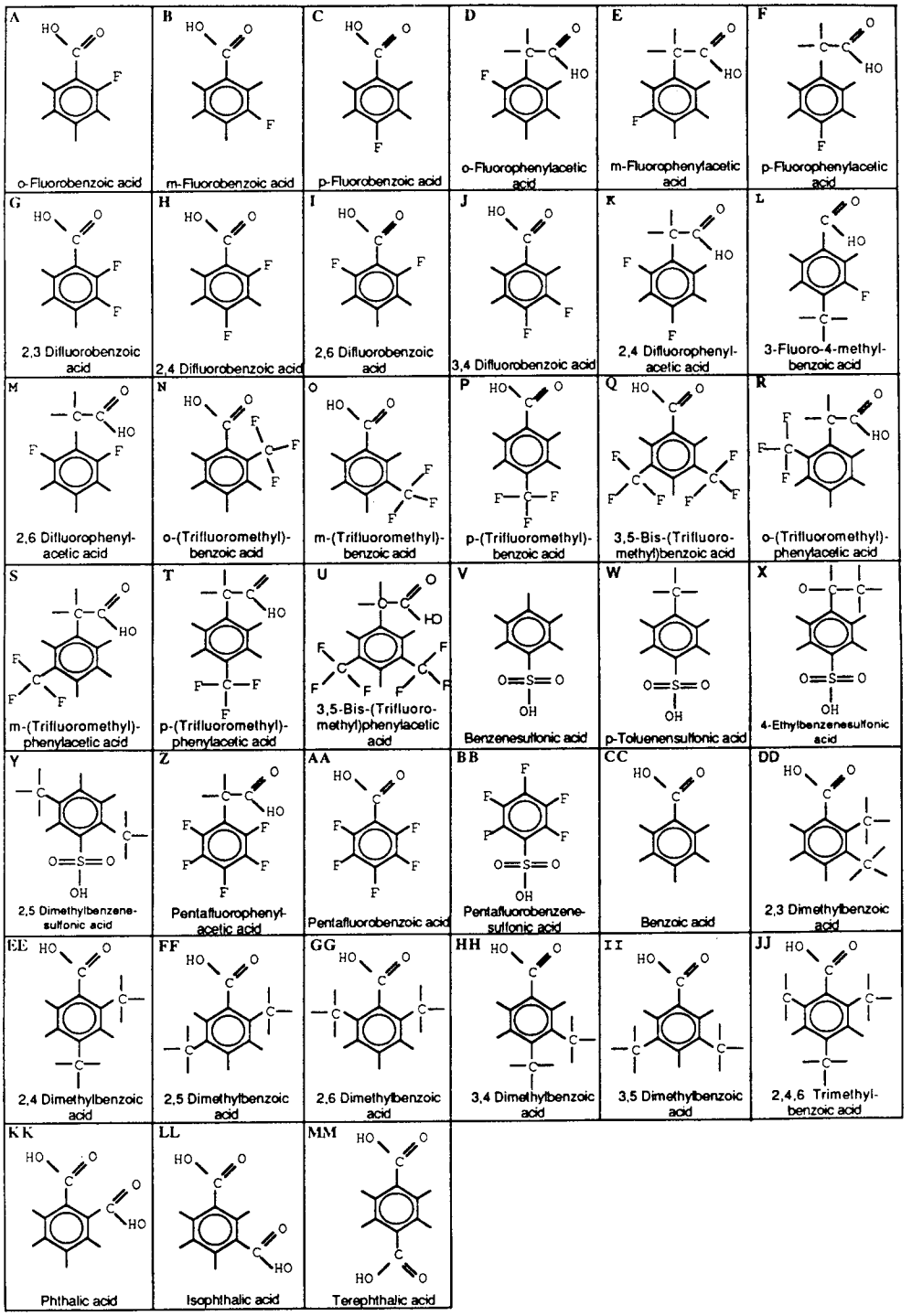

Figure 1. Chemical names and structures of hydrocarbons being tested.

is to extend the use of tracers to vapor-dominated systems. Therefore, we have attempted to include potentially stable tracers with a variety of volatilities. This will enable steam as well as liquid to be tagged; and if the distribution coefficients are known, subsurface processes can be elucidated. To this end we have also been testing the less volatile sulfonic- and acetic-derivatives. Methylated derivatives were also tested because of their probable thermal stability. The compounds tested are shown in Figure 1.

EXPERIMENTAL PROCEDURES

Five experimental reaction vessels have been put into operation since 1985. These vessels are housed at the University of Utah's Department of Metallurgy. One of these is capable of sustaining temperatures of up to 350°C. The use of multiple reaction vessels makes it possible to perform experiments of relatively long duration on several different tracers or under different conditions simultaneously.

At the beginning of each experiment, aliquots of the solutions containing the tracer are encapsulated in sealed quartz tubes (Fig. 2). The ampules are filled with approximately 30 ml of solution and sealed in an oxygen-methane flame. At least two ml of the ampule are occupied by a gas phase during each experimental run. The gas phases used for these experiments are pure nitrogen or an atmospheric mixture of oxygen and nitrogen that is approximately 20% oxygen by volume. The solutions of the experimental runs that used a nitrogen gas phase were purged with nitrogen gas in the ampule for up to 2 hours. The neck of the ampule (see Fig. 2) was aspirated to prevent oxygen contamination from the oxymethane flame during sealing.

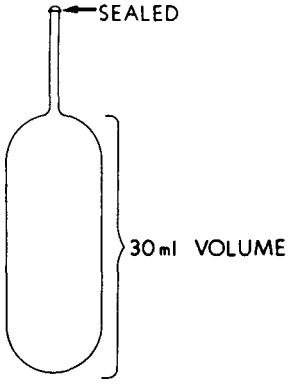

Figure 2. Illustration of quartz tube used for hydrothermal experiments.

Three oxygen concentrations were used in the test solutions in order to bracket the variable oxidation potentials that may result from surface treatment prior to injection. These oxygen concentrations were created by: 1) allowing the solution to equilibrate with atmospheric oxygen at room temperature and leaving atmospheric oxygen in the head space, 2) equilibration of the solution with atmospheric oxygen and filling the head space with nitrogen, and 3) nitrogen-purging of the solution and filling the head space with nitrogen. Oxygen concentrations were measured and oxygen to fluorescein molar ratios calculated for several of these solutions. Oxygen conditions in (1) and (2) averaged 6.9 ppm O_2 and in (3) ranged from .27 to .05 ppm, depending on purge time. Molar ratios of oxygen to fluorescein were 351, 18, and .69 to .13, for oxygen conditions 1, 2 and 3, respectively.

ANALYTIC METHODS

Analysis of hydrocarbons down to the 20 ppb level can be achieved by direct injection of up to 0.2 ml of solution into a high pressure liquid chromatograph (HPLC). If desired, on-column enrichment techniques can be utilized to significantly lower detection limits (Stetzenbach et al., 1982). For HPLC analysis of the benzoic acids, the eluent buffer is prepared by adding sufficient phosphoric acid to reduce the pH to 1.9 with acetonitrile added in the 17-45% range. For analysis of benzene sulfonic acids, an ion-pairing reagent is added (tetrabutyl ammonium phosphate) and the pH adjusted to 6.0. In both cases, the column used is polymer based which is more resistant to degradation than silica-based resins. Detection is by UV absorption at 200-205 nm.

Fluorescein and rhodamine WT were analyzed using a colorimeter and a fluorometer for high and low concentrations, respectively.

EXPERIMENTAL RESULTS

The initial experimental runs were designed to produce a rapid evaluation of the thermal stability of many derivitized hydrocarbons. These runs were carried out at 250°C with high and low oxygen concentrations. In addition, because of its past usage as a tracer and ease of analysis, fluorescein was tested under a variety of other conditions.

The factors chosen to test fluorescein stability were temperature, pH, salinity, and oxygen concentration. Our results indicate that oxygen is the major destabilizing factor. At high oxygen concentrations, high pH and salinity have a stabilizing effect, while high temperatures have a very slight destabilizing effect.

The effect of varying the oxygen concentration is shown in Figure 3. These data demonstrate that fluorescein is very stable in oxygen concentrations typical of geothermal reservoirs. Any scatter in the nitrogen curve is probably due to the variable oxygen concentrations left from the purging pro-

cess. In a geothermal reservoir the oxygen would be even lower than that in the nitrogen purged fluid, and fluorescein should be very stable. In contrast, higher oxygen concentrations result in rapid degradation of fluorescein (Fig. 3).

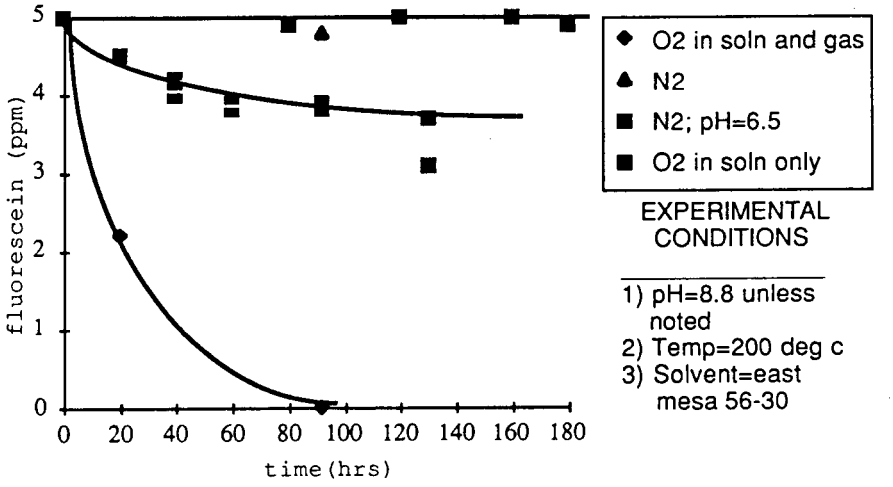

Figure 3. Fluorescein decay vs. time. The initial concentration of fluorescein was 5 ppm.

The effect of varying the solution pH is shown in Figure 4. These data are for experimental runs at an oxygen concentration of approximately 7 ppm. It can be seen that lower pH values strongly promote degradation of fluorescein. This is most likely due to a fluorescein species change in the pH range of 6 to 8.

field by Adams (1985). During one of the injection tests at that field, a 2500 gallon slug of fluorescein and thiocyanate (SCN) was injected and left in the 174°C reservoir for six months, before the fluid was drawn back from the well and analyzed. This data is presented in Figures 5a and b. Here it can be seen that the fluorescein to SCN ratio was frequently higher than the injection ratio, implying that SCN and not fluorescein was lost to the formation. Furthermore, the fluorescein/SCN ratio is consistently subequal to the injected ratio at the tail end of the fluid withdrawn, where the pH and oxygen concentration were identical to the reservoir conditions. Thus fluorescein

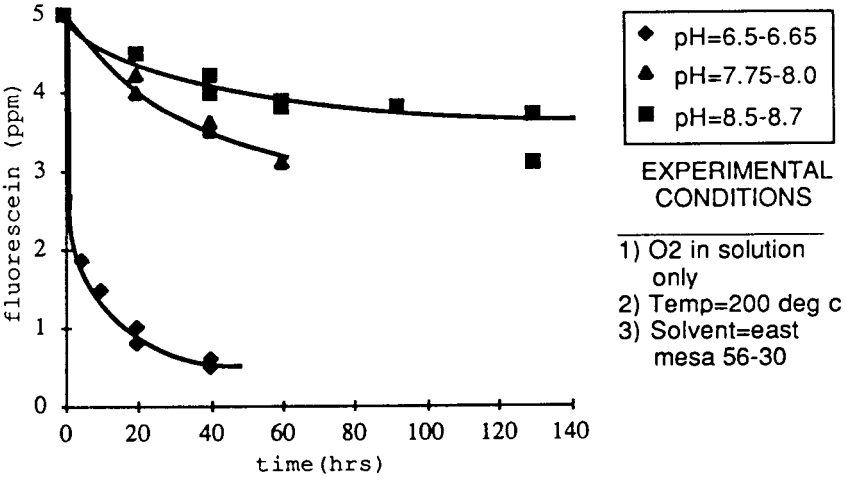

Figure 4. Fluorescein decay vs. time. The initial concentration of fluorescein was 5 ppm.

The in-situ stability of fluorescein has been demonstrated at the East Mesa geothermal

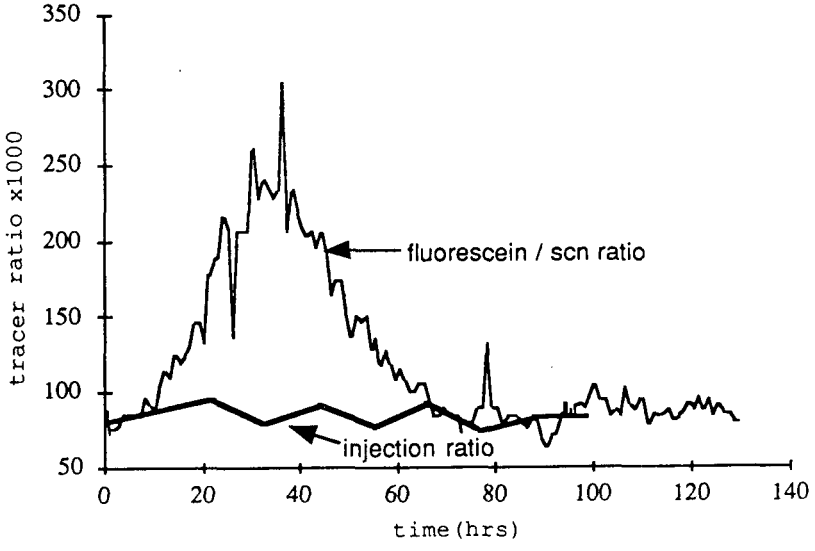

Figure 5a. Ratio of two tracers, SCN and fluorescein, after remaining in the 174°C reservoir for 6 months. The zero time on the x-axis represents the beginning of fluid withdrawal.

appears to be thermally stable, in accordance with the experimental results.

One set of tests was performed on rhodamine WT at 200°C in oxygen and in nitrogen. The results show that rhodamine WT is similar to fluorescein in its sensitivity to the presence of oxygen. In addition, however, it was found that rhodamine WT adsorbs onto colloidal silica as well as filter paper at room temperature. We hope to quantify these effects in the future.

Two sets of experiments were conducted on the hydrocarbons. One set used a monofluorinated, a perfluorinated, and a trifluoromethyl substituted benzoic acid as well as two forms of sulfonic acid. These were tested at temperatures of up to 150°C for 172 hours and in oxygen and nitrogen atmospheres. The results are shown in Figure 6. All compounds were stable with the exception of the perfluorinated benzoic acid. This is the opposite of what would be expected from groundwater studies where the perfluorinates are the most stable tracers.

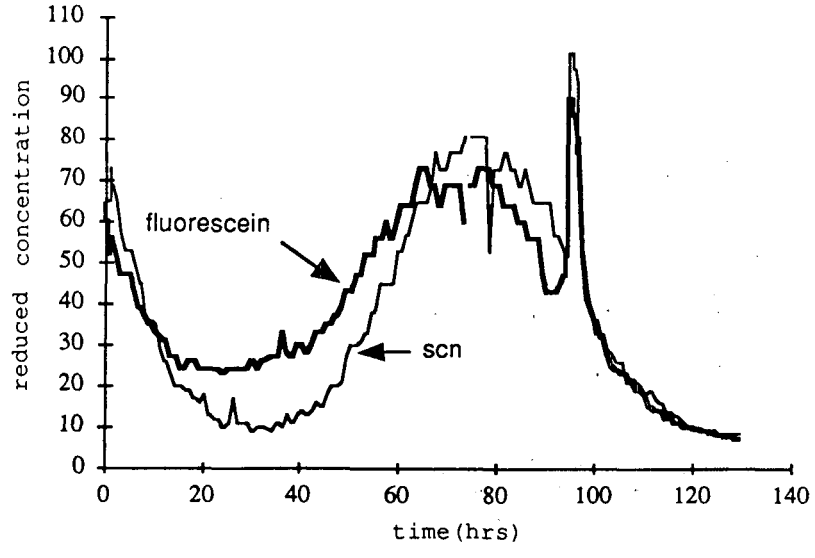

Figure 5b. Reduced concentration normalized to injected concentration of tracers vs. time. Time axis is as in Figure 5a.

The second set of experiments was run for 168 hours at 250°C in oxygen and in nitrogen atmospheres. At the present time 26 of the tracers have been tested and analyzed. Of the 26, only 7 were reasonably stable. Those were compounds B, L, Q, DD, FF, HH, and II, shown in Figure 2. The unifying factor of the stable species appears to be related to a low degree of fluorination and the location and inclusion of a methyl group on the benzene ring, primarily at the carbon that is meta to the carboxyl group. Results on the remaining hydrocarbons are expected during January of 1986.

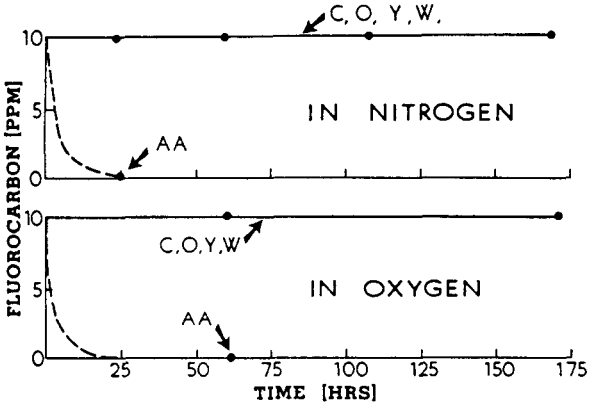

Figure 6. The stability with time of five commonly used groundwater tracers. Compound names and structures are listed in Figure 1.

CONCLUSIONS

Twenty-six derivitized hydrocarbons as well as fluorescein and rhodamine have been tested for thermal stability in pressurized autoclaves. Of these 28 compounds, 7 derivitized hydrocarbons and fluorescein have proven to be stable at high temperatures. The compounds have a variety of liquid-steam distribution coefficients, and will thus be applicable to vapor- as well as liquid-dominated geothermal systems. Testing of additional tracers is in progress.

ACKNOWLEDGEMENTS

This report was funded under U. S. Department of Energy Contract No. DE-AC07-85ID12489. Patrick Daubner drafted the figures and Joan Pingree typed the manuscript. We are grateful to them both.

REFERENCES

Adams, M. C., 1985, Tracer stability and chemical changes in an injected geothermal fluid during injection-backflow testing at the East Mesa geothermal field: 10th Workshop on Geothermal Reservoir Engineering, Stanford Univ., p. 247-252.

Bentley, H. W., 1983, Development and use of groundwater tracers at the Waste Isolation Pilot plant, Southeastern New Mexico: EOS, 64.

Bentley, H. W., 1982, Selection and design of tracers for evaluation of aquifer parameters: ACS Symposium on the Hydrology of Mining and Industrial Wastes, El Paso, Abstracts with program.

Davis, S. N., Campbell, D. J., Bentley, H. W., Flynn, T. J., 1985, An introduction to groundwater tracers: EPA Manual (in review).

Davis, S. N., Thompson, G. M., Bentley, H. W., Stiles, G., 1980, Groundwater tracers - A short review: Groundwater, v. 18, p. 14-23.

Gudmundsson, J. S., Hauksson, T., Thorhallsson, S. Albertsson, A., and Thorolfsson, G., 1984, Injection and tracer testing in Svartsengi field, Iceland: Proc. 6th N. Z. Geothermal Workshop, p. 175-180.

Hydro Geo Chem, Inc., 1985a, Convergent flow tracer tests at the H-6 hydropad at the Waste Isolation Pilot Plant (WIPP) in southeastern New Mexico: Prepared for Sandia National Laboratories.

Hydro Geo Chem, Inc., 1985b, Field investigation to evaluate the hydraulic characteristics of the Lewis Shale and Almond sandstone in the vicinity of the proposed "B" pond: Prepared for Pacific Power and Light Company.

McCabe, W. J., Barry, B. J., and Manning, M. R., 1983, Radioactive tracers in geothermal underground water flow studies: Geothermics, v. 12, p. 83-110.

Stetzenbach, K. J., Jensen, S. L., Thompson, G. M., 1982, Trace enrichment of fluorinated organic acids used as ground-water tracers by liquid chromatography: Environmental Science and Technology, v. 16, p. 250-254.

PROCEEDINGS, Eleventh Workshop on Geothermal Reservoir Engineering
Stanford University, Stanford, California, January 21-23, 1986
SGP-TR-93

THERMAL STABILITY OF CHELATED INDIUM ACTIVABLE TRACERS

Costas Chrysikopoulos and Paul Kruger

Stanford University, CA 94305

ABSTRACT

The thermal stability of indium tracer chelated with organic ligands ethylenediaminetetraacetic acid (EDTA) and nitrilotriacetic acid (NTA) was measured for reservoir temperatures of 150, 200, and 240°C. Measurements of the soluble indium concentration was made as a function of time by neutron activation analysis. From the data, approximate thermal decomposition rates were estimated. At 150°C, both chelated tracers were stable over the experimental period of 20 days. At 200°C, the InEDTA concentration remained constant for 16 days, after which the thermal decomposition occurred at a measured rate constant of k_{obs} = 0.09 d^{-1}. The thermal decomposition of InNTA at 200°C showed a first order reaction with a measured rate constant of k_{obs} = 0.16 d^{-1}. At 240°C, both indium chelated tracers showed rapid decomposition with rate constants greater than 1.8 d^{-1}. The data indicate that for geothermal reservoir with temperatures up to about 200°C, indium chelated tracers can be used effectively for transit times of at least 20 days. These experiments were run without reservoir rock media, and do not account for concomitant loss of indium tracer by adsorption processes.

INTRODUCTION

Reinjection of thermally spent geothermal brines is attractive for two distinct advantages. For environmental protection, it provides disposal of hazardous waste brines which cannot be discharged to surface waters. For operational efficiency, it serves to maintain reservoir pressure and enhance thermal energy recovery from the reservoir formation. However, uncertainties exist about the long-term potential of reinjection, such as the possibility of permeability reduction, inducement of seismic events, and the reduction of discharge enthalpy by initial breakthrough of cooled recharge fluid causing losses in steam production. To study these uncertainties, several tracer investigations have been performed to investigate reservoir structure and path networks (e.g., Horne, 1982). The features of tracer response important for these studies are early breakthrough time, peak tracer concentration, fractional recovery, and shape of retardation tail. Many tracers are not sufficiently sensitive for determining breakthrough time and retardation tail. Among the properties of suitable tracers for such studies, problems exist with thermal stability and adsorption processes leading to losses and retardation of the tracer with respect to the recharge fluid. Activable tracers are considered for their high sensitivity by radioactivity measurement and wide variety of stable materials compatible with the high-temperature and adsorption-prone geothermal reservoir environment. This paper discusses the selection of suitable activable tracers for liquid-dominated reservoirs and thermal stability of complexed activable tracers over a range of geothermal reservoir temperatures.

NEUTRON ACTIVATION ANALYSIS

The technique of neutron activation analysis is a unique combination of nuclear and chemical processes selected to optimize the precision and accuracy of trace-element chemical analysis or a high-dilution tracer study. Very few analytical methods offer the versatility and sensitivity achievable by neutron activation analysis. The advantages of neutron activation analysis and its application to ground water aquifers are described by Kruger (1971). For a tracer study a suitable stable material with proper chemical and nuclear properties must be selected so that upon thermal neutron irradiation it will produce the desired activation product. Irradiation with thermal neutrons is preferable because thermal neutron capture cross sections are large and production of interfering radioisotopes are minimized. Several devices are readily available with large thermal neutron fluxes, such as low-power nuclear research reactors and radioisotope sources. The quantity of tracer material needed as a geothermal reservoir tracer is dependent upon the neutron flux available. The higher the neutron flux the smaller the quantity of stable element required. The amount of the radioisotope produced at the end of irradiation period is proportional to the parent isotope and its disintegration rate is given by the radioactivation equation:

$$D_0 = n\,\sigma\,\varphi\,(1-e^{-\lambda\tau}) \qquad (1)$$

where, D_0 = amount of radioactivity of the product radionuclide at the end of irradiation (disintegrations per second, dps); φ = incident neutron flux (n/cm^2 sec); σ = neutron capture cross section (cm^2); n = number of atoms present in the sample which can give rise to the product activity; λ = decay constant of the product radionuclide (sec^{-1}); and τ = length of irradiation (sec).

After the end of irradiation, the activity of the product radionuclide decreases according to the radioactivity decay law:

$$D_t = D_0\,e^{-\lambda t} \qquad (2)$$

where, t = the elapsed time from the end of irradiation to the start of measurement; D_t = amount of radioactivity of the product radionuclide at time t.

The minimum amount of a tracer element required for efficient detection under given irradiation and counting conditions is given by the sensitivity equa-

tion:

$$w_{min} = \frac{N_{min} M}{\varepsilon \sigma \varphi A' f (1-e^{-\lambda \tau}) e^{-\lambda t}} \quad (3)$$

where, w_{min} = minimum weight of target element (grams); f = fractional isotopic abundance; A' = Avogadro's number; M = atomic weight of the element; $\varepsilon = N/D$, counting efficiency; and N_{min} = minimum number of counts during counting time interval (cps). Other parameters, such as chemical yield if chemical separations are required, can be included in the sensitivity equation. For similar irradiation and measurement conditions of the tracer and a known standard, the activable tracer measurement reduces to the simple form of:

$$w_{tr} = w_{std} \frac{D_{tr}}{D_{std}} \quad (4)$$

where the subscripts tr and std indicate tracer and standard respectively.

The irradiation duration is a relative parameter and depends upon the nuclear properties of the selected isotopic tracer as well as on the design characteristics of the activation analysis. When tracer concentrations are close to the limits of sensitivity, it is desirable to irradiate enough time for the tracer to approach a level of steady state or saturation, in which radioactive products disintegrate at the same rate at which they are formed. If the irradiation is terminated before the steady state is achieved, then the disintegration rate of the active nuclide is less than its rate of formation. For short-lived active nuclides the approach to saturation activity level is fast. On the other hand, for long-lived nuclides a careful estimation of the minimum desired level of radioactivity reduces the time period of the activation process.

The radioactivity of the tracer is measured by monitoring selectively the energies and intensities of the gamma-rays emitted by the product radionuclide with a radiation detector coupled with a multichannel analyzer system. Several radiation detectors are commercially available but the sodium-iodide thalium, NaI(Tl), detectors are most useful when sensitivity is the main concern or low levels of radioactivity are to be measured (Friedlander et al., 1981).

Occasionally, samples may contain major constituents whose activation would lead to high levels of radiation or to generation of radionuclides with gamma radiation interfering with the radiations from the product nuclide. These samples require chemical preconcentration of the trace elements prior to neutron activation. Several techniques are available for separation of the interfering constituents; however, the most favorable is the rapid ion exchange separation technique (Matthews and Riley, 1970). If ion exchange is not applicable, an alternative preconcentration method is coprecipitation (Navada et al., 1981; Drabaek, 1982). Postirradiation separation is necessary when the highest possible sensitivity is required. Postirradiation separations are more reliable because once the radioactive species are produced any chemical manipulation can be performed on the sample without contamination of the radioelements being measured.

SELECTION OF ACTIVABLE TRACERS

The requirements for a suitable activable tracer are: (a) a background concentration as close as possible to the minimum detectable amount of tracer by available detection systems, (b) large natural isotopic abundance, (c) large neutron activation cross sections, (d) appropriate gamma radiation of the product radionuclide for measurement by gamma-ray spectrometry, and (e) optimum half-life of the product radionuclide.

An optimization analysis for external tracers, based on a literature survey on the chemical composition of geothermal effluents taking into account the criteria for activable tracer, was conducted and four potential activable tracers were identified: vanadium (V), cobalt (Co), indium (In), and dysprosium (Dy). Table 1 summarizes the sensitivity calculations of the elements based on 10-minute irradiation in thermal neutron flux of 2×10^8 n/cm^2-sec and 30-minute delay time until measurement. The minimum value of N = 60 cpm at the measurement time was set as an additional sensitivity requirement. This arbitrary counting rate value is high enough to permit efficient detection of the gamma-ray of interest. Indium is considered to be the most promising of the four potential activable tracers, because of its unique combination of good detection sensitivity and relatively high energy of major gamma-ray emission. High-energy gamma-rays are preferred when interfering radionuclides with low gamma-energy are present because their Compton scattering contribution to the tracer full-energy peak is negligible. However, counting efficiency decreases with increasing gamma-ray energy.

Indium is a member of the Group IIIA elements of

Table 1. Laboratory Sensitivity for the Potential Activable Tracers

TARGET NUCLIDE			
Element	Isotope	f *	$\sigma_{(n,\gamma)}$ *
V	^{51}V	0.997	4.88
Co	^{59}Co	1.000	19
In	^{115}In	0.957	70
Dy	^{164}Dy	0.281	900
PRODUCT NUCLIDE			
Isotope	$T_{1/2}$ *	Major-γ (MeV)*	Sensitivity (mg)
^{52}V	3.75 m	1.434	126.06
^{60m}Co	10.47 m	0.059	2.24
^{116m}In	54.12 m	1.294	0.59
^{165}Dy	2.33 h	0.095	0.10

* The nuclear data have been adapted from Lederer and Shirley (1978). f = isotopic abundance; $\sigma_{(n,\gamma)}$ = thermal neutron cross section in barns.

the Periodic table, and has only two naturally occurring isotopes with mass numbers 113 and 115. The cross sections for $^{113}_{49}In(n,\gamma)^{114}_{49}In$ and $^{113}_{49}In(n,\gamma)^{114m}_{49}In$ reactions are relatively small, 3 and 5 barns respectively. Also, ^{114}In has a relatively short half-life (71.9 seconds), while ^{114m}In has a half-life of 49.5 days which is very long for an activable tracer. In addition to these unfavorable properties, ^{115}In has a small isotopic abundance (4.3%); therefore, this natural isotope of indium is not useful for geothermal tracing. On the other hand, the cross sections for $^{115}_{49}In(n,\gamma)^{116}_{49}In$ and $^{115}_{49}In(n,\gamma)^{116m}_{49}In$ reactions are quite large, 41 and 70 barns respectively. The 14.1 second ^{116}In is easily excluded from any tracing applications because of its extremely short half-life. The unique combination of good isotopic abundance of $^{115}_{49}In$ (95.7%) and the fairly good half-life of its activation product (54.12 minute-^{116m}In) is the chief reason that makes indium an excellent activable tracer. The gamma-ray spectrum of this isotope consists of several gamma rays ranging from 0.138 to 2.225 MeV. Its major gamma ray is 1.2935 MeV with an absolute intensity of 85 percent, which makes its detection tractable by scintillation detectors.

Indium is a relatively rare metal and is widely distributed in combined form. The metal occurs in minerals either as an isomorphous replacement for other elements of similar ionic radii or as structural member of the principal mineral (Linn and Schmitt, 1972). The indium concentration of natural waters is very low. Hot spring waters in Bulgaria were reported to contain up to 40 ppb indium (Smith et al., 1978), while indium concentration in Pacific Ocean water was found to be 4 ppt (chow and Snyder, 1969). The exact indium concentration of any representative geothermal fluid has not been evaluated, however Cosner and Apps (1978) reported that the indium content of geofluids is less than 100 ppb.

Indium exhibits positive oxidation states from one through three, but the common valence is three. Since the use of a cation tracer is not advisable (Adams, 1985) and because anionic solute species tend to be more conservative than cationic species, chelation of indium is necessary to ensure chemical stability in geofluids.

The organic ligands ethylenediaminetetraacetic acid (EDTA) and nitrilotriacetic acid (NTA) form strong water-soluble complexes with a variety of elements, and were chosen to enhance the solution stability of the selected tracer. Both chelating agents have the ability of ionizing each one of their carboxyl groups. In general, EDTA can form coordination bonds at six sites, the four oxygen and the two nitrogen sites. The metal complexes of EDTA form five five-membered rings and reduce the charge on the central atom by four. On the other hand, NTA can form coordination bonds at four sites, the three oxygen and one nitrogen sites. The metal complexes of NTA form three five-membered rings and reduce the charge of the central atom by three. The two indium chelates are similar but InEDTA possesses two additional rings. The stability constant for InEDTA is K_s =24.9 and for InNTA is K_s = 15.9. The principal factor influencing the stronger stability of InEDTA over InNTA is the extra number of rings, or more specifically the stability of the metal complex increases with increasing number of chelate rings (Dwyer and Mellor, 1964).

The thermal stability of the chelated tracers is an important consideration for their use in geothermal reservoirs. Venezky and Moniz (1969) reported that EDTA in aqueous solutions is stable up to 200°C. They observed a secondary degradation process at this temperature in which the decomposition products retain chelating ability. At higher temperatures primary degradation occurs forming products without evident chelating characteristics. Martell et al. (1975) reported that NTA does not cleave at temperatures up to 260°C but decomposes above 290° through a stepwise decarboxylation. Since the information available in the literature is based primarily on the free organic ligands, the thermal stability of indium chelated complexes in particular, required experimental determination.

EXPERIMENTAL

The study concentrated mainly on the laboratory investigations needed to provide a linkage between current information about indium chelated tracers and their unknown behavior in liquid-dominated geothermal systems. The experimental work consisted of two parts. First, batch experiments were carried out at room temperature to evaluate and compare the time stability of indium solubility as EDTA and NTA complexed ions. Second, thermal stability measurements of the indium chelates were performed for reservoir temperatures of 150, 200, and 240°C, to determine thermal decomposition rates from the experimental data.

Apparatus: Gold plated pressure vessels of approximately 40-ml volume, provided by the U.S. Geological Survey, Menlo Park, were employed for the high temperature experiments. The choice of gold plated pressure vessels was dictated by the desire to minimize interactions between tracer solution and vessel wall. The pressure vessels were housed in an air-bath at constant temperature within ±0.5°C. The samples were activated in the Stanford Linear Accelerator Center (SLAC) ^{252}Cf neutron irradiation source at a thermal neutron flux of $2x10^{8}$ n cm^{-2} s^{-1}. Measurement of 54.12 minute-^{116m}In radioactivity was performed by gamma-ray NaI(Tl) scintillation spectroscopy with a multichannel analyzer in the Stanford Environmental Engineering laboratory.

Reagents: The indium standard solution was prepared by dissolving high-purity indium metal in concentrated HNO_3. The disodium salts of analytical reagent grade EDTA and NTA were used for the ligand standards. Milli-Q reagent grade deionized water was used as solvent. The indium solution was acidified to reduce adsorption onto container walls. The pH of the organic ligand standards was adjusted to a pH slightly above the last pK value of the corresponding ligand, because chelating agents are polyprotic acids and usually only the fully deprotonated form of the acid gives complexes with the metal ion. The indium tracer solutions were formed with a chelon to metal mole ratio of 10 to increase the stability of the indium-chelate complexes.

Procedure: The time stability experiments at room temperature (20-22°C) were conducted over a two month period. Stock solutions of indium chelated tracers at a concentration of 505 ppm were prepared and stored in glass containers with ground glass stoppers. At regular intervals two 5-ml samples of

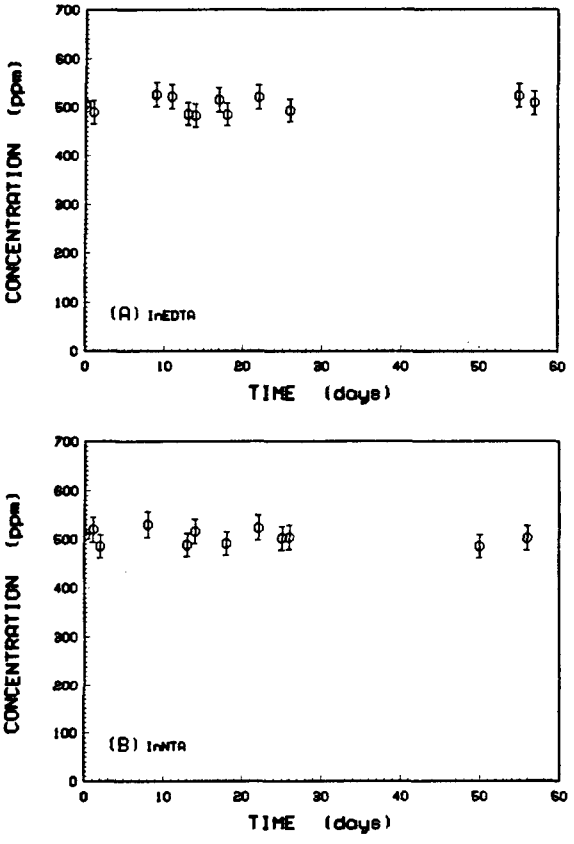

Figure 1. Indium chelated time stability behavior

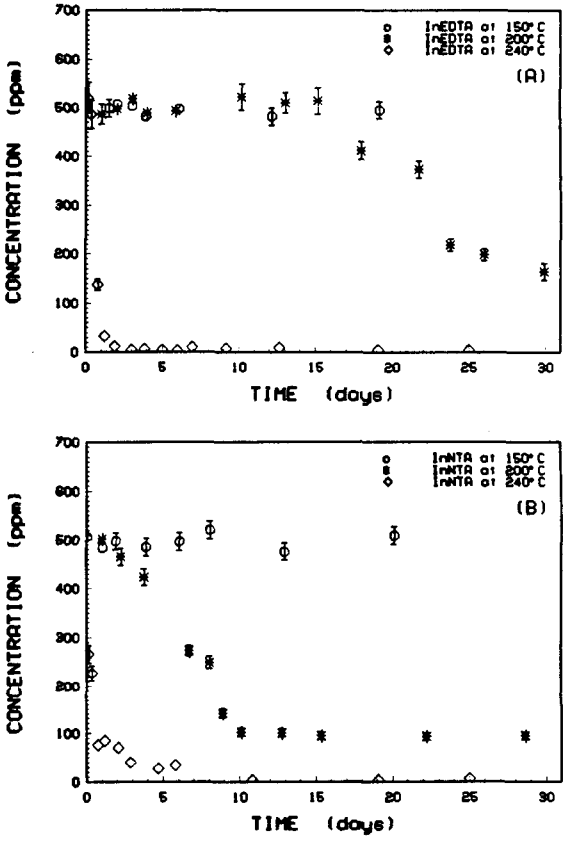

Figure 2. Indium chelated thermal stability behavior

tracer solution were transferred by pipette from each glass container to 15-ml polystyrene centrifuge tubes. After centrifugation at 3500 rpm for ten minutes, 2-ml of the supernatant liquid were removed from each centrifuge tube to a 6-ml Wheaton scintillation capsules for neutron irradiation and gamma-ray spectroscopy. Comparator standards were prepared and encapsulated with the unknown samples and were treated identically under the same irradiation flux conditions. The thermal stability high temperature experiments were conducted over 20 to 30 day periods. The pressure vessels were filled with 10-ml tracer solution and were sealed with teflon discs to prevent sample leakage. Geothermal reservoir temperatures were simulated with an air-bath. The vessels were taken from the air-bath and quickly quenched by immersion in a cool water-bath. The samples were transferred to centrifuge tubes and the detection of the soluble indium concentration was performed with the same analytical procedure as the one described for the room temperature experiments.

RESULTS AND DISCUSSION

The results of the tracer time stability investigations are given in parts A and B of Figure 1. The average concentration of 502 ppm indicates that there was no change in the soluble indium concentration during the experimental time. Any unchelated indium ions would be expected to adsorb onto container walls and to precipitate as indium hydroxide. The precision of the analytical procedure was estimated to be ±14 ppm. The error bars express only the counting error of the radioactivity measurements.

The experimental data from the high temperature runs are given in parts A and B of Figure 2. At 150°C, both chelated tracers were stable over the experimental period of 20 days. At 200°C, the soluble indium concentration of the InEDTA tracer solutions remained constant for 16 days, and then decreased with a measured rate constant of $k_{obs} \cong 0.09\ d^{-1}$. The time lag before the occurrence of any significant change in the total soluble indium concentration can be attributed to the secondary degradation products of EDTA. The thermal decomposition of InNTA at 200°C showed a first order reaction with a measured rate constant of $k_{obs} \cong 0.16\ d^{-1}$. At 240°C the data were not suitable for quantitative analysis because the time required for the first few pressure vessels to reach air-bath temperature was an appreciable fraction of each heating period. Nonetheless, both indium chelated tracers showed rapid decomposition with rate constants greater than $1.8\ d^{-1}$.

CONCLUSIONS

From the experimental results it was concluded that the organic ligands EDTA and NTA form stable time persistent complexes with indium at room temperature. The results from the thermal stability measurements showed that indium chelated tracers can be used effectively in geothermal reservoirs with temperatures up to about 200°C for transit times of at least 20 days. The data indicate that indium chelation with EDTA is favorable for high-temperature reservoirs.

Experiments are underway to investigate the effects of temperature and organic complexing ligands on the adsorption of indium on geothermal rock types, such as graywacke. Initial experiments are being run to determine adsorption and precipitation phenomena of In^{+3} at room and elevated temperatures.

ACKNOWLEDGEMENTS

The authors would like to thank Mike Thompson of USGS, Menlo Park for many stimulating discussions and for permission to the high-temperature laboratory; as well as Don Busick and Gary Warren of Health Physics, SLAC for allowing us to use the ^{252}Cf neutron source. This work was funded by U.S. Department of Energy under contract number DE-AT03-80SF11459.

REFERENCES

Adams, M. C. (1985), "Tracer Stability and Chemical Changes in an Injection Geothermal Fluid During Injection-Backflow Testing at the East Mesa Geothermal Field," Tenth Workshop on Geothermal Reservoir Engineering, Stanford Univ., pp. 247-252.

Chow, T. J. and Snyder, C. B. (1969), "Indium Content of Sea Warter," *Earth and Planetary Science Letters*, **7** , pp. 221-223.

Cosner, S. R. and Apps, J. A. (1978), "Compilation of Data on Fluids from Geothermal Resources in the United States," U. S. Dept of Energy, W-7405-ENG-48.

Drabaek, I. (1982), "Analysis and Time Stability of Activable Hydrospheric Tracers," *J. Radioanal. Chem.*, **75** , pp. 97-106.

Dwyer, F. P. and Mellor, D. P. (1964), *Chelating Agents and Metal Chelates*, Academic Press, New York, NY.

Friedlander, G., Kennedy, J. W., Macias, E. S. and Miller, J. M. (1981), *Nuclear and Radiochemistry*, Wiley Interscience, New York, NY.

Horne, R. N. (1982), "Effects of Water Injection Into Fractured Geothermal Reservoirs: A Summary of Experience Worldwide, Stanford Geothermal Program, SGP-TR-57, Stanford CA.

Kruger, P. (1971), *Principles of Activation Analysis*, Wiley Interscience, New York, NY.

Lederer, C. M. and Shirley, V. S., Eds. (1978), *Table of Isotopes*, Wiley Interscience, New York, NY.

Linn, T. A. and Schmitt, R. A. (1972), "Indium," in *Handbook of Geochemistry* Vol. 2, Wedepohl, K. H., Ed., Springer-Verlag, Berlin, Heidelberg.

Martell, A. E., Motekaitis, R. J., Fried, A. R., Wilson, J. S. and MacMillan, D. T. (1975), "Thermal Decomposition of EDTA, NTA, and Nitrilotrimethylenephosphonic Acid in Aqueous Solution," *Can. J. Chem.*, **53** , pp. 3471-3476.

Matthews, A. D. and Riley, J. P. (1970), "The Determination of Indium in Sea Water," *Anal. Chim. Acta*, **5** , pp. 287-294.

Navada, S. V., Kulkarni, V. P. and Rao, S. M. (1981), "Study of Tracer Analysis of Iodide by the Cerium(IV)-Arsenic(III) Catalytic Method and Indium-EDTA Neutron Activation Method for Hydrological Investigation," in *Trace Analysis and Technological Development*, Spec. Contrib. Pap. Int. Symp., pp. 257-271. Sankar, D. M., Ed., Wiley Interscience, New York, NY.

Smith, C. I., Carson, B. L. and Hoffmeister, F. (1978), *Trace Metals in the Environment, Vol. 5-Indium*, Ann Arbor Science, Ann Arbor, MI.

Venezky, D. L. and Moniz, W. B. (1969), "Nuclear Magnetic Resonance Study of the Thermal Decomposition of Ethylenedinitrilotetraacetic Acid and its Salts in Aqueous Solutions," *Anal. Chem.*, **41** pp. 11-16.

PROCEEDINGS, Eleventh Workshop on Geothermal Reservoir Engineering
Stanford University, Stanford, California, January 21-23, 1986
SGP-TR-93

NATURAL STATE MODEL OF THE NESJAVELLIR GEOTHERMAL FIELD, ICELAND

G. S. Bodvarsson, K. Pruess,* V. Stefansson,** B. Steingrimsson,***
S. Bjornsson,† A. Gunnarsson,† and E. Gunnlaugsson†

*Lawrence Berkeley Laboratory, Earth Sciences Division
University of California, Berkeley, California 94720

**National Energy Authority of Iceland
Reykjavik, Iceland

†Reykjavik Municipal District Heating Service
Reykjavik, Iceland

ABSTRACT

The Nesjavellir geothermal system in southern Iceland is very complex from both a thermal and hydrologic point of view. There are large pressure and temperature gradients in the wellfield and zones with drastically different pressure potentials. Thus, natural fluid flow is substantial in the system and flow patterns are complex. We have developed a two-dimensional natural state model for the Nesjavellir system that matches reasonably well the observed pressure and temperature distributions. The match with field data has allowed determination of the energy recharge to the system and the permeability distribution. Fluids recharge the system at rate of 0.02 kg/s/m with an enthalpy of 1460 kJ/kg. The permeability in the main reservoir is estimated to be in the range of 1.5 to 2.0 md, which agrees well with injection test results from individual wells. Permeabilities in shallower reservoirs are about an order of magnitude higher. Most of the main reservoir is under two-phase conditions, as are shallow aquifers in the southern part of the field. The model results also suggest that the low temperatures in the shallow part of the northern region of the field may be due to the young age of the system; i.e., the system is gradually heating up. If this is the case the estimated age of the system near the wellfield is on the order of a few thousand years.

INTRODUCTION

The Nesjavellir high temperature geothermal field is located in the northern part of the Hengill geothermal area, which is estimated to be one of the largest geothermal areas in Iceland. The Nesjavellir field is now under extensive investigation by the Reykjavik Municipal District Heating Service for possible cogeneration of hot water and electricity.

The geothermal system at Nesjavellir is extremely complex from a hydrological standpoint (Stefansson, 1985). There are very large lateral pressure gradients in the present wellfield as well as large differences in pressure potential between feed zones in many of the wells. There are also large temperature variations in the field, generally with high temperatures to the south and lower temperatures in the north. It has been postulated from the pressure and temperature data that the southern part of the field is boiling, and that the northern part is in sub-cooled liquid conditions (Steingrimsson and Stefansson, 1979; Stefansson, 1985).

The present paper describes a two-dimensional model of the natural state of the Nesjavellir system. When the model was developed, field data were available for wells 2 - 10, and these data were used in the model development. Since then six additional wells have been drilled in the field and data from these recent wells change somewhat the conceptual model of the field. The new data will be incorporated into future models, including a three-dimensional natural state model.

CONCEPTUAL MODEL

To date, sixteen wells have been drilled at Nesjavellir (Fig. 1). The depth of the wells varies from 400 to 2200 m. Stefansson (1985) has described the pressure and temperature conditions as inferred from well data. Figure 2 shows feed zone pressures in wells 3 - 10. These data suggest the presence of several different aquifers with different pressure potentials (Stefansson, 1985; the pressure gradient from southwest to northeast can be seen in Figure 6). The temperature distribution in the system is also very complex, as illustrated in Figure 3. Temperatures are highest in the southwest, especially at shallow depths.

Stefansson (1985) presents a plausible conceptual model of the Nesjavellir system. He suggests that the main upflow zone feeding the system is southwest of the present wellfield. The fluids flow toward the northeast between well 12 and the other wells in the field, recharging the main wellfield. Feed zone pressures (Fig. 3) suggest that there are four zones with different pressure potentials in the wellfield area, but chemical characteristics of the fluids suggest a common origin.

In developing a two-dimensional natural state model, the complex temperature distribution of the system has to be explained. Of particular importance is the large SW-NE temperature gradient in shallow regions of the system (Fig. 3).

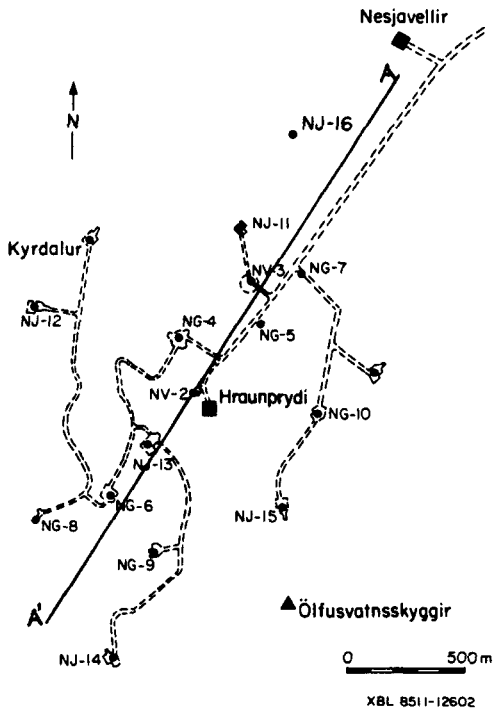

Figure 1. The wellfield at Nesjavellir. The line A-A' represents the cross-section considered in the two-dimensional natural state model.

There are several possible explanations for the declining temperature towards the northeast, including:

(1) *Fluid mixing:* Fluids flowing from the south mix with colder groundwater and cool down as they flow towards the north.

(2) *Rainfall cooling:* The hot fluids flowing to the north are cooled down due to mixing with cold infiltrating rainwater.

(3) *Steam losses:* Vaporization (boiling) occurs as fluids flow from the south, and steam escapes to surface manifestations, leaving behind colder fluids (e.g., Krafla field, Bodvarsson et al., 1984).

(4) *Permeability barriers:* Low permeability zones prevent the hot fluids from the south from flowing into the shallow aquifers in the northern part.

(5) *Young system:* The system is very young and still heating, with the thermal anomaly gradually extending to the north.

At present it is difficult to determine which one(s) of these alternatives is most likely to explain the observed trends. However, it appears that the first alternative, fluid mixing, is rather unlikely because the shallow pressure gradient is rather consistently from southwest to northeast at all depths; hence, fluid mixing is probably limited. One also expects that cooling due to rainfall infiltration cannot explain the temperature decrease to the north, because the very shallow groundwater aquifers in the northern part of the field have very different pressure potentials from those deeper. In the top 100 m, the water level is around 10 m below

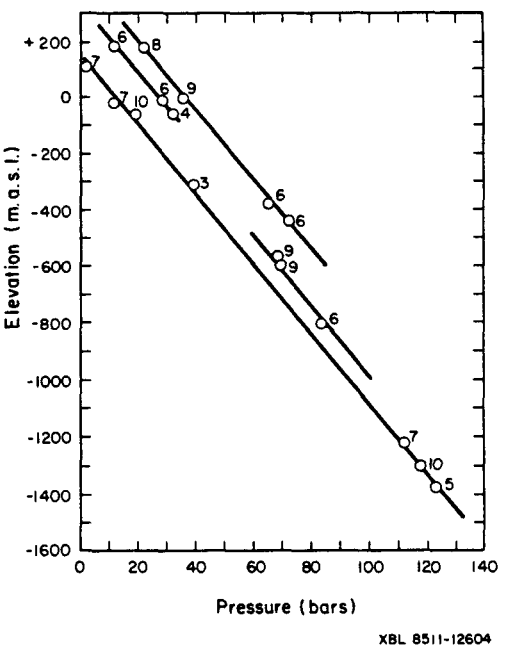

Figure 2. Pressures at feed zones in the wells.

ground surface, whereas below a depth of approximately 100 m the water level is approximately 70 m below ground surface. This suggests very low vertical permeability in the shallow part of the northern region; hence, it is unlikely that significant percolation to deeper aquifers occurs.

Vaporization of steam and flow to surface manifestations can also explain the sharp decrease in temperature to the north. At present, we do not have sufficient data regarding flow rates and enthalpies of fluids feeding the surface springs to judge if this is a realistic alternative explanation.

In the present work we investigate alternatives 4 and 5. In the basic model we assume that there is limited hydraulic communication between the shallow aquifers in the south and north. We use this model to calculate steady-state temperatures and pressures and compare them to the observed data. Then we investigate briefly the transient thermal development of such a system and the possibility that the Nesjavellir system is young and still developing based upon the thermal and hydraulic data that have been collected.

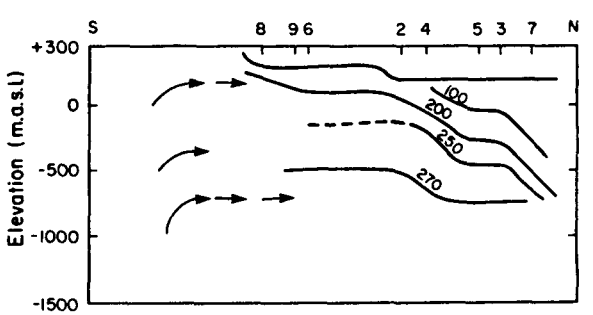

Figure 3. A north-south cross-section of the temperature distribution in the system. XBL 8511-12607

APPROACH

The fluid and heat flow patterns within the Nesjavellir systems are very complex, and cannot be explained entirely in terms of the simple two-dimensional model. However, in all modeling work it is best to start with as simple a model as possible in order to reproduce the main features of the geothermal systems. From such a simple model, more complex models can be developed in order to reproduce more details of the geothermal system. With this in mind, we have developed a simplified two-dimensional model of the Nesjavellir system. This model can readily be extended to three dimensions.

The model developed is a two-dimensional cross-section extending from southwest to northeast through the wellfield, as shown by line A-A' in Fig. 1. The model is intended to reproduce the main features of the temperature- and pressure-distributions in the system. Figure 4 shows the computational grid used. An upflow zone is assumed to be southwest of the the present wellfield. Fluids from the upflow zone flow upwards and then laterally from southwest to northeast (Fig. 3). Boundary nodes to the north are used to absorb the flowing fluids. The shaded areas in Fig. 4 are assumed to be low permeability zones.

Permeabilities and the flow rate and enthalpy of fluids recharging the system in the upflow zone were adjusted in order to obtain a match with the pressure and temperature distributions. Values for parameters assumed constant are given in Table 1. The numerical code MULKOM (Pruess 1982) was used in this work.

Table 1.
Constant parameters used in the simulations.

Parameter	Value
Porosity:	5%
Rock density:	2650 kg/m^3
Heat capacity:	1000 J/kg/°C
Thermal conductivity:	2.0 W/m/s/°C
Relative permeability:	X-curves
	$S_{rl} = 0.4$, $S_{rv} = 0.05$

BEST MODEL

After a number of iterations a steady state model was developed which gave a reasonable agreement between the calculated and observed pressure and temperature distributions in the system. Table 2 shows the thermodynamic values assumed for the boundary nodes. Figure 5 shows the calculated pressure distribution, and Figure 6 shows comparisons between observed and calculated pressure contours at 500 m below sea level. Figures 7 and 8 show the calculated temperature distribution and comparison with measured temperatures, respectively.

In general the figures show a rather good agreement with the measured data. There are certainly three-dimensional effects in the data that the two-dimensional model cannot resolve, and the model is not capable of matching large differences in pressure potential between different feed zones. Otherwise the agreement between calculated and observed values is reasonably good.

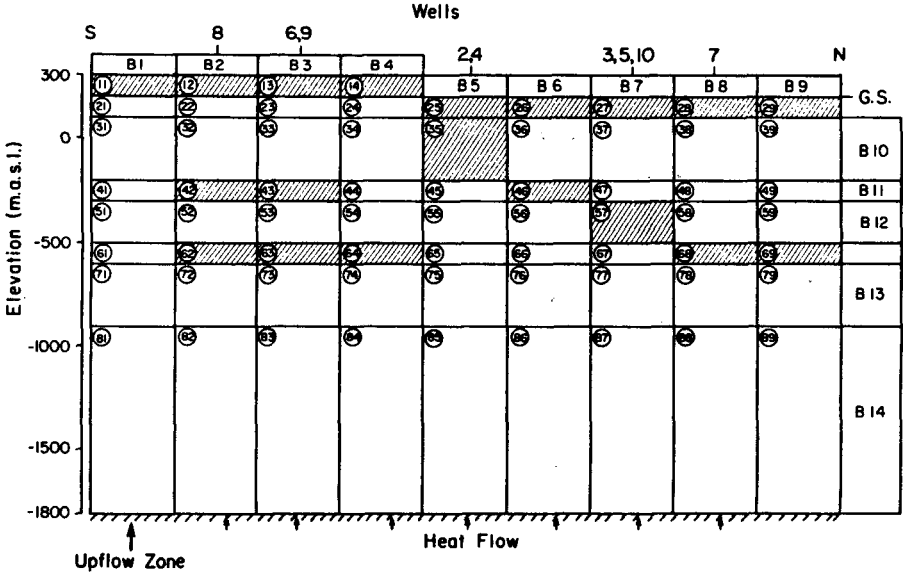

Fig. 4. Internal and boundary elements used for the two-dimensional natural state model. (Low permeability zones are shaded.) XBL 8511-12628

Table 2.
Thermodynamic condition of boundary nodes and mass flow rates into boundary nodes.

Boundary node	Temperature (°C)	Pressure (MPa)	Mass flow rate (kg/s/m)
B-1 to B-9	5	0.1	~ 0.
B-10	50	1.5	~ 0.
B-10	125	3.0	~ 0.
B-12	175	4.0	0.0020
B-13	270	7.0	0.0031
B-14	300	11.0	0.0149

In order to match the measured data, various zones with different horizontal and vertical permeabilities were included in the model. Figure 9 shows the various zones with different permeabilities; the permeability values are given in Table 3. The results indicate that the main reservoir below a depth of 800 - 900 m has a horizontal permeability of 1.5 - 2.0 md, and that the permeability is somewhat higher in the southern part of the reservoir than in the northern part. In the shallow regions in the southern part of the reservoir the calculated permeability is considerably higher than in the main reservoir, or 8 md both horizontally and vertically. The confining layers and the caprock are estimated to have permeabilities in the range 0.1 - 0.001 md.

In the best model 0.02 kg/m/s of fluids with an enthalpy of 1460 kJ/kg recharge the system through the upflow zone. This enthalpy corresponds to a temperature of approximately 320 °C, which is approximately the calculated temperature at the bottom of the model. Heat inflow of some 1.0 W/m^2 was specified at the bottom of the model in order to represent conductive heat flow or steam rising from depth. Figure 10 shows the mass fluxes in the system at steady state conditions. Most of the fluids flow laterally in the

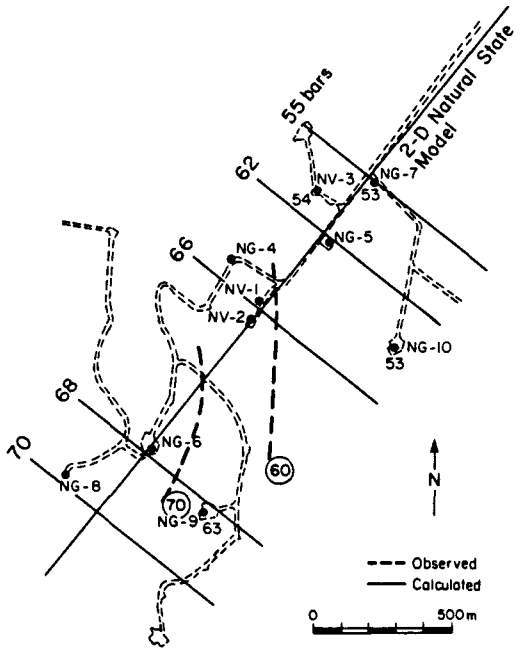

Figure 6. Comparison between calculated and observed pressures at 500 m.b.s.l. XBL 8511-12627

main reservoir from south to north. The mass flow rates into the boundary nodes are given in Table 2.

The calculated vapor saturation distribution is shown in Figure 11. Most of the main reservoir is in two-phase conditions, except for the region nearest the upflow zone. The calculated vapor saturation in the main reservoir is low and close to the residual steam saturation for the relative permeability curves used. In the shallow two-phase zone in the southern part of the field, the calculated vapor saturation is much higher, or close to 0.6. This high vapor saturation is in agreement with field data.

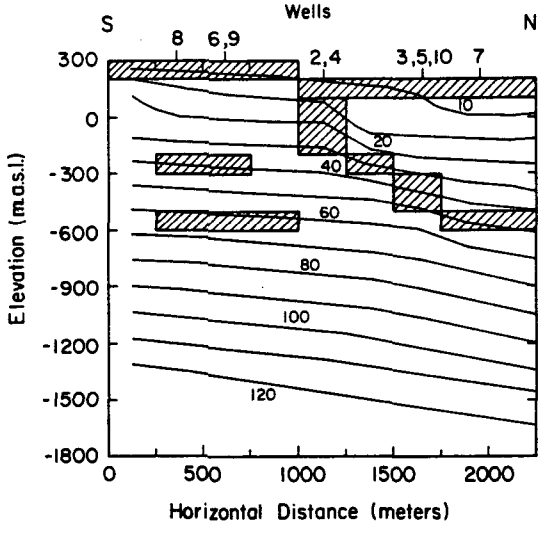

Figure 5. The calculated pressure distribution using the best model (steady state). XBL 8511-12605

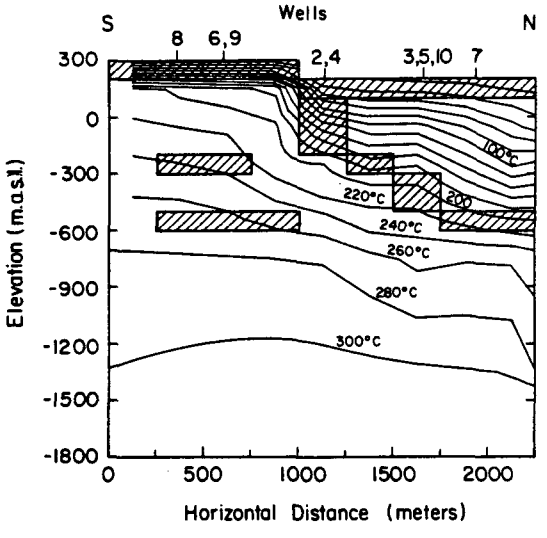

Figure 7. The calculated temperature distribution. XBL 8511-12606

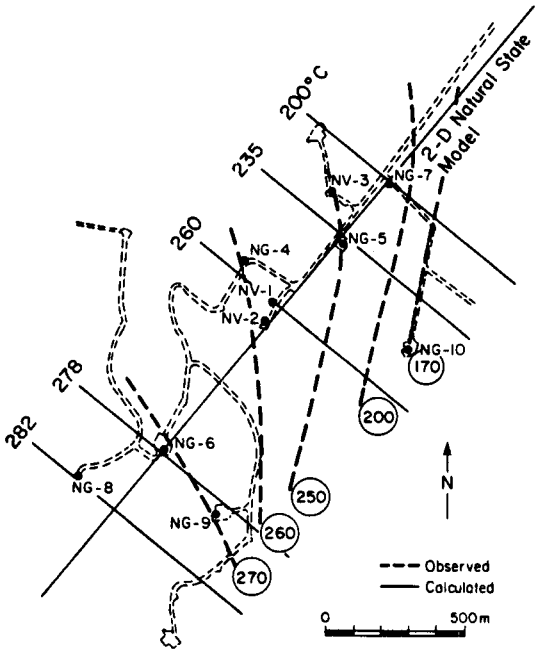

Figure 8. Comparison between calculated and observed temperatures at 500 m.b.s.l. XBL 8511-12626

Table 3. Permeabilities of the various reservoir zones.

Pattern	Permeability (md) Horizontal	Vertical
	0.001	0.001
	0.1	0.1
	8.0	8.0
	2.0	8.0
	1.0	1.0
	2.0	1.0
	1.5	1.0

XBL 8511-12663

TEMPERATURE EVOLUTION

The results from the best model were used to simulate the natural evolution of the system. The simulation is initiated with the entire system at a temperature of 20 ° C and corresponding hydrostatic pressure distribution. Fluids are removed from the northern-most internal elements (elements to 39, 49, 59, 79 and 89) at the rate determined by the best model. The boundary nodes (B10 - B14) are not used, because they would disturb the initial hydrostatic pressure distribution. At time zero fluid flow into the upflow zone begins at the rate and enthalpy determined from the best model.

Figure 12 shows the temperature distribution after 3,000 years of the evolution. The figure shows that the thermal anomaly in the shallow regions of the system has extended approximately to the assumed low permeability layers. Thus, it appears quite possible that the rather low temperatures observed in shallow regions of the northern part of the system may reflect its young age rather than the presence of low permeability confining layers. If this hypothesis is true, the age of the hydrothermal system is in the range 2000 - 3000 years. There are several observations suggesting that the geothermal system at Nesjavellir is geologically young, such as little mineral alteration at shallow depth, and the lack of equilibrium between the mineral assemblages and observed temperatures (Tomasson et al., 1974; Kristmannsdottir and Tomasson, 1974; Stefansson et al., 1983).

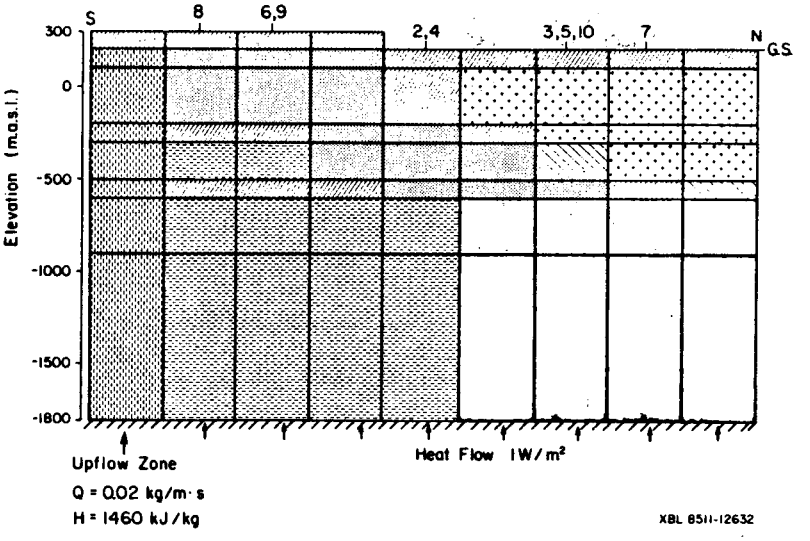

XBL 8511-12632

Fig. 9. The various reservoir zones with different permeabilities.

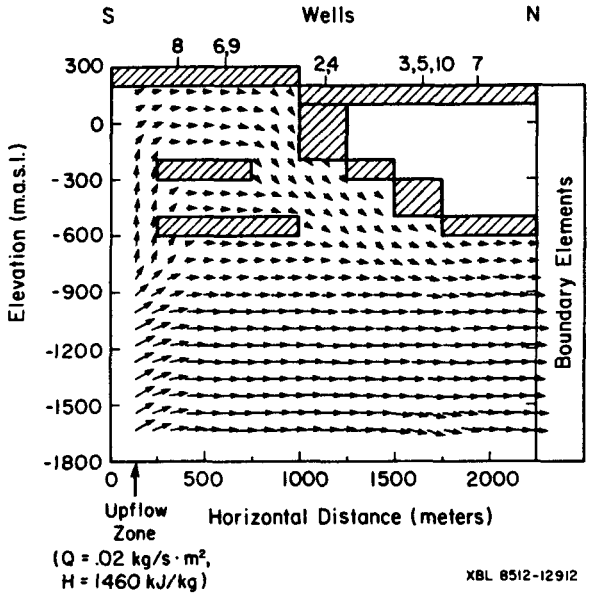

Figure 10. The steady-state flow field.

DISCUSSION

The non-uniqueness of the parameter values determined in this study is probably not a major problem for the system modeled. The main parameters determined from the natural state modeling are the recharge rate, enthalpy of the recharge fluids, and the permeability distribution in the system. It is well known that for isothermal problems the observed pressure distribution can be used to estimate either the mass flow rates or the permeabilities, but not both. In the present model, the temperature distribution is also matched and this allows for the determination of both mass flow rate and permeabilities within some limits. In fact, it is possible to determine approximately the permeability distribution and the total energy recharge rate, which is the product of the mass recharge rate and the enthalpy. Thus, for a given enthalpy, the mass recharge rate and the permeability distribution may be determined.

In the best model a recharge enthalpy of 1460 kJ/kg is used together with a mass recharge rate of 0.02 kg/s/m. Theoretically, the enthalpy of the recharge fluids could be as high as 2800 kJ/kg, but in that case the flow rate would be about 0.01 kg/s/m, and permeabilities would also be about half the values estimated. However, this would require the calculated pressure gradient to be close to vaporstatic in the upflow zone. Such conditions have not been observed so far in the Nesjavellir system. Therefore, the estimated values of the recharge rate and permeability distribution should be within a factor of two of the real values (given the two-dimensional model).

CONCLUSIONS

A two-dimensional natural state model of the Nesjavellir geothermal system has been developed. The model extends north-south through the present wellfield. It matches reasonably well the observed pressure and temperature distributions in the system. The major conclusions of this work are:

(1) In order to match the observed pressure and temperature distributions in the region modeled, an energy recharge rate of 30 kJ/s/m is required. A mass recharge rate of 0.02 kg/s/m and an enthalpy of 1460 kJ/kg were used in the simulations. However, it is possible that the recharge enthalpy is somewhat higher; this would reduce the mass recharge rate accordingly.

(2) Permeabilities in the main reservoir deduced from the natural state modeling are in the range of 1.5 - 2.0 md, which compares reasonably well with the results of injection tests performed on individual

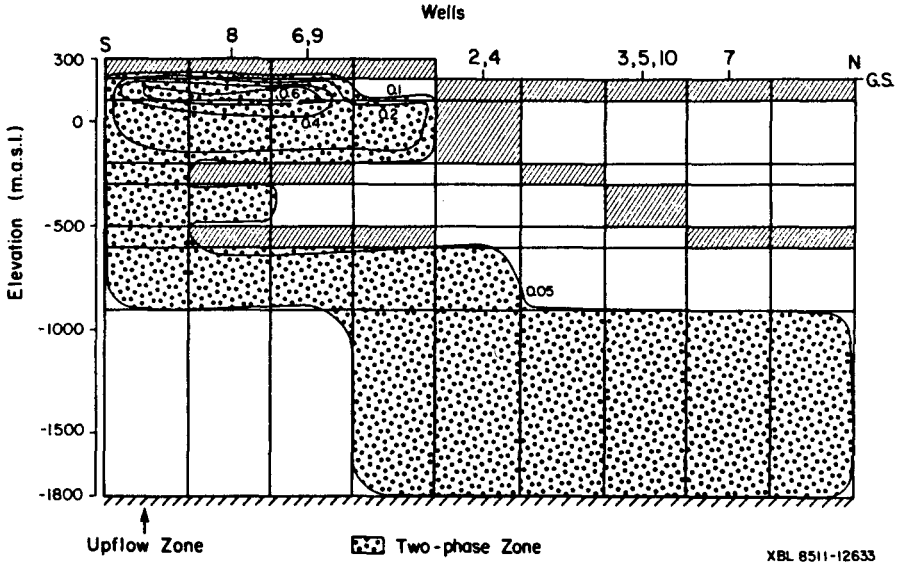

Fig. 11. The location of the two-phase zone in the system.

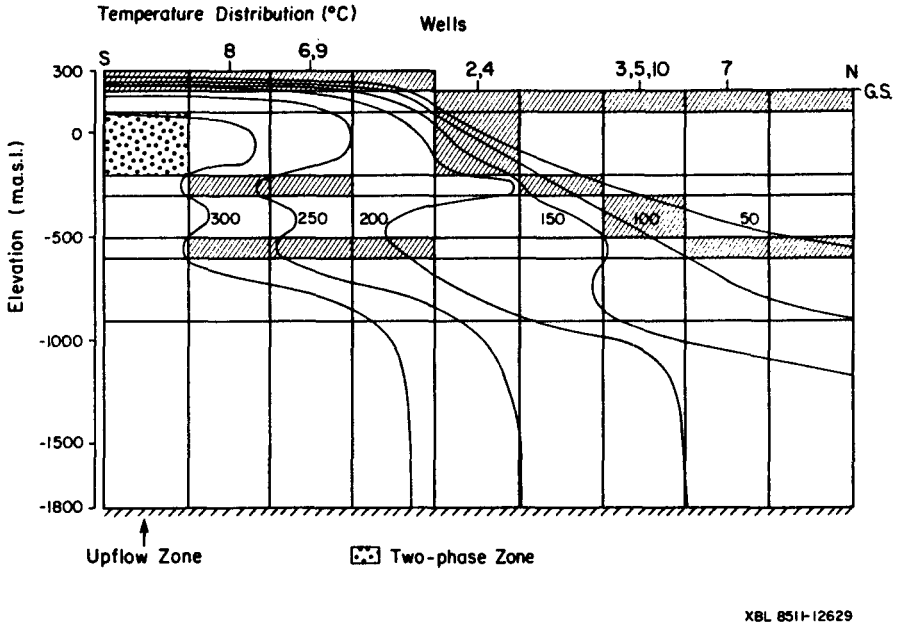

Fig. 12. The temperature evolution after 8,000 years for the evolution model.

wells. Permeabilities in the shallow aquifers in the southern part of the field are estimated to be considerably higher, or about 8 md.

(3) It appears possible from the modeling that the relatively low shallow temperatures in the northern part of the field are simply due to the young age of the system; i.e., the system is still heating up. If this is true, the modeling of the evolution of the system suggests that the age of the system is in the range of 2000 to 3000 years. There is an obvious need to determine if there are actually low permeability layers separating the hot reservoir from the shallower cooler zones.

ACKNOWLEDGEMENT

The Reykjavik Municipal District Heating Service is thanked for permission to publish data from the Nesjavellir high temperature geothermal field. This work was supported by the Reykjavik Municipal District Heating Service and through the Assistant Secretary for Conservation and Renewable Energy, Office of Renewable Technology, Division of Geothermal Technology.

REFERENCES

Bodvarsson, G.S., Pruess, K., Stefansson, V., and Eliasson, E.T., 1984, The Krafla geothermal field, Iceland 2. The natural state of the system, Water Resources Research, vol. 20, pp. 1531-1544.

Kristmannsdottir, H., and Tomasson, J., 1974, Nesjavellir - Hydrothermal alteration in a high temperature area, International Syposium on Water - Rock Interaction, Prague (September).

Pruess, K., 1982, Development of the general purpose simulator MULKOM, 1982 Annual Report, Earth Sciences Division, Lawrence Berkeley Laboratory, Berkeley, Ca.

Stefansson, V., 1985: The Nesjavellir high temperature geothermal field in Iceland, Proceedings, 10th Annual Workshop on Geothermal Reservoir Engineering, Stanford University, Stanford, CA, 1984.

Stefansson, V., Tomasson, J., Gunnlaugsson, E., Sigvaldason, M., Franzson H. and Sigurdsson, O., 1983, Nesjavellir hola NG-6, Borun, rannsoknir og vinnslueiginleikar, Orkustofnun 0S-83023/JHD-04, Reykjavik (in Icelandic).

Steingrimsson, B., and Stefansson, V., 1979: Nesjavellir. Hitastig og thrystingur i jardhitasvaedinu. Orkustofnun, 0S79032/JHD15, Reykjavik, 31 s.

Tomasson, J., Gronvold, K., Kristmannsdottir, H., and Thorsteinsson, Th., 1974, Nesjavellir, Well 5, report OSJHD-7423, National Energy Authority (in Icelandic), 47 pp.

PROCEEDINGS, Eleventh Workshop on Geothermal Reservoir Engineering
Stanford University, Stanford, California, January 21-23, 1986
SGP-TR-93

THE EVOLUTION AND NATURAL STATE OF LARGE-SCALE VAPOR-DOMINATED ZONES

S.E. Ingebritsen

U.S. Geological Survey, Menlo Park, CA 94025

ABSTRACT

Numerical simulation is used to define the rather special conditions under which large-scale vapor-dominated zones can evolve. Given an adequate supply of heat, a vapor-dominated zone can evolve within low-permeability barriers without changes in rock properties or boundary conditions. However, the evolution of the system is accelerated in cases involving an initially high fluid throughflow rate that decreases with time. Near-steady-state pressures within the vapor-dominated zone are shown to vary with depth to the caprock.

INTRODUCTION

Within a hydrothermal convection system, vapor-dominated conditions may be extensive areally (to 10's of square kilometers) and vertically (more than 3 km), as at The Geysers, California, or they may be very localized, confined to a few fractures or fracture systems. This paper presents results from a series of numerical experiments designed to illustrate the evolution and natural state of large-scale vapor-dominated zones. The numerical models are used to address a number of fundamental questions about the occurrence and behavior of such zones.

A classic paper by White and others (1971) proposed a model of vapor-dominated hydrothermal systems and compared such systems with the more common liquid-dominated or hot-water type. The essence of this model is that within part of a vapor-dominated system liquid is relatively immobile and steam is the pressure-controlling phase, and that springs fed by vapor-dominated systems are low in chloride, gassy, and generally acidic. As figure 1 shows, any distinction between vapor-dominated and liquid-dominated conditions based on the vertical pressure gradient, the relative mass flux of steam and liquid (q_s/q_w) or relative permeabilities (k_{rs}/k_{rw}) is arbitrary. However, it seems reasonable to assume that natural vapor-dominated zones of the type described by White and others would fall in the lightly patterned region of figure 1. Within this region

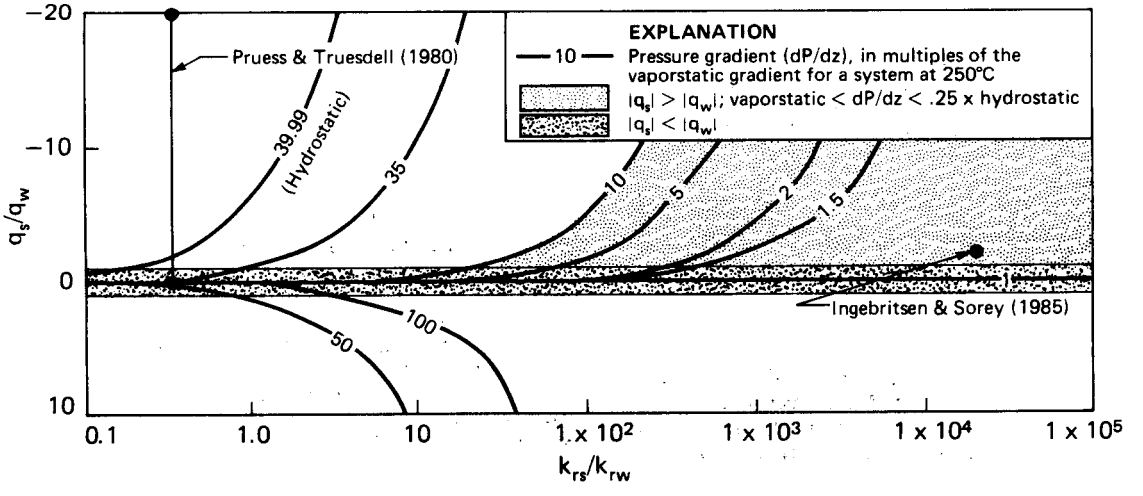

Fig. 1 Relationship between the vertical mass flux ratio of steam (q_s) to liquid (q_w) and the relative permeability ratio (k_{rs}/k_{rw}) for various vertical pressure gradients. A pressure gradient of one is vaporstatic.

there is vapor/liquid counterflow, with the vapor flux greater than the liquid flux, and the pressure gradient is less than 25 percent of hydrostatic.

The hydrothermal convection systems at The Geysers, California, Kamojang, Indonesia, and several areas (including Larderello) in Tuscany, Italy are generally referred to as vapor-dominated systems. The Matsukawa system, Japan is sometimes included in this group. The Geysers, Kamojang, and the Tuscany systems are all characterized by extensive vapor-dominated zones with near-vaporstatic vertical pressure gradients. Because of the low pressure gradients, these vapor-dominated zones are generally underpressured with respect to local hydrostatic pressures. They are apparently shielded from surrounding flow systems by low-permeability barriers, and are overlain by a zone that is liquid saturated or nearly saturated with a mixture of steam condensate and shallow groundwater. This shallow layer is sometimes referred to as the condensate zone.

Pressures in the upper parts of the vapor-dominated zones at the Geysers, Kamojang, and Larderello are generally near 30.6 bars, the pressure of saturated steam at maximum enthalpy. Wells completed into the vapor-dominated zones at The Geysers, Kamojang, and the Tuscany systems produce saturated or slightly superheated steam and little or no water. Wells at Matsukawa also produce "dry" steam, but the pressure gradient within the reservoir is apparently closer to hydrostatic than vaporstatic (Donaldson and Grant, 1981).

PREVIOUS WORK

There has been little quantitative analysis of the physical processes controlling the evolution and natural state of vapor-dominated zones. This is largely attributable to the general lack of analytical solutions to geologically meaningful two-phase flow problems, and to the computational difficulty and expense of simulating two-phase flow problems numerically over time scales of geologic interest.

Schubert and Straus (1979, 1980; Straus and Schubert, 1981) modeled certain aspects of vapor-dominated zones analytically. However, their reliance on analytical methods limited them to one-dimensional, steady-state cases, and often required additional simplifying assumptions.

Pruess and Truesdell (1980) attempted to simulate the evolution of a vapor-dominated system numerically with a radial model involving conductive heat flow at the lower boundary (approximately 30 hfu)[1/], a constant pressure/temperature condition at the upper boundary, and no-flow lateral boundaries. Their steady-state result involved a zone of two-phase counterflow beneath a 400 m thick low-permeability (3×10^{-12} cm^2) caprock. Within this two-phase zone the ratio k_{rs}/k_{rw} was approximately 0.3 and the pressure gradient was necessarily near hydrostatic (see figure 1).

Pruess and others (1983) simulated approximately 15 years of production from the vapor-dominated zone at Serrazzano, Italy. They incorporated what was known about the geology of the system into their model, but did not attempt to simulate the evolution and natural state. They also assumed that liquid was immobile within the vapor-dominated zone, and that the system was closed to recharge and discharge.

Ingebritsen and Sorey (1985; Sorey and Ingebritsen, 1984) described numerical simulations of the evolution and natural state of a "parasitic" vapor-dominated zone overlying and fed by a lateral flow of thermal water. The pressure gradient in the vapor-dominated zones in their models was near-vaporstatic (see figure 1).

Most recently, Pruess (1985) demonstrated numerically that a brief period of limited discharge through a low-permeability caprock could cause a transition from "liquid-dominated heat pipe" conditions (a slightly subhydrostatic pressure gradient and a boiling point with depth temperature distribution) to vapor-dominated conditions. With the exception of the controlled discharge event, the system was treated as closed.

CONCEPTUAL AND NUMERICAL MODELS

Figure 2 is a schematic diagram of the conceptual model that White and others (1971) developed, based largely on observations from The Geysers and Larderello. Within the extensive vapor-dominated zone in this model, the pressure gradient is somewhat above vaporstatic. Saturated steam and water coexist within the vapor-dominated zone, and there is steam/liquid counterflow, as a fraction of the steam rising through the larger channels condenses and flows down

---

[1/] One heat flow unit (hfu) = 41.84 mW/m^2

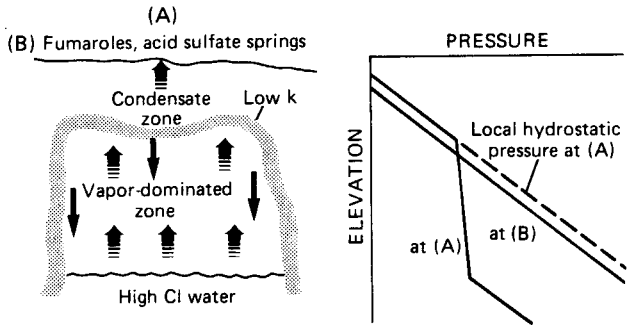

Fig. 2 Conceptual model of large-scale vapor-dominated zone with solid limited throughflow. Solid arrows for liquid, broken arrows for vapor flow.

in narrower channels and pore spaces. The vapor-dominated zone is presumably underlain by a zone of high-chloride liquid, but unlike the "parasitic" vapor-dominated zone (Ingebritsen and Sorey, 1985; Sorey and Ingebritsen, 1984) there is no evidence for significant liquid throughflow.

The low-permeability aureole surrounding the vapor-dominated zone (figure 2) may be related to deposition of silica, calcite, or gypsum, as discussed by White and others (1971); argillization, natural structural barriers, or a combination of these factors. For example at The Geysers, the main vapor-dominated reservoir is overlain by relatively impermeable caprocks consisting of serpentinite, melange, and metagraywacke (figure 3a). Argillic alteration also apparently helps to seal the top of the reservoir (Hebein, 1985). The reservoir may be bounded laterally, at least in part, by mineralization along the Mercuryville and Collayomi fault zones. At Larderello (figure 3b), steam is found mainly in antiforms within carbonate and evaporitic (dolomitic-anhydrite) rocks. The carbonates are overlain by low-permeability shales and sandstones which isolate the vapor-dominated zones both laterally and vertically. At Matsukawa (figure 3c), the Matsukawa Andesite is the caprock and the margins

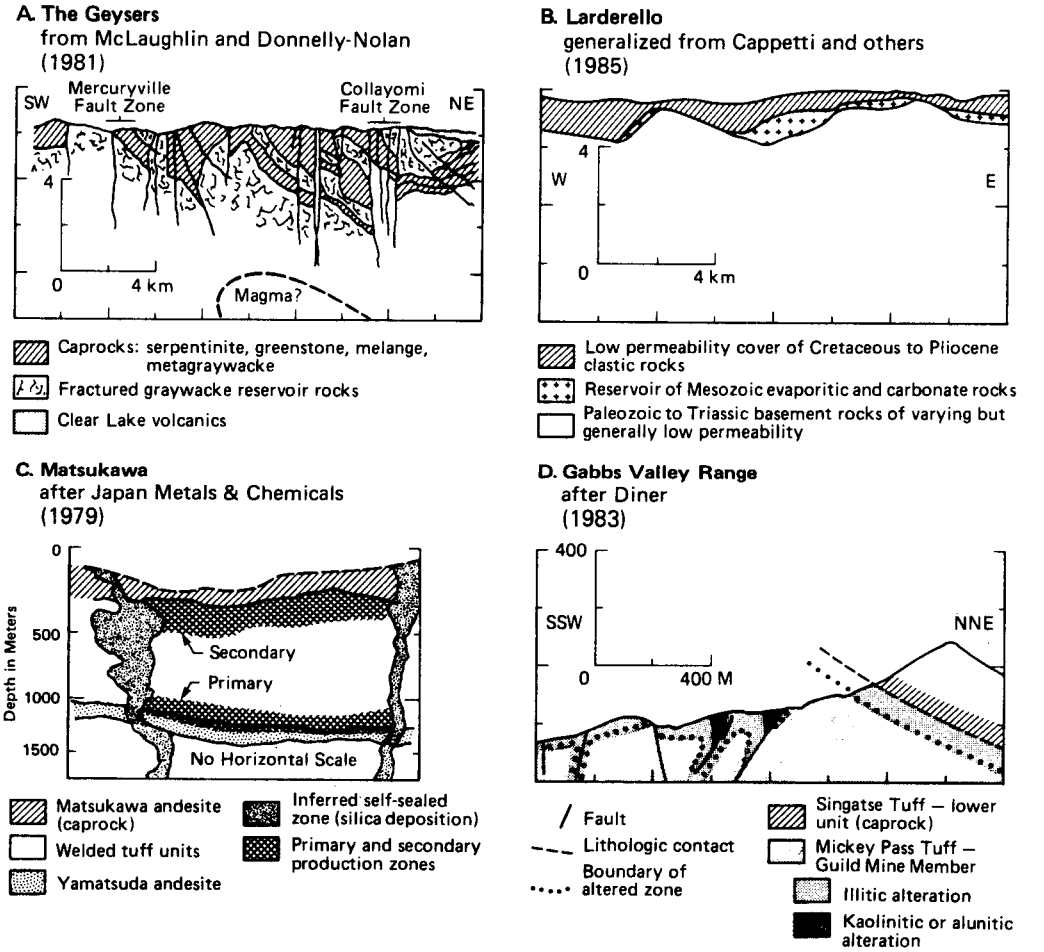

Fig. 3 Simplified geologic cross sections of various vapor-dominated systems, showing suggested low permeability boundaries to the vapor-dominated zones.

of the reservoir appear to be self-sealed by deposition of silica (M. Hanano, oral communication, 1985). At a possible fossil vapor-dominated system in the Gabbs Valley Range, Nevada (figure 3d; Diner, 1983; Stearns, 1982), the caprock was a poorly welded ash flow tuff. The pattern of mineralization suggests that fluid circulation beneath this unit was largely confined to fault zones, each of which may have comprised an isolated vapor-dominated heat pipe.

Isolation due to self-sealing - by deposition of silica due to cooling at the margins of a system, or by deposition

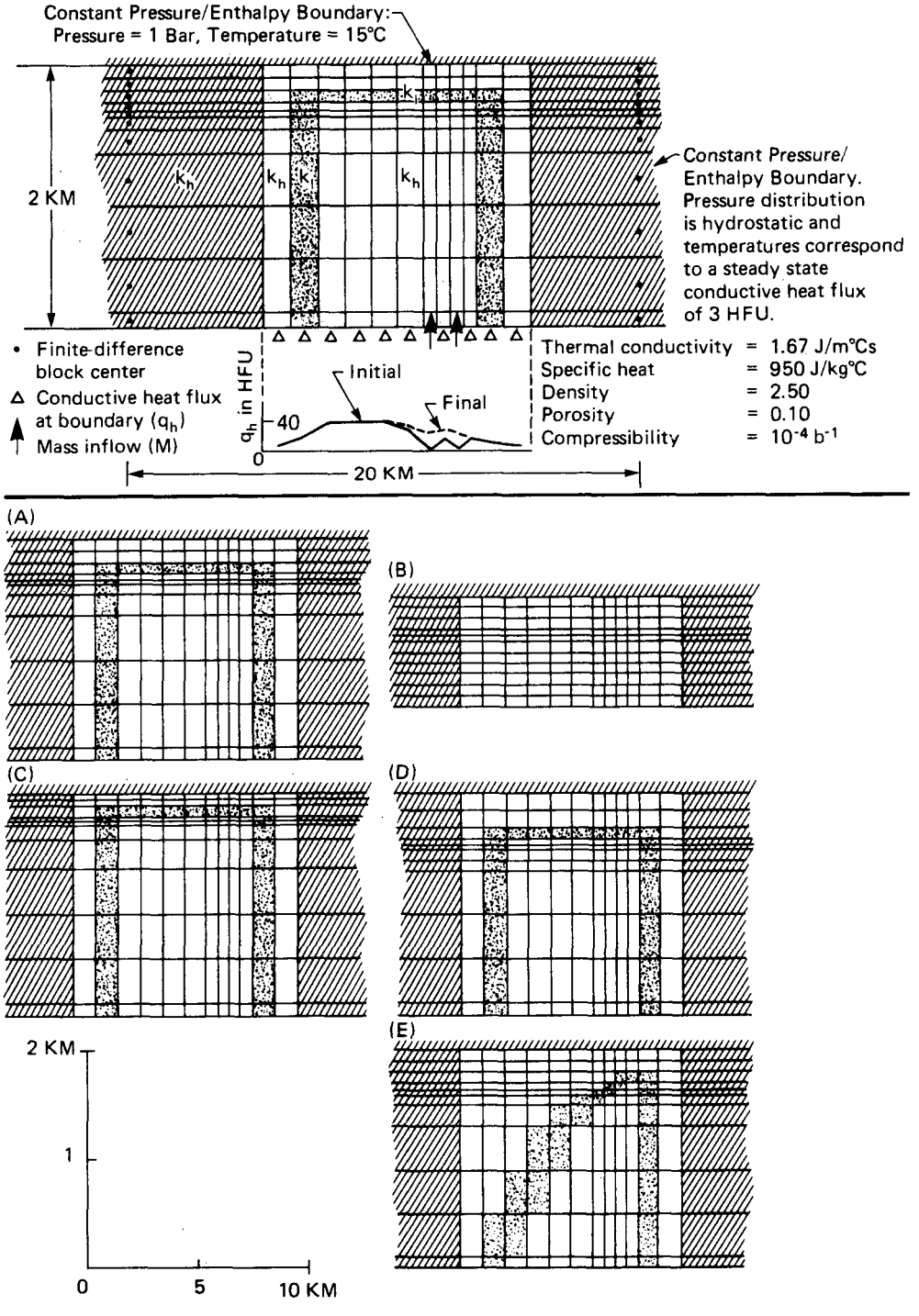

Fig. 4 Geometric models used in simulations of the conceptual model shown in figure 2.

of calcite, gypsum, or anhydrite as recharge water warms - is likely to be more effective during a liquid-dominated stage that precedes development of vapor-dominated conditions. At Reykjanes, Iceland, self-sealing by silica and calcite sustains a pressure difference of nine bars across the lateral boundaries of a high-temperature liquid-dominated system (Tomasson and Smarason, 1985).

Figure 4 shows the geometric models used to represent the conceptual model shown in figure 2 and, in a more generalized fashion, the real systems shown in figure 3. These geometric models are simplified, but adequate to represent the essential features of large-scale vapor-dominated systems. They are two-dimensional vertical cross sections, with no boundaries closed to mass or energy. The system is flanked by nonthermal groundwater systems, represented by constant pressure/enthalpy boundaries, but buffered to some extent by low-permeability zones (k_l). There is input of mass (M) and heat (q_h) (by both convection and conduction) at the base, and discharge of heat and recharge or discharge of mass at the land surface.

The computer code used to simulate heat and mass transport within these geometric models was a modified version of the three-dimensional, two-phase program described by Faust and Mercer (1979). With this program, solutions for fluid pressure and enthalpy at selected times are obtained using finite-difference techniques. Other system properties such as liquid-steam saturation and rock-fluid temperature are obtained from the calculated pressures and enthalpies. Modifications to the original code were made to improve the scheme for upstream weighting of fluid properties and to allow conductive heat flux to be specified as a boundary condition (Ingebritsen, 1983), and to extend the allowable temperature range.

RESULTS

The results presented here are abstracted from a Ph.D. dissertation in progress (Ingebritsen, 1986). The simulations discussed in this section are summarized in Table 1. Those marked with an asterisk in Table 1 led to extensive vapor-dominated zones with near-vapor-static pressure gradients, while the others led only to short-lived (Run 3) or very localized vapor-dominated conditions (Runs 5 and 6), or did not lead to the formation of vapor-dominated zones at all. Comparison of these various results leads to a number of interesting conclusions.

Initial conditions for each simulation were a hydrostatic pressure distribution and a low-temperature conductive temperature regime. Total simulation times ranged from 10,000 to 40,000 years.

Table 1. Summary of numerical simulations discussed in the text. Runs marked with an asterisk led to extensive vapor-dominated zones.

Run	Geometry[1]	k_h,[1] in cm	k_l,[1] in cm	$\bar{q}_{hf}$,[2] in hfu	M_i,[3] in kh/s	M_f,[4] in kg/s	Time to M_f, in years	Total simulation time, in years
1*	A	1.0×10^{-9}	5.0×10^{-13}	27.5	100	2	3500	10,000
2*	A	1.0×10^{-9}	5.0×10^{-13}	27.5	100	2	5500	10,000
3	A	1.0×10^{-9}	5.0×10^{-13}	0	100	2	3500	10,000
4*	A	1.0×10^{-9}	5.0×10^{-13}	27.5	0	0	N.A.	40,000
5	A	1.0×10^{-9}	5.0×10^{-13}	27.5	100	5	3500	10,000
6	A	1.0×10^{-9}	5.0×10^{-13}	27.5	100	10	3500	10,000
7*	A	1.0×10^{-9}	5.0×10^{-15}	27.5	0	0	N.A.	40,000
8	A	1.0×10^{-9}	5.0×10^{-11}	27.5	100	2	5500	10,000
9	B	1.0×10^{-12}	1.0×10^{-12}	27.5	0	0	N.A.	25,000
10	B	1.0×10^{-11}	1.0×10^{-11}	27.5	0	0	N.A.	25,000
11*	C	1.0×10^{-9}	5.0×10^{-13}	27.5	100	2	3500	10,000
12*	D	1.0×10^{-9}	5.0×10^{-13}	27.5	100	2	3500	10,000
13*	E	1.0×10^{-9}	5.0×10^{-13}	27.5	100	2	3500	10,000

[1] See Figure 4.
[2] Final mean conductive heat flow at base of model.
[3] Initial mass inflow rate.
[4] Final mass inflow rate.

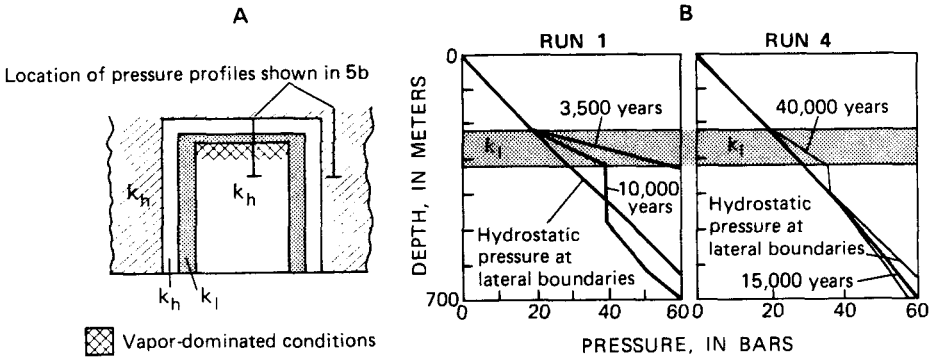

Fig. 5 (a) Extent of vapor-dominated conditions at the end of Run 1, and location of pressure profiles shown in 5b. (b) Pressure profiles at selected times during Runs 1 and 4.

These times were sufficient to allow most of the simulations to reach a near-steady-state condition.

The simulations demonstrate the feasibility of two different evolutionary pathways: a decrease in mass inflow over time (e.g. Table 1 - Run 1), and conductive heating at a constant rate with no changes in boundary conditions (e.g. Run 4). Both of these scenarios led to extensive vapor-dominated zones, although the system evolved more rapidly in runs that involved an early period of high liquid throughflow. Figure 5a shows the extent of vapor-dominated conditions for such a case (Run 1) at the total simulation time of 10,000 years. Figure 5b shows pressure profiles at selected times during this run and during a simulation that involved conductive heating only (Run 4). At later times in both cases pressures are greater than hydrostatic above the vapor-dominated zone, and the vertical pressure gradient is near-vaporstatic within the vapor-dominated zone and near-hydrostatic below the vapor-dominated zone. In both cases the pressures at the top of the vapor-dominated zone are somewhat above hydrostatic. This explains the stability of the liquid saturated layer above the vapor-dominated zone, and is related to the permeability contrast between k_l and k_h (figure 4). Superhydrostatic pressures in shallow steam zones have been reported at The Geysers (Allen and Day, 1927; up to approximately 150 percent of hydrostatic at 150 m depth), Mud Volcanoes, Yellowstone (White and others, 1971; approximately 125 percent of hydrostatic at 106 m depth), and Svartsengi, Iceland, where a "steam cap" is forming in response to exploitation (Gudmundsson and Thorhallson, 1986).

Note that the vapor-dominated zones in both cases are relatively thin (figure 5b) - much thinner than that at The Geysers, for example. At a total simulation time of 40,000 years the conduction-only run (Run 4) is far from steady state, but the run involving a decrease in mass inflow (Run 1) is approaching steady state at the total simulation time of 10,000 years. Thus the vapor-dominated zone in Run 1 may be near an equilibrium thickness. As the thickness of the vapor-dominated zone increases, the lateral pressure gradient into the vapor-dominated zone increases (figure 5b). Eventually, the amount of steam flowing vertically out of the vapor-dominated zone is balanced by lateral inflow. The factors affecting the thickness of the vapor-dominated zone at equilibrium include the rate of conductive heating at

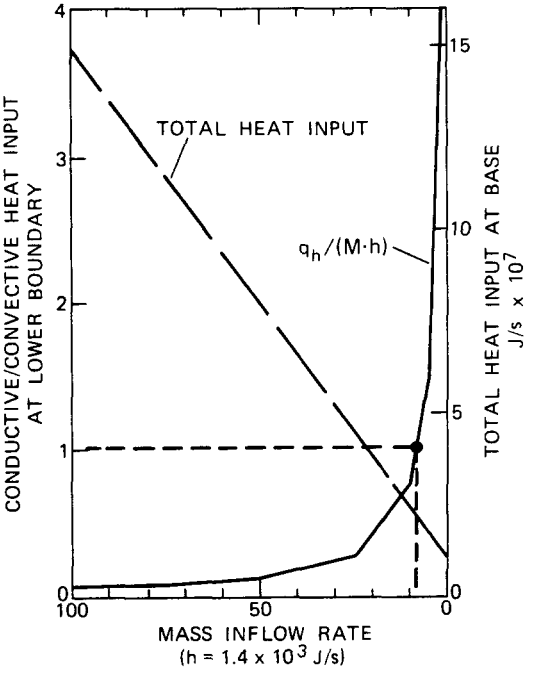

Fig. 6 Total heat input at the lower boundary of the geometric model and conductive/convective heat input ratio, both as functions of mass inflow rate M. For $M < 10$ kg/s, conductive heat input is greater than convective.

the base of the model and the permeability of the low-permeability barriers that inhibit lateral flow (k_l). An increase in the heat input would increase the rate of steam loss and lead to a thicker vapor-dominated zone. If the lateral barriers (k_l) were completely impermeable (preventing inflow), the vapor-dominated zone would keep growing indefinitely. Of course, if the vapor-dominated zone reached the lower boundary of the geometric model the boundary condition used would become inappropriate.

A series of simulations (Runs 4, 1, 5, and 6) illustrates the effect of varying the final rate of mass inflow M at the base of the model. The final rates range from 0-10 kg/s. Rates of 0 and 2 kg/s (Runs 4 and 1) lead to extensive vapor-dominated zones. Mass inflow rates of 5 and 10 kg/s (Runs 5 and 6) lead to higher pressures such that vapor-dominated conditions are only very localized (one to five finite-difference blocks) and pressures are above hydrostatic throughout the system. For these geometric models, this implies that the conductive heat input must exceed the convective heat input at the lower boundary (figure 6) in order for an extensive vapor-dominated zone to form.

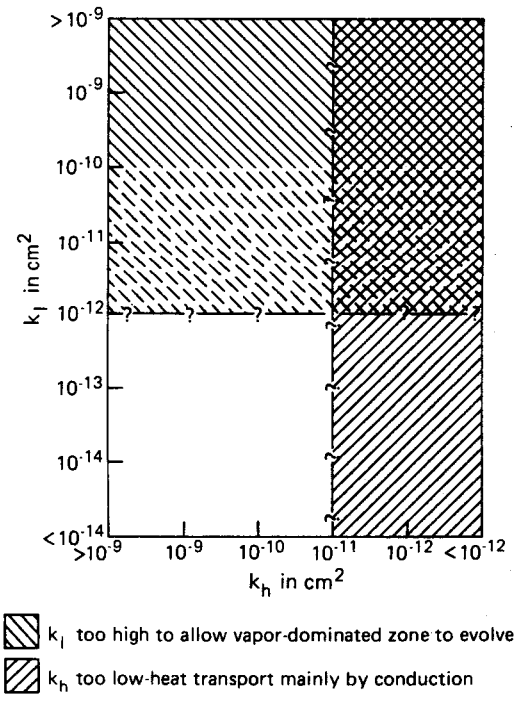

Fig. 7 Permeabilities favorable for the evolution of vapor-dominated conditions within the geometric models shown in figure 4.

The conductive heat input used in the simulations implies an underlying heat source of great intensity. Assuming no convection below the boundary, the depth to magmatic temperatures implied by the lower boundary condition is given by

$$D = K \frac{(T_m - T_b)}{\bar{q}_{hf}}$$

where K is thermal conductivity, T_m is the magmatic temperature, T_b is the temperature at the lower boundary, and $\bar{q}_{hf}$ is the average conductive heat flux at the lower boundary. The temperature at the base of the model equilibrates at about 300°C, and the average heat flow is 27.5 hfu. Assuming a magmatic temperature of 800°C and using a thermal conductivity value of 5 tcu[1/], D =.9 km. Given active convection at depths below two km (the base of the model), the calculated depth to magma would be greater. In contrast, the "parasitic" vapor-dominated zone (Ingebritsen and Sorey, 1985; Sorey and Ingebritsen, 1984) does not necessarily require such a potent local heat source, as heat can be supplied by a voluminous liquid throughflow.

Another series of simulations (Runs 1 and 7-10) shows the effect of varying the permeability distribution (figure 4: k_h versus k_l). For $k_l \gtrsim 10^{-12}$ cm², the interior of the system is insufficiently isolated from the constant pressure/enthalpy boundaries for vapor-dominated conditions to evolve. For $k_h \leq 10^{-11}$ heat transport throughout the system is dominantly conductive, so no vapor-dominated zone could evolve. (The near-isothermal conditions within the vapor-dominated zones imply convective heat flux >> conductive). This might have been anticipated by a Rayleigh number analysis of a slightly idealized version of Runs 9 ($k_h = k_l = 10^{-12}$ cm²) and 10 ($k_h = k_l = 10^{-11}$ cm²), which shows R ~ .27 and R ~ 2.7, respectively. These values are approximately equal to or below R_c for the onset of convection (Straus and Schubert, 1977). This series of simulations suggests that a permeability contrast ($k_h > k_l$) is needed to allow a vapor-dominated zone to evolve (figure 7). Straus and Schubert (1981) reached a similar conclusion. Their earlier work (Schubert and Straus, 1980) had shown that a permeability of 4×10^{-13} cm² or less was required for gravitational stability of water over steam. In their later work (1981), they found that higher permeabilities were needed within the vapor-dominated zone itself, and, thus, recognized the need for a permeabi-

---

1/ One thermal conductivity unit (tcu) = 418.4 mW/m-°k

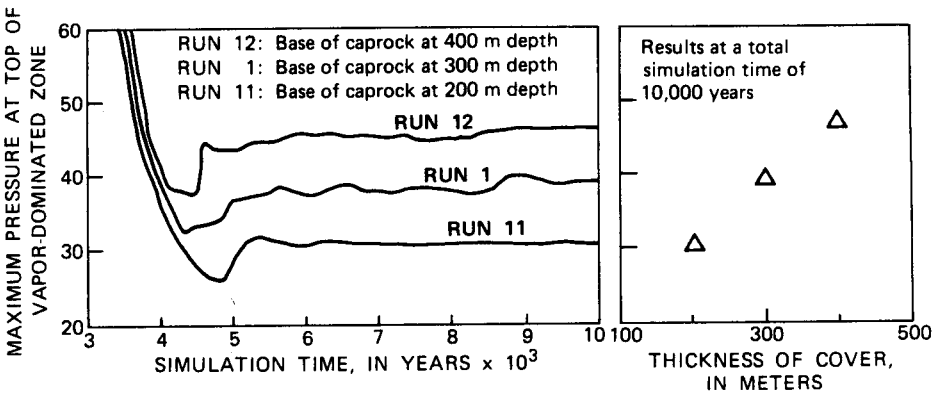

Fig. 8 Pressure at the top of the vapor-dominated zone as a function of time in runs that involve different depths to the caprock, and near-steady-state pressures as a function of thickness of cover.

lity contrast at the top of the vapor-dominated zone.

Near-steady-state pressures within the vapor-dominated zone vary regularly in response to changes in the depth to the low permeability caprock (figure 8; Runs 1, 11, 12). This is predictable, for in order to sustain a flux of steam into the base of the caprock, pressures at the top of the vapor-dominated zone must exceed the overlying weight of water. Pressures within the vapor-dominated zone are also sensitive to the geometry of the caprock (Run 13 - not shown).

The minimum rate of heat loss from a vapor-dominated zone at various depths or pressures can be estimated by assuming that the heat loss is largely by conduction to the land surface, that the temperature at the top of the vapor-dominated zone lies on the boiling point with depth curve, and that K = 5 tcu (figure 9). An equivalent rate of heat input could be the minimum required to sustain the vapor-dominated zone. Somewhat surprisingly, this analysis suggests that a deeper/higher pressure vapor-dominated zone might require a less intense heat source.

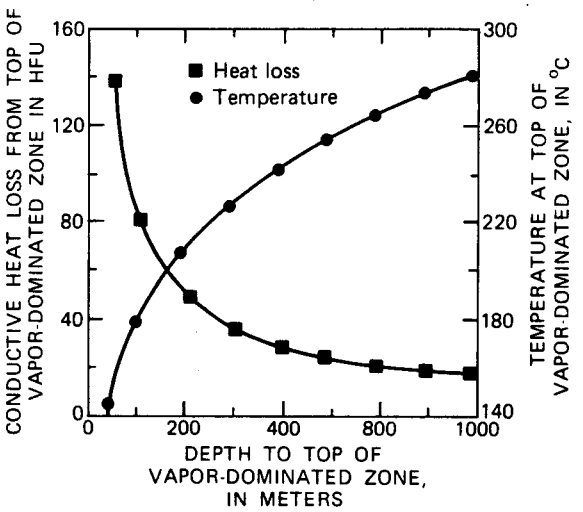

Fig. 9 Minimum heat input rates necessary for evolution of a vapor-dominated zone at various depths. Conditions at the top of the vapor-dominated zone are assumed to fall on the boiling point with depth curve.

Several of the simulations led to vapor-dominated zone pressures greatly in excess of the pressure of maximum enthalpy of saturated steam. Field evidence for such high pressures is scarce. However, Stefanssson (1985) has suggested vapor-dominated conditions at a pressure of 84 bars at the Nesjavellir high-temperature field, Iceland. Dry steam entries at pressures of 40 bars (in shallow horizons; Celati and others, 1978) to 70 bars (in deeper horizons; Cappetti and others, 1985) have been reported at Larderello, and pressures of around 60 bars have been reported in both shallow and deep horizons at Travale, Tuscany (Cappetti and others, 1985). However, there are not enough pressure measurements in any of these cases to show whether the pressure profile is near vaporstatic. Since the rate of heat loss from such deep/high pressure vapor-dominated zones is relatively small (figure 9), they might be encountered near the margins of known vapor-dominated systems or on the flanks of intense heat flow anomalies, rather than at the centers of such anomalies.

These experiments show that the pressure of maximum enthalpy of saturated steam does not control pressures in large-scale vapor-dominated zones. An alternate explanation is needed for the

coincidence of several known systems at pressures of 30-35 bars.

SUMMARY

Given an adequate supply of heat, a large-scale vapor-dominated zone can evolve within low-permeability barriers without changes in boundary conditions or rock properties. However, the evolution of the system is accelerated in cases involving an initially high fluid throughflow rate that decreases through time. The conductive/convective heat flow ratio at the lower boundary of the system must be >>1, because the low permeability aureole surrounding the vapor-dominated zone and the near-vapor-static pressure gradient within the vapor-dominated zone preclude high throughflow rates.

Although low permeability barriers are necessary to buffer the vapor-dominated zone from surrounding and overlying zones with near-hydrostatic pressure gradients, permeability within the vapor-dominated zone itself must be relatively high, since vertical heat transport is dominantly by a heat-pipe mechanism rather than conduction. Thus, vapor-dominated zones cannot exist in a medium of uniform low permeability - some permeability contrast is necessary. Given low permeability barriers with permeability/thickness ratios low enough to allow a vapor-dominated zone to evolve, the system is relatively insensitive to the permeability of surrounding and overlying normally-pressured flow systems. Heat transfer in these zones may be dominantly convective or conductive. The stability of a liquid saturated zone overlying the vapor dominated zone is readily explained by pressures at the top of the vapor-dominated zone that are somewhat in excess of local hydrostatic pressures.

Near-steady-state pressures within the vapor dominated zone are not controlled by the pressure of maximum enthalpy of saturated steam (30.6 bars). They are shown to vary regularly with depth to the caprock (i.e., thickness of cover). The coincidence of a number of systems at pressures near the pressure of maximum enthalpy of saturated steam is yet to be explained.

ACKNOWLEDGEMENTS

I would like to thank the members of my Ph.D. research committee for their advice and support; they are: J.D. Bredehoeft, J.S. Gudmundsson, Roland Horne, R.J.P. Lyon, Irwin Remson, M.L. Sorey, and D.E. White. Drs. Gudmundsson, Sorey, and A.H. Truesdell reviewed this manuscript and made numerous helpful suggestions. This work was partially supported by a U.S. Department of Energy grant to the Stanford Geothermal Program. Rebecca Munn typed the manuscript.

REFERENCES CITED

Allen, E.T., and Day, A.L., 1927, Steam wells and other thermal activity at "The Geysers", California: Carnegie Institution of Washington Publication No. 378, 106 p.

Cappetti, G., Celati, R., Cigni, U., Squarci, P., Stefani, G., and Taffi, Learco, 1985, Development of deep exploration in the geothermal areas of Tuscany, Italy: Geothermal Resources Council Transactions, International Volume, p. 303-309.

Celati, R., Squarci, P., Stefani, G., and Taffi, L., 1978, Study of water levels at Larderello for reconstruction of reservoir pressure trends: Geothermics, 6, p. 183-198.

Diner, Y. A., 1983, The HY precious metals lode deposit, Mineral County, Nevada: M.S. thesis, Stanford University, 220 p.

Donaldson, I.G., and Grant, M.A., 1981, Heat extraction from geothermal reservoirs, in Rybach, L., and Muffler, L.J.P., eds., Geothermal Systems (:) Principles and Case Histories: Chichester, Wiley and Sons, p. 145-180.

Faust, C.R., and Mercer, J.W., 1979, Geothermal reservoir simulation (:) 2. Numerical solution techniques for liquid and vapor-dominated hydrothermal systems: Water Resources Research, 15, p. 31-46.

Grant, M.A., 1979, Interpretation of downhole pressure measurements at Baca: Proc. Fifth Workshop on Geothermal Reservoir Engineering, Stanford Univ., Stanford, p. 261-268.

Gudmundsson, J.S., and Thorhallsson, S., 1986, The Svartsengi reservoir in Iceland: Geothermics, in press.

Hebein, J.J., 1985, Historical hydrothermal evolutionary facets revealed within the exploited Geysers steam field: Geothermal Resources Council Bulletin, 14, no. 6, p. 13-16.

Ingebritsen, S.E., 1983, Evolution of the geothermal system in the Lassen Volcanic National Park area: M.S. thesis, Stanford Univ., Stanford, 90 p.

Ingebritsen, S.E., and Sorey, M.L., 1985, A quantitative analysis of the Lassen hydrothermal system, north-central California: Water Resources Research, 21, p. 853-868.

Japan Metals and Chemicals Co., 1979, Matsukawa geothermal power development: Japan Metals and Chemicals Co., Ltd., Tokyo, 17 p.

McLaughlin, R.J., 1981, Tectonic setting of pre-Tertiary rocks and its relation to geothermal resources in the Geysers-Clear Lake area, in McLaughlin, R.J., and Donnelly-Nolan, J.M., Research in the Geysers-Clear Lake Geothermal Area, Northern California: U.S.G.S. Professional Paper 1141, p. 3-24.

Pruess, K., 1985, A quantitative model of vapor-dominated geothermal reservoirs as heat pipes in fractured porous rock, Geothermal Resources Council Transactions, p. 353-361.

Pruess, K., and Truesdell, A.H., 1980, A numerical simulation of the natural evolution of vapor-dominated hydrothermal systems: Proc. Sixth Workshop on Geothermal Reservoir Engineering, Stanford Univ., Stanford, p. 194-203.

Pruess, K., Weres, O., and Schroeder, R., 1983, Distributed parameter modeling of a producing vapor-dominated geothermal reservoir (:) Serrazzano, Italy: Water Resources Research, 19, p. 1219-1230.

Schubert, Gerald, and J.M. Straus, 1979, Steam-water counterflow in porous media: Journal of Geophysical Research, 84, p. 1621-1628.

Schubert, Gerald, and J.M. Straus, 1980, Gravitational stability of water over steam in vapor-dominated geothermal systems: Journal of Geophysical Research, 85, p. 6505-6512.

Sorey, M.L., and Ingebritsen, S.E., 1984, A quantitative analysis of the hydrothermal system in Lassen Volcanic National Park and Lassen KGRA: U.S.G.S. Water Resources Investigations Report 84-4278, 80 p.

Stearns, S.W., 1982, Disseminated epithermal precious minerals in the Santa fe district, Mineral County, Nevada: M.S. thesis, Stanford University, 109 p.

Stefansson, V., 1985, The Nesjavellir high-temperature field in Iceland: Proc. 10th Workshop on Geothermal Reservoir Engineering, Stanford Univ., Stanford, p. 23-31.

Straus, J., and Schubert, G.M., 1977, thermal convection of water in a porous medium (:) Effects of temperature and pressure-dependent thermodynamic and transport properties: Journal of Geophysical Research, 82, p. 325-333.

Straus, J.M., and Schubert, Gerald, 1981, One-dimensional model of vapor-dominated geothermal systems: Journal of Geophysical Research, 86, p. 9433-9438.

Tomasson, J., and Smarason, O.B., 1985, Developments in geothermal energy: Hydrogeology in the Service of Man, Memoires of the 18th Congress of the International Association of Hydrogeologists, Cambridge, p. 189-211.

White, D.E., Muffler, L.J.P., and Truesdell, A.H., 1971, Vapor-dominated hydrothermal systems compared with hot-water systems: Economic Geology, 66, p. 75-97.

PROCEEDINGS, Eleventh Workshop on Geothermal Reservoir Engineering
Stanford University, Stanford, California, January 21-23, 1986
SGP-TR-93

Quantitative Model of the Cerro Prieto Field

S. E. Halfman, M. J. Lippmann, and G. S. Bodvarsson

Lawrence Berkeley Laboratory
Earth Sciences Division
University of California
Berkeley, California 94720

ABSTRACT

A three-dimensional model of the Cerro Prieto geothermal field, Mexico, is under development. It is based on an updated version of LBL's hydrogeologic model of the field. It takes into account major faults and their effects on fluid and heat flow in the system. First, the field under natural state conditions is modeled. The results of this model match reasonably well observed pressure and temperature distributions. Then, a preliminary simulation of the early exploitation of the field is performed.

The results show that the fluid in Cerro Prieto under natural state conditions moves primarily from east to west, rising along a major normal fault (Fault H). Horizontal fluid and heat flow occurs in a shallower region in the western part of the field due to the presence of permeable intergranular layers. Estimates of permeabilities in major aquifers are obtained, and the strength of the heat source feeding the hydrothermal system is determined.

INTRODUCTION

The Cerro Prieto geothermal field is located in the southern part of the Salton Trough--about 20 miles south of the United States-Mexico border in Baja California, Mexico (Fig. 1). Approximately, 140 deep wells have been drilled in the area (Fig. 2); the wells produce from three major aquifers (α, β and γ reservoirs). To date, the installed electrical power generating capacity at the field is 400 MWe; by the end of 1986 it is expected to reach 620 MWe. A reliable model of the field is needed to assess its ultimate generating potential and to optimize the reservoir exploitation strategy. The model must consider the pre-exploitation conditions of the system and be able to predict reservoir pressure and temperature changes during fluid production. This paper presents preliminary results of a three-dimensional numerical simulation of the pre-exploitation and early production states of the Cerro Prieto field.

The basis for the three-dimensional numerical model presented here is an updated version of Halfman et al.'s (1984) hydrogeologic model that depicts preproduction subsurface geothermal fluid flow patterns in the Cerro Prieto field (Fig. 3). This model explains the role of layers of different permeabilities (i.e., sandstones, sandy shales, and shales) and the effects of major faults on fluid flow. According to Halfman's model, the hot fluids originate at great depths in the eastern portion of the field flowing through the deepest reservoir identified up to now (the γ reservoir; not shown in Fig. 3). Then the fluids

(1) rise along Fault H,
(2) flow westward through the Z sandstone (between wells M-117 and M-123) corresponding to the β reservoir,
(3) ascend into a sandy gap in the O shale (in the vicinity of M-10),
(4) flow westward through a sandy shale layer within the O shale [between M-14 and M-25 (1200-1400 m)] corresponding to the α reservoir,
(5) rise up Fault L, and
(6) flow westward through the shallower sandstone [between M-29 and M-9 (800 - 1000 m)].

Eventually the geothermal fluids either mixes with the cold water surrounding the geothermal anomaly or discharge to the surface in mudpots, fumaroles, hot springs, and hot pools. These postulated fluid flow patterns are consistent with mineralogic (Elders et al., 1981, 1984), thermal (Mercado, 1976), and reservoir engineering and geochemical (Grant et al., 1984) studies conducted on the Cerro Prieto field.

Lippmann and Bodvarsson (1983) developed a two-dimensional numerical model of the field that was based on a portion of Halfman et al.'s (1984) hydrogeologic model. They obtained a good match with the observed natural-state pressures and temperatures. However, because of the two-dimensional nature of the model (not allowing recharge of the system along a horizontal direction perpendicular to the cross section), a good match with reported 1973-1979 pressures was not possible. The three-dimensional model presented here extends the Lippmann and Bodvarsson's (1983) model to three dimensions, thereby not restricting the recharge to the produced reservoir. First, a natural-state model of the field will be discussed, giving estimates for the mass and heat flow and for the permeability distributions in the system. Then, using the same model preliminary results of reservoir behavior under exploitation will be described.

METHODOLOGY

A natural steady-state model of Cerro Prieto was developed by varying the rock properties and boundary conditions of the model until reasonable matches between calculated and observed temperatures (Navarro et al., 1982; Rivera et al., 1982) and pressures (Ayuso, 1984) were obtained. After that, the early (1973-1979) exploitation of the field was simulated to validate the model against the observed reservoir pressure decline (Bermejo et al., 1979).

A three-dimensional, multi-phase, multi-component simulator MULKOM (Pruess, 1983) was used to compute the heat and mass flow in the system.

Computational Mesh

The three-dimensional mesh used in this study was designed on the basis of the geologic characteristics of the field. One side of the model is oriented in a NW-SE direction along the approximate strike of Fault L (Fig. 4). The SW-NE side of model is parallel to Fault H. Both of these faults are important features in the hydrogeological model of Cerro Prieto (Halfman et al., 1984). In plan view, the region modeled extends over an area of 8600 m (SW-NE) by 9000 m (NW-SE). The thickness of the model varies, considering depths between 800 and 4000 m. The mesh consists of 242 elements: 146 internal elements and 96 boundary blocks.

Figure 5 shows the computational mesh for a SW-NE cross section in the upthrown block. The elements are designed to reproduce schematically the geology and characteristics of the various layers comprising the system. The region modeled is below 800 m depth; the shale layer above 800 m is assumed to be impermeable. In general, the lateral boundaries are also assumed impermeable. The recharge of hot fluids is modeled by injection into the mesh elements representing the deep γ reservoir. The discharge of the fluids is through boundary elements located along the western margin of the grid, at 800 m depth. We also assume that the rocks below the β reservoir are of low permeability, except for the sandy γ reservoir. Similar assumptions are made for the corresponding downthrown block.

Material Properties

Different material properties were assigned to various zones in the mesh (Figs. 6A and 6B). In the early simulations, we used values for rock densities, porosities, permeabilities, and heat conductivities similar to those defined from the modeling work of Lippmann and Bodvarsson (1983). Later on, during the matching process with observed temperatures and pressures, the material properties (especially permeablities and thermal conductivities) were adjusted somewhat. Those used in the "best" model are given in Table 1.

Figure 6A shows the materials used in the cross section given in Figure 5. The K1 zone represents the thick sandstones lying to the west of the main geothermal anomaly. The S1 zone is the cooler aquifer overlying the α and β reservoirs. The C1 zone is a leaky caprock to the α reservoir (S2 zone). The relatively low permeability C2 zone separates the α and β reservoir in the western portion of the field. The F1 zone corresponds to Fault L. The S3 and S3B zones are the β reservoir in the western portion of the field. S4 is a sandy zone overlying the C4 zone which is the caprock to the sandy β reservoir (S5 zone) in the eastern portion of the field. The C5 is a low-permeability zone due to mineral precipitation in the upper part of the sandy gap (S7 zone). C6 is a shaly zone separating the β reservoir from the sandy γ reservoir (S6 zone).

Figure 6B shows the zones (materials) in a cross section along a SW-NE downthrown row of elements. The K1 and S1 sandstones are equivalents to those of the upthrown block. A new C7 shaly zone is identified in this cross section because no α reservoir exists in this area of the downthrown block. A shale zone (C8) is arbitrarily assigned to part of this section because of lack of well data in the area. The rest of the zones in this section are similar to those of the upthrown section (Fig. 6A).

The result of our model indicates that the permeabilty of the shale layers varies generally between 0.005 and 1 md, and that of the sandy materials between 1 and 100 md. In the three reservoirs (α, β, and γ), the horizontal permeability is 100 md and the vertical permeability ranges between 1 and 10 md. These values agree reasonably well with the results of well tests and with permeabilities used in earlier simulations of the field (Lippmann and Bodvarsson, 1983; Ayuso, 1984).

A thermal conductivity of 2.0 W/m °C is used for the different zones except for a few zones where it is slightly higher. A constant rock density of 2,650 kg/m^3 is assumed for all materials.

Boundary Conditions

In our model, boundary elements are located along the west, north, and top sides. Conductive heat transfer is allowed from all boundary elements. The temperatures for these elements were selected on basis of temperature log data (Bermejo et al., 1979; and Bermejo, personal communication, 1982). Five of the boundary elements located along the western edge on the top row were open to fluid flow. The constant pressure for the fault and two upthrown open boundary elements is 68 bars and those for the two downthrown open boundary elements are 100.3 and 101.1 bars, respectively. For the best model, a constant rate of hot fluid recharge of 100 kg/s is assumed in the γ reservoir along the eastern edge of the model.

Natural State Model

The natural state model describes the heat and fluid flows, and the distribution of pressures, temperatures, and steam saturations in the system before commercial

fluid production is initiated. The model discussed in this paper is the one that presently best matches the field data.

The properties of the different zones in this "best" model are given in Table 1. The total rate of hot (1512 kJ/kg) water recharge along the eastern side of the model is about 100 kg/s. Figures 7A and 7B show the observed and computed isotherms respectively, for the SW-NE cross section shown in Figure 5. In the eastern portion of the field (east of the sandy gap), there is a good temperature match. The isotherms between 150° to almost 300° C indicate a high-temperature gradient in the caprock (hatched zone). As the hot fluids ascend through the sandy gap in the caprock, the isotherms rise to shallower depths, as is confirmed by the field data. In the western part of the cross section (west of sandy gap) the agreement between observed and computed temperatures is not as good; the computed ones are generally too high (about 50° C).

The discrepancies in the western region may be due partly to two factors. First, the field temperatures used reflect temperatures more closely associated to those found along cross section A-A' of Halfman et al.'s (1984). This section is about 1000 m northwest of the section shown in Figures 7A and 7B. There is evidence that a few wells such as M-181 are hotter, especially west of Fault L. This suggests that the temperatures given in Figure 7A should be somewhat higher towards the west.

The second and probably more accurate reason for the temperature discrepancy along the western region is the existence of cold water recharge between 1200 and 1400 m depth along the western margin of the field (Lippmann and Bodvarsson, 1983). This recharge was not considered in the model discussed here; it will be taken into account in our future modeling work.

The temperature distribution at 1300 and 1750 m depth are given in Figures 8 and 9, respectively. Figures 8A and 9A show observed values as reported by Navarro et al. (1982); Figure 8B and 9B are the computed ones. For the temperatures at 1300 m there is a reasonable match. East of the railroad tracks, the regions between isotherms are narrow, reflecting the presence of Fault H that controls the upflow of hot fluids. West of the tracks, the isotherms spread out; in a N-S direction (Fig. 8A) and in a NW-SE direction (Fig. 8B). The main difference between observed and calculated temperatures is that the computed temperature distribution along the western edge of the field is spread over a wider area than that shown on Figure 8A. One could argue that the actual temperature distribution in this part of the field is not well known because of a scarcity of well data. However, an alternate possibility is natural cold water inflow along the western margin of the field; this will be tested in future simulations.

Figure 9A shows the observed temperatures at 1750 m depth. East of the railroad tracks the 150° and 100° C isotherms are not given. Ignoring the corresponding two contours in Figure 9B, in the eastern region the calculated and observed temperature contours show a similar trend of converging towards Fault H. West of the tracks, both the observed and calculated isotherms show a general trend of spreading, in an N-S direction (Fig. 9A) and in a NW-SE direction (Fig. 9B). However, the observed temperature contours delineate a smaller region and show a distinct elongation to the SW which is not shown in Figure 9B. The differences between observed and calculated temperatures can again be explained by the scarcity of data or by cold water inflow. There is very limited well data for the western region of the field, especially below a depth of 1750 m. An influx of colder waters, if included in our model, could improve the match between observed and computed temperatures.

Table 2 shows some comparisons of observed pressures (Ayuso, 1984), calculated pressures from Lippmann and Bodvarsson's (1983) two-dimensional modeling study, and our calculated pressures. In the α and the western β reservoirs, the calculated pressures are lower (6 and 13 bars, respectively) than those computed by Lippmann and Bodvarsson's (1983). Our calculated pressures should increase somewhat when cold water recharge from the west is added to the model. In the section modeling Fault H the calculated pressure agrees well with the observed pressure. In the eastern β reservoir, the calculated pressure is 4.5 bars higher than the one reported by Ayuso (1984).

From Halfman et al.'s (1984) hydrogeologic model, it was concluded that the general geothermal fluid flow pattern is from large depths in the east to shallower depths in the west, and that some of the hot fluids escape to the surface along the western margin of the field. Our three-dimensional model essentially shows the same flow pattern (e.g., Fig. 10). Hot fluid enters the system through the γ reservoir in the east. The fluid moves westward and then up Fault H into the Z sandstone (β reservoir) where it slightly spreads to the NE and SW. Then, the fluid in the Z sandstone flows predominately westward. In the vicinity of the sandy gap, most of the fluid in the model is either flowing through the SW-NE upthrown row of elements next to or in Fault H zone, itself. A good portion of the fluid rises up the sandy gap, then flows westward into the α reservoir, up Fault L, and westward in the shallow sandstone aquifer and out the model through the top western elements. Because of the three-dimensional nature of the model, the fluid flow pattern shown on Figure 10 is only schematic. Perpendicular to this cross section there is also some fluid movement especially from the Fault H zone, located to the SE, and at the western edge of the section from the sandy region (zone K1).

Production Model

As part of the validation of our three-dimensional model of Cerro Prieto we simulated the exploitation of the α reservoir from 1973 to the end of 1979. At this stage, we assumed yearly constant production rates.

For the period considered, the flow rates were 345, 590, 603, 695, 751, and 716 kg/sec. In Figure 11 the agreement between computed and observed α reservoir pressures is quite reasonable. This is very encouraging since it indicates that the physical parameters assumed for the model, especially for the α reservoir, are generally correct. As we improve the natural state model of the field we expect to obtain a better match with the pressures reported by Bermejo et al. (1979).

CONCLUSIONS

A three-dimensional model of Cerro Prieto is under development. For pre-exploitation conditions the model gives fluid flow patterns consistent with those of Halfman et al. (1984). The calculated and observed temperature distributions match reasonably well. The computed pressures are somewhat lower than the observed ones. The computed pressure drawdown in the α reservoir also matches well with the observed 1973-1979 pressure decline. We expect to improve the agreement between observed and computed data by refining our three-dimensional model and by including in the calculation cold water recharge along the edges of the field. These future improvements of the model will allow its use for predicting the behavior of Cerro Prieto as fluid production is expanded to the eastern areas and to deeper reservoirs.

ACKNOWLEDGEMENTS

We thank our colleagues of the Comisión Federal de Electricidad for providing the data used in this study. This work was supported by the Assistant Secretary for Conservation and Renewable Energy, Office of Renewable Technology, Division of Geothermal Technology of the U. S. Department of Energy, under Contract No. DE-AC03-76SF00098.

REFERENCES

Ayuso, M. A., 1984. Gerencia de Proyectos Geotermoeléctricos, Com. Fed. de Electr. internal report 1384-027 and 028, Departamento de Evaluación y Yacimientos, 15 p.

Bermejo, M., F. J., F. X. Navarro O., F. Castillo B., C.A. Esquer, and C. Cortez A., 1979. Pressure variations at the Cerro Prieto reservoir during production, in Proceedings, Second Symposium on the Cerro Prieto Geothermal Field, Com. Fed. de Electr. Mexicali, Mexico, Oct. 17-19, 1979, pp. 473-493.

Elders, W. A., A. E. Williams, D. A. Bird, and P. Schiffman, 1984. Hydrothermal flow regime and magmatic heat source of the Cerro Prieto geothermal system, Baja California, Mexico, Geothermics, v. 13, p. 27-47.

Elders, W. A., A. E. Williams, and J. R. Hoagland, 1981. An integrated model for the natural flow regime in the Cerro Prieto hydrothermal system based upon petrological and isotope geochemical criteria, in Proceedings, Third Symposium on the Cerro Prieto geothermal field, March 24-26, 1981, San Francisco, California; Lawrence Berkeley Laboratory Report LBL-11967, pp. 102-109.

Grant, M. A., A. H. Truesdell, and A. Mañón, 1984. Production induced boiling and cold water entry in the Cerro Prieto geothermal reservoir indicated by chemical and physical measurements, Geothermics, v. 13, pp. 117-140.

Halfman, S. E., M. J. Lippmann, R. Zelwer, and J. H. Howard, 1984. A geologic interpretation of the geothermal fluid movement in Cerro Prieto field, Baja California, Mexico, Assoc. Pet. Geol. Bull., v. 68, pp. 18-30.

Lippmann, M. J., and G. S. Bodvarsson, 1983. Numerical studies of the heat and mass transport in the Cerro Prieto geothermal field, Mexico, Water Resources Research, v. 19, no. 3, pp. 753-767.

Mercado, G. S., 1976. Movement of geothermal fluids and temperature distribution in the Cerro Prieto geothermal field, in Proceedings, Second United Nations Symposium on the Development and Use of Geothermal Resources, May 20-29, 1975, Washington, D.C., U.S., Government Printing Office, v. 1, pp. 489-494.

Navarro, F.X., F. J. Bermejo, F. Castillo, and R. Rivera, 1982. Update of temperature behavior and distribution in Cerro Prieto I, in Proceedings, Fourth Symposium on the Cerro Prieto Geothermal Field, Com. Fed. de Electr., Guadalajara, Mexico, Aug. 10-12, 1982, pp. 81-91.

Pruess, K., 1983. Development of the general purpose simulator MULKOM, in 1982 Annual Report Earth Sci. Div., Lawrence Berkeley Laboratory report LBL-15500, pp. 133-134.

Rivera, R. J., F. Bermejo, F., Castillo, H. Pérez, and A. Abrajān, 1982. Update of the temperature behavior and distribution in Cerro Prieto II and III, in Proceedings, Fourth Symposium on the Cerro Prieto Geothermal Field, Com. Fed. de Elect., Guadalajara, Mexico, August 10-12, 1982, pp. 93-112.

Table 1. Properties of the materials assigned to the zones used in the model, as shown in Figure 6A and 6B.

Zones	Porosity (%)	Permeability (md) x	y	z
K1,S1,S2,S3,S4	16	100	100	10
S3B,S5,S6	14	100	100	1
S7	14	100	10	10
C1,C2	22	1	1	0.1
C4,C5,C6,C7,C8	25	.5	.005	.005
F1	14	50	50	50

Table 2. Natural state model validation. Pressure comparisons.

Region	Depth (m)	Pressure (bars)		
		Observed Ayuso(1984)	Calculated (Lippmann & Bodvarsson, 1983)	Calculated in this study
α reservoir	1300	-	118.8	112.8
β reservoir (west of sandy gap)	1700	-	156.0	143.5
Fault H	2600-2900	235	-	233.8
β reservoir (east of sandy gap)	2500-2840	228	-	232.5

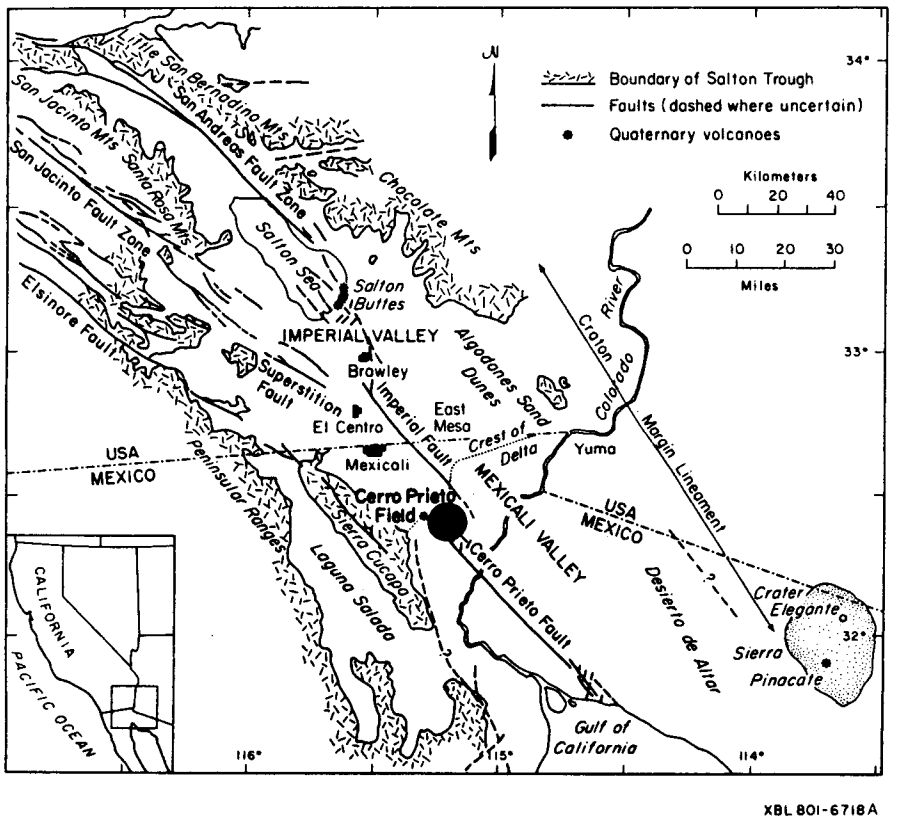

Figure 1. Regional geology of Salton Trough (i.e., Imperial and Mexicali Valleys) and location of the Cerro Prieto field.

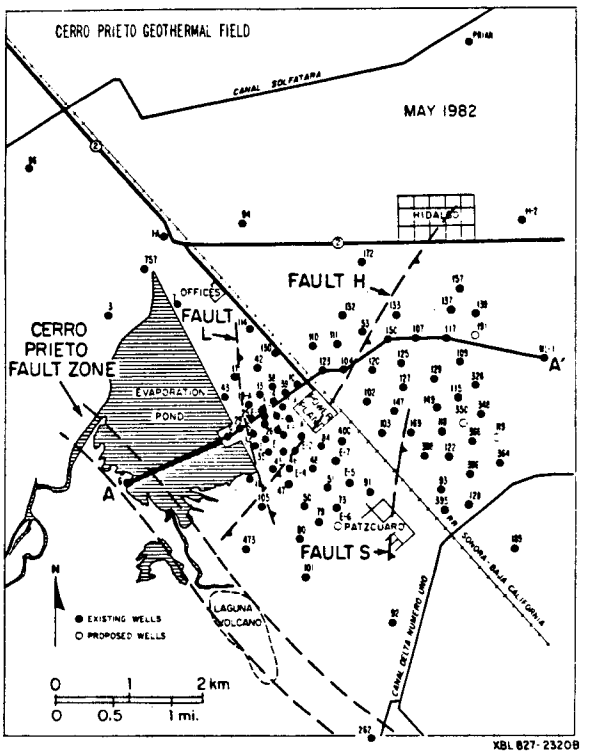

Figure 2. Location of some of the wells, principal faults, and cross section A-A' at Cerro Prieto.

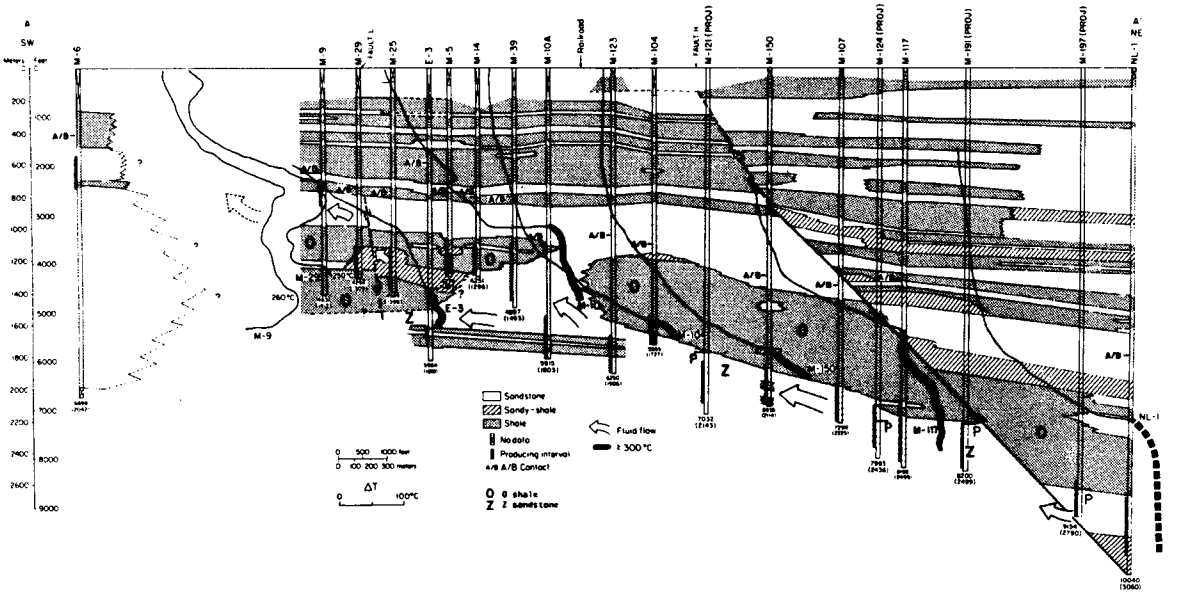

Figure 3. Lithofacies cross section A-A', showing well locations, lithofacies groups, faults, temperature profiles, producing intervals, A/B contacts, shale unit O, sand unit Z, and arrows indicating direction of fluid flow. On temperature profiles, points corresponding to 300 ° C are placed under the location of the respective wells. Parts of temperature profiles shown by heavy lines indicate temperatures 300 ° C or higher.

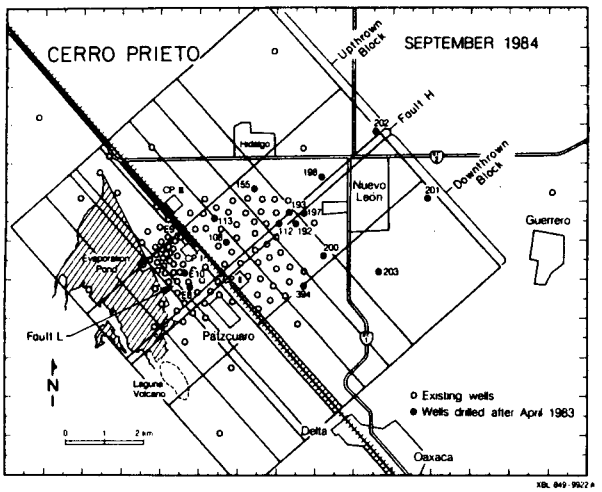

Figure 4. Plan view of the computational mesh used in the work.

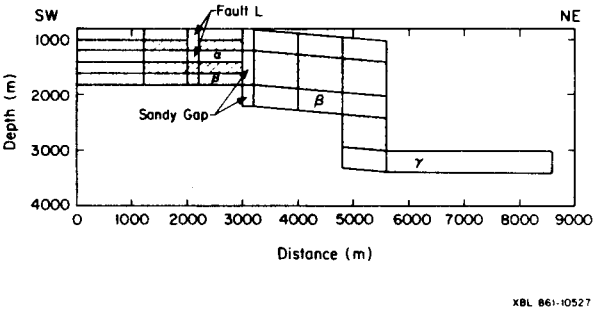

Figure 5. Cross section through the SW-NE row of elements just north of the Fault H. Grid elements are shown, hatched zones represent layers of lower permeability.

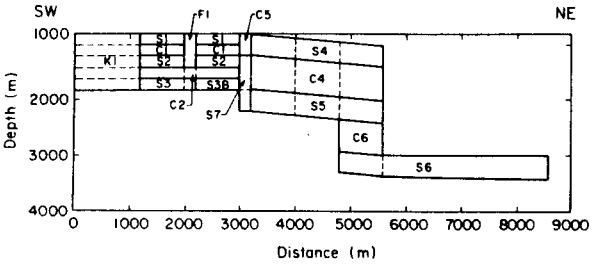

Figure 6A. Cross section given in Figure 5 showing different materials used for the upthrown block.

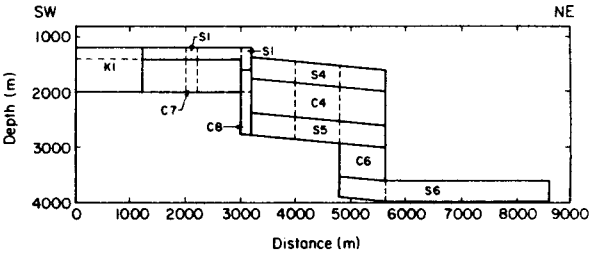

Figure 6B. Cross section through the southernmost SW-NE row of elements representing different materials used for the downthrown blocks.

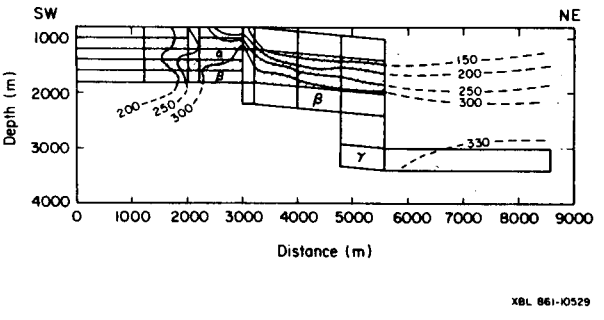

Figure 7A. Cross section given in Figure 5 showing observed temperature distribution (° C).

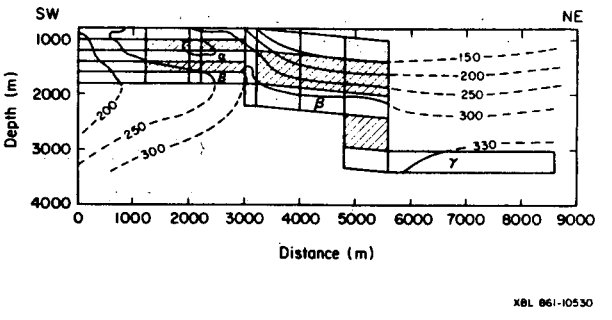

Figure 7B. Cross section given in Figure 5 showing calculated temperature distribution (° C).

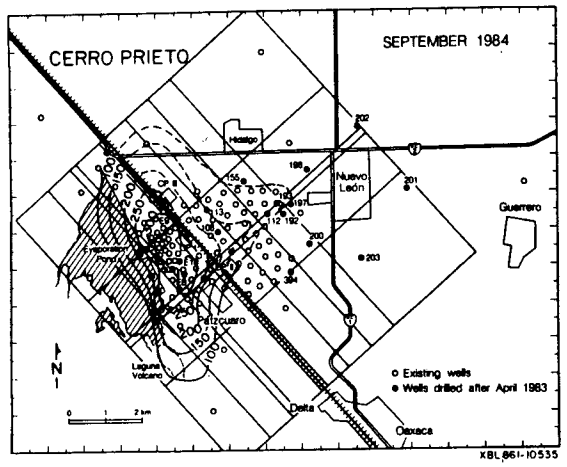

Figure 8A. Observed temperature distribution (° C) at 1300 m depth (Navarro, et al., 1982).

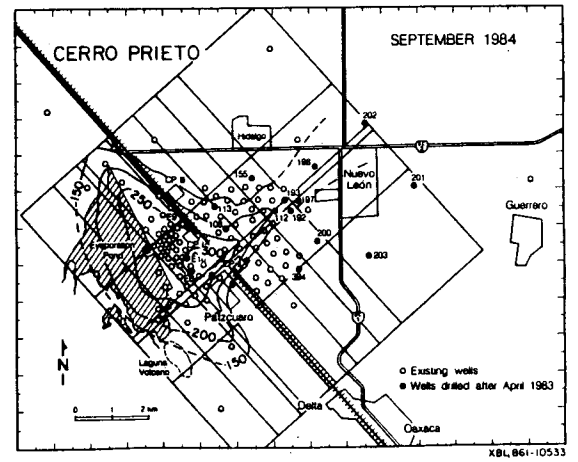

Figure 8B. Calculated temperature distribution (° C) at 1300 m depth.

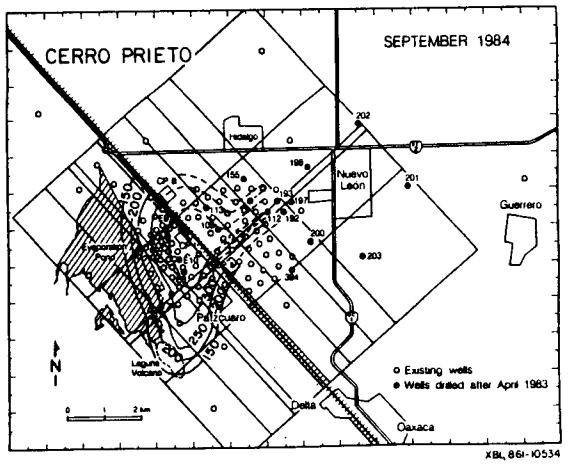

Figure 9A. Observed temperature distribution (° C) at 1750 m depth (Navarro et al., 1982).

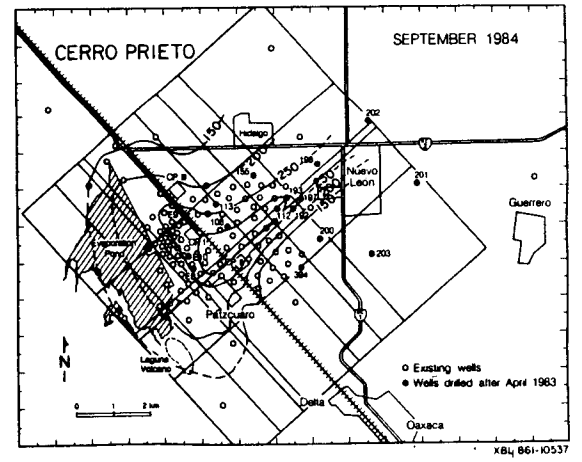

Figure 9B. Calculated temperature distribution at 1750 m depth.

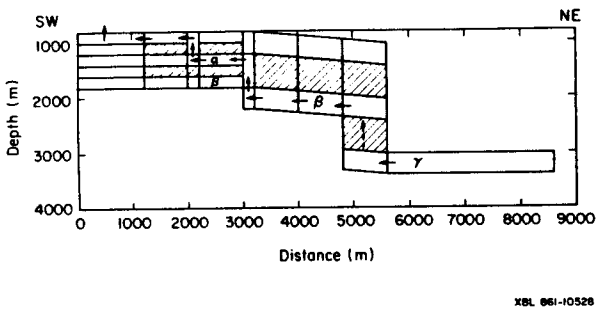

Figure 10. Generalized fluid flow pattern for the cross section shown in Figure 5. The dashed arrow between the β and γ reservoirs indicates vertical flow in the fault zone (located to the southeast).

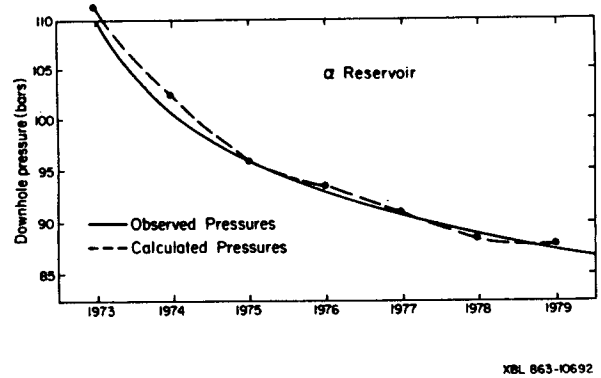

Figure 11. Comparisons of observed (Bermejo et al., 1979) and calculated pressure changes (in bars) in the α reservoir.

PROCEEDINGS, Eleventh Workshop on Geothermal Reservoir Engineering
Stanford University, Stanford, California, January 21-23, 1986
SGP-TR-93

THE INFLUENCE OF GROUNDWATER FLOW ON THERMAL REGIMES IN MOUNTAINOUS TERRAIN

Craig Forster and Leslie Smith

Department of Geological Sciences
University of British Columbia
Vancouver, British Columbia, Canada V6T 2B4

ABSTRACT

Active circulation of cool groundwater in mountainous terrain can cause an advective disturbance of the thermal regime. This factor complicates interpretation of data collected in geothermal exploration programs. An isothermal free-surface model has been developed which provides qualitative insight into the nature of an advective disturbance as it is affected by topography, permeability and climate. A fully coupled model of fluid and heat transfer is being developed for quantitative study of idealized mountain hydrothermal systems.

INTRODUCTION

Geothermal exploration in the Pacific Northwest is hampered by the advective disturbance of thermal regimes. Active circulation of cool groundwater in this region of steep topography and abundant precipitation can complicate interpretation of temperature gradients measured in shallow boreholes (La Fleur, 1983). Furthermore, shallow groundwater flow may suppress high-temperature surface manifestations of a geothermal resource and mask an underlying hydrothermal flow system (Duffield, 1983). In regions of low relief, and/or low permeability, advective heat transfer is minimized and high-temperature thermal phenomena such as geysers, fumaroles and hot springs are more likely to occur. Geothermal exploration in such environments is simplified due to the close association of surface phenomena with underlying free-convection cells, thermal sources and possible reservoirs.

Conventional exploration strategies often use data from thermal springs to draw inferences on the nature of the thermal regime. In mountain hydrothermal systems, the character of thermal springs is determined largely by topographically-induced groundwater flow systems which are difficult to relate to possible exploration targets. For example, at Meager Creek, in the Coast Mountains of British Columbia, a localized thermal anomaly has been identified in close proximity to a thermal spring (Lewis et. al., 1978). However, despite a significant exploration effort, the relationship between thermal springs, possible reservoirs and thermal sources has yet to be resolved.

An improved understanding of the interaction of groundwater flow and thermal regimes in mountain systems will help refine exploration strategies. To this end, we have initiated a model study of the mechanism of coupled heat and fluid transfer in mountainous terrain. A first step in our study has involved formulating a method to simulate isothermal groundwater flow in mountain systems. The isothermal model has been developed and is being incorporated in a fully-coupled model of fluid and heat transfer. In the following discussion, results of isothermal simulations demonstrate our approach to modeling groundwater flow in mountain systems and provide qualitative insights into the nature of advective disturbance of thermal regimes in mountainous terrain.

MODELING APPROACH

An idealized isothermal groundwater flow system in mountainous terrain is shown in Figure 1. In order to emphasize the relatively steep slopes, the system has been drawn without vertical exaggeration. We are interested in the bulk flow of groundwater through the mountain massif rather than the details of flow in thin surficial deposits. Thus, the top boundary is viewed as the bedrock surface with vegetation and surficial deposits removed. Impermeable vertical and basal boundaries allow recharge and discharge only across the top boundary.

In taking the bedrock surface as the top boundary of the flow system, we assume that overlying surficial deposits act as a thin high-permeability skin on the bedrock surface. Precipitation either crosses the bedrock surface as recharge, or is lost as runoff. We lump overland flow, subsurface flow through surficial deposits and evapotranspiration in a single runoff term. These processes are strongly influenced by the variable magnitude, frequency and duration of precipitation events. However, in the context of large-scale mountain systems, a steady-state approach is reasonable. We define an available infiltration rate to represent the maximum rate of recharge expected for specified climatic, geologic and topographic conditions (Figure 1). Depending upon the nature of the flow system, recharge rates may be less than this maximum. If available infiltration exceeds recharge, additional runoff is generated (Figure 1).

Groundwater recharge is controlled by hydraulic gradients near the bedrock surface. Hydraulic gradients are governed by the permeability and geometry of the overall flow system and reflect the capacity for flow through the system. Low gradients and low permeability can produce recharge rates less than available infiltration rates. High permeability and high gradients may enable a flow system to accept all the available infiltration.

Saturated and unsaturated regions of flow occur along the bedrock surface. They are separated by a water table which meets the bedrock surface at a point of detachment (POD). Note that the POD does not necessarily coincide with the boundary between recharge and discharge (shown as the hinge point in Figure 1). Where the water table coincides with the ground surface, the saturated zone is recharged directly by incident precipitation. Elsewhere, recharge at the bedrock surface is transferred to the water table by unsaturated flow. Significant lateral flow in the unsaturated zone may cause patterns of flux across the water table to differ from patterns of recharge at the bedrock surface. The nature and magnitude of lateral flow in unsaturated regions of mountain flow systems is not well known. In our modeling approach, we use the simplest assumption of one-dimensional vertical flow in the unsaturated zone. This approach implies that fluid flux rates across the water table correspond exactly to recharge rates at the bedrock surface, allowing us to neglect the unsaturated zone. Thus, the water table is the effective upper boundary of the entire flow system.

In using the water table as the upper boundary of the flow system, we require information on water table elevations in mountainous terrain. Such data are sparse and assumptions must be made to estimate realistic water table elevations. One possibility is to arbitrarily fix the water table position with reference only to surface topography. This method can result in flow systems which erroneously have recharge rates in excess of available infiltration rates. In order to maintain reasonable recharge patterns we adopt a free-surface modeling approach which does not require explicit definition of the water table. This method provides a constraint on water table estimates by incorporating available infiltration rates in the computations. For example, if recharge accepted by the system is everywhere less than available infiltration, the water table will be at the bedrock surface. If the capacity of the system to accept recharge exceeds available infiltration, the water table lies at some distance below the bedrock surface.

A vertical, planar/axisymmetric model of steady-state groundwater flow in two-dimensional mountain systems has been developed using a free-surface method similar to that of Neuman and Witherspoon (1970). Linear triangular elements and one-dimensional line elements are used. Line elements have been included to allow simulation of thin, high-permeability fault zones.

The free-surface method involves iterative solution of the groundwater flow equation using a finite element mesh which can deform in the vertical direction. For initial and subsequent iterations, a mixed boundary condition is specified on the top surface (Figure 1). Fixed heads are specified where the water table coincides with the bedrock surface. Elsewhere, an available infiltration rate is assumed. The solution proceeds by solving this initial problem and computing the corresponding head distribution. The resulting head values are used to extrapolate a new water table position and the finite element mesh is deformed to conform to the shape of the new upper boundary. At each iteration, the POD is moved along the top surface to ensure a balance of recharge and discharge. The iterative procedure is repeated until a stable water table configuration is determined.

Conventional techniques in free-surface models track the movement of the point of detachment (POD) along the bedrock surface. Groundwater recharge is assumed to occur only above the POD, which is implicitly assumed to coincide with the hinge point. In developing our modeling approach, it was observed that the POD does not necessarily coincide with the

boundary between recharge and discharge (hinge point) in steep terrain with relatively low permeability. Thus, recharge can occur downslope of the POD where the water table coincides with the bedrock surface in recharge areas (Figure 1). This situation cannot be handled by conventional methods which may produce solutions with unrealistic water table configurations.

We have adopted the conventional approach of tracking the movement of the point of detachment (POD) along the top surface. However, we do not assume that the POD marks the lowest point of recharge. Rather, we identify the POD as the uppermost point where hydraulic heads are known to equal the surface elevation (Figure 1). Although recharge rates are not initially known for the region between the POD and hinge point, they can be computed following solution of the flow problem. Recharge rates are computed at each iteration using hydraulic heads in the vicinity of the bedrock surface. Computed recharge rates are compared to available infiltration rates at each iteration. If recharge rates exceed infiltration rates, additional water table adjustments are made within the iteration.

The accuracy of each solution is estimated by performing a fluid flux balance. A total balance of fluid crossing all system boundaries is computed, in addition to a balance of fluxes across only the top surface. Because vertical grid lines in the deforming mesh are rarely orthogonal to the sloping top boundary, computation of fluid flux normal to the surface using hydraulic heads can be inaccurate. After the final iteration is complete, the problem is reformulated in terms of stream functions and solved for the velocity potential distribution. This technique enables direct computation of fluxes normal to the water table. Differences between boundary fluxes obtained from the hydraulic head and stream function solutions can be used to identify regions where the finite element mesh may be too coarse. If discrepancies are significant, the mesh is refined and the problem is solved again using the new mesh. Contour plots of the stream function solutions are particularly useful in visualizing patterns of groundwater flow in mountain systems and relating them to the thermal problem.

ISOTHERMAL GROUNDWATER FLOW SYSTEMS

Isothermal fluid flow in mountainous terrain is strongly controlled by topography, climate and the distribution of rock mass permeability. The effect of these factors on water table configurations and groundwater flow patterns can be demonstrated by modeling a series of idealized systems. In this discussion we neglect the influence of thermal bouyancy on fluid flow patterns. This effect will be addressed upon completion of the fully coupled model.

Figure 2a shows the flow system and water table configuration computed for the homogeneous isotropic rectilinear system described in the previous section. A uniform available infiltration rate is arbitrarily assigned as 20 percent of a reference hydraulic conductivity K_o. In regions where recharge accepted by the flow system exceeds available infiltration, the water table lies below the bedrock surface (Figure 2a). Increased infiltration rates would produce higher water table positions with corresponding POD's at higher elevations on the bedrock surface.

Streamlines shown in Figure 2a demonstrate the pattern of flow. In nonisothermal systems, heat within a streamtube is transferred by fluid motion parallel to streamlines. If thermal dispersion is neglected, heat is transferred between streamtubes by thermal conduction. A qualitative impression of advection-dominated heat transfer can be obtained from the density of streamlines and their proximity to a thermal source. Thermal gradients are enhanced where streamlines downgradient of a heat source are closely spaced. Conversely, thermal gradients are reduced upgradient of a thermal source and in regions where streamlines are more widely spaced. As groundwater flow rates decrease, thermal conduction between streamtubes increases.

A reservoir at depth is simulated by including a region of increased hydraulic conductivity in the rectilinear system of Figure 2a. Figure 2b shows the flow system for a basal reservoir, 400 meters thick, with hydraulic conductivity 50 times that of the homogeneous isotropic system (K_o). The pattern of flow is significantly altered by the reservoir, suggesting that cool fluids might penetrate more deeply into the system. Convergence of streamlines within the reservoir implies that thermal anomalies in the mountain massif and in the discharge region might be more localized than in the previous example (Figure 2a). The increased permeability at depth causes a maximum water table decline of 200 meters and an increased net flux through the system of 20 percent.

The effect of surface topography on mountain flow systems is illustrated in Figure 3. Figure 3a represents a vertical section of a concave ridge with volcano-like form. A vertical section of a convex ridge which might be found in glaciated crystalline terrain is shown in Figure 3b. The total relief and overall geometry of

these systems are the same as in the previous case. Again, the reference homogeneous, isotropic hydraulic conductivity K_0 is assumed with uniform available infiltration rates equal to 20 percent of K_0.

Water table configurations and net flux through each flow system are affected by the surface topography. The relatively flat upland of the convex system (Figure 3b) results in a more extensive recharge area than is found in the other topographic types (Figures 2a and 3a). This effect results in greatest flux and the highest water table elevation in the system with convex topography. The smallest net flux and lowest water table elevation occur in the concave system where the extent of the recharge area approximately equals that of the discharge area (Figure 3a). Convergent streamlines in the restricted discharge area of the convex system suggest that convex topographies will produce localized surface thermal anomalies of greater magnitude than those in concave topographies. The general nature of this effect has been identified by Smith and Chapman (1985) in modeling of systems with low topographic relief.

Anisotropy and heterogeneity in rock mass permeability affects both water table configurations and flow patterns. Figure 4a shows how the flow system of Figure 3b is modified by increasing the vertical hydraulic conductivity by a factor of 5 relative to the horizontal hydraulic conductivity, which is held at K_0. This anisotropic system is intended to simulate uniform sub-vertical fracturing. Figure 4b shows how the flow system of Figure 3b is modified by a vertical fault zone 100 meters wide with hydraulic conductivity 5 times that of the surrounding rock mass (K_0). Overall patterns of flow through each system are similar. However, streamline densities in the discharge regions of each system are markedly different. The vertical fault and vertical anisotropy contribute to an increased density of streamlines in discharge areas suggesting an enhanced thermal expression at the surface. Note that relatively minor geologic features, such as the 100 meter wide fault zone of Figure 4b, can significantly affect the water table configuration despite the subtle difference in hydraulic conductivity between the fault zone and the surrounding rock mass.

Regional variations in climate influence the spatial variation of precipitation and available infiltration rates. For each flow system, a threshold infiltration rate can be defined above which the water table is everywhere at the bedrock surface. The threshold rate defines the maximum recharge rate which can be accepted by a particular system and depends upon surface topography and rock mass permeability. Low permeability systems in humid climates will have threshold rates which may be less than available infiltration rates. Thus, water tables are at or near the bedrock surface (Figure 5a). The converse is true for high permeability systems in arid environments where threshold rates may exceed available infiltration rates and produce water tables well below the bedrock surface (Figure 5b). When assigning arbitrary infiltration rates or water table positions, it is important to check that computed recharge rates are within the limits expected for the specified topographic and climatic conditions. The free-surface technique helps to reduce uncertainty in this regard by employing an internally consistent method to assign water table postions and ensure that available infiltration rates are not exceeded.

Figure 5a shows the fully saturated system occurring in a convex system with infiltration rates in excess of the threshold. The threshold rate for the convex system equals 29 percent of the reference hydraulic conductivity K_0. Threshold rates for the rectilinear and concave systems are equal to 56 percent and 72 percent of K_0, respectively. Therefore, the restricted discharge area produced by the convex topography of Figure 5a results in a significantly lower threshold infiltration rate.

Figures 5b and 3b show the lower water tables and modified flow patterns found for the convex system using sub-threshold infiltration rates equal to 10 percent of K_0 and 20 percent of K_0, respectively. Note that the total flux through a fully saturated system is the maximum which can be attained even if infiltration rates exceed the threshold rate. Using the computed flux through the fully saturated convex system as a reference, dimensionless fluxes of 0.96 and 0.52 correspond to the progressively lower water tables indicated in Figures 3b and 5b. Thus, water table configurations and total flux through the flow system are significantly affected by available infiltration rates. Similar results are found for other topographic types. Arbitrary definition of water tables in mountain regions may imply infiltration rates which do not adequately reflect the climatic environment.

Model results presented here indicate that water table configurations depend strongly on the magnitude and distribution of hydraulic conductivity and available infiltration rates. Arbitrary estimation of water table elevations with reference only to surface topography cannot easily account for the influence of these factors. Using the free-surface method, we employ assumed available infiltration rates and hydraulic characteristics

of the flow system to calculate plausible water table configurations. It is recognized that infiltration rates depend upon a variety of complex factors which are not easily evaluated. Thus, there is a certain subjectivity involved in estimating infiltration rates, just as there is a subjective element in defining permeability distributions in mountain-scale systems. However, estimating these parameters by iterative comparison of field data and model results is expected to provide reasonable estimates of water table configurations and flow patterns in mountainous terrain.

SUMMARY

Isothermal free-surface modeling of groundwater flow in mountainous terrain illustrates the influence of topography, rock mass permeability and climate on water table configurations and groundwater flow patterns. Contoured plots of the velocity potential provide qualitative insights into the possible nature of thermal regimes in mountain systems. This isothermal model forms the basis for a fully coupled model of fluid and heat transfer in mountainous terrain.

The fully coupled model currently in development uses this method to solve the steady-state groundwater flow equation. The isothermal model is modified to include a thermal bouyancy term in the flow equation and to account for the temperature dependence of fluid viscosity and density. Steady-state thermal regimes can be simulated by solving the equation of heat transfer. Both thermal conduction and heat transfer by fluid flow are considered. Thermal boundary conditions include a basal heat flux and insulated vertical boundaries. On the top surface, temperatures in recharge areas can be fixed at an ambient air temperature which varies as a function of elevation. In discharge areas, surface temperatures can also be fixed at air temperature or computed using an iterative process. In the iterative procedure, surface temperatures are related to ambient air temperature through a simple linear cooling law. This method uses a highly simplified representation of the complex processes of heat transfer at the surface. However, this approach should provide useful insights into the nature of thermal regimes in mountainous terrain and aid in establishing relationships between thermal springs, thermal sources and possible reservoirs.

REFERENCES

Duffield, W.A. (1983), "Geologic Framework for Geothermal Energy in the Cascade Range", Trans. Geoth. Res. Council, Vol. 7,pp 243-246.

La Fleur, J. (1983), "An Exploration Overview", Trans. Geoth. Res. Council, Vol. 7, pp 253-261.

Lewis, J.T. and J.G. Souther. (1978), "Meager Mt. B.C.- Possible Geothermal Energy Resource", Energy Mines and Resources of Canada, Earth Physics Branch, Geothermal Series No. 9. Ottawa, 17pp.

Neuman, S.P. and P.A. Witherspoon. (1970), "Finite Element Method of Analyzing Steady Seepage With a Free Surface", Water Resources Research. Vol. 6, No. 3, pp 889-897.

Smith, L. and D.S. Chapman. (1985), "The Influence of Water Table Configuration on the Near-Surface Thermal Regime", Journal of Geodynamics, November, 1985.

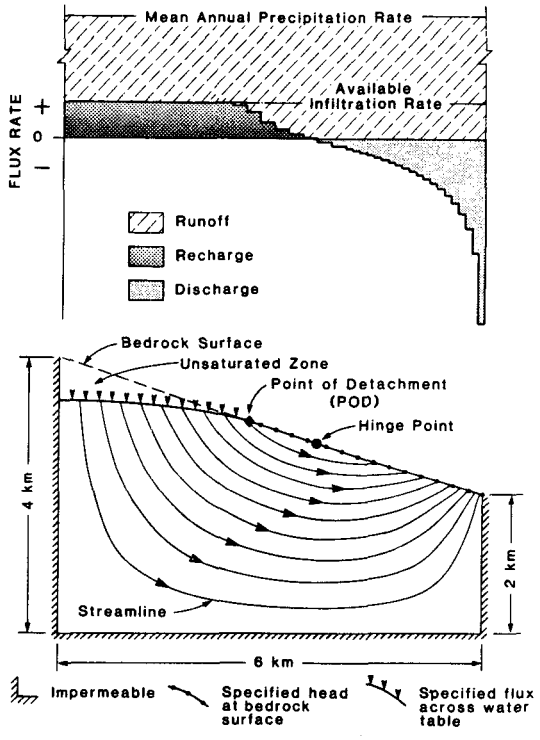

FIGURE 1. Schematic boundary value problem for isothermal groundwater flow in mountainous terrain.

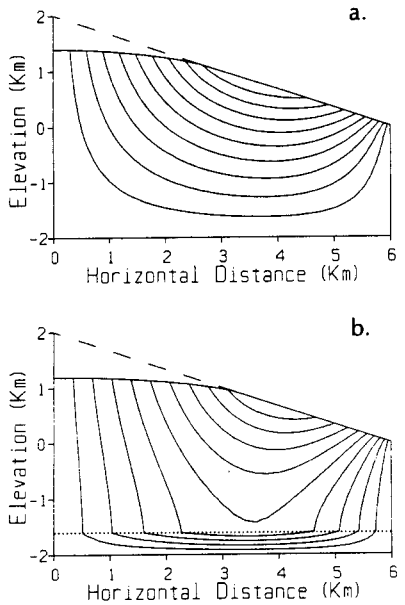

FIGURE 2. Influence of a reservoir at depth on patterns of flow in a rectlinear system. a) Homogeneous isotropic system with hydraulic conductivity K_o. b) Basal reservoir 400 meters thick with hydraulic conductivity 50 times K_o.

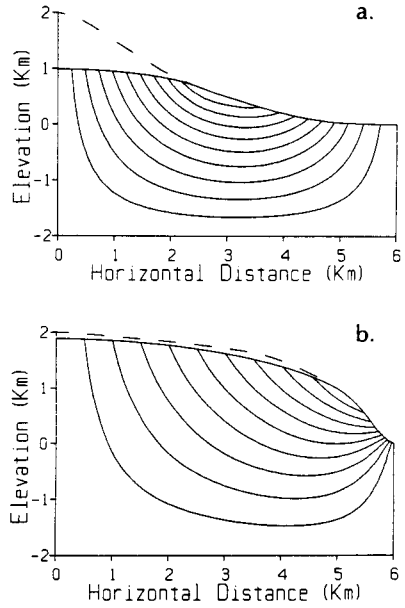

FIGURE 3. Influence of topography on patterns of flow in mountainous terrain. a) Concave volcano-form system. b) Convex glaciated system in crystalline terrain. Both systems have homogeneous isotropic conductivity K_o.

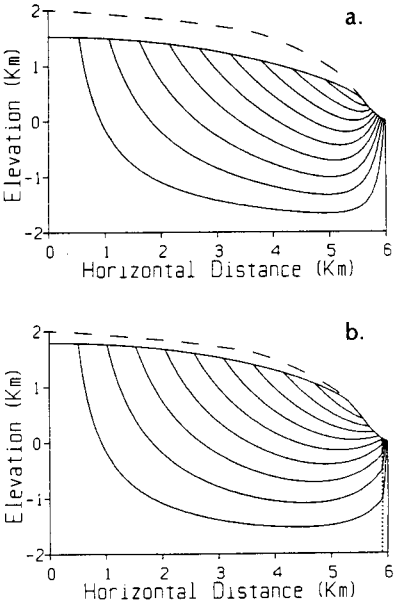

FIGURE 4. Influence of anisotropy and heterogeneity on patterns of flow in a convex system. a) Anisotropic system with vertical hydraulic conductivity 5 times K_o. b) Vertical fault zone 100 meters wide with hydraulic conductivity 5 times K_o.

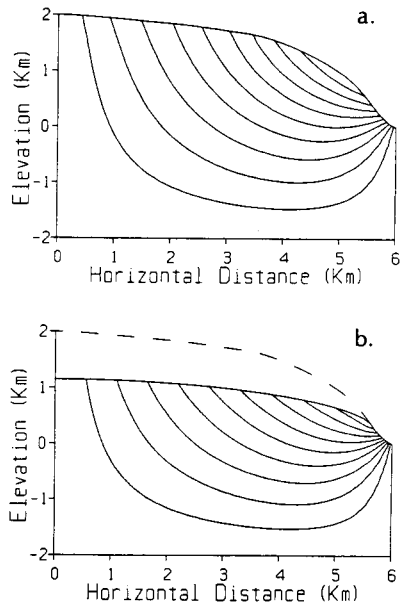

FIGURE 5. Influence of climate on patterns of flow in a convex system. a) Humid climate; infiltration rates exceed the threshold rate and the water table coincides with the ground surface. b) Arid climate; infiltration rates are less than the threshold rate and the water table falls below the bedrock surface. Both systems have homogeneous isotropic hydraulic conductivity K_o.

PROCEEDINGS, Eleventh Workshop on Geothermal Reservoir Engineering
Stanford University, Stanford, California, January 21-23, 1986
SGP-TR-93

HOT SPRING MONITORING AT LASSEN VOLCANIC NATIONAL PARK, CALIFORNIA 1983-1985

Michael L. Sorey

U.S. Geological Survey
Menlo Park, California

ABSTRACT

Data collected on several occasions between 1983 and 1985 as part of a hydrologic monitoring program by the U.S. Geological Survey permit preliminary estimation of the natural varability in the discharge characteristics of hydrothermal features in Lassen Volcanic National Park and the Lassen KGRA in northern California. The total rate of discharge of high-chloride hot springs along Mill Creek and Canyon Creek in the Lassen KGRA has averaged 20.9 $\pm$ 1.7 L/s, based on seven measurements of the flux of chloride in these streams. Measured chloride flux does not appear to increase with streamflow during the spring-summer snowmelt period, as observed at Yellowstone and Long Valley Caldera. The corresponding fluxes of arsenic in Mill Creek and Canyon Creek decrease within distances of about 2 km downstream from the hot springs by approximately 30%, most likely due to chemical absorption on streambed sediments. Within Lassen Volcanic National Park, measurements of sulfate flux in streams draining steam-heated thermal features at Sulphur Works and Bumpass Hell have averaged 7.5 $\pm$ 1.0 and 4.0 $\pm$ 1.5 g/s, respectively. Calculated rates of steam upflow containing dissolved H_2S to supply these sulfate fluxes are 1.8 kg/s at Sulphur Works and 1.0 kg/s at Bumpass Hell.

INTRODUCTION

This paper summarizes data collected in a hydrologic monitoring program conducted by the U.S. Geological Survey between 1983 and 1985 in the vicinity of Lassen Volcanic National Park (LVNP). The area of study is located in north-central California at the southern end of the Cascade Range and includes LVNP and the adjacent Lassen Known Geothermal Resource Area (KGRA, fig. 1). The monitoring program has been funded by the National Park Service in an effort to determine the natural level of variability in the discharge characteristics of surficial hydrothermal features in this area. Such information may be needed to assess the impacts of future geothermal development on the Lassen hydrothermal system. An Environmental Impact Statement is currently being prepared for geothermal leasing of federal lands adjacent to LVNP.

Late Pliocene to Holocene volcanic rocks in the Lassen region were extruded from several long-lived volcanic centers, each producing composite cones of andesite to rhyolite lavas and pyroclastics (Clynne, 1984, 1985). A silica magma chamber associated with the Lassen volcanic center (0.6 m.y. to present) provides heat for the present-day hydrothermal system which occurs primarily within the southern half of LVNP and the adjacent KGRA (fig. 2).

Surface thermal discharge includes fumaroles and steam-heated hot springs at relatively high elevations within the Park and high-chloride hot springs at relatively low elevation in the KGRA. Geochemical evidence and temperature measurements in a 1.2 km deep well near Terminal Geyser indicate that the Lassen hydrothermal system is liquid-dominated but includes a parasitic vapor-dominated region associated with the central upflow zone beneath Bumpass Hell (Muffler et al., 1982, Sorey and Ingebritsen, 1984, Ingebritsen and Sorey, 1985). Zones of lateral outflow of hot water derived from this upflow zone trend southward and southeastward, extending to discharge points within the KGRA. Thermal fluid discharge occurs in high chloride hot springs at Growler and Morgan Hot Springs and in diluted low chloride springs at Domingo Springs (fig. 2). Additional thermal fluid may flow in shallow aquifers south of Morgan Hot Springs and may discharge as seeps

into Willow Creek and Warner Creek (Sorey and Ingebritsen, 1984).

THE MONITORING PROGRAM

The monitoring program described in this paper includes periodic streamflow measurements and chemical sampling at several sites in Mill Creek, Canyon Creek, and at Domingo Springs, and similar measurements in streams draining steam-heated thermal features at Sulphur Works and Bumpass Hell (fig. 2). Such data permit calculation of hot spring discharge within the KGRA from measurements of the flux of chemical elements contributed to the streams by hot spring waters. With few exceptions, the flow of hot springs in the Lassen area cannot be gaged directly and much of the thermal water occurs as streambed seepage. Hence thermal fluid discharge must be calculated from chemical flux measurements.

Chemical flux measurements in the Lassen KGRA have been made for three conservative thermal fluid elements - Cl, B, and As. The precision of this technique is enhanced by the relatively high concentration of these elements in the hot springs (table 1). Such concentrations may be indicative of a fluid component of marine origin within the Lassen hydrothermal system (Sorey and Ingebritsen, 1984; Thompson, 1985). Although the fraction of hot-spring water in Mill Creek and Canyon Creek at the measuring sites ranges from about 0.5% to 5% during the year, concentrations of Cl, B, and As remain well above detection limits. As noted below, however, a significant portion of the arsenic contributed to these streams by the hot springs appears to be taken out of solution by adsorption on streambed sediments, making chloride flux measurements the most reliable for calculating hot spring discharge.

At Domingo Springs, water that flows from several vents at temperatures near 9°C is channeled through a culvert. Streamflow measurements and chemical samples have been taken below the discharge end of the culvert. Although the measured chloride concentrations in this water (11-19 mg/L) are signifcantly lower than chloride concentrations in Growler and Morgan Hot Springs, they are approximately 10 times higher than chloride concentrations in other cold springs in the KGRA. This indicates that some component of thermal water from the Lassen hydrothermal system discharges in Domingo Springs. In results shown in the next section, thermal fluid discharge at Domingo Springs is calculated from the measured flow of the springs by assuming that the chloride concentration of the thermal component is equal to that measured in water produced from the well at Terminal Geyser (2180 mg/L). This, in turn, is based on the assumption that some or all of the thermal water flowing southeast in the lateral outflow zone beneath Terminal Geyser eventually discharges in Domingo Springs.

The rate of discharge of fluids from thermal areas within LVNP cannot be determined by the same type of chemical flux measurements because of the loss of steam in fumaroles and the lack of conservative elements such as Cl in the steam-heated hot springs. The discharge characteristics of individual vents in such areas may undergo considerable fluctuation due to seasonal and annual hydrologic variations. Published and unpublished data on the temperature and gas concentration of selected steam vents at thermal areas in LVNP document some of these changes that have occurred since 1975 (Muffler et al., 1982; Truesdell et. al., 1983; Janik, written communication, 1986). For the purposes of delineating changes in the rate of upflow of steam and gas from underlying vapor-dominated zones, measurements of the total heat output from each thermal area would be most useful. Such measurements, although difficult to obtain, have been successfully made at Wairakei, New Zealand, to quantify changes in steam upflow induced by geothermal development (Allis, 1981). Total heat output determinations require measurements of heat loss by advection in hot springs and fumaroles, by conduction, and by evaporation.

Data collected during the present monitoring program on the flux of sulfate in streams draining thermal areas at Sulphur Works and Bumpass Hell provide a preliminary basis on which to assess the natural variability in heat discharge at these areas. Some or all of this sulfate flux must come from near-surface oxidation of H_2S which originates along with steam upflow from underlying vapor-dominated zones. If the ratio of H_2S to steam in such upflow is known, the sulfate flux measurements provide an estimate of the fraction of the total steam upflow that is condensed in the hot spring waters in these areas. Such measurements were originally suggested by A.H. Truesdell (written communication, 1984), based on the work of Giggenbach and Stewart (1982). Complicating factors include

the possibility that sulfate is also contributed to the streams draining these areas from products of rock weathering and that some H_2S reacts with near-surface rocks to form pyrite and sulfur. Measurements of sulfate flux and the associated steam upflow reported here are compared with estimates of steam upflow made by other means and by other investigators to evaluate the effects of such complicating factors.

THERMAL WATER DISCHARGE IN LASSEN KGRA

The rate of discharge of thermal water from hot springs along Mill Creek and Canyon Creek can be estimated from the difference in the flux of chloride at sites above and below the hot springs divided by the chloride concentration in the spring waters. Data for the site on Mill Creek at Highway 36 (table 2) exemplify the way this is done. Calculated values of hot spring flow (thermal water component) are based on an average chloride concentration of 2300 mg/L in hot springs above this site. The average spring flow is calculated as 17.2 L/s with a standard deviation of 1.2 L/s. Thermal water discharge at Morgan Hot Springs and Growler Hot Springs contributes to this total.

Differences between calculated values of hot spring discharge at this site and other sites within the KGRA between the seven sampling visits during the 1983-1985 period could be caused by several factors. These include errors in streamflow measurements and chloride determinations, loss (or gain) of stream water to the shallow ground-water system below the hot spring areas, and actual differences in hot spring discharge. Data from chemical analysis on duplicate water samples and subjective ratings of stream gaging accuracy suggest that the accuracy of the flux measurements at this site is $\pm$ 10%. Thus, most if not all of the variation in calculated spring flow at this site could be due to errors in streamflow and chloride concentration determinations. There does not appear to be a consistent increase in chloride flux at this site (or any of the other sites in the KGRA) with increasing streamflow. Such a correlation has been shown for hot spring areas at Yellowstone National Park (Norton and Friedman, 1985) and Long Valley Caldera (Farrar, et al., 1985). In those areas the correlation has been attributed to a release of chloride from storage within drainage basins accompanying the spring-summer runoff period.

Results of hot spring discharge calculations based on chloride flux determinations for each thermal area in the KGRA are listed in table 3. The total hot spring flow along Mill Creek (from Morgan Hot Springs) and Canyon Creek (from Growler Hot Springs) has average 20.9 L/s with a standard deviation of 1.7 L/s. Note that the total for Morgan Hot Springs is calculated from the thermal component in Mill Creek at Highway 36 (17.2 L/s from table 2) less the thermal component in Canyon Creek below Growler Hot Springs (2.19 L/s from table 3) plus the thermal component (3.7 L/s) in a tributary to Mill Creek at Highway 36 that is also derived from hot springs at Morgan Hot Springs. At Domingo Springs, chloride flux measurements indicate an average thermal component of 0.93 $\pm$ 0.18 L/s with chloride concentration equal to that measured in the well at Terminal Geyser.

Measured fluxes of arsenic in Mill Creek and Canyon Creek are significantly lower than values calculated from estimates of the thermal-fluid component in these streams (based on measured chloride fluxes). This is not true for the measured boron fluxes, which agree with the calculated fluxes. Data for Mill Creek at Highway 36 (table 4) indicate that 10-39% of the hot-spring derived arsenic is lost between the springs and this measurement site over a distance of 2.5 km. The most likely explanation for this loss is chemical adsorption on streambed sediments. Similar calculations for Canyon Creek show arsenic losses of 19-50% over a distance of 1.6 km.

SULFATE DISCHARGE IN LVNP

Measurements of sulfate flux in streams draining steam-heated thermal features at Sulphur Works (SW) and Bumpass Hell (BH) in LVNP are reported in table 5. Measurements at SW have been made at four culverts through which branches of West Sulphur Creek flow. Data in table 5 apply to two of these branches which drain active thermal features; sulfate discharge in the other two branches is contributed entirely by erosion of sulfate-rich surficial deposits. The total hot-spring derived sulfate flux at SW averages 7.5 $\pm$ 1.0 g/s, and the corresponding total for BH averages 4.0 +

1.5 L/s. At both areas, the reported sulfate flux does not vary significantly with streamflow, indicating that the sulfate contribution from nonthermal sources is minimal.

As discussed previously, the sulfate flux estimates can be converted to estimates of steam condensed in the hot springs, assuming the sulfate is derived from oxidation of H_2S and that the ratio of oxidized H_2S to condensed steam is the same as the H_2S to steam ratio in the vapor-dominated reservoir. Data from Muffler et. al. (1982) based on analyses of fumarolic gases at BH indicate that the steam to H_2S molar ratio in the vapor-dominated reservoir is 1290. The corresponding weight ratio of steam to SO_4 would be 242. Thus the average sulfate fluxes at BH and SW noted above convert to 1.1 kg/s and 1.8 kg/s of condensed steam, respectively. For comparison, the rate of steam condensation required to provide the advective heat loss in the streams draining these areas is approximately twice the values calculated from the sulfate measurements. This suggests that the actual ratio of condensed steam to oxidized H_2S is at least twice the steam to H_2S ratio in the vapor-dominated reservoir. The higher steam to H_2S ratios implied by the advective heat loss rates may be accounted for by near surface loss of H_2S to form pyrite and sulfur deposits and by surficial discharge of H_2S in gas vents and seeps.

Estimates of the total rate of steam upflow at Bumpass Hell can also be obtained from the calculations of total heat flow at this area discussed by Friedman and Frank (1978). Their data, based on ground temperature measurements and meterological calculations, together with the advective heat loss estimates from the current monitoring program, indicate a total heat loss of 36 MW over an area of 0.045 km^2 at Bumpass Hell (fig. 3). This total does not include heat loss in fumarolic steam discharge. The rate of steam upflow required to maintain this heat flow is approximately 13 kg/s, or ten times flow rate suggested by the sulfate flux measurements. Additional study and field observations will be required to verify this heat flow estimate and to delineate more clearly the processes responsible for these differences in steam upflow estimates.

REFERENCES

Clynne, M.A., 1984, Stratigraphy and major-element geochemistry of the Lassen Volcanic Center, California: U.S. Geological Survey Open-File Report 84-224, 168 p.

Clynne, M.A., 1985, Quaternary volcanism in the Southern Cascade Range, California: in Proceedings of the Workshop on Geothermal Resources of the Cascade Range, ed. Guffant, M., and Muffler, L.J.P.: U.S. Geological Survey Open-File Report 85-521, p. 24-30.

Farrar, C.D., Sorey, M.L., Rostaczer, S.A., Janik, C.J., Mariner, R.H., Winnett, T.L., and Clark, M.A., 1985, Hydrologic and geochemical monitoring in Long Valley caldera, Mono County, California 1982-1984: U.S. Geological Survey Water Resources Investigations Report 85-4183, 137 p.

Friedman, J.D. and Frank, D., 1978, Thermal surveillance of active volcanoes using Landsat-1 Data Collection System: Part 4, Lassen volcanic region: National Technical Information Services, NTIS N78 23499/LL, 46 p.

Giggenbach, W.F. and Stewart, M.K., 1982, Processes controlling the isotopic composition of steam and water discharge from steam vents and steam-heated pools in geothermal areas: Geothermics, v. 11, p. 71-80.

Ingebritsen, S.E. and Sorey, M.L., 1985, A quantitative analysis of the Lassen hydrothermal system, north-central California, Water Resources Research, v. 21, no. 6, p. 853-868.

Muffler, L.J.P., Nehring, N.L., Truesdell, A.H., Janik, C.J., Clynne, M.A., and Thompson, J.M., 1982, The Lassen geothermal system: Proceedings of the Pacific Geothermal Conference, Auckland, New Zealand, p. 349-356.

Norton, D.R., and Friedman, I., 1985, Chloride flux out of Yellowstone National Park: Journal of Volcanology and Geothermal Research, v. 26, p. 231-250.

Sorey, M.L., and Ingebritsen, S.E., 1984, Quantitative analysis of the hydrothermal system in Lassen Volcanic National Park and Lassen Known Geothermal Resource Area: U.S. Geological Survey Water

Resources Investigations Report 84-4278, 80 p.

Thompson, J.M., 1985, Chemistry of thermal and nonthermal springs in the vicinity of Lassen Volcanic National Park: Journal of Volcanology and Geothermal Energy, v. 25, p. 81-104.

Truesdell, A.H., Mazor, E., and Nehring, N.L., 1983, The origin of thermal fluids at Lassen Volcanic National Park: Evidence from noble and reactive gas abundances: Geothermal Resources Council Transactions, v. 7, p. 343-348.

Table 1. Average concentrations of selected ions in thermal waters from the Lassen area, based on analytical results from the U.S. Geological Survey Central Laboratory, Arvada, Colorado on samples collected 1983 - 1985 (except for data for the Terminal Geyser well which are from Thompson, 1985).

Location	T °C	Cl mg/L	B mg/L	As mg/L
Growler Hot Springs	94	2500	87	11
Morgan Hot Springs	94	2300	80	10
Terminal Geyser Well	175	2180	62	10
Domingo Springs	9	15	0.5	0.03

Table 2. Data on streamflow and chloride concentration in Mill Creek at Highway 36 and corresponding calculated values of chloride flux and thermal-water component.

Date	Streamflow (L/s)	Cl (mg/L)	Cl flux (g/s)	Thermal component (L/s)
8/83	4840	7.5	36	15.8
10/83	1146	34	39	17.0
6/84	4871	8.5	41	18.0
8/84	1170	31	36	15.8
11/84	1034	40	41	18.0
7/85	793	46	36	15.9
10/85	1025	45	46	20.1

Average springflow = 17.2 $\pm$ 1.2 l/s

Table 3. Average values of thermal-water discharge at thermal areas in the Lassen KGRA, based on chloride flux measurements between 1983 and 1985. Standard deviations for each set of values shown with ±.

Spring area	Thermal water discharge (L/s)
Growler Hot Springs	2.19 ± 0.35
Morgan Hot Springs	18.7 ± 1.67
Domingo Springs	0.93 ± 0.18
Total	21.8 ± 1.72

Table 4. Calculated losses of hot-spring derived boron and arsenic in Mill Creek above Highway 36, based on hot spring discharge computed from measured chloride fluxes (see table 2).

Date	Streamflow (l/s)	Arsenic			Boron flux		
		Calculated (g/s)	Measured (g/s)	Lost (o/o)	Calculated (g/s)	Measured (g/s)	Lost (o/o)
6/84	4871	0.18	0.12	32	1.44	1.46	-1
8/84	1170	0.16	0.10	39	1.27	1.17	8
11/84	1034	0.18	0.12	31	1.44	1.34	7
7/85	793	0.16	0.14	10	1.27	1.31	-3
10/85	1025	0.20	0.16	18	1.61	1.54	4

Table 5. Sulfate flux measurements at Sulphur Works and Bumpass Hell.

Date	Sulphur Works			Bumpass Hell		
	Streamflow (L/s)	SO_4 (mg/L)	SO_4 flux (g/s)	Streamflow (L/s)	SO_4 (mg/L)	SO_4 flux (g/s)
8/83*	280	13	3.6	57	68	3.9
8/84	54	118	6.4	5.4	440	2.4
11/84	52	148	7.7	6.2	850	5.3
5/85*	72	60	4.3	36	180	6.5
7/85	52	117	6.1	4.0	740	3.0
10/85	39	203	7.9	2.8	990	2.8

*Measurements made only at "central" culvert - SO_4 flux applies only to "central" culvert; measurements on all other dates made at "central" culvert and "east" culvert - SO_4 flux applies to the total for both culverts.

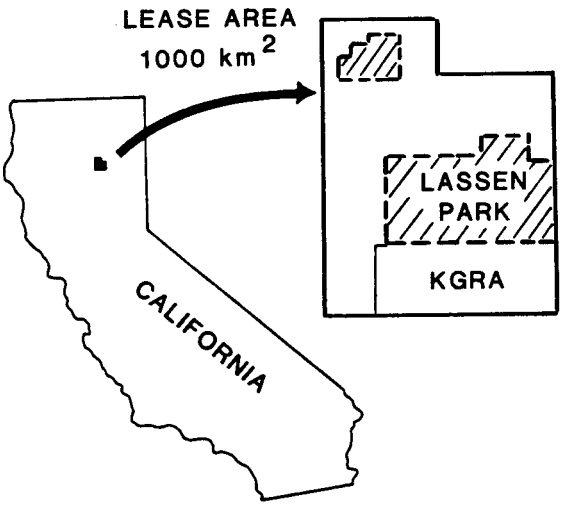

Figure 1. Map showing location of the Lassen study area in north-central California, which includes Lassen (Volcanic National) Park, Lassen KGRA, and Thousand Lakes Wilderness Area (cross-hatched pattern in upper left). All or part of the study area excluding the cross-hatched areas may be leased for geothermal development by the Bureau of Land Management during 1986.

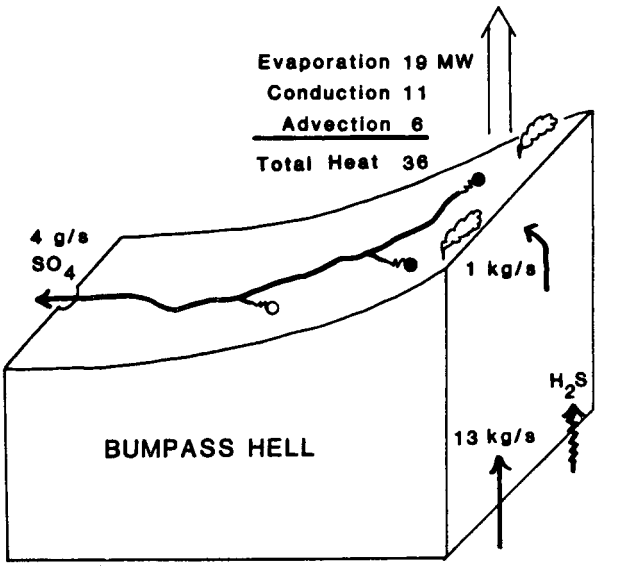

Figure 3. Diagram of Bumpass Hell thermal area depicting the average value of sulfate flux in Bumpass Creek (4 g/s) and the corresponding rate of steam condensation (1 kg/s) assuming a steam to H_2S molar ratio of 1290. Also shown are heat flow estimates based on the work of Friedman and Frank (1978) and the results of this study and the corresponding rate of steam upflow required to supply a total heat flow of 36 MW (13 kg/s).

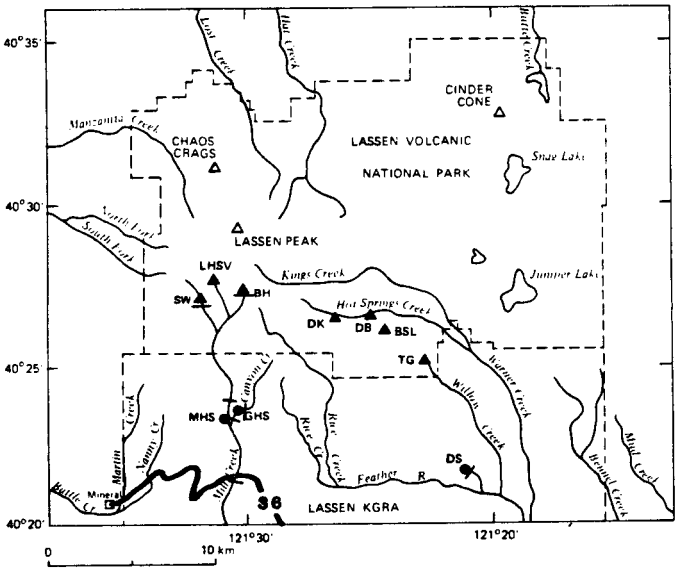

Figure 2. Map showing areas of thermal-fluid discharge and surface drainage in the Lassen region. Areas with fumaroles and steam-heated hot springs are shown as triangles (BH = Bumpass Hell, LHSV = Little Hot Springs Valley, SW = Sulphur Works, DK = Devils Kitchen, DB = Drakesbad, BSL = Boiling Springs Lake, TG = Terminal Geyser). Areas with high-chloride thermal water discharge are shown as dots (GHS = Growler Hot Springs, MHS = Morgan Hot Springs, DS = Domingo Springs). Short lines crossing streams at right angles signify sites where chemical flux measurements have been made for estimation of thermal-fluid discharge.

PROCEEDINGS, Eleventh Workshop on Geothermal Reservoir Engineering
Stanford University, Stanford, California, January 21-23, 1986
SGP-TR-93

Inert and Reacting Tracers for Reservoir Sizing in Fractured, Hot Dry Rock Systems

J. W. Tester, B. A. Robinson, and J. H. Ferguson
Chemical Engineering Department
Massachusetts Institute of Technology
Cambridge, MA 02139

Abstract

Flow characterization and volumetric sizing techniques using tracers in fractured hot dry rock reservoirs are discussed. Statistical methods for analyzing the residence time distribution (RTD) are presented. Tracer modal volumes and RTD shape are correlated with reservoir performance parameters such as active heat transfer area and dispersion levels. Chemically reactive tracers are proposed for mapping advance rates of cooled regions in HDR reservoirs, providing early warning of thermal drawdown. Important reaction rate parameters are identified for screening potential tracers. Current laboratory research and field work is reviewed.

Nomenclature

A= effective heat transfer area
A_r = pre-exponential factor
C, C(t)= tracer concentration
C_p = fluid heat capacity
D^p= dispersion coefficient
E_a = activation energy
E(V) or E(t) = exit RTD for a pulse
k = reaction rate constant
L = characteristic reservoir length
m_p = mass of tracer pulse
Pe = dispersional Peclet number = uL/D
Q = volumetric flowrate
R = Universal gas constant
t = time
T = fluid temperature
u = fluid velocity
$\mathring{V}$, <V> = modal, mean reservoir volume
x,y,z = reservoir postion coordinates
w1/2 = width of the RTD at 1/2 height
ρ = fluid density
α = thermal diffusivity of rock
λ_2= thermal conductivity of rock
σ^2= statistical variance of the RTD

Introduction and Motivation

This paper reviews the research and development work on tracers that has occurred in the last 11 years at Los Alamos and MIT. Details are contained in the following publications by the author and his co-workers (Tester, Bivins and Potter (1982), Robinson and Tester (1984), Robinson (1985), Robinson, Tester, and Brown (1984), Robinson and Tester (1986 a,b,c), and Grigsby and Tester (1986)).

The primary motivation for our work with tracers has been to provide an independent estimate of reservoir lifetime in multibore, hot dry rock (HDR) geothermal systems. Because these reservoirs have been activated by the hydraulic fracturing of inherently low permeability crystalline rock, their geometry and flow characteristics deviate markedly from the more traditional assumptions applied to dispersion in homogeneous porous media. In every case we have examined in the field, the observed flow patterns are complex resulting primarily from superimposed effects of multi-dimensional flow in a discrete set of interconnected fractures. The major challenge facing us at this point is to develop suitable models of these reservoirs in order to permit estimation of performance before thermal drawdown is observed under a prescribed set of injection conditions of flow rate, temperature, and pressure. We recognized at the outset that some non-uniqueness would result in these models, reflecting a common difficulty encountered in deconvolution problems of this type where the geometry and flow patterns within the reservoir are incompletely specified.

Fortunately, tracers have become a reliable diagnostic tool as they provide a direct measure of reservoir flow characteristics that are important in determining how efficiently energy is being extracted from the fractured rock. Inert tracers have been used in field tests of HDR reservoirs at the Fenton Hill site in New Mexico (Murphy et al (1981)) and at the Rosemanowes quarry in Cornwall, U.K. (Batchelor (1986)). Model-independent information, such as fracture volumes and dispersive characteristics, obtained from inert tracer measurements has provided a means of quantifying the behavior of these fractured geothermal systems. Because, however, the information supplied by conventional inert tracers is insufficient to construct detailed reservoir models with extensive predictive capabilities, we are also developing new techniques that use temperature-sensitive, chemically reacting compounds as tracers. These reactive tracers will measure directly the

cooldown rate of the primary flow paths in the geothermal reservoir. Reactive tracers should also be useful in diagnosing some conventional geothermal reservoirs where reinjection may accelerate thermal drawdown.

To date theoretical modeling and bench-scale screening tests have been conducted to identify potential reactive tracers for field use and to explore the strengths and limitations of the reactive tracer concept for sizing HDR systems.

Statistical Definitions

1. Residence Time Distribution, E(t): E(t)dt is the fraction of the injected fluid which leaves the system between t and t + dt. An effective tracer follows the same flow paths as the reservoir fluid, and the concentration-time response measured at the outlet to a pulse injected at the inlet is:

$$C(t) = m_p E(t)/Q \quad (1)$$

where m_p is the mass of tracer injected, and Q is the volumetric flow rate of fluid. The residence time distribution (RTD) curve can be also expressed as E(V), where E(V)dV is the fraction of the produced fluid which entered at t = 0 that emerges between V and V + dV where V is the cumulative produced fluid volume corrected for the finite volume of the wellbores. Thus, E(V) = E(t)/Q. With this convention fracture volumes measured in tracer experiments at different flow rates can be compared.

2. Modal Volume, $\mathring{V}$: the volume corresponding to the peak of the RTD curve. $\mathring{V}$ most likely represents the volume of low impedance fracture connections which follow a direct route from inlet to outlet.

3. Integral Mean Volume <V>:

$$\langle V \rangle = \int_0^\infty VE(V)dV \quad (2)$$

In fractured media, <V> is the void volume of all fractures which accept flow, regardless of their impedance.

4. Variance, σ^2: the variance is a measure of the overall spread of the distribution. It can be defined on a volume basis as:

$$\sigma^2 = \int_0^\infty (V - \langle V \rangle)^2 E(V)dV \quad (3)$$

The V and $(V - \langle V \rangle)^2$ terms in the integrals of Eqns. (2) and (3) cause the tail of the distribution at large volumes to have a significant effect on the magnitude of both <V> and σ^2. Because tracer concentrations are very low in the tail region, inherent inaccuracies arise, frequently causing substantial uncertainty in estimating <V> and σ^2.

5. Width at Half Height, w1/2: the width between the two points on either side of the peak for which the tracer response is one-half its peak value. This parameter, defined analogously in chromatographic separation theory, is a measure of the outlet dispersion of the main fracture flow paths. Unlike the variance of the distribution σ^2, the magnitude of w1/2 does not depend on the tail of the RTD.

Dispersion Mechanisms

The spreading of the outlet tracer concentration in a fractured geothermal reservoir potentially results from three major mechanisms: (1) large-scale flow heterogeneities caused by the superposition of flows from fractures of different size and flow impedance, (2) crossflow between different fractures, and (3) dispersion within a single fracture.

The extent of dispersion in single-fracture flow can be affected by roughness along the fracture surface, tracer holdup caused by fluid permeation and molecular diffusion of tracer into the rock matrix surrounding the fracture, molecular diffusion within the fracture across a velocity gradient perpendicular to the mean direction of flow (Taylor dispersion), and two-dimensional invicid potential and/or buoyantly-driven convective flow between the inlet and outlet zones of the fracture. Horne and Rodriguez (1983) and Robinson and Tester (1984) have evaluated the magnitude of various single-fracture dispersion mechanisms for conditions likely in fractured geothermal reservoirs. Table 1 summarizes the results of these studies, using the axial dispersion Peclet number (Pe = uL/D) as the parameter characterizing the level of dispersion. A large Peclet number indicates that the mechanism produces very little of the observed outlet dispersion. The table shows that the amount of dispersion produced within a single fracture is smaller than the overall level of tracer dispersion measured in the field.

This strongly suggests that superimposed flow from and crossflow between multiple fractures of different size and flow capacity are major contributors to the level of dispersion observed in HDR reservoirs.

Dispersion Models for Reservoirs

Given the complex nature of flow in a set of multiple fractures of largely unspecified geometry, many models have been used to describe tracer dispersion. These can be divided into two major categories: Deterministic and stochastic models. On the deterministic side, a steady state flow field is usually specified with appropriate geometric parameters, such as inlet to outlet well spacing, aperture size, fracture lateral or radial extent, and fracture volumes.

Table 1. Magnitudes of Different Single-Fracture Dispersion Mechanisms in Fractured HDR Reservoirs.

Sources: Horne and Rodriguez (1983), Robinson and Tester (1984).

Mechanism	Dispersional Peclet Number Pe	Comments
Fracture Roughness	$>10^3$	scale of dispersion (fracture aperture) is very small compared to overall length scale (well-bore separation distance)
Matrix Diffusion	$>10^3$	large apertures and rapid flow velocities minimize matrix diffusion effect
Taylor Dispersion	$(0.15 - 30) \times 10^3$	molecular diffusion coefficient varies strongly with temperature, causing wide range in Pe
Point Source-Point Sink Potential and Buoyantly-Driven Flow	55-70	calculated assuming dispersion is caused solely by flow streamlines of different length and velocity
Actual Measured Dispersion in Fractured Geothermal Reservoirs	0.5-5	observed dispersion is much greater than can be explained by flow in a single fracture

The most simplistic of these deterministic approaches couples the two extremes of infinite dispersion in a so-called continuous stirred tank reactor (CSTR) to a zero-dispersion in a plug flow reactor (PFR) to provide a best fit to the data. Although reasonable fits to data may result by treating the number of PFR's and CSTR's and their relative arrangement as adjustable parameters, the final model may bear little resemblance to the real reservoir, thus making prediction of performance impractical.

The remaining deterministic models would either deal with the flow pattern and resulting dispersion as a result of (1) a distribution of apertures and therefore flow velocities in a network of fractures that obeys Darcy's law or (2) multidimensional flow with or without molecular diffusion effects in a single fracture or in a discrete fracture set that follows the convective-dispersion equation.

Tester et al (1982) and Batchelor et al (1985) have used aperture distribution models to account for observed RTD's in HDR systems. Under Darcy flow conditions the flow rate varies with the cube of the aperture and can cause a wide RTD even with a modest distribution of apertures in a parallel set of fractures of equal length. Batchelor et al (1985) have used an orthogonal block model of the fracture system (FRIP) to provide a consistent RTD. A distribution of fluid residence times results from the 3-D nature of flow through the jointed rock network between the injection and production zones of the reservoir. The variations in the stress field surrounding the pressurized injection region are used to determine individual joint apertures which specifies the flow impedances and fluid velocities within each joint. In many cases, it is difficult for these aperture models to simultaneously match both the RTD shape (w1/2 and σ^2) and the fracture volumes ($\langle V \rangle$) observed.

Use of the convective-dispersion equation has been widespread in chemical and petroleum engineering as a basis of flow modeling (Robinson (1985), Horne and Rodriquez (1983), and Tester et al (1982)). The general form of the equation is

$$\nabla \cdot (\underset{\approx}{D} \nabla C) - \underset{\sim}{u} \cdot \nabla C = \frac{\partial C}{\partial t} \qquad (4)$$

where $\underset{\approx}{D}$ is the dispersion coefficient tensor, and $\underset{\sim}{u}$ the flow velocity vector. Although Eq (4) can be regarded as a rigorous statement of mass conservation it cannot be applied in practice unless the $\underset{\approx}{D}$ tensor terms are known. In most practical applications, a 1-D or 2-D steady flow field is assumed and $\underset{\approx}{D}$ is reduced to one or two terms that may be constant or dependent on the local velocity in a straightforward manner. Thus with this heuristic simplification, $\underset{\approx}{D}$ becomes an effective dispersion coefficient that is empirically fit to the data. It includes the combined effects of molecular diffusion and local mixing and turbulance on a macroscopic as well as microscopic or pore size level.

Given knowledge of individual fracture zone flow fractions and volumes, the convective-dispersion approach can be formulated to deal with superimposed flows (Tester et al (1982)). However, any application of this model for predictive purposes requires that the assumed reservoir geometry and flow patterns are being respresented realistically. For example, treating the effective dispersion coefficient as an adjustable parameter to match the RTD does not guarantee that it will result in reservoir sizes (apertures and lengths) that will predict the proper thermal drawdown history of the system. A certain amount of non-uniqueness is inevitable in modeling such complex reservoirs.

Purely stochastic models would seem justified because of the geometric uncertainties in these fractured reservoirs. Deterministic simulations of hydrodynamics, although appealing because of their "mathematical exactness," can in practice become no more than exercises in curve-fitting when only limited information is known about the reservoir. In a typical stochastic analysis, flow patterns are simulated for different randomly-constructed fracture networks. Monte Carlo methods may be used to generate such structures where such parameters as fracture length, orientation, and aperture will be specified within known or assumed distribution functions (Long, et al (1982)).

We are currently working on hybrid models that incorporate a deterministic approach for the main fracture zones with a stochastic approach for the secondary flow paths. We believe this will provide a realistic model for heat extraction performance prediction while requiring only a small number of adjustable parameters.

Field Results with Inert Tracers

The observed levels of dispersion in the Fenton Hill and Rosemanowes systems studied to date are dominated by multi-fracture flow. This conclusion was corroborated in some radioactive ^{82}Br tracer experiments at Fenton Hill using gamma logging in the production wellbore. As shown in Figure 1, distinct concentration-time curves were identified for three exit regions in the production wellbore (Tester, et al (1982)). Thus at least three different fractures were contributing to the observed total dispersion. Not only were the three fracture zones identified, but the dispersion from each individual fracture zone was too great to result from any combination of single-fracture dispersion mechanisms (Robinson and Tester (1984)). Crossflow among the different fractures was occurring, perhaps in a highly-fractured region near the inlet to the reservoir as depicted in Figure 2.

Recent tracer test results for the Phase II reservoirs at Fenton Hill and Rosemanowes are shown in Figure 3 where the characteristic shape of the RTD is similar for both reservoirs (see also Robinson (1986) and Batchelor (1986) for additional data and analysis). Superimposed, multi-fracture flow is probably the dominant mechanism contributing to the overall RTD but it cannot be proven from the tracer tests alone. A direct comparison to the observed thermal performance of these prototype HDR reservoirs is necessary as discussed in the next section.

Tracer-Determined Flow and Thermal Performance

In analyzing past tracer experiments in the Fenton Hill and Rosemanowes systems, we have found an empirical approach to be very useful in comparing the nature of flow and heat transfer in these reservoirs.

Large scale heterogeneities such as the superposition of flows from multiple fractures undoubtedly exert great influence on heat transfer behavior, since the positioning of low impedance conduits effectively defines the accessible volume of rock. In many systems, the onset and subsequent rate of thermal drawdown is probably controlled by the surface area of the smallest low impedance connection. Because the modal volume $\mathring{V}$ corresponds to the low impedance fracture connections, it should correlate with the reservoir's heat transfer capacity which can in turn be estimated from a simplified model: Assuming plug flow up a single vertical, rectangular fracture of surface area A (on one face of the fracture), the fluid temperature within the fracture during long-term operation is given by (Murphy et al (1981)):

$$\frac{T-T_i}{T_r-T_i} = \mathrm{erf}\left[\frac{\lambda A(z/L)}{\rho C_p Q \sqrt{\alpha t}}\right] \qquad (5)$$

in which T, T_i, and T_r are the temperatures of the fluid at point z, at the inlet, and throughout the rock initially, respectively. The parameters λ and α are the thermal conductivity and thermal diffusivity of the rock, ρ and C_p the average density and heat capacity of the fluid, and t is the time of operation of the reservoir. The outlet fluid temperature is obtained by setting $z/L = 1$. Although simplistic, this model conveniently describes the thermal behavior of a fractured reservoir with a single adjustable parameter, A. Assuming Figure 4 is correct, a single inert tracer experiment can provide a modal volume and thus a crude estimate of the heat extraction capability of a fractured reservoir.

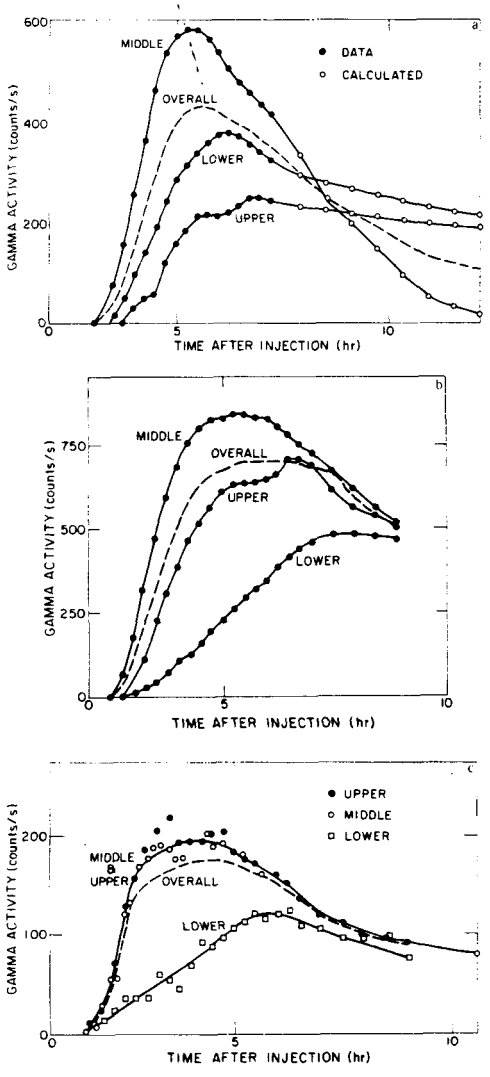

Figure 1 Individual fracture zone concentration-time curves obtained by ^{82}Br pulse injection followed by gamma logging in the production well bore. (a)Exp. 217-A2, 5/9/80. (b)Exp. 217-A4, 12/2/80. (c) Exp. 217-A5, 12/12/80.

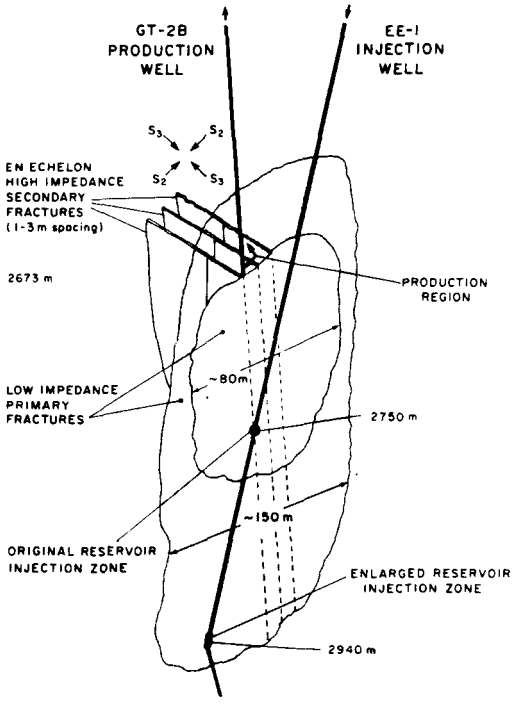

Figure 2 Conceptual schematic of the EE-1/GT-2 fracture system (adapted from Tester et al (1982). Schematic of the fracture-well bore geometry.

The Rosemanowes Phase II points in Figure 4 are extrapolated, as extensive energy extraction has not yet been carried out in this reservoir, so measurable drawdown has not been observed. Only the modal volume has been plotted. For this new larger reservoir and for commercially-sized systems in general, use of the modal volume to estimate A is as yet unjustified because of the large extrapolation required from smaller sized systems. A more legitimate approach for large systems with multiple entrance and exit regions perhaps would be to size individual fracture zones using preferential injection of a radioactive tracer and production well gamma logging (Tester, et al (1982)). These zones or subsystems are likely to be small enough to warrant the use of Figure 4 without extrapolation.

Another factor regarding Figure 3 is the fact that the slope of the line through the data is about 0.7 and statistically different than unity. Thus the effective aperture of fracture comprising the modal volume must change disproportionally with changes in effective heat transfer surface area. This simple analysis ignores the fluid that does not flow through the low impedance fractures. Based on modeling of quartz dissolution kinetics in the main fracture flow path, it was recognized that at least 30% of the production fluid during Run Segment 5 must have flowed through long residence time flow paths which had experienced no thermal drawdown (Grigsby and Tester (1986)). This observation is supported by tracer experiments (5/9/80 to 12/12/80) where roughly 70% of the tracer is recovered in the main peak of the RTD and the remainder is recovered in the tail of the distribution. This result appears to be quite common in the HDR reservoirs tested to date: flow through several low impedance joints accounts for the early tracer response, while a substantial secondary flow travels through a large volume of rock, probably at the periphery of the reservoir.

A comparison of the volumes of the low impedance primary flow paths and the high impedance secondary paths can be made. The modal volume represents the low impedance volume and the integral mean volume [Eqn. (2)] is the total fracture volume (main fractures plus secondary flow paths). As seen in Table 2, the computed integral mean volumes for the ^{82}Br tracer experiments of Run Segment 5 are much larger than the corresponding modal volumes. The enormous potential capacity of this reservoir appears to have gone largely unused due to the tendency of the fluid to short-circuit through low impedance joints. Total reservoir size estimates using microseismic mapping and geochemical information substantiate this conclusion.

In addition to the absolute sizes of the low-impedance fractures and the total reservoir, reservoir growth during energy extraction may be monitored using V and $\langle V \rangle$ from a series of tracer tests. Fracture volume growth may be caused either by thermal contraction and stress cracking of rock during cooldown, or through opening new fractures by water permeation into pre-exisitng joints in the rock matrix (hydraulic fracturing). For example, the increases in modal and integral mean volumes during the Run Segment 5 are plotted against total energy extracted in Figure 5. The maximum amount of new fracture volume possible via thermal contraction of rock is denoted by the free thermal expansion line. The large increase in integral mean volume suggests that additional fracturing must have been occurring along with thermal contraction. However, much of this new volume is apparently not available for heat extraction as shown by the modest increase in modal volume.

Reservoir Analysis Using Reacting Tracers

Thermal drawdown analysis of small, prototype reservoirs was possible because a measurable temperature decline in the produced fluid occurred after only a few months of operation. However, for larger systems, reservoir simulators will have to be used in a predictive way, since years could pass before produced fluid temperature measurements yield useful modeling information. More importantly, commercialization of HDR requires that a method exists for predicting a priori the lifetime of a reservoir. The normal battery of diagnostic experiments (pressure transient, well logging, inert tracer, microseismic, and fluid geochemical) will not provide all the information necessary to construct these detailed reservoir models with predictive capability. Chemically reactive tracers, which are sensitive to internal changes to the reservoir's temperature field, may help solve this problem in future HDR systems.

The kinetics of most chemical reactions are extremely temperature-sensitive. For first-order reactions carried out in batch reactors, the following equation is often used to express the instantaneous rate of conversion of reactant at concentration C to product:

$$dC/dt = -kC \qquad (6)$$

The rate constant k is the parameter which contains the temperature sensitivity. It normally can be described by an equation of Arrhenius form:

$$k = A_r \exp(-E_a/RT) \qquad (7)$$

For typical reactions in solution, k will vary by several orders of magnitude for the range of temperatures typically encountered in an operating HDR reservoir.

Suppose a tracer is injected into an initially hot reservoir, and the reaction proceeds about half way to completion during its stay in the system. Then, after some cooldown has been achieved, a second experiment should show less conversion because of the shorter time the fluid spends in hot zone of rock. A series of reactive tracer experiments will, in theory, map the rate of progress of the cooled region as it approaches the exit well, giving an early warning of thermal drawdown.

In practice, the transient response of a reacting tracer depends on both the temperature field and the dispersive nature of the fluid flow within the reservoir. To illustrate this coupled dependence conceptually, we assumed that the tracer behavior could be modeled using the one-dimensional form of the convective-dispersion equation with a first-order chemical reaction included:

$$D\left(\frac{\partial^2 C}{\partial z^2}\right) - u\left(\frac{\partial C}{\partial z}\right) - kC = \frac{\partial C}{\partial t} \qquad (8)$$

Equation (8) is directly coupled to the rate of heat extraction because k is a strong function of temperature (Eqn. (7)). Thus, in order to solve Eqn. (8) for C(t,z) we must know the axial (z-direction) temperature field. The single-fracture temperature solution [Eqn. (5)] was used in preliminary calculations. This simplified temperature field assumption is perhaps questionable given the evidence for superimposed multifracture flow. Each fracture is likely to have unique temperature characteristics, e.g. the small ones (corresponding to short residence times) cooling down more rapidly than the large ones. Nonetheless, the model as formulated should be sufficient for parameter sensitivity studies.

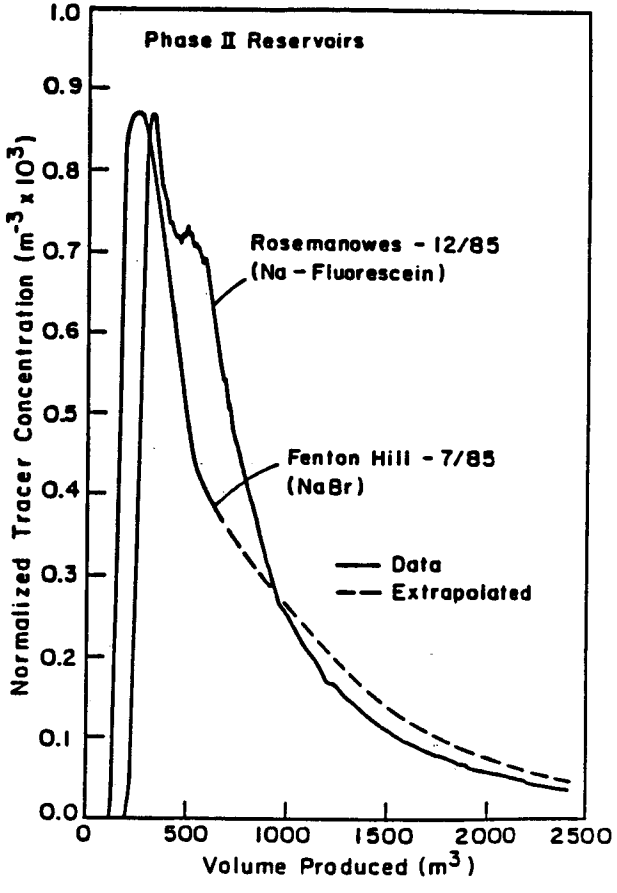

Figure 3 Comparison of RTD from pulse tracer injections in the Fenton Hill and Rosemanowes Phase II HDR reservoirs. Curves are normalized with respect to peak tracer concentrations at the modal volume.

*Rosemanowes data uncorrected for wellbore volumes

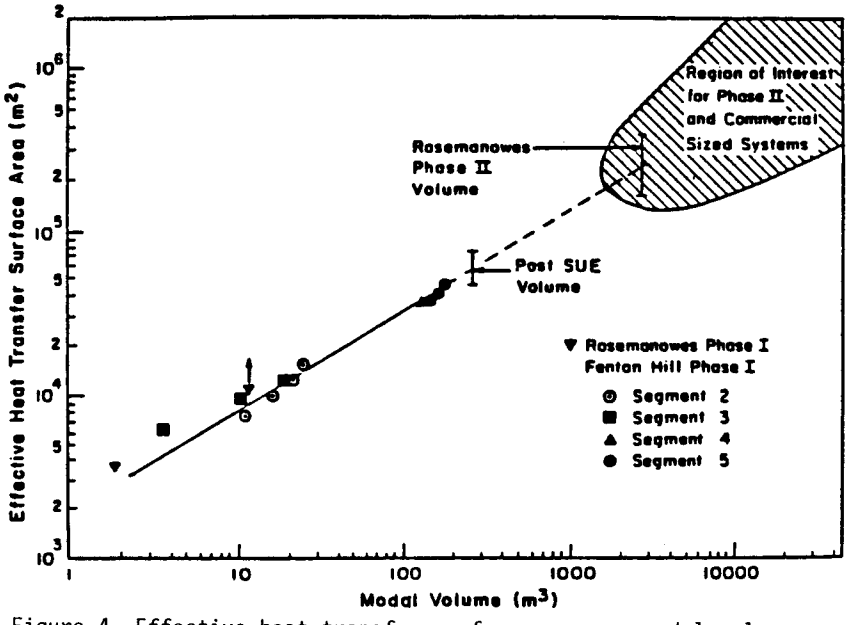

Figure 4 Effective heat transfer surface area vs. modal volume.

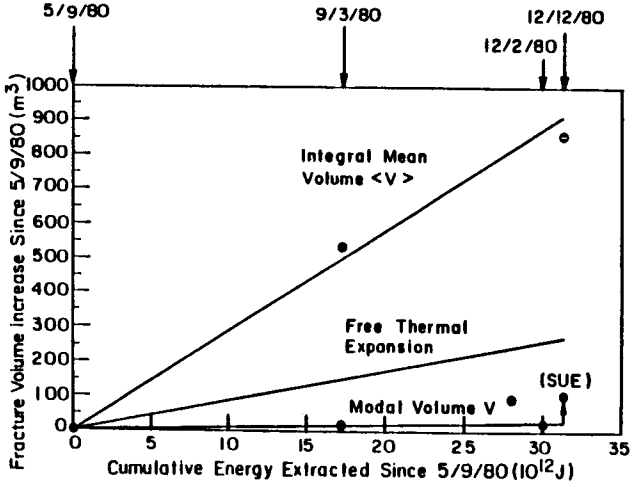

Figure 5 Fracture volume growth vs. cumulative energy extracted.

Table 2. Summary of Tracer Field Experiments

Fenton Hill Experiments

Date(tracer)	$\mathring{V}$ (m^3)	<V> (m^3)	w1/2 (m^3)	w1/2/$\mathring{V}$
Phase I (GT2B-EE-1)				
2/9/78(NaF)	11.4	-	18.1	1.59
3/1/78(NaF)	17.0	-	40.3	2.37
3/23/78(NaF)	22.7	-	62.5	2.75
4/7/78(NaF)	26.5	-	70.8	2.67
5/9/80(Br)	161	1311	227	1.41
9/3/80(Br)	178	1845	323	1.81
12/2/80(Br)	187	-	303	1.62
12/12/80(Br)	266	2173	479	1.80
Phase II (EE-2 - EE-3)				
7/85(NaF/NaBr)	300	-	279	0.93

Rosemanowes Tracer Experiments

Phase I				
RH6A(1982)(NaF)	1.42	-	1.68	1.18
RH12(1983)(NaF)	12.3	-	7.0	0.57
Phase II (RH11-RH12)				
#3(1984)(NaF)	2390	-	4870	2.04
Phase IIB (RH12-RH15)				
#4(9/85)(NaF)	136	964	545	4.01
#5(10/85)(NaF)	122	1058	509	4.17
#6(11/85)(NaF)	123	982	509	4.14
#7(12/85)(NaF)	119	913	473	3.98
(EA)	119	-	298	2.43
(EtOH)	119	-	474	3.98
(ISO-PA)	119	-	710	5.97

NaF - sodium fluorescein
Br - $^{82}Br^-$ isotope
EtOH - ethanol
NaBr - sodium bromide
EA - ethyl acetate
ISO-PA - isopentyl acetate

The internal temperature field for a particular model reservoir at various times is shown in Figure 6. To achieve 10°C of produced fluid thermal drawdown (a practical minimum for estimating reservoir size), over five years of continuous operation are required.

The reactive tracer response to a step change in inlet concentration for the same model system is shown in Figure 7. Just 1 to 2 years of operation are required to obtain a sensitive estimate of heat exchange capacity.

Parameter studies using the 1-D convective-dispersion model also support the following trends:

1) For thermal behavior such as that in Figure 6, reactions with higher activation energies are more sensitive to small levels of thermal drawdown.

2) Tracer dispersion affects the shape of the response curves, but not the sensitivity of the measurement. However, if dynamic shifts in reservoir size occur during production, inert tracers should also be used in conjunction with reactive tracers.

3) The reactive tracer response is sensitive to the extent of thermal drawdown, but not to the specific shape of the temperature field. Reactions which are moderately fast at the highest reservoir temperature are extremely slow at temperatures 100°C below this. Thus, the exact shape of the temperature field in the cooled region of the reservoir is unimportant. The conversion of a reacting tracer is essentially a measure of the amount of hot rock remaining between the two wellbores.

Reactive Tracer Screening Studies

A significant portion of our research efforts have been and are currently directed toward identifying appropriate reactive tracers for use in HDR systems having a range of mean residence times and rock temperatures. The desired kinetic parameters (A_r and E_a) should be such that the reaction time ($1/k$ for a 1st order reaction) at the average reservoir temperature is approximately of the same order as the mean residence time. In addition, each reactive tracer must have the same characteristics required of an inert tracer in that it must be non-adsorbing and easily detectable in low concentrations.

In our early work, the kinetics of alkaline hydrolysis of a number of organic esters and amides were determined in aqueous solutions for temperatures varying from 100 to 300 °C (Robinson (1984) and Robinson, Tester, and Brown (1984)). For this system a pseudo-first order reaction was created by conducting the hydrolysis in excess OH^- or in a buffered solution. The results of these early studies are summarized in Fig. 8. Ethyl acetate, ethyl propionate and isopentyl acetate would be suitable for HDR systems at 70 to 125°C having reaction times ranging from 10 to 200 hr.

The first test of reactive tracers in the field was conducted in December of 1985 in the redrilled Phase II reservoir at Rosemanowes in the U.K. operated under continuous circulation conditions (Batchelor (1986)). Na-fluorescein as an inert tracer was injected simultaneously with concentrated solutions of ethyl acetate and isopentyl acetate. Figure 9 shows the preliminary response curves for all three tracers. The shape of all three curves is very similar indicating that ethyl acetate (EA) and isopentyl acetate are not selectively adsorbed on the formation. The RTD for ethanol (EtOH) which is a reaction product of the hydrolysis of ethyl acetate was determined as well. By proper weighting of the EA and EtOH RTD's with their molecular weights (MW), we can sum the curves to estimate the RTD of EA had it not reacted:

$$\frac{[EA]}{MW_{EA}} + \frac{[EtOH]}{MW_{EtOH}} = \frac{[EA_{non\text{-}reactive}]}{MW_{EA}} \quad (9)$$

where the [] brackets refer to concentrations.

Using Eqn. (9) to calculate the peak non-reactive EA concentration, a value of 20 ppm results. This is consistent with the estimated peak concentration of 20.2 ppm for non-reactive EA for a 27 kg injection scaled to the observed 1.8 ppm peak for Na-Fluorescein which resulted from a 2 kg injection of dye. At constant pH, EA hydrolysis will follow a pseudo-first order mechanism with $k = (A_r \exp(-Ea/RT))[OH^-]$. If we assume that the average pH seen by the tracer was 8.5 with $A_r = 3.05 \times 10^6$ liter/mols and $E_a = 40.9$ kJ/mol, an average reservoir temperature of 94°C is estimated from the ratio of the measured peak for EA of 10 ppm at 13.4 hr after injection to the calculated non-reactive EA peak of 20.2 ppm. This estimated temperature is within 5°C of actual measured rock temperature and is a strong indicator that the EA tracer is working as expected. Ethyl pivalate and acetamide would work well for reservoirs between 150 to 200°C over the same residence time range. We are presently involved with identifying reactive tracers for use in hotter reservoirs at 200 to 300°C. A number of thermal decompositions involving fluorinated, low molecular weight hydrocarbons, peroxides, and organic dyes and the hydrolysis of bromobenzene and its substituted derivatives are currently under laboratory study with field tests planned for the near future.

Conclusions

1. Levels of tracer dispersion from field experiments in HDR reservoirs indicate a dominant mechanism caused by the superposition of flow from multiple fractures of different size and impedance. At Fenton Hill, about 70% of flow is through a number of low impedance fractures with the remaining 30% contained in high impedance secondary flow paths of large volume and long residence time.

2. Reservoir heat transfer capacity measured by effective heat transfer surface area A correlates with tracer modal volume $\hat{V}$.

3. Preliminary modeling and field test results suggest that the injection of chemically reactive tracers should be a sensitive reservoir test for measuring thermal drawdown far in advance of actual produced fluid temperature decline.

4. Laboratory kinetic studies have identified several chemically reactive tracers for use in geothermal reservoirs having temperatures ranging from 80 to 200°C.

Acknowledgements

We would like to thank the HDR project staffs at Los Alamos National Laboratory and the Camborne School of Mines for their support in the field. Special thanks go to C. Grigsby, H. Murphy, R. Potter, and R. Bivins from Los Alamos and A.S. Batchelor, K.A. Kwakwa, and R. McCartney from Camborne. The financial support provided collectively by the U.S. and U.K. Departments of Energy is gratefully acknowledged.

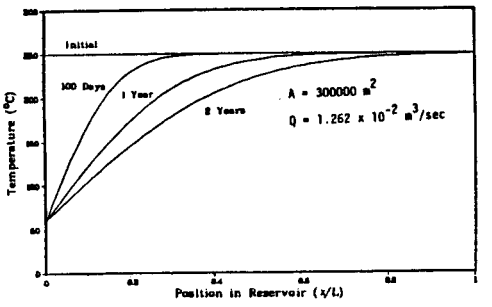

Figure 6 Internal temperature profiles during long-term energy extraction in a single fracture.

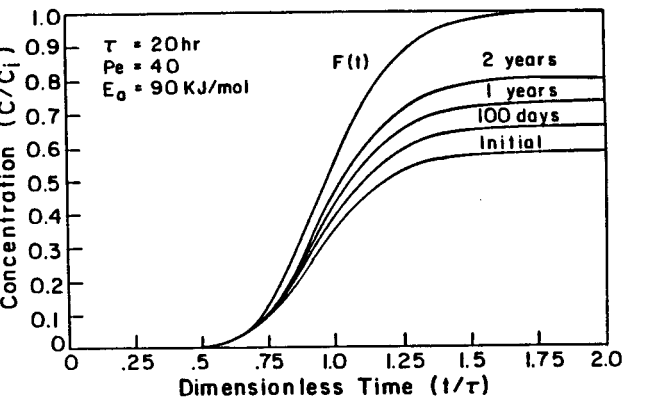

Figure 7 Reactive tracer behavior during long-term energy extraction in the single fracture as described in Fig. 6.

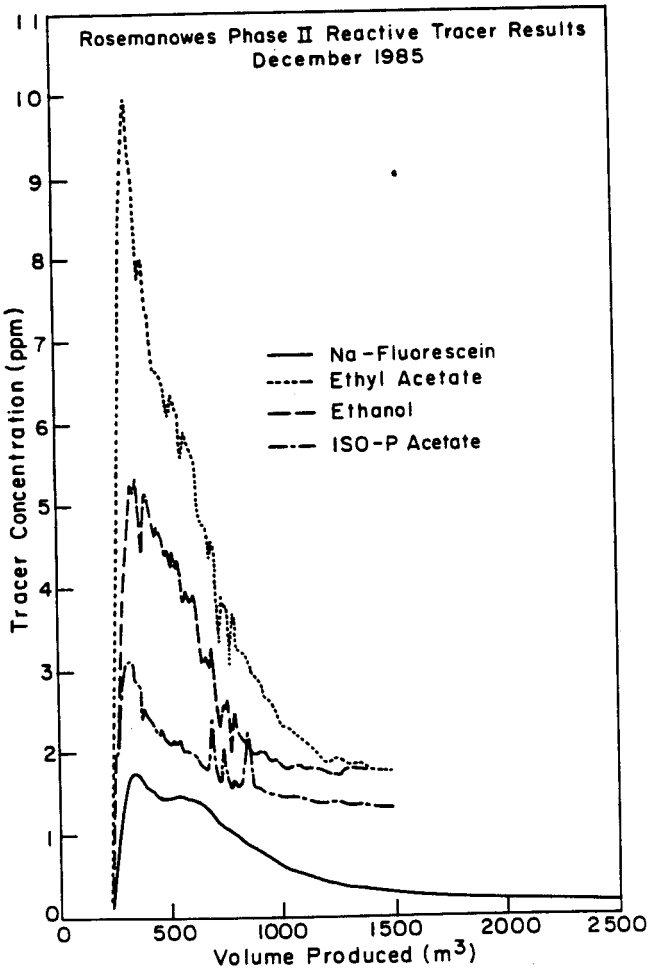

Figure 9 Results of the first reactive tracer field test in the Phase II Rosemanowes Reservoir (December 1985).

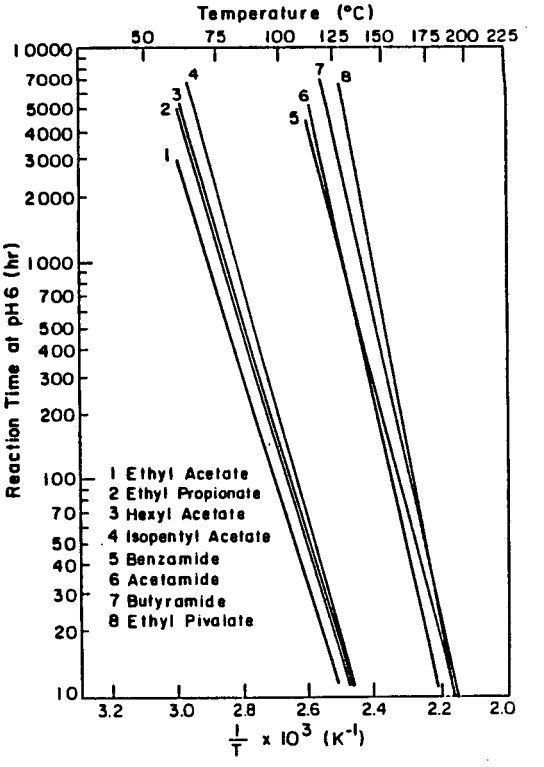

Figure 8 Summary of kinetic results for the ester and amide hydrolysis reactions: characteristic reaction time as a function of reciprocal temperature.

References

Batchelor, A.S. (1985), Personal Communication, Camborne School of Mines, Cornwall, U.K. (1985).

Batchelor, A.S. (1986), "Reservoir Behavior in a Stimulated HDR System," 11th Annual Workshop on Geothermal Reservoir Engineering, Stanford University, Stanford, CA (Jan. 21-23, 1986).

Dash, Z. V., H.D. Murphy, et al (1981), "Hot Dry Rock Geothermal Reservoir Testing: 1978-1980," J. Volcanology and Geothermal Research 15, 59-99 (1981).

Grigsby, C.O. and J.W. Tester (1986), "Rock-water Interactions in Hot Dry Rock Geothermal Systems: III. Geochemical Modeling of a recirculating reservoir (in preparation).

Horne, R.N., and F. Rodriguez (1983), "Dispersion in Tracer Flow in Fractured Geothermal Systems," Geophys. Res. Letters, 10, 289, (1983).

Long, J.C.S., J.S. Remer, C.R. Wilson, and P.A. Witherspoon (1982), "Porous Media Equivalents for Networks of Discontinuous Fractures," Water Resources Res., 18 (3), 645-658 (1982).

Murphy, H. D., J.W. Tester, C.O. Grigsby, and R.M. Potter (1981), "Energy Extraction from Fractured Geothermal Reservoirs in Low-Permeability Crystalline Granite," J. Geophys. Res. 86 (B8) 7145 (1981).

Robinson, B.A., and J.W. Tester (1984), "Dispersed Fluid Flow in Fractured Reservoirs: An Analysis of Tracer-Determined Residence Time Distributions," J. Geophys. Res. 89(B12), 10374 (1984).

Robinson, B. A., J.W. Tester, and L. Brown (1984), "Reservoir Sizing Using Inert and Chemically Reacting Tracers," SPE paper 13147, presented at the 59th Annual Technical Conference and Exhibition, Houston, TX (September 16-19, 1984).

Robinson, B.A. (1985), "Non-Reactive and Chemically-Reacting Tracers: Theory and Applications." Ph. D. Thesis, Massachusetts Institute of Technology, Cambridge, MA (February, 1985).

Robinson, B.A. and J.W. Tester (1986a), "The Temperature-Sensitive Chemically Reactive Tracer I. Theory," (submitted to AIChE J., February, 1986).

Robinson B.A. and J.W. Tester (1986b), "The Temperature-Sensitive Chemically Reactive Tracer II. Experimental Demonstration in a Laminar Flow Heat Exchanger," (submitted to AIChE J., February, 1986).

Robinson, B.A. and J.W. Tester (1986c), "Hydrolysis of Organic Esters and Amides in High Temperature, Buffered Aqueous Solutions from 100 to 300°C," (to be submitted to J. of Chemical Engineering Data, 1986).

Robinson, B.A. (1986), "A Field Study of Tracer and Geochemistry Behavior During Hydraulic Fracturing of a Hot Dry Rock Geothermal Reservoir," 11th Annual Workshop on Geothermal Reservoir Engineering, Stanford University, Stanford, CA (Jan. 21-23, 1986).

Tester, J. W., R.L. Bivins, and R.M. Potter (1982), "Interwell Tracer Analyses of a Hydraulically Fractured Granitic Geothermal Reservoirs," Soc. Pet. Eng. J., 22, 537 (1982).

Zyvoloski, G.A. (ed.) (1981), "Evaluation of the Second Hot Dry Rock Geothermal Energy Reservoir: Results of Phase I, Run Segment 5," Rept. LA-8940-HDR, Los Alamos National Laboratory, Los Alamos, NM (1981).

PROCEEDINGS, Eleventh Workshop on Geothermal Reservoir Engineering
Stanford University, Stanford, California, January 21-23, 1986
SGP-TR-93

Modeling Studies of Cold Water Injection into Fluid-Depleted, Vapor-Dominated Geothermal Reservoirs

C. Calore, K. Pruess**, and R. Celati**

*International Institute for Geothermal Research
Pisa, Italy

**Earth Sciences Division
University of California
Lawrence Berkeley Laboratory
Berkeley, California 94720

INTRODUCTION

Reinjection experiments in the strongly fluid-depleted reservoir of Larderello have revealed the possibility of increasing production rates and overall heat extraction by injection into high permeability, low pressure zones of the reservoir (Giovannoni et al., 1981; Cappetti et al., 1982; Bertrami et al., 1985). A large fraction (over 80%) of the injected water was recovered as steam in the most favorable area and, despite the short distance between injection and producing wells (the minimum distance being about 150 m), no significant temperature change has been observed in the latter, after 3 years of injection at a rate ranging from 10 to 50 kg/s (Bertrami et al., 1985).

The physical processes involved in cold water injection into a "superheated" fractured reservoir are not yet fully understood, and this insufficient knowledge of the fundamental mechanisms limits the possibility of forecasting future reservoir behavior and optimizing the heat extraction process. Numerical simulation can be a very effective tool in the study of the complex phenomena involved, allowing a rapid examination of different situations and conditions, a systematic investigation of the effects of various parameters on reservoir performance, and some insight into long term behavior. We have performed simulation experiments on simple one-dimensional, porous and fractured reservoir models in order to study the migration of injected water, thermodynamic conditions in the boiling zone, heat extraction, and vapor generation. A two-dimensional radial porous medium model, with some characteristics typical of the high productivity zones of Larderello, has also been applied for studying the evolution of the shape and the thermodynamic conditions of the injection plume in the presence of gravity, reservoir heterogeneities and anisotropy.

The MULKOM code was used for the simulations (Pruess, 1983).

One-dimensional, porous medium column

For our first simple case of injection of cold water into a "superheated" reservoir we consider a one-dimensional porous column initially at 240 °C and 6 bars. Water at 30 °C is injected at one end of the column and the other end is maintained at a constant pressure of 6 bars; gravity is ignored. The parameters of the system simulated are shown in Table I.

A sharp boiling front develops and advances through the column (Fig. 1). Temperature, saturation and fluid velocity change abruptly at this front. Liquid saturation passes from 1 behind the front to 0 in front of it, temperature jumps from the boiling temperature for the pressure existing at the front to the undisturbed reservoir temperature, and velocity is that of the injected liquid on one side and that of the vapor generated by its vaporization at the other.

Behind the front is a "hot liquid zone" where the liquid saturation is 1 and temperature is nearly constant. Still further behind, the temperature decreases to that of injected liquid. The hot liquid-cold liquid front is the classical "temperature front" of liquid saturated systems (Bodvarsson, 1972). In Fig. 1 this second front appears strongly smeared out by conduction and numerical dispersion.

Figure 2 shows typical variations with time of steam flow-rate, temperature of the liquid at the boiling front, and the volume of liquid water accumulated in the system. After an initial transient, production rate and boiling temperature tend to stabilize. The boiling temperature is always controlled by the pressure at the boiling front. As in our simulation the liquid-saturated interval remains small with respect to the total length

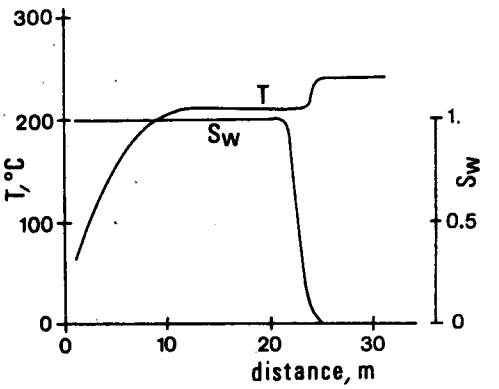

Fig. 1. One-dimensional, porous medium column. Temperature and saturation profiles for q_{inj} = 2.75e-3 kg/sm^2, k=5e-13 m^2.

Table I. Parameters used in one-dimensional models

Parameter	Problem		
	1-D linear porous	1-D linear fractured	1-D radial fractured
Length, m	300	300	
Cross sectional area, m^2	1	1	
Radius, m			300
Thickness, m			50
Initial temperature, °C	240	240	240
Initial pressure, bars	6	6	6
Const. pressure boundary, bars	6	6	6
Injection enthalpy, J/kg	125800	125800	125800
Injection rate, kg/s	6.3e-6 -2.34e-2	3.e-4	2.78
ROCKS			
Density, kg/m^3	2600	2600	2600
Porosity	8%	8%	8%
Heat conductivity, W/m °C	2.51	2.51	2.51
Specific heat, J/kg °C	920	920	920
Permeability, m^2	5e15 -1e-12	5e-18	5e-18
Relative permeability: (Corey curves)	S_{rw} =.30 S_{rv} = .05	S_{rw} =.30 S_{rv} = .05	S_{rw} =.30 S_{rv} = .05
FRACTURES			
Two vertical orthogonal sets spacing, m		25	25
Equivalent continuum porosity		1%	1%
Equivalent continuum permeability		5e-13	5e-13
Relative permeability:		liquid vapor	$k_{rw} = (S_w\text{-}0.01/0.99$ $k_{rv} = (0.99\text{-}S_w)/0.99$

of the column, boiling temperature and steam production remain almost constant during the simulation and the temperature in the hot liquid zone almost uniform. When injection starts and some of the injected water is vaporized, the pressure at the boiling front and the steam flow increase. As pressure (and temperature) at the boiling front increase, however, the heat released by the rock, and the boiling rate, decrease. Stabilization of temperature and steam flow-rate occur when the (increasing) steam flow equals the (decreasing) boiling rate.

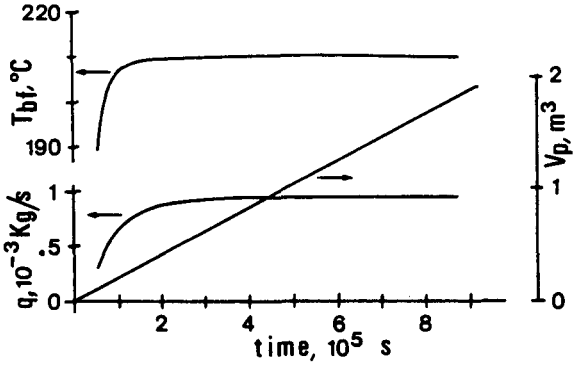

Fig. 2. One-dimensional, porous medium column. Production rate, boiling temperature and volume of liquid phase versus time for q_{inj} = 2.75e-3 kg/sm^2, k=5e-13 m^2.

The phenomena involved when stabilization of temperature and flow-rate are reached can be approximately described by a simple set of equations. Under the hypothesis that the heat released by the cooling rock equals the heat required for vaporization of liquid water, the heat balance for a column of unit cross section can be written as

$$v_{bf}(1-\phi)\rho_R C_R \Delta T = q_v h_{lv} \qquad (1)$$

The velocity of advancement of the boiling front is less than the velocity of liquid behind it, as a fraction of the liquid arriving at the front is vaporized. For a column of unit cross section we have

$$v_{bf} = \frac{q_{liq} - q_v}{\phi \rho_w} \qquad (2)$$

The steam flow in the dry steam zone is

$$q_v = k\frac{m_{bf} - m_c}{L} \qquad (3)$$

m being the pseudopressure at initial reservoir temperature. As q_{liq} is approximately equal to q_{inj}, and $p_{bf} = p_{sat}$ the system can be solved for q_v and ΔT. From this set of equations it follows that the boiling temperature depends on the group q_{inj} L/k, and the ratio q_v/q_{inj} depends on ΔT.

These relations are shown in Figures 3 and 4, where the results of several numerical simulations (with injection rates and permeabilities varying by several orders of magnitude) are compared with those of the above system of equations. Other parameters being equal, boiling temperature increases when q_{inj} increases, since a higher pressure at the boiling front is required to sustain a higher rate of steam flow. For the same reason, boiling temperature increases when permeability decreases, or the length of the steam flow path, L, increases.

The ratio of production to injection rate increases with the cooling undergone by the rock.

One-dimensional, fractured-porous medium models

The phenomena occurring when cold water is injected into a porous medium are largely controlled by the solid-fluid temperature equilibrium. In fractured media the heat transfer between the rock and the fluid flowing through the fractures occurs at a finite rate, which entails some differences in behavior compared to ideal porous media. The porous media thermal fronts are typically sharp whereas in fractured media they become very diffuse (Lauwerier, 1955).

Two simple reservoir models have been adopted to study the phenomenology of injection into fractured-porous media: a one-dimensional column and a one-dimensional radial system. In the first case cold water is injected at one end of the column and a constant pressure is maintained at the other end. In the second case water is injected at the center of the system and a constant pressure is maintained at the outer boundary.

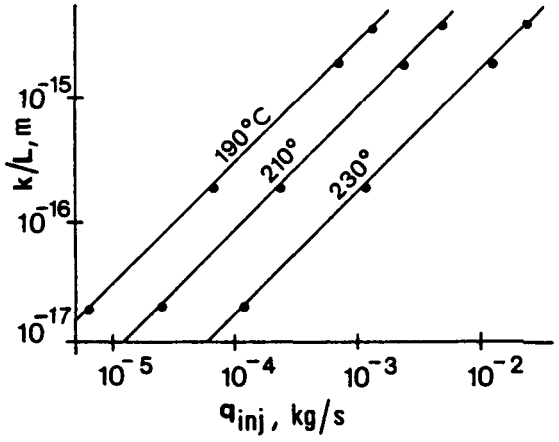

Fig. 3. One-dimensional, porous medium column. Dependence of stabilized boiling temperature on injection rate, permeability, and length of steam flow-path. Lines: from equations (1) to (3); solid circles: from numerical simulations.

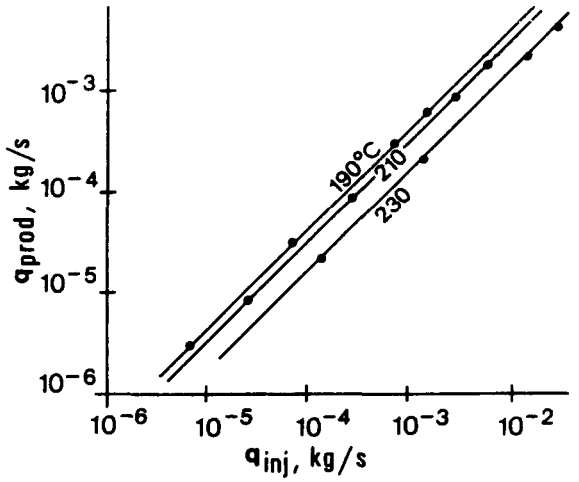

Fig. 4. One-dimensional, porous medium column. Dependence of q_{prod} on q_{inj} and boiling temperature. Lines: from equations (1) to (3); solid circles: from numerical simulations.

In both cases initial conditions are uniform temperature of 240 ° C and uniform pressure of 6 bars. The simulations have been performed using the method of "multiple interacting continua" (Pruess and Narasimhan, 1982, 1985). The parameters used for the simulations are shown in Table I.

Figure 5 shows a typical spatial distribution of temperature and saturation in the fractures for the one-dimensional column case. The liquid moves fast in the fractures and a wide two-phase zone is formed. Boiling takes place throughout the two-phase zone, at a rate which, at each point, depends essentially on the conductive heat flow from the matrix to the fractures. The hot liquid zone observed in the porous column is replaced, in this case, by an extended two-phase zone. The temperature is nearly uniform in the two-phase zone as it is controlled by the local pressure, which is nearly uniform due to the large fracture permeability. The temperature jumps abruptly to the initial reservoir temperature at the boundary between the two-phase and the dry zones. The temperature difference between the outermost elements of the matrix and the fractures is also shown in Fig. 5. This quantity is proportional

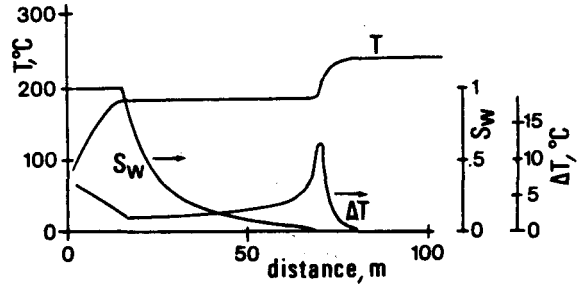

Fig. 5. One-dimensional, fractured medium column. Profiles of temperature and saturation in the fractures and temperature difference between outermost matrix elements and fractures for q_{inj} = 3e-4 kg/sm^2, k=5e-13 m^2

to the rate of matrix-fracture conductive heat flow, and reaches a maximum value at the leading edge of the two-phase zone.

The time evolution of some relevant quantities is shown in Figure 6. As in the porous column, boiling temperature and vapor production tend to stabilize after a short transient and temperature remains nearly uniform in the boiling zone (Fig. 6a). The flow rate of liquid entering the two-phase, boiling zone is slightly less than the injected water, as a fraction of the latter penetrates into the matrix (Fig 6b). This penetration is significant in the zone where the fractures are fully liquid-saturated, and is negligible in the two-phase zone. Both rates of liquid entering the matrix and the boiling zone tend to stabilize rapidly. The rate of vapor leaving the boiling zone also tends to stabilize to a lower value than the liquid inflow. The nearly constant difference between these two quantities causes the continuous widening of the boiling zone (Fig. 6). Due to this widening the distance between the boiling zone and the production boundary of the column is shortened considerably with a consequent slow decrease of the boiling temperature. It is interesting to observe that, while the boiling zone is spreading, the total heat flow from the matrix to the fractures in the boiling zone tends to stabilize. This means that the effect of decreasing heat flux from the matrix is compensated by an increase of the heat exchange surface. As in the porous column, the stabilization of temperature and flow rate occurs when the boiling rate equals the rate of vapor flow towards the production end.

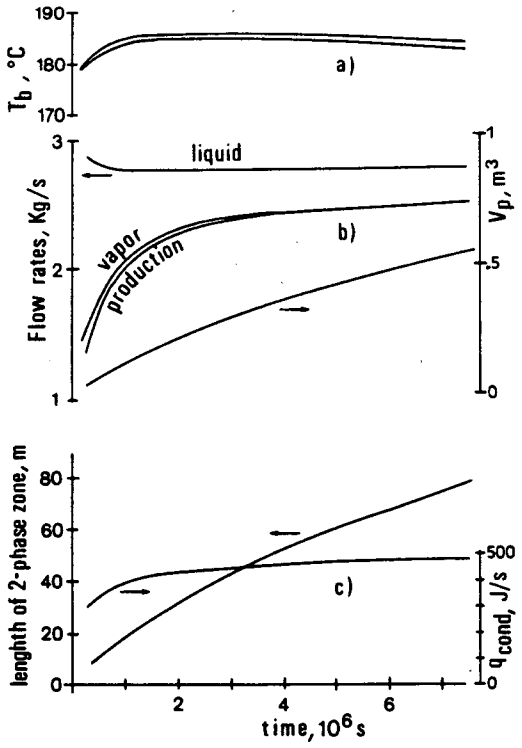

Fig. 6. One-dimensional column, fractured-porous medium. (a) Minimum and maximum temperature of two-phase fluid in the fractures. (b) Flow rates of liquid entering the two-phase zone in the fractures and flow of steam out of it; production rate at the constant pressure boundary; volume of liquid in the column (including the liquid fraction of the two-phase fluid). (c) Width of the zone with two-phase fluid in the fractures and total conductive matrix-fracture heat flow in this zone.

In the porous medium the velocity of the boiling front and the rock cooling adjust during the injection process so as to reach this condition. In the fractured medium, the rock-fluid heat transfer is limited and this condition is reached and maintained by enlargement of the boiling zone.

Figures 7 and 8 show results for the one-dimensional radial model. The only significant difference to the case with 1-D linear flow is that the width of the two-phase zone increases more slowly with time. In both cases the role of matrix blocks is essentially that of absorbing liquid from the fractures and releasing heat to them by conduction. The liquid inflow into the blocks becomes significant only when the surrounding fractures are fully liquid saturated. From this moment on, the liquid continues to flow into the block while the block is cooled by conduction. This process continues until the block is fully saturated with liquid at the temperature of the injected water.

TWO-DIMENSIONAL RADIAL, POROUS MEDIUM MODELS

Numerical experiments were also performed using more complex two-dimensional models, to obtain insight into fluid migration and phase transformation processes induced by injection on a reservoir scale, taking gravity into account. We consider a two-dimensional, radial porous medium system with a radius of 600 m (Fig. 9 and Table II). The injection well is placed at the center of the system and the production wells are assumed to be uniformly distributed in the region 150 m $<$ R $<$ 600 m. The reservoir is assumed to be 1000 m thick, with initial liquid saturation $S_w = 0$, and bounded below by a constant pressure surface with p = 64.1 bars and T = 280 ° C. All wells are assumed to have 50 m open intervals at the top of the reservoir. The production wells are placed on deliverability, with a bottom-hole pressure of 5 bars. Before starting injection, the system is run to steady-state heat conduction

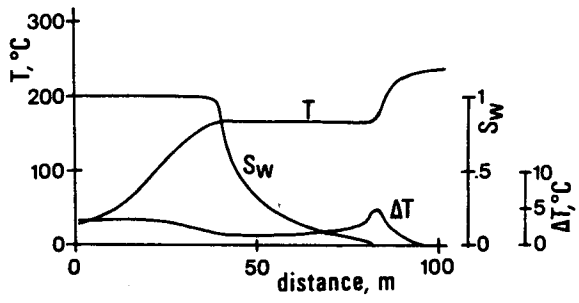

Fig. 7. One-dimensional radial, fractured-porous medium model (injection rate = 2.78 kg/s, k=5e-13 m^2). Variation with radial distance of temperature and liquid saturation in the fractures, and temperature difference between the outermost matrix elements and fractures.

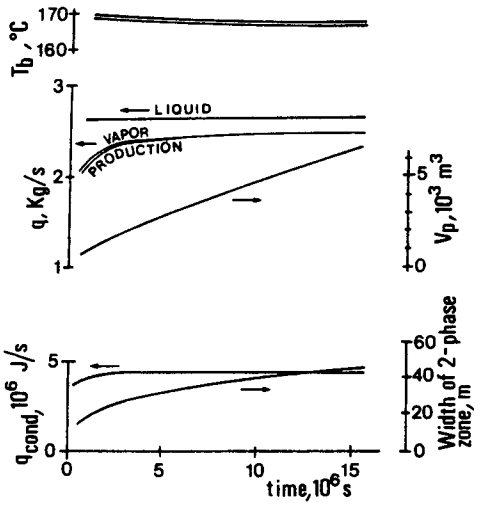

Fig. 8. One-dimensional radial, fractured-porous medium model. Temporal evolution of the same quantities as shown in Fig. 6.

(240 °C in the uppermost elements and 280 °C at the bottom) and quasi-steady mass flow at that temperature distribution. The production and recharge rates in this state are 58 kg/s, which is equal to the total pre-injection flow-rate of the wells at a distance of less than 600 m from the injection well for the field experiment reported by Giovannoni et al. (1981).

The simulations performed include three cases of injection into isotropic formations and one of anisotropic permeability, with vertical permeability one order of magnitude lower than horizontal. The permeability in zone c (see Table II) was adjusted so as to have the same initial production of the isotropic case. The parameters for the four cases are reported in Table II. The following general observations are made from the results obtained in all four cases (Figs. 10, 11, 12):

(1) The injection plume tends to move primarily downward from the injection well rather than laterally outward;

(2) most of the plume is in single-phase liquid conditions, with boiling restricted to the outer "skin" of the plume; (If the fractured-porous nature of the reservoir were taken into account we would expect more extensive two-phase zones.)

Table II. Parameters used in two-dimensional models

Parameter	Case 1	Case 2	Case 3	Case 4
Injection rate, kg/s	5	27.8	55.6	27.8
Injection enthalpy, J/kg	125800	125800	125800	125800
Wells on deliverability:				
productivity index per unit area, m^3/m^2	1.81e-15	1.81e-15	1.81e-15	1.81e-15
bottomhole pressure, bars	5	5	5	5
Initial liquid saturation	0	0	0	0
Specific heat, J/kg °C	920	920	920	920
Relative permeability: (Corey curves)	S_{rw}=.30 S_{rv}=.05	S_{rw}=.30 S_{rv}=.05	S_{rw}=.30 S_{rv}=.05	S_{rw}=.30 S_{rv}=.05
ZONE A				
Density, kg/m^3	2600	2600	2600	2600
Porosity	8%	8%	8%	8%
Heat conductivity, W/m °C	2.51	2.51	2.51	2.51
Horizontal permeability, m^2	5e-13	5e-13	5e-13	5e-13
Vertical permeability, m^2	5e-13	5e-13	5e-13	5e-14
ZONE B				
Density, kg/m^3	2700	2700	2700	2700
Porosity	5%	5%	5%	5%
Heat conductivity, W/m °C	2.87	2.87	2.87	2.87
Horizontal permeability, m^2	5e-13	5e-13	5e-13	5e-13
Vertical permeability, m^2	5e-13	5e-13	5e-13	5e-14
ZONE C				
Density, kg/m^3	2700	2700	2700	2700
Porosity	1%	1%	1%	1%
Heat conductivity, W/m °C	2.93	2.93	2.93	2.93
Permeability, m^2	4.5e-14	4.5e-15	4.5e-15	5.1e-15

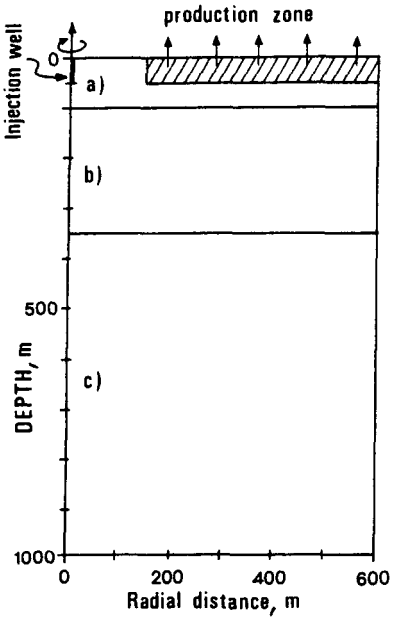

Fig. 9. Two-dimensional radial, porous medium model.

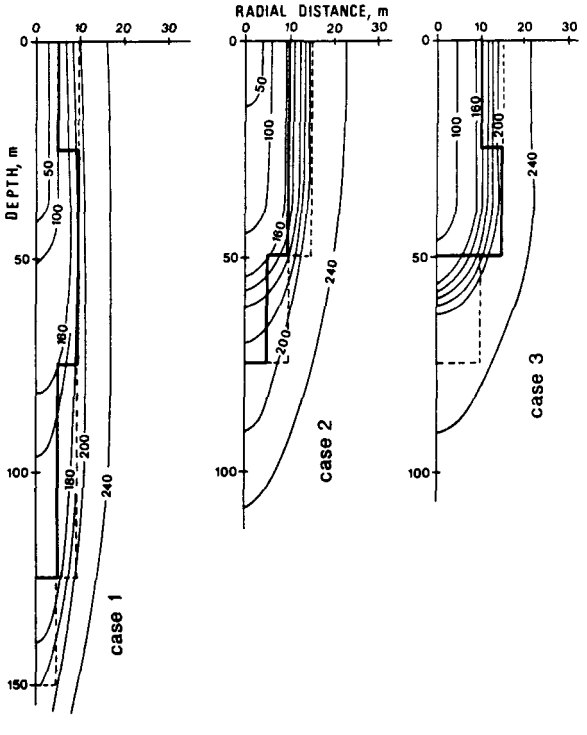

Fig. 10. Two-dimensional radial, isotropic porous medium model. Shape of the injection plume and isotherms for different injection rates. In all three cases the liquid volume (including the liquid in the two-phase elements) is about 2800 m^3. Continuous line: limit of liquid-saturated region. Dashed line: limit of two-phase region.

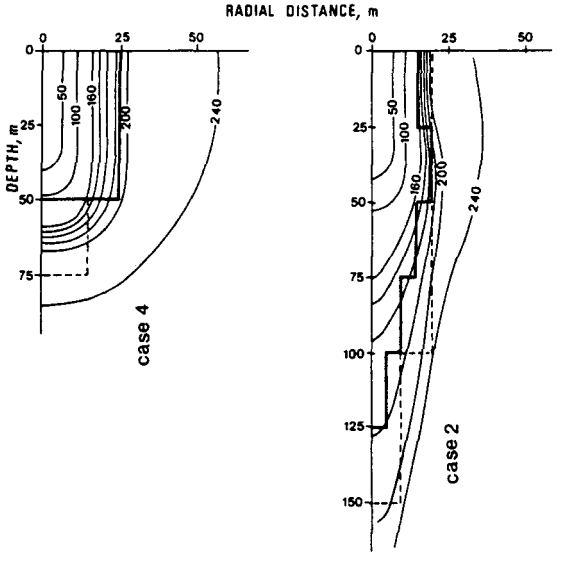

Fig. 11. Shape of the liquid plume and isotherms for the anisotropic and isotropic cases after approximately three weeks of injection, when liquid volume (including that in the two-phase elements) is about 8500 m^3. Continuous line: limit of liquid-saturated region. Dashed line: limit of two-phase region.

(3) after an initial transient, boiling temperatures again tend to stabilize and the temperature differences between different parts of the outer surface of the plume are limited to a few tens of degrees.

Once injection starts, the plume expands both downward and laterally. The shape assumed by the plume during its evolution depends on the relative importance of pressure and gravity forces. The lateral expansion is more pronounced for higher injection rate (Fig. 10). As the plume continues to expand, both its horizontal cross-section and the height of the liquid column increase, thus facilitating the downward movement of liquid water and decreasing the pressure in the upper parts of the plume. With time the lateral expansion of the plume slows down and eventually terminates. Other conditions being equal, the horizontal cross section reached is higher for higher injection rates. When the plume reaches the permeability discontinuity at 350 m depth below reservoir top, its downward propagation slows down considerably, and liquid migration occurs radially outward above the discontinuity surface. The liquid can propagate to below the producing area, but a thick layer of steam saturated, high temperature rock still separates the liquid-invaded reservoir volume from the shallow producing wells (Fig. 12). The boiling temperature is still controlled by the pressure in the boiling zone and tends to stabilize when boiling rate equals the steam flow towards the producing zone. In a two-dimensional system the spatial distribution of boiling temperature depends on the steam flow pattern. Boiling temperature is higher for higher injection rates (Fig. 10), as higher pressure in the boiling zone is needed to maintain a higher rate of steam flow. Boiling temperature also increases with depth due to the

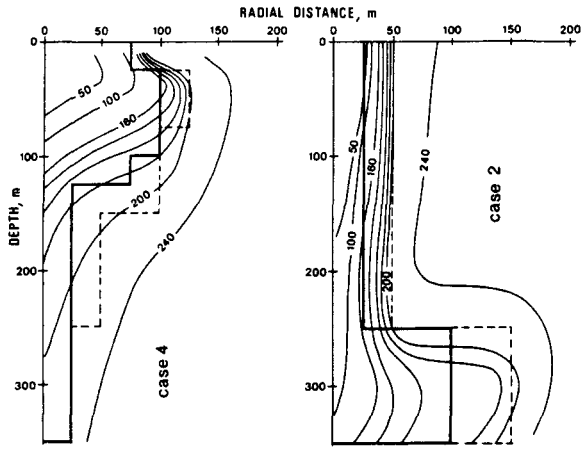

Fig. 12. Shape of the liquid plume and isotherms for the anisotropic and isotropic cases after approximately one year of injection, when liquid volume (including that in the two-phase elements) is about 356,000 m^3. Continuous line: limit of liquid-saturated region. Dashed line: limit of two-phase region.

higher initial reservoir temperature, and the greater distance from the producing zone. Due to the high permeability assumed in our models in the upper part of the reservoir, these differences remain limited.

After the lateral expansion of the plume has stopped, the temperature inside the plume continues to decrease due to flow of cold injected water. The temperature of the stationary (at shallower depth) skin of the plume would also tend to decline. However, this process can not go very far because of the coupling between temperature and pressure in a two-phase system. In response to very small temperature-and-pressure declines at the lateral boundary of the plume the vaporization process terminates there. Subsequently vapor flows towards the shallow surface of the plume, where it condenses, depositing its latent heat. The "skin" of the plume is still kept at a high temperature by steam condensation and conductive heat flow. In such conditions, the downflow of liquid inside the plume is larger than the injection flowrate.

Figures 11 and 12 compare the plumes for cases 2 and 4 (anisotropic) at different stages of evolution. Figure 11 shows the shape of the plume and the isotherms in an early stage of its evolution. In both cases the lateral expansion of the plume is still underway. Although the coarse mesh used was inadequate for a detailed analysis of the long time behavior of the systems, Fig. 12 nevertheless reveals some significant differences between the two cases and illustrates some of the above-described phenomena. After about one year of injection, in the anisotropic case, the bottom of the plume has only just reached the permeability discontinuity. The plume still continues to expand laterally, and the two-phase zone has advanced to near the production zone. In case 2 the lateral expansion of the upper parts of the plume has already ended and the horizontal movement of the plume above the permeability discontinuity surface is evident. Figure 13 shows the pressure distribution in the dry steam zone for case 2 at the same time as Fig. 12. The pressure distribution clearly shows the flow of steam from the deep boiling zones to the upper condensing zones of the plume "skin".

CONCLUSIONS

Injection of cold water into depleted vapor zones gives rise to complex coupled processes of fluid flow and heat transfer. Temperature and phase fronts tend to be sharp in porous medium models, but become very diffuse in fractured media, where the thermal equilibration between fluids in the fractures and reservoir rock is delayed. The following observations were made in our numerical experiments.

(1) After an initial transient, boiling temperature at the surface of the injection plume tends to stabilize.

(2) Stabilized boiling temperature depends primarily on injection rate and reservoir permeability, being larger for larger rate and smaller permability.

(3) When gravity effects are included the injection plume tends to move primarily downward from the injection point rather than laterally outward.

(4) Vaporization and condensation processes tend to keep temperature variations limited over the entire surface of the plume.

In summary, it appears that a number of fluid flow and heat transfer processes combine to make cold water injection into depleted vapor zones an efficient heat extraction process.

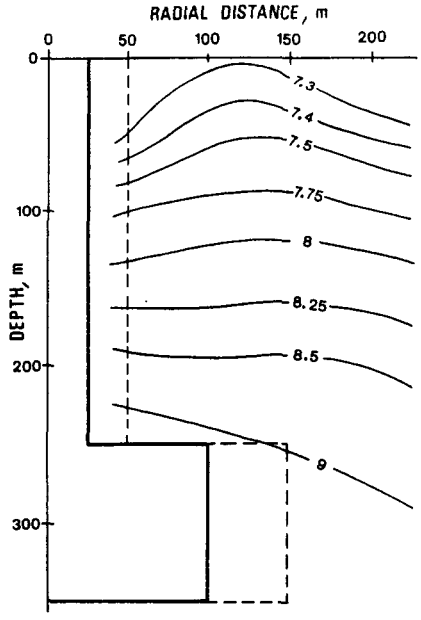

Fig. 13. Pressure distribution (bars) around the "plume" for case 2.

NOMENCLATURE

c_r	specific heat of rock, J/kg °C
h_{lv}	latent heat of vaporization, J/kg
k	permeability, m^2
L	distance of boiling front from the constant pressure boundary, m
m	pseudopressure, Pa s/m^2
p	pressure, Pa
p_{sat}	saturation pressure, Pa
q	flux, kg/s·m^2
q_{cond}	total conductive heat flow, J/s
q_{inj}	injection flux, kg/s·m^2
q_{liq}	flux of liquid behind the boiling front, kg/s·m^2
q_{prod}	production flux, kg/s·m^2
q_v	steam flux, kg/s·m^2
R	radius, m
S	saturation, dimensionless
S_{rw}	irreducible liquid saturation, dimensionless
S_{rv}	irreducible vapor saturation, dimensionless
T	temperature, °C
v_{bf}	boiling front velocity, m/s
V_w	volume of liquid in the system, including that in the 2-phase fluid, m^3
ϕ	porosity, dimensionless
ρ	density, kg/m^3

Subscripts

b	boiling zone
bf	boiling front
c	constant pressure boundary
r	rock
v	vapor
w	liquid

ACKNOWLEDGEMENT

This work was supported by the Progetto Strategico Valorizzazione Materie Prime Minerali, CNR, Italy, and by the U.S. Department of Energy, Geothermal Technology Division, under Contract No. DE-AC03-76SF00098. For assistance in the preparation of the manuscript, the authors are indebted to M. H. Dickson, G. Gori, E. Klahn, L. Fairbanks, and M. Bodvarsson.

REFERENCES

Bertrami, R., Calore, C., Cappetti, G., Celati, R., D'Amore, F., 1985, A three-year recharge test by reinjection in the general area of Larderello field: analysis of production data. 1985 International Symp. on Geothermal Energy, Kailua-Kona, Hawaii, Vol. 9, pt. 2, pp. 293-298.

Bodvarsson, G., 1972, Thermal problems in the siting of reinjection wells, *Geothermics,* Vol. 1, No. 1, pp. 63-68.

Cappetti, G., Giovannoni, A., Ruffilli, C., Calore, C., Celati, R., 1982, Reinjection in the Larderello geothermal field, Proceedings International Conference on Geothermal Energy, Firenze, BHRA Fluid Engineering, Cranfield, Bedford (England), pp. 395-408.

Giovannoni, A., Allegrini, R., Cappetti, G., Celati, R., 1981, First results of a reinjection experiment at Larderello, Proceedings of 7th Workshop Geothermal Reservoir Engineering, Stanford, California, pp. 77-84.

Lauwerier, H. A., 1955, The transport of heat in an oil layer caused by the injection of hot fluid, Appl. Sci. Res., Martinus Nijhoff, Publisher, The Hague, Vol. 5, Section A, No. 2-3, pp. 145-150.

Pruess, K., 1983, Development of the general purpose simulator MULKOM, Annual Report 1982, Earth Science Division, Report LBL-15500, Lawrence Berkeley Laboratory.

Pruess, K. and Narasimhan, T. N., 1982, On fluid reserves and the production of superheated steam from fractured, vapor-dominated geothermal reservoirs, *Journal of Geophysical Research,* Vol. 87, No. B11, pp. 9329-9339.

Pruess, K. and Narasimhan, T. N., 1985, A practical method for modeling fluid and heat flow in fractured porous media, *SPE Journal,* February, pp. 14-26.

PROCEEDINGS, Eleventh Workshop on Geothermal Reservoir Engineering
Stanford University, Stanford, California, January 21-23, 1986
SGP-TR-93

COOLING OF THE WAIRAKEI RESERVOIR DURING PRODUCTION

Paul F. Bixley

Ministry of Works and Development
Wairakei Geothermal Projects Office

ABSTRACT

After nearly 30 years of power generation, parts of the present production area at Wairakei are near the end of their economic life due to local cooling. To the west of the present production area there remains a large volume of high temperature resource whose deep liquid temperatures have not changed from those measured during the 1960's. Power generation can be maintained for many more years by producing from this high temperature resource.

INTRODUCTION

In 1988 the Wairakei power station will celebrate 30 years of generation and it is anticipated that the existing plant can operate economically until about the year 2000 (Stacey & Thain, 1983). Even a cursory examination of production data shows that although parts of the present production area are also approaching the end of their economic life, a large, essentially unexploited resource remains to the west of this area. Proper planning for the maintenance of steam supply, possible power station replacement and the incorporation of reinjection into the system have recently led to renewed interest in the application of reservoir engineering to obtain optimum value from the resource.

Definitions: Throughout the paper several essentially geographic areas are referred to (fig 1):

- Production Reservoir - area within 230°C contour (fig 1), between depths 200-1000m (elevation +200 to -600m).
- Production area - original production area, about 1 km², near northeast field boundary; sometimes subdivided into eastern and western production areas.
- Western investigation area. To the west and southwest of the production area, delineated by several high temperature exploration wells, three of these were connected to steam supply system in 1982.
- Peripheral wells - non-productive "cold" (less than 220°C wells) outside the boundary of the high temperature reservoir, but showing pressure response to the reservoir.

BACKGROUND

Prior to exploitation Wairakei was a liquid-dominated field with a vertical pressure profile about 10% above hydrostatic (Grant & Horne, 1980). Water at base temperature 260°C rose through the reservoir, reaching boiling point at about 500m depth (elevation 100m). Above this level limited two-phase conditions were present with fluid ascending through fissures in the otherwise poorly permeable Huka Formation "caprock" to feed the surface features. Mass and heat flow from these was about 400 kg/s and 400 MW (Allis, 1981).

Up to 1958 pressure variations within the reservoir were transmitted rapidly to peripheral wells near the southern and eastern boundaries (no suitable wells were available to the west at this time), with detailed response to changes in mass withdrawal rate from the reservoir, implying liquid conditions between reservoir and these wells (WK12, 36 & others, see fig 2). At this time total pressure change from the natural conditions was less than three bars. With the commissioning of the first stage of the power station in 1958 and an accompanying sustained increase in mass withdrawal rate (from 600 to 1300 kg/s), liquid pressures began to fall rapidly and response from the above wells took a new trend (fig 2), indicating that widespread boiling had commenced and that pressure response in these wells was now being buffered by a steam or two-phase zone.

From 1958 to 1965 reservoir response in the production area was governed by saturation conditions with temperatures falling rapidly as pressures decreased. After 1965 liquid temperatures in the production area have slowly, but steadily decreased while in the unexploited high temperature western investigation area no changes in deep liquid temperatures have been observed.

of maximum subsidence and it is most likely that this water is entering the reservoir by the same channels that allowed hot chloride water to travel upwards before exploitation reduced pressures (Allis, 1980).

VAPOUR PRESSURES

A few wells at Wairakei have been specifically completed into the vapour zone(s), but many wells have dual, or multiple feed points, and are open to both vapour and liquid pressures. When these wells are shut-in, the steam zone pressure can be readily monitored at the wellhead. The shut-in wellhead pressure has been routinely monitored on production and non-production/ investigation wells since 1964, and the resulting data classifies the wells into four distinct groups (figs 3 & 4). A few wells lie slightly off these trends, but the close agreement of distinct pressures over wide areas of reservoir is quite remarkable, and implies:

- throughout each area there is very good horizontal communication (at the level of the vapour zone),
- there are boundaries between the different zones.

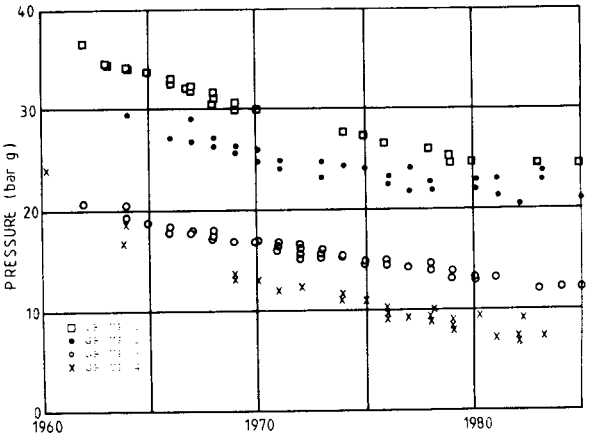

Fig 3 Vapour pressure decline 1964-1985

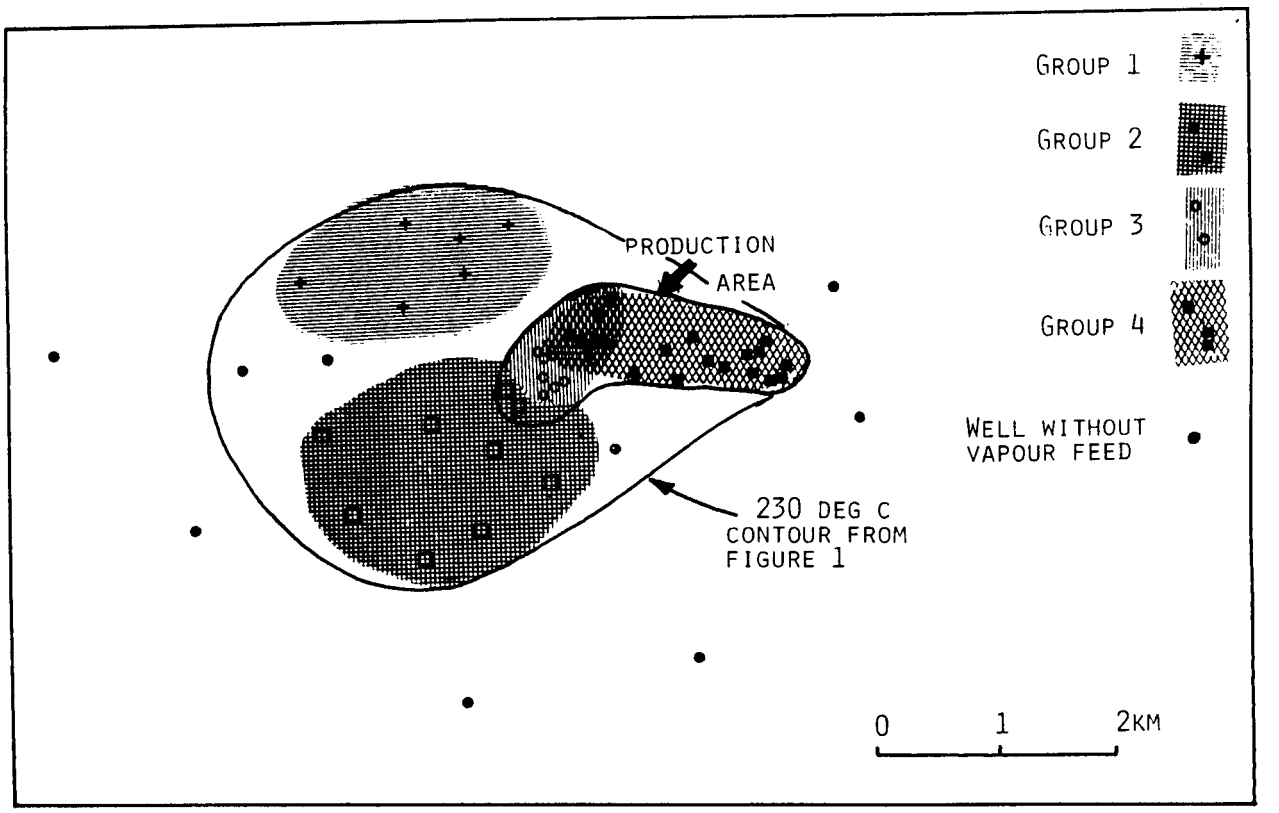

Fig 4 Distribution of vapour pressure zones across field

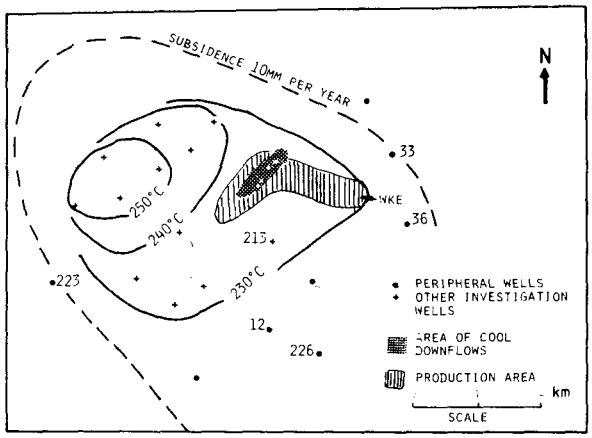

Fig 1 Plan of Wairakei field. Not all wells are shown. Temperatures are at -370m a.s.l. after Hitchcock (1978).

Direct evidence of cooling comes from chemical data, changes in vapour pressure on shut-in wells, measured feedwater temperature, temperatures in wells with "cool" downflows, and changes in well and field enthalpy. Indirect support is obtained from pressure changes in the cold peripheral wells and shallow wells over the reservoir. These different kinds of information are discussed below.

PRESSURE RESPONSE - LIQUID

Liquid pressures in the western production and western investigation areas have always changed together with a ±1 bar range reflecting the very high permeability over the whole area. Pressures in the eastern production areas are 2 to 3 bars below the western trend. Locations of some peripheral wells are shown on fig 1 and their pressure responses to exploitation on figure 2.

Pressures in the peripheral areas around the unexploited reservoir are likely to have been slightly less than those within the reservoir, as most showed inversion-type temperature profiles typical of outflow zones when first drilled. It is very difficult to identify the level of connection between these wells and the reservoir to obtain an absolute comparison between hot reservoir pressure and cold peripheral pressure, so data on figure 2 has been adjusted to show changes in pressure assuming no difference in the unexploited condition.

Figure 2 shows that drawdown has in fact travelled out into the cooler regions around the reservoir. An idea of how far it has propagated may be given by ground surface subsidence surveys (fig 1).

The pressure response of one shallow (50m) water level well is shown on figure 2. Contours of the shallow water table surface show there is a steep pressure gradient across the field from west to east, generally following the topography. To the west the piezometric surface is at elevations of about 470m falling across the reservoir to 360m at Wairakei Stream/Waikato River. Changes in the water table indicate that the shallow flow is now being diverted toward the area

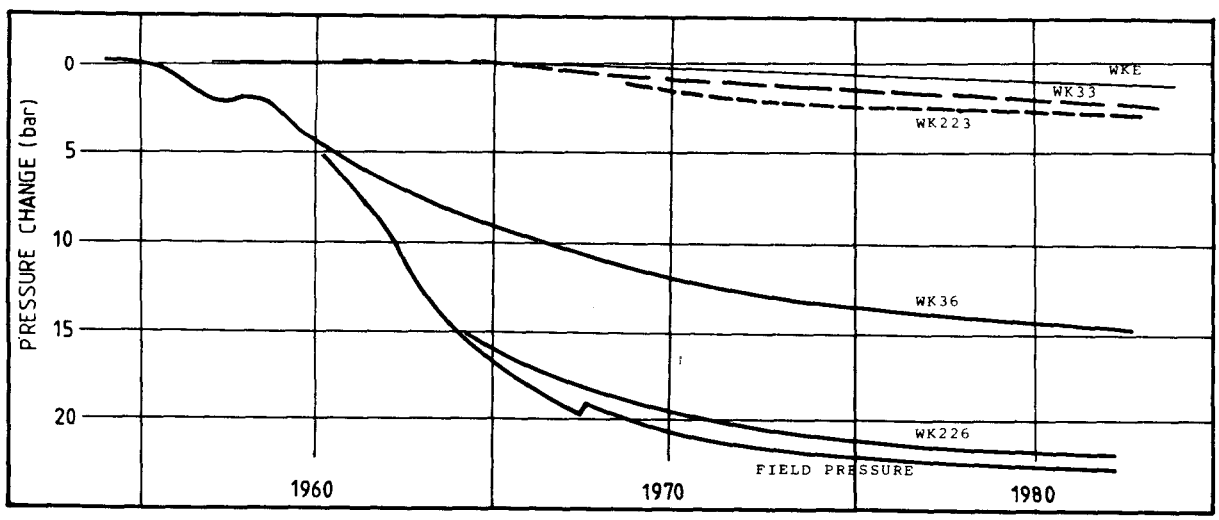

Fig 2 Pressure response of liquid zone to exploitation. See fig 1 for well locations.

COOL DOWNFLOWS

These downflows, now common in parts of the production area, were first recognised by Hitchcock in 1974, after WK107 had suddenly died when taken off production for routine maintenance. Subsequent flowmeter runs showed this downflow to be 50 l/s. Evidence of rapidly cooling feedwater temperature in some wells had actually been available since 1965 (Wainwright). Chemical data showed wells 31, 80, 101 & 109 all had potential problems at that time. WK31 and 101 died soon after, but the problem never became too severe in 109 due to poor permeability limiting the cool inflow.

Data from wells with known or inferred cool inflows is tabulated below. In some cases a downflow can be inferred from the development of a blockage (near the inflow point) and generally low temperatures above the blockage (less than 200°C). Proven downflows on WK80, 101 & 107 all developed blockages due to calcite deposition at the inflow level.

Well	Elevation of Inflow (m)	Inflow Temp (1982) (°C)	Rate l/s
80	+ 55	176 ?	?
101	+ 60	148	40
107	+129	140	50
109	+ 89	195 (1967)	15
118	+130	?	?
213	- 50	198	?

Table 1 : Data from wells with cool downflows

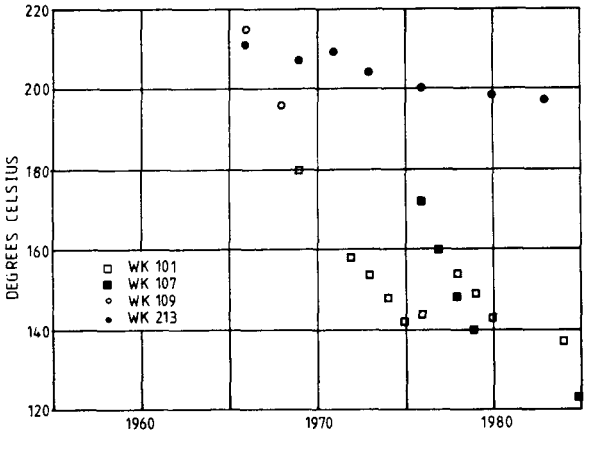

Fig 5 Feed temperature in wells with cool downflows

A comparison of inflow elevation with well location indicates that the inflows are more likely to be controlled by a horizontally oriented permeable zone than by vertical zones (faults). However tracer return data between downflow wells and other production wells shows that faults control the rapid return paths - but may equally act as barriers to restrict lateral distribution on the field-wide scale (McCabe et al 1983).

There has also been a strong trend of temperature decrease of these cool downflows with time. The "original" downflows in WK101 and 109 in 1968 were 180-200°C. These had decreased to 120-140°C in 1984 (fig 5).

VERTICAL PRESSURE DISTRIBUTION

Using the data from table 1 and pressure data obtained from routine measurements and repair operations on downflow wells, vertical pressure profiles can be constructed for the downflow area. This is shown together with the profiles in the eastern production area and western investigation area on fig 6. To appreciate the three-dimensional picture, fig 6 should be read in conjunction with fig 4.

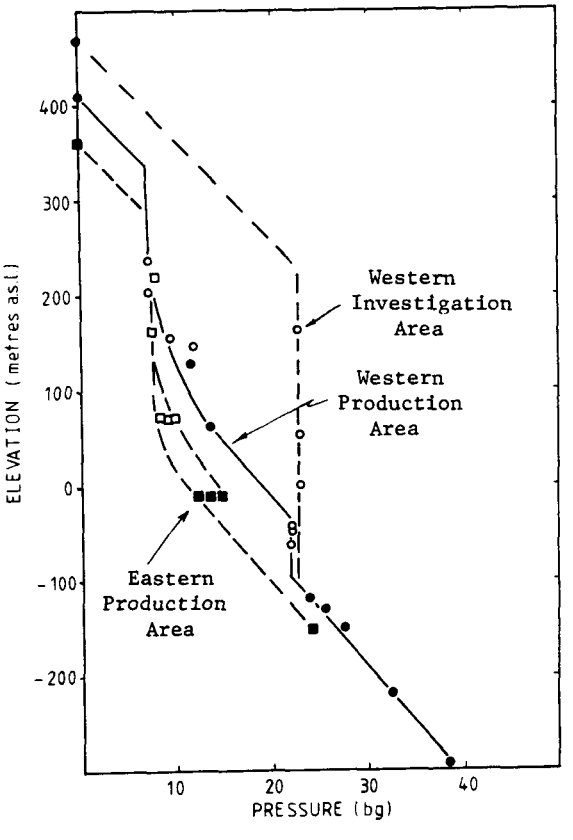

Fig 6 Vertical pressure distribution

FEEDWATER TEMPERATURES

One of the more definitive prediction tools at Wairakei has been obtained from the programme of measuring feedwater temperatures on flowing wells. This can be done only on highly permeable liquid-fed wells. Such measurements have been made since 1968 only. Data plotted (fig 7) prior to this time is taken from shut-in profiles.

The pre-1965 data shows the expected rapid decrease associated with pressure drawdown. Since 1968 there has been a near-linear decrease of about 0.8°C/year in the production area, with 1985 feed temperatures of about 225°C.

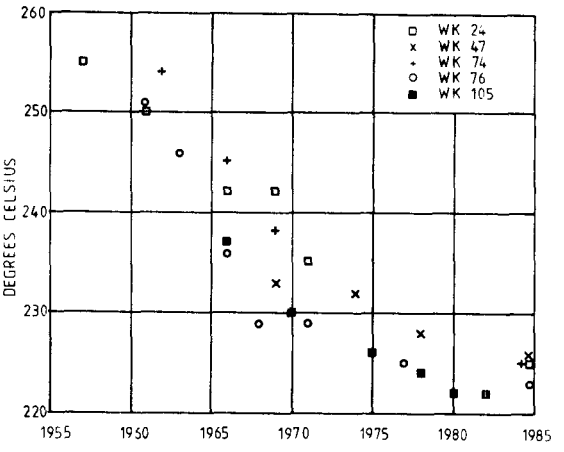

Fig 7 Feedwater temperatures in selected highly permeable production wells. Data pre-1968 is from shut-in profiles; post-1968 data is measured in flowing conditions

FIELD ENTHALPY

The variation of total discharge enthalpy from 1960 to 1980 is shown on fig 8. After 1974 the absolute accuracy of the data is poor as from this time most of the separated water from HP and IP wells was collected and flashed to IP and LP steam, and water flows from individual wells measured once or twice each year. The trend in field enthalpy is clear with continuing decrease following the 1965 maximum. This trend cannot be directly correlated with liquid feed temperature as the steam flow rate from the "dry" and high enthalpy wells runs down at 3-4 times the rate of liquid wells.

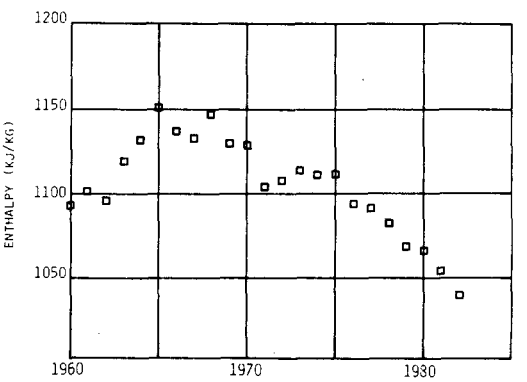

Fig 8 Total field discharge enthalpy 1958-84

CONCEPTUAL MODEL

Interpretation of the above data poses two major problems:

- what are the reasons for rundown in vapour pressures?
- does exploitation of the vapour zone influence the fluid quality in the liquid zone?

Aspects of these questions are discussed in detail by Hitchcock (1978), Grant (1978) and Allis (1981).

At this stage it appears there is no single reason for vapour zone rundown. Rundown rate in these zones varies between 0.4 and 1.0 bar/year 1965-1980. The most rapid rundown being in the lowest pressure, exploited zone, and least in the areally extensive group 4 wells. Heat loss rate appears to be controlled by a combination of:

- exploitation via wells,
- heat loss to cooler water percolating through the vapour zone,
- heat loss to surface features,
- steam flow between zones.

Other factors may also be important, such as heat input from the boiling upflow in the high temperature western investigation area, and heat transfer rate between reservoir rock and fluid.

Chemical data and physical measurements conclusively demonstrate that cooler waters from above the reservoir are flowing down to mix with the high temperature liquid in the production area. Although pressure measurements indicate that there is undoubtedly cooler lateral inflow, as yet there has been no physical evidence of reduced temperatures in wells within the high temperature reservoir. (Note that the southeast "boundary" is actually hot, and connected to the Tauhara reservoir, so that inflows from here are already hot).

In general the steam zones appear to have formed just below layers of restricted permeability (Huka Formation), with the initial pressure being controlled by elevation, hence temperature of the boiling zone. The group 2, 22 bar (1985) steam zone in the production area appears to be an anomaly - but more probably shows that there is likely to be a good geological reason for a boiling zone to form within the Waiora Breccia, which is in places a well stratified formation of varying physical properties.

Individual well tests in the vapour zone give high permeabilities. Grant (1978) obtained kh values of 20-80 darcy-metres for 8-inch steam producers in the production area, and a 12-inch steam well completed in 1985 gave a kh of 400 darcy-metres! (production rate 180 t/h steam at 6 bar from the 23 bar steam zone). Thus the intuitive feelings that high (horizontal?) permeability must exist within the steam zones is confirmed by measurements.

Modelling of fluid flows within the liquid zone gives horizontal permeabilities of 30-300 darcy-metres and vertical permeability an order of magnitude less at 5-7 darcy-metres (Grant, 1984).

FUTURE PRODUCTION

Within 10 years production rate from many of the existing producing wells will have decreased to uneconomic rates. However a large high temperature resource still exists to the west of these wells which with proper engineering will sustain power generation for at least another 30 years.

ACKNOWLEDGEMENTS

The permission of the General Manager, Electricity Division of Ministry of Energy and the Commissioner of Works to publish this data is acknowledged. We are indebted to David Wainwright who was the first person to really come to grips with the multitude of physical data collected at Wairakei and who instituted the monitoring programmes from which much of the data presented was obtained. Also Malcolm Grant and Rick Allis who have researched and published much information relating to cooling of the Wairakei reservoir.

REFERENCES

Allis, R.G. (1981), "Changes in heat flow associated with exploitation of Wairakei Geothermal Field, New Zealand", Journal of Geology and Geophysics, V24.

Allis, R.G. (1982), "Geologic controls on shallow hydrologic changes at Wairakei field", Proceedings of 4th New Zealand Geothermal Workshop, p139-144.

Ellis, A.J. ; Mahon, W.A.J. (1977), "Chemistry and geothermal systems", Academic Press.

Grant, M.A. (1978), "Pressure changes in the two-phase zone at Wairakei", Geothermal Circular MAG 20, Applied Maths Division, D.S.I.R.

Grant, M.A. ; Horne, R.N. (1980), "The initial state and response to exploitation of Wairakei Geothermal Field", Geothermal Resources Council transactions 4, p333-336.

Grant, M.A. (1984), "Preliminary Modelling of Wairakei reinjection", D.S.I.R. Applied Maths Division Report.

Hitchcock, G.W. (1976), "Report on Bore 107", Ministry of Works and Development internal report.

McCabe, W.J. ; Barry, B.J. ; Manning, M.R. (1983), "Radioactive tracers in underground water flow studies", Geothermics V12, No 2/3.

Hitchcock, G.W. (1978), "Physical Model of the Wairakei-Tauhara reservoir, Internal Ministry of Works report.

Stacey, R.E. ; Thain, I.A. (1983), "25 Years of Operation at Wairakei Geothermal Power Station", Proceedisngs of 5th New Zealand Geothermal Workshop p79-90.

Wainwright, D.K. (1970) "Wairakei geothermal power project, prediction of steam output", Ministry of Works internal report.

PROCEEDINGS, Eleventh Workshop on Geothermal Reservoir Engineering
Stanford University, Stanford, California, January 21-23, 1986
SGP-TR-93

THE COUPLING OF THE NUMERICAL HEAT TRANSFER MODEL OF THE PAUZHETKA HYDROTHERMAL SYSTEM (KAMCHATKA, USSR) WITH HYDROISOTOPIC DATA

A.V.Kiryukhin and V.M.Sugrobov

Institute of Volcanology,
Petropavlovsk-Kamchatsky,
683006, USSR

ABSTRACT

The application of the two-dimensional numerical heat-transfer model to the Pauzhetka hydrothermal system allowed us to establish that

1. A shallow magma body with the anomalous temperature of 700-1000°C and with a volume of 20-30 km^3 may be a heat source for the formation of the Pauzhetka hydrothermal system.
2. The water feeding source of the Pauzhetka hydrothermal system may be meteoric waters which are infiltrated at an average rate of 5-10 $kg/s \cdot km^2$.

The coupling of the numerical heat-transfer model with hydroisotopic data (D,T,^{18}O) obtained from the results of testing of exploitation wells, rivers and springs is the basis to understand more clearly the position of recharge areas and the structure of water flows in the hydrothermal system.

INTRODUCTION

The hydrothermal systems in Kamchatka occur in the volcanic zone of north-eastern trend 25 km wide and 1000 km long. The Pauzhetka hydrothermal system is the most studied among them (Fig.1). In the early sixtieth of our century a decision was taken to use the geothermal resources of Pauzhetka for the production of the electrical power and since 1966 the 5MW and later 11MW Power Plant has operated here.

Owing to exploration works we have obtained information on (1) temperature distribution in the interiors and natural heat discharge; (2) geological structure and magmatism; (3) geometry and permeability of reservoir; and (4) conditions of water recharge and discharge of the hydrothermal system. Of great importance were the studies made by V.V.Averiev, V.I.Belousov, S.I.Naboko and V.M.Sugrobov (Pauzhetka Hot Waters ..., 1965).

The surface discharge includes the discharge of hot springs (31 kg/s) with temperature of 98°C and steam vents with the whole heat capacity of $4.6 \cdot 10^3$ kcal/s (Fig.2). The temperature penetrated by wells is 150-200°C. The geothermal reservoir is composed of fractured psephitic tuffs. In this area acid extrusions (dacites and rhyolites), the intrusion of which took place in the Middle and Upper Pleistocene and Holocene (6000 yrs ago) were also found (Belousov et al., 1976).

The geometry of the reservoir is characterized by the distribution of thermal occurrences at the surface. This reservoir is located at the junction of the permeable zones of north-

western and meridional trends. The analysis of the results of well testing gives evidence that there is no correlation between the stratigraphic sequence and production zones that points to a deep enhancement of the geothermal reservoir (Fig.3).

The recharge areas of the Pauzhetka hydrothermal system include high parts of the Kambalny Ridge and the Kurile and Vitaminnoe Lakes which are situated at +104 - +273 m a.s.l. (see Fig.1). Data on well sampling for O^{18} and D support an idea on meteoric feeding of the hydrothermal system (Fig.4).

To explain the mechanism of hydrothermal activity in the region of the Pauzhetka structure a numerical heat transfer model was suggested. This model is 2-dimensional and is based on the laws of mass and heat conservation and on the equations of movement of water flows (Kiryukhin and Sugrobov, 1985).

DISCUSSION

The results of numerical modelling made earlier (Kiryukhin and Sugrobov, 1985) yielded a somewhat higher value of temperature gradient (in comparison with actual data on geothermal wells) in the lower parts of the section. Besides, new hydroisotopic data (D, O^{18}) obtained recently, make us revise our model.

In particular, from these data, the hydroisotopic composition of thermal waters is intermediate between that of the Kurile lake and meteoric waters of the Kambalny Ridge. Meanwhile, within the framework of the previous model the source of heat feeding, namely a shallow magma chamber, did not differ in filtrational properties from ambient rocks and therefore the infiltrational waters could freely penetrate to this chamber. If it was really so, then the hydroisotopic composition in the discharge area should approach the hydroisotopic composition of "magmatogenic waters" which have $-71 < D < -40$, $0 < O^{18} < +6.6$ (Sakai and Matsubaya, 1976; Kononov and Polyak, 1982; Serezhnikov and Seletsky, 1982; Matsuo et al., 1985). Contrary to this, the water in the discharge area of the Pauzhetka hydrothermal system penetrated by wells has $-100 < D < -60$, $-11.5 < O^{18} < -6.5$ (see Fig.4).

Thus, it is necessary to use this model to find the mechanism owing to which the water penetration to the magma chamber decreases. This may be achieved by decreasing the permeability of magma body. In this connection, the sensitivity of the model to variations in filtrational properties of magma body was examined.

In order to regard the filtrational heterogeneity , it was necessary to improve the numerical model 1985 algorithm; to solve the hydrodynamic part of the model, the iteration method for finite-difference scheme which approximates the elliptic type equations with variable coefficients, was used.

For these reasons, a new model differs from the previous one (1985) in lower permeability of magma body, also in an increased by 1.5 times size of reservoir for considering the possible water recharge from the Kurile lake. The most important parameters for modelling are given below.

The size of reservoir L - 15 km
Heat conductivity λ-$5.0 \cdot 10^{-3}$cal/cm °C s
Volumetric heat capacity C-0.6cal/cm^3°C
Heat capacity of fluid C_0-1.0cal/g cm^3°C
Thermal expansion of fluid α -10^{-3} °C^{-1}
Average infiltration in recharge area $\frac{\partial \psi_0(x)}{\partial x}$ -3-13 kg/s km^2
The modelling time t_1 - 15000 yrs
The size of magma body S - 29 km^2
Initial magma body temperature T_2 - 700°C
Reservoir permeability K - 0.015 m/day
Magma body permeability K_u- 0.0015 m/day
Nondimensional parameters Ra= $\frac{K L \alpha T_2 C_0}{\lambda}$ =3000 Fo= $\frac{t_1 \lambda}{c L^2}$ =$1.76 \cdot 10^{-3}$
Inf= $\frac{\varphi}{\lambda}$ max $\psi_0(x_1) - \psi_0(x_2)$=50-200
Fe=S/L^2=0.13

The action of the hydrodynamic model is expressed, as in the 1985 model, as a succession of temperature and hydrodynamic fields (stream function) corresponding to different periods of time which have passed from the moment of the origin of magma body (Fig.5).

Before the emergence of magma body ($t<0$) the temperature increases linearly with depth in accordance with gradient G=0.02 °C/m. The ground water flow conditions in the considered permeable zone are defined by recharge in the right part of the model which imitates the eastern flank of the Kambalny Ridge and areas adjacent from the east, and by discharge in the left part of the model imitating the valley of the Pauzhetka river (see Figs.5.1, 5.2).

Then, when t=0, we consider that the intrusion of heat body occurs which imitates the impulse of magmatic activity in Holocene-Upper Pleistocene (see Figs. 5.3, 5.4).

However, the convective cells evolve with difficulty (as distinct from the variant considered earlier) because of the existence of a large impermeable zone, i.e. a hot magma body with low filtrational properties. Nevertheless, heat is extracted from this magma body rather intensively owing to washing of its surface by infiltrational flows. In addition, a small part (~10%) of meteoric waters penetrates to the magma body. As a result, a hot water flow forms; with time it approaches the surface (see Figs.5.5, 5.6, 5.7, 5.8).

To obtain the more reliable model parameters, data on temperature distribution in the interior of the Pauzhetka hydrothermal system and on its surface heat discharge were used. Values of the size of magma body, reservoir permeability and water feeding in the recharge areas were selected so as to reach the agreement between the observed and calculated thermohydrodynamic fields (see Fig.5.9).

Besides, in terms of this model we can find a more clear explanation to the fact that the isotopic composition of thermal waters in the discharge area becomes heavier. This is due to throughmagmatic filtration of meteoric waters.

It is worthy of note that if our conceptual model of the Pauzhetka hydrothermal system is true (see Fig.5.10), then some time later we must find the higher contents of tritium in the ascending high-temperature water flow (see Fig.4). If the water with the anomalous content of tritium penetrated to the system from the recharge area 25 years ago and if we take the average

length of the way of filtration to be 15 km and the average rate of filtration $1.3 \cdot 10^{-8}$ m/s, then when the effective porosity is 0.01-0.001, the tritium water must emerge in the discharge area 400-40 years later, respectively. Anyhow, inasmuch as we cannot find tritium now, then the effective porosity of the reservoir is not less than 0.001.

CONCLUSION

As a result of hydroisotopic studies, the numerical thermohydrodynamic model-1985 of the Pauzhetka hydrothermal system was revised. In this connection, the mechanism of the final phase of evolution of the Pauzhetka hydrothermal system may be as follows.
I. The emergence of a hot magma body occurred 15000 yrs ago. II. The thermal interaction between the relatively impermeable magma (intrusive) body and permeable water saturated rocks is manifested in washing of the hot magma body by water flows with insignificant penetration of the latter into the magma body. III. The formation of the ascending hot water flow is caused by gradual cooling of the magma body.

In further investigations it is necessary to improve understanding of the interaction between the magma body and water saturated rocks since this mechanism determines the efficiency of heat extraction from high-temperature hydrothermal systems connected directly with the magma chambers.

REFERENCES

Belousov, V.I., Sugrobov,V.M. and Sugrobova,N.G., 1976. Geological structure and hydrogeological peculiarities of the Pauzhetka hydrothermal system. In: Hydrothermal Systems and Thermal Fields of Kamchatka. Vladivostok,p.23-57 (in Russian).

Kiryukhin,A.V. and Sugrobov,V.M.,1985. On the conditions of water and heat feeding of the Pauzhetka hydrothermal system (S.Kamchatka,USSR). Proc. 10th Geothermal Eng.Workshop, p.57-64.

Kononov,V.I. and Polyak,B.G., 1982. The problem of finding the juvenile component in recent hydrothermal systems.Geokhimiya, No.2, p.163-178 (in Russian).

Matsuo,S., Kusanabe,M., Niwano,M., Hirano,T. and Oki,Y., 1985. Origin of thermal waters from the Hakone geothermal system, Japan. Geochemical Journal, v.19, p.27-44.

Pauzhetka Hot Waters in Kamchatka, 1965, Moscow, 205 pp. (in Russian).

Sakai,H. and Matsubaya,O., 1976.Stable isotopic studies of Japanese geothermal systems. Geothermics, v.5, p.97-125.

Serezhnikov,A.I. and Seletsky,Yu.B., 1982. Deuterium, O^{18} and tritium in thermal waters of South Kamchatka. Geokhimiya, No.2, p.178-192 (in Russian).

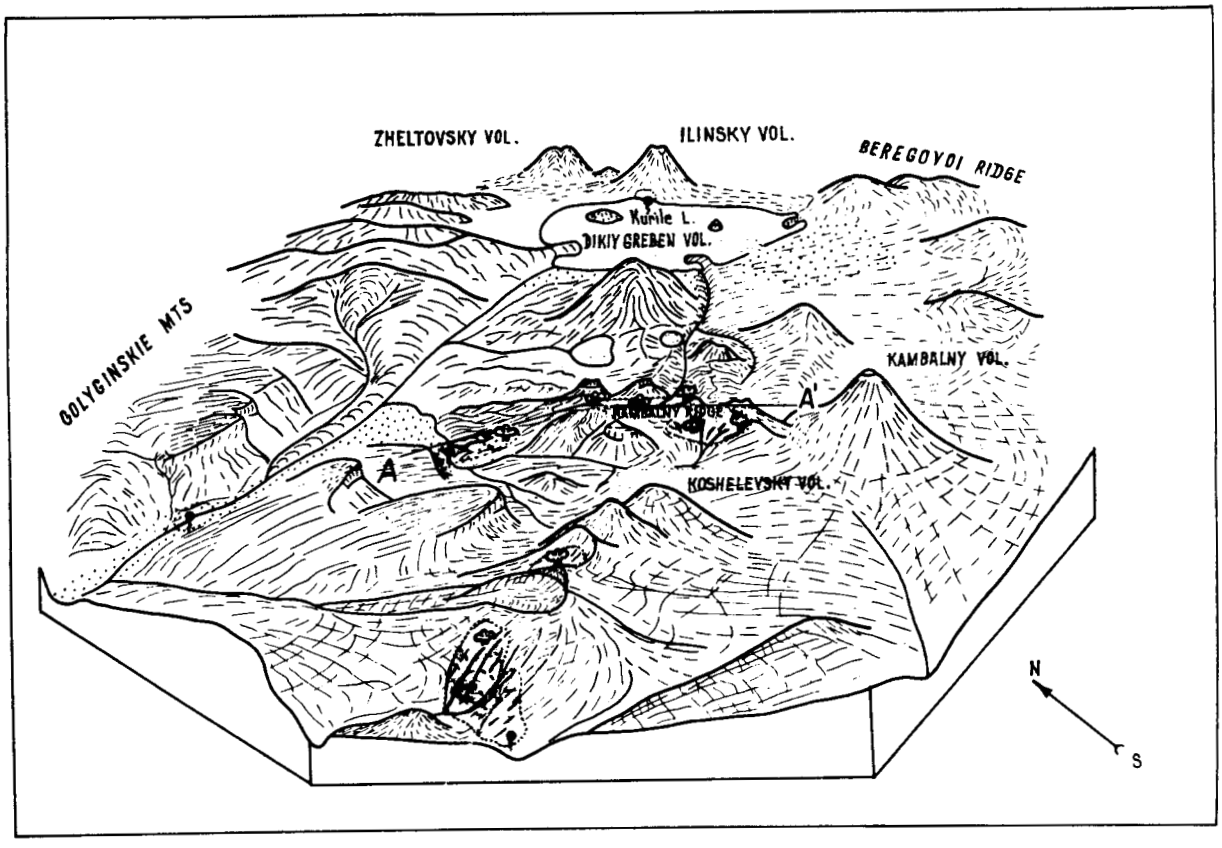

Fig.1. The block scheme of the Pauzhetka hydrothermal system.

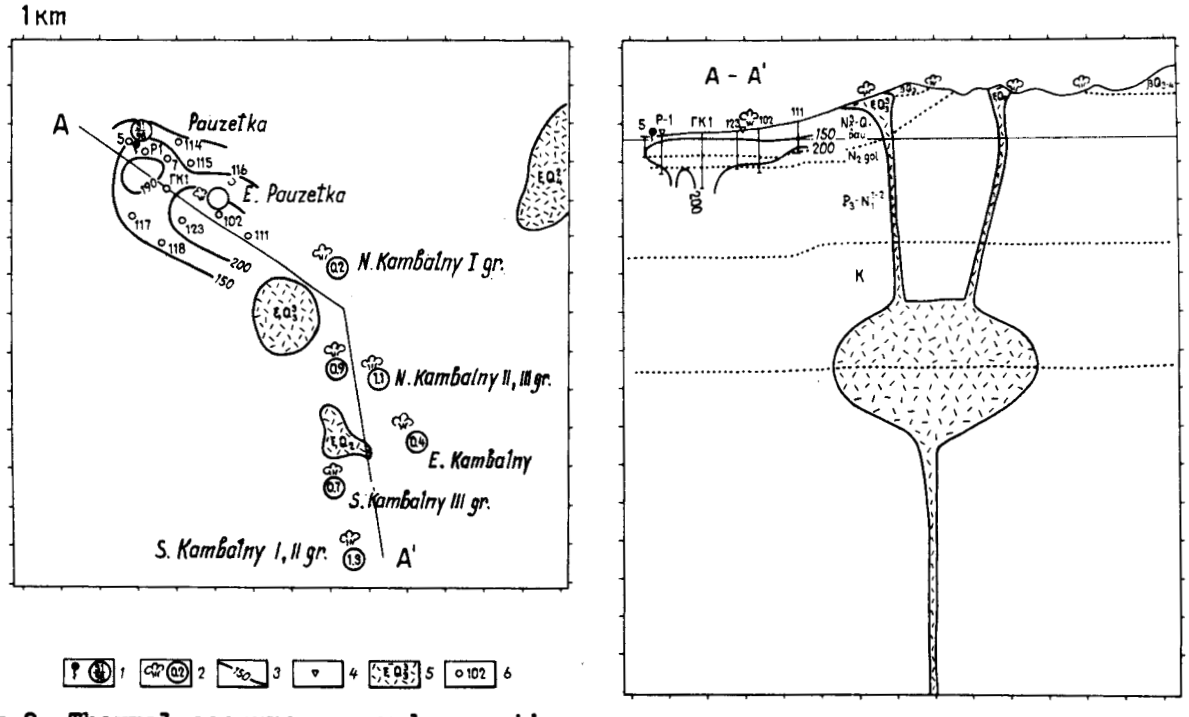

Fig.2. Thermal occurrences and magmatic activity within the Pauzhetka hydrothermal system: 1 - hot springs, the numerator denotes the discharge, kg/s, and the denominator denotes the temperature °C; 2 - steam grounds, heat capacity 10^3 kcal/s; 3 - geoisotherms; 4 - piezometric levels of thermal waters; 5 - acid extrusions; 6 - wells.

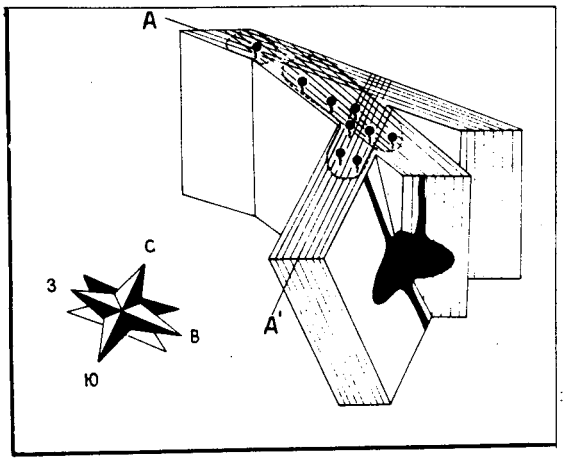

Fig.3. Geometry of the reservoir (cross section from Fig.1).

Fig.4. Hydroisotopic composition of thermal and meteoric waters within the Pauzhetka hydrothermal system (O^{18} and D were determined by V.A.Polyakov and T was determined by V.V.Romanov): a) deuterium and ^{18}O; 1 - data obtained by Serezhnikov and Seletsky (1982) from wells; 2 - data obtained by the authors from wells (sampling in 1983); 3 - cold waters from the Kambalny Ridge (sampling in 1983); 4 - water from the Kurile Lake,

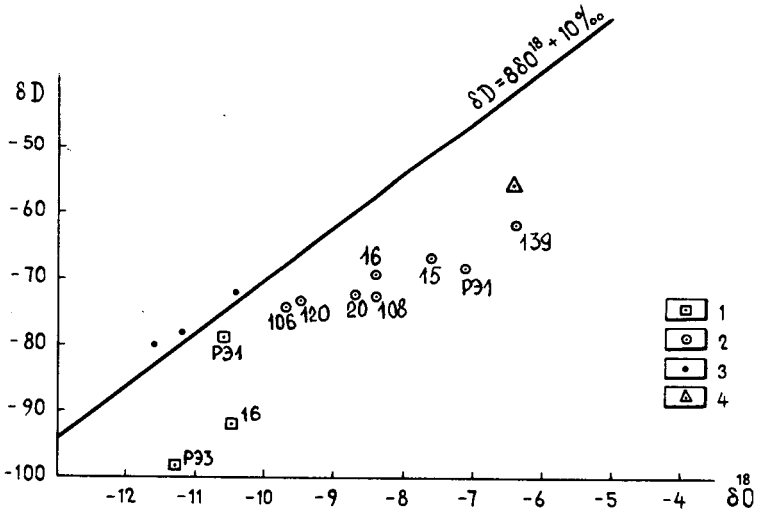

depth 300 m (sampling in 1983); b) the tritium concentration (in T.U.); 1 - well numbers are shown to the right of the circle, to the left- the numerator denotes the T concentration in 1981 and the denominator denotes the T.concentration in 1983; 2 - tritium isolines.

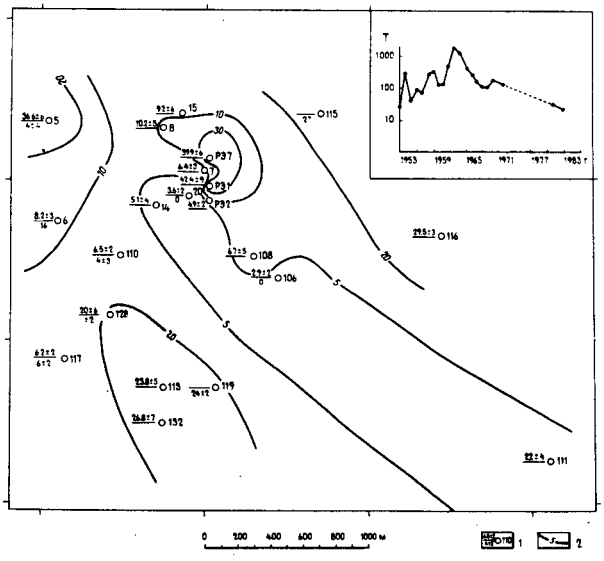

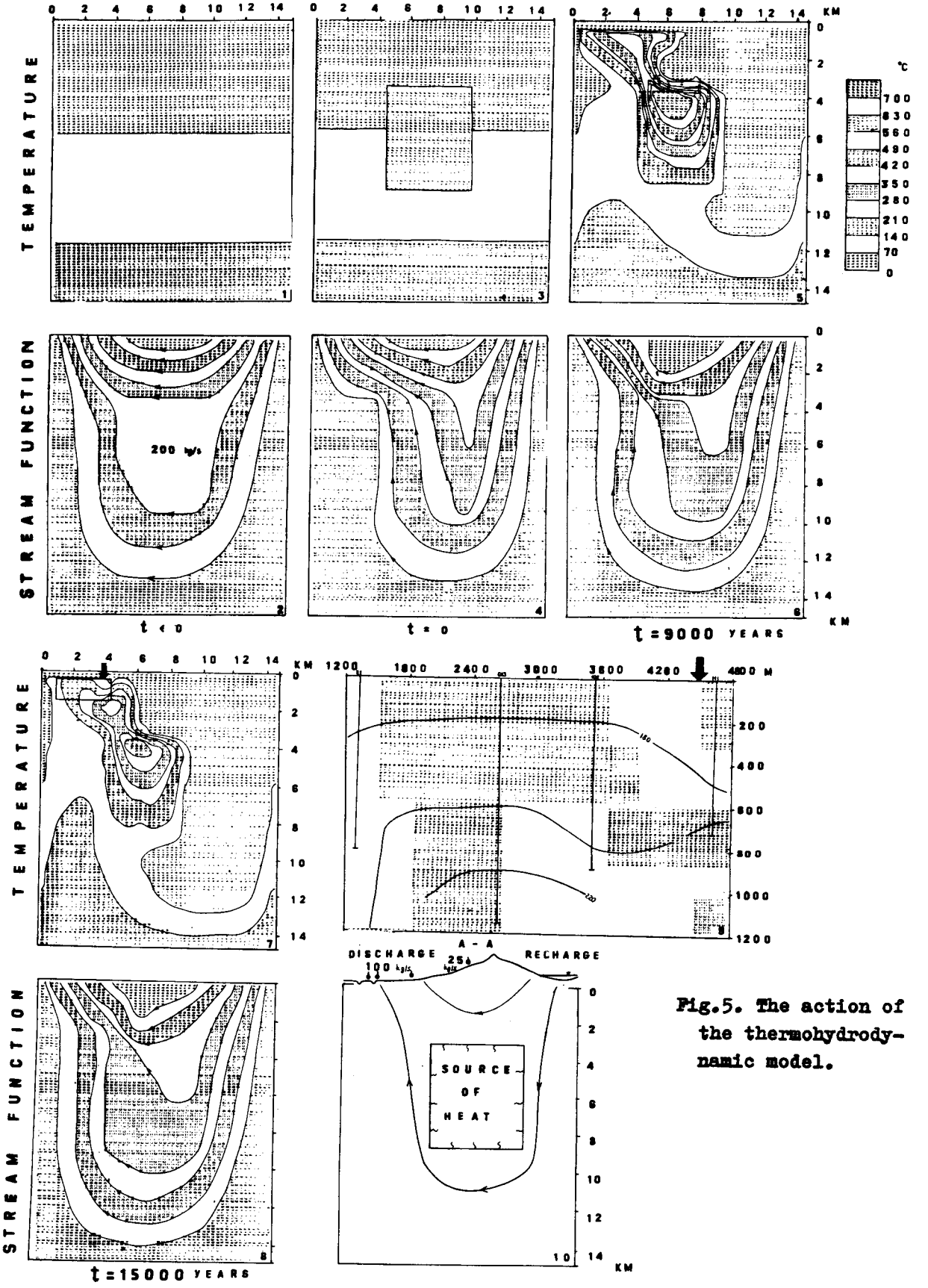

Fig.5. The action of the thermohydrodynamic model.

PROCEEDINGS, Eleventh Workshop on Geothermal Reservoir Engineering
Stanford University, Stanford, California, January 21-23, 1986
SGP-TR-93

PRESSURE PROFILES IN TWO-PHASE GEOTHERMAL WELLS: COMPARISON OF FIELD DATA AND MODEL CALCULATIONS

A.K. Ambastha and J.S. Gudmundsson

Petroleum Engineering Department, Stanford University

Abstract

Increased confidence in the predictive power of two-phase correlations is a vital part of wellbore deliverability and deposition studies for geothermal wells. Previously, the Orkiszewski (1967) set of correlations has been recommended by many investigators to analyze geothermal wellbore performance. In this study, we use measured flowing pressure profile data from ten geothermal wells around the world, covering a wide range of flowrate, fluid enthalpy, wellhead pressure and well depth. We compare measured and calculated pressure profiles using the Orkiszewski (1967) correlations.

Introduction

Two-phase steam/water flow occurs in geothermal reservoirs, wellbores, and surface pipelines. The production of steam/water mixtures depends on how the reservoir, wellbore, and surface facilities operate in series. It means that the overall performance of the system can be dominated by poor performance by any of its components. Improved understanding of the system components, therefore, may lead to better production methods for geothermal resources of the liquid- and boiling-dominated type. In this paper we consider the wellbore part of the system.

A feature common to previous studies of geothermal wellbore flow, is that several two-phase flow correlations are compared to a single or few data sets, and the best-fit correlation identified. A limitation of this approach is that a particular correlation can be matched to a single set of flowing data by adjusting a number of parameters. This leaves open the question of generalizability; that is, the application of the best-fit wellbore model to other geothermal wells. It may also not be clear what wellbore correlations to use for predictive purposes. Furthermore, the several-models and single-data-set approach may hide what aspects of modeling and measurements would benefit from research and development. In this paper we address the issue of generalizability by adopting an approach of a single-model and several-data-sets.

The Orkiszewski (1967) wellbore correlations and simulator used in our work are discussed in a companion paper (Ambastha and Gudmundsson, 1986). A related paper is that of Gudmundsson *et al.* (1984).

Field Data

Flowing pressure and temperature profiles from 10 geothermal wells were collected for the purpose of our study. The wells are in 6 countries: the United States, Mexico, New Zealand, the Philippines, Iceland, and Italy. The discharge data for these wells are shown in Table 1. The total flowrate ranges from 12.9 kg/s to 68.6 kg/s; the mixture enthalpy from 965 kJ/kg to 1966 kJ/kg (corresponding to liquid water at 225°C and up); wellhead pressure from 2.3 bar-g to 56.5 bar-g (245 kPa to 6027 kPa); well depth from 913 m to 2600 m. The wellbore diameter is also given in Table 1, the nominal casing size near the surface ranging from 7-5/8" to 9-5/8". We were not able to compile the chemical data (dissolved solids and non-condensible gas content) for the wells.

Flowing data for wells Cerro Prieto 90, East Mesa 6-1, and Utah State 14-2 are given by Ortiz-R. (1983), who in turn obtained the data from Castaneda (1983), Fandriana *et al.* (1981), and Butz and Plooster (1979), respectively. The different sources of the same data sets are listed here to assist investigators in further studies. The data for well East Mesa 6-1 has been used in several studies; for example, Gould (1974), Nathenson (1974), and Juprasert and Sanyal (1977). The original East Mesa reference is that of Lundberg (1973). A reference for the Roosevelt Hot Springs well Utah State 14-2 data is that of Butz and Mickley (1982). Flowing data for well Cerro Prieto 91 was obtained from Ryley and Parker (1982), who in turn used a paper by Goyal *et al.* (1980). The Ryley and Parker (1982) paper was also the source for the data for Krafla 9 in Iceland. The data for well Okoy 7 in the Philippines were taken from a report by Catigtig (1983). A paper authored by Chierici *et al.* (1981) provided the data for the Italian well Mofete 2. Information on well HGP-A in Hawaii was taken from Kihara *et al.* (1977) and Yuen *et al.* (1978). The New Zealand data on well Ngawha 11 was provided by Bixley (1984); the Mexican data on well Los Azufres 18 was provided by Molinar (1985). More wellbore profile data are found in Upadhyay *et al.* (1977), Barelli *et al.* (1982), Butz and Mickley (1982), and Wilson (1984).

Wellbore Simulation

The pressure and temperature profiles for the 10 wells, respectively, are shown in Figure 1 and Figure 2. However, well Utah State 14-2 had no temperature profile data. Using the data in Table 1, we used the Orkiszewski-based simulator discussed in the companion paper (Ambastha and Gudmundsson, 1986), to calculate the flowing profiles. All calculations were done from the surface to well bottom. The matches we obtained with the measured profiles ranged from good to not-so-good. It is not possible to show all the matches in this paper. Instead, we determined the average pressure gradient in the first 500 m

Table 1. Data used to calculate pressure and temperature profiles from wellhead to bottom

Well	Total Flowrate kg/s	Mixture Enthalpy kJ/kg	Wellhead Pressure bar-g	Wellbore String Design	Total Depth m
A-- Cerro Prieto 90	45	1343	40.7	0.5808 ft from 0-bottom	1299
B--Los Azufres 18	26.7	1607	30.0	0.7296 ft from 0-959 m 0.5153 ft from 959 m-bottom	1324
C--Ngawha 11	68.6	965	19.8	0.652 ft from 0-673.5 m 0.4934 ft from 673.5 m-bottom	950
D--Okoy 7	13.2	1403	46.5	0.7251 ft from 0-1308 m 0.523 ft from 1308 m-bottom	2600
E--Cerro Prieto 91	34.2	1372	56.5	0.5361 ft from 0-1942 m 0.3370 ft from 1942 m-bottom	2294
F--Mofete 2	16.4	1834	3.5	0.7283 ft from 0.1272 m 0.5118 ft from 1272 m-bottom	1989
G--HGP-A	13.9	1966	3.2	0.802 ft from 0-680 m 0.5833 ft from 680 m-bottom	1966
H--East Mesa 6-1	12.9	1197*	2.3	0.7267 ft from 0-bottom	2134
I--Krafla 9	25	1532*	16.3	0.7297 ft from 0-1053 m 0.5856 ft from 1053 m-bottom	1251
J--Utah State 14-2	40.9	1648*	26.7	0.7433 ft from 0-bottom	913

* --- Based on measured bottom-hole temperature

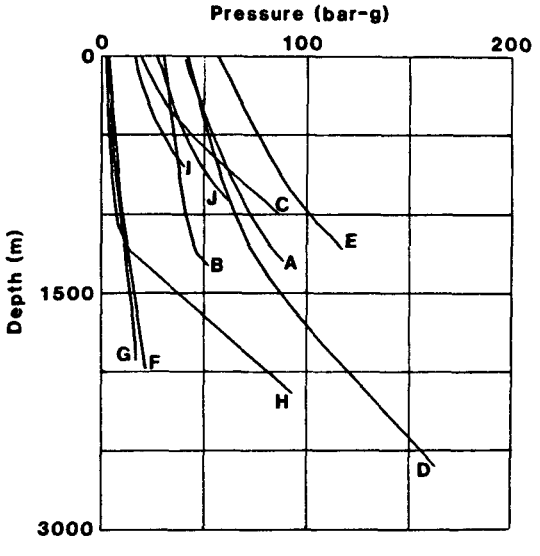

Figure 1. Measured pressure profiles.

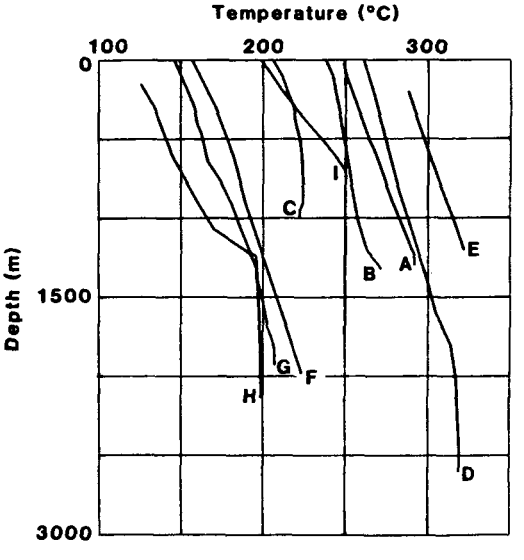

Figure 2. Measured temperature profiles.

Table 2. Values representing two-phase nature of flow at/near wellhead

Well	Total Mass Flux kg/s-m^2	Quality at Wellhead	Steam Mass Flux kg/s-m^2	Wellhead Pressure bar-g	Measured Pressure Gradient bar/m	Calculated Pressure Gradient bar/m	Ratio
A--Cerro Prieto 90	1830	0.15	275	40.7	0.0275	0.0275	1.00
B--Los Azufres 18	687	0.33	227	30.0	0.0104	0.0088	0.85
C--Ngawha 11	2211	0.025	55	19.0	0.0494	0.0770	1.56
D--Okoy 7	344	0.16	55	46.5	0.0207	0.0220	1.06
E--Cerro Prieto 91	1630	0.11	179	56.5	0.0398	0.0333	0.84
F--Mofete 2	424	0.57	242	3.5	0.0064	0.0071	1.11
G--HGP-A	296	0.63	187	3.2	0.0042	0.0049	1.17
H--East Mesa 6-1	335	0.14	47	1.5	0.0030	0.0060	2.00
I--Krafla 9	644	0.08	52	20.9	0.0274	0.0117	0.42
J--Utah State 14-2	1015	0.08	83	30.6	0.0275	0.0192	0.70

of each well (from the wellhead and 500 m down) and compared the measured and calculated values. These values are shown in Table 2 for the 10 wells. Also given is the ratio of the calculated and measured pressure gradients. A pressure gradient ratio of unity indicates a good match; a gradient ratio less than unity means that the measured is greater than the calculated; a gradient ratio greater than unity means that the calculated pressure gradient is greater. Our visual inspection of the measured and calculated profiles suggested that the matches were reasonable when the calculated pressure gradient was within about 20 percent of the measured gradient. This means that not-so-good matches were obtained for wells Ngawha 11, East Mesa 6-1, Utah State 14-2 and Krafla 9. Well Cerro Prieto 90 gave a good match, and other wells reasonable matches. Well Okoy 7 was a special case. The calculated and measured pressure gradients near the wellhead were similar, but diverged with depth.

We looked at the quality of matches by estimating mean and standard deviation of error and percent error, as follows:

$$e_i = p_{calc} - p_{meas} \tag{1}$$

$$d_i = \frac{p_{calc} - p_{meas}}{p_{meas}} \times 100 \tag{2}$$

where p_{calc} and p_{meas} are calculated and measured pressures at any point respectively.

$$\bar{e} = \frac{\sum_{i=1}^{n} e_i}{n} \tag{3}$$

$$\sigma_e = \left[\frac{\sum_{i=1}^{n}(e_i - \bar{e})^2}{n-1}\right]^{1/2} \tag{4}$$

$$\bar{d} = \frac{\sum_{i=1}^{n} d_i}{n} \tag{5}$$

$$\sigma_d = \left[\frac{\sum_{i=1}^{n}(d_i - \bar{d})^2}{n-1}\right]^{1/2} \tag{6}$$

where e_i is the error, $\bar{e}$ is arithmetic mean error, σ_e is the standard deviation about $\bar{e}$, and n is the number of data points. Similarly, d_i is the percent error, $\bar{d}$ is mean percent error, and σ_d is the standard deviation about $\bar{d}$. Such statistical parameters have been used before to evaluate the accuracies of two-phase correlations (Vohra *et al.*, 1975). Results of our calculations are summarized in Table 3. For a good match, we should have a low mean and standard deviation. Looking at the mean and standard deviation of error, we find that Ngawha 11, Okoy 7, East Mesa 6-1, Krafla 9 and Utah State 14-2 fall in the category of not-so-good matches. Similar conclusion is drawn by looking at the columns of mean percent error and standard deviation of percent error, except that now it seems that Mofete 2 and HGP-A are also not-so-good matches. But these two wells are low pressure wells and hence small deviation in calculated pressure gets magnified when we calculate percent error. So mean and standard deviation of percent error is not necessarily a good way to determine the quality of matches in low pressure cases. Thus three different criteria to determine the quality of matches suggest that we have not-so-good matches for 5 wells.

The Cerro Prieto 90 , Ngawha 11 (ratio greater than unity), and Krafla 9 (ratio less than unity) pressure profiles are shown in Figures 3, 4, and 5, respectively. They demonstrate the range of results obtained in our work. All the wellbore calculations reported here were done assuming no heat transfer to/from the formation; the absolute casing

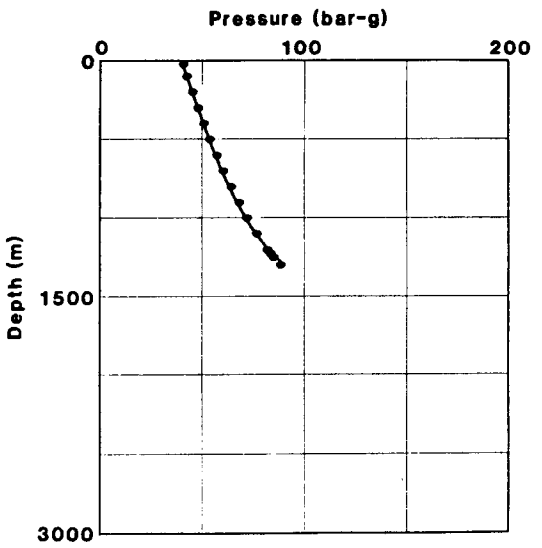

Figure 3. Pressure profile match for well Cerro Prieto 90.

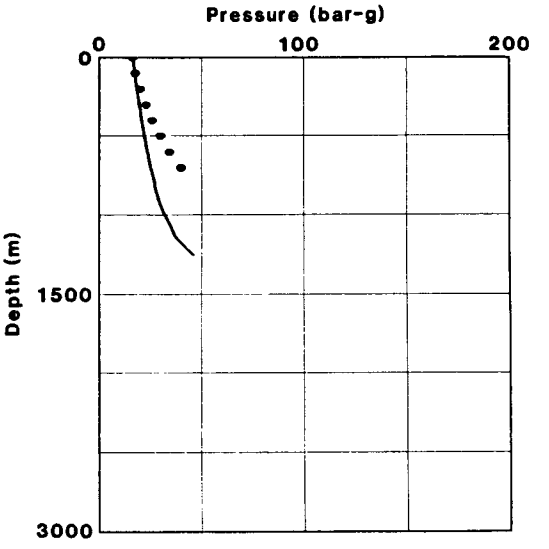

Figure 5. Pressure profile match for Krafla 9.

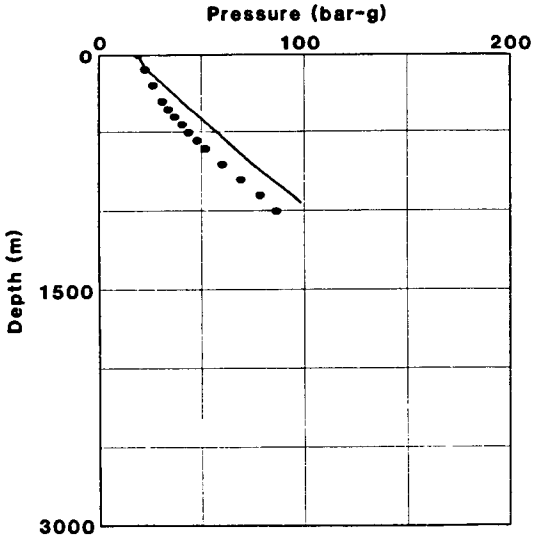

Figure 4. Pressure profile match for well Ngawha 11.

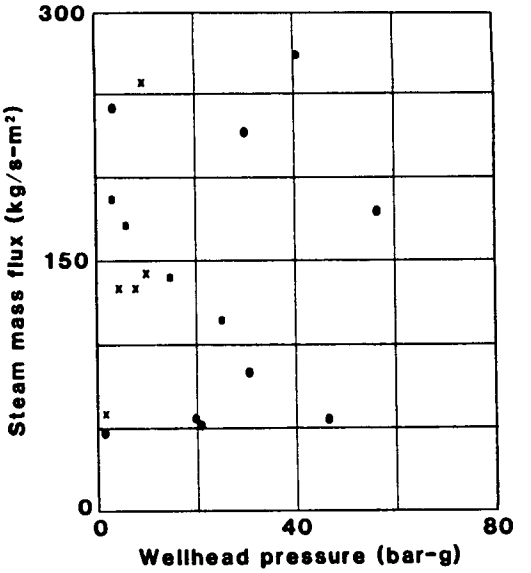

Figure 6. Steam mass flux vs. wellhead pressure

roughness used throughout was 0.0006 feet; the wellbore was divided into about 50 segments in most cases. The effects of noncondensible gases and dissolved solids were not considered.

We think that the Orkiszewski (1967) method performs as well as any other method for geothermal wellbore flow; that is, the method seems to have general applicability. What we would like to know also, is under what conditions it performs best, and under what conditions it should not be expected to give good results. We looked at the 10 matches of calculated and measured profiles, and tried to group the good and not-so-good wells using two-phase flow related criteria such as mass flux, void fraction, and pressure. We found that by plotting the "steam mass flux at the wellhead" against "wellhead pressure," the wells exhibiting not-so-good matches formed a group away from the better matched wells. This result is shown in Figure 6. The values used to draw this figure are given in Table 2. The rationale for Figure 6 are these: (1) the steam mass flux represents the dryness or void fraction of the flow, arbitrarily taken at the wellhead; (2) the wellhead pressure correlates the physical properties of steam and water.

There are more points in Figure 6 than are given in Table 2. Nine of the wells in Table 2 are represented by circles in Figure 6. The well not shown by a circle is HGP-A in Hawaii; it is represented by stars. There are four stars in Figure 6. The highest flowrate one is that given in Table 2. The other three are lower flowrate profiles that we also matched using the wellbore simulator. The five crosses in Figure 6 are data points from a paper by Upadhyay *et al.* (1977), from wells in the Philippines

Table 3. Comparison of measured and calculated pressure profiles

Well	Data Points	Measured Pressure Range, bar-g	Mean Error bar-g	Standard Deviation of Error, bar-g	Mean Percent Error	Standard Deviation of Percent Error
A--Cerro Prieto 90	16	40.9-88.5	-0.3	0.8	-0.6	1.1
B--Los Azufres 18	18	30.0-52.1	-1.1	1.2	-2.65	2.2
C--Ngawha 11	14	19.0-86.3	10.8	5.1	22.8	10.4
D--Okoy 7	14	41.7-162.9	5.3	4.1	5.1	3.9
E--Cerro Prieto 91	13	56.5-117.0	-0.15	2.6	-0.66	2.9
F--Mofete 2	5	3.5-21.5	0.4	0.4	4.9	5.7
G--HGP-A	17	3.2-16.7	0.6	0.4	6.1	2.7
H--East Mesa 6-1	15	2.3-92.9	11.0	9.4	59.5	53.2
I--Krafla 9	8	16.3-40.0	-5.5	5.4	-17.5	13.8
J--Utah State 14-2	30	27.0-61.6	-6.7	4.6	-13.6	6.9

and the United States. Upadhyay *et al.* (1977) stated that reasonable matches were obtained when comparing measured profiles to calculated profiles using a wellbore simulator based on Orkiszewski's (1967) correlations. The total flowrate of these two-phase wells ranged from 3 kg/s to 11 kg/s. It appears from Figure 6 that the Orkiszewski (1967) correlations do not work as well when the steam mass flux is below 100 kg/s-m^2.

Discussion

In general, the Orkiszewski (1967) correlations work well for different geothermal wellbore flow situations. The mean percent errors for Ngawha 11, East Mesa 6-1, Krafla 9 and Utah State 14-2, however, were larger than 10%. Ngawha 11 has 1.4% of noncondensible gas in the total flow. This may be the reason for the bad match, because the wellbore simulator does not consider the effect of noncondensible gases.

Krafla 9 is said to have wellbore deposition problems which reduces the effective area open to flow in the wellbore and this could be the reason for the bad match. If we reduce the wellbore string diameter, we will have larger pressure drop and can match the measured pressure profile. We are not aware of any problems with well Utah State 14-2, so we can not propose a reason for the not-so-good match in this case.

East Mesa 6-1 is a special case. The mean percent error and standard deviation about mean percent error for East Mesa 6-1 were unusually large. This match is shown in Figure 7. We see that calculated pressure profile is displaced away from the measured pressure profile by a constant positive pressure in single-phase section of the wellbore. This means that the predicted depth of flashing is higher up in the wellbore than the actual depth of flashing. The calculated depth of flashing is highly dependent on the fluid enthalpy value used. Thus fluid enthalpy is an important parameter which determines the depth of flashing and hence the quality of match.

Conclusions

The Orkiszewski (1967) correlations have been used to compare the measured and calculated pressure profiles from ten wells that cover a wide range of flowrate, fluid enthalpy, wellhead pressure and well depth. We conclude

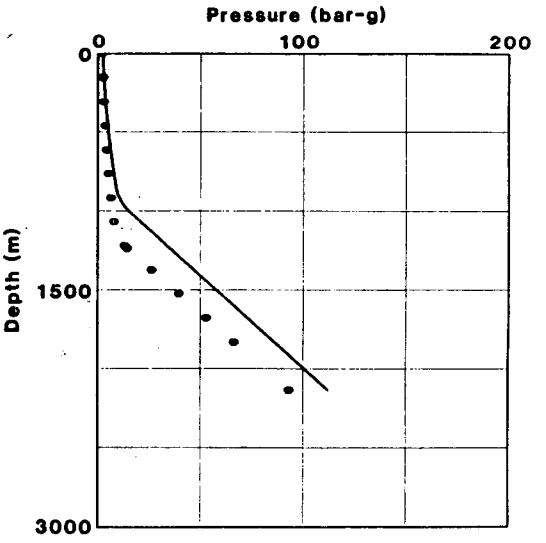

Figure 7. Pressure profile match for well East Mesa 6-1.

the following:

1. The Orkiszewski (1967) correlations seem to have general applicability for geothermal wellbore flow, and work well under a variety of situations.
2. Good matches between the calculated and measured pressure profiles were obtained using the correlations if the steam mass flux is larger than 100 kg/s-m^2.
3. Gas content and fluid enthalpy are important parameters in determining the depth of flashing and hence the agreement between calculated and measured pressure profiles.

Acknowledgments

This work was supported by the Stanford Geothermal Program, through contract DE-AT03-80SF11459 with the U.S. Department of Energy. This work was carried out in cooperation with CFE in Mexico, METU in Turkey, and MWD in New Zealand.

References

Ambastha, A.K. and Gudmundsson, J.S.:"Geothermal Two-Phase Wellbore Flow: Preesure Drop Correlations and Flow Pattern Transitions," Proc., 11th Workshop on Geothermal Reservoir Engineering, Stanford Univ., Stanford, CA (Jan. 21-23, 1986).

Barelli, A., Corsi, R., Delpizzo, G. and Scali, C.:"A Two-Phase Flow Model for Geothermal Wells in Presence of Non-condensable Gases," Geothermics, Vol. 11, No. 3 (1982) 175-191.

Bixley, P.F.:"Personal Communication" (1984).

Butz, J. and Mickley, M.C.:"Theoritical and Experimental Research on Two-Phase Flow in Geothermal Wells," Denver Research Institute, Report DOE/ET/27141-3 (DE82011702), U. of Denver, Denver, CO, (1982).

Butz, J. and Plooster, M.:"Subsurface Investigations at the Roosevelt Hot Springs, Utah, KGRA," Report DOE/ET/28389-1 (Oct. 1979).

Castaneda, M.:"Personal Communication" (1983).

Catigtig. D.C.:"Boreflow Simulation and its Application to Geothermal Well Analysis and Reservoir Assessment," Report 1983-8, UNU Geothermal Training Programme, Reykjavik, Iceland, (1983).

Chierici, G.L., Giannone, G., Sclocchi, G. and Terzi, L.:"A Wellbore Model for Two-Phase Flow in Geothermal Reservoirs," SPE of AIME, Paper SPE 10315, Presented at 56th Annual Fall Tech. Conf. and Exhibition, San Antonio, TX (Oct. 5-7, 1981).

Fandriana, L., Sanyal, S.K. and Ramey, H.J., Jr.:"A Numerical Simulator for Heat and Fluid Flow in a Geothermal Well," Pet. Eng. Dept., Stanford U., Stanford, CA (1981).

Gould, T.L.:"Vertical Two-Phase Steam-Water Flow in Geothermal Wells," J. Pet. Tech. (Aug. 1974) 833-842.

Goyal, K.P., Miller, C.P. and Lippman, M.J.:"Effect of Measured Wellhead Parameters and Well Scaling on the Computed Downhole Conditions in Cerro Prieto Wells," Proc., Sixth Workshop on Geothermal Reservoir Engineering, Stanford Univ.,Stanford, CA (Dec. 1980) 130-138.

Gudmundsson, J.S., Ortiz-R., J., and Granados, E.E.:"Two-Phase Flow and Calcite Deposition in Geothermal Wells," SPE of AIME, SPE Paper 12741, Presented at California Regional Meeting, Long Beach (April 11-13, 1984).

Juprasert, S. and Sanyal. S.K.:"A Numerical Simulator for Flow in Geothermal Wellbores," Trans., Geothermal Resources Council, Vol. 1 (1977) 159-161.

Kihara, D., Chen, B., Yuen, P. and Takahashi, P.:"Summary of Results of HGP-A Well Testing," Proc., Third Workshop on Geothermal Reservoir Engineering, Stanford Geothermal Program, Report SGP-TR-25, (1977) 138-144.

Lundberg, E.A.:"Geothermal Resource Investigations: Special Report on Test Well Mesa 6-1," U.S. Bureau of Reclamation, (Feb. 1973).

Molinar-C. R.:" Personal Communication" (1985).

Nathenson, M.:"Flashing Flow in Hot-Water Geothermal Wells," J. Research U.S. Geological Survey (Nov.- Dec. 1974) 743-751.

Orkiszewski, J.:"Predicting Two-Phase Pressure Drops in Vertical Pipe," J. Pet. Tech. (June 1967) 829-838.

Ortiz-R., J.: "Two-Phase Flow in Geothermal Wells: Development and Uses of a Computer Code," Stanford Geothermal Program, Report SGP-TR-66 (June 1983).

Ryley, D.J. and Parker, G.J.:"Flowing Geothermal Wells: Cerro Prieto Well M-91 and Krafla Well KJ-9; Computer Analysis Compared with Experimental Data," International Conference on Geothermal Energy, Florence, Italy, Paper C4 (May 11-14, 1982) 187-194.

Upadhyay, R.N., Hartz, J.D., Tomokoria, B.N. and Gulati, M.S.:"Comparison of the Calculated and Observed Pressure Drops in Geothermal Wells Producing Steam-Water Mixtures," SPE of AIME, Paper SPE 6766, 52nd Annual Fall Tech. Conf. and Exhibition, Denver, CO., (Oct. 9-12, 1977).

Vohra, I.R., Hernandez, F., Marcano, N. and Brill, J.P.:"Comparison of Liquid-Holdup and Friction-Factor Correlations for Gas-Liquid Flow," J. Pet. Tech. (May 1975) 564-568.

Wilson, D.J.:"Computer Modeling of Output From Geothermal Wells," Master of Engineering Project Report, Dept. Mech. Eng., University of Canterbury, New Zealand (Feb. 1984).

Yuen, P.C, Chen, B.H., Kihara, D.H., Seki, A.S. and Takahashi, P.K.:"HGP-A Reservoir Engineering," U. of Hawaii, Honolulu, HI (Sept. 1978).

PROCEEDINGS, Eleventh Workshop on Geothermal Reservoir Engineering
Stanford University, Stanford, California, January 21-23, 1986
SGP-TR-93

A FIELD STUDY OF TRACER AND GEOCHEMISTRY BEHAVIOR DURING HYDRAULIC FRACTURING OF A HOT DRY ROCK GEOTHERMAL RESERVOIR

Bruce A. Robinson

Earth and Space Sciences Division
Los Alamos National Laboratory
Los Alamos, NM 87545

ABSTRACT

Tracer and geochemistry measurements in fractured Hot Dry Rock (HDR) geothermal reservoirs are usually performed after a fracture connection has been established and constant, nearly equal inlet and outlet flow rates have been achieved. However, during hydraulic fracturing experiments designed to create a low-impedance fracture connection between two wells, the inlet and outlet flow rates can be dramatically different and can vary during the test, forcing us to revise the common analytical methods for interpreting tracer response curves and geochemistry behavior.

This study presents tracer and geochemistry data from several hydraulic fracturing experiments at the Fenton Hill, NM, HDR geothermal reservoir. Tracers have been injected at various times during these tests: 1) initially, before any flow communication existed between the wells; 2) shortly after a flow connection was established; and 3) after the outlet flow had increased to its steady state value. An idealized flow model consisting of a combination of main fracture flow paths and fluid leakoff into secondary permeability explains the different tracer response curves for these cases, and allows us to predict the fracture volume of the main paths.

The geochemistry during these experiments supports our previously developed models postulating the existence of a high concentration indigenous "pore fluid." Also, the quartz and Na-K-Ca geothermometers have been used successfully to identify the temperatures and depths at which fluid traveled while in the reservoir. The quartz geothermometer is somewhat more reliable because at these high temperatures (about 250°C) the injected fluid can come to equilibrium with quartz in the reservoir. The Na-K-Ca geothermometer relies on obtaining a sample of the indigenous pore fluid, and thus is somewhat susceptible to problems of dilution with the injection fluid.

INTRODUCTION AND BACKGROUND

The hot dry rock geothermal concept currently being developed at the Fenton Hill, NM and Rosemanowes Quarry, Cornwall UK geothermal sites consists of creating a network of high-permeability fractures between two wellbores drilled into hot granite or crystalline basement rock of low inherent permeability (see Figure 1). Water is circulated down one wellbore, through the large volume of hot rock defined by the fracture network, and is collected and brought to the surface as heated, pressurized water to be utilized for electricity generation. The creation and characterization of the downhole fracture network of the Fenton Hill reservoir has been the goal of the Los Alamos HDR project for the past three years. The role of tracers and geochemistry in this effort is reported in the present study.

In previous HDR reservoir studies, tracers and geochemistry have been used extensively in systems which have already been created and steady state circulation established (Tester et al., 1982, Grigsby, 1983, Robinson and Tester, 1984). Tracers are used to measure the fracture volume of both main and secondary flow paths and to estimate the flow split among fractures of various permeabilities (Robinson and Tester, 1984). The tracer modal volume V, the produced fluid volume corresponding to the peak of the tracer response curve, is a good measure of the fracture void volume of the main flow paths. In previously operated reservoirs in which tracer and long-term energy extraction measurements have been made, V can be correlated roughly with the effective heat transfer surface area as determined from produced fluid temperature decline over time. Figure 2 illustrates this correlation. The effective heat transfer surface area is the area of a single fracture which would result in the measured rate of produced fluid cooldown, and thus is obviously a simplification. Nonetheless, the correlation implies that a single measurement of fracture volume using tracers can provide an estimate, subject to uncertainties, of the heat

transfer capacity of an HDR reservoir. Geochemical behavior in these circulating systems can be treated with analytical techniques similar to those of tracer studies. Grigsby (1984) has outlined the theory necessary to evaluate experiments in which the geochemical content of the injected fluid is changed temporarily. The quartz and Na-K-Ca geothermometers have also been used in reservoir evaluation.

Unfortunately, during the hydraulic fracturing of an HDR reservoir, the interpretation of tracer and geochemistry data is much more complex and subject to uncertainty. In the fracturing experiments described below, little or no hydraulic communication existed when pumping began. As a test proceeded, the outlet flow rate increased, and the ratio of fluid produced to fluid stored in the fracture system decreased. Thus the timing of the tracer injection and the inlet and outlet fluid flow rates affect the tracer response in a manner unlike that experienced in the steady state tests. Geochemistry is difficult to interpret as a tracer in these experiments, but the geothermometers are actually more useful in these transient tests for determining temperatures and depths at which fluid is being produced. Fracturing experiments of the so-called Phase II reservoir at Fenton Hill are described below, and tracer and geochemical techniques are developed to evaluate the reservoir fracture system.

THE FENTON HILL PHASE II CAMPAIGN

The Phase II campaign at the Fenton Hill geothermal site is designed to demonstrate the commercial feasibility of the HDR geothermal energy concept. The first reservoirs proved the technical merits of the concept, but the reservoir lifetimes and thermal energy production levels were too small in these prototype systems to be commercially interesting. Figure 3 provides a useful reference for the following description of events. In August 1982, two new wellbores (EE-2 and EE-3) were drilled to a depth of about 3.9 km, with the final 1.4 km inclined at an angle up to 35° from vertical. Several hydraulic fracturing experiments were performed in both wells without achieving the desired flow communication between EE-2 and EE-3. The most important of these was Experiment 2032, in which a total of 21000 m^3 of water was injected in EE-2 at an average flow rate of 0.1 m^3/sec and 48 MPa surface pressure. House et al. (1985) presented an analysis of the microseismic events located during this fracturing experiment, and one perspective of these events are shown in Figure 3.

As evidenced by the seismicity, the injected fluid stimulated a series of fractures which were essentially parallel to the two wellbores, and thus the intersection of the two holes with a network of flowpaths was not possible with this wellbore/fracture geometric configuration. Thus it was decided to redrill the bottom portion of wellbore EE-3 to intersect the 3-dimensional "cloud" of microseismicity located during Experiment 2032. Figure 3 also shows the nearly vertical trajectory of the new section of wellbore called EE-3A.

This redrilling was interrupted and followed by several hydraulic pressurization experiments in the new EE-3A wellbore, two of which were successful in creating the desired fracture flow communication between the two holes. Hydraulic fracturing is almost certainly a misnomer here, as the pumping most likely resulted in restimulation of the existing flowpaths created during Experiment 2032 described above. However, after several years of fluid diffusion away from this stimulated zone, the joints required more pressurization to increase their hydraulic conductivity. This was done using a newly designed openhole packer, which allowed specific intervals of wellbore EE-3A to be pressurized independently. Another essential reason for the openhole packer is the existence in the openhole region at 3.1 km (10250 ft) of a high-permeability zone which accepts large amounts of fluid at low pressures. This zone is not connected to EE-2, and eliminates any attempt to pump fluid into the formation at lower depths without a packer.

There are four packer flow stimulation tests for which there are tracer and/or geochemistry data of interest. Experiment 2032, the massive hydraulic fracturing experiment in wellbore EE-2, was described earlier. Experiment 2059 was the first successful attempt in the Phase II reservoir to achieve hydraulic communication between the wells. It was performed with the packer set at a relatively shallow depth in EE-3A. A second stimulation test, Experiment 2061, pressurized a region much deeper in the wellbore, with a much greater separation distance between the injection and target production regions. In this instance hydraulic communication was not established. Finally, Experiment 2062 created a second set of flow paths connecting the wells. The packer was set at an intermediate depth, and after 8 hours of pumping, interwell flow was achieved.

TRACER DATA ANALYSIS

The primary goal of HDR reservoir modeling is to estimate the reservoir heat transfer capacity and thus the potential lifetime of the system. The tracer modal volume $\bar{V}$ has been shown to be useful in this regard when steady state circulation experiments are

performed (Figure 2). Since this volume is best thought of as the fracture volume associated with the main fracture flow paths, this correlation is not surprising: the most direct hydraulic connections are likely to cool most rapidly, and thus control the heat transfer capacity.

When tracer experiments are carried out during the pumping experiments described below, the inlet flow rate was larger than the outlet rate as the hydraulic connection was developed. This net accumulation of water in the reservoir must be accounted for to calculate the volume of the main fracture flow paths. This situation is depicted schematically in Figure 4, which assumes interwell flow through the main joints and fluid leakoff into secondary permeability. Tracer travels through the main fractures most rapidly near the inlet and slows down due to water leakoff with distance or volume until it is traveling at the production flow rate when it leaves the system. The unknown is the main fracture volume (assumed to be the tracer modal volume V), which is found from the following integration:

$$\overset{\circ}{\tau} = \int_0^{\overset{\circ}{V}} \frac{dV}{Q} \qquad (1)$$

$\overset{\circ}{\tau}$ is the measured modal residence time and the independent variable V is the fractional volume of the main paths (0 at the entrance and V at the exit). An expression for $Q = Q(V)$ is needed to derive an analytical expression for V. The simplest possible relation is obtained by assuming a linear decline in flow rate with V, or

$$Q = Q_{in} - \frac{(Q_{in}-Q_{out})V}{\overset{\circ}{V}} \qquad (2)$$

Substituting Eqn. (2) into (1), we obtain, after integration and rearrangement:

$$\overset{\circ}{V} = \frac{\overset{\circ}{\tau}(Q_{in}-Q_{out})}{\ln\left(\frac{Q_{in}}{Q_{out}}\right)} \qquad (3)$$

Perhaps a more realistic representation of the flow rate is obtained by assuming a linear pressure decline along the main fractures, implying that the fractional water loss linearly decreases. Assuming no water loss to the formation at V=V, the appropriate expression for the flow rate for this model is

$$Q = Q_{in} - 2(Q_{out}-Q_{in})\left(\frac{1}{2}\left[\frac{V}{\overset{\circ}{V}}\right]^2 - \frac{V}{\overset{\circ}{V}}\right) \qquad (4)$$

When Eqn. (4) is substituted into Eqn. (1), the resulting expression for V is

$$\overset{\circ}{V} = \frac{-\overset{\circ}{\tau}\, Q_{out}(Q_{in}-Q_{out})}{\tan^{-1}\left(-\sqrt{\frac{Q_{in}-Q_{out}}{Q_{out}}}\right)} \qquad (5)$$

Equations (3) and (5) will be used to evaluate two of the tracer experiments below.

Experiment 2059: This experiment was the first fracturing test in the Phase II reservoir which resulted in a successful connection between the wells. To prove that the vent fluid at EF-2 was indeed caused by fluid injected at EE-3, 1 kg of sodium fluorescein dye was placed in the injection well before pumping began. Colorimetric measurements of the produced fluid using a UV-visible spectophotometer verified the presence of the dye. Unfortunately, the strategy of placing the tracer in the well before pumping began made the extraction of quantitative information about the reservoir nearly impossible. After the production well had vented the entire wellbore volume, tracer immediately appeared in the fluid, suggesting that the tracer front had traversed the entire wellbore separation distance before venting began. Given this situation, it is difficult to estimate the tracer transit time $\overset{\circ}{\tau}$ to use in Eqns. (3) and (5).

The only reliable quantitative information from this tracer test is the total mass of tracer collected during the vent. In this test 32% of the tracer injected into EE-3 was collected at EE-2, compared to an expected maximum of 47%, which is the ratio of the water volume vented to the amount injected. This recovery (68% of the expected maximum) seems quite high, especially since the reservoir was not a closed, confined system with limited boundaries during the test. Thus the data suggest that a short-circuiting flow path probably exists between the wells, allowing most of the injected tracer to reach the production wellbore rapidly. Since a commercially viable hot dry rock reservoir requires a sweep of fluid through a large rock volume, this direct interwell connection is not an acceptable result, and further hydraulic fracturing experiments were carried out.

Experiment 2062: This test was the second successful attempt to connect wellbores EE-3 and EE-2 with a set of hydraulically stimulated fractures, this time with the injection region at a depth about 150 m deeper in EE-3A. The difficulties in quantitatively analyzing the data of the previous tracer test led to changes in the tracer interrogation strategy for this experiment, with significantly improved results. The foremost rule learned from Experiment 2059 was that tracer should be injected only after a hydraulic connection is achieved. Also, during the tracer test the inlet and outlet flow rates should be kept as constant as possible to minimize unwanted

transients. Two tracer experiments were performed during Experiment 2062. The first was a 0.91 kg (2 lb) sodium fluorescein dye pulse injected early after the production vent began. In the second experiment, after the inlet and outlet flow rates were more nearly equal, three tracers were injected: 0.91 kg (2 lb) sodium fluorescein dye, 113.6 kg (250 lb) sodium bromide, NaBr, and 22.7 kg (50 lb) sodium nitrate, $NaNO_3$. The NaBr and $NaNO_3$ were analyzed for Br^- and NO_3^-, respectively, using an anion chromatograph. Figures 5 and 6 show the tracer responses for these two experiments, with the ordinate corrected for background levels and wellbore residence times, and the concentration is normalized so that the area under the curve would be unity for complete recovery of all injected tracer. Figure 5 compares the normalized response curves for the three tracers injected in the second experiment. Since the peak response for all three tracers occurred simultaneously, all tracers are non-adsorbing to within the limit of measurability. The differences in response curves are most likely due to measurement difficulties at high concentration in the case of the dye, and possible degradation of NO_3^- for the nitrate. Nonetheless, the modal volume V can be accurately determined: based on the produced fluid volume, V is 260 $\pm$20 m^3.

Figure 6 compares the dye tracer responses for the two tracer tests in Experiment 2062. The discrepancy in peak response volumes can be explained using the conceptual reservoir models described earlier. The first test was operated at higher injection and lower outlet flow rate. Using Eqns. (3) and (5) the modal volume estimates for the two experiments are:

Experiment 1:	550 m^3	Eqn. (3)
	371 m^3	Eqn. (5)
Experiment 2:	470 m^3	Eqn. (3)
	388 m^3	Eqn. (5)

For either of the models, the calculated values of V for the two tracer tests agree adequately. However, the choice of the model affects the result, making it difficult to assign a precise value to V. In round numbers, 400 m^3 is our best estimate for modal volume for Experiment 2062. As seen in Figure 2, this volume is larger than that of any fracture system previously created at Fenton Hill. Consequently the reservoir lifetime should be correspondingly higher. Future operations will attempt to enlarge the reservoir still more and increase the hydraulic conductivity between the wells.

GEOCHEMISTRY RESULTS

Geochemistry in the Fenton Hill reservoir is controlled by both active dissolution of minerals and displacement of indigenous pore fluid. In the steady state operational mode, injection of fresh water low in concentration of dissolved ions results in behavior quite similar to an interwell tracer. However, during a hydraulic fracturing experiment, transient effects dominate the early geochemical behavior. When a pressurized, shut-in production well is first opened, a rush of almost pure pore fluid enters the wellbore. As time proceeds and the interwell connection improves, the pore fluid becomes more and more diluted with injection fluid until constant concentrations are reached. This situation, though simple to describe qualitatively, does not provide much information about fracture volume or dispersive characteristics.

Despite this fact, geochemistry in the form of chemical geothermometers provides valuable information about the fluid temperature and hence depth when it resided in the reservoir. This temperature, combined with a background temperature log, yields the depth at which fluid traveled in the fracture system. The two most effective geothermometers for the Fenton Hill HDR reservoirs are the quartz and Na-K-Ca geothermometers, although their application is somewhat different due to the difference in equilibration times, as described below.

Quartz Geothermometer: The solubility of quartz in water is a strong function of temperature, and thus the concentration of silicic acid in a fluid sample can be related to an underground fluid temperature. Rimstidt (1979) compiled the available equilibrium data and obtained the following correlation:

$$C^{\infty} = 6\times10^{4} \times 10^{(1.881-2.028\times10^{-3}T-1560/T)} \quad (6)$$

where C^{∞} is the equilibrium solubility (in ppm) and T the absolute temperature (in K).

The main question of the applicability of this relation resides in the assumption of equilibrium. If injected fluid does not stay in the reservoir long enough to reach equilibrium, erroneously low geothermometer readings will result. The kinetics of quartz dissolution has been studied by many workers (Kitahara, 1960, Van Lier et al., 1960, Siebert et al., 1963, Weill and Fyfe, 1964, Stober, 1967, and Rimstidt, 1979), and the results were reviewed and further experiments performed by Robinson (1982). The accepted rate law in a closed vessel is:

$$\frac{dC}{dt} = ka^*(C^{\infty} - C) \quad (7)$$

where k is the dissolution rate constant (in m/sec) and a* the rock surface area to fluid volume ratio (m^{-1}). Thus $1/ka^*$ is a characteristic reaction time, and equilibrium may be safely assumed for downhole fluid residence time greater than three times this reaction time, or $\tau_r > 3/ka^*$. In a fractured

reservoir, a* = 2/b, where b is the average fracture aperture. In reality the fraction of rock which is quartz should also be included, but for this approximate calculation this correction is unnecessary. The rate constant k was found by Robinson (1982) to obey an Arrhenius temperature dependence with E_a = 78.3 kJ/mol and A_r = 2.712 m/sec. Thus the criterion for equilibration of the quartz geothermometer is

$$\tau_r > 1.5\times10^{-4}\ b(e^{9418/T}) \qquad (8)$$

where τ_r is in hours, b in m, and T in K. Equation (8) should always be used to evaluate the likelihood of chemical equilibium of the quartz geothermometer, as a lack of equilibrium will result in erroneously low temperatures. A typical average fracture aperture for HDR reservoirs is on the order of 10^{-3} m (1 mm). Using this value, the approximate equilibration times for flow in hyraulically stimulated fractures at 150, 200, and 250°C are 690 hr, 66 hr, and 10 hr respectively. In the fracturing experiments analyzed here, the downhole residence times are long enough and temperatures high enough for equilibration. Note however that in geothermal systems of intermediate temperature (150-200°C) the quartz geothermometer must be used with caution when evaluating the geochemistry of injection-flow experiments of limited duration.

Other potential problems with the quartz geothermometer are polymerization or deposition of silica, mixing of fluids of different temperatures, and flashing during sample collection. In general, the quartz geothermometer is not affected strongly by deposition unless long residence times at large degrees of supersaturation are encountered, such as in an above ground heat exchanger or in an injection well. As a result, if a fluid equilibrates with respect to quartz at one temperature and then encounters a section of reservoir at a lower temperature, the geothermometer reading at the higher temperature is preserved. Fluid dilution and mixing will obviously affect the reading, although reequilibration after mixing can in many cases eliminate the problem. Flashing of steam will result in a higher concentration in the remaining fluid sample, but this effect can be accounted for precisely by calculating the steam fraction using an enthalpy balance.

Na-K-Ca Geothermometer: This geothermometer provides a measure of rock temperature through the ratios of these ions in solution, which are controlled by cation exchange reactions among the feldspars and feldspar alteration minerals (Fournier and Truesdell, 1973). The empirical relationship proposed by Fournier and Truesdell is

$$T = \frac{1647}{\log_{10}(Na/K)+\beta[\log_{10}(\sqrt{Ca}/Na)+2.06]+2.47} \qquad (9)$$

where concentrations are in ppm, T in K, and β = 1/3 for T > 100°C and 4/3 for T < 100°C. The major difference of this geothermometer from the quartz measurement is that the dissolution/alteration reactions require much longer times for equilibrium. Thus only fluid present in the reservoir for long periods of time will reflect the downhole temperature, and injected fluid will not reach equilibrium in a typical short term flow test. Nonetheless, the effects of dilution caused by injection of clean fluid are not great since the ratios of ions in solution are used in Equation (9). As long as the fluid samples contain some of the reservoir pore fluid, the geothermometer will provide a good measure of downhole temperature. Mixing of fluids of somewhat different temperatures will affect the reading, with the measured result falling in between the temperatures of the fluids before mixing.

Experiment 2032: In this fracture experiment which resulted in the microseismic events shown in Figure 3, equipment failure resulted in an uncontrolled vent back up the injection wellbore after pumping 21000 m^3 of fluid. After 34 hours of venting the situation became safe enough to collect several fluid samples. Table 1 shows the quartz and Na-K-Ca geothermometer readings of these samples. Since flashing occured during the vent, the quartz geothermometer readings using the simple equilibrium relationship are artificially high. Grigsby and Matsunaga (1984) have corrected these values for the conditions at Fenton Hill (where the boiling point of water is 90°C) and obtained an average value of 216°C. Both geothermometers give a temperature of about 215°C, which is approximately equal to the initial rock temperature at the injection depth during this experiment. This suggests that the injected fluid traveled away from the injection region with no tendency to flow preferentially either upward or downward. The seismic event locations (Figure 3) agree with this conclusion. Although this may not seem surprising, a later experiment described below (Experiment 2061) resulted in a different conclusion, and the geochemistry evaluation added to the interpretation of the test.

Experiment 2059: This test was the first to result in interwell flow, and the geochemical measurements in this case were of produced fluid rather than water being vented back up the injection well. The first few samples were simply fluid residing in the production well and not indicative of reservoir chemical conditions. Once this fluid was displaced, the Na-K-Ca concentrations listed in Table 1 indicate a fluid temperature of 240-250°C. This range agrees with the initial rock

temperature at the known injection region, determined precisely from a temperature log performed after the experiment. The fluid apparently short-circuited directly from one well to the other, and showed no tendency to take a more circuitous route downward before reaching the production well. If it had traveled downward, higher geothermometer measurements would have been obtained. The decline in the geothermometer temperatures during the experiment are probably due to fluid mixing which occured during the experiment. These effects are difficult to discern with the geothermometers, which smear the actual downhole temperatures into an average temperature.

Experiment 2061: During this unsuccessful attempt to create more fracture flow connections between the wells, samples of the ventback fluid were collected. The quartz and Na-K-Ca geothermometers do not agree in this case. We believe that dilution and mixing probably affected the Na-K-Ca readings and that the quartz values are more representative of the reservoir fluid. The values of the quartz geothermometer (277 and 286°C) are much higher than the rock temperature at the injection region, indicating that the vented fluid was being recovered from a region much deeper than the injection depth. Since the target depth in the production well was above the injection zone but the water traveled preferentially downward, it is not surprising that the desired flow connection was not achieved. This explanation agrees with microseismic event locations during this experiment, which clustered far below the injection region. The geochemical evidence cited here augments that finding and provides a more complete picture of the downhole flow geometry at remote locations away from the injection wellbore.

Experiment 2062: This experiment, like Experiment 2059, resulted in an interwell connection, and the samples collected were production fluid samples. The geothermometer data were quite similar to the previous test, with downhole temperatures close to that of the rock near the injection region. Once again the injected fluid swept pore fluid from this depth to the production well, and the geothermometer readings reflect the temperature of the rock at this depth.

In summary, the geothermometer measurements can provide additional information about reservoir geometry during a hydraulic fracturing experiment. Specifically, the depths at which fluid resided when in the reservoir, and hence the flow direction (e.g. upward or downward) can be determined from geochemical analyses, knowing the initial rock temperature as a function of depth from a background temperature survey. In the experiments described above, this geochemical information agreed well with microseismic event locations, which indicate where the fluid is traveling in space. This suggests that in pumping experiments in which no microseismicity is induced, geothermometer readings can be used to determine the location of fluid flow paths (in the vertical direction). In one such interwell flow experiment performed recently at Fenton Hill (Brown, 1985) there was no microseismicity, and a temperature log indicated two possible depths for fluid entering the wellbore. The geochemical evidence ruled out the shallower of the two entrance depths, and the flow geometry was thus determined.

CONCLUSIONS

The Fenton Hill field tests have identified several practical conclusions regarding the use of tracers and geochemistry during hydraulic fracturing experiments.

1. Tracer and geochemical information must be interpreted differently during hydraulic fracturing due to unequal inlet and outlet flow rates and transient effects.
2. Two simple models of flow in main fractures with water storage in secondary joints were developed. These models allow the volume of the main fracture flow paths to be estimated from an interwell test.
3. During hydraulic fracturing tests, tracer should be injected only after flow communication has been established between the wells.
4. The quartz and Na-K-Ca geothermometers are useful to identify the downhole temperature and hence depth at which fluid is traveling.
5. The quartz geothermometer equilibrates rapidly enough in fractured reservoirs at 250°C to be used accurately. An approximate criterion has been developed to evaluate the likelihood of equilibration.
6. The Na-K-Ca geothermometer does not equilibrate rapidly, but still may be used in injection-flow experiments because sufficient quantities of indigenous pore fluid are contained in the fluid samples. It is somewhat more susceptible to problems due to fluid mixing and dilution, however.

ACKNOWLEDGEMENTS

This work was funded by the U. S. Department of Energy. Field data were collected and analyzed primarily by Pat Trujillo and Dale Counce, with help from Ron Aguilar, Chuck Grigsby, and George Cocks.

NOMENCLATURE

$\dot{a}$	rock surface area to fluid volume ratio (m^{-1})
A_r	reaction rate pre-exponential factor (m/sec)
b	fracture aperture width (m)
C	dissolved silica concentration (ppm)
C^{∞}	equilibrium solubility of quartz (ppm)

E_a	reaction rate activation energy (kJ/mol)
k	quartz dissolution reaction rate constant (m/sec)
Q	volumetric flow rate (m^3/sec)
Q_{in}	inlet volumetric flow rate (m^3/sec)
Q_{out}	outlet volumetric flow rate (m^3/sec)
T	temperature (K)
V_f	fracture volume (m^3)
V_m	modal volume (m^3)
τ	modal residence time (sec)
τ_r	characteristic reaction time for quartz dissolution (sec)

REFERENCES

Brown, D. W. (1985), "Analysis of the EE-3A Temperature Logs Following the Experiment 2064 Pre-Pump," Los Alamos National Laboratory ESS Division Internal Memorandum, Dec. 24, 1985.

Fournier, R. O. and A. H. Truesdell (1973), "An Empirical Na-K-Ca Geothermometer for Natural Waters," Geochim. et Cosmochim. Acta, 37, 1255-1275.

Grigsby, C. O. (1983), "Rock-Water Interactions in Hot Dry Rock Geothermal Systems: Reservoir Simulation and Modeling," S. M. Thesis, Massachusetts Institute of Technology Department of Chemical Engineering.

Grigsby, C. O. and I. Matsunaga (1984) in Murphy, H. D. (ed), "Experiment 2032 Report," Los Alamos National Laboratory ESS Division Internal Memorandum, ESS-4-70-84, March 26, 1984.

House, L., H. Keppler and H. Kaieda (1985), "Seismic Studies of a Massive Hydraulic Fracturing Experiment," Transactions Geothermal Resources Council, Vol 9 - Part II, paper presented at 1985 Geothermal Resources Council annual meeting, Honolulu, Hawaii.

Kitahara, S. (1960), "The Solubility Equilibrium and the Rate of Solution of Quartz in Water at High Temperatures and High Pressures," Rev. Phys. Chem. Japan, 30, 2, 122-130.

Rimstidt, J. D. (1979), "Kinetics of Silica-Water Reactions," PhD Thesis, The Pennsylvania State University Department of Geosciences.

Robinson, B. A. (1982), "Quartz Dissolution and Silica Deposition in Hot Dry Rock Geothermal Systems," S. M. Thesis, Massachusetts Institute of Technology Department of Chemical Engineering.

Robinson, B. A. and J. W. Tester (1984), "Dispersed Fluid Flow in Fractured Reservoirs: An Analysis of Tracer-Determined Residence Time Distributions," J. Geophys. Res., 89, B12, 10374-10384.

Siebert, H., W. V. Youdelis, J. Leja and E. O. Lilge (1963), "The Kinetics of the Dissolution of Crystalline Quartz in Water at High Temperatures and High Pressures," Unit Processes in Hydrometallurgy, The Metallurgical Society of A.I.M.E. Conference, 24, 284-299.

Stober, W. (1967), "Formation of Silicic Acid in Aqueous Suspensions of Different Silica Modifications," Equilibrium Concepts in Natural Water Systems, American Chemical Society, 67, 161-182.

Tester, J. W., R. L. Bivins and R. M. Potter (1982), "Interwell Tracer Analyses of a Hydraulically Fractured Granitic Geothermal Reservoir," Soc. Pet. Eng. J., 22, 537-554.

Van Lier, J. A., P. L. de Bruyn and J. Th. G. Overbeek (1960), "The Solubility of Quartz," J. Phys. Chem., 64, 1675-1682.

Weill, D. F. and W. S. Fyfe (1964), "The Solubility of Quartz in H_2O in the Range 100-4000 Bars and 400-550°C," Geochim. et Cosmochim. Acta, 28, 1243-1255.

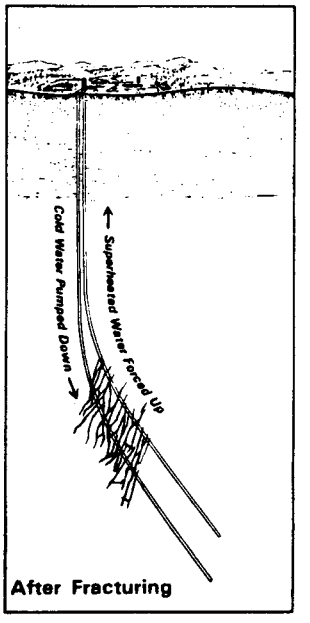

Figure 1. Hot Dry Rock Geothermal Concept

TABLE 1
CHEMICAL CONCENTRATIONS AND GEOTHERMOMETER RESULTS

EXPERIMENT	DATE	TIME	Na	K	Ca	SiO_2	GEOTHERMOMETER TEMPERATURES (°C) Na-K-Ca	Quartz
2032*	12/10/83	15:30	900	100	52.4	380	210	240
	12/11/83	15:30	1310	142	43.3	440	218	258
	12/12/83	10:30	1360	154	98	415	213	251
		13:30	1410	164	93	430	216	255
		16:15	1480	167	80.3	438	216	257
	12/14/84	09:30	1410	157	129	417	210	251
		16:00	1480	167	138	420	211	252
2059	5/28/85	02:15	1220	98	14		209	
		03:30	1630	175	65		217	
		04:20	2860	468	174		247	
		05:00	2770	414	113		245	
		05:30	2750	411	115		245	
		06:00	2430	354	93		243	
		07:00	2010	316	72		247	
		09:00	1900	283	55		245	
		10:00	1360	181	40		233	
		11:00	1350	221	59		242	
		13:00	1160	175	58		233	
		16:00	1320	177	38		233	
		20:00	1425	192	42		234	
	5/29/85	02:00	1340	182	35		235	
		08:00	1400	180	36		232	
		15:00	1360	176	38		232	
2061	7/2/85	10:00	2010	280	47	510	243	277
		17:00	2010	283	50	542	243	286
2062	7/18/85	17:00	1720	220	232	410	216	249
		18:45	2250	350	148	430	240	255
		19:00	2010	292	107		237	
		20:00	1920	318	108		244	
		21:30	1900	265	77		236	
		22:45	1560	239	62		241	
	7/19/85	00:30	1670	219	55		233	
		03:00	1270	184	50		235	

*Quartz geothermometer values not corrected for flashing.

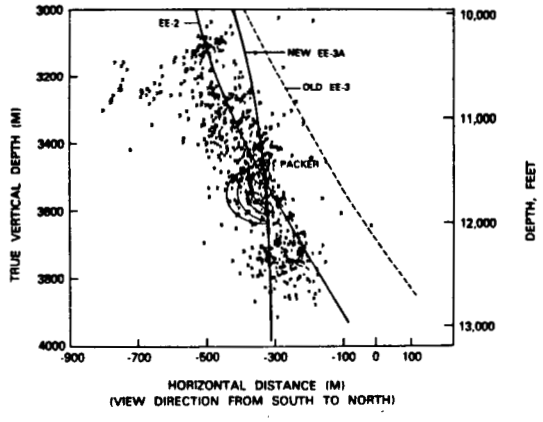

Figure 3. Elevation View of Phase II Wellbores and Experiment 2032 Microseismicity

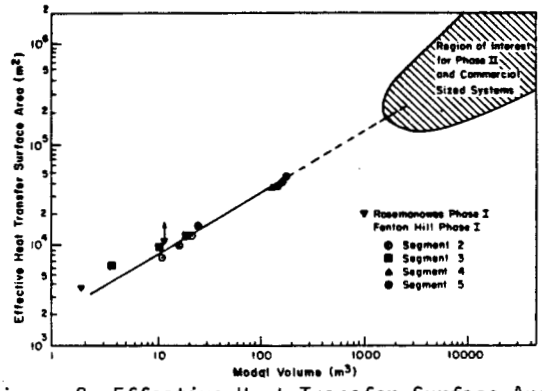

Figure 2. Effective Heat Transfer Surface Area Versus Modal Volume Correlation

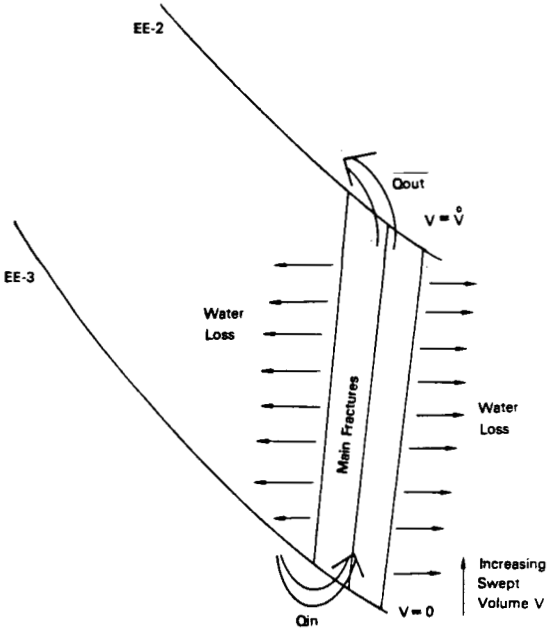

Figure 4. Schematic of Fracture Flow, Water Loss Model

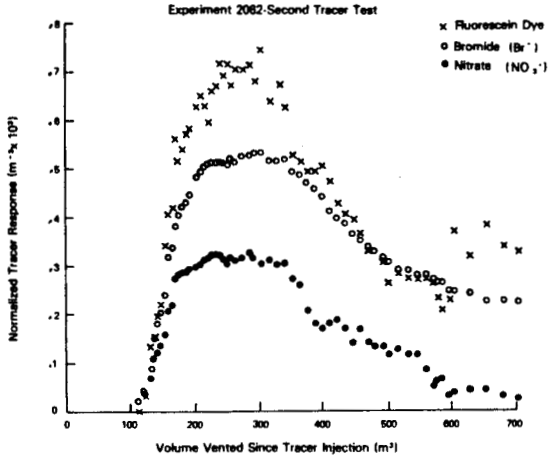

Figure 5. Normalized Tracer Response Curves for 2nd Tracer Test of Experiment 2062

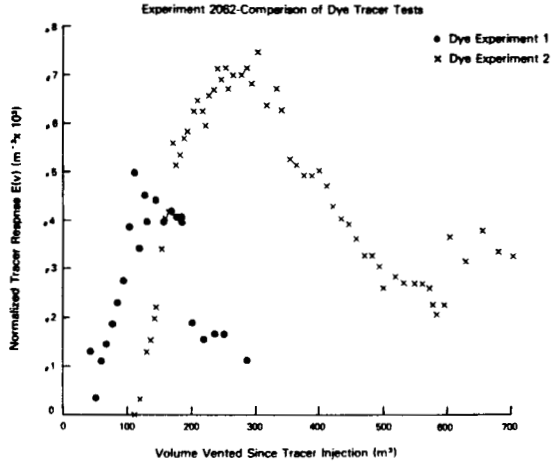

Figure 6. Comparison of Tracer Response Curves for the 1st and 2nd Tracer Tests of Experiment 2062

PROCEEDINGS, Eleventh Workshop on Geothermal Reservoir Engineering
Stanford University, Stanford, California, January 21-23, 1986
SGP-TR-93

PRESSURE-TEMPERATURE-SPINNER SURVEY IN A WELL AT THE GEYSERS

Andy Drenick

GEO Operator Corporation
1330 North Dutton, Suite A
Santa Rosa, CA 95401

ABSTRACT

This paper presents results from a flowing pressure-temperature-spinner log run in a well drilled by GEO Operator Corporation (GEOOC) at The Geysers. Analysis and interpretation of the log data are also presented. The data indicated superheated steam with a temperature of 600°F (316°C) and an enthalpy of 1316 BTU/lbm (725 cal/gm) entered the wellbore below 8000 feet (2438 meters). This temperature and enthalpy is much higher than most Geysers steam wells which produce steam at or below 475°F (246°C) and 1240 BTU/lbm (683 CAL/gm). The high temperature and enthalpy are even more puzzling since static pressure and temperature measurements conducted with Kuster type instruments six months later, indicate a "normal" vapor-dominated system existing at 475°F (246°C) and 500 psia (35 Kg/cm^2). Conceptual reservoir models which can explain these unusual thermodynamic conditions are presented.

INTRODUCTION

The purpose of this paper is threefold: (1) to describe the pressure-temperature-spinner survey run by GEO Operator Corporation (GEOOC), a wholly owned subsidiary of Geothermal Resources International, Inc., in a well at The Geysers; (2) to present and analyze the data obtained; and (3) to describe several conceptual models which can account for the observed thermodynamic behavior.

The activities of GEOOC personnel at The Geysers are currently focused in two separate areas. GEOOC leases and operates the Unit 15 steam field located in the southwest portion of The Geysers, providing steam to the Pacific Gas and Electric Unit 15. GEOOC is also exploring and developing the northwest area of The Geysers (see Figure 1). In this northwest Geysers area, a 130 MWg power plant is being constructed by Central California Power Agency No. 1, which GEOOC has dedicated approximately 1495 acres to and is under contract to supply steam. GEOOC is also actively drilling step-out wells from this proven acreage.

In 1984, GEOOC drilled a successful step-out well in the northwest Geysers area. Results from a standard flow test of 56 hours conducted upon completion of drilling were: a flowrate of 158,000 lbs/hr at a flowline pressure of 153 psia, and a flowline temperature of 405°F. During the last 5 hours of flow, a pressure-temperature-spinner log was successfully run to the total depth of the well.

The purpose of the pressure-temperature-spinner log was: (1) to identify the location and relative productive size of steam entries, and (2) to measure the flowing pressure and temperature profile. Both of these objectives were met, with details of the results being presented herein. It was determined that steam with a temperature of 600°F and an enthalpy of 1316 BTU/lbm was entering the wellbore below 8000 feet.

Following completion of the logging and flow testing, the well was shut-in and the wellbore filled with gas (primarily nitrogen) to preserve the integrity of the wellbore, miti-

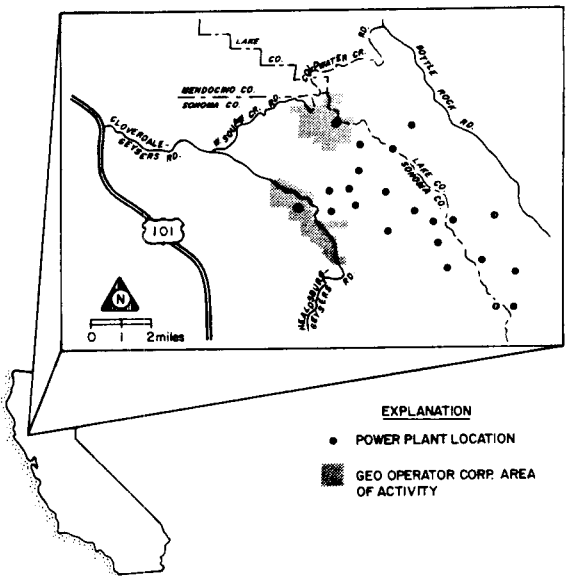

FIGURE 1. GEO Operator Corporation areas of activity at The Geysers, California.

gate any potential corrosion and prevent release of steam to the atmosphere. It was not possible to record a conventional buildup when the well was shut-in.

Approximately six months after being shut-in, a pressure-temperature survey was run utilizing conventional Kuster tools. A static pressure of 500 psia and a temperature of 475°F was measured at approximately sea level, typical of vapor-dominated systems and in particular The Geysers reservoir.

The high temperatures encountered in this well during flowing conditions is the primary subject of this paper. Geological, geochemical, and pressure transient data and analysis have not yet been incorporated in this work.

DESCRIPTION OF THE PRESSURE-TEMPERATURE-SPINNER TOOL AND RESULTS

The pressure-temperature-spinner tool was manufactured by Hot Hole Instruments (HHI) of Los Alamos, New Mexico. The tool simultaneously monitors pressure, temperature, spinner revolutions per second (RPS) and internal tool temperature. The sensitive tool electronics are insulated from the high temperature geothermal environment with a Dewar filled with an eutectic fluid. This insulation system allows the tool to be utilized in a high temperature environment for approximately four hours, after which time the tool must be pulled and allowed to cool. Individual signals from the four measurements are sent to the surface once every two seconds via a high temperature single conductor electrical line. Data is received, processed and recorded at the surface with conventional logging equipment. Product information sheets provided by HHI state that the tool is 13 feet long, 3 inches in diameter and weighs 170 pounds. The stated accuracy is 0.2% of full scale, with a resolution of 0.2 psi.

Results from the logging run made with this tool are presented in Figure 2, which is a reduced copy of the actual log. The data in Figure 2 was obtained as the tool was being pulled up from the bottom of the well. Log data obtained while lowering the tool are not

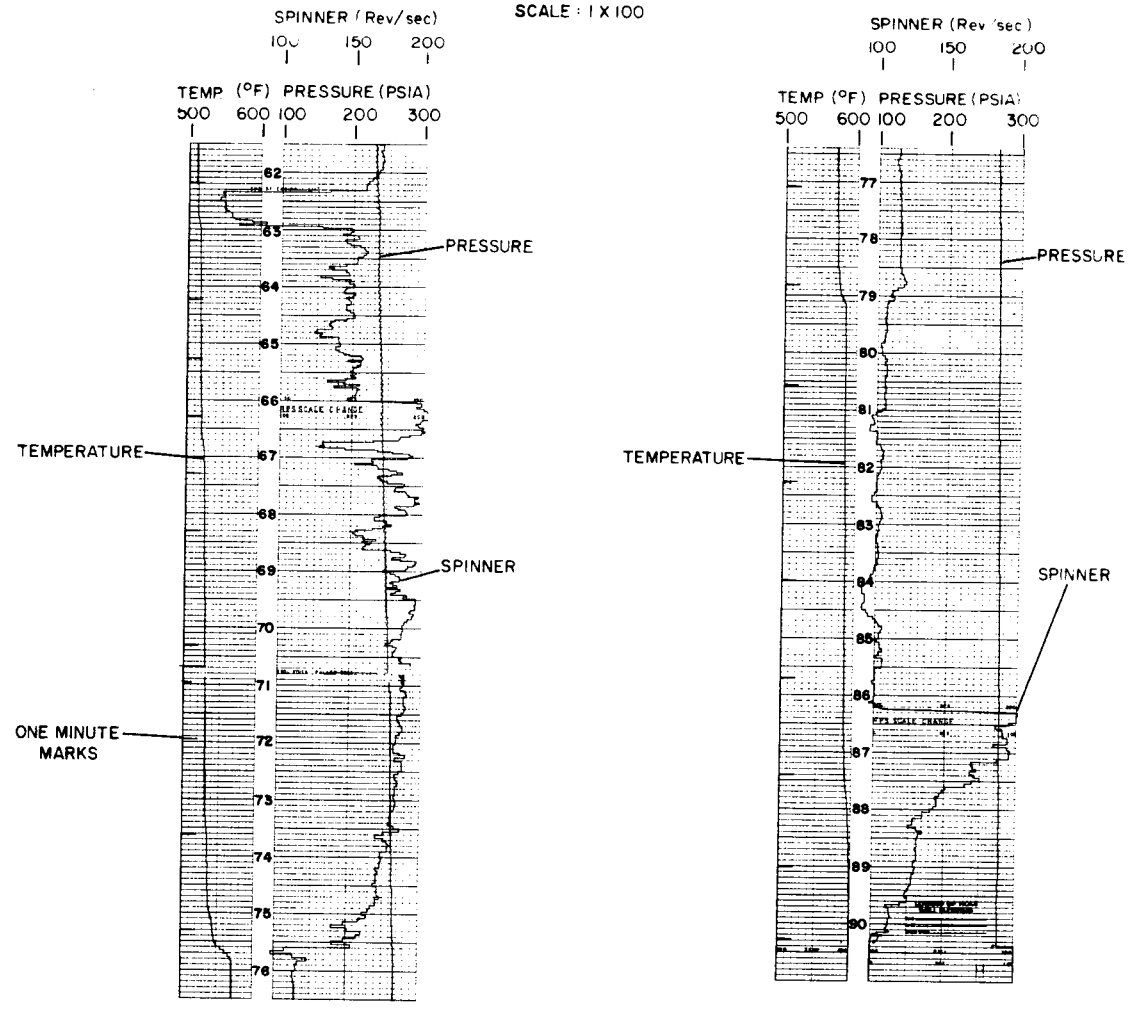

FIGURE 2. Section of the actual well log from 6200 ft.to 9030 ft.

presented as it was essentially identical. The log is not compensated for the stretch or thermal expansion of the electrical cable.

The step-like nature of the log data can be explained as follows. The logging speed was normally between 150 feet per minute and 200 feet per minute (note one minute time marks on left side of log). As previously stated, one signal for each measurement is transmitted to the surface once every two seconds. At a logging speed of 200 feet per minute, this means a measurement is being recorded once every 6.7 feet of vertical depth, which is the vertical length of each step.

The jagged nature of the spinner data is due to irregularities in the open-hole diameter caused by wash-outs and tight spots, in addition to the turbulent flow regime of the steam.

The pressure and temperature measurements recorded at the surface agreed with wellhead measurements made manually by GEOOC field operators. Manual measurements, made with conventional equipment, of pressure and temperature at the time of the logging were 154 psia and 405°F, respectively. Additionally, data from other wells in which this logging tool was used compare favorably with data obtained from tools of competitors run in the same well. For these reasons, the log data reported herein can confidently be accepted as accurate.

ANALYSIS OF SPINNER DATA

Data from the spinner portion of the log have been interpreted to determine where steam is entering the wellbore, and the relative productive size of each such entry (see Figure 3). Interpretation of this nature is possible because changes in the spinner rotational speed (RPS) are related to changes in the velocity of steam in the wellbore. When additional steam enters the wellbore at an open fracture, the steam velocity increases due to increased mass flowing through the unchanged cross-sectional area. Thus, zones where spinner RPS increase are identified as steam entries. The relative productive size of each steam entry can be estimated by assuming a linear relationship between spinner RPS and steam mass rate. The percent contribution for each entry identified has been calculated in this manner, and is shown in Figure 3.

Steam entries can be detected and their relative size estimated from measurements made at the surface during drilling. These measurements include:

1) increases in the injection pressure necessary to circulate the drilling fluid (air), caused by increased friction losses in the annulus due to the increased steam flow;

2) temperature increases in the flow line as a result of increased steam flow;

3) changes in the chemical composition of the returning fluid (air and steam);

4) drilling breaks, i.e., rapid changes in the rate of penetration;

5) flow measurements made with orifice plates and/or pitot tubes. These measurements require extensive, costly rig time and are usually only conducted upon completion of a well.

The entries detected with these methods are shown in Figure 3. In this particular well there is very good agreement between the entries detected at the surface and those detected with the log.

In higher flowrate wells, good agreement between log data and surface data would not be expected. Entries deep in high flowrate wells are often undetected as they are masked by the shallower entries. In such cases, use of a pressure-temperature-spinner log can identify the location and relative productivity of the deep steam entries.

One final point is made regarding the data presented in Figure 3. The steam entries are essentially clustered into two groups, with each group producing approximately 50% of the steam flow. One group is centered at about

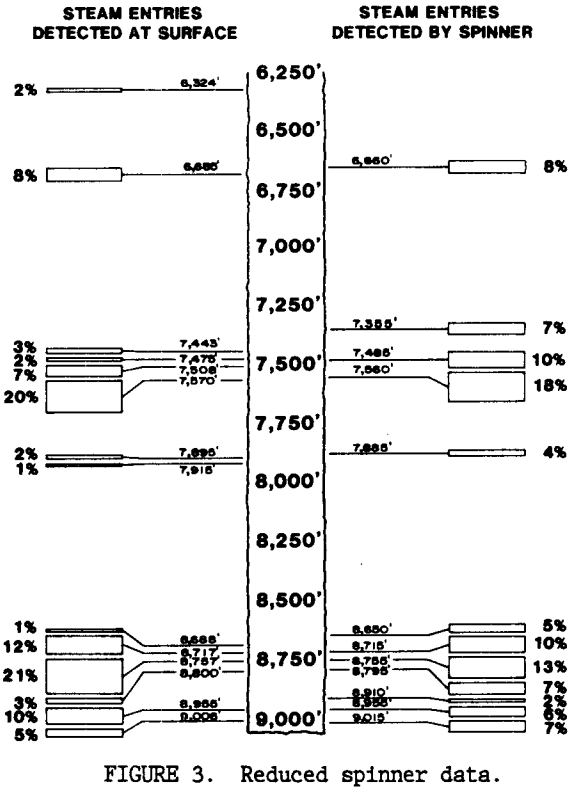

FIGURE 3. Reduced spinner data.

7500 feet, while the other group is centered at about 8800 feet. The temperature and enthalpy of the steam in these two groups is surprisingly different, as will be seen in later sections.

ANALYSIS OF PRESSURE DATA

Pressure data from the log are presented in Figure 4(b). Casing and open-hole diameters are shown alongside in Figure 4(a). As expected, the frictional losses are greatest in the 11-3/4-inch liner.

Also shown in Figure 4(b) are pressure profiles calculated from wellhead flow conditions using two relatively simple calculations. The Fritzche equation (King, 1967), normally used for calculating friction losses in horizontal pipeline flow, was modified to include pressure changes due to the piezometric head of steam. The other profile was calculated using a method published by Economides (1979) in a past Stanford workshop. Both methods can easily be run on hand-held calculators, and yield results within 10% of measured values.

ANALYSIS OF TEMPERATURE DATA

Data from the temperature portion of the log have been reduced and are presented in Figure 4(c). Since the steam in the wellbore is superheated, the pressure data from Figure 4(b) is used in conjunction with the temperature data to obtain the enthalpy which is also shown in Figure 4(c). A steam properties computer program was used to calculate these enthalpies. Two features on Figure 4(c) deserve mention. The sudden temperature and enthalpy change of the steam which occurs between 7500 feet and 8000 feet, and the high temperature and enthalpy of the steam entering the wellbore below 8000 feet.

The sudden temperature and enthalpy change can be explained as follows. The steam entering the wellbore below 8000 feet has an enthalpy of about 1310 BTU/lbm. The steam entering the wellbore above 8000 feet is "typical" Geysers steam, that is, its enthalpy is about 1205 BTU/lbm. The shallow steam cools the hotter steam from below and produces a mixture with an enthalpy of about 1257 BTU/lbm.

Wellbore heat losses for the flowing conditions present during logging were calculated using the method published by Ramey (1964). The data used in the calculations and subsequent results are presented in the Appendix. Wellbore heat losses were calculated to be 93,464,000 BTUs per day or 25 BTU per pound of steam. Kinetic energy changes have been neglected. Subtracting the 25 BTU/lbm heat loss from the previously calculated enthalpy of 1257 BTU/lbm means steam with an enthalpy of 1232 BTU/lbm should have been measured at the surface. The actual enthalpy measured at the surface with the pressure-temperature-spinner tool was 1227 BTU/lbm. The difference is attributed to the inaccuracy of determining the percent steam flow from each zone, and/or the possibility that the steam entering the wellbore above 8000 feet has an enthalpy lower than 1205 BTU/lbm.

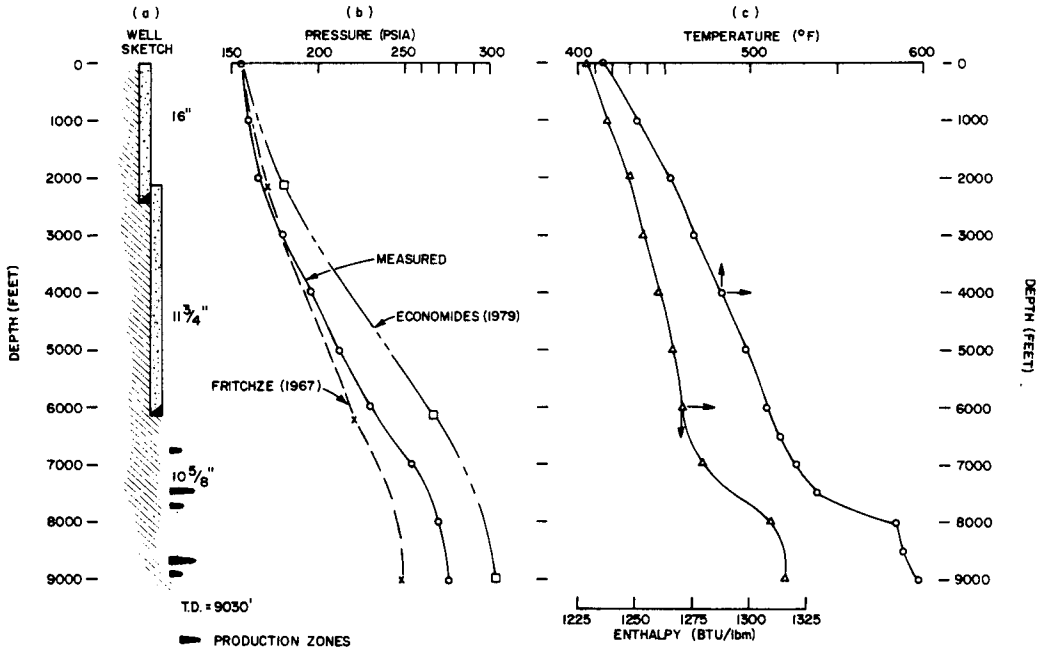

FIGURE 4. Reduced flowing pressure and temperature data.

This explanation of higher temperature and enthalpy steam entering the wellbore below 8000 feet and being cooled by a shallower steam entry is also supported by temperature measurements made during drilling. Downhole temperatures were routinely measured while taking directional surveys during the drilling process. These data are listed in Table 1. The measured temperatures were considerably higher once drilling proceeded past 8000 feet, supporting the concept of higher rock and steam temperatures below 8000 feet.

TABLE 1

Summary of Temperatures Measured during Drilling

Drilled Depth (feet)	Temperatures Measured during Directional Surveys (°F)	Flow Line Temperature of Returning Fluid (Air and Steam) (°F)
6347	209	175
6625	217	150
7194	330	167
7347	351	200
7630	452	205
7736	370	210
7975	364	212
8137	530	220
8348	550	207
8716	548	210
8825	560	227
8923	577	230
9030	N/A	231

The source of this deeper, high temperature and enthalpy steam is difficult to explain as it is unusual for vapor-dominated systems to produce steam of this nature. Before this is discussed further, it is appropriate to first consider the static pressure and temperature measurements made in the well.

STATIC PRESSURE AND TEMPERATURE DATA AND ANALYSIS

The static pressure and temperature data add a puzzling contrast to the flowing pressures and temperatures previously discussed. A static pressure and temperature survey was run in the well approximately six months after completion of the pressure-temperature-spinner log. The well was completely shut-in for the six month period. Data from this survey is typical of a static well in The Geysers. A temperature and pressure of about 475°F and 500 psia, respectively, were recorded near sea level (see Figure 5). Unfortunately, the tools would not go below 8100 feet, presumably due to a bridge or ledge in the open-hole section of the wellbore. Pressures and temperatures above 4000 feet are indicative of the gas filling the wellbore, steam exists below about 4000 feet.

The pressure gradient between the last two pressure measurements, at 8000 feet and 8100 feet, is 0.370 psi/ft indicating a static water column exists. This may only be condensate which has accumulated on top of an impermeable bridge in the well. Accumulation of condensate at the bottom of other Geysers wells has been previously reported by Lipman et al. (1978). However, it could also indicate the top of a liquid-dominated region. If an impermeable bridge exists at 8100 feet, it would isolate the deeper, hotter zone from wellbore. This would account for the difference between flowing and static temperature measurements. Further testing will be necessary to determine if such a bridge exists.

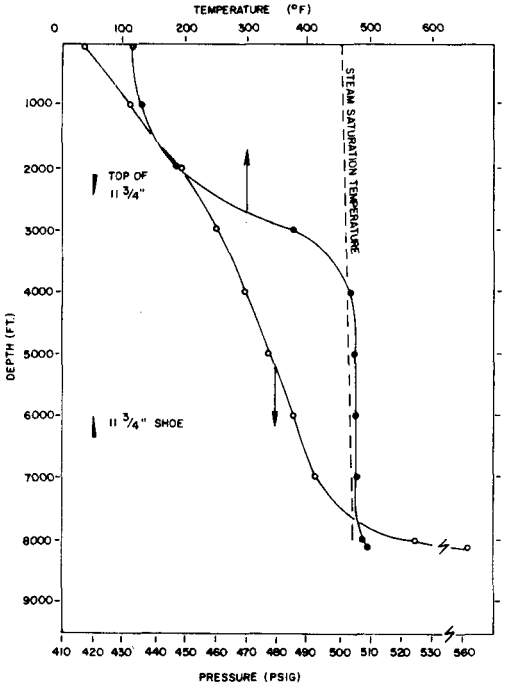

FIGURE 5. Static temperature and pressure survey conducted after 6-month shut-in.

DISCUSSION

Downhole measurements made during the flowing conditions previously described indicate steam with a temperature and enthalpy considerably greater than previously reported for The Geysers is entering the subject well below 8000 feet. Previously published data from wells at The Geysers indicate a vapor-dominated system existing at about 475°F and 514 psia (Lipman et al., 1978). James (1968) convincingly argued that vapor-dominated systems must exist at this pressure and temperature, which is essentially at the maximum enthalpy of dry saturated steam. Production of steam from a reservoir of this type, assuming isothermal expansion from 500 psia to 250 psia in the reservoir results in steam with a maximum temperature of 475°F and enthalpy of 1240 BTU/lbm being delivered to the wellbore (after Truesdell and White,

1973). Assuming no heat loss in flow up the wellbore (isoenthalpic expansion), a maximum temperature of 450°F and the same enthalpy of 1240 BTU/lbm would be expected at the surface (see Figure 6). However, decompression and flow through the reservoir probably does not occur along a perfectly isothermal path, but along some path between isothermal and isoenthalpic. Flow up the wellbore definitely is not isoenthalpic - heat losses to the cooler earth results in a 5 to 25 BTU/lbm loss. Thus, wells at The Geysers typically produce steam with an enthalpy at the surface of 1220 BTU/lbm or less as shown by the shaded area in Figure 6.

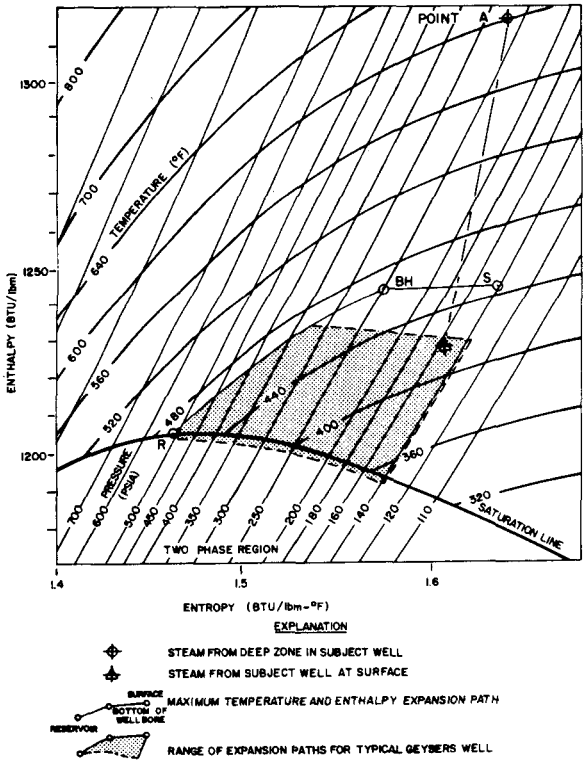

FIGURE 6. Expansion paths for production of steam from vapor-dominated reservoirs (after Truesdell and White, 1973).

Although the surface temperature and enthalpy of the subject well falls in the range of "typical" Geysers wells, the unusual nature of the steam entering the well below 8000 feet is clearly evident in Figure 6. The decrease in entropy shown by the expansion path of the subject well supports the interpretation that mixing of steam from two different zones is occurring. Flow from two different zones raises an interesting possibility. The deep, hotter steam mixes with shallower, "typical" Geysers steam to produce an enthalpy at the surface which is only slightly higher than normal Geysers wells. It is therefore possible that other Geysers wells with a surface enthalpy greater than 1220 BTU/lbm may be producing steam from two distinctly different zones. Flowing downhole temperature measurements would be necessary to detect such deeper, high temperature zones.

Since 600°F steam is entering the subject well at depth, rocks with a temperature of at least 600°F must be in contact with the reservoir fluids. Yet this temperature exceeds previous temperature measurements made at The Geysers (Lipman et al., 1978; Thomas et al., 1979) by at least 100°F. What production mechanisms can account for these high steam temperatures? What is the original state of this steam and where is it located in relation to the "typical" Geysers reservoir? Several different conceptual models which can answer these questions are presented next.

CONCEPTUAL MODELS

The conceptual models presented herein attempt to explain the thermodynamic behavior encountered. Work to include geochemical and geological studies, which will be necessary to fully understand this well and the reservoir it produces from, are underway.

The conceptual models must include a "typical" Geysers vapor-dominated system existing to a depth of about 8000 feet. This is necessary to explain the temperatures and pressures measured during static conditions, and to account for the measurements made during drilling prior to 8000 feet. Below 8000 feet, transition to a high temperature region must rapidly occur. This requires a sudden increase in the temperature gradient from less than 1°F/100 feet to about 10°F/100 feet to obtain temperatures of 600°F in 1000 feet. The pressure gradient may be that of a static steam column, or a hot water column depending on whether or not an impermeable bridge in the well at 8100 feet. If an impermeable bridge exists, a static steam gradient below 8100 feet is possible. However, if the bridge does not exist, the last two static pressure measurements indicate the start of a liquid-dominated system. Further testing of the well is necessary to determine if the impermeable bridge exists.

Vapor-Dominated System with Local Heat Source

The first model considers a localized heat source which acts like a furnace and supplies heat to produce 600°F steam from 475°F steam (see Figure 7). The heat source would likely be a local intrusion of magmatic material, such as a dike or pluton. Drilling and completing a new well acts as a stimuli which creates a new fracture flow path or paths through the previous hot dry impermeable rock. Fluid originates at 475°F and is superheated to 600°F as it flows through the hotter rock to the wellbore. Envisioned on the Mollier diagram shown in Figure 6, steam originates at 475°F (maximum enthalpy of dry saturated steam) and expands along a path much steeper than isothermal to reach Point A. A path steeper than isothermal is pos-

sible due to heat transfer from 600°F rocks. Note that the well can be outside the hot dry rock area and still produce 600°F steam as long as the fractures go through the hot dry rock. The existence of very hot dry rocks near productive wells have been noted in the Latera Field in Italy (Cavarretta et al., 1985). Static temperatures as high as 650°F at 9100 feet have been measured in dry holes near productive wells.

When the well is static, cooler, shallower steam flows down the well masking the higher temperatures below 8100 feet. This simple model is consistent with the temperatures encountered, is physically possible, but does not seem very probable.

Liquid-Dominated System below the Vapor-Dominated System

In the second model, we consider a liquid-dominated system located just below the vapor-dominated system, but isolated due to an impermeable section. The two sections were at one time connected, but the liquid-dominated system sealed itself due to mineral deposition. Fournier (1983) has hypothesized that such a system could exist at depth, but never be detected since it is self-sealed. The impermeable section permits a very high temperature gradient to exist between the vapor-dominated system and the liquid-dominated system (see Figure 8). The subject well penetrates the seal and produces water which is flashed to dryness while flowing to the wellbore. Low permeability and high pressure drops would be necessary to flash the liquid to complete dryness. Additionally, the fluid in the liquid-dominated system must be high (greater than 25%) in salt content to raise the boiling point of water to about 600°F (Truesdell and White, 1973). In effect the salt raises the saturation line shown on the Mollier diagram in Figure 6. Thus, brine exists at 600°F and 514 psia, then boils when decompressed to produce 600°F steam. If pure water existed in the liquid-dominated system, and the pressure at its free surface is 514 psia, the level would have to drop about 3000 feet to obtain the pressure corresponding to a saturation temperature of 600°F. This is calculated as follows:

Saturation pressure for 600°F - pressure at top of water surface ÷ pressure gradient = depth of 600°F water.

(1550 psia - 514 psia) ÷ .323 psi/foot
= 3100 feet

A standing liquid column and/or flooding of the vapor-dominated system has not occurred because the liquid-dominated system is underpressured relative to hydrostatic, hence, the pressure at the free surface of the water is 514 psia.

The problem with this model is that it seems unlikely that water could flash to dryness prior to entering the wellbore (James, 1968; Truesdell and White, 1973). Additionally, the effect of noncondensible gases, which are known to exist, would be to lower the boiling point of water. Once geochemical data is incorporated with this work, it should be possible to verify the validity of this model.

Fossil Liquid-Dominated System

The last conceptual model is an extension of the previous one. In this model, the liquid-dominated system has boiled to dryness, leaving behind superheated steam existing in the fractures and major voids. Liquid water remains adsorbed to the rocks and held in any existing small pores and fracture interstices. The ability of water to exist on rock at higher temperatures than saturation has been confirmed by laboratory work (Hsieh and Ramey, 1981; Herkelrath et al., 1983), however, their work was conducted at temperatures considerably lower than 600°F. The fossil liquid-dominated system would allow the high temperature gradients necessary for rock temperatures to reach 600°F.

The nature of the connection between the vapor-dominated system and the fossil liquid-dominated system could be physical or evolutionary. A physical barrier, such as an impermeable region, may exist which separates the two regions and prevents them from mixing to create more uniform temperature gradients. However, the boundary between the zones may be due to the evolution of the vapor-dominated system over time (Walters, M. A., personal communication). Recent work by Pruess (1985) has quantified the evolution of a vapor-dominated system from a liquid-dominated system as proposed by James (1968) and later Truesdell and White (1973). It seems possible that this northwest area of The Geysers could still be evolving into the "typical" Geysers reservoir. Hence, the deeper, hotter zone has not yet cooled down. The high temperature gradient could be due to the slow nature of the evolutionary process, especially if an area of reduced permeability is present.

Stated another way, heat transfer into this area by conduction has been greater than heat transfer out by convection, causing increased temperature. This heat transfer imbalance is probably caused by the better insulation resulting from the greater depth of the steam reservoir in this area. Pressure has not increased because the hotter zone is in communication with the typical Geysers zone.

A similar evolution process appears to be occurring in Hawaii. It has been hypothesized that the Puna Geothermal System, an apparent liquid-dominated system, is in the process of boiling to form a vapor-dominated system (Iovenitti and D'Olier, 1985). Fluids with temperatures as high as 650°F have been produced from this system.

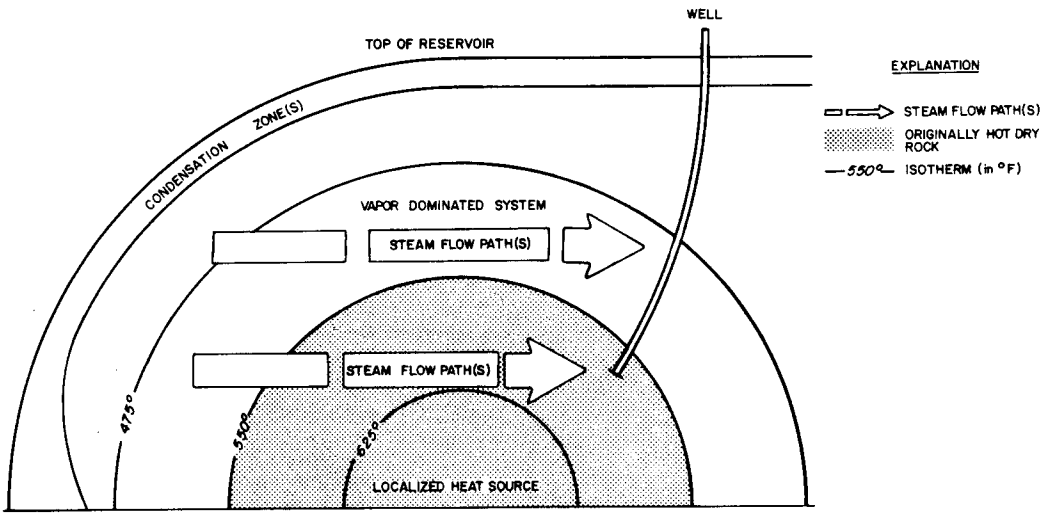

FIGURE 7. Drilling well causes new permeable fracture through previously hot dry rock. Localized heat source adds heat to steam as it flows to well.

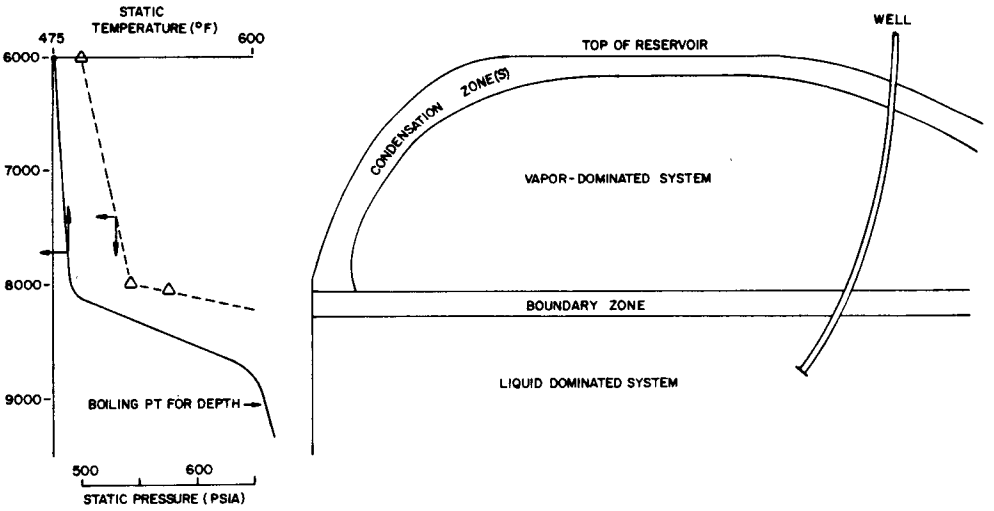

FIGURE 8. Well penetrates liquid-dominated system with high (+25%) salt content, previously sealed from vapor-dominated system.

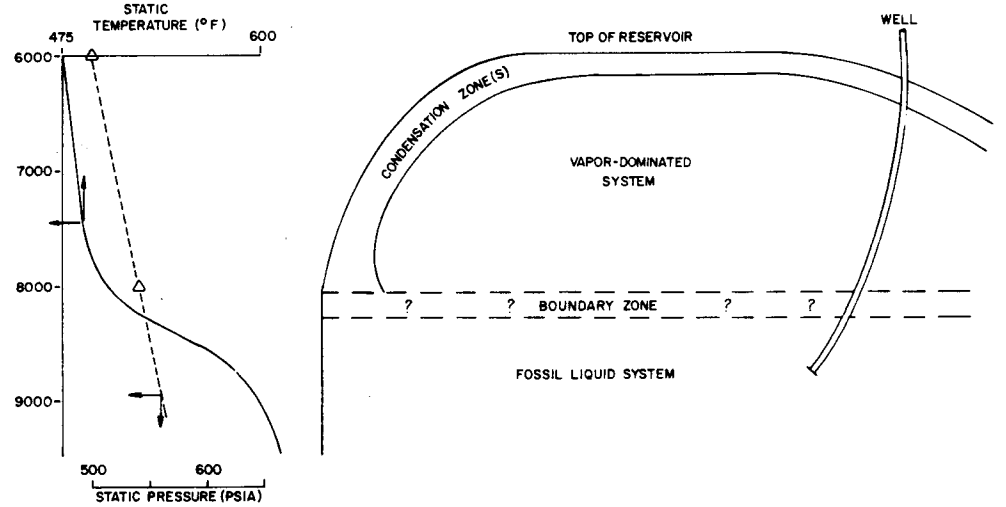

FIGURE 9. Well penetrates fossil liquid-dominated system which has evolved to high temperature vapor-dominated system.

CONCLUSIONS

1) Two separate and thermodynamically distinct zones are feeding the well described in this paper. The shallow zone supplies typical Geysers steam with a temperature less than 475°F. The deeper zone supplies steam at a temperature of about 600°F. Conceptual models of reservoirs which can produce 600°F steam have been presented.

It is possible that other wells at The Geysers are producing steam at depth with temperatures that approach 600°F, but is being masked by cooler, shallower steam and cannot be detected at the surface. Use of downhole logging tools are necessary to detect such deeper, high temperature zones.

2) The spinner data obtained from the log agrees well with conventional methods of detecting steam entries. Hence, conventional methods for detecting and quantifying steam entries can be used with more confidence in average flowrate wells (100,000 to 180,000 lbs/hr).

3) The thermodynamic data and analysis presented in this paper must be integrated with geochemical and geological studies to more precisely and fully explain the high temperatures and enthalpies encountered, and the reservoir from which they are being produced.

ACKNOWLEDGEMENTS

I would like to thank the management of Geothermal Resources International, Inc., for support and permission to publish this work. I would also like to thank Dr. Jim Combs and the technical staff of GEOOC for guidance and critical review and D. Darling and S. Mason at GEOOC for help in preparation of the manuscript and figures.

REFERENCES

Cavaretta, G., Ginaelli, G., Scandiffio, G., and Tecce, F., (1985), "Evolution of the Latera Geothermal System II: Metamorphic, Hydrothermal Mineral Assemblages and Fluid Chemistry", Journal of Volcanology and Geothermal Research, 26, pp. 337-364.

Economides, M. J., (1979), "Shut-In and Flowing Bottom Hole Pressure Calculation for Geothermal Steam Wells", Proceedings Fifth Workshop Geothermal Reservoir Engineering, Stanford University, pp. 127-138.

Fournier, R. O., (1983), "Active Hydrothermal Systems as Analogues of Fossil Systems", Geothermal Resources Council, Special Report No. 13, pp. 263-279.

Herkelrath, W. N., Moench, A. F., and O'Neal II, C. F., (1983), "Laboratory Investigations of Steam Flow in a Porous Medium", Water Resources Research, Vol. 19, No. 4, Paper No. 3W0738, pp. 931-937.

Hsieh, C. H., and Ramey, H. J. Jr., (1981), "Vapor Pressure Lowering in Geothermal Systems", Society of Petroleum Engineers of AIME, SPE 9926, pp. 435-441.

Iovenitti, J. L., and D'Olier, W. L, (1985), "Preliminary Results of Drilling and Testing in the Puna Geothermal System, Hawaii", Proceedings, Tenth Workshop on Geothermal Reservoir Engineering, Stanford Univ., pp. 65-71.

James, R., (1968), "Wairakei and Larderello: Geothermal Power Systems Compared", New Zealand Journal of Science, Vol. 11-706-719.

King, R. C. (1967), "Piping Handbook", Fifth Edition, McGraw-Hill Book Company, pp. 3-138 to 3-155.

Lipman, S. C., Strobel, C. J., and Gulati, M. S., (1978), "Reservoir Performance of The Geysers Field", Geothermics, Vol. 7, pp. 209-219.

Pruess, K., (1985), "A Quantitative Model of Vapor-Dominated Geothermal Reservoirs as Heat Pipes in Fractured Porous Rock", GRC Transactions, Vol. 9, Part II, pp. 353-360.

Ramey, H. J. Jr., (1964), "How to Calculate Heat Transmission in Hot Fluid Injection", Petroleum Engineer, Nov., pp. 110-120.

Thomas, R. P., Chapman, R. H., and Dykstra, H. (1979), "A Reservoir Assessment of The Geysers Geothermal Field", California Department of Conservation, Division of Oil and Gas, Publication No. TR27.

Truesdell, A. H., and White, D. E., (1973), "Production of Superheated Steam from Vapor-Dominated Geothermal Reservoirs", Geothermics, Vol. 2, Nos. 3-4, pp. 154-173.

Willhite, G. P., (1967), "Over-all Heat Transfer Coefficients in Steam and Hot Water Injection Wells", Journal of Petroleum Technology, pp. 607-615.

APPENDIX - WELLBORE HEATLOSS CALCULATION

Nomenclature

a - geothermal gradient, $^{o}F/ft$
K - earth thermal conductivity, BTU/day ^{o}F ft
K_{cem} - cement thermal conductivity, BTU/day ^{o}F ft
Q - heat loss rate, BTU/day
r_i - inside radius of casing, ft
r_h - radius of hole, ft
r_o - outside radius of casing, ft
t - time from start of flow, days
T_e - temperature of earth at top of section, ^{o}F
T_s - temperature of steam at top of section, ^{o}F
U - overall heat transfer coefficient, BTU/day ft^2 ^{o}F
Z - depth change, ft

Heat loss for cased sections of well (Ramey, 1964)

$$Q = \frac{2\pi r_i U K}{K + r_i U f(t)} [(T_s - T_e) Z - 0.5 a Z^2]$$

Heat loss for open hole sections of well (Ramey, 1964)

$$Q = \frac{2\pi K}{f(t)} (T_s - T_e) Z - 0.5 a Z^2)$$

Overall heat transfer coefficient (Willhite, 1967)

$$U = [r_o (\ln (r_h/r_o))/K_{cem}]^{-1}$$

Transient heat-conduction time function for earth (Ramey, 1964)

$$f(t) = \ln (2 \sqrt{.96t}/r_h) - .29$$

Values used for calculations

t = 8 days
K = 42.4 BTU/ft day ^{o}F
K_{cem} = 7 BTU/ft day ^{o}F
Well Flowrate = 158,000 lbs/hr

HEATLOSS SCHEMATIC

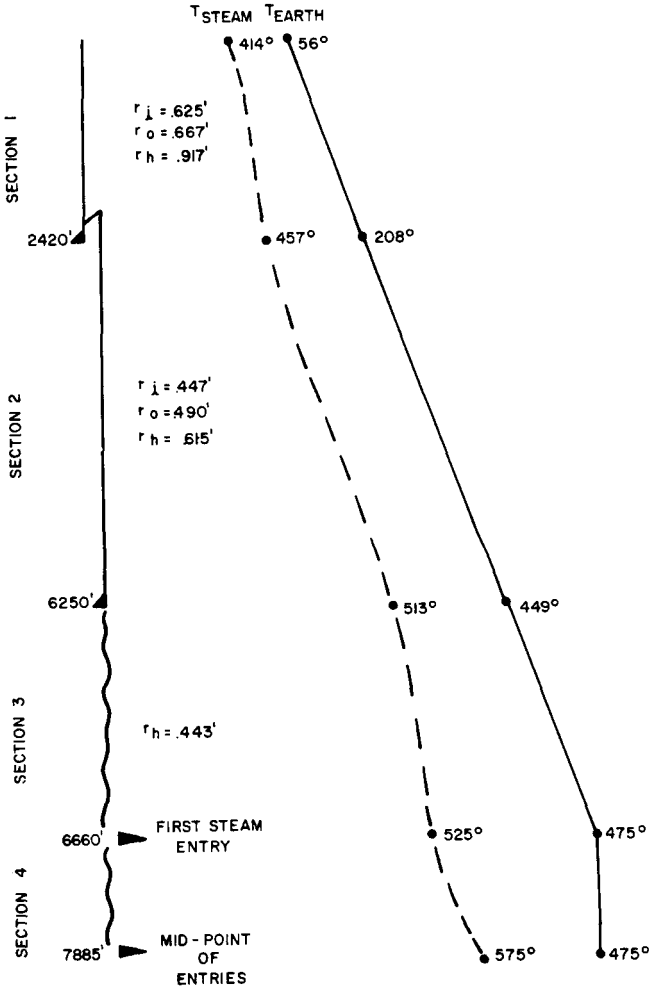

SUMMARY OF CALCULATIONS

Section	Z	T_s	T_e	f(t)	U	1000 BTU/day	BTU/lbm
1	2420	414	56	1.51	33.0	50,947	13.4
2	3830	457	208	1.91	62.9	38,353	10.1
3	410	513	449	2.24	∞	2,492	0.7
4	1225	525	475	2.24	∞	1,672	0.5
					TOTALS	93,464	24.7

PROCEEDINGS, Eleventh Workshop on Geothermal Reservoir Engineering
Stanford University, Stanford, California, January 21-23, 1986
SGP-TR-93

FRACTURE DETECTION: INTERPRETATION OF WELL LOGS TO SELECT PACKER SEATS AND LOCATE INJECTION INTERVALS

D. S. Dreesen, K. L. Burns, P. Chavez, Z. V. Dash, S. Kelkar, J. Kolar, and S. S. Levy

Earth and Space Sciences Division
Los Alamos National Laboratory
Los Alamos, New Mexico 87544

ABSTRACT

A wireline and mud logging program has been conducted in conjunction with redrilling operations in well EE-3 at the Fenton Hill Hot Dry Rock (HDR) site near Valles Caldera, New Mexico. The trajectory for the new bore, EE-3A, penetrated a fractured zone stimulated from adjacent well EE-2 and thereby established hydraulic communication. To test and stimulate selected zones in EE-3A inflatable open hole packers designed for high temperature service were used. Proper identification and selection of packer seats was crucial to the success of the project. The logging program successfully identified five competent packer seats in six attempts. Wireline temperature, caliper, sonic televiewer and natural gamma ray logs were used in conjunction with mud logs, drill cuttings and drilling parameter data to locate fractures, out-of-gage hole, temperature anomalies and mineralized zones which were avoided in selection of the packer seats.

INTRODUCTION

The Los Alamos National Laboratory has been engaged for the past decade in developing technology for energy extraction from hot dry rock reservoirs. As a part of the development of a second, deeper, hotter reservoir (Phase II), field experiments are in progress at the HDR test site. The primary objective of the field operations has been to achieve hydraulic communication between wells EE-2 and EE-3 at depths ranging from 11,500-13,200 feet. Thus cold water can be injected down one well and hot water produced at the other well. The rock mass surrounding the two wells was stimulated with the injection of large volumes of water. Subsurface microseismic detectors were used to map the micro-earthquakes during and after the massive injections (House et al., 1985). After failing to establish a connection, EE-3 was sidetracked and redrilled (EE-3A) on a lower trajectory to intersect a high density region in the cloud of microseismic events surrounding EE-2 resulting from the largest injection which used five million gallons of fresh water. The 8-1/2 inch wellbore was drilled from 9,300 to 13,180 feet encountering temperatures in excess of 260°C.

A number of reservoir stimulation tests were conducted at various depths during redrilling operations. Due to the existence of a low pressure region at 10,250 feet, the lower intervals had to be isolated from this zone and open hole packers were selected as the only practical method to effectively stimulate and interrogate the wellbore. This was accomplished with the use of a recently improved, open hole, inflatable packer (Dreesen et al., 1985 and 1986). The high initial temperature, large thermal cycles, high differential pressures and abrasive open hole environment created an extremely challenging environment for open hole packer operations. Packer seats had to be selected to avoid enlarged, fractured, incompetent or mechanically weak borehole. A reliable logging program was essential for successful packer operations and the reservoir development and testing program.

LOGGING PROGRAM

The logging program included in the EE-3A drilling plan sought to identify and locate effective packer seats. Most of the wellbore was assumed to be unsuitable due to one or more of the following conditions: oversized, irregular broken out or washed out bore, open fractures intersecting the bore, mineral filled fractures and jointed or weak rock more susceptible to fracturing than the targeted injection zone (Hickman et al., 1985; Warren, 1981). Potential packer seats were located by using mud logs, temperature logs and caliper logs. Open hole and through-drill-pipe gamma ray/collar locator logs were used to correlate drill pipe and open hole wireline depths. The USGS high temperature televiewer was run to investigate caliper log data of unusual character. Figure 1 presents a composite correlation of the various logs used over one region of interest. Table 1 summarizes the stimulation tests and packer seats by packer run.

Mud Logging and Geological Interpretation: Drill cuttings were collected and examined at the wellsite by commercial mud loggers. A complete geothermal drilling data log including drill pipe depth, drill rate (Figure 1a), lithology, flowline temperatures, gas content and supporting drilling data were also

collected and presented on a ten feet per sample display. Mineral identification and fracture examination by binocular and petrographic microscope, x-ray diffraction, and electron microprobe analysis were performed. Results were used to prepare a lithologic log (Figure 1b) showing the approximate location of geologic unit boundaries, dikes and mineral filled fractures. Gross gamma measurements of cutting samples were made (Figure 1c) in a region of particular interest to compare drilling pipe depths with wireline gamma ray depths (Figure 1d).

Wireline Logging and Procedures: A 7-conductor, tetrafluoroethylene (TFE) teflon insulated logging cable and cable head rated for continuous service at 320°C were used to run the Los Alamos project logging sondes (Dennis et al., 1985) and the USGS high temperature televiewer. Pressure control equipment for the high temperature logging cable was limited to 1000 psig. A casing collar locator was run in conjunction with other sondes for depth calibration.

A commercial "slim hole" gamma ray/collar locator provided a through-drill-pipe log in a drill string cooled with low flow rate circulation.

Temperature Logging: The temperature sonde uses a thermistor probe with high accuracy and resolution. It is readily fielded, reliable and more easily replaced than other sondes. Therefore it was run prior to running other logging sondes. Cable tension and tool turnaround were monitored carefully to assure hole conditions were suitable for the caliper logging to follow. Surveys were run at 60 to 150 ft/min both into and out of the well. Depths were corrected for thermal lag time and cable stretch (turnaround).

Temperature surveys were run in well EE-3A preceding and following each packer experiment. Anomalies and variations from the background temperature gradient were used to infer fracture inlets/outlets within +10 feet (Figure 1g, Figure 2). More precise location of fractures was often precluded by the high pressures that prevented logging during injection or early shut-in. The packer configuration prevented logging below it. Venting and circulation of the well was required prior to removal and this resulted in a smearing of fluid entrances and made it difficult to determine the fracture locations.

Caliper Logging: The Los Alamos caliper tool is a 3-independent-arm tool configured to measure hole diameters from 5 to 14 inches. Mechanical linkage, magnetic couplings and high temperature, rotary potentiometers are used to convert borehole radius to an electronically measured output. The sonde was run with the arms retracted. They were extended to log out over the interval of interest and then retracted for removal. Logging speeds varied from 5 to 40 ft/min. Pre-log and post-log calibrations were made to calculate corrections for the caliper pad wear which was significant on runs of over 200 feet. The tool was run with two bow centralizers straddling the measuring arms. A slip and stick movement of the tool was indicated by caliper log quality below 12,600 feet.

Accurate caliper logs were required to select packer seats (Figure 1f). Over-extension of the high temperature design inflatable packer element (in the range of 9.5 inch diameter) made the element susceptible to rupture. Washouts, breakouts or ledges which could easily go undetected using a single or dual arm caliper can also rupture the element. After the packer ruptured during initial inflation on run five (Table 1) a repeat caliper log showed that an inoperative arm on the previous log had, in fact, tracked through a washed out fracture with no significant response by the other two arms (Figure 3). A new packer seat was selected 30 feet above the previous packer depth and a successful injection of 1-1/2 million gallons was completed with no evidence of a packer leak.

Televiewer logging: The motor in the logging sonde would not operate in the primary interval of interest below 12,400 feet, but was operational above 12,200 feet so logs were run over several alternate depth intervals. A logging speed of 5 ft/min provides the most detailed image. However stick-slip motion of the sonde at low logging speeds resulted in imagery that was totally incoherent at 5 ft/min and only partially coherent at 10 ft/min. A logging speed of 20 ft/min was used. The best logs were obtained in the depth interval between 11,200 and 12,000 feet, where hole inclination (from the vertical) was about 10 degrees. Below that interval, wire-line drag aggravated the stick-slip motion. Above that interval, the inclination was as high as 20 degrees and image quality deteriorated due to poor centralization of the tool and an increase in stick-slip motion. The results emphasize the need for improved centralizing assemblies for imaging tools.

Studies of the texture of the imagery indicate that coherent images were obtained for about 95 percent of the logged intervals. Incoherent imagery is characterized by a texture termed "shading" as illustrated by Clark (1981). The 5 percent of incoherent imagery, from comparison with caliper logs, probably corresponds with zones of multiple, open fractures. It is, in fact, reasonable to interpret all the incoherent portions of the imagery as open fracture zones. This means that the televiewer yielded, preferentially, coherent imagery for non-fractured parts of the wellbore. While this result is disappointing for studies of the hydraulic apertures, it was turned to advantage in selecting locations for packer seats.

Two types of geological features were extracted from imagery (Figure 1h and 1i). The first is the discrete, dark, linear feature which, as is well-known, corresponds to fractures or joints. The textural appearance is probably due to wave-guide absorption (Burns, 1986). The second is a diffuse, or dispersed feature with two possible causes. It may be due to foliation or to fractures of aperture less than the sonic wavelength. The two types are shown separately on the accompanying figures. Whatever the geological cause of the second type, it was found that it is clear and distinctive in smooth regions of the wellbore, as indicated by the caliper log, and obscured or invisible in rough sections.

There were therefore two criteria for finding smooth, sound, unfractured portions of the wellbore from televiewer logs which were supported by caliper results: the lack of incoherent "shading" and the visibility of diffuse features. These were felt to give a reliable diagnosis of hole condition and were a major consideration in choosing the final packer seat.

Open Hole Gamma Ray Logging: A geiger detector gamma ray sonde was run in the open hole of EE-3A to tie the natural gamma ray depth signature to project wireline depths. The commercial design electronics for the tool are thermally protected in a dewar housing with a cerrobend heat sink. The tool operates at temperatures of 300°C for more than 6 hours. The gamma ray signature obtained was readily correlated with signatures obtained with the commercial through-drill-pipe log. Most logs were run at 60 to 80 ft/min. Logging speeds as low as 40 ft/min were required to obtain a good repeat signature with the dewared tool.

Gamma Ray/Collar Locator Correlation Log: A commercial high temperature gamma ray / collar locator log was run through drill pipe. It was determined that a packer rupture occurred as a result of setting the packer in enlarged hole. There were two possible explanations for positioning the packer at an improper depth: (1) The depth correlation between the caliper log and drill pipe was incorrect. Open hole and through-drill-pipe gamma ray logs confirm that the packer had been set at the proper depth. Tag bottom depths had been successfully used to correct wireline depth to drill pipe depth. (2) The caliper arm pads failed to track through a washout. This in fact occurred as is discussed under caliper logging.

RESULTS OF THE LOGGING PROGRAM

The logging program provided input to the successful packer operations and also added significantly to the reservoir description process complementing injection and tracer data. Results that contributed to the reservoir description included depth correlation of drilling data with wireline data, location of active fractures, mineral filled fractures and foliations and formation changes.

Depth Correlation: Table 2 shows correlations between wireline and drill pipe depths. Depth measurements made on various runs using the same wireline varied less than four feet. Depths measured using different wirelines varied as much as 20 feet. When working within 600 feet of the bottom of the hole, tag bottom depths were used successfully to make the drill pipe / wireline depth correction.

A logging run was required for each sonde run since multiplexing equipment for the Los Alamos open hole logging tools (now under development) was not available. Where accurate packer depths were required, an open hole gamma ray log was run on the wireline currently in use to correlate with a through-drill-pipe gamma ray log.

There was also concern that drill pipe depth discrepancies may have occurred. Gamma ray measurements were made on the drill cuttings over an interval of specific concern in selecting the packer seat for run 7, to assure that the mud log depths at the packer seat were on depth with the through-drill-pipe gamma ray log being used to position the packer. The resulting measurements led to an alternate correlation presented in Figure 1a, b and c (dashed line).

Active Fractures: Active fractures were located using pre- and post-injection temperature logs. Full interpretation of post-injection logs required modeling or simulation using a wellbore heat transfer code in order to calculate the flow split. However the raw log data were adequate to detect fractures and select packer seats. Temperature logs of the EE-3A wellbore are shown on Figures 1g and 2. The major active fractures inferred using these and other logs are also depicted in Figure 2. Oriented cores were obtained but there is considerable evidence that the orientations were not representative of most of the wellbore. Where log quality is adequate the televiewer log provides the best information on fracture orientation.

Lithology and Structure: Lithological banding was detected in mud logs, televiewer logs and cores. More detailed lithologic information was obtained by laboratory examination. Comparison of core and televiewer data is continuing to resolve the question of detectability of fabric elements such as cleavage and foliation (diffuse features).

Early in the drilling, a possible correlation between large drill cuttings/high drilling rates and high biotite concentrations (based on wellsite measurements) was observed. Packer seats were selected to avoid regions of large or irregular cuttings, high biotite concentrations, high secondary mineral concentrations and high penetration rates

based on the assumption that any of these might be indicative of weak or incompetent rock. Subsequent laboratory study has shown that simple biotite content is not the controlling factor, but may provide some indication of rock strength or competence. All of the packers were set in granodiorite with biotite concentrations of less than 10%.

Mineral-Filled Fractures: Mineral-filled fractures were identified by laboratory examination of the drill cuttings and core where available. The use of high viscosity sepiolite gel drilling fluid removed cuttings up to 0.2 inches long and complete fractures up to 0.08 inches wide were detected. Cuttings containing fracture surfaces broken during drilling were also observed. Several thousand cuttings per sample had to be examined to detect even moderately abundant fractures. From this study, regions with high density of mineral-filled fractures were identified (Figure 1b).

Textural relations within fracture fillings show that many fractures have been repeatedly reactivated in the past and could be activated during packer inflation and reservoir stimulation. Information about mineral-filled fractures was used in selecting the last two packer seats.

Microseismic Earthquake Density Plot: An earthquake density plot was constructed using earthquakes mapped during the 5 million gallon injection into EE-2. The number of earthquakes located within 300 feet (100 meters) of a given measured well depth are compared with the active fractures inferred from temperature logs (Figure 2). There is a correlation between the seismic density and the connecting and non-connecting fractures. Regions of high density surround and in some cases overlap the connecting fracture entrances.

Stimulation Testing Program: The stimulation testing program, summarized in Table 1, achieved two goals: (1) Stimulate the reservoir in the vicinity of the new wellbore (EE-3A) to establish and enhance hydraulic connections with EE-2. (2) Assess injection potential and determine injection pressure/rate relationships for the stimulated intervals. The first two tests below the low pressure region were primarily for the purpose of evaluating packer performance while the subsequent testing had specific reservoir testing objectives (Kelkar et al., 1986). Volumes up to 1-1/2 million gallons of water and test durations up to 100 hours were achieved using the packer system. Hydraulic communication between the two wells was established through several well defined fracture entrances at depths between 11,700 and 12,550 feet.

Packer Results: Packer performance was much better than expected. Out of seven runs two packers ruptured during initial inflation. Leakage around the packer was observed on only two packer runs. Packer damage caused the leak on run 2. A packer seat located between two fractures which were both connected to EE-2 explained the leakage observed during run 7. The ability to select suitable intervals for packer seats and a well planned and systematic approach to the experimental plans played a major role in the successful program.

CONCLUSIONS

The EE-3A logging program was crucial in selection of packer seats for the reservoir testing program. The mud logging program provided wellsite input to focus the caliper logging on regions with good potential packer seats. The three arm caliper log was needed to eliminate sections of bore that were too large for the high temperature packer element. This was confirmed on packer run 5 where the packer element ruptured after it was set using two arm output from the three arm caliper sonde. Temperature logs provided sufficiently accurate location of fractures to select packer seats. The logging program has also contributed to the understanding of reservoir structure which at this point is in good agreement with other reservoir data.

The importance of multiple arm caliper logging and good wireline depth corrections was demonstrated during these operations. High temperature wireline logging has been shown to be a useful investigative tool in granitic rock. A six arm, hot hole caliper, a high temperature multiplexing system and high pressure well control equipment for large diameter hot hole wirelines are needed to make the techniques described commercially viable. A method to eliminate the severe stick-slip movement of the the caliper and televiewer sondes in the inclined, abrasive wellbores at Fenton Hill would make the caliper/televiewer and open hole packers a powerful and complementary wellbore evaluation system.

ACKNOWLEDGMENTS AND DISCLAIMER

Reference to a company, product, service or equipment does not imply approval or recommendation of the same by the University of California (Los Alamos National Laboratory) or the U. S. Department of Energy to the exclusion of others that may be suitable. The project described in this paper was funded by the U. S. Department of Energy, Division of Geothermal Technology as well as the Governments of the Federal Republic of Germany and Japan.

The authors acknowledge the many individuals and firms who supported the work described herein. We especially thank Leigh House for his contribution to the seismic density plots and Richard Hodges with the Water Resources Division of the USGS who provided and operated the televiewer.

TABLE 1. PACKER SEAT SELECTION AND RESERVOIR TEST DATA

RUN	TEST INTERVAL+ (ft.)	BOREHOLE DESCRIPTION* DIAMETER (in)	SECONDARY MINERALS %	BIOTITE %	INJECTION VOLUME (gal)	TIME (hr)	COMMENTS
1	10,829-10,875	8.75	1	3-5	6,000	1.5	Initial packer test, no leakage observed.
2	10,841-11,615	8.75	2	3-5	140,000	10	Packer deflated, moved and leaked.
3	11,537	8.9	2	5-7			Packer damaged during run in and failed to set.
4	11,537-12,203	8.9	2	5-7	420,000	20	Small leak via fracture suspected. Connection to EE-2 established.
5	12,585	9.2**	1	<5			Packer ruptured during initial inflation.
6	12,555-13,180	9.2	1	<5	1.4×10^6	38	No leakage observed.
7	11,976-12,550	9.1	2	<10	1.5×10^6	84	2nd connection to EE-2 established, 1 BPM leak observed. Bypass to upper EE-2 connection formed leak path.

* Diameter based on caliper log. Mineral percentages based on wellsite mud log estimates. Country rock lithology was identified as biotite granodiorite on the mud log.

\+ Initial depth corresponds to packer setting depth.

** Repeat caliper log showed a 4.9 inch radius wash out or break out on one side of bore.

TABLE 2. DEPTH CORRECTIONS FROM COMMERCIAL AND LOS ALAMOS WIRELINE GAMMA RAY LOGS USED FOR RUN 6 AND 7 PACKER SEAT SELECTIONS.

FEATURE	DEPTHS PIPE	THRU DP	OPEN HOLE	DEPTH CORRECTIONS THRU DP LOG	OPEN HOLE LOG
Whipstock	9,391*		9,376		15
GR Spike**	9,584	9,573	9,571	11	13
GR Spike	10,048	10,036	10,040	12	8
GR Spike	10,910	10,896	10,902	14	8
GR Spike	11,761	11,746	11,755	15	6
GR Spike	12,454	12,440	12,453	14	1
GR Spike	13,038	13,021	13,037	17	1
Tag Bottom	13,170	13,155		15	

* Top of whipstock set at 9,380 ft. with previous rig and drill string.

** High gamma ray count over a narrow interval.

REFERENCES

Burns, K.L. (1986), "Geological structures from televiewer logs of GT-2, Fenton Hill. Part 1 - feature extraction", LA-MS report, Los Alamos National Laboratory, 25 pp., in press.

Clark, W.P. (1981), "Landsat 3 Return Beam Vidicon response artifacts. A report on RBV photographic product characteristics and quality coding system", EROS Data Center, Department of Interior, Sioux Falls, 13 pp.

Dennis, B.R., Koczan, S.P. and Stephani, E.L. (1985), "High-Temperature Borehole Instrumentation," LA-10558-HDR, UC-66b.

Dreesen, D.S. and Miller, J.R. (September 12, 1985), "Open Hole Packer and Running Procedure for Hot Dry Rock Reservoir Testing," Proceedings Fourth Annual Department of Energy Geothermal Program Review, Washington, D. C.

Dreesen, D.S., Miller, J.R., Halbardier, F.A. and Nicholson, R.W. (1986), "Open Hole Packer for High Pressure Service in a Five Hundred Degree Farenheit Precambrian Wellbore," Proceedings IADC/SPE 1986 Drilling Conference, Dallas, Texas.

Hickman, H.H., Healy, H.H. and Zoback, M.D. (June 1985), "In Situ Stress, Natural Fracture Distribution, and Borehole Elongation in the Auburn Geothermal Well, Auburn, New York," Journal of Geophysical Research, Vol. 90, No. B7, p. 5497-5512.

House, L., Keppler, H. and Kaieda, H. (August 1985), "Seismic Studies of a Massive Hydraulic Fracturing Experiment," Transactions Geothermal Resources Council, Vol. 9-Part II.

Kelkar, S., Zyvoloski, G. and Dash, Z. (1986), "Pressure Testing of a High Temperature, Naturally Fractured Resevoir," this workshop.

Warren, W.E. (December 1981), "Packer-Induced Stresses During Hydraulic Well Fracturing," Transactions of the ASME, Vol. 103, p. 336-343.

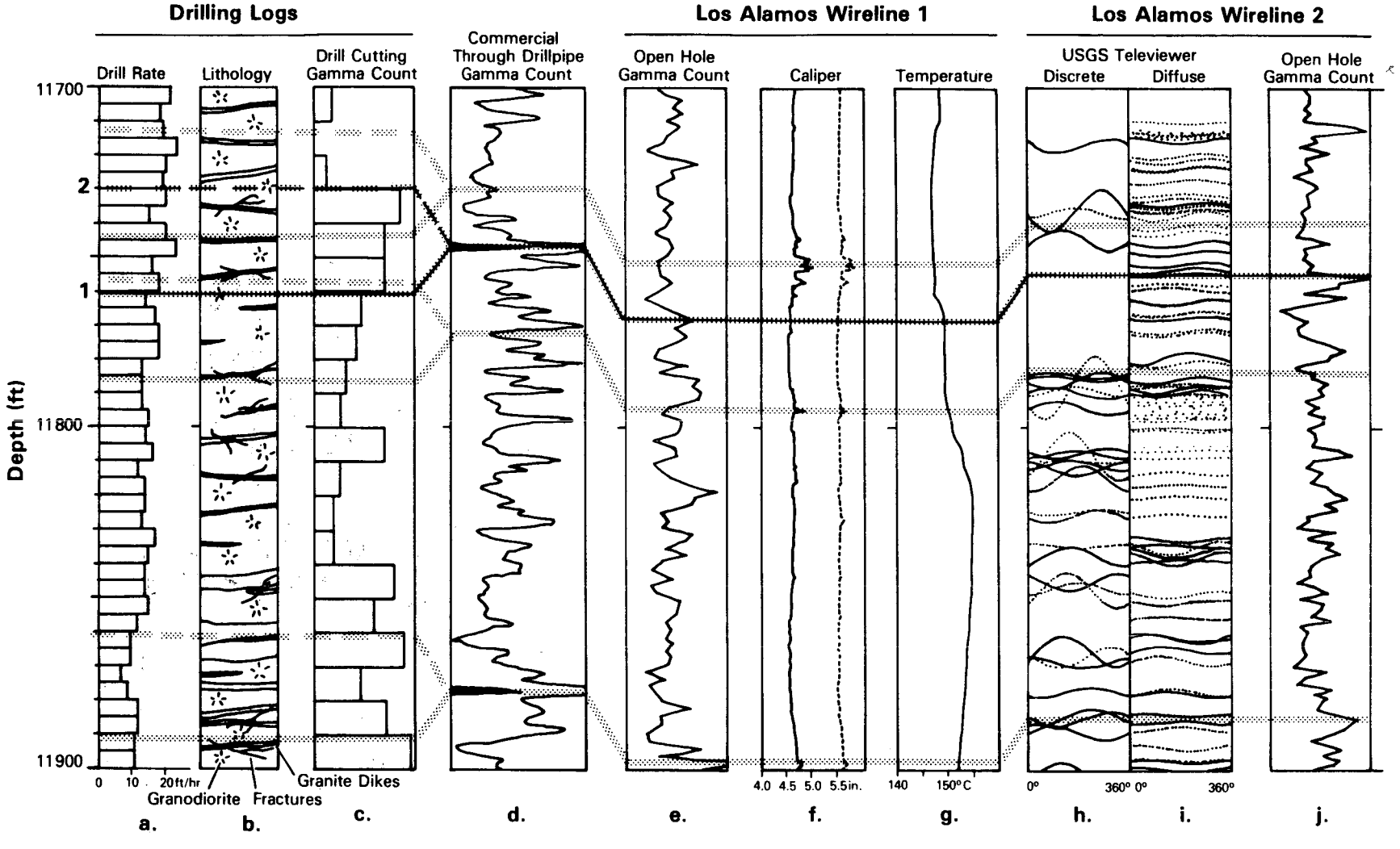

Figure 1. Example of well logs used for selecting packer seats.
1. Correlation based on through-drill-pipe and wire-line gamma ray logs run after drilling was completed.
2. Alternate correlation of drilling logs based on gamma ray counts of drill cuttings.

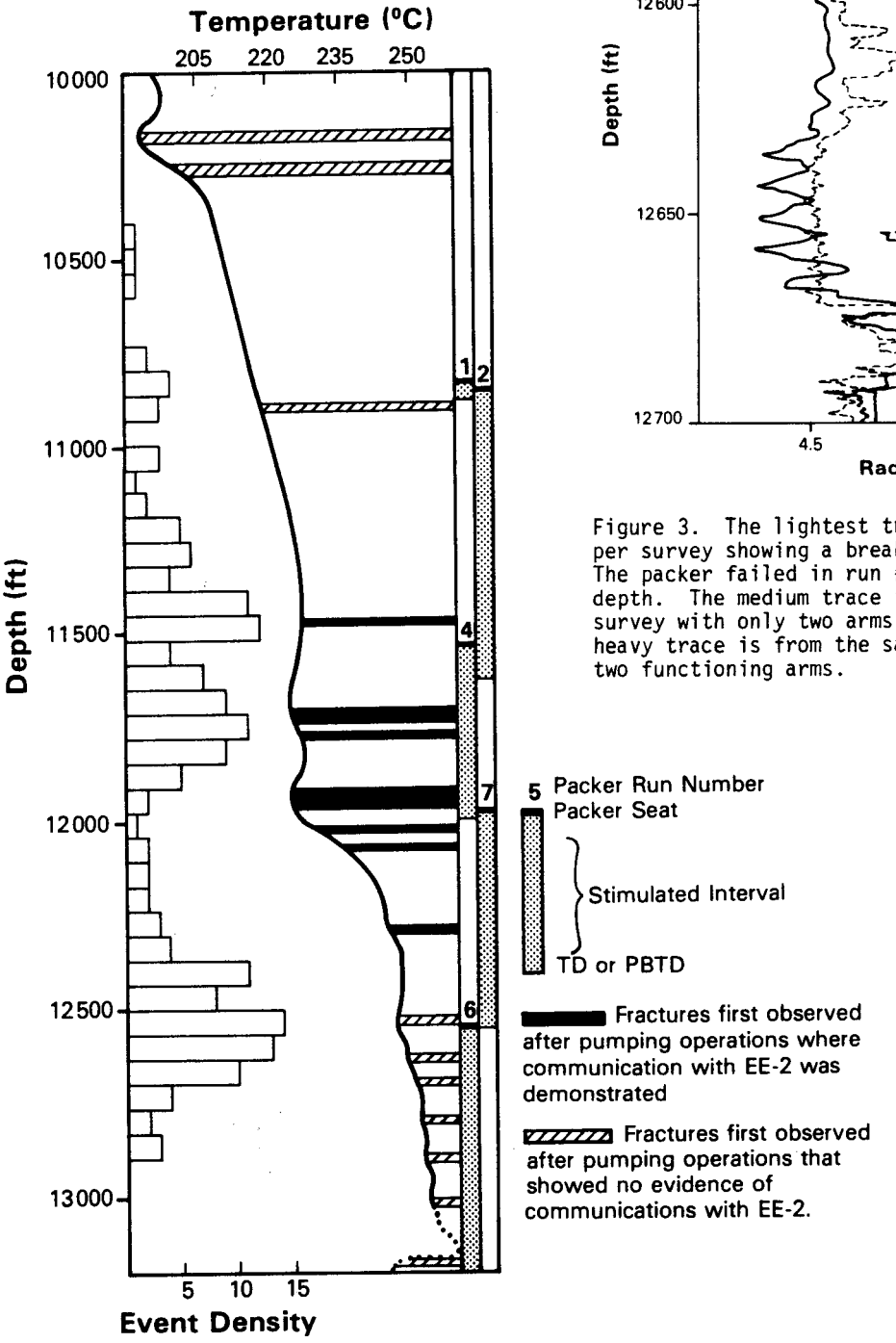

Figure 2. A histogram of microseismic event densities and a typical temperature log compared to fracture entrances detected in stimulation test # 1 to 7.

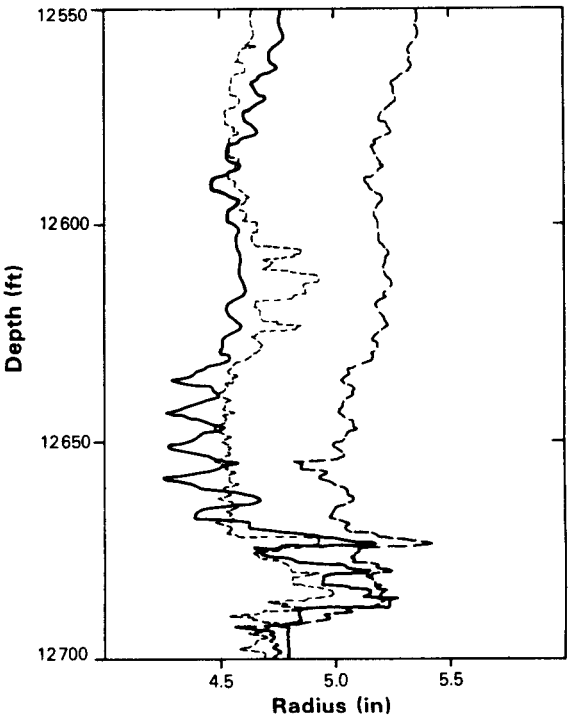

Figure 3. The lightest trace is a 3-arm caliper survey showing a break-out near 12,600 feet. The packer failed in run #5 when set at this depth. The medium trace is an earlier caliper survey with only two arms functioning. The heavy trace is from the same survey using the two functioning arms.

PROCEEDINGS, Eleventh Workshop on Geothermal Reservoir Engineering
Stanford University, Stanford, California, January 21-23, 1986
SGP-TR-93

SINGLE BOREHOLE GEOTHERMAL ENERGY EXTRACTION SYSTEM FOR ELECTRICAL POWER GENERATION

George E. Lockett

Total Energy Conservation & Management Co. Ltd.
Whelmar House, Skelmersdale, Lancashire WN8 6NN, England
Tel.: +44 695 33255 Telex: 666387 AMSTEL-G ATTN.TECAM Fax: +44 695 29668

ABSTRACT

The Extraction System utilises heat transfered from the geothermal fluids into a closed combined Heat Pipe/Organic Rankine Cycle. The system overcomes problems of reinjection, two phase fluid movement and enviromental pollution by bringing a clean secondary fluid to the surface. Reservoir fracturing and primary fluid movement will also be covered.

HOW THE SYSTEM WORKS

One of the innovations is the use of thermal/fluid heat transfer. Special fluids operate in a closed pipe circuit to transfer heat from the bottom of the well to the top via vaporised fluids moving at near sonic velocities. The minimum depth of hole needed to provide power enough to drive turbogenerators depends on the geothermal gradient: in some geographical areas this is from as shallow as 900m.

Downhole, these wells are completed by casing and perforating through up to 1,000m of fractured hot rocks, in either a dry or a hydrothermal field. Reservoir heat is transferred to the wellbore by convection-type circulation over the 1,000m of exposed formation. Additional horizontal drilling and hydraulic fracturing to aid this process can be utilised. In truly dry holes, addition of a second working fluid to the formation makes internal circulation possible.

Inside the casing, a closed 203mm tube is inserted, containing a sintered copper or stainless capillary type liner (see Fig. 1). This liner extends over the lower 1,000m of its interior surface. Inside the tubing, a concentric, well-insulated 63mm diameter working fluid return string sprays condensed liquid through perforations onto the sintered metal heat exchanger. The capillary action of the sintered wick transfers a thin film of working fluid around the circumference. The vaporised fluid then flows up the tubing return annulus, to the surface turbine unit. Cooling water provides a strong temperature differential for efficient energy extraction.

The working fluid flows down the 63mm return tube by gravity, against reduced backpressure of the hot vaporised fluid. A backup feed pump is available to start the system.

Since there is no interchange between working fluids and external heat source fluids located in the casing-tubing annulus, the system life is as high as 20-25 years.

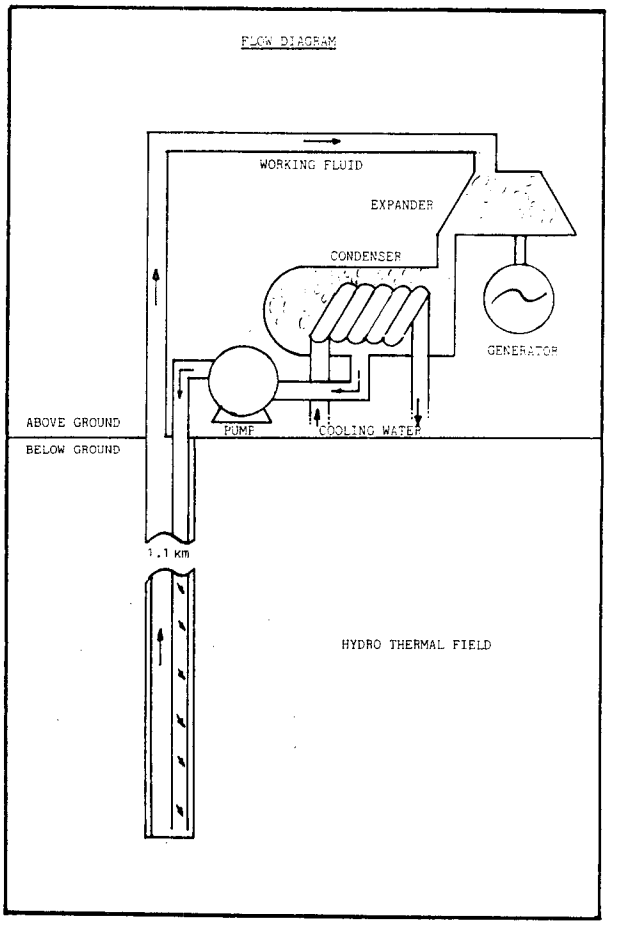

FIGURE 1

THE ADVANTAGES OF A SINGLE BOREHOLE SYSTEM

Most geothermal power stations today are based on two-hole extraction systems, the reason being that the geothermal fluids are not pure: there are many contaminants that cause environmental pollution. These two-hole systems normally extract geothermal fluids from one hole and re-inject the cooled fluids down a second well. This removal of fluid itself causes a whole host of problems: corrosion, silting of well, two-phase fluid movement, subsidence and many other lesser problems.

With the single borehole system, pressure in the geothermal fluids is maintained as the fluid is not removed from the field. This has many advantages, as no drop in pressure means that the geothermal fluids do not turn into aggressive corrosive contaminants. Also, because the pressure is maintained, suspended solids stay in suspension and do not drop out to silt up the well.

However, by far the most important advantage of the single borehole system is that no environmental pollution is caused. This is a very important claim, as all the traditional methods of power generation cause environmental pollution. Some examples are:

- Fossil fuels cause "acid rain"

- Nuclear power causes radioactive waste

CREATION OF A RESERVOIR

Single borehole systems to date are very rare. This is due to the inability to create a dynamic method of heat extraction. The creation of a suitable geothermal reservoir which can transfer geothermal heat from a large catchment area, not by conduction but by the circulation of either a naturally occuring or an artificially created geothermal fluid, is also a necessity for a single borehole system.

There are many areas around the world where there are natural reservoirs: obvious examples are geysers and hot springs (Ref. 1). Hydrothermal and steam fields are also suitable sites for single borehole systems. Hot dry rock applications, though, need the creation of an artificial reservoir (Ref. 2). This is normally achieved by a combination of horizontal drilling, downhole fracturing and the use of special circulating fluids.

ECONOMIC ADVANTAGES OF THE ONE-HOLE SYSTEM

One of the major advantages of a single borehole system is that wells drilled for other purposes can be utilised for geothermal. Some examples are: unsuccessful or dried-up oil and gas wells and test bores. Normally, the high cost of drilling these is just written off. The conversion of these wells is quite simple if utilisation has been decided before the borehole has been plugged.

As the single borehole extraction system makes use of low boiling point organic fluids, then these wells, which are not normally drilled in geothermally rich areas, still have high enough bottomhole temperatures to be an economic proposition.

UTILISING READY-DRILLED HOLES FOR GEOTHERMAL

In areas like the North Sea (U.K.), oil drilling is carried out from platforms. Normally up to 20 wells are drilled from one platform, though not all of these are productive. The use of a small proportion of wells for the extraction of geothermal heat could provide adequate electrical supply for the platform.

The North Sea has got the added advantage of a large volume of relatively cold (5 deg. C) sea water that provides a good heat sink.

DRILLING HOLES SPECIALLY IN GEOTHERMALLY RICH AREAS

It is economically viable to drill purpose-made bores in areas where the earth's crust is thin, such as the offshore regions of China, the Middle East, Southeast Asia, down the Atlantic Ocean and along the west coast of North and South America.

Studies show (Ref. 3) the system can extract 2.5mw of electrical power from rocks hotter than 150 degrees Centigrade. In isolated areas the geothermally powered generator can supply economical power for irrigation pumps, lighting, heating and other applications.

For further technical information and licence details, contact the writer.

REFERENCES

1. Freeston, D.H. (1985), "The Application and Design of Downhole Heat Exchanger": Geothermics, Vol. 14, No. 2/3, pp 343-351.

2. Foster, J.W. (1984), "Method for Producing a Geothermal Reservoir in a Hot Dry Rock Formation for the Recovery of Geothermal Energy": Author, Illinois State University.

3. Rice, G. (1985), "Predicted Performance of a Heat Pipe/Geothermal Energy System for Total Energy Conservation and Management Co. Ltd.": by request from author.

PROCEEDINGS, Eleventh Workshop on Geothermal Reservoir Engineering
Stanford University, Stanford, California, January 21-23, 1986
SGP-TR-93

Deliverability and its Effect on Geothermal Power Costs

J.S. Gudmundsson and J.A. Marcou

Petroleum Engineering Department
Stanford University

Abstract

The deliverability of liquid-dominated geothermal reservoirs is presented in terms of reservoir performance, and wellbore performance. Water influx modeling is used to match the performance of Wairakei in New Zealand, and Ahuachapan in El Salvador. The inflow performance is given in terms of a linear productivity index for liquid-only flow, and a solution-gas drive relationship for two-phase flow. A 9-5/8" production well is assumed, flowing 250°C water from 900 m depth, with a wellhead pressure of 100 psia. A Geothermal Development Model, that couples reservoir deliverability and power plant performance, and assigns costs to both, is used to illustrate how the development cost of geothermal electric power projects can be estimated.

Introduction

The performance of reservoir/wellbore systems is perhaps the major cause of uncertainty in geothermal field development decisions, at least in comparison to the performance of surface facilities and power plants. Because of this uncertainty it is difficult to optimize the development of liquid-dominated resources for electric power production. This may be the reason why issues of geothermal resource exploitation and power plant operations tend to be dealt with separately in the literature. In this paper, we couple the reservoir and economical issues in a Geothermal Development Model, and consider the effect of deliverability on the cost of geothermal electric power from liquid-dominated resources. The overall performance of a reservoir/wellbore system with time is what we call deliverability. It has three components: reservoir performance, inflow performance, and wellbore performance.

Reservoir Performance

A reservoir model describes the change in reservoir pressure as a function of fluid production. The reservoir models available range from simple decline curves, through lumped-parameter models, to distributed-parameter models. Grant (1983) has reviewed these for geothermal uses. Figure 1 shows the drawdown in reservoir pressure versus cumulative mass withdrawal for three liquid-dominated reservoirs: Ahuachapan, Svartsengi, and Wairakei. These data were taken from Vides (1982) and Quintanilla (1983) for Ahuachapan, and from Gudmundsson et al. (1985) and Stacey and Thain (1983) for Svartsengi and Wairakei, respectively. Figure 1 shows that the drawdown in the three reservoirs is similar. The Wairakei reservoir is known to be larger than the others. In terms of surface area, it is reported to be about 15 km^2 (Donaldson and Grant, 1978), while Ahuachapan and Svartsengi are likely to be in the range 5-10 km^2. Figure 1 suggests that Svartsengi is the smallest of the three; it shows greater drawdown at lower levels of production. Through 1982, the average rate of fluid production from Wairakei was about 1500 kg/s; the rate at Ahuachapan was about 600 kg/s through 1983; from Svartsengi the average rate was about 150 kg/s, currently it is about 300 kg/s. The three fields are reaching nearly the same level of drawdown as cumulative mass production increases. The long-term drawdown appears to be about 3 MPa, although the drawdown in the two smaller fields has not leveled off as much as Wairakei. We observe that these geothermal liquid-dominated reservoirs exhibit a similar drawdown characteristic; their overall uniform behavior suggests they can be modeled using similar reservoir engineering techniques. The Wairakei, Ahuachapan, and Svartsengi reservoirs have a steam/vapor-dominated zone above the main liquid-dominated zone; see Donaldson and Grant (1981), Rivera-R. et al. (1983), and Gudmundsson and Thorhallsson (1986) for details, respectively.

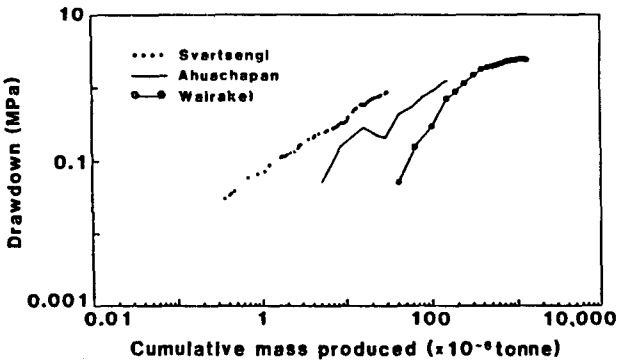

Figure 1. Drawdown in reservoir pressure in three liquid-dominate reservoirs.

We elected to use a lumped-parameter model with water influx to study the performance of the three liquid-dominated reservoirs; specifically, the simplified method of Hurst (1958). This method was used by Olsen (1984) and Gudmundsson and Olsen (1985) to match the production history of the Svartsengi reservoir. Marcou (1985) extended this work to include Ahuachapan and Wairakei - the latter match will be discussed here. We assumed the reservoir to be radial and finite, and the supporting aquifer to be radial and infinite. In water influx modeling we focus on fluid flow across the boundary between the hot reservoir and surrounding warm aquifers. The reservoir is taken to have homogeneous properties and uniform pressure. The model equation is given in terms of the warm aquifer physical properties; the permeability-thickness product of the reservoir and aquifer are taken to be equal; the compressibility of the reservoir and aquifer provide the

main contrast in properties. In a general way, the pressure response of the reservoir is dominated by the flow of water into the main reservoir volume from surrounding aquifers. If there was no fluid flowing into the reservoir, it could be modeled as a constant volume tank under decompression or drainage. There are three constants used in the Hurst (1958) simplified method

$$A = \frac{\mu_a}{2\,\pi\,kh\,\rho_a}$$

$$B = \frac{k}{\phi\,\mu_a\,c_a\,r_r^2}$$

$$C = \frac{2\,c_a}{c_r}$$

where the symbols have the usual meaning, and the subscripts a and r stand for aquifer and reservoir, respectively. Grant et al. (1982) showed that for typical geothermal reservoir conditions, the compressibility of liquid water is of the order of 10^{-9} Pa^{-1}, steam vapor 10^{-7} Pa^{-1}, and a two-phase mixture 10^{-6} Pa^{-1}. This range of several orders of magnitudes affects greatly the pressure response of geothermal reservoirs, particularly when two-phase zones are present.

We matched the Wairakei data using 3 years, 6 years, 12 years, and 25 years of production history. The match parameters obtained from the partial data sets were then used to predict the drawdown in reservoir pressure for the 25 years of history. Our matches are shown in Figure 2. We wanted to test the forecasting ability of the model. Using the first three years of history, the model overpredicts the drawdown; using six years or more the match between model and actual drawdown was reasonable. That is, using six years of production history, we were able to forecast the next twenty years of drawdown with reasonable success. The following values of model constants were obtained from the full match: $A = 6.7 \times 10^2$ pa.s/kg; $B = 9.3 \times 10^8$ s^{-1}; $C = 0.19$. For an aquifer compressibility of 2.4×10^{-9} Pa^{-1}, the reservoir compressibility becomes 2.6×10^{-8} Pa^{-1}. It appears from this result that boiling in the two-phase zones does not significantly influence the compressibility of the Wairakei reservoir.

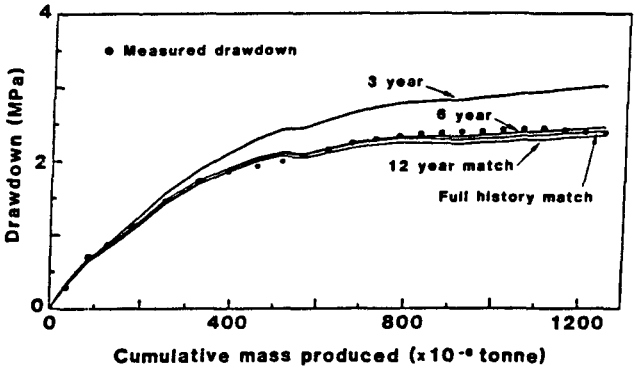

Figure 2. History match and forecast of drawdown for Wairakei.

Inflow Performance

The relationship between reservoir pressure and wellbore flowing pressure we call inflow performance. In general, the mass flowrate w increases with increasing difference between the two pressures, as expressed by the relationship

$$w = J\,(p_r - p_{wf})$$

where J is a constant called the productivity index. This equation usually applies for single-phase laminar flow into the wellbore; single-phase Darcy-type flow. In the case of geothermal wells, the well flowing pressure p_{wf} ought to be measured at the depth of the well's main feedzone fracture. The linear productivity index has been used by Gudmundsson (1984) in the calculation of output curves of geothermal wells with single-phase feedzones, using a wellbore simulator. We use it here for single-phase flow from the reservoir into the wellbore; when the well flowing pressure p_{wf} is greater than the saturation pressure p_{sat} of water. Figure 3 shows that inflow performance of well Utah State 14-2 in the Roosevelt Hot Springs geothermal area. The data were taken from Butz and Plooster (1979), and Butz (1980); see also Menzies (1982). The productivity index of this well was determined to be about 40 tonne/hr.MPa (600 lb/hr.psi), which is an average-kind of a well. A more productive well is well 12 in the Svartsengi field, which was reported by Gudmundsson (1984b) to have a productivity index of about 100 tonne/hr.MPa (1500 lb/hr.psi). We note that the productivity index is the inverse slope of the line above p_{sat} in Figure 3. A larger productivity index, therefore, means that a greater flowrate is achieved for the same pressure drive. Furthermore, the advantage of increased casing size is greater for wells with a large productivity index.

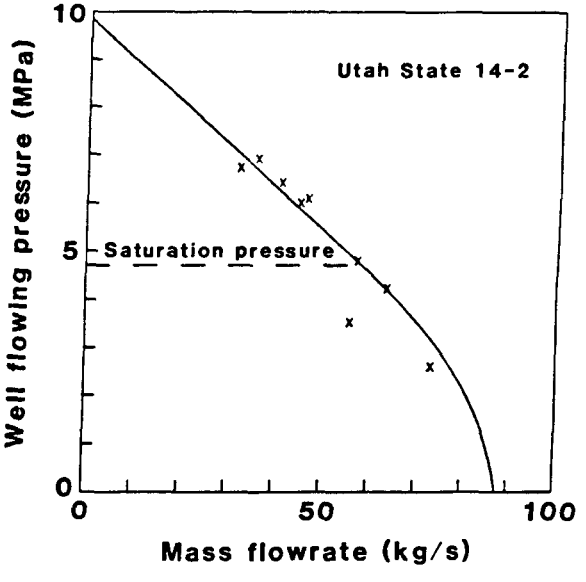

Figure 3. Inflow performance of well Utah State 14-2.

At relatively high flowrates, and when a steam/water mixture flows from the reservoir into the wellbore, the relationship between mass flowrate w and driving pressure $(p_r - p_{wf})$, is likely to become non-linear. This problem was

investigated by Vogel (1968) for solution-gas drive reservoirs in the petroleum industry; Menzies (1982) considered a similar problem of steam/water flow in fractures, including the effect of heat transfer from the rock to two-phase mixture. The Vogel-method was used in our work because of its simplicity.

The Vogel (1968) inflow performance curve is an empirical relationship, obtained for the situation where gas is coming out of solution; the flow of oil from its bubble point to increasing gas/oil ratio. We decided to apply the Vogel (1968) relationship to only the two-phase flow part of the geothermal inflow performance curve. For this situation the relationship takes the form

$$\frac{\Delta w}{\Delta w_{max}} = 1.0 - 0.2\left[\frac{p_{wf}}{p_{sat}}\right] - 0.8\left[\frac{p_{wf}}{p_{sat}}\right]^2$$

The Δw is the incremental mass flowrate we achieve by lowering the well flowing pressure below the fluid's saturation pressure. The Δw_{max} is what would ideally be achieved if the well flowing pressure be became negligible; in other words, if there was negligible pressure drop in the wellbore. The square term in the modified Vogel (1968) relationship takes into account turbulent losses and other non-linear effects. The inflow performance below the saturation pressure in Figure 3 is a solution-gas-type relationship. We see that the inflow performance of well Utah State 14-2 can be matched with a linear productivity index at pressures above the saturation presure, and a combined linear and non-linear relationship at lower pressures.

Wellbore Performance

We considered wells that produce steam/water mixtures at the wellhead. In the main they will have liquid water feedzones; in some cases the fluid will be two-phase, as in Figure 3 when the well flowing pressure falls below the saturation pressure. Wellbore performance concerns the pressure drop from the bottom or main feedzones to the wellhead. This performance depends on many variables, including: fluid enthalpy, reservoir pressure, well diameter and depth, and wellhead pressure. Ambastha and Gudmundsson (1986) present flowing pressure and temperature profiles in 10 two-phase geothermal wells; they also match the data using a wellbore simulator based on the Orkiszewski (1967) pressure drop correlations. Such a simulator can be used to construct performance curves for two-phase geothermal wells. Butz and Plooster (1979) and Butz (1980) have published performance curves for well Utah State 14-2. The curves are based on a fluid enthalpy of 1100 kJ/kg (liquid water at 250°C), a reservoir pressure of about 9.7 MPa (1430 psia) at a depth of 900 m, and a wellhead pressure of 0.69 MPa (100 psia). We present these curves in Figure 4 as wellbore performance curves for a 9-5/8" and 13-3/8" casing from 900 m depth to surface. The wellbore performance curves are independent of inflow performance and reservoir performance; when we couple them, however, we obtain the reservoir/wellbore system deliverability.

Geothermal Development Model

Decision making about geothermal developments deals with objectives, choices, and constraints. To optimize this decision making process, we need a model that includes both the physical and economic features of development. We have made such a model from the point

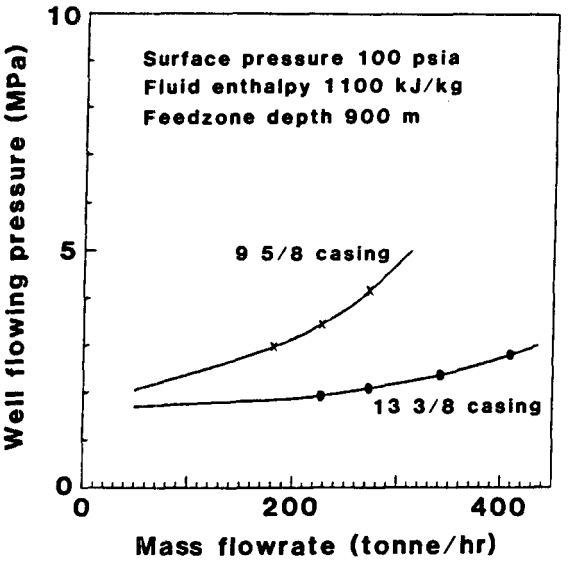

Figure 4. Wellbore performance of 9 5/8" and 13 3/8" wells.

of view of reservoir engineering, to study the effect of deliverability on electric power costs. The elements of the Geothermal Development Model are shown in Figure 5. Several physical models or features can be selected for each of these elements; similarly, different problems can be investigated: (1) reservoir can be modeled using decline curves, lumped-parameter models, or distributed-parameter models, (2) wellbore flow can be modeled using generalized, or flow pattern specific two-phase flow models, (3) surface facilities can have separators at each wellhead, or a central separator station (4) wellhead units and a central station are typical power plant choices (5) spent fluids can be disposed of at the surface or injected back into the reservoir, with or without chemical treatment. And, for whatever choices we make, there are associated costs, and constraints.

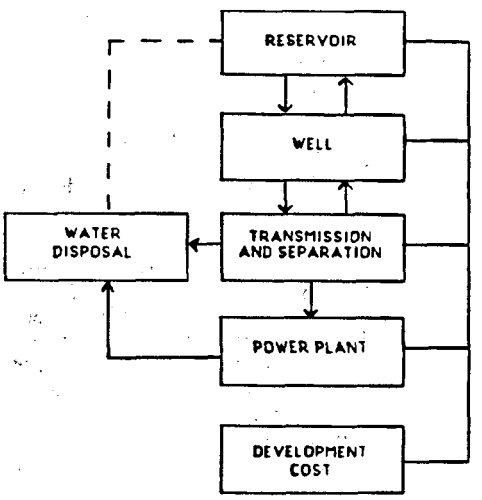

Figure 5. Elements of geothermal development model.

Above we presented the main features of the reservoir, inflow, and wellbore performances used. The following are a few details needed to complete the coupling of the individual performances to get the reservoir/wellbore system deliverability. We decided to use a 9-5/8" wellbore casing. The inflow performance curve in Figure 3, the 9-5/8" wellbore casing performance curve in Figure 4, intersect at a total flowrate of 220 tonne/hr (60 kg/s). This flowrate then, is the initial flowrate from a well like Utah State 14-2, for a wellhead pressure of 0.69 MPa (100 psia). With decreasing reservoir pressure, this flowrate will also decrease, because the inflow performance curve will move down in parallel with the initial curve, because it is constrained to go through the current reservoir pressure. We determined the deliverability of our typical well to follow the approximate relationship

$$w = 30p_r - 60$$

where w is mixture flowrate (kg/s) and p_r the average reservoir pressure (MPa). We used this equation in the development model to determine how many wells are needed at start-up, and when new wells are needed.

For a mixture enthalpy of 1100 kJ/kg and a separator pressure of 0.69 MPa, the mass fraction of steam is 22 percent. We reviewed a number of publications on geothermal electric power plants to obtain a value for the conversion efficiency of steam to electric power (see Marcou, 1985). We found that the following value were representative: condenser plants 8 tonne/hr.MW and back-pressure plants 15 tonne/hr.MW. We assumed negligible pressure loss from the wellhead to power plant. It follows that a well like Utah State 14-2 can generate about 6 MW of electric power initially. The average capacity of wells in liquid-dominated reservoirs worldwide is about 5 MW.

We divided the total cost of development into steamfield costs and power plant costs. Again, we reviewed a number of publications on geothermal electric power developments. The studies reviewed indicated that steamfield costs range from 25 to 50 percent of total development cost. Two of the references are reports by Holt and Ghormley (1976) and Southan et al. (1983). We decided to select typical cost values for use in the development model. The intial investment cost of central power plants was taken as 1.3 M$ per installed MW. This is cost in 1984 dollars, and includes expenses during construction. The initial investment cost of condenser wellhead units was taken as 0.7 M$ per MW. The cost of backpressure wellhead units was taken as 0.5 M$ per MW. We used an annual cost of 0.03 M$/year per MW for central plants, 0.06 M$/year per MW for condenser wellhead units, and 0.03 M$/year per MW for backpressure wellhead units. The wellhead units were assumed 5 MW in capacity. The investment cost values used in the development model can be thought of as total cost at start-up.

Steamfield costs include production wells, separators, pipelines, and injection wells; that is, the total cost of delivering steam to a power plant. We lumped these costs into one value and assigned them to a production well. In other words, we assumed that total steamfield costs are proportional to the number of production wells. We selected 2.2 M$ per production well as a representative value. The annual steamfield expenses we estimated 0.3 M$/year per production well. Note that the cost of injection wells, for example, is included in this cost value; we are simply using the production wells as our yardstick. Like the power plant costs, the steamfield costs ought to be thought of as the total cost at start-up.

A project life of 25 years and a discount rate of 10 percent were selected for our study. Costs were discounted to find their net present value at the start of the project.

For a project involving a central plant, the total development cost was arrived at as follows. The initial plant investment cost, plus the sum of the discounted annual plant cost, were added to the initial steamfield investment cost, plus the discounted annual steamfield costs. In addition, as the deliverability of each well declines with time, more wells need to be drilled to maintain steam production. The cost of the additional wells was discounted to present value along with their annual steamfield costs. For a project involving a wellhead unit, the plants and wells were installed at the same time in pairs. Wells and wellhead plants added after the first year of the project, were discounted to the first year; that is, their investment and annual costs.

The steamfield was assumed to operate every day of the year; at 100 percent capacity. The power plant was assumed to be operated at 80 percent capacity. Therefore, the drawdown in reservoir pressure was calculated assuming the wells were on-line all the time; the cost of electricity was calculated assuming the power plant was on-line 80 percent of the time.

Results and Discussion

The general form of our results is shown in Figure 6. The total cost of project development in million dollars, based on net present value at start-up, is plotted against generation level or installed electric power in megawatts. Consider the nature of this curve. Point A is a 50 MW power project, and point B a 150 MW project. The net present value development cost of the 50 MW project is 100 M$, while the 150 MW project costs almost 450 M$ (447 M$), which give 2000 $/kW and about 3000 $/kW as specific costs, respectively. Figure 6 happens to be based on Ahuachapan match parameters and 5 MW wellhead plants with condensers. The slope of the curve in Figure 6 gives the energy cost from different size developments. For example, at point A the gradient corresponds to a levalized energy cost of 31 mills/kWh, at point B it is 83 mills/kWh, and at point C (90 MW plant) it is 47 mills/kWh. We distinguish between the average and marginal cost. The average cost of energy is found from the slope of a line connecting some point on the curve with the origin. The marginal cost is found from the slope of the tangent to some point on the curve. At point A both the average and marginal costs are the same. At point B, however, the average cost is 47 mills/kWh, but the marginal cost 83 mills/kWh.

Why does the marginal cost of energy increase with generation level? The main reason, we think, is that the flowrate of the production wells decreases more rapidly at high generation levels than low, but also because we assumed no economy of scale in power plant costs. To illustrate this point: 11 wells are required for the 50 MW project in Figure 6, yet 78 wells are requried for the 150 MW project. Therefore, while the generation level tripled, the required number of wells (over the life of the project) increased about seven times. Neither did we lower the cost associated with production wells with time; that is, we assumed the same ratio of injection to production wells at start-up and later. We are forced to conclude that geothermal power developments shown dis-economy of scale when steamfield costs and power plant costs are coupled

The Geothermal Development Model can be used to study any number of reservoir/wellbore deliverability and

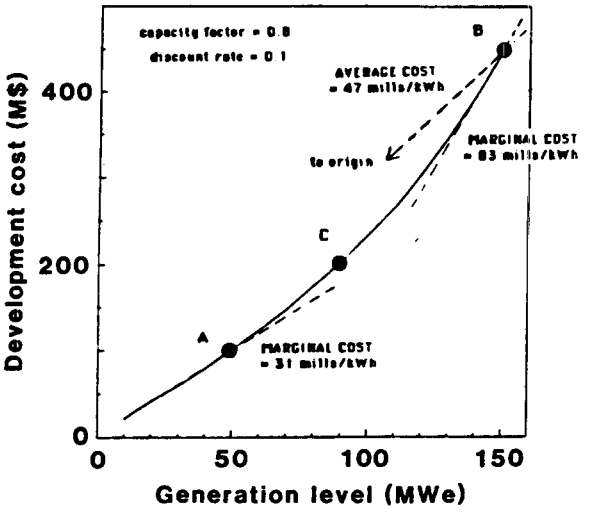

Figure 6. General form of results from development model.

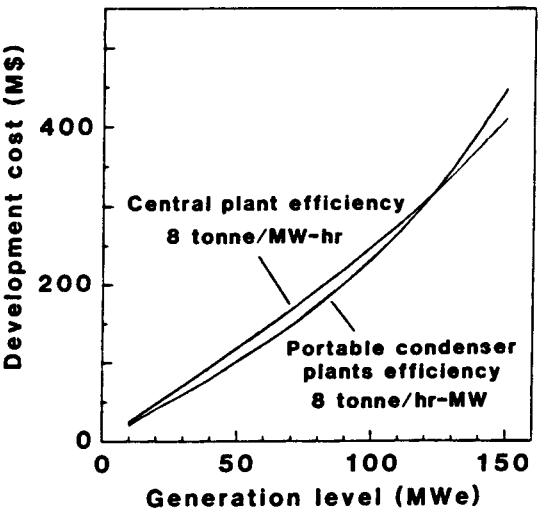

Figure 7. Effect of plant choice on development cost for Ahuachapan match parameters.

power project scenarios. We used the reservoir and economic parameters already discussed, to study the effect of different reservoirs, different power plant choices, and different wellfield operations. In the last of these, we contrasted the effect of constant wellhead pressure production, against constant flowrate production (choked wells). We found that lower development costs were achieved in the constant wellhead pressure case. In our study of different power plant choices, we found the backpressure option was in all cases much more expensive than the condenser option; the reason being the large difference in their conversion efficiency from thermal to electric power.

Figure 7 shows the effect of different types of power plants; that of wellhead units with condensers (same as Figure 6), and a central power station (with condensers). We used the reservoir match parameters for Ahuachapan. At low generation levels the wellhead option costs less, but at high generation level it costs more. This results comes about due to the constraint of having each wellhead unit hooked up to just one well. At high generation levels the flowrate of the wells declines much more than at low generation levels. Each of the wellhead units is generating below what it is capable of generating, resulting in over-installed capacity. In the central plant scenario, on the other hand, the installed capacity is always the same, because make-up wells can be connected to the plant as required. We did the same calculation using match parameters from the Wairakei reservoir. Unlike that shown in Figure 7, the cental power plant option costs more at all generation levels, because the reservoir/wellbore deliverability does not decline as much as at Ahuachapan.

The scenario of different size reservoirs for the same type of power plant project, is shown in Figure 8. Using the deliverability of Ahuachapan and Wairakei, we calculated the development cost for wellhead units with condensers. The message of Figure 8 is that there is a great cost advantage in having a large reservoir over that of having a medium or small reservoir. This advantage becomes more pronounced with increasing generation level. At 150 MW the Ahuachapan option has a marginal energy cost of 83 mills/kWh, while the Wairakei option has a marginal cost of 40 mills/kWh.

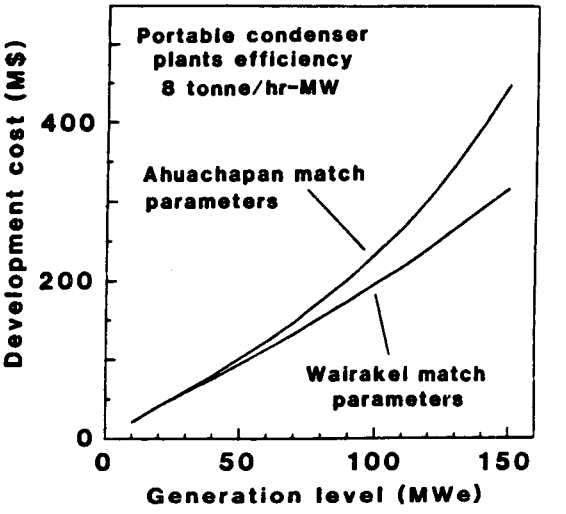

Figure 8. Effect of reservoir/wellbore deliverability on development cost for wellhead condenser plants.

Conclusions

- The production histories of the liquid-dominated Ahuachapan, Svartsengi, and Wairakei reservoirs, were successfully matched using the radial form of Hurst's simplified water influx method. In the case of Wairakei, for example, six years of production data were sufficient to match the full twenty-five years of history.
- The deliverability of reservoir/wellbore systems consists of reservoir performance, inflow performance, and wellbore performance. Methods and data are available to model the deliverability of liquid-dominated geothermal reservoirs. The methods selected here were intentionally kept simple, so there is ample scope for improvements.

- The Geothermal Development Model can be used to study the effect of reservoir/wellbore deliverability and different power plant schemes on the economics of geothermal electric power. With model refinements, it ought to be possible to optimize geothermal field developments.
- The cost of geothermal electric power and energy increases more rapidly than linearly with the size of development; there exists a dis-economy of scale in geothermal power developments. This effect is especially true for large developments and small and medium sized reservoirs.

Acknowledgements

This work was supported by the Stanford Geothermal Program, through contract DE-AT03-80S11459 with the U.S. Department of Energy. Thank you, Marty Molloy, for the four-years of cooperation.

References

Ambastha, A.K. and Gudmundsson, J.S. (1986): "Pressure Profiles in Two-Phase Geothermal Wells," Proc., 11th Workshop Geothermal Reservoir Engineering, Stanford University, Stanford, CA.

Butz, J.R. (1980): "A Case Study of Two-Phase Flow at the Roosevelt Hot Springs, Utah KGRA," Trans., Geothermal Resources Council, 4, 439-442.

Butz, J. and Plooster, M. (1979): "Subsurface Investigations at the Roosevelt Hot Springs, Utah, University of Denver Research Institute, Report DOE/ET/28389-1, Denver, CO.

Donaldson, I.G. and Grant, M.A. (1978): "An Estimate of the Resource Potential of New Zealand Geothermal Fields for Power Generation," Geothermics, 7(2-4), 243-252.

Donaldson, I.G. and Grant, M.A. (1981): "Heat Extraction from Geothermal Reservoirs," Geothermal Systems: Principles and Case Histories, Rybach, L. and Muffler, L.J.P. (eds.), John Wiley, Chichester, England.

Grant, M.A. (1983): Geothermal Reservoir Modeling, Geothermics, 12, 251-263.

Grant, M.A., Donaldson, I.G. and Bixley, P.F. (1982): "Geothermal Reservoir Engineering," Academic Press, Inc., New York, N.Y.

Gudmundsson, J.S. (1984): "Discharge Analysis of Two-Phase Geothermal Wells," Trans., Geoth. Resources Council, 8, 295-299.

Gudmundsson, J.S. and Olsen, G., (1985): "Water Influx Modeling of Svarsengi Geothermal Field, Iceland," SPE Paper 13615, Society of Petroleum Engineers, California Regional Meeting, Bakersfield, CA.

Gudmundsson, J.S. and Thorhallsson, S. (1986): "The Svartsengi Reservoir in Iceland," Geothermics, 1986, in press.

Gudmundsson, J.S., Olsen, G. and Thorhallsson, S. (1985): "Svartsengi Field Production Data and Depletion Analysis," Proc., 10th Workshop Geothermal Reservoir Engineering, Stanford University, Stanford, CA.

Holt, B. and Ghormley, E.L. (1976): Energy Conversion and Economics for Geothermal Power Generation at Heber, California; Valles Caldera, New Mexico; and Raft River, Idaho - Case Studies, Electric Power Research Institute, Report EPRI ER-301, Palo Alto, CA.

Hurst, W. (1958): "The Simplification of the Material Balance Formulas by the Laplace Transformation," Trans. AIME, 213, 292-303.

Marcou, J.A. (1985): Optimizing Development Strategy for Liquid Dominated Geothermal Reservoirs, Stanford Geothermal Program, Report SGP-TR-90, Stanford University, Stanford, CA.

Menzies, A.J. (1982): "Flow Characteristics and Relative Permeability Functions for a Two-Phase Geothermal Reservoir from a One-Dimensional Thermodynamic Model, Stanford Geothermal Program, Report SGP-TR-59, Stanford University, Stanford, CA.

Olsen, G. (1984): "Depletion Modeling of Liquid-Dominated Geothermal Reservoirs, Stanford Geothermal Program, Report SGP-TR-80, Stanford University, Stanford, CA.

Orkiszewski, J. (1967): "Predicting Two-Phase Pressure Drops in Vertical Pipe," J. Pet. Tech., (June), 829-838.

Quintanilla, A. (1983): "Computer Modelling of Ahuachapan Geothermal Field," Project Report, Geothermal Institute, University of Auckland, Auckland, New Zealand.

Rivera-R., J. Vides-R., A., Cuellar, G., Samaniego-V., F. and Neri, G. (1983): "A Status Report on the Exploitation Conditions of the Ahuachapan Geothermal Field," Proc., 9th Workshop Geothermal Reservoir Engineering, Report SGP-TR-74, Stanford University, Stanford, CA, 97-106.

Southan, J.A.N., Wigley, D.M., Carey, B.S., Constable, L.K., Hall, N.R., Mills, T.P. and Sell, P. (1983): Report on Small Geothermal Power Development in New Zealand, Ministry of Works and Development, Ministry of Energy, Auckland, New Zealand.

Stacey, R.E. and Thain, I.A. (1983): "25 Years of Operation at Wairakei Geothermal Power Station," Proc., 5th New Zealand Geothermal Workshop, University of Auckland, Auckland, New Zealand, 79-90.

Vides, J.R. (1982): "Model Simulation of the Behaviour of Ahuachapan Geothermal Field, Project Report, Geothermal Institute, University of Auckland, Auckland, New Zealand.

Vogel, J.V. (1968): "Inflow Performance Relationships for Solution-Gas Drive Reservoirs," J. Pet. Tech., 20(1), 83.

PROCEEDINGS, Eleventh Workshop on Geothermal Reservoir Engineering
Stanford University, Stanford, California, January 21-23, 1986
SGP-TR-93

Enhancement of Steam Phase Relative Permeability Due to Phase Transformation Effects in Porous Media

A. Verma and K. Pruess

Lawrence Berkeley Laboratory
Earth Sciences Division
University of California
Berkeley, California 94720

An experimental study of two-phase concurrent flow of steam and water conducted (Verma et al., 1985) and a set of relative permeability curves was obtained. These curves were compared with semi-empirical results (Brooks and Corey, 1964) and experimental results obtained by other investigators (Johnson et al., 1959, and Osoba et al., 1951) for two-phase, two-component flow (oil/gas; gas/water; gas/oil). It was found that while the wetting phase relative permeabilities were in good agreement, the relative permeability for the steam phase was considerably higher than the relative permeabilities of the non-wetting phase (oil in oil/water and non-condensing gas in gas/oil or gas/water) in two-component systems (Figs. 1 and 2). This enhancement of steam relative permeability is attributed to phase transformation effects at the pore level in flow channels.

There are two separate mechanisms by which phase transformation affected relative permeability curves (1) phase transformation in converging-diverging flow channels with hydrophilic walls can cause an enhancement of steam phase relative permeability; and (2) phase transformation along the interface of a stagnant phase and the phase flowing around it controls the irreducible phase saturation of the stagnant phase (Verma, 1986).

A pore level model was considered to study the first mechanism. In this model a pore space, shown in Figure 3, is idealized as a torroidal flow channel (Fig. 4) with a throat radius r_t and pore body radius r_b. Flow of steam and water through the throat portion of a pore was modeled using the MULKOM simulator (Pruess, 1983). The results indicate that when steam encounters a pore throat of a highly constricted flow channel (i.e., $\frac{r_t}{r_b} \ll 1$) in high conductivity solid, a fraction of the flowing steam condenses upstream from the constriction, depositing its latent heat of condensation. This heat is conducted through the solid grains around the pore throat, and evaporation takes place downstream. Therefore, for a given bulk flow quality, a smaller fraction of steam actually flows through the throat segments. Since steam has much higher kinematic viscosity than liquid water, and since the throat segments are the primary contributors to the overall flow resistance in the flow channels, the phase transformation effects reduce the overall resistance to steam flow along channels with varying cross sections. This pore-level effect manifests itself as relative permeability enhancement on a macroscopic level. However, our numerical studies indicate that for typical pores found in sandstone this effect is negligible.

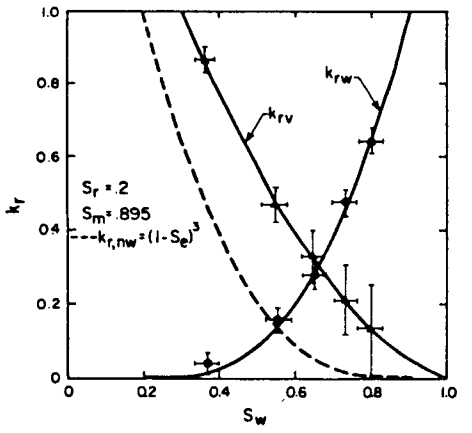

Figure 1. Relative permeability curves. Data points indicate the experimental results; the solid lines indicate the best fit. The broken curve is the relative permeability of the nonwetting phase according to the data of Brooks and Corey (1964).

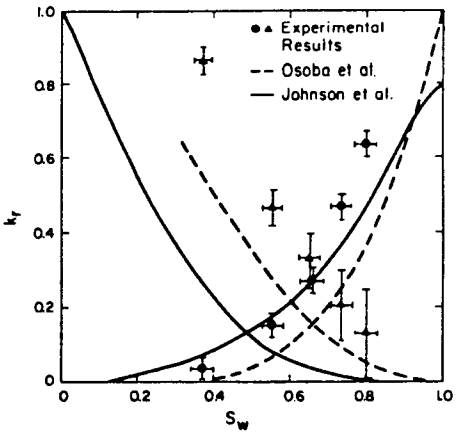

Figure 2. Comparison of our experimental results with those of Johnson et al. (1959) for oil-water and Osaba et al. (1951) for oil-gas. The wetting phase relative permeabilities compare well, but the steam phase relative permeabilities are higher than nonwetting phase relative permeabilities obtained by other investigators.

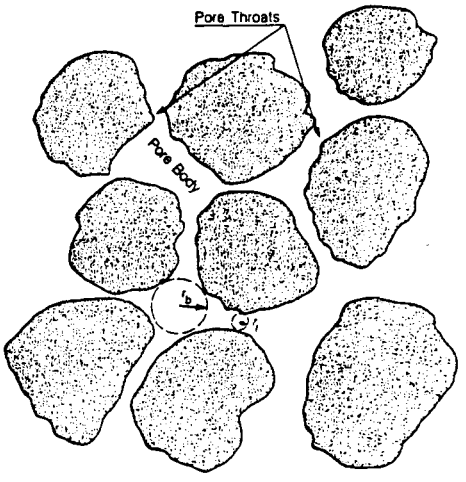

Figure 3. Schematic of pore space showing pore bodies and the throats connecting them.

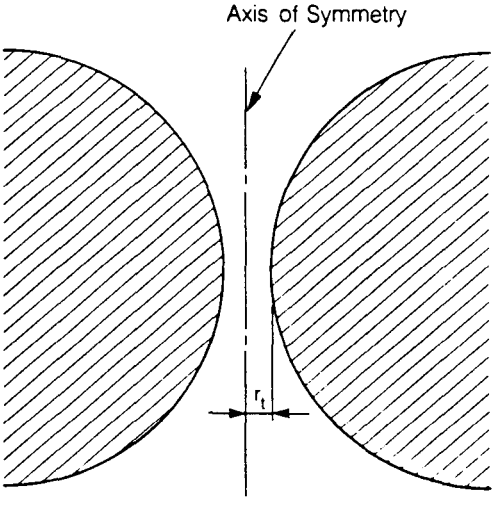

Figure 4. Idealized representation of a pore throat as a torroidal flow channel.

The second effect was studied by applying thermodynamic stability criteria to stagnant phases in pore space. Our study indicates that: (1) irreducible phase saturation for the steam phase will be negligible small when the liquid phase is flowing in the direction of lower thermodynamic pressure and temperature; and (2) irreducible phase saturation for the liquid phase will generally be negligible when steam is flowing in the direction of lower thermodynamic pressure and higher temperature. Detailed derivation of these results is given in a forthcoming report (Verma, 1986).

We conclude that the enhancement of steam relative permeability observed in our experiment is due to a reduction in irreducible steam phase saturation in comparison to the irreducible phase saturations for the non-wetting phase in the oil-water and oil-gas experiments with which we have compared our results.

References

Brooks, R.H., and Corey, A.T., 1964: Hydraulic Properties of Porous Media, Colorado State University, Hydro. Paper No. 3., March, vol. 19, pp. 38-41.

Johnson, E.F., Bossler, D.P. and Nauman, V.O., 1959: Calculation of Relative Permeability from Displacement Experiments, Trans. AIME, Vol. 216, pp. 370-376.

Osoba, J.S., Richardson, J.G., Kerner, J.K., Hanford, J.A. and Blair, P.M., 1951: Laboratory Measurement of Relative Permeability, Pet. Trans., AIME, vol. 192, pp. 47-55.

Pruess, K., 1983: Development of the General Purpose Simulator MULKOM in Annual Report 1982, Earth Sciences Division, Lawrence Berkeley Laboratory Report LBL-15500, pp. 133-134.

Verma, A.K., 1986: Effects of Phase Transformation on Steam Water Relative Permeability, Ph.D. Dissertation, University of California, Berkeley, May.

Verma, A.K., Pruess, K., Tsang, C.F. and Witherspoon, P.A., 1985: A Study of Two-Phase Concurrent Flow of Steam and Water in an Unconsolidated Porous Medium, in Heat Transfer in Porous Media and Particulate Flows (HTD Vol. 46), Proceedings, 23rd ASME/AIChE National Heat Transfer Conference, Denver, Colorado, August 4-7, 1983, pp. 135-143.

PROCEEDINGS, Eleventh Workshop on Geothermal Reservoir Engineering
Stanford University, Stanford, California, January 21-23, 1986
SGP-TR-93

THE STREAMING POTENTIAL GENERATED BY FLOW OF WET STEAM IN CAPILLARY TUBES

S. S. Marsden, Jr., and Craig K. Tyran

Stanford University

ABSTRACT

For a constant pressure differential, the flow of wet steam generated electric potentials which increased with time and did not reach equilibrium values. These potentials were found to increase to values greater than 100 volts. The reason for this kind of potential build-up behavior was the presence of tiny flowing water slugs which were interspersed with electrically nonconductive steam vapor slugs. The measured electric potential for wet steam increased with pressure differential, but the relationship was not linear. The increase in potential with pressure drop was attributed both to an increase in fluid flow rate and changes in the wet steam quality.

INTRODUCTION

Streaming potential is an electrokinetic potential generated by the flow of a fluid through a conduit such as a tube or porous medium. It results from the physical transfer of ions in the diffuse double layer of the fluid along and out of the conduit. This is counter-balanced by and eventually comes into equilibrium with charge transfer either through the conductive solid material forming the conduit or along its surface or else by ionic conduction in the fluid itself. With especially low electrical conductivity of all three paths, streaming potentials of more than 100 volts are easily generated in the laboratory and more than 10,000 volts in large pumping systems for petroleum products (Klinkenberg and van der Minne 1958). The latter can lead to electrical discharges and sparks which have undoubtedly been the cause of many explosions and fires in oil tankers, terminals and refineries.

The phenomenon of streaming potential was first described and explained almost a century ago by Quincke (1888) and has been studied over the decades by many physical and colloid scientists. An excellent monograph has been published by Klinkenberg and van der Minne (1958) and more recently another on the importance in the petroleum industry by Bustin and Dukek (1983). The streaming potential generated by flowing foam was studied by Raza and Marsden (1967) and an equation derived for describing the potential generated by the flow of such a non-Newtonian fluid. This was later extended to emulsions by Dowdle and Marsden (1974).

The SP (self potential) log is widely used in the petroleum industry. It is believed to be derived from the sum of two electrical potentials, the first being a static electrochemical or concentration potential and the second a streaming potential. While the former is more important under most circumstances, the latter can be significant under some.

A number of investigators, including Zohdy et al. (1973), Corwin (1976), Anderson and Johnson (1976) and Banwell (1970), have reported self-potential anomalies which are associated with geothermal activity. It is believed that the streaming potential due to the presence of circulating fluid in a geothermal reservoir contributes to the anomalous electrical potential fields which have been measured at the earth's surface. Whether this is a streaming potential or whether it is due to electrochemical potentials caused by fluid redistributions is not known.

Because we had considerable experience with and still had equipment left for measuring streaming potentials in glass capillary tubes, we felt it was desirable simply to see if these potentials are generated by steam flow, and if so, what were some of the parameters describing the system. The development of the equipment and description of the results are presented here briefly. More detail is given in a M.S. Degree Research Report by one of the authors (C.K.T.) (1983) and results with another worker will be described at a later date (Wheatall and Marsden 1986).

EXPERIMENTAL

Apparatus

The components of the equipment used fell into two general categories, namely, the fluid handling and flow system plus the electrical measurement instrumentation. These will be described in general terms only because exact specifications are unnecessary here and are given elsewhere by Tyran (1983).

A schematic diagram of the equipment is shown in Fig. 1. Steam was generated by heating distilled water in a 2 *l* metallic tank (pressure bomb) wrapped with electrical resistance heating tape and enclosed in thermal insulation. The water was flashed to steam through a needle control valve and then introduced into the pyrex tube. This part of the system also had calibrated, Bourdon pressure gauges (tank and at pyrex tube entrance and exit), thermocouples (at the pyrex tube entrance and exit), and several valves (tank filling, pressure relief, flow control, condensate collector). All lines were also heated electrically and enclosed in sponge-ceramic thermal insulation (Fiberfrax).

A pyrex tube 48.0 cm long and 0.0775 cm inside diameter was used. The latter was determined by weighing

---

The paper is based on the experimental work of C. K. Tyran for his M.S. Degree Research Report submitted in June 1983 to the Petroleum Engineering Department at Stanford University. A portion of it was the basis of a paper presented at the Geothermal Resources Council Meeting in Hawaii in August 1985 and the remainder is presented here.

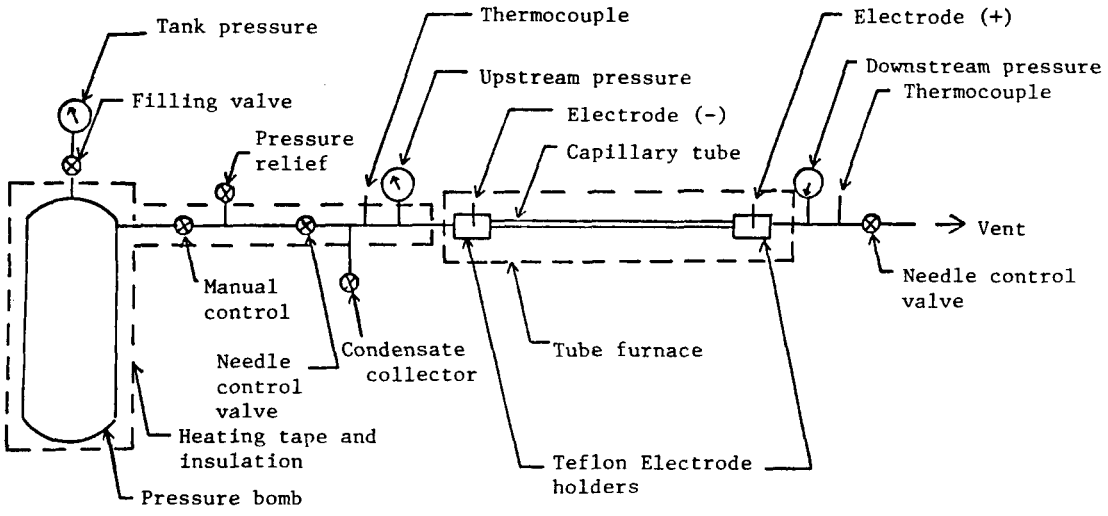

Fig. 1 - Schematic diagram of the streaming potential apparatus

it empty and then filled with H_g. This was enclosed at both ends in especially made teflon holders which also contained Pt-Ir wire electrodes. At the tube exit, pressure and temperature were again measured just upstream of another needle control valve. This part of the system was contained in a horizontal tube furnace.

The streaming potential was measured with the Keithley Model 610A Electrometer used previously by Raza and Marsden (1967). The output of this was also put into a voltage divider and a section of this was connected to a recording potentiometer. A 0.43 F capacitor was connected across the voltage divider to improve stability of the voltage tracing. It was determined that the tube furnace provided electrical shielding for the pyrex tube and its teflon holders, and a braided metallic shield was used for the usually positive (downstream) electrical lead. All measuring components were properly grounded, which is very important in this kind of work to avoid drift, and were carefully calibrated before the work and later rechecked.

Procedure

The cleaning procedure for the pyrex tube was similar to that used by Raza and Marsden (1967), i.e. nitric acid, distilled water and heating to about 150°C, and for the electrodes nitric acid and distilled water.

After measuring the electrical conductivity of the water used to fill the tank, the latter, the flow system and the tube were all heated until the bomb pressure was 30-35 psig (207-241 kPa). Before flow started the static electrical potential across the tube was checked. The tube furnace was shut off to eliminate the slight effect it had on potential measurements and then the control valves opened to start steam flow. After a period of adjustments to get flow stabilization, measurements were started. Condensate was removed intermittantly while attaining stabilization and frequently thereafter. Pressure drops and potentials generated were measured along with visual observations of water slugs and their effects on the potentials.

RESULTS AND DISCUSSION

To check the performance of the system, a temporary modification was made to allow nitrogen pressure to force distilled water to flow through it at room temperature. Using several samples of distilled water with slightly different resistivities in different runs, the ratio of measured streaming potential, ΔE, to pressure drop, ΔP, was constant, as it should have been. A graph of ΔE vs ΔP (Fig. 2) gave straight lines that extrapolated to a slightly positive ΔE value of about 0.5 volt, which was probably due to the not uncommon polarization effect reported by Korpi (1960). The calculated zeta potential values of 0.048 to 0.054 volts certainly agreed well with those in the literature of 0.046 to 0.054 volts for the glass-water interface (Glasstone 1946).

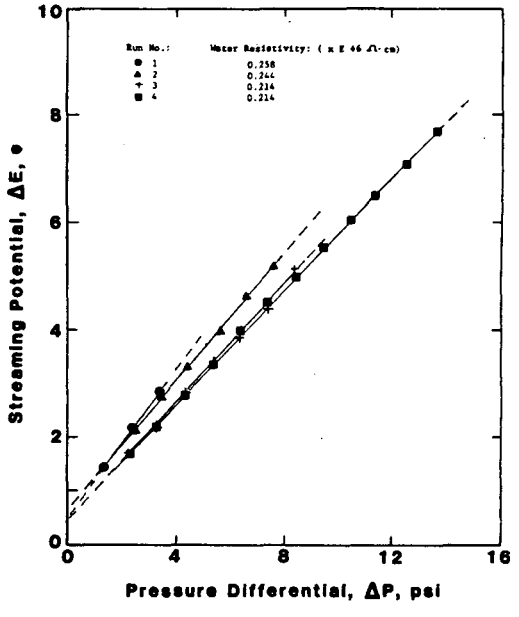

Fig. 2 - Streaming potential, ΔE, vs pressure differential, ΔP, for several samples of distilled water at 68°F.

Dry Steam

The first series of experiments after the blank runs with water was on dry (superheated) steam. The tube furnace was heated to well above 100°C and with downstream pressure maintained at atmospheric, the upstream temperature varied from 129°C for a ΔP of 15 psi (103 kPa) down to 116°C for a ΔP of 4 psi (28 kPa). Condensate was carefully and completely bled off before it reached the capillary tube and no condensed water came out of the fluid exit. The dry steam came out with a whistling sound rather than the soft gurgling sound observed later on for the wet steam.

No electrical potential due to the flow of dry steam through the capillary tube was observed. A small constant potential of 0.2 volts independent of temperature and ΔP was observed, but this was only the electrode polarization mentioned earlier. It also existed here at these temperatures when steam was not flowing.

It is evident that there is no transport of ions or other charged particles here leading to generation of a streaming potential. If there is adsorption of water vapor, which is likely to at least a modest extent, then this is an essentially immobile water layer under these experimental conditions.

In a separate experiment, dry nitrogen was flowed through the system and no streaming potential was also observed. Thus steam behaved like an inert gas here.

Wet Steam

To get wet steam flowing in the system, the tube furnace was heated to nearly 100°C and the steam source operated at conditions of temperature and pressure which would produce high quality steam. (Please note that the term quality here refers to the mass ratio of vapor to total fluid and not the volume ratio as is used for foam (Raza and Marsden, 1967)). Pressure drops along the capillary ranged from 5 to 25 psi (34 to 172 kPa), upstream temperatures from 119°C to 134°C and downstream temperatures slightly under 100°C. Even with these relatively large pressure and temperature drops along the capillary tube, stable flow of the wet steam was possible. Large slugs of water, which led to erratic electrical behavior, were avoided by draining the condensate trap frequently but small slugs, which had little effect on the potential readings, were impossible to eliminate entirely.

In contrast to dry steam, easily measurable streaming potentials were found for wet steam. These potentials, however, did not reach equilibrium values but instead increased with time. It was observed that in many cases the potentials were still increasing when they reached 100 volts, the maximum that could be measured with this electrometer and voltage divider combination. These large electrical potentials could be attributed to the very high electrical resistances that existed between the electrodes and decreased the flow of the reverse or conduction current. Not only was the resistivity of the condensed steam high but that of the vapor itself even higher.

In order to compare the potential data recorded for different pressure drops, a procedure was adopted which dissipated the charge accumulated at the electrodes by shorting them momentarily, and thus allowing the observed potential to return to essentially zero. This was done at an arbitrary but consistent time period of 50 s before being short-circuited again. During this time period, the potential built-up as is shown in Figs. 3 & 4 for a number of consecutive periods at the same temperature and pressure, before the latter was changed for another series of measurements.

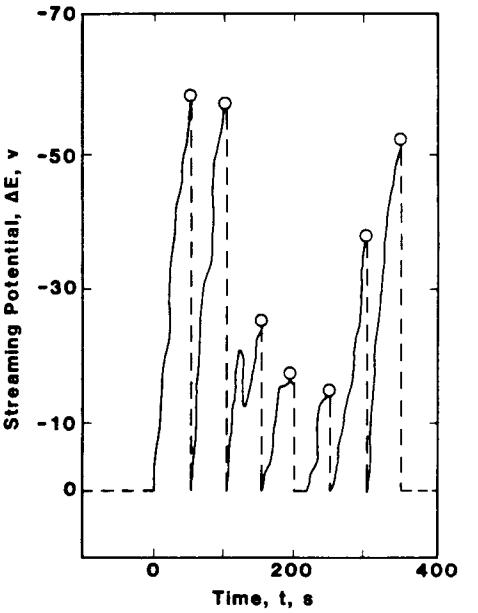

Fig. 3 - Streaming potential, ΔE, vs time, t, for a pressure differential of 10 psi. Upstream temperature 124°C and downstream temperature 97°C.

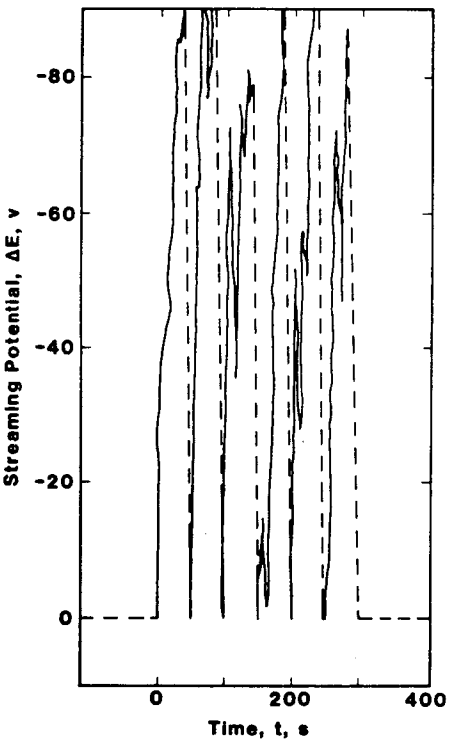

Fig. 4 - Streaming potential, ΔE, vs time, t, for a pressure differential of 20 psi. Upstream temperature 129°C and downstream temperature 96°C.

The chart readings of Streaming Potential vs Time for ΔP's of 10 psi (69 kPa) and less were fairly stable, but those for higher ΔP's were somewhat erratic. The latter often went off scale (90 volts for the recorder and 100 volts for the electrometer). While the trends of an increase ΔE with time were evident, the reproducibility from one 50 s interval to the next was poor, probably because of instabilities and variations in the two-phase flow in the capillary tube.

Data similar to that in Figs. 3 and 4 were collected for ΔP values starting at 5 psi (35 kPa), increasing in intervals of 5 psi (35 kPa) to 25 psi (173 kPa) and then decreasing stepwise again. The maximum ΔE's were then read from the chart for each of the 50 s periods and these averaged. These average ΔE values were then plotted vs ΔP in Fig. 5 with the points connected by curved lines with arrowheads merely to show the sequence.

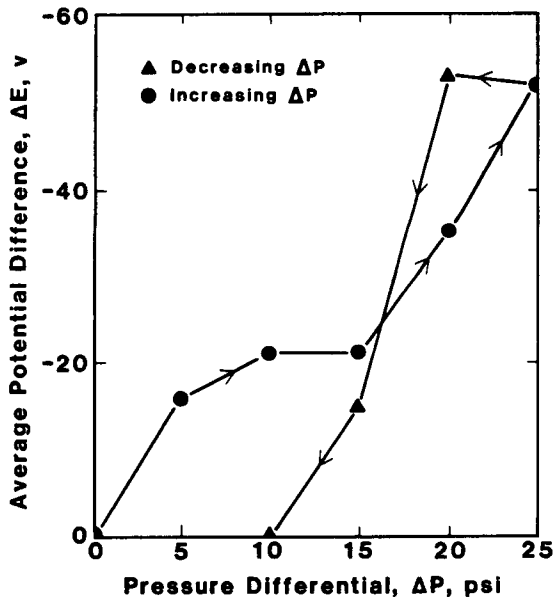

Fig. 5 - Average potential difference, ΔE vs pressure differential, ΔP, for wet steam.

It is certainly evident that the magnitude of the electrical potentials generated increased with pressure drop in a non-linear manner and then decreased again with hysteresis. We cannot say if this increase in charge transport was due to a greater fluid flow rate or to a change in steam quality or possibly both, but it is certainly evident. This question has been addressed in a subsequent study to be reported elsewhere (Wheatall and Marsden, 1986).

Application to Natural Geothermal Systems

We have shown here that streaming potentials can be generated in the laboratory by the flow of wet steam but not dry steam in a clean, single-channel conduit made of a good dielectric (pyrex glass). The phenomenon has been demonstrated but no attempt made to scale the results for application to any situation in nature. Although higher ΔP's and flow rates have been used than exist in nature and higher ΔE's observed, proper modelling and scaling may show that this is acceptable.

In the equipment used here, the electrical resistance for the conduction current is much lower than is likely in a subsurface formation. Alternate electrical paths containing immobile water such as those existing in porous media, as well as the possible presence of electrolytes in this water and conductive minerals such as clays in the pores all contribute to conductivity. Additional laboratory experiments simulating some of these conditions have been done and will be reported elsewhere (Wheatall and Marsden 1986).

CONCLUSIONS

The following conclusions apply to wet steam flowing through a pyrex capillary tube at somewhat elevated temperatures and pressures:

1. The flow of wet steam under a constant pressure differential generated a streaming potential which increased with time but did not reach equilibrium values. This potential was found to increase to values of at least 100 volts, the upper limit of measurement in our equipment. This behavior was probably due to the presence of small flowing water slugs interspersed and alternating with non-conductive steam slugs.
2. The measured electrical potential for wet steam increased with pressure differential but not linearly. This was probably due to an increase in fluid flow rate as well as changes in steam quality.

ACKNOWLEDGEMENTS

We are indebted to NL Industries, Inc. for their generous financial support of this study as well as a grant from the Institute for Energy Studies of Stanford University. We would also like to thank the Stanford Geothermal Program for its support of the preparation and presentation of this manuscript.

REFERENCES

Anderson, L.A., and Johnson, G.R. (1976), "Application of Self-Potential Method to Geothermal Exploration in Long Valley, California," J. Geop. Res. 81, 1527.

Banwell, G.J. (1970), "Geophysical Techniques in Geothermal Exploration," Proceedings of the U.N. Symposium of the Development and Utilization of Geothermal Resources, vol. 1, 32.

Bustin, W.M., and Dukek, W.G. (1983), Electrostatic Hazards in the Petroleum Industry, Research Studies Press, N.Y.

Corwin, R.F., (1976), "Self-Potential Exploration for Geothermal Reservoirs," Proceedings of the Second U.N. Symposium on the Development and Use of Geothermal Resources, vol. 2, 937.

Dowdle, W.L., and Marsden, S.S. (1974), "The Streaming Potential of Emulsions in Tubes and Porous Media," J. Coll. and Interface Sci. 48, No. 3, 523.

Glasstone, S., (1947), Textbook of Physical Chemistry D. Van Nostrand Co., New York, 1224.

Klinkenberg, A., and van der Minne, J.L., (1958), Electrostatics in the Petroleum Industry, Elsevier Publishing Co., Amsterdam.

Korpi, G.K., (1960), "Measurement of Streaming Potentials," M.S. Dissertation, M.I.T., 41.

Quincke, M., (1888) Wied. Ann., 35, 593.

Raza, S.H., and Marsden, S.S., (1967), "The Streaming Potential of Foams in Tubes and Porous Media," Soc. Pet. Eng. J. (Dec.) 359.

Tyran, C.K., (1983), "The Streaming Potential of Steam," M.S. Report, Stanford University.

Wheatall, M.W., and Marsden, S.S. (1986), To be presented at Fifth International Symposium on Water-Rock Interaction, Reykjavik, Iceland, Aug. 1986.

Zohdy, A.A.R., Anderson, C.A., and Muffler, L.S.P. (1973), "Resistivity, Self-Potential, and Induced Polarization Surveys of a Vapor-Dominated Geothermal System," Geophysics, vol. 38, No. 6, 1130.

PROCEEDINGS, Eleventh Workshop on Geothermal Reservoir Engineering
Stanford University, Stanford, California, January 21-23, 1986
SGP-TR-93

A TOOL AND A METHOD FOR OBTAINING HYDROLOGIC FLOW VELOCITY MEASUREMENTS IN GEOTHERMAL RESERVOIRS

C. R. Carrigan[1], J. C. Dunn[2] and H. C. Hardee[1]

(1) Geoscience Department
(2) Exploratory Energy Systems Department
Sandia National Laboratories
Albuquerque, NM 87185

ABSTRACT

Downhole instruments based on a thermal perturbation principle are being developed to measure heat flow in permeable formations where convective transport of heat is important. To make heat flow measurements in these regions, the ground water velocity vector must be determined. A downhole probe has been designed to measure the local ground water velocity vector. The probe is a cylindrical heat source operated at a constant heat flux. In a convecting environment, surface temperatures on the probe are perturbed from those values of a purely conductive environment. With the aid of analytical and numerical models, these temperature differences can be related to the local velocity vector.

INTRODUCTION

Hot wire or hot film anemometry is commonly used in engineering applications to determine flow velocities of gases in pipes, channels and other configurations. A simple hot wire anemometer measures the velocity of a gas indirectly by relating the power supplied to the sensor to the velocity of the fluid in a direction normal to the sensor (Dally et al, 1984). Heat produced by ohmic dissipation within the sensor element is removed by the flow of cooler gas past the element. The resultant cooling of the element causes a change in its electrical resistance that can be related to the fluid velocity. We describe here a tool based on a similar approach that can be used to estimate flow velocity in a permeable medium. It is found that application of the hot wire approach is relatively uncomplicated if the tool is placed in a permeable formation so that the porous matrix surrounding it is left more or less undisturbed. This circumstance could be achieved for a shallow well drilled into a sandy zone with backfilling of the hole. Calculations indicate that the tool can also be used in the wire-line mode in an uncased hole if the effects of the well pressure distribution on the pressure field in the porous medium are considered.

ANALYSIS OF OPERATION

A three dimensional analytical model for flow in a permeable medium past a heated prolate spheroidal body has been developed by Romero (1983a). The geometry of the problem solved by Romero is illustrated in Figure 1. Here a slender body of radius, a, and length, 2l, is aligned parallel to the vertical axis, z. The azimuthal coordinate of the Darcy velocity is given by ϕ while its angle to the vertical is given by θ_0. The dimensionless quantity η, which defines the axial location on the probe, is scaled by the half length, l.

In a saturated porous medium, Darcy's law and the Boussinesq approximation are assumed to apply. For a given velocity U_∞ , which characterizes Darcy flow in the far field of the tool, a solution for the pressure and temperature fields in the vicinity of the heated tool was obtained. In particular, the solution for the temperature distribution on the tool surface as a function of both the far field velocity and prescribed heat flux across the tool surface is required. There are two significantly different length scales that characterize the problem. One is the characteristic dimension of the tool while the other is the thermal diffusion length, α/U_∞, where α is the thermal diffusivity. The ratio of the two lengths is given by the Peclet number Pe. The typical

difference in length scales (Pe<<1) necessitates matching between an inner region near the tool and an outer region to obtain a perturbation solution. Details of the mathematical analysis can be found in Romero (1983a) who obtains a general solution for the problem valid for Pe <1. The resulting equation for the temperature, T, on the surface of the probe is

$$\frac{-T + T_\infty}{Q\ a/k} = T_o + \frac{\pi}{8} Pe + Pe\ Cos\theta_o\ g(\eta)$$

$$+ \frac{a}{l} Pe\ sin\theta_o\ cos\phi\ h(\eta) - \frac{a}{l} Ra\ f(\eta) \quad (1)$$

Temperature is a function of the heat flux, Q; the conduction solution, $T_o(\eta)$; the Peclet number,

$$Pe = \frac{Ul}{\alpha}$$

the Rayleigh number,

$$Ra = \frac{\rho_o g \beta K Q l^2}{k \alpha \mu}$$

and the functions $f(\eta)$, $g(\eta)$ and $h(\eta)$ that are plotted in Figure 2. We point out that the Rayleigh number used here is a measure of the convection induced in a region of permeability, K, subject to gravitational acceleration, g, by local buoyancy associated with the heat flux from the probe and the volumetric thermal expansion, β. Ideally this effect should be small allowing the term involving the Rayleigh number to be neglected compared to terms containing the Peclet number. For most field conditions that have been encountered this has indeed been the case. If Ra is comparable to Pe, then it is apparent from the equation that terms associated with forced convection, i. e., terms involving Pe, can be masked by the term involving Ra that includes the effect of natural convection induced by the probe heater. When the flow is entirely vertical, i. e., parallel to the probe axis, manipulation of the above equation for surface temperature yields the following result for the temperature difference between two locations that are symmetrical about the mid line:

$$\frac{-T(\eta) + T(-\eta)}{Qa/k} = Pe[g(\eta) - g(-\eta)] - Ra\ \frac{a}{l}[f(\eta) - f(-\eta)] \quad (2)$$

This result indicates that the temperature difference between the two locations is linearly related to the flow velocity through the nondimensional Peclet number. A similar result was also obtained by Romero (1983b)for purely vertical flow using a slender body analysis that applies for all values of the Peclet number. For small values of this parameter it is found to be in good agreement with the perturbation result. However, at larger values (Pe> 1), the temperature change becomes smaller for a given change in velocity, i. e., the tool becomes less sensitive at higher Darcy flow rates. We will further consider this equation as well as the more general one (1) in conjunction with laboratory and field tests of a full size convective flow probe. The theory for the convective flow probe has also been tested using bench scale laboratory experiments that were particularly well controlled. These help to illustrate the role of the induced convection in affecting the sensitivity of the probe to groundwater flows.

BENCH SCALE EXPERIMENTS

In the scaled down laboratory experiments and analysis of Hickox, Dunn and Gartling (1985), the geometry of the probe model was essentially that assumed for the theoretical model in Figure 1. A typical probe model consists of a long (aspect ratio 20), chromel wire wrapped rod (10 cm heated length) with at least two thermistors located at different positions along its electrically heated length. In the absence of any flow in the surrounding permeable medium, the axial temperature distribution is symmetric about the midpoint of the heated length. When there is flow in the permeable medium, the temperature distribution is skewed along the heated length of the model. Thus a temperature difference will be measured between the symmetrically positioned thermistors. This difference can be related to the magnitude and direction of flow using Equation 1.

A 61 cm long plexiglass cylinder filled with sand contained the probe which was embedded parallel to the centerline. For this case the porosity and permeability were .35 and 16 darcies, respectively. A vertical upward flow was produced in the cylinder by maintaining a constant pressure difference across

the bed. The observed relation between measured temperature difference and axial flow velocity is plotted in Figure 3 using the dimensionless quantities $\Delta\Theta$ and Pe where the former quantity is given by $\Delta\Theta = 2\Delta T\alpha l / Q$. For a given heat output, Hickox et al. found a more or less linear change in the temperature difference for a change in axial flow velocity just as predicted by Romero for small Pe. Further, they found that the sensitivity (slope) was greatest for Peclet numbers less than 1. Beyond this value, increases in velocity result in much smaller increases in the temperature difference. This result is consistent with the slender body analysis of Romero.

FULL SCALE LABORATORY TESTS

A prototype wire line tool was developed for carrying out both full scale laboratory and down hole tests. The tool is shown in Figure 4. Because of the additional features required for wire line operation, the probe is significantly more complicated mechanically than the simple probes used in the bench scale experiments. The tool's overall length is approximately 2 m. and its diameter is about 5.7 cm when the heater and sensor pads are in the fully retracted position. The frame and most of the components of the tool are machined from 304 stainless steel. A dc motor mounted in the tool sets the compression packers as well as driving a scissors mechanism that extends the segmented cylindrical heater and sensor pads until they contact the borehole wall. The current tool can function in wells up to 3 inches (7.7 cm) in diameter. The four laminated silcon rubber heating/sensing pads are the heart of the tool. A thin strip heater runs the full length (56 cm) along the base (tool side) of each pad. In addition, four calibrated thermistors, symmetriclly arranged in a diamond pattern, are positioned above the heating element near the top side (borehole wall side) of each pad. In principle, at least three thermistors are necessary for determining a velocity unambiguously. However, sixteen are used to improve resolution of the velocity vector and to provide redundancy in measurements. For shallow holes (short cable lengths) it was considered adequate to make only two wire thermistor measurements especially since the characteristic resistance of the thermistors was several hundred thousand ohms. Periodic heater wattage and thermistor resistance measurements were obtained and recorded using a Hewlett Packard data acquisition system that included a portable HP 85 computer.

For testing and calibration, the probe was embedded in a 1.2 m diameter tank filled with sand. Water was pumped at a uniform rate through a plenum in the base of the tank. Flow up the cylindrical tank was extracted at the top and returned to the pump reservoir. Temperature measurements at various locations in the tank were made using calibrated thermocouples embedded in the sand. Typical pumping rates of about a liter per hour yielded Darcy velocities of about 2×10^{-7} m/s or roughly 8 m/yr. Three pumping rates were used during the test corresponding to a low value of .89 l/hr, a medium value of 1.39 l/hr and a high rate of 1.9 l/hr. Three power levels were also used during the series of tests. Values of 32, 62 and 126 watts are characteristic of power levels that would be used in downhole environments. While higher heater power levels permit larger temperature differences to be measured and, hence, smaller flow rates, an upper limit is imposed on heating rate both by the tendency to induce natural convective flow and by the possibility of exceeding the boiling point of the groundwater. The predicted linear relationship between temperature difference and flow velocity was generally suported by the results as indicated in Figure 5.

NUMERICAL SIMULATION OF FLOW AROUND PROBE IN WELL

Because the probes are buried in the porous medium in both the bench scale and full size experiments, the analysis of Romero applies directly. However, if the tool is used in a borehole, some modification of the analysis is necessary. For general usage, it is found that the more or less hydrostatic pressure distribution in a borehole will significantly affect flows in the vicinity of the tool. In an uncased hole, the hydrostatic pressure distribution on the borehole wall requires that the vertical component of flow vanish in the porous medium at the wall.

Figure 6a illustrates how the pressure distribution would be modified in the vicinity of an uncased hole. Below the hole, isobars are horizontal indicating vertical flow. Near the hole, however, the isobars are severely distorted and become vertical giving rise to a purely radial flow at the borehole wall. (Obviously continuity does not permit fluid to flow into or out of the hole everywhere if fluid is not being removed or added to the well. A change in sign of the radial component of flow must occur at some depth although it is not shown here.)

A tool such as the convective flow probe will further modify the near field pressure distribution. Along the portion of the hole containing the tool, the flow through boundary condition will no longer apply. Fluid is prevented from flowing radially into the hole and must flow along the tool. If either by design or error, small quantities of borehole fluid can be communicated past or through the tool causing the hole to remain in hydrostatic equilibrium, then a bidirectional flow along the probe will be set up as shown in Figure 6b. For a short (1 m) probe, the induced bidirectional flow is found to be virtually symmetric near the tool independent of the direction of the vertical flow in the far field. Longer probes (5 m) give rise to asymmetry in the bidirectional flow that is associated with the direction of the far field flow. It would also appear that the probe's sensitivity to the azimuthal direction of the flow improves with increasing length of the packed off region.

FIELD TESTS--LONG VALLEY, CA.

The full scale probe was field tested in two drill holes in Long Valley Caldera, CA. The holes were located near existing USGS heat flow holes where temperature profile data had been obtained. The Sandia hole SLV1 is in a region of suspected upflow while hole SLV2 is in a region of suspected horizontal flow. During the tests electrical leakage problems developed in two of the four instrument pads. While the heater function was not inhibited in these pads, accurate measurement of the temperature was prevented. However, the eight thermistors in the other two pads provided quite sufficient information for estimating the fluid velocity vectors. Before placement of the probe in a drill hole, caliper logs were run to determine uniformity of the side walls as well as the depth to the uncased portion of the hole. A depth interval having the most uniform hole diameter was then selected. After the tool was lowered to this depth, the internal motor was operated to extend the heater pads against the borehole wall and the isolation packers were set. The probe was then allowed to equilibrate thermally in the holes for two hours. The heaters were then powered and data were recorded as a function of time using the computer controlled data acquisition system. Power levels used in SLV1 were 137 and 215 W. After steady state was achieved a vertical temperature difference of about 4 C, related to the upward component of groundwater flow, was measured. Using a modified slender body analysis valid for higher Pe than the original perturbation analysis of Romero, a very large upward velocity of $U=2.4 \times 10^{-5}$ m/s (760 m/yr) was estimated. Using a similar procedure in SLV2, a velocity vector of magnitude 6.8×10^{-7} m/s oriented at 79° to the vertical was obtained. The influence of the borehole in the SLV2 flow measurements was fortuitously minimized by packing off one end of the probe in the well casing while the pads extended beyond into the uncased part of the hole.

CONCLUSION

From the results presented here, we conclude that hot probe anemometry provides a realistic approach to estimating Darcy velocities in a permeable regime. Probes which are embedded in a permeable medium can produce data that is readily modeled using the theory of Romero (1983a,b). However, if a probe is used in a borehole, the effect of the hydrostatic pressure distribution in the borehole on the measured velocity vector becomes a factor. However, numerical calculations indicate that substantially lengthening the probe will minimize this effect. Preliminary field tests of the probe have yielded results which appear consistent with the geothermal settings of the wells.

ACKNOWLEDGEMENTS

We wish to thank R. Striker for his helpful discussion. The tool has been assigned patent number 4547080. This work performed at Sandia National Laboratories is supported by the U. S. Department of Energy under contract number DE-AC04-76DP00789 for the Office of Basic Energy Sciences.

REFERENCES

1. Dally, J. W., Riley, W. F. and McConnell K. G. (1984), "Instrumentation for Engineering Measurements," John Wiley and Sons, New York, NY.

2. Hickox C. E., Dunn, J. C. and Gartling, D. K. (1985), "Fundamental Studies of Flow Processes in Porous Media," Internal Final Report, Sandia National Laboratories, Albuquerque, NM.

3. Romero, L. A. (1983a), "Low Peclet Number Convection Past a Spheroid in a Saturated Porous Medium," Sandia Report (SAND83-0291), Sandia National Laboratories, Albuquerque, NM.

4. Romero, L. A. (1983b), "Forced Convection Past Slender Bodies in a Saturated Porous Medium," Sandia Internal Memorandum (May 13), Sandia National Laboratories, Albuquerque, NM.

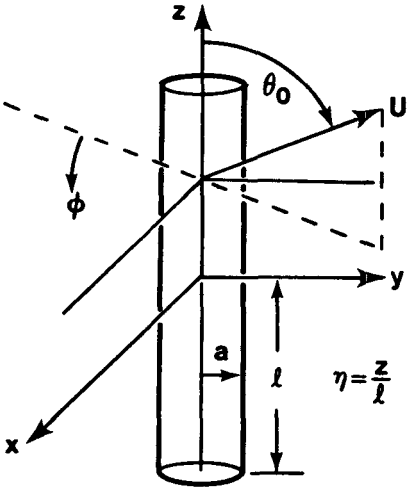

Figure 1. Heated cylinder is embedded in porous matrix. Darcy flow vector is expressed in cylindrical coordinates.

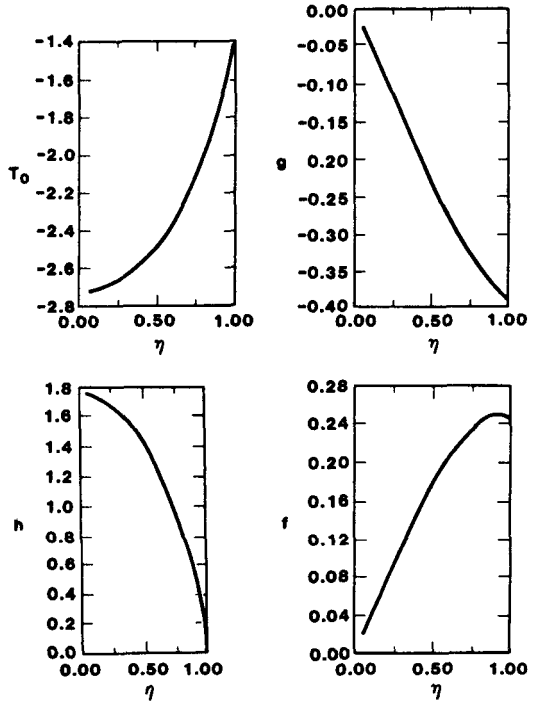

Figure 2. Plots of nondimensional functions and conductive temperature solution appearing in Equation 1.

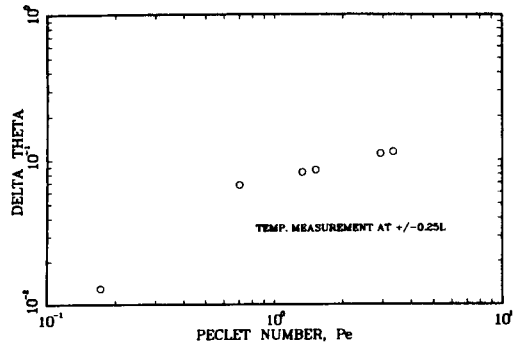

Figure 3. Relationship between temperature difference and flow velocity as expressed by Peclet number. Result obtained from bench-scale experiments.

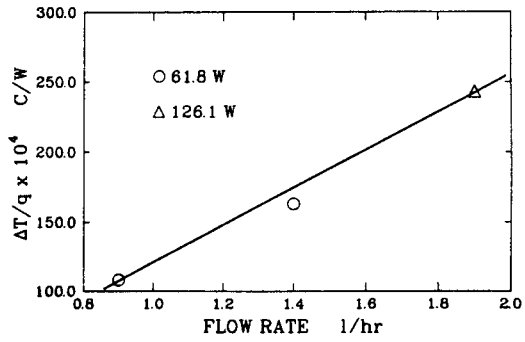

Figure 5. Linear relationship between temperature difference measured at points symmetric about midline and flow rate is supported by full scale laboratory tests.

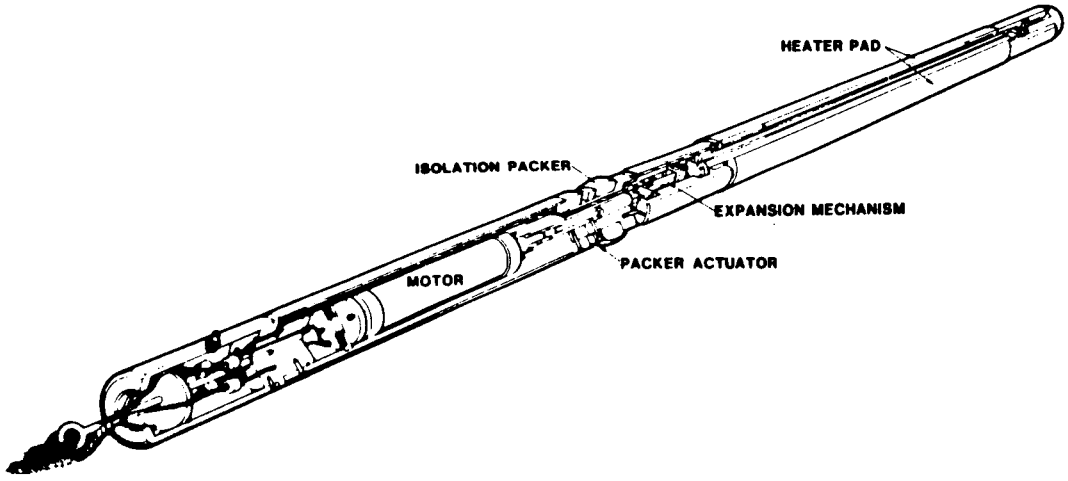

Figure 4. Full size probe design suitable for downhole usage.

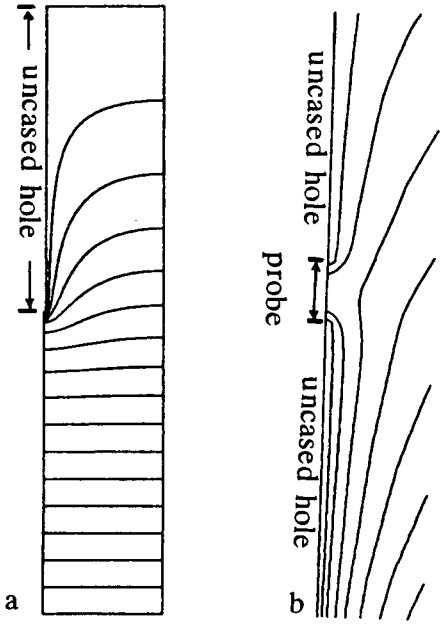

Figure 6. a) Far field isobars are strongly affected by hydrostatic pressure distribution in uncased well. Horizontal isobars give rise to vertical flow. Near well isobars become vertical resulting in radial flow. b) For short tool in uncased well, more or less symmetric isobar pattern implies existence of bidirectional flow.

PROCEEDINGS, Eleventh Workshop on Geothermal Reservoir Engineering
Stanford University, Stanford, California, January 21-23, 1986
SGP-TR-93

NATURAL VERTICAL FLOW IN THE LOS AZUFRES, MEXICO, GEOTHERMAL RESERVOIR

E.R. Iglesias and V.M. Arellano
Instituto de Investigaciones Electricas
Apartado Postal 475
Cuernavaca, Morelos 62000, Mexico
and
J. Ortiz-Ramirez
Comision Federal de Electricidad
Melchor Ocampo 35 Pte.,
Cd. Hidalgo, Michoacan, Mexico

ABSTRACT

This work focuses on estimating the mass (M) and energy (E) flow rates, the permeability k, and the relative permeability functions R_L and R_V associated with the natural vertical flow in the reservoir. To estimate M and E we used the standard 1-D vertical equations for two-phase flow, complemented with boundary conditions at the boiling and dew interfaces. These boundary conditions were derived in an earlier stage of this study that established an approximate 1-D vertical model of the reservoir. The estimated values of M and E were then used together with the previously established liquid saturation vertical profile of the reservoir, and the differential equation expresing the pressure gradient, to fit, by trial and error, the observed natural pressure profile. The accuracy of the fit depends on the assumed value for the vertical permeability and on the chosen forms for the relative permeability functions. We estimated $M \sim 6.9\times10^{-8}$ kg m^{-2} s^{-1} and $E \sim 0.2$ W m^{-2}. These results lie well within the ample ranges of mass and energy flowrates per unit area found in geothermal fields worldwide. The estimated values of M and E support the previous inference that there is an extensive caprock in the reservoir. Our best fit to the natural pressure gradient implies a vertical permeability of about 0.08 mD, residual water- and steam-saturations of about 0.04 and 0.00 respectively, and "fracture relative permeabilities" (i.e., $R_L+R_V=1$). This work addresses a major obstacle for a succsesfull analysis of the Los Azufres geothermal reservoir, which is characterized by an extensive two-phase region: the former unavailability of reasonably reliable relative permeability functions. Furthermore, the present characterization of the vertical natural flow provides important constraints for both lumped- and distributed-parameter models of the reservoir. Finally, this work gives information on reservoir properties that would be difficult to obtain by other means.

INTRODUCTION

Geothermal reservoir assesment generally requires a conceptual model, a quantitative mathemathical model based on the former, initial conditions, and boundary conditions. For Los Azufres we recently developed a quantitative-conceptual 1-D vertical model (Iglesias et al., 1985a, 1985b, 1985c). However, in order to charactherize the initial conditions for the model, we needed information about the natural mass and energy output of the field, for which no direct measurements exist. Furthermore, for the mathematical model we lacked reasonably reliable relative permeability functions, and knowledge about the magnitude of the vertical permeability.

In this paper we estimate the mass and energy flowrates per unit area, the permeability, and the relative permeability functions associated with the natural vertical flow in Los Azufres. The basic equations and some of the ideas on which the present work is based were presented by Pritchett (1979). This author discussed 1-D vertical two-phase flow and heat transfer in high-temperature hydrothermal systems. In particular, Pritchett stressed the possibility of obtaining insight on the relative permeabilities from comparison of synthetic vertical profiles of pressure, temperature, saturation and the like, whose forms depend on the details of the chosen relative permeability functions, with downhole measurements.

Our estimates are also based on data concerning the conditions at the boiling and dew elevations of the system, and on the natural vertical saturation and pressure profiles taken from our previous conceptual-quantitative 1-D vertical model of the Los Azufres reservoir (Iglesias et al., 1985a, 1985b, 1985c). Figure 1 summarises this model. The model reveals the existence of a "stack" composed of a deep compressed-liquid zone, a two-phase liquid-dominated zone, a two-phase vapor-dominated zone, and a dry-steam zone (this last zone in the fractures and cracks that vent the steam to the surface). Another important feature of the model is that the pressures of the natural reservoir were approximately fitted by a composite boiling-point-for-depth/vaporstatic pressure profile. Figure 2 illustrates the liquid saturation vertical profile obtained from this model.

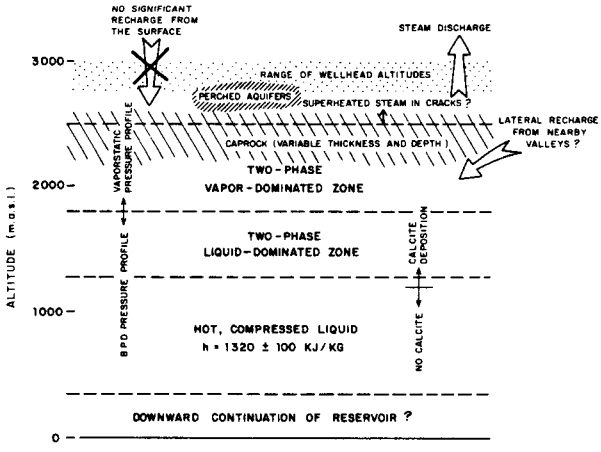

Fig. 1 A schematic 1-D vertical, conceptual model of the reservoir (after Iglesias et al., 1985c).

METHOD

Pritchett (1979) combined the equations describing the conservation of mass, momentum, and energy for vertical two-phase flow in porous media, in two compact equations: the pressure gradient law,

$$\frac{dP}{dz} = -g\left(\frac{R_V\,\rho_V^2\,\mu_L + R_L\,\rho_L^2\,\mu_V + M\,\frac{\mu_L\,\mu_V}{k\,g}}{R_V\,\rho_V\,\mu_L + R_L\,\rho_L\,\mu_V}\right) \qquad (1)$$

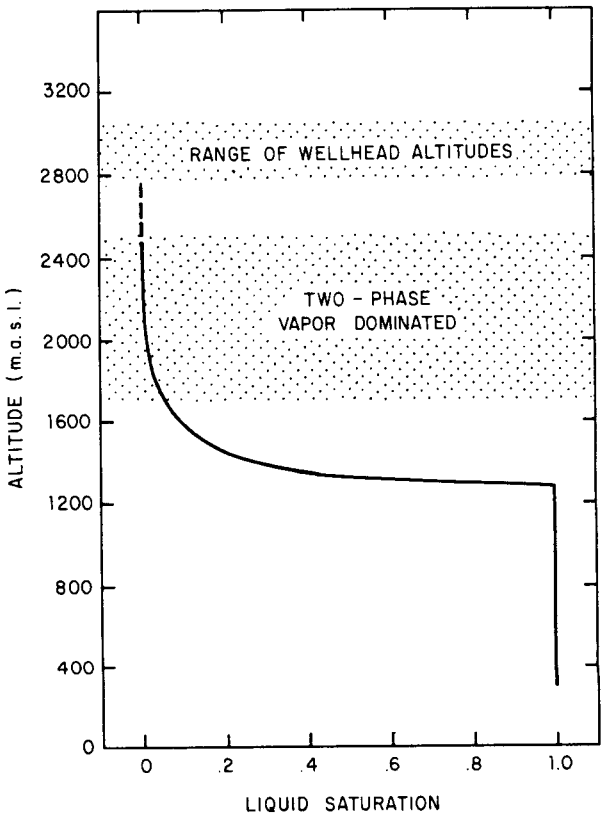

Fig. 2 The vertical profile of the liquid saturation in the model (after Iglesias et al., 1985c).

and the constitutive constraints equation,

$$R_V\left[\left(\frac{E}{k\,g}\right)\left(\frac{\mu_L}{\rho_L^2\,h_V}\right) - \left(\frac{M}{k\,g}\right)\left(\frac{\mu_L}{\rho_L^2}\right) - \left(\frac{K}{k}\right)\left(\frac{\gamma\,\rho_V\,\mu_L}{\rho_L^2\,h_V}\right)\right] + R_L\left[\left(\frac{E}{k\,g}\right)\left(\frac{\mu_V}{\rho_L\,\rho_V\,h_V}\right) - \left(\frac{M}{k\,g}\right)\left(\frac{\mu_V\,h_L}{\rho_L\,\rho_V\,h_V}\right) - \left(\frac{K}{k}\right)\left(\frac{\gamma\,\mu_V}{\rho_V\,h_V}\right)\right]$$

$$-R_L\,R_V\left(1-\frac{\rho_V}{\rho_L}\right)\left(1-\frac{h_L}{h_V}\right) = \left(\frac{M}{k\,g}\right)\left(\frac{K}{k}\right)\left(\frac{\mu_L}{\rho_L^2}\right)\left(\frac{\gamma\,\mu_V}{\rho_V\,h_V}\right) \qquad (2)$$

(notation at the end of the paper).

In the compressed-liquid region $S = 1$, $R_L = 1$ and $R_V = 0$, and the pressure gradient is given by

$$\frac{dP}{dz} = -\left(g\,\rho_L + \frac{M\,\mu_L}{k\,\rho_L}\right) \qquad (3)$$

To estimate M and E, we applyed the boundary conditions

$S = 1,\ R_L = 1\ ,\ R_V = 0$ at $z = z_B$,

$S = 0,\ R_L = 0\ ,\ R_V = 1$ at $z = z_D$,

at the boiling (B) and dew (D) elevations, to (1) and (2). Thus we obtained a system of 4 equations in 4 unknowns: M, E, k_B, and k_D. The corresponding solutions are:

$$M = \frac{K\left[\gamma_B\left(\frac{dP}{dz}\right)_B - \gamma_D\left(\frac{dP}{dz}\right)_D\right]}{(h_{VD} - h_{LB})} \qquad (4)$$

$$E = M\,h_{LB} + K\,\gamma_B\left(\frac{dP}{dz}\right)_B$$

$$= M\,h_{VD} + K\,\gamma_D\left(\frac{dP}{dz}\right)_D \qquad (5)$$

$$k_B = \frac{M}{\frac{\rho_{LB}}{\mu_{LB}}\left[\left(\frac{dP}{dz}\right)_B - g\,\rho_{LB}\right]} \qquad (6)$$

$$k_D = \frac{M}{\frac{\rho_{VD}}{\mu_{VD}}\left[\left(\frac{dP}{dz}\right)_D - g\,\rho_{VD}\right]} \qquad (7)$$

Solutions (4)-(7) assume that the thermal conductivity is a simple constant, independent of altitude. This is frequently a reasonable assumption (e.g., Pritchett, 1979), and there seems to be no reason to invalidate it in Los Azufres.

We were able to use equations (3) and (4) to estimate M and E for Los Azufres. The necessary values of the pressure gradients, enthalpies, and γ's were known from the previous quantitative vertical model (Iglesias et al., 1985a, 1985b, 1985c). However, the permeabilities k_B and k_D could not be estimated by means of (5) and (6) because that requires evaluation of the differences $(dP/dz - g\rho_L)_B$, $(dP/dz - g\rho_V)_D$, between the dynamic and the static pressure gradient. Normally these differences are of the order of 10% of the value of the static gradient (e.g., Grant et al., 1982). Unfortunately, the dispersion of the measured pressure profile (fig. 3) precludes reasonably reliable evaluation of said differences in our case. Therefore, we resorted to another approach to obtain information on the vertical permeability.

If estimates of M and E are available, the pressure gradient equations (1) and (3) can be used together with the liquid saturation vertical profile (fig. 2) to fit, by trial and error, the measured pressure profile (fig. 3). The fit depends on the vertical distribution assumed for **k**, and on the forms of the relative permeability functions $R_L(S)$ and $R_V(S)$ chosen for the synthetic profile.

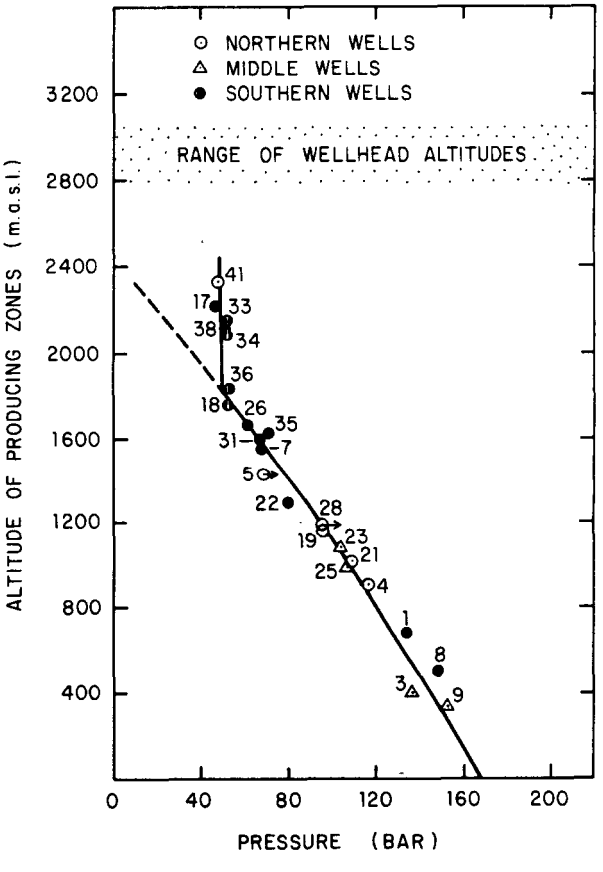

Fig. 3 The measured pressure profile, with the composite BPD-vaporstatic profile (after Iglesias et al., 1985c).

Lacking information about the vertical distribution of **k**, we adopted the simplest assumption: **k** is a constant independent of altitude. Thus, the magnitude of **k** derived from the fitting process must be regarded as an equivalent vertical permeability representative of the areally-lumped 1-D vertical model.

To compute the synthetic pressure profiles, equations (1) and (3) were numerically integrated subjected to the constraints

$$S = S(z); \quad R_L = R_L(S); \quad R_V = R_V(S),$$

and to the boundary conditions

$$P(z_{min}) = Pmax; \quad P(z_D) = P_D,$$

where z_{min} is the elevation corresponding to the maximum pressure of the quantitative-conceptual model. Naturally, the forms of the relative permeability functions must be defined *before integration can proceed.*

The actual fitting procedure involved manipulation of the fitting parameters (k and the relative permeability functions) and repeated integrations until a satisfactory fit was achieved.

Like other inverse (in the mathematical sense) methods, the method just described does not guarantee the uniqueness of the solution. Fortunately, the observed pressure profile at Los Azufres is particularly difficult to fit due to the existence of a pronounced "knee" at about 1800 m a.s.l., the altitude corresponding to the transition from a water-dominated to a vapor-dominated system (e.g., fig. 3). The greater difficulty hopefully circumscribes the range of fitting parameters that reasonably represent solutions.

RESULTS AND DISCUSSION

Using $K = 1.8\ W\ m^{-2}$ in (4) and (5), as suggested by the, so far, only available direct measurements of thermal conductivity for andesites from Los Azufres (Contreras et al., 1986), we estimated

$$M = 6.9 \times 10^{-8}\ kg\ m^{-2}\ s^{-1},$$

$$E = 0.2\ W\ m^{-2}.$$

The computed mass flux is well within the ample range of mass fluxes found in geothermal fields worldwide. Adopting 30 km^2 as the area of the reservoir (e.g., de la Cruz and Castillo, 1984; Iglesias et al., 1985b, 1985c), the value inferred for M implies a natural discharge for Los Azufres of about 50 ton/hr of steam [no geothermal liquid is discharged in the field (Rodriguez et al., 1984; Iglesias et al., 1985c)]. This small natural discharge is compatible with the field discharging exclusively steam and with the fact that the discharge area is small with respect to the reservoir area. As is well known, the natural discharges in Los Azufres are far from reaching the intensity and spectacularity observed in other geothermal fields. This result reinforces the available evidence indicating the existence of an extensive caprock in the reservoir. If the system is in steady state, as indicated by some evidence (Iglesias et al., 1985b, 1985c), this result also indicates the magnitude of the **natural** recharge.

The value inferred for the natural thermal flow is significantly greater than the normal average thermal flow. The average heat flow in thermally "normal" continental regions is 0.05-0.06 $W\ m^{-2}$ (e.g., Goguel, 1976; Elder, 1976; Jessop et al., 1976). Thus, the natural thermal flow in Los Azufres is clearly within the range of the thermally anomalous regions, as expected. The relative importances of the conductive and convective componentes of the deep thermal flow in Los Azufres can be assesed by means of equation (5); in this way it is easy to show that the contributions of both components are comparable at the boiling and dew altitudes. Adopting, as before, 30 km^2 as the reservoir area, the value inferred for E implies a natural thermal discharge for Los Azufres of about 6 MW.

Our best-fit estimates of the vertical permeability and relative permeability functions were obtained from the fit ilustrated in fig. 4; compare with the composite BPD-vaporstatic profile of fig. 3. The estimates are

$$k = 0.08 \times 10^{-15}\ m^2,$$

$$R_L = [(S-S_0)/(1-S_0)]^a, \qquad (8)$$

$$R_V = 1-R_L, \qquad (9)$$

$$S_0 = 0.04, \quad S_{0V} = 0, \qquad (10)$$

$$a = 0.2, \qquad (11)$$

where S_0 is the liquid irreducible saturation, S_{0V} the vapor irreducible saturation, and **a** a real, positive exponent.

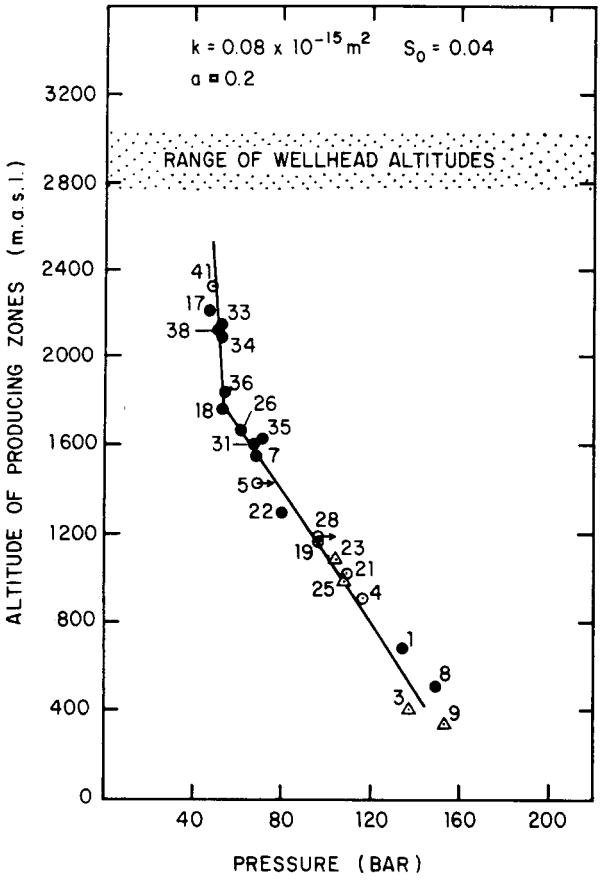

Fig. 4 Best fit to the measured pressure profile.

The inferred vertical permeability is significantly smaller than the horizontal fracture permeabilities deduced from pressure well tests, which span the range 10^{-15} to 30×10^{-15} m^2 (e.g., Iglesias and Arellano, 1985); however, its magnitude is comparable with those of the matrix permeabilities measured in drill cores from Los Azufres, which vary approximately from less than 0.002×10^{-15} to 0.2×10^{-15} (Contreras et al., 1986).

For the relative permeability functions we adopted the so called "fracture relative permeabilities" condition (9) (e.g., Grant et al., 1982). This was done because (a) there is compelling geologic (e.g., Razo, 1984; Garfias, 1984; Huitron, 1985; de la Cruz and Castillo, 1984) and well testing (e.g., Iglesias and Arellano, 1985) evidence that Los Azufres is a naturally fractured reservoir; and (b) we were unable to obtain a satisfactory fit with Corey-type or other multicomponenet-oriented relations.

The successful fit of the observed pressure profile provides circumstantial evidence in favor of the validity of the "fracture relative permeabilities" condition. A non-zero liquid irreducible saturation and a zero vapor irreducible saturation were also necessary for a succsessful fit. The forms of the resulting relative permeability functions are shown in fig. 5.

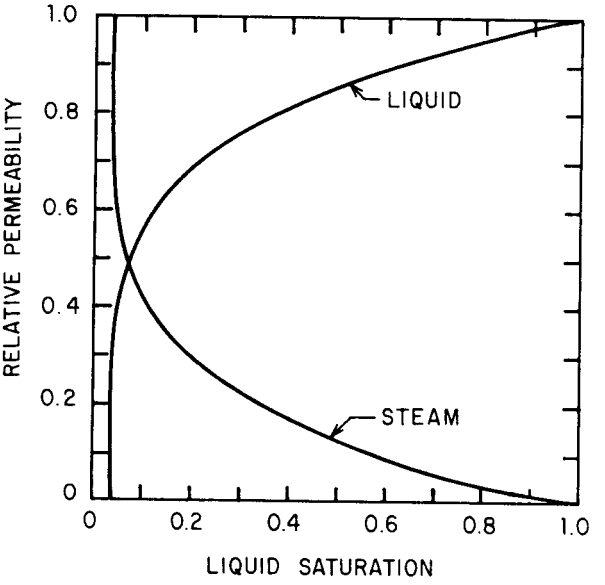

Fig. 5 Derived relative permeability functions.

The sensitivity of the fit to the fitting parameters **k**, S_0 and **a** is illustrated in figs. (6)-(8) respectively. In these figures the continuous line indicates the best fit.

SUMMARY

We have estimated the mass and energy fluxes, the permeability and the relative permeability functions associated with the natural vertical flow in the reservoir. The results for M ($\sim$ 6.9×10^{-8} kg m^{-2} s^{-1}) and E ($\sim$ 0.2 W m^{-2}) lie well within the ample ranges of mass and energy flowrates per unit area found in geothermal fields worldwide. These results support the previous inference that there is an extensive caprock in the reservoir. Our best fit to the natural pressure gradient implies a vertical permeability of about 0.08 mD, residual water- and steam-saturations of about 0.04 and 0.00 respectively, and "fracture relative permeabilities" (i.e., $R_L+R_V=1$). This work addresses a major obstacle for a succsesfull

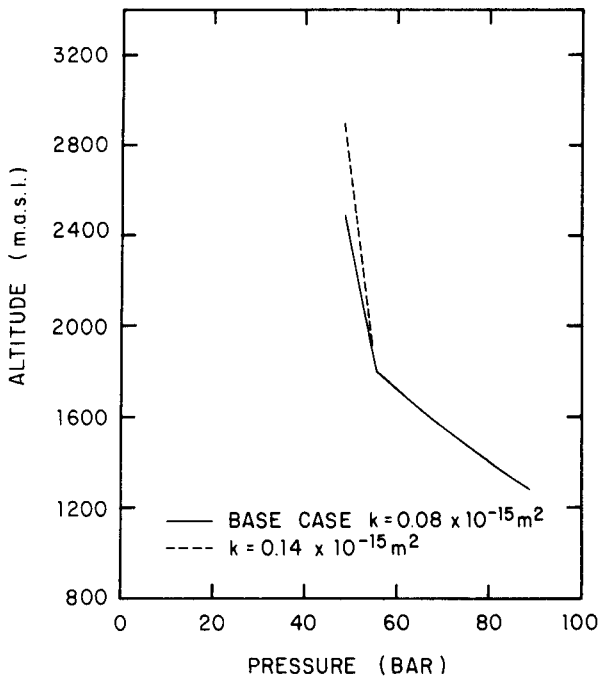

Fig. 6 Sensitivity of the fit to the vertical permeability.

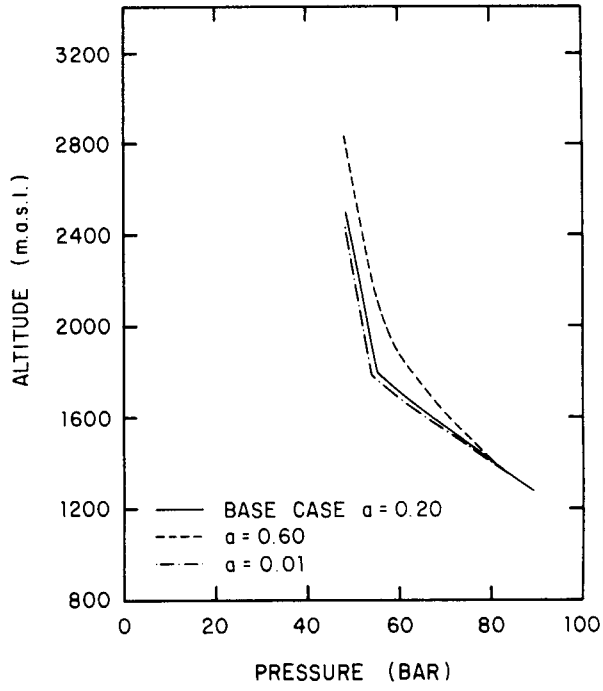

Fig. 8 Sensitivity of the fit to the exponent **a**.

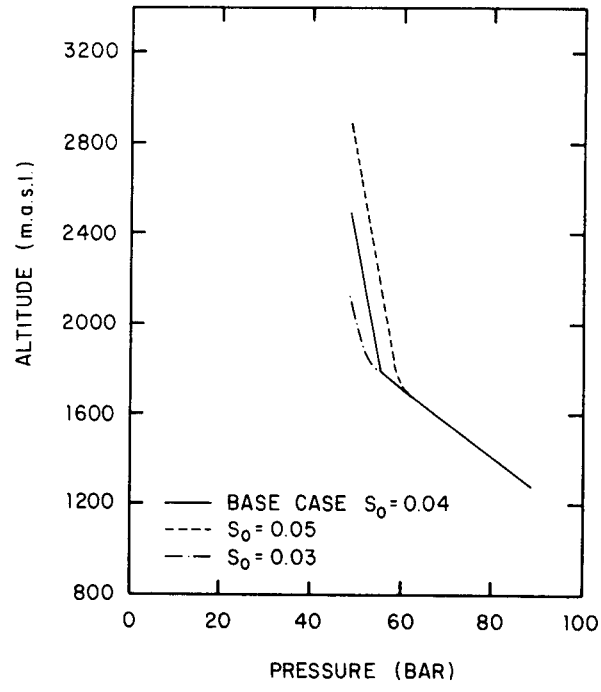

Fig. 7 Sensitivity of the fit to the irreducible liquid saturation.

analysis of the Los Azufres geothermal reservoir, which is charactherized by an extensive two-phase region: the former unavailability of reasonably reliable relative permeability functions. Furthermore, the present characterization of the vertical natural flow provides important constraints for both lumped- and distributed-parameter models of the reservoir. Finally, this work gives information on reservoir properties that would be difficult to obtain by other means.

ACKNOWLEDGEMENTS

The authors are indebted to Ing. Ramon Reyes S., Head of the Coordinadora Ejecutiva de Los Azufres for his encouragment. This work has been partly supported by CFE contract 832004.

NOMENCLATURE

E : upward energy flux ($W\ m^{-2}$)

g : gravity ($m\ s^{-2}$)

γ : dT/dP ($^{o}C\ Pa^{-1}$)

h_L : enthalpy of liquid phase ($J\ kg^{-1}$)

h_V : enthalpy of vapor phase ($J\ kg^{-1}$)

k : vertical permeability (m^2)

K : vertical thermal conductivity ($W\ m^{-1}\ C^{-1}$)

M : upward mass flux ($kg\ m^{-2}\ s^{-1}$)

μ_L : liquid-phase viscosity (Pa s)

μ_V : vapor phase viscosity (Pa s)

P : fluid pressure (Pa)

R_L : liquid-phase relative permeability (dimensionless)

R_V : vapor-phase relative permeability (dimensionless)

ρ_L : liquid-phase density ($kg\ m^{-3}$)

ρ_V : vapor-phase density ($kg\ m^{-3}$)

S : liquid saturation (dimensionless)

T : temperature (^{o}C)

z : altitude (m a.s.l.)

REFERENCES

Contreras E., Iglesias E. and Razo A. (1986) Initial measurements of petrophysical properties on rocks from the Los Azufres, Mexico, geothermal field, these Proceedings.

De la Cruz V. and Castillo D. (1984) Modelo geotermico conceptual del campo de Los Azufres, Mich., CFE Internal Report 13-84, Comision Federal de Electricidad, Mexico.

Elder J. (1976) The bowels of the Earth, Oxford University Press.

Garfias A. (1984) Personal communication.

Goguel J. (1976) Geothermics, McGraw-Hill Book Company.

Grant M.A., Donaldson I.G. and Bixley, P.F. (1982) Geothermal reservoir engineering, edit. Denton J., Academic Press.

Huitron R. (1985) Personal communication.

Iglesias E., Arellano V., Garfias A., Miranda C. and Aragon A. (1985a) The natural thermodynamic state of the fluids in the Los Azufres geothermal reservoir, Proc. 10th Stanford Workshop Geoth. Res. Eng., pp. 241-246, Stanford University, SGP-TR-84.

Iglesias E., Arellano V., Garfias A., Miranda C. and Aragon A. (1985b) A one-dimensional vertical model of the Los Azufres, Mexico, geothermal reservoir in its natural state, GRC Transactions, vol. 9, part II, pp. 331-336.

Iglesias E., Arellano V., Garfias A., Miranda C. and Aragon A. (1985c) Los Azufres geothermal field, Mexico: I. The natural state of the fluids, submitted to Geothermics.

Iglesias E. and Arellano V. (1985) Integracion de un modelo basico actualizado del campo geotermico Los Azufres, Informe IIE/11/1864/I 04/F, Instituto de Investigaciones Electricas, Mexico.

Jessop A.M., Hobart M.A. and Sclater G.J. (1976) The world heat flow data collection 1975, Geothermal Service of Canada, Geotherm. Ser. vol. 5. pp. 175.

Pritchett J.W. (1979) Vertical two-phase flow in geothermal reservoirs, Report SSS-R-80-4341, Systems Science and Software, La Jolla, CA.

Razo A. (1984) Personal communication.

Rodriguez C., Villa S. and Quijano J. (1984) Modelo geoquimico del campo geotermico Los Azufres, CFE Internal Report 10-84, Comision Federal de Electricidad.

PROCEEDINGS, Eleventh Workshop on Geothermal Reservoir Engineering
Stanford University, Stanford, California, January 21-23, 1986
SGP-TR-93

PERMEABILITY ENHANCEMENT USING HIGH ENERGY GAS FRACTURING

T. Y. Chu, J. F. Cuderman, J. Jung, R. D. Jacobson

Sandia National Laboratories
Albuquerque, New Mexico 87185

ABSTRACT

This paper reports the results of a preliminary study of using High Energy Gas Fracturing (HEGF) techniques for geothermal well stimulation. Experiments conducted in the G-tunnel complex at the Nevada Test Site (NTS) showed that multiple fractures could be created in water-filled boreholes using HEGF. Therefore, the method is potentially useful for geothermal well stimulation.

INTRODUCTION

Drilling is often a substantial fraction of the overall cost of a geothermal well. It may, therefore, be more economical to stimulate a nonproducing well instead of redrilling a new well. Because permeability in geothermal reservoirs is typically fracture dominated any stimulation method must have the potential of connecting the wellbore to the existing productive fractures.

Attempts to stimulate sub-commercial wells using hydraulic fracturing have generally been unsuccessful because hydraulic fractures usually run parallel to natural fractures.

Sandia National Laboratories with funding from the U. S. Department of Energy carried out a series of experiments to evaluate the potential of the High Energy Gas Fracturing (HEGF) technique for stimulating geothermal wells. HEGF was developed at Sandia for stimulating gas wells [1,2]. The geothermal application represents an extension of this technology from gas filled to liquid filled boreholes.

The HEGF technique uses propellants to pressurize a wellbore. By proper design it can produce multiple radial fractures emanating from a wellbore with typical fracture length of 30 ft (10 m) or more [1,2]. This fracture length is comparable to typical distances between productive geothermal fractures. Therefore, HEGF produced radial fractures can be potential conduits connecting the wellbore to existing productive fractures.

Four experiments were conducted at the G-Tunnel complex at NTS in horizontal boreholes with mine back following the experiments to examine the fracture patterns. The fracture patterns were compared with the results from finite element analyses. Propellant burn tests in steel pipes were also performed to qualify canister designs, and to test propellants and propellant mixtures.

THE HIGH ENERGY GAS FRACTURING TECHNIQUE

The Pressure Risetime Criterion

The basic concept of HEGF is that fracture patterns achieved in pressurizing a borehole are dependent on the rate of pressurization or the pressure risetime. A typical pressure time profile in a gas filled borehole shows a monotonic initial pressure rise, followed by a slight drop in pressure at fracture initiation and then again a pressure increase until the propellant burn is complete. The pressure risetime is defined as the time span of the initial pressure rise; it is a convenient measure of the pressurization rate.

For explosives or very fast propellants (0.1 ms risetimes), a crushed zone is produced about the wellbore resulting in decreased permeability. For very slow pressurizations (1 ms risetime), only hydraulic type fracture occurs. For intermediate burn rates (0.1 to 1 ms risetimes), four or eight major fractures emanate from the wellbore, oriented along principal in situ stress directions. The number of fractures

generally increases with shorter risetimes.

Experimentally, the multiple-fracture regime can be correlated in terms of pressure risetime (t_m) by [1]:

$$\frac{\pi D}{2C_R} \lesssim t_m \lesssim \frac{8\pi D}{C_R} \qquad (1)$$

where C_R is the Raleigh surface wave speed and D is the borehole diameter. The term at the left is derived by Cuderman [1,2] based on a surface standing wave concept; it represents the multiple-explosive crushing boundary. The term at the right is an empirical fit to the hydraulic-multiple boundary. The expression D/C_R is a measure of the communication time between surface elements of the borehole. For the 4-in boreholes in ashfall tuff in the present experiments, equation (1) reduces to:

$$0.15\text{ms} \lesssim t_m \lesssim 2.4\text{ ms} \qquad (1a)$$

Propellant Specification

M5A, M5B, M30A and M30B artillary propellants were used in HEFG experiments [3]. Pressurization rates calculated from ballistics data are inadequate for HEFG applications because ballistics data are for much higher pressures. The risetimes are, therefore, experimentally determined for each propellant for cases where the borehole is filled with the propellant [1,2]. When the propellant canister is smaller than the borehole, the free volume (volume not occupied by the propellant) is increased by the annular space between the canister and the borehole. There is a corresponding increase in risetime. The risetime variation is directly proportional to the free volume [1]:

$$\frac{t_m'}{t_m} = \frac{V'}{V} \qquad (2)$$

where the primed symbols correspond to the larger free volume and risetime.

When the desired risetime cannot be achieved by using a single propellant a mixture is formulated using a logarithmic mixing law [1].

Fracture Geometry

Figure 1 is a mapping of a multiple-fracture pattern radiating from a borehole. The maximum principal stress in the plane normal to the borehole is designated σ_{max}, the minimum σ_{min}. The vertical and horizontal fractures are thus in the two principal stress planes. The fracture in each quadrant corresponds to plane of maximum in situ shear stress. The average fracture length was found to be proportional to the square root of energy content per unit length of the propellant canister [1].

STEEL PIPE PROPELLANT BURN EXPERIMENTS

The design of the pipe experiment is shown in Figure 2. The propellant canister consisted of a 48 in. (1.22m) long RIP igniter co-axial with a PVC pipe; propellant grains filled the space between the pipe and the ignitor. The canister size varied from 0.04m to 0.08m. For most tests 72 in (1.83m) long, extra heavy duty 4-in. pipes (4.1 in., 0.10m, I.D.; 5.6 in., 0.14m, O.D.) with screwed-on end caps were used.

A total of fourteen experiments were conducted, with canister size, propellant and annular fill (water, air) as variables. Unlike gas filled experiments, the pressure histories of water filled experiments exhibit high frequency oscillations superimposed on the general trend of increasing pressure. The pressure histories were also spatially non-uniform, see Figure 3. The oscillations and non-uniformities are related to pressure transient effects in water.

The pipe experiments show that the main effect of water is to decrease the free volume thus decreasing the risetime. The risetime can be scaled within a factor of about two by the free volume ratio, equation (2). Risetimes in the 0.1ms to 4ms range were obtained in water filled pipes spanning the values required for HEGF applications. The pipe experiments also showed that all of the propellants used obey the same mixing laws [2,3].

NTS BOREHOLE EXPERIMENTS

Four experiments (GT1-GT4) were performed in water-filled boreholes [3]. GT1 was used to test canister design and ignition schemes; only results of GT2-4 are reported here.

The experiments were all done in 4-in. (0.1m) diameter boreholes

drilled into the face of a horizontal drift. Four holes with a 3 1/2° dip to horizontal were drilled into each 12 ft x 14 ft (3.7m x 4.3m) face. Two out of the four holes were used for GT experiments. Lithologies of the experiment zones for GT 1-2 and GT 3-4 show two types of ashfall tuff - Red and Peralkaline, in bandlike intervals. Because the intervals are shifted upward down the drift, different rock types are encountered down the axis of the boreholes. Of the two rocks, the red is more competent [4].

The experiment assembly consists of the propellant canister, pressure transducer, packer, and cable tube, Figure 4. Upon installation of the experiment package, the borehole is backfilled with water and the packer pressurized with air or water. The borehole beyond the packer is stemmed with damp sand. A foot of 50/50 mix of sand and sulfate-based cement at the collar ensures containment of the stemming.

Experiment GT2

Experiment GT2 used a 3.2 in (0.08 m) ID, 8-ft (2.4m) long propellant canister filled with 11.2kg of M5B propellant, at the bottom of a 40-ft (12.2 m) borehole. The test zone was in a mixture of Peralkaline and Red Ash. A 0.7 ms risetime was predicted assuming the only effect of water was to reduce the free volume. The observed risetime was 0.3 ms, Figure 5. Both values are within the multiple fracture regime. The fracture pattern is shown in Figure 6. A large hydraulic type fracture started near the pressure transducer end of the test zone, then propagated both toward the collar of the borehole and over the test zone, total length 23 ft (7 m). Just before the test zone, a horizontal fracture was observed between 25 ft and 31 ft (8.8 and 9.4 m); in this region, the fracturing is characterized as multiple. In the test zone itself, multiple fractures were initiated; but crushing prevented propagation. The same risetime in a liquid-free borehole would have produced a multiple fracture pattern. But here the pattern is a combination of hydraulic, multiple, and explosive fracturing. The fact that the test zone was partially in Peralkaline may be a contributing factor for crushing.

Experiment GT 3

Experiment GT3 used a 1.75-in (0.044 m) diameter 4-ft (1.22 m) propellant canister with 1.36 kg of M30A propellant. The borehole was 25 ft (7.62 m) deep. The test zone was mainly in Red Ash. A pressure risetime of 1.2 ms was predicted. Figure 7 shows the measured pressure history with two major pressure pulses having risetimes of 0.25 ms, and 1.9 ms, respectively. The 1.9 ms risetime is consistent with pipe results. These risetimes in a 4-in borehole, should result in multiple, and multiple-hydraulic fracturing, respectably.

The mineback results are summarized in Figure 8, showing major fractures at 55 degrees and at 215 degrees (measured from the direction of maximum principle stress) about 5 ft (1.52m) long. In addition, a small fracture nearly parallel to the 55° orientation broke out near the center of the test zone. In gas-filled boreholes, the predominant fractures are in the principal planes of stress; fractures in the quadrants between the principal stresses, corresponding to the principal shear planes, were secondary, but in liquid filled boreholes there appears to be no preference. Borehole televiewer observations indicated that horizontal and vertical fractures were clearly initiated but they did not propagate.

Experiment GT 4

Experiment GT 4 used a 3.2 in (0.08m) diameter 4-ft (1.22 m) propellant canister with 5.27 kg of 50/50 mixture of M30A/M30B propellants. The borehole was 25-ft (7.62 m) deep. The test zone was predominately in Peralkaline. A pressure risetime of 0.5 ms was predicted. Figure 9 is a plot of the pressure history. The peak pressure for the overall pulse occurred at 7.4 ms. But, three sharp pressure spikes are observed in the first millisecond of pressure buildup, with risetimes ranging from 0.07 ms to 0.2 ms. The 0.07 ms spike is expected to initiate crushing, the 0.2 ms multiple fracturing. The third spike is probably most important because of its larger impulse. If either the first three pulses or the second and third acted collectively resulting in effective risetimes of 1 ms and 0.3 ms respectively, multiple fractures should result.

Figure 10 is a 3-dimensional drawing of the GT-4 mineback. Four main fracture sets, labeled 1-4, were mapped. The borehole televiewer and mineback showed significant borehole crushing in the test zone. A vertical hydraulic fracture, see fracture 1 and 1A (Sec. A-A and C-C) Figure 10, above the borehole, was present in most of the mineback. The other major fractures were mainly in principal shear plane directions.

A multiple fracture pattern was again initiated at the borehole, but only one to three of these fractures propagated into the formation at any given section, see fracture 2 (Sec. B-B) and fracture 3 (Sec. DD) in Figure 10. Fracture 4 originated at the end of the borehole and proceeded well beyond the mineback region (Sec D-D).

The combination of fracture patterns observed in GT-3 and GT-4 both indicated that the fracture behaviors are best understood as the cumulative effects of individual pressure pulses.

NUMERICAL ANALYSIS

Two dimensional finite element analyses of the experiments were conducted for comparison with the experimental results. Since the observed fracture patterns are actually three dimensional, the comparison must be recognized as qualitative. The pressure histories were calculated via a propellant burn model, and rock cracking and crushing were represented with an elastic-plastic cracking material model and a tensile cracking criterion [4]. Water was modeled simply as an incompressible solid. Because of the aforementioned problems with ballistics data, the calculated pressure rates and peak pressures were only within a factor of two to three of the measured values. Therefore, the experimentally measured borehole pressure histories were used as inputs in a separate series of analyses.

Results

GT2

When the experimentally measured pressure was used, the calculations showed significant cracking adjacent to the borehole and the radius of the borehole increased to approximately 4.5 inches. These results are in qualitative agreement with the mineback data, Figure 6.

GT3

The analyses predicted a major vertical fracture, and some short fractures adjacent to the borehole. The result agrees qualitatively with the initiation of multiple fracture observed by the televiewer. However, the predicted fracture directions are not consistent with the experimental results.

GT4

The analyses using the burn model predicted one major vertical crack Figure 11a. However, when the experimental pressure history containing the pressure spikes was used, short cracks adjacent to the borehole of approximately the length of the observed ones also formed, Figure 11b. This result corroborates the observation that individual pressure spikes are important to the formation of the fractures.

CONCLUDING REMARKS

Multiple fractures along hydraulic fracture directions and principal shear planes such as those observed in GT 3 and GT 4 were created in water-filled boreholes, using the HEGF technique, thus demonstrating the potential of HEGF for Geothermal Stimulation.

The fracturing behavior is considerably more complex in liquid-filled boreholes than the liquid-free case. More research is needed with longer test zones, where the influences of end effects and pressure transients are expected to be less. Experiments should also be conducted in naturally fractured or prefractured test beds to simulate reservoir conditions. Finally, application in geothermal wells requires development and testing of high temperature propellant systems or temperature control of wells during stimulation.

REFERENCES

1. Cuderman, J. F. (1984) "High Energy Gas Fracturing Development--Final Report to Gas Research Institute, SAND84-0247, Sandia National Laboratories, Albuquerque, NM.
2. Cuderman, J. F., and Northrop, D. A. (1984) "A Propellant-Based

Technology for Multiple Fracturing Wellbores to Enhance Gas Recovery: Application and Results in Devonian Shale. "SPE/DOE/GRI 12838, Unconventional Gas Recovery Symposium," Pittsburgh, PA.

3. Cuderman, J. F., T. Y. Chu, J. Jung, and R. D. Jacobson, (1985) "High Energy Gas Fracturing Experiments in Liquid Boreholes--Potential Geothermal application," SAND85-2809, Sandia National Laboratories, Albuquerque, NM.

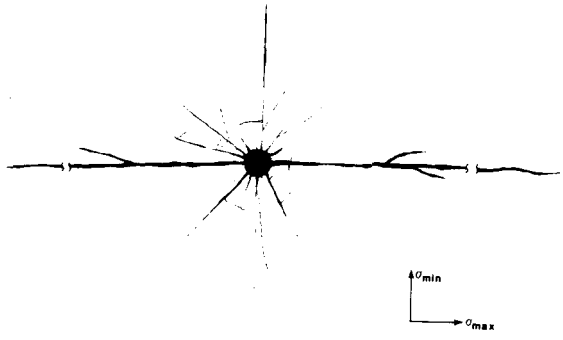

Fig. 1 Optimal Multiple Fracture Pattern

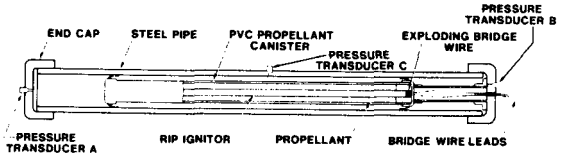

Fig. 2 Design of Pipe Propellant Burn Experiment

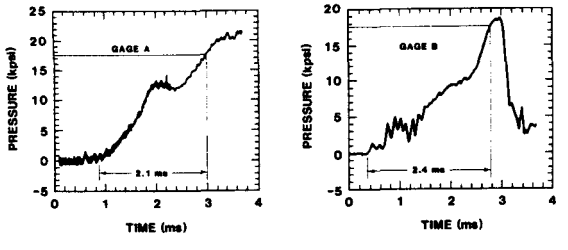

Fig. 3 Pipe Experiment P12 [3] Pressure at two locations, see Fig. 2 for transducer location designation

4. Taylor, Lee M., Daniel V. Swenson, and P. W. Cooper, (1984) "A Coupled Gas Flow/Solid Dynamics Model for Predicting the Formation of Fracture Patterns in Gas Well Simulation Experiments," SAND84-0016, Sandia National Laboratories, Albuquerque, NM.

This work was supported by the U. S. Department of Energy at Sandia National Laboratories under Contract DE-AC04-76DP00789.

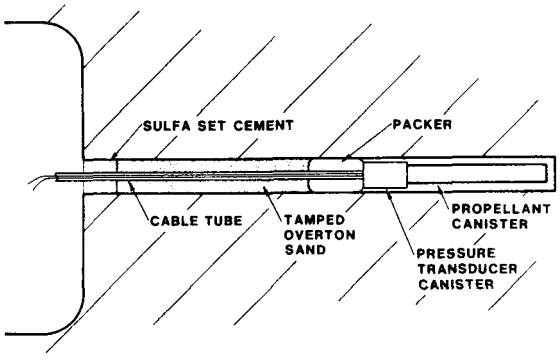

Fig. 4 Typical Borehole Experiment Installation

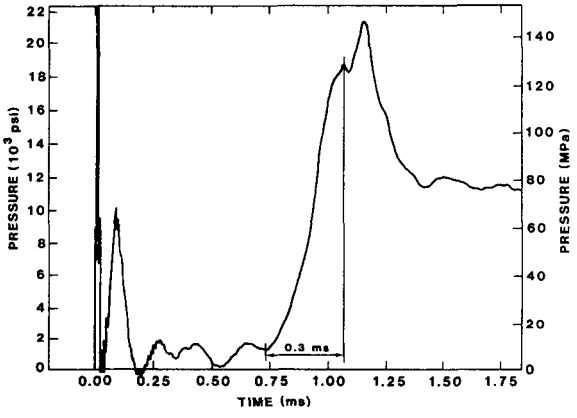

Fig. 5 GT2 Experiment Pressure History

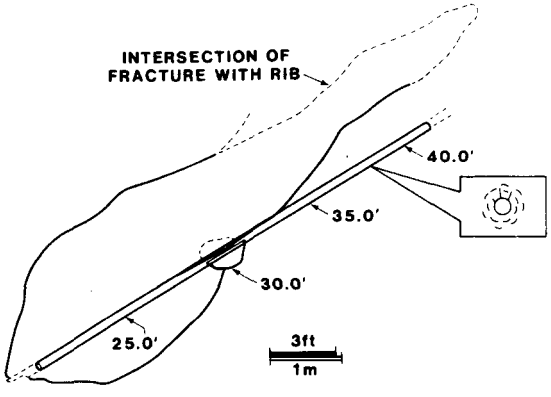

Fig. 6 GT2 Fracture Mapping

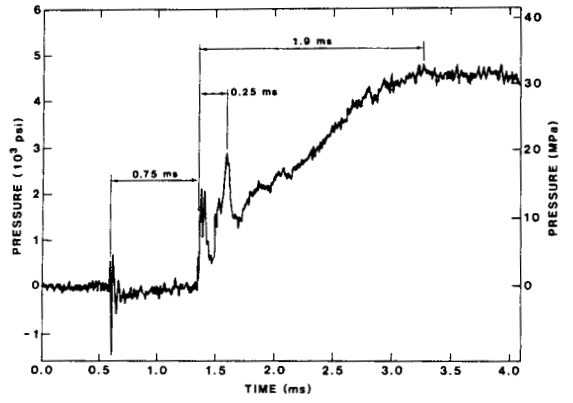

Fig. 7 GT3 Experiment Pressure History

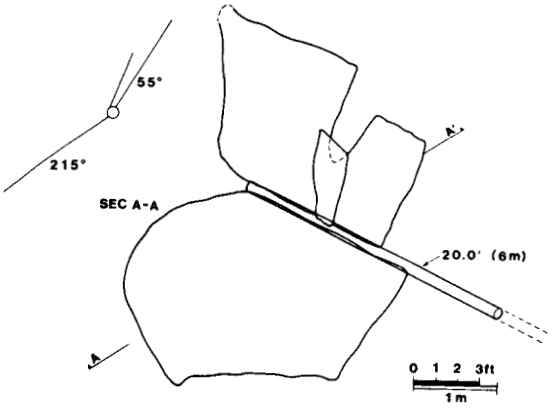

Fig. 8 GT3 Fracture Mapping

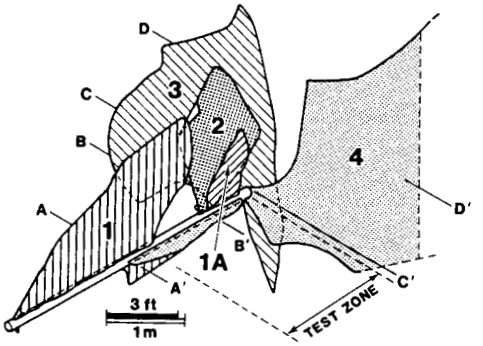

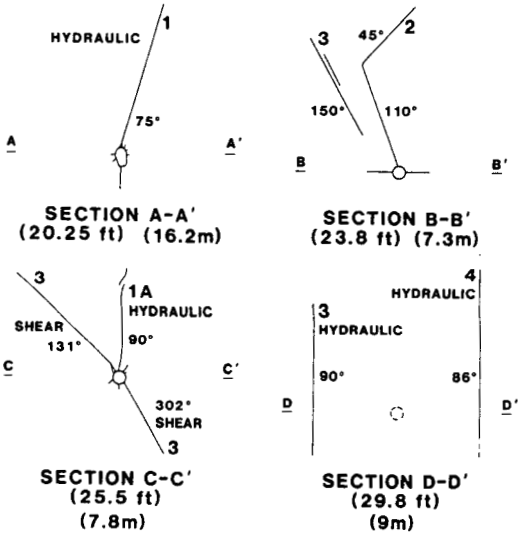

Fig. 10 GT4 Fracture Mapping

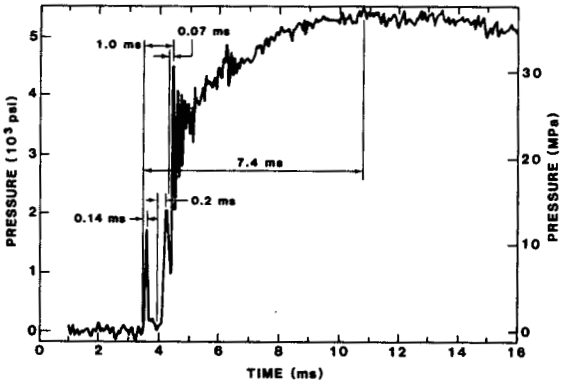

Fig. 9 GT4 Experiment Pressure History

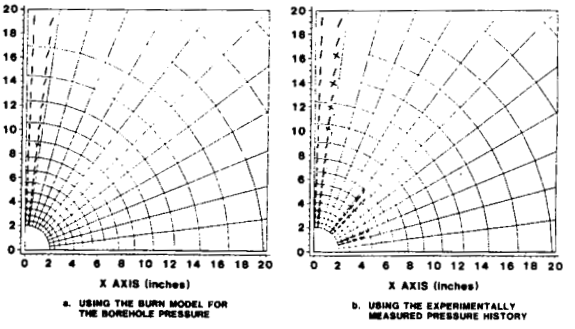

Fig. 11 GT4 Calculated Fracture Pattern

PROCEEDINGS, Eleventh Workshop on Geothermal Reservoir Engineering
Stanford University, Stanford, California, January 21-23, 1986
SGP-TR-93

CONCEPTUAL SCHEMATIC GEOLOGIC CROSS-SECTIONS OF THE GEYSERS STEAM FIELD

Jeffrey J. Hebein

Diamond Shamrock Thermal Power Co.
3333 Mendocino Avenue, Suite 120
Santa Rosa, California 95401

ABSTRACT

While formerly studied in terms of ancient Franciscan stratigraphy, The Geysers Steam Field now offers new views and interpretations on the deeper structure and importance of the lithocap, main metagraywacke, and felsic intrusive basement units with respect to the huge fractured reservoir. The Big Sulphur Creek enhanced tectonic disruption area provides the best situation for shallow felsite injection, shallow reservoir top, metasomatism transformation, and profound fracture permeability. Steam cells commonly extend to great depths and laterally drop off sharply, with relatively flat lateral continuance in some resource areas. Injectate ponding may offer a third fluid interface for reservoir steam reserves. A possible boiled down residuum of complex evaporates and hematite has been viewed in one area of the field where the reservoir (proper) bottom was encountered. Such a deposit may exist along all reservoir cell(s) bottoms, where in numerous cases the reservoir proper has been seen to pass into a somewhat mysterious ultra-superheated reservoir.

INTRODUCTION

Former subsurface conceptions of The Geysers field concentrate on nearer-surface structure with particular emphasis on Franciscan stratigraphy, speculating little on the third dimension, reservoir depth and lateral continuance. Many publically and privately held ideas concerning the deeper reservoir nature are superficial and lack enhanced tectonic thought. This critique presents a simplistic, yet realistic view of the reservoir and its surroundings on a megalithologic/megatectonic scale, utilizing proper hydrothermal thought and conservatively constructive speculation.

GEOLOGIC/HYDRAULIC DISCUSSION

The steam field (Figures 1-6) exists in an ancient metamorphic-Quaternary felsic intrusive complex with fieldwide traceable contours of a main graywacke (very brittle), undefined lithocap (more plastic partial seal), felsic intrusives (many brittle differentiated phases), and reservoir top (ultimate sericitic seal). The main graywacke and felsite usually plunge together, while the felsite contact can be traced downward by various hydrothermal alteration haloes, even when contacting below maximum drilling depths. The reservoir can extend upward into the lithocap in the core areas of the field (more profound tectonic disruption), due to former enhanced hydrothermal metasomatism (embrittlement) of the lithocap. The reservoir runs deep into the felsite (somewhat elusive, variable, yet sometimes profound, permabilities), its bottom perhaps even below the implied bounds detected by production strain seismicity. Section 7 offers a generalized view of the most metasomatized area of the steam field. Felsic differentiation (granite, quartz monzonite, granodiorite, quartz diorite; both plutonic and hypabyssal) is somewhat speculative, yet should be realistic.

Injectate (creekwater, steam condensate, tower rainwater, chemical tracers, sump fluids, etc.) ponding may offer a third reserves interface. The reservoir (proper) bottom has been adequately detected in one area of the steam field, evidence suggesting that the entire reservoir(s) bottom may be filled with a boiled down residuum of complex evaporates (chlorides, etc.) and hematite. The absolute depth and extent of the ultra-superheated (somewhat mysterious) reservoir is unknown.

Virgin vapor cell geochemical signatures have been obliterated and perhaps are now rendered interpretationally useless due to much injectate contamination. Non-condensible gas distributions over the field are of high surviellance importance.

Sections utilized private data, published data, public well records and drilling surveys, and some of the author's personal speculation, especially on the extreme lateral slopes of the reservoir and felsite. Competitor data was considered, however not revealed in the sections.

ACKNOWLEDGEMENT

The views and conclusions expressed herein are those of the author and may not necessarily represent the views and conclusions of Diamond Shamrock Thermal Power Company, its affiliated companies, its venture partners, or any other entity.

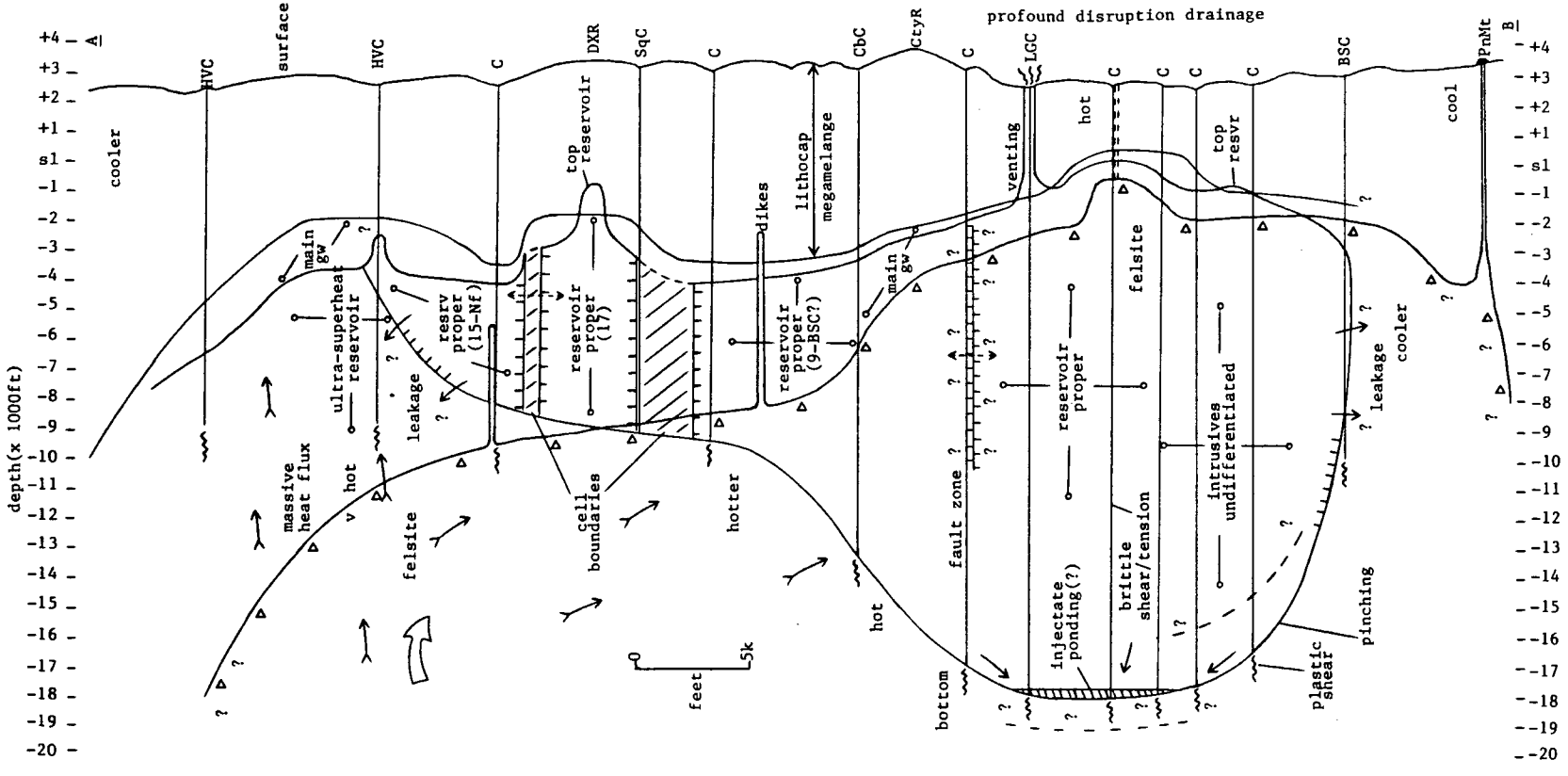

Figure 1. Cross-section A-B. The felsite line closely follows the lithocap line along the more structurally disrupted areas(core) of the steamfield. Steeply plunging felsite at the field's flanks probably relates to the termination of intense rock metasomatism. Certain localized tectonic effects allow the reservoir to perpetuate into the lithocap. Stratigraphic definition of the metamorphic complex is unnecessary; rock mechanics are applied at the surface in plan view to correctly define projectable reservoir fracturing. In the northern portions of the steamfield, the reservoir proper passes into an ultra-superheated reservoir, with perhaps minor crossflow from vaporstatic steam convective flow (470°-485°F) to much drier conductive flow(485°++F) regimes. The resource's main heat flux undoubtedly emanates from the northeastern reaches; wells drilled out of the reservoir proper penetrate into much hotter rock, while wells drilled out of the reservoir in the westernmost and southern portions exhibit temperature declines. The ultra-superheated reservoir appears only to exist in the northernmost portion of the resource. Contours and lithologic contacts are approximate and are probably somewhat irregular. The deepest roots of the resource are well defined in some areas and a bit speculative in several other reaches. Lithology and hydraulic paramaters are modified in part after Thomas(1981).

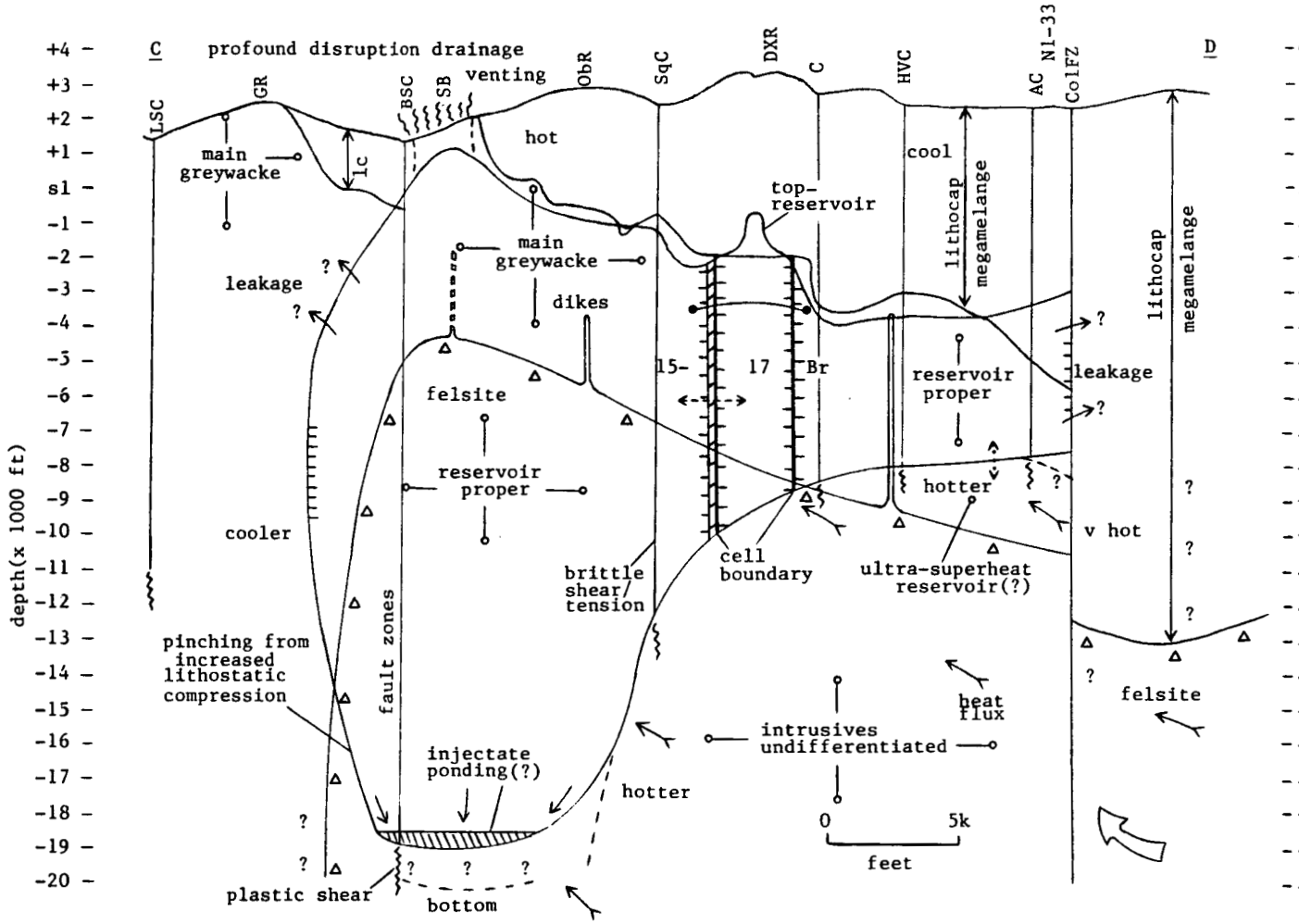

Figure 2. Cross-section C-D. Felsic magma has stoped to its shallowest levels along the highly disruptive Big Sulphur Creek Fault zone. Production-induced seismicity infers great reservoir depth(±21,000 feet) in the Geysers sector. The reservoir probably pinches off at depth, where rocks become more plastic from increased lithostatic compression. Evidence points toward two stacked reservoirs in the Bottlerock area. The Collayomi Fault forms the ultimate eastern reservoir proper boundary. Vertical fault zones beneath major drainage probably penetrate to appreciable crustal depths. Certain reservoir cells could form smaller isolated enclaves within what is a larger area dominated by the hydraulic continuity of a separate reservoir cell(s). Minor cross-flow may occur between separate reservoir cells and/or enclaves. Complete definition of all the steamfield's cells is not entirely aquirable. Lithology and hydraulic parameters are modified in part after Thomas(1981).

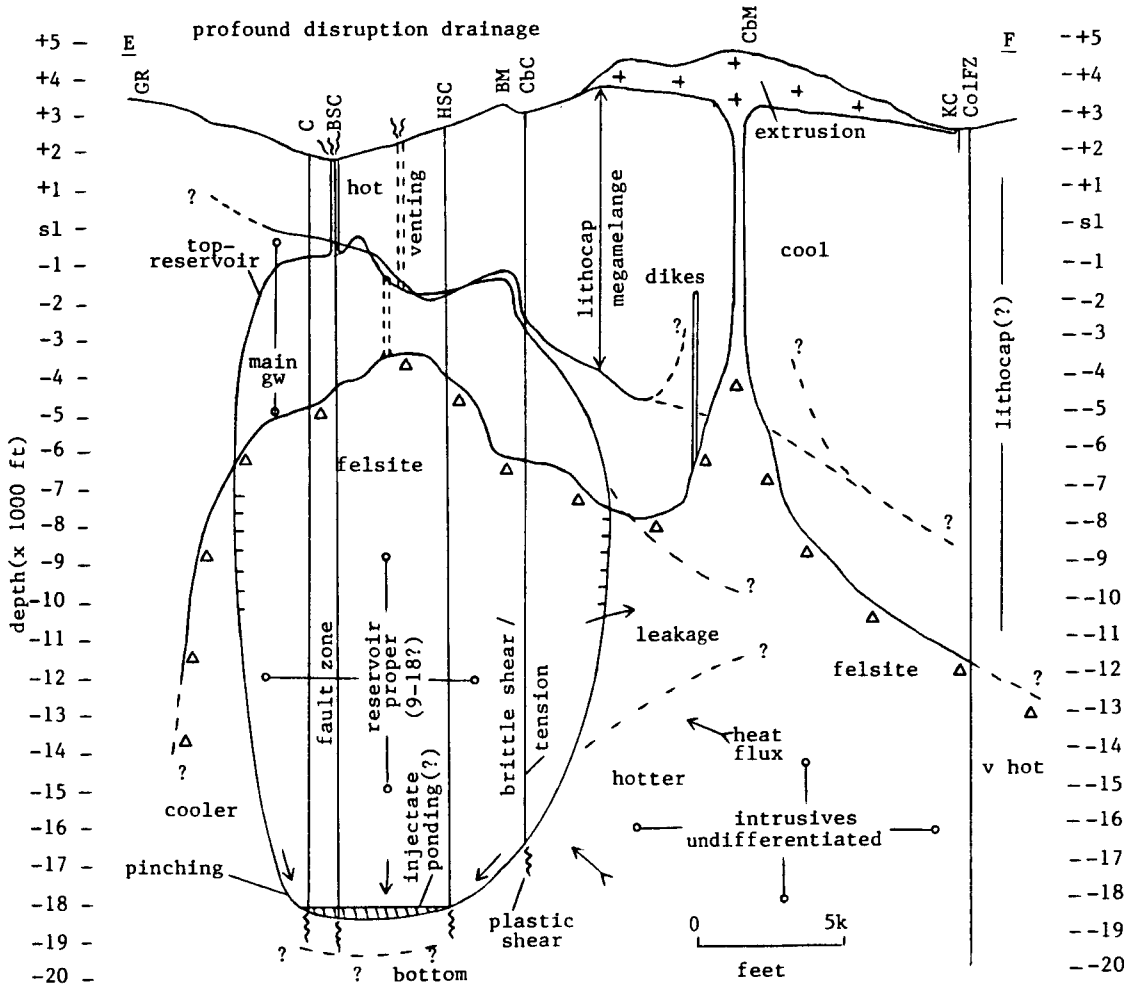

Figure 3. Cross-section E-F. Here, Felsic intrusive basement assumes much larger portions of the reservoir volume. Surface reservoir venting occurs along enhanced disruption features. The less brittle lithocap becomes very thick under Cobb Mountain(and probably east of the Collayomi Fault: Clear Lake Volcanic Field), allowing for the igneous injection and extrusion of volcanics along selective fault planes of weakness(entire volcanic field). With shallower main metagraywacke occurence, felsic magmas stoped higher into the crust with minimal diking and virtually no surface extrusion. Felsic stock formation was probably favored over voluminous extrusion and caldera formation(batholitic doming) due to highly fractured metagraywacke being easily assimilated which allowed gentle continuous stoping to occur over long time frames. This tectonic/intrusive regime is analogous to the shear-rhombochasmic/plutonic complex at Tongonan, Philippines(and other nearby areas), which has experienced a similar long history of intrusive/hydrothermal events. Deep unknown extentions of the reservoir could exist in intrusive rocks.

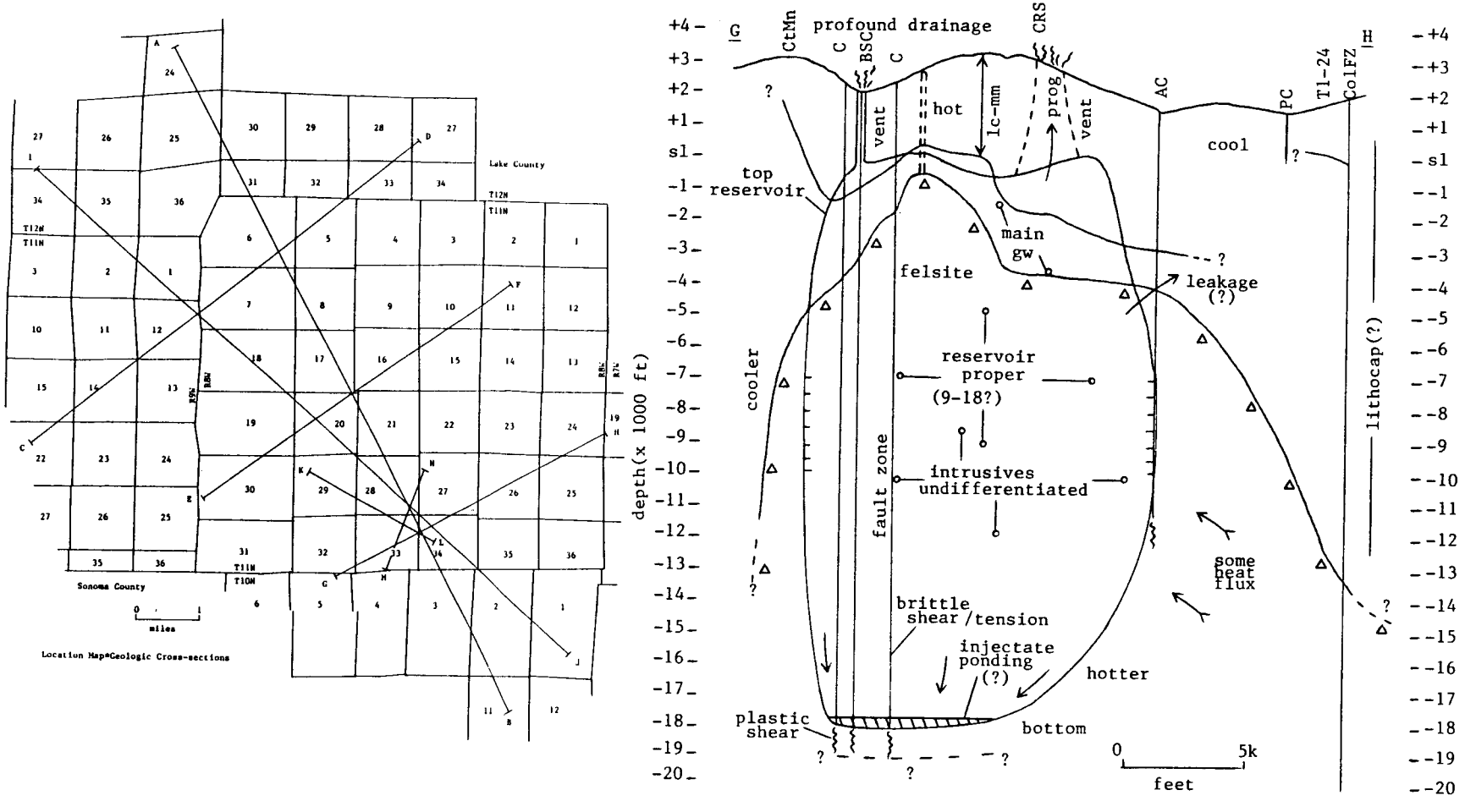

Figure 4. Cross-section G-H. The reservoir proper and felsite line can drop off sharply as the resource flanks are approached. The felsite dives deeply under the suspected lithocap near and beyond the Collayomi Fault zone. Selective structural disruption facets may offer conduits for the reservoir to vertically rise upward through the metasomatized lithocap and to the surface. Here, such an area appears analogous to the normal shallow trend usually found along the Big Sulphur Creek shear zone. The reservoir bottom may penetrate to nearly the same depths as that in the Big Geysers area. The known reservoir does not extend all the way to the Collayomi Fault zone, as is the case in the Bottlerock area. Localized tectonic deviations may leave certain certain crustal blocks relatively unfractured, even though long-ancestral hydrothermal activity may have existed. Lithology and hydraulic parameters are modifided in part after Thomas(1981).

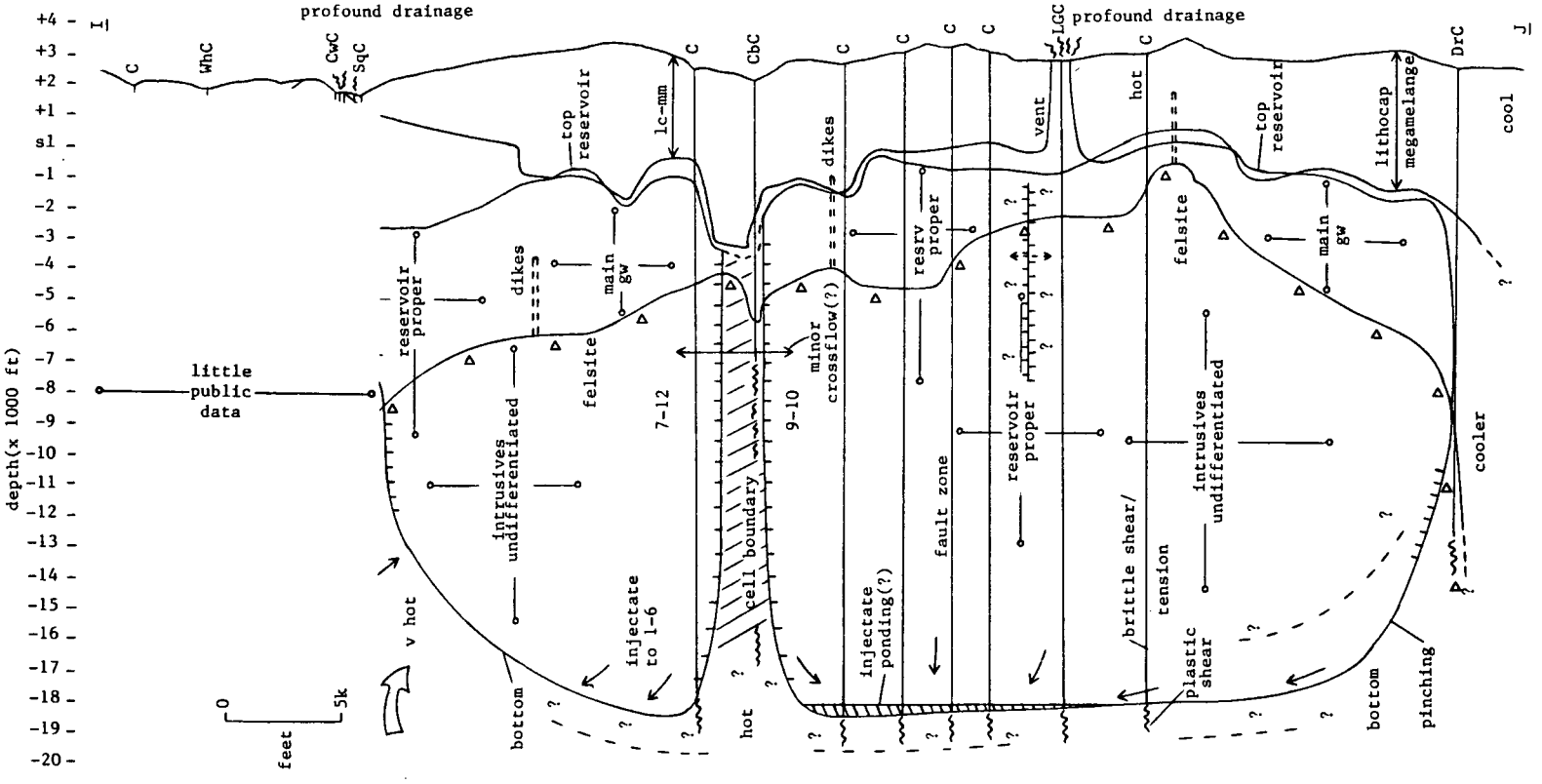

Figure 5. Cross-section I-J. The felsite represents a huge, deep to shallow plutonic complex of wide timeframes and lithologic compositions. Reservoir cell boundaries are probably the result of differing tectonic stresses/strains and lithologic changes in somewhat localized linear trends, perhaps major cross-fault controlled. The lowest portions of the reservoir(s) may act as catch basins for all the injectate that escapes initial reflash and percolates down to the reservoir base. An abrupt drop in the felsite line could equate with an abrupt appearence of the ultra-superheated reservoir. The felsic intrusive plutonic basement comprises a large portion of the reservoir in the core trend of the steamfield. Through long periods of time, the specific positioning of favorable parts of a brittle metamorphic complex, enhanced regional and localized tectonic faulting and jointing, and numerous phases of igneous intrusive injection has allowed a prolific hydrothermal system(s) to perpetuate in the past and present. Lacking some of the aforementioned requirements, the remainder of the Clear Lake Volcanic/Hydrothermal Field probably exists as a very deep lithocap(no main metagraywacke?) underlain by igneous intrusives, with hydrothermal flow restricted to selectively random faults with classic liquid-domination properties. Besides favorable tectonics, a massive easily and highly fractured reservoir rock must exist in order for a huge hydrothermal system to propogate. Both the main metagraywacke and the felsic intrusive basement along with specific tectonics offered an appropriate setting for the developement of such a large and uniquely evolved hydrothermal system. Lithology and hydraulic parameters are modified in part after Thomas(1981)

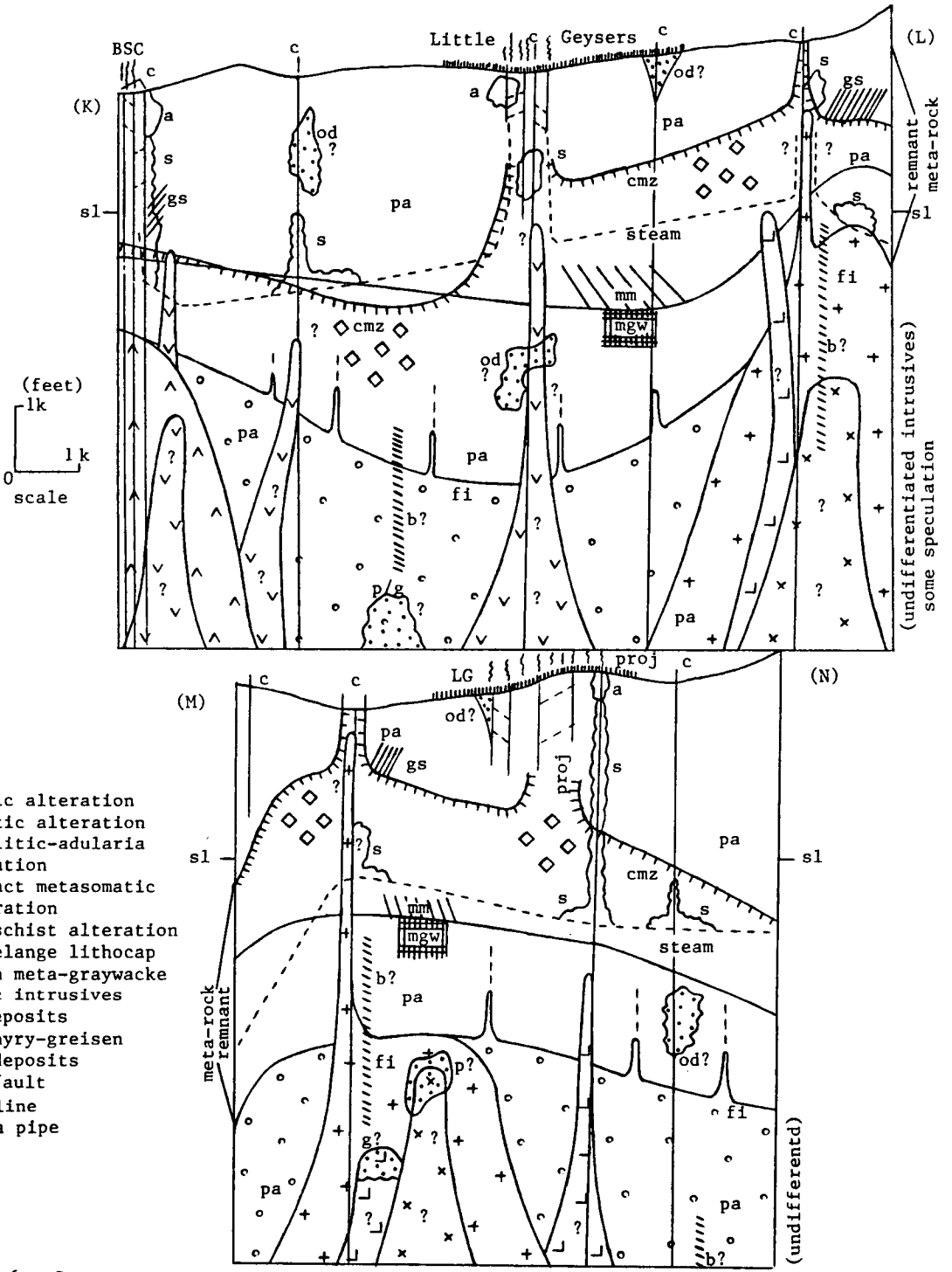

Figure 6. Cross-sections K-L and M-N. Petrologically, the most intensely metasomatized area of the steamfield/intrusive complex. Some alteration and deposition zones will trend outward into the third dimension. Numerous intrusive phases penetrate the ancient metamorphic complex, stoping higher into the highly fractured brittle meta-graywacke base. Other intrusive phases probably underlie the drilled limits of the basement igneous complex. In the steamfield core trend, the reservoir will penetrate deep into the felsic basement, untill brittle shear yields to plastic shear(depth still unknown). This area has witnessed many concurrent and/or successive hydrothermal fluxes over the last 2.5 million years of thermal history. Thermal fluxes will undoubtedly propogate into the future for quite some time to come. Contacts and contours are generalized, probably being a bit irregular in actuality.

PROCEEDINGS, Eleventh Workshop on Geothermal Reservoir Engineering
Stanford University, Stanford, California, January 21-23, 1986
SGP-TR-93

SIGNIFICANT SILICA SOLUBILITY IN GEOTHERMAL STEAM

Russell James

D.S.I.R., Wairakei,
New Zealand

ABSTRACT

Although it is widely believed that silica solubility in low pressure (5 to 10 bar) geothermal steam is negligible, when one takes into account steam flows exceeding 10 million tonnes a year - at Wairakei, for instance - it is found that the amount transmitted in the vapour has the potential to give significant deposits on turbine nozzles and blades.

A 150 MWe power station, when based on flows from a hot water reservoir at (a) 250 C or (b) 315 C, and with separator pressures of 6 bar, is found to carry about 100 and 200 kg/year respectively in the steam phase. In the case of a similar sized station exploiting a dry steam reservoir such as The Geysers, equivalent silica flows are obtained, dissolved in steam and carried as dust - the latter as solid particles precipitating from the vapour en route from source to turbine, and not pre-existing in the formations as is commonly considered. Choking or coating of subterranean rock near such dry steam wells due to exsolving silica, may be the principal cause of declining steam discharge under production.

Silica from completely dry or superheated steam can also seal the cap and sides of steam reservoirs when expanding below the criticus temperature (236°C) in a way previously thought possible only by hot water or wet steam.

INTRODUCTION

The concentration of silica in subterranean hot water reservoirs is proportional to temperature; figures presented by Fournier (1973), Ellis and Mahon (1977), show that a value of 484 ppm would be associated with reservoir water at 250°C. When discharged at constant enthalpy from wellheads into separators at 6 bar pressure, the concentration increases to 604 ppm due to the generation of steam. To determine the small concentration of silica dissolved in this steam, Figure 1 is shown plotted from data presented by Coulter et al. (1956) for concentration ratios versus density ratios in steam and water. A fairly straight line can be drawn through the points for the usual near-neutral hot water of pH 6 to 8, and this enables the following equation to fit the data:

$$\frac{\text{Silica concentration in water}}{\text{Silica concentration in steam}} = \left(\frac{V_g}{V_f}\right)^2 \qquad (1)$$

where V_g and V_f are the specific volumes of steam and water respectively, which at 6 bar are 315.7 and 1.1006 litres/kg. At the separator pressure of 6 bar,

$$\frac{604}{\text{Silica concentration in steam}} = \left(\frac{315.7}{1.1006}\right)^2$$

Hence, silica concentration in steam = 0.00835 ppm

If the wellhead separators were 100% efficient - which is apparently the aim of some manufacturers - there would be no carryover water at 604 ppm escaping into the overland steam transmission pipelines and therefore the only silica passing towards the power house would be the amount dissolved in the steam phase with the very low concentration given above. The steam power rate for turbines operating between 4.5 bar entrance pressure and 150 millibar condenser pressure is about 9.5 tonne/MWh, James and Meidav (1977), and so the required steam flow for a 150 MWe project is:-

$150\ (9.5)\ 8760 = 1.25\ (10)^7$ tonne/year

Hence silica transported in steam =

$$\frac{0.008335}{(10)^6}\ 1.25\ (10)^7$$

= 0.0917 tonne silica in steam/year
= 91.7 kg silica in steam/year

For a higher temperature reservoir water at 315 C, the silica concentration would also be higher at 798 ppm compared with 484 ppm for the 250°C reservoir. The concentration in separated water at 6 bar would be 1255 ppm and in the separated steam would now attain 0.01526 ppm which gives an amount of silica transmitted in steam lines for a 150 MWe project as 190.5 kg/year compared with 91.7 kg/year for the 250°C reservoir.

It is clear that, although the higher temperature reservoir is more attractive from a power potential viewpoint James (1986), it has some retrograde features with regard to

possible silica deposition in both separated water lines for reinjection, and in steam transmission lines. Silica concentrations at these locations is now more than twice that of the comparable 250°C reservoir.

Silica deposition from reinjection water can take place within the overland water transmission pipelines, the reinjection wells and also in the interstices of the reservoir rocks. Much research is continuing in many countries into inhibiting such a deposition technically and economically but, up to the present, no technique has succeeded in both. Raising the pressure of separation has its advocates but lowers the efficiency of exploitation, increases costs and reduces the life of the field, hence is unacceptable if a more attractive alternative can be developed.

CYCLONE SEPARATOR EFFICIENCY

Since the tests of Bangma (1961) observations at Wairakei show that some water escapes into the steam line of an amount equal to about 0.03% of the steam flow and that this carry-over water is in the form of a fine spray or mist with droplets averaging about 1 micrometre in diameter. Such fine drops are virtually impervious to the centrifugal action of the separator under normal running conditions and are captives of the viscous inertia of the steam. If the steam pipe connecting the separators to the power house is short, a mist extractor with fresh water reflux (spray) removes this water prior to the turbines, as at Hatchobaru, Japan. For long pipelines as at Wairakei, heat loss causes growth of the drops while turbulence and differential velocity brings them to coalesce on the moist pipe wall (the 'fly-paper' effect) followed by drainage to the bottom of the pipeline. Extraction pots situated at intervals of about 100 m remove this mixture of carry-over and condensate so that the silica carried is reduced by 3 to 5 orders of magnitude, with correct design, James (1975).

For both short or long steam pipelines, silica dissolved in steam will not penetrate far down the line as carryover mist from separators would scrub it almost entirely from the steam. Calculations indicate that, for the flows considered, water droplets of 1 micrometre diameter would be spaced a mere 100 micrometres apart in the carryover mist entering the steam pipeline. This degree of intimacy is much greater than that afforded by the wet pipe wall and effective due to heat radiation causing growth in droplet size (see Appendix 1).

In fact, if it was not for the 'inefficiency' of cyclone separators, geothermal projects would probably have many problems with silica in steam exsolving within the nozzles and first blades of turbines. A senario to guarantee this condition would involve a separator of 100% efficiency followed by an insulated pipeline whose pressure-drop is designed to avoid condensate developing. In this case, silica would be kept dissolved in the steam until the highly localised temperature drop in the turbine nozzles made exsolving inevitable. Metastable flow in such nozzles means that the expanding (and cooling) dry saturated steam does not get wet until almost through the so-called Wilson zone (see Appendix 2). For an entrance steam pressure of 4.5 bar, the nozzle steam falls in temperature by 20°C before becoming wet at about 2.5 bar; after this point increasing wetness keeps blades free from deposition.

PROPORTION OF SILICA IN STEAM

Under normal operating conditions similar to Wairakei, for a reservoir at 250°C and a project of 150 MWe, the mass of water escaping into steam lines is about 0.03% and steam flow is $1.25\ (10)^{10}$ kg/year; hence the mass of water entering the steam

$$= \frac{0.03}{100}\ 1.25\ (10)^{10} = 3.75\ (10)^{6}\ \text{kg/year}$$

Silica content of this water is 604 ppm, so the mass of silica transported in water =

$$\frac{604}{(10)^{6}}\ 3.75\ (10)^{6}\ \text{kg/year} = 2265\ \text{kg/year}$$

$$\frac{\text{Silica in Steam}}{\text{Silica in Water}}\ \% = \frac{91.7}{2265}\ (100) = 4.05\%$$

This result is, of course, independent of the size of project and is indeed also independent of the reservoir temperature due to proportional factors cancelling, so we may take it that for 0.03% water carryover and 6 bar separator pressure, the mass of silica dissolved in the steam line is only about 4% of that carried in water entering the line. This explains why work has concentrated on removing water while considering silica in steam as negligible.

WORST CASE FOR DEPOSITION

If a 'normal' Wairakei-style cyclone separator is followed by a well insulated pipeline but with a pressure-drop designed to keep the flowing steam completely dry or even slightly superheated, then the mist of carryover water will completely dry out to be replaced by a host of minute, probably sticky, mineral particles. These particles, together with the silica dissolved in the steam, will not only give trouble at the turbine, but no doubt will adhere to the pipe walls especially nearer the power station. Under such a design, it may be unattractive to rectify the condition by decreasing pressure-drop as this would reduce flow and megawatts. The economic solution requires spraying scrubbing water into the

line, followed by a separator prior to the turbine entrance. In this context, the balance between pipeline heat loss through insulation, and frictional pressure-drop of the flowing steam, is important enough to be the subject of another study, James (1986). Attempts at Wairakei to increase steam flow beyond design recommendations have resulted in just such deposition on the pipe wall and presumably in the turbines, and the practice has been discontinued, Keith Wilson (pers. comm.).

CONDENSATE CORROSION IN STEAM LINES

Effective extraction of carryover water has its drawbacks, however, as mineral-free condensate has corroded some of the long Wairakei steam pipelines, James (1980). To retard such corrosion to acceptable levels, it has been found necessary to retain a few ppm of silica in water, especially near the end of pipelines, where extraction pots finally remove this residual amount before steam enters turbines.

Earlier on, it was anticipated that difficulties would be met in attempts to transmit steam-water mixtures to power stations, and also in piping saturated hot water for reinjection purposes while dry saturated steam should present relatively few problems. In practice, it has been found that the first two proved fairly easy to handle, James et al (1970), James (1979), whereas steam alone has continued to produce some surprising and inconvenient phenomena.

ORIGIN OF GEYSER DUST

The steam discharged from boreholes at The Geysers field, California, is believed to originate from water in the reservoir at about 236°C, James (1968), Truesdell and White (1973); such steam, after disengaging from the subterranean liquid, travels through reservoir rock to the well feed horizon before rising to the wellhead and being piped overland to turbines of the power house.

Taking a typical well, Budd (1973), as 0.254 m internal diameter (average for a telescopic profile), depth 1.5 km and flow 75 tonnes/hr at a wellhead pressure of 9 bar, the bottom-hole pressure is calculated as 19 bar taking into account frictional pressure-drop and hydrostatic head of the steam column. Overland piping of this steam to a turbine entry pressure of 8 bar is assumed.

According to Budd (1973) the steam carries a continuous mass of dust requiring wellhead separators which remove 99% of the particles; dirt-legs are also placed at selected points in the overland pipeline to be discharged occasionally.

Silica dissolved in reservoir steam can be calculated as previously from the concentration in water which, for a temperature of 236°C, comes to about 419 ppm.
From Equation 1, for 236°C and saturated steam

$$\frac{419}{\text{silica concentration in steam}} = \left(\frac{64.2}{1.2208}\right)^2$$

Silica concentration in steam = 0.15 ppm

This is close to the value of 0.2 ppm given on Figure 2 from Sohre (pers. comm.) which is preferred here as the steam solubility can be followed along the path of declining pressure with flow, from reservoir to turbine. There is no significant difference between the solubility of silica in steam whether expanding along the dry saturated line of Figure 2 or whether at a constant temperature of 236°C, hence values close to the saturated line will be taken. We shall assume a superheat of 5°C at the wellhead pressure of 9 bar which, from Figure 2, gives a solubility of 0.011 ppm. Hence the mass of silica exsolving en route from its origin at 236°C for the well described above is:-

$$\frac{75\,000\ (8760)\ (0.2 - 0.011)}{10^6} = 124.2 \text{ kg/year}$$

For equilibrium solubility to prevail, this amount must precipitate as solid particles (the so-called Geyser dust) and as previously stated 99% of this is removed by the wellhead separators, leaving 1.24 kg/y entering the overland pipeline. This quantity is supplemented by a further amount which exsolves as solubility declines to 0.009 at the end of the pipeline near the turbine entrance, and which equals:-

$$\frac{75\,000\ \ (8760)\ \ (0.011 - 0.009)}{10^6} = 1.31 \text{ kg/y}$$

The amount of silica still dissolved in steam at the turbine entrance is:-

$$\frac{75\,000\ \ (8760)\ \ (0.009)}{10^6} = 5.91 \text{ kg/y}$$

The total of these three quantities
= 8.46 kg/y
This applies to one well, the power potential steam rate from which = 8.62 kg/kWh, James and Meidav (1977), for steam expanding through a turbine from 8 bar to 150 millibar condenser pressure.
Hence gross power potential of one well =

$$\frac{75\,000}{8.62\ (1000)} = 8.7 \text{ MWe}$$

Silica transported in overland pipelines for a 150 MWe scheme =

$\frac{150}{8.7}$ (8.46) = 146 kg/year which is intermediate between the amounts transported for

hot water fields at reservoir temperatures of 250°C and 315°C.

DEPOSITION WITHIN THE TURBINE NOZZLE

For a single well, the amount of solid particles reaching the turbine is 1.24 + 1.31 ≃ 2.55 kg/y while the quantity still dissolved in steam is 5.91 kg/y. If we presume that only the rapid cooling of steam when expanding in nozzles and first blades can create conditions in which silica exsolves and forms an impermeable and tenacious coating, then only the latter figure will be considered. The solid particles are more likely to pass through the turbine intact and dispersed in the wet region, to add to the sludge in the base of cooling towers.

Steam at 8 bar and 5°C of superheat when expanding at high speed through a nozzle, does not have sufficient time to get wet until it attains the Wilson line (theoretical wetness of 2%) which, for this initial condition, is about 4.5 bar pressure at which point the silica solubility has fallen to 0.0025 ppm from Figure 2. Hence, silica amount depositing in nozzle =

$$\frac{75\,000\ (8760)\ (0.009 - 0.0025)}{10^6} = 4.27 \text{ kg/y}$$

Although the time for steam to pass through the nozzle is too short (less than a millisecond) for the thermodynamic equilibrium of water substance to occur - hence the delayed wetting of the steam - it is assumed that the chemical kinetics of silica deposition is fast enough to form the hard glass-like layer of silica which has been found in turbines at The Geysers and at the Kamojang dry steam field (Indonesia). The mass of silica coating nozzles and first blades for a 150 MWe scheme is therefore:-

$$\frac{150}{8.7}\ (4.27) = 73.6 \text{ kg/y}$$

As has been pointed out*, the maximum acceptable deposition is about 7.5 kg/y for a 150 MWe installation, hence the above amount is one order of magnitude high.

Such deposits can lead to unbalance vibration and can also concentrate corrosives - althouth not necessarily corrosive themselves - and unless removed or avoided, can lead to blade failure. This has happened at The Geysers, but the problem has now been solved with water spray injection near the end of the pipeline followed by a terminal separator, J. Farison (pers. comm.).

A patented wet scrubber has also been successfully used at the Dieng field, Indonesia, G. Shulman (pers. comm.), to remove dissolved minerals from the carryover mist escaping into the very short steam line connecting a water separator to an atmospheric exhaust turbine, after scaling was found on nozzle and blades.

Although the transportation of silica is fundamentally different for these two cases - being dissolved in steam in one, and in water droplets in the other, it is encouraging to find that the same solution for cleaning the steam, is effective for both.

For the long steam pipelines of hot water fields similar to Wairakei, however, extraction pots are an efficient and economical technique in eliminating transported minerals. A casual observer at Wairakei might however be disconcerted to find spray injection into some steam lines taking place, but as has been mentioned, this mineralized water injection is to replace silica and inhibit corrosion caused by the virtually complete removal of this mineral from the reactive and slightly acidic condensate formed en route.

DEPOSITION IN RESERVOIR RESTRICTING STEAM FLOW?

A considerable proportion of the solid particles calculated as being trapped by the wellhead separator of a typical Geyser borehole may, in fact, not reach the well at all having been retained in the surrounding rock of the feed zone. For dry saturated steam leaving water at 236°C with a silica concentration of 0.2 ppm and arriving at the well bottom pressure of 19 bar at constant enthalpy, a temperature of 212°C is obtained (2°C of superheat) with a silica concentration of 0.06 ppm. The amount of silica exsolved from source to well bottom is:-

$$\frac{75\,000\ \ (8760)\ \ (0.2 - 0.06)}{10^6} = 92 \text{ kg/y}$$

If this quantity is retained in the underground formation either as dust or as scale, it may of course be an explanation of the decline in well discharge of about 50% in 5 years observed by Budd (1973). Rock heat may initially buffer the steam temperature at the well bottom to higher than the equilibrium value of 212°C but even if it was held at 236°C this would only increase the silica content from 0.06 to 0.065 ppm giving 89 kg/y instead of 92 kg/y - an insignificant difference.

SILICA IN STEAM SEALS THE CAPROCK

Dry saturated steam at a temperature higher than 236°C becomes wet on expanding through porous-permeable rock at constant enthalpy; if this takes place within a geothermal reservoir with an expansion upwards towards

* *James (1975) suggested a maximum deposition rate of 0.5 lb/y for a 5 MWe turbine.*

the ground surface, then the water formed will drain downwards dissolving silica and thereby increasing the rock permeability, James (1984). However, continued expansion upwards at temperatures below 236°C results in the steam becoming not only completely dry but with progressively increasing superheat at lower pressures and temperatures. Its solubility for silica is also progressively reduced as indicated in Figure 2. Hence the small amount of silica dissolved in this steam at 236°C will have to decline still further as the steam rises in the reservoir. The amount of exsolved mineral which is necessary to sustain equilibrium solubility will therefore coat or choke the interstices or fissures of the media above the level at which the temperature of 236°C exists, known here as the 'criticus'* temperature. It follows from this that there exists a strong tendency for increasing permeability below the criticus temperature and reducing permeability above it, hence sharply delineating the reservoir as a discrete entity with depth. Expanding towards the reservoir periphery should, similarly, result in sealing of the boundary walls although the integrity of such sealing may be suspect in tectonic regions.

* *"Critical" is an over-worked word as it is also used for the steam temperature (374.14°) above which pressure alone will not cause condensation; it is also employed as the flow condition at which sonic velocity occurs, James (1962), and at lesser velocities as the boundary between viscous and turbulent Reynolds' number, Streeter (1966), therefore its extended use here can only result in ambiguity. Hence, because of the importance of the temperature at which dry saturated steam has a maximum enthalpy (234 to 238°C, depending which steam tables are used) for an understanding of steam reservoirs, it would appear appropriate to employ another term which has inherent the concept of criticality. And just as the critical temperature can be altered by the presence of dissolved chemicals or gases, so also can the criticus temperature, James (1968), Sestini (1970), White et al. (1971), Tuesdell and White (1973), consequently it is not a term of immutable value divorced from the chemistry of associated fluids, liquid and vapour).*

CONCLUSIONS

Silica dissolved in steam creates problems in pipes and plant of geothermal schemes which exploit both dry steam and hot water reservoirs where similar amounts are transported from wellhead to turbine for the same power generated. Because it is highly disposed to enter any water present, it can be successfully eliminated by water extraction devices on long pipelines, or if the steam is completely dry (or superheated) by injecting spray water first.

Sealing of steam reservoirs can be caused by silica leached from rocks by steam which first becomes wet when flowing at constant enthalpy, followed by drying-out of the condensate formed, James (1984). But it is shown here that even completely dry steam (below the criticus temperature of 234 to 238°C) which expands through rock at ever increasing superheat with constant enthalpy can also seal the reservoir boundaries - top and sides - with silica. The precipitation of solid silica particles from such steam within The Geysers reservoir, wells and overland pipelines is probably the genesis of the so-called Geyser dust which is a contaminant of the discharge and thought to exist in the subterranean formations of the reservoir. It is hard to believe, however, that steam drag forces would not have swiftly cleared the formation of such small particles existing close to the well. For those further off, the formation itself should retain them more efficiently than the wellhead separators, as steam velocities fall-off rapidly with distance. If the viewpoint presented here is correct, however, a continuous stream of particles is to be expected.

REFERENCES

Bangma, P. (1961): The Development and Performance of a Steam-Water Separator for use on Geothermal Bores. Proc. U.N. Conf. New Sources of Energy, Vol. 3 Geo. Energy 2.

Budd, C.F. Jr. (1973): Steam Production at The Geysers Geothermal Field. In Geothermal Energy, P. Kruger and C. Otte, Eds., Stanford Univ. Press, Stanford, Calif., p. 129.

Coulter, E.E., Pirsh, E.A. and Wagner, E.J. (1956): Selective Silica Carryover in Steam. ASME, Trans, May 1956, p. 869-873.

Ellis, A.J. and Mahon, W.A.J. (1977): Chemistry and Geothermal Systems. Academic Press, New York, U.S.A.

Fournier, R.O., (1973): In Proc. Symp. Hydrogeochem. Biogeochem. 1, 122-139, Clarke Co., Washington, D.C., U.S.A.

James, R., (1962): Steam-Water Critical Flow through Pipes. Proc. I. Mech. E. 176, 26, p 741.

James, R., (1968): Wairakei and Larderello; Geothermal Power Systems Compared. N.Z.J. Sc., 11, 4, 706.

James, R., McDowell, G.D., and Allen, M.D. (1970): Flow of Steam-Water Mixtures through a 12-inch Diameter Pipeline; Test results. Geothermics, v. 2, pt 2, p. 1581.
James, R., (1975): Control Orifices Replace Steam Traps on Overland Transmission Pipelines. Proc. 2nd U.N. Symp. Develop. and Use of Geothermal Resources, San Francisco, U.S.A.
James, R., and Meidav, T., (1977): Thermal Efficiency of Geothermal Power. Geo. Energy, 5, 4, 8.
James, R., (1980a): Suppression of Steam Condensate Corrosion at Wairakei Geothermal Project, Geothermal Energy, 8, 3, 11.
James, R., (1980b): Transmission of Pressurized Hot Water at the Boiling Point. Proc. N.Z. Geothermal Workshop, Univ. of Auckland, Part 1 p. 166.
James, R., (1984): Geothermal Steam Flow through Porous-Permeable Rock. Proc. CSIRO/DSIR Seminar on Convective Flows in Porous Media, DSIR, Wellington, New Zealand.
James, R. (1986a): Power Potential of Geothermal Wells Related to Reservoir Temperature. Proc. 12th Workshop Geothermal Reservoir Engineering, Stanford Univ., Stanford, Calif., U.S.A.
James, R., (1986b): Heat Loss and Pressure-Drop Balance for Steam Transmission, Geothermal Energy Mag. (in press).
Sestini, G., (1970): Superheating of Geothermal Steam. Geothermics Special Issue 2, v. 2, pt 1, p. 622.
Streeter, V.L., (1966): Fluid Mechanics. McGraw-Hill, New York, U.S.A.
Truesdell, A.H. and White, D.E., (1973): Production of Superheated Steam from Vapor-Dominated Reservoirs. Geothermics, 2, 3-4, 154.
White, D.E., Muffler, L.J.P., and Truesdell, A.H., (1971): Vapor-Dominated Hydrothermal Systems compared with Hot-Water Systems. Econ. Geol. 66, 1, 75.

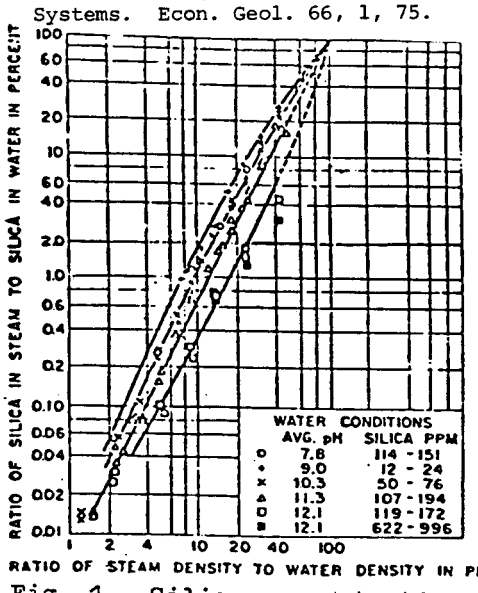

Fig. 1. Silica concentration ratio

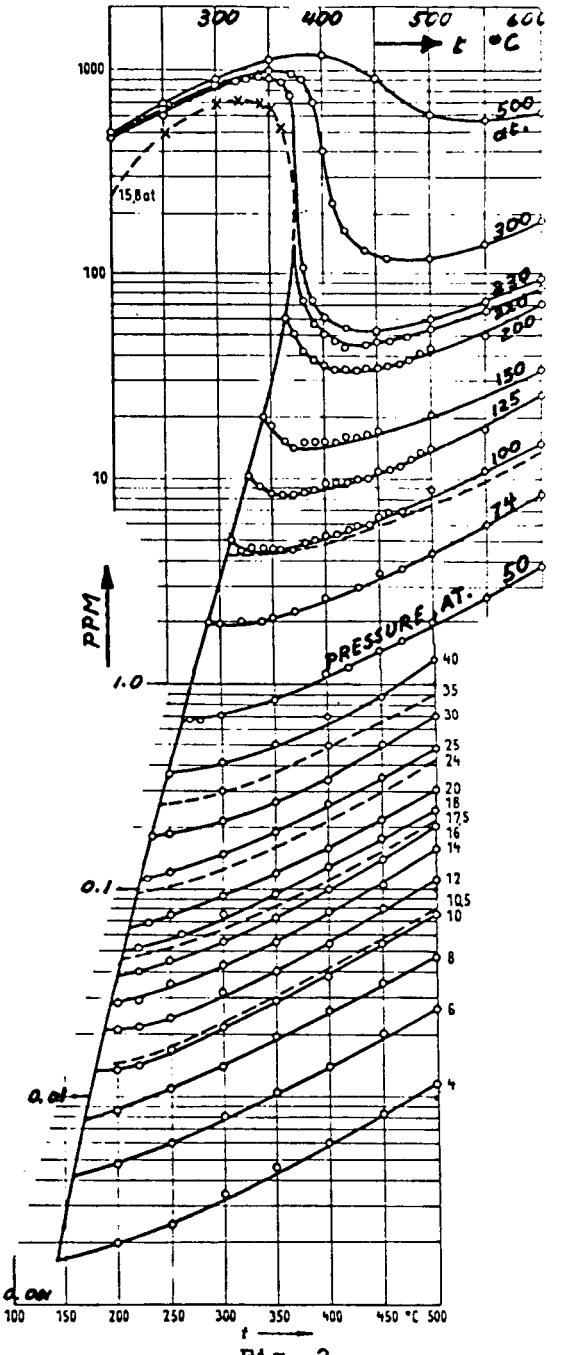

Fig. 2
Solubility of Silica (SiO_2) in Steam as Function of Pressure and Temperature, Parts per Million (1 at. = 14.22 psi; Temperatures are °C).

APPENDIX 1

SCRUBBING OF SILICA FROM STEAM

On a first examination, it might seem impossible that a mist of brine droplets which escape into the steam pipeline would be successful in removing silica dissolved in the accompanying steam, as the two phases have already coexisted in equilibrium within the swirling confines of the separator vessel, and are now moving along a pipeline at roughly the same pressure.

The reason is that the mass of liquid droplets now constitute only about 0.03% of the steam mass and this is also approximately equal to the amount of pure condensate which forms over 100 m length of a short geothermal steam pipeline, James (1986b). Heat loss from these droplets by heat radiation to the cooler pipe wall results in their becoming nucleation sites for condensation from the steam matrix. This leads to growing droplets consisting of a brine core surrounded by a pure condensate layer into which can dissolve silica from the vapour phase. Hence from the steam viewpoint, the droplets would be 'seen' as pure water since it is unlikely that diffusion of brine minerals into the condensing layer would exceed the rate at which the layer thickens. Therefore it appears probable that even for a short pipeline, brine droplets would scrub most of the silica from the steam into the liquid phase, (as has been pointed out, subsequent dry-out of these drops can occur within the highly localised pressure decline of turbine nozzles and blades, leading to mineral scaling). It is known that this phenomenon (of droplet growth) takes place on long pipelines as the minute brine droplets which initially are impervious to gravity and centrifugal forces (at bends) attain a size which eventually renders them sensitive to these effects so that they settle-out and coalesce on the pipe wall. Glass viewing ports in a 0.762 m diameter steam line at Wairakei have been used to examine the pipe flows at night employing artificial lighting. The steam is lucid with occasional patches of mist and a small stream of condensate runs along the bottom of the pipe.

APPENDIX 2

DELAYED WETTING OF TURBINE NOZZLES AND BLADES

If dry saturated steam expands through a convergent nozzle from 4.5 bar to 2.5 bar most of the steam follows an isentropic path so that the final wetness theoretically is 3.5% and the temperature has fallen by 20°C. The wetness has increased progressively from the dry entry condition and should arrest any tendency to deposition taking place on the wall of the nozzle. However, close to the wall is a layer of fluid which is moving very slowly (the so-called laminar sub-layer) within which streamline or viscous conditions prevail. The pressure in this layer declines in harmony with that of the steam mass expanding in the central region of the nozzle but due to the negligible velocity change within the layer, its expansion is isenthalpic with a decline in temperature theoretically of 8°C from 4.5 bar to 2.5 bar. Hence, at the lower pressure, instead of being 3.5% wet as for the greater mass of steam, it is not only dry but has a superheat of 12.0°C or at least it would have if considered as a separate and discrete entity free from turbulent mixing with the central steam. Between the laminar sub-layer and the high speed steam flux, is a turbulent region with velocities up to about 100 m/s within which mainly isenthalpic expansion still pertains and which tends to buffer the wall micro-climate against change. The high acceleration of central steam up to the speed of sound (~500 m/s) over a nozzle length of a few centimetres, would cause rapid thinning of the laminar sub-layer, turbulence within it and finally wall wetting. This may be the explanation of the phenomenon of delayed wetting of steam down to the theoretical 3.5% wetness; in other words, the steam becomes truly wet throughout its core but remains dry on the nozzle wall until a location is reached downstream at which moisture penetrates to the surface.

Hence, it appears likely that silica from dry steam will adhere to the nozzle wall until downstream a point is reached at which the presence of water makes this impossible.

PROCEEDINGS, Eleventh Workshop on Geothermal Reservoir Engineering
Stanford University, Stanford, California, January 21-23, 1986
SGP-TR-93

POWER POTENTIAL OF GEOTHERMAL WELLS RELATED TO RESERVOIR TEMPERATURE

Russell James

D.S.I.R., Wairakei, New Zealand

ABSTRACT

For equal flows of hot water wells, the electric power which can be generated increases with feed water temperature. However, high temperature wells discharge greater flows than that of lower temperature wells of similar permeability, with the result of enhanced power potential.

In fact, where fluids are exploited utilising two-stage flash, these factors combine to give a power potential which is proportional to the cube of the feed water temperature in degrees celcius. Hence a feed of 315°C would generate twice the power of that of water at 250°C for wells of good permeability and where the reservoir exists under conditions of boiling point with depth.

Higher temperature water (exceeding 300°C) has, however, a commensurate higher tendency to mineral deposition in reinjection water lines and this disposes design to single-stage flash with slightly reduced power, compared with the two-stage alternative.

INTRODUCTION

After the discovery and exploitation of the Larderello field in Italy, drillers have sought reservoirs which produce dry or super-heated steam and have had successes with The Geysers (U.S.A.), Kamojang (Indonesia), Matsukawa (Japan) and others. Most reservoirs penetrated, however, have proved to contain hot water at or near the boiling point for depth and many have been developed since the building of the Wairakei station. Early theory, James (1966), urged shallow drilling (order of 350 m) into hot water reservoirs, so as to exploit the 'top of the boiler' and tap the thin layer of steam believed to exist there. By this means a steadily increasing volume of vapour should spread over the top reaches of the reservoir supplied by the underlying water which boils and draws heat from the rock matrix. The efficiency of such an approach was calculated as far higher than the alternative of simply discharging boiling water as the latter would have less than half the power-life of the former which more effectively utilizes the rock heat. To judge by the power generated at Larderello and The Geysers, this may be so, especially as it is believed that such dry steam reservoirs are indeed under-pinned by large volumes of water either beneath the steam zone, James (1968) or co-mingling with it, Truesdell and White (1973). In the initial development of a hot water field, a putative steam zone may be of small thickness or possibly non-existent and in the latter case, a well drilled to about 350 m would merely initially tap hot water at about 236°C whereas deeper drilling would most probably find higher temperature water capable of greater power potential even though having to discharge through a longer length of borehole. Statistics indicate that this is so, as the average depth of hundreds of wells drilled in geothermal regions in the U.S.A. over the last few years has reached 2 km, which, for a classical boiling point with depth (BPD) reservoir would attain 339°C. This would be an attractive result so long as bottom hole permeability was good and that the mineral concentration in the brine was not too high to present problems with reinjection or in-hole scaling. And nowadays, reinjection is a mandatory part of nearly all world-wide geothermal schemes, even for dry steam reservoirs with their relatively small quantity of condensate to be disposed.

It may be appropriate to reasses drilling strategy and make a determined effort to exploit the top of water reservoirs in the expectation of evolving a steam zone with fewer problems and more energy efficiency potential. However, one cannot be dogmatic, as drilling is an exacting and expensive business with first discharge awaited with nervous anticipation, and reputations dependent, to some extent, on the results. Higher temperature water does, of course, produce more steam than lower temperature water and consequently more electric power can be generated. It is also found that higher temperature water, even though at greater depth, discharges greater flows than lower temperature water for equivalent feed-zone permeabilities, hence the trend to tap deeper horizons is a logical one. Up to now, no quantitative assessment has been possible into the comparative merits of higher water temperature with depth except to be aware that deeper is better. This is because it has

not been possible to sensibly compare the discharge of wells which are drilled to various depths without being aware that permeability variation controls, more often than not, whether a well is a good producer, and so a low temperature shallow well can have a greater discharge and power potential than a deeper higher temperature well drilled into tighter formations. Although, as has been pointed out, statistics indicate that the deeper wells are generally a better investment, this may be because unknown factors conspire to increase permeability at around a depth of 2 km in a similar way that good permeability is found at about 350 m depth, James (1984a).

Therefore, for equivalent permeabilities, and assuming that boiling point with depth (BPD) obtains, a good deep well is superior to a shallow well within the depth common to geothermal drilling, which is down to about 2.5 km. At greater depths, the cost of drilling increases rapidly and begins to exert its influence on the cost-benefit analysis, but in this study that aspect will be ignored, and will only be resurrected if deeper drilling becomes an intrinsic part of geothermal technology.

MAXIMUM WELL DISCHARGE

This has been calculated, James (1980) for infinite permeability at the feed zone, boiling point with depth, and wide-open stable vertical discharge. The following formula is employed.

$$P_c = d_c^{0.602} \left(\frac{C}{72.2}\right)^{2.195} \quad \text{for } 180 < C < 350 \qquad (1)$$

P_c = lip pressure in bar; C = the feed temperature, degree celcius. For the boiling point with depth relationship where H is depth in metres, James (1980).

$$C = 69.56\ H^{0.2085} \quad \text{for } 30 < H < 3\ 000 \qquad (2)$$

Formula (1) has been confirmed in practice James (1984b), and applies whether the feed is reservoir water which is just at the boiling point (for the hydrostatic pressure), or whether it is dry saturated steam at the same temperature. The relationship between flow, lip pressure, pipe diameter and fluid enthalpy is derived from James (1962) and in the metric form:-

$$W = 5.2\ (10)^6\ \frac{P_c^{0.96}\ d_c^{2}}{h_o^{1.102}} \qquad (3)$$

W = Flow t/h;
d_c = Inside diameter of well and discharge pipe, m
h_o = Enthalpy of discharge, kJ/kg

We now require a relationship between water enthalpy and temperature and a plot of these factors derived from steam tables, gives:-

$$h_o = 1.475\ C^{1.197} \quad \text{for } 210 < C < 350 \qquad (4)$$

Substituting (1) in (3), we have

$$W = 5.2\ (10)^6\ \frac{d_c^{2.578}}{h_o^{1.102}} \left(\frac{C}{72.2}\right)^{2.1072} \qquad (5)$$

Now substitute (4) in (5),

$$W = \frac{5.2(10)^6\ d_c^{2.578}}{\left(1.475\ C^{1.197}\right)^{1.102}} \left(\frac{C}{72.2}\right)^{2.1072}$$

$$W = 410.82\ d_c^{2.578}\ C^{0.788} \text{ tonne/hr} \qquad (6)$$

Although this result gives the maximum flow from a well which can be expected, it can increase with displacement upwards of boiling point with depth in the reservoir; also for low enthalpy wells, high gas content can boost flow to higher values than that determined from equation (6), James (1982). Lower discharge than the maximum can be due to (a) mineral deposition which reduces the well diameter, (b) impermeability of the feed horizon, or (c) displacement downwards of the boiling point with depth relationship.

Equation (6) shows that flow is directly proportional to both the diameter of well and feed water (or steam) temperature; however, the index of diameter is greater than the expected square law and emphasises the importance of increasing well diameters where excellent permeability exists.

To determine the amount of electric power which can be generated from the flow of equation (6), we require the specific power rate for hot water expanding by two-stage flash into turbo-condensers under optimum design conditions. Fortunately, this has been accomplished, James and Meidav (1977) who present the following relationship:

$$\text{Megawatt (electrical)} = W \left(\frac{C}{1260}\right)^{2.2233} \quad \text{for } 210 < C < 350 \qquad (7)$$

Substituting (6) in (7), we obtain:-

$$\text{Megawatt (electrical)} = \frac{5.26}{(10)^5}\ d_c^{2.578}\ C^{3.0112} \qquad (8)$$

This shows that the electrical power which can be generated from hot water reservoirs is proportional to the cube of the feed temperature, and tapping a reservoir at 315C for example, should give twice the power of a

reservoir at 250°C, all other factors being equal.

Interestingly enough, James (1986) shows that at these reservoir temperatures, the amount of silica transported in the separate steam and water pipelines (for power and injection) is also twice as high for the higher temperature reservoir when exploited for equal electricity generated. Because of potential scaling problems anticipated in the reinjection water lines of higher temperature fields (exceeding about 300°C), it may be that only single-stage flash will be employed rather than the more efficient two-stage flash, in which case the power relationship of equation (7) will have to be replaced with that derived for single-stage, James and Meidav (1977), as:-

$$\text{Megawatt (electrical)} = W \left(\frac{C}{1055}\right)^{2.611} \quad \text{for } 235 < C < 365 \tag{9}$$

Substituting (6) in (9), we obtain:-

$$\text{Megawatt (electrical)} = \frac{5.247}{(10)^6} d_c^{2.578} C^{3.399} \tag{10}$$

For single-stage flash and condensing sets, the relationship of equation (10) shows that a reservoir temperature of 306.6°C would generate twice the power of a reservoir of 250°C. It should be noted that, although the index of temperature now exceeds the cube, the power will be less than that of the two-stage alternative, due to the equation constant being smaller by approximately 10. For example, if a well diameter of 0.2 m is taken and a reservoir hot water temperature of 250°C, then the power potential for two-stage flash from equation (8) comes to 13.8 MWe compared with 11.7 MWe for the single-stage alternative. Actual values when flows are reduced by discharging horizontally instead of vertically would lower these figures to about 75%, namely to 10.3 MWe and 8.8 MWe. Further decline would also be expected over the years as reservoir pressures fall with time and exploitation.

MAXIMUM POWER FROM DRY STEAM RESERVOIRS

The shallower depths of dry steam reservoirs are usually at a temperature close to about 236°C and at a horizon which agrees with that calculated from equation (2), namely 350 m and because of this, the lip pressure of equation (1) can be determined independently of whether steam or hot water is the fluid involved. Therefore, inserting 236°C in equation (1) we have:-

$$P_c = d_c^{0.602} \left(\frac{236}{72.2}\right)^{2.195} = 13.46\, d_c^{0.602} \tag{11}$$

Substituting this value of P_c in equation (3) and letting h_o = 2804.1 kJ/kg which is the enthalpy of dry saturated steam at 236°C, we obtain

$$W = d_c^{2.578} (10)^4 \text{ tonne/hr} \tag{12}$$

Taking a steam power specific rate of 10 tonne/MWh, James and Meidav (1977), we can now determine the maximum electric power which can be generated by a dry steam reservoir as

$$\text{Megawatt (electrical)} = \frac{d_c^{2.578} (10)^4}{10} = (10)^3 d_c^{2.578} \tag{13}$$

Hence, for a well diameter of 0.2 m, the power potential = 15.8 MWe. If we substitute this value in equations (8) and (10) for the same well diameter, we can determine the temperature of hot water reservoirs which give identical power to the steam reservoir, as follows:-

Hot water reservoir employing two-stage flash to give 15.8 MWe, and d_c = 0.2 m.

$$15.8 = \frac{5.26}{(10)^5} (0.2)^{2.578} C^{3.0112}$$

Equivalent hot water reservoir temperature = 261.5°C

For hot water reservoir employing single-stage flash to give 15.8 MWe,

$$15.8 = \frac{5.247}{(10)^6} (0.2)^{2.578} C^{3.399}$$

Equivalent hot water reservoir temperature = 273°C.

As has been pointed out, unless there is a technical and economic break-through in the control of mineral scaling from the separated injection water, it is likely that the single-stage design will be increasingly prevalent, especially as deeper drilling is gaining momentum and higher temperature water reservoirs discovered.

Although it might be thought from these figures that a hot water reservoir which exceeds 273°C has the advantage over a dry steam reservoir at 236°C, the simplicity and low overall cost of the latter together with its avoidance of massive water injection (with largely unknown side effects) makes the exploitation of dry steam reservoirs a much more attractive proposition.

CONCLUSIONS

Because of the greatly increased power potential of hotter water at deeper horizons, there is considerable incentive to ignore shallow drilling. However, high temperature water usually contains increased concentrations of dissolved minerals which can lead to scaling of reinjection water lines,

reinjection wells, and the surrounding reservoir, with serious consequences for the "life" of a project.

As reinjection is an inherent part of most future power developments and the problem of scaling not yet solved technically and economically, it is recommended that a sustained effort be made into locating (and subsequently exploiting) the dry steam believed to exist at close to the criticus temperature of 236°C, James (1986). Such steam horizons would be situated above hot water reservoirs and ideally located at a depth of about 350 m. Even if hot water is found at this level, it will most probably be temporary or at least have a relatively low level of dissolved minerals which will permit two-stage flash exploitation, with reinjection free from scaling problems; a not unattractive scenario. And continued production of water will lead (it is hoped) to eventual changeover to steam flows with development of a spreading vapour-filled zone.

REFERENCES

James, R. (1962): Steam-Water Critical Flow through Pipes. Proc. I. Mech. E., 176, 26, 741.

James, R. (1966): Power-Life of a Hydrothermal System. Proc. 2nd Australasian Conf. Hydraulics and Fluid Mechanics. Univ. of Auckland, New Zealand.

James, R. (1968): Wairakei and Larderello: Geothermal Power Systems compared. N.Z.J.Sc., 11, 4, 706.

James, R. and Meidav, T. (1977): Thermal Efficiency of Geothermal Power. Geothermal Energy, 5, 4, 8.

James, R. (1980): Estimating Maximum Discharge of Geothermal Wells. Proc. 6th Workshop Geothermal Reservoir Engineering, Stanford Univ., Stanford, Calif. U.S.A.

James, R. (1982): Large Flows of Low-Enthalpy Geothermal Wells can be due to Non-Condensible Gas-Lift. Geothermal Energy, 10, 5, 14.

James, R. (1984a): Geothermal Steam Flow Through Porous-Permeable Rock. Proc. CSIRO/DSIR Seminar of Convective Flows in Porous Media, DSIR, Wellington, N.Z.

James, R. (1984b): Successful Prediction of Mokai 5 Discharge. Geothermal Energy, 12, 2, 7.

James, R. (1986): Significant Silica Solubility in Geothermal Steam. Proc. 12th Workshop Geothermal Reservoir Engineering, Stanford Univ., Stanford, Calif., U.S.A. (in preparation).

Truesdell, A.H. and White, D.E. (1973): Production of Superheated Steam from Vapour-Dominated Reservoirs. Geothermics, 2, 3-4, 154.

PROCEEDINGS, Eleventh Workshop on Geothermal Reservoir Engineering
Stanford University, Stanford, California, January 21-23, 1986
SGP-TR-93

THE RESPONSE TO EXPLOITATION OF ROTORUA GEOTHERMAL FIELD

Malcolm A. Grant

Geothermal Coordinator, Head Office,
D.S.I.R., Private Bag, Wellington, New Zealand.

ABSTRACT

The concern about possible decline in Whakarewarewa spring activity led to the creation of the Rotorua Monitoring Program and the Rotorua Task Force. Both will shortly issue their final reports (Ministry of Energy 1985a,b). Under the Monitoring Program a considerable database was collected about aquifer, well and spring behaviour. From this it has been concluded that exploitation has had the following effects:

* geothermal aquifer pressures have fallen by up to 0.5 bar;
* geothermal aquifer pressures beneath Whakarewarewa have fallen by about 0.2 bar;
* geothermal flow from Whakarewarewa has been reduced by about half.

The effects on the springs could be reduced by reducing withdrawal particularly near Whaka, reinjection (including the use of downhole heat exchangers), or a combination of these.

INTRODUCTION

The analysis of possible changes at Rotorua due to exploitation has always been hampered by a lack of the most important data for field modelling, a history of past response. We have instead an intensive series of measurements over a brief period: zero to three years. In this paper I describe the data and my interpretations. The resulting model has been used as the basis of a simulation (Grant et al. 1985). The simulation is not described here except to note that, by matching the interpreted data, it confirms the consistency of the interpretation and conclusion.

THE AVAILABLE DATA

The Monitoring Program has a number of monitor wells and groundwater wells. In these water level or wellhead pressure is recorded continuously or at intervals. In addition temperature profiles and water levels have been measured in another 100 wells.

A number of springs are instrumented and flow, water level and/or temperature recorded. The flow and temperature of Puarenga Stream, which drains Whaka, is recorded above and below Whaka.

The flow of the wells drawing from the geothermal aquifer has been measured or estimated, and also the amount by which the flow varies seasonally. (Ministry of Energy, 1985b).

Lake level, rainfall, atmospheric pressure and temperature are all recorded.

This forms a fairly complete set of physical data covering the present state of the field, although for various reasons some vital instrument installations have only recently begun functioning.

AQUIFER PRESSURE

The geology of Rotorua has been described by Wood (1985). Figure 1 shows a map of the field and a few features. A major fault, Inner Caldera Boundary Fault (ICBF), crosses the field just north of Whaka. North of this fault there are two rhyolite domes, one of which reaches surface at Pukeroa Dome (Hospital Hill). In the east of the field the rhyolite is absent and Mamaku Ignimbrite is found. Both rhyolite and ignimbrite are very permeable in their top surface, and are covered by lake sediments of poor permeability. Thus the major permeable feature is a well-defined surface, and this represents the geothermal aquifer from which most wells produce.

This aquifer is reached at 70-130 m depth over much of the field. To obtain comparable data water levels or downhole pressures were reduced to equivalent pressure data at a fixed elevation, RL+180 m, which is about 100 m below surface over much of Rotorua. For most wells this data is the same as measured downhole pressure at RL+180 m. For wells with feed depth markedly different from RL+180 m it was necessary to correct for the difference between downhole and reservoir pressure gradients.

Figure 2 shows this pressure distribution. Figure 3 shows the temperature at feed depth (i.e. not a RL+180 m). In Figure 3 the region at boiling point is shaded. Temperature differences within these areas reflect only

FIGURE 1

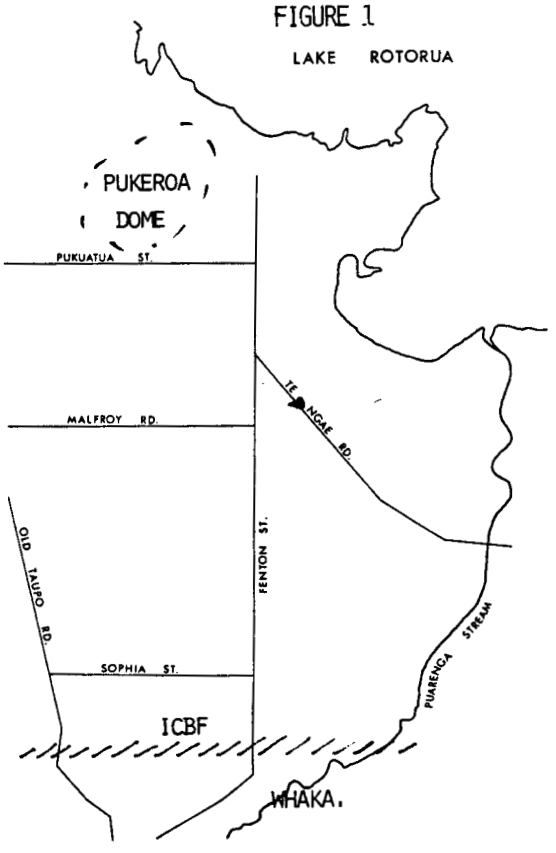

FIGURE 2

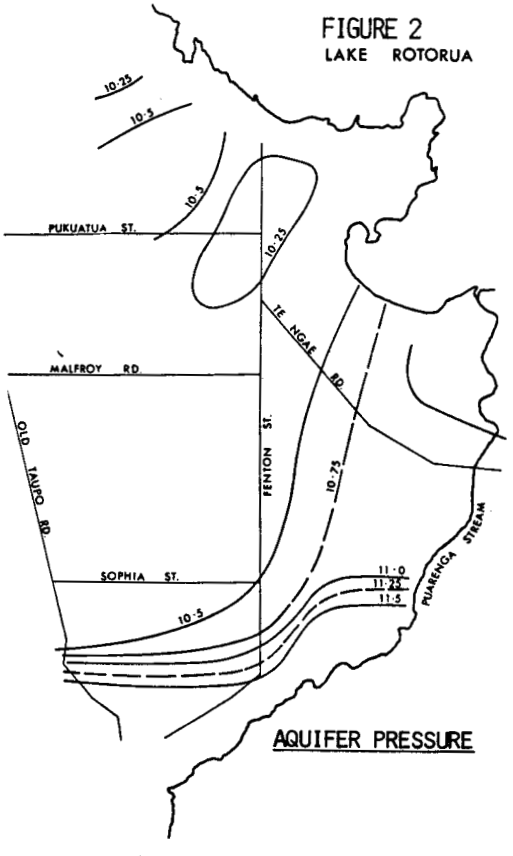

FIGURE 3

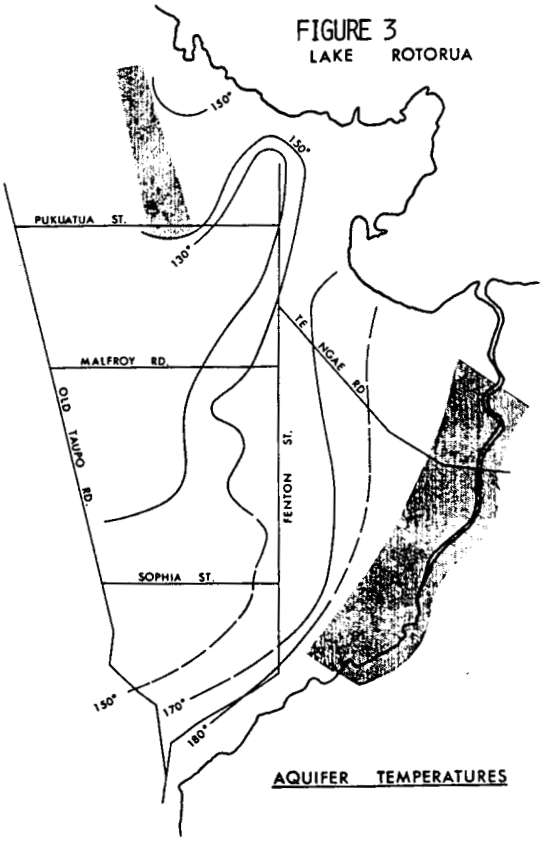

difference in aquifer elevation.

The pressure and temperature distribution clearly reflect a number of features, most of them already known or conjectured. (Glover 1974, Grant 1979, Donaldson 1980, Simpson 1985). Pressure and temperature maxima at Whaka along the eastern edge of the field and at Pukeroa Dome reflect upflow of deep geothermal fluid into the aquifer. A pressure minimum under the business district reflects the heavy density of withdrawal. The ICBF is very clearly marked in the south by a steep pressure gradient. The permeable aquifer is displaced at the fault, making a resistance to horizontal flow of fluid.

SEASONAL CHANGES

There is a well-marked seasonal cycle in aquifer pressures. Figure 4 shows some data (Bradford 1983). Geothermal pressures reach a minimum in winter, the fall beginning at the first cold spell in autumn, and recover in summer. The cycle, the opposite of groundwater change, is clearly related to withdrawal. Total withdrawal reaches a maximum of 31,000 t/d in winter, and drops to about 25,000 t/d in summer. (Ministry of Energy 1985b).

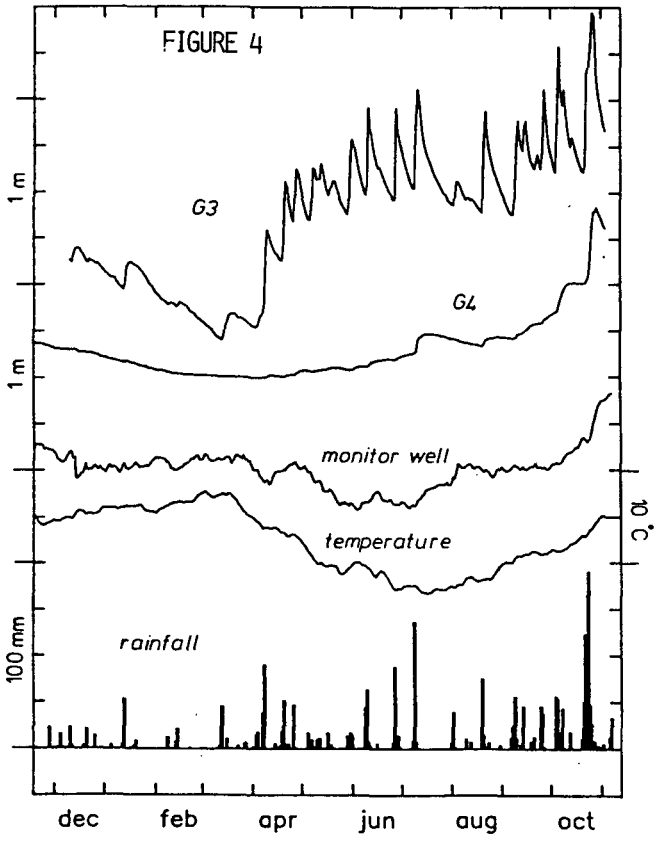

SPRINGS

Total flow from Whaka is 158 MW (Simpson 1985b), equivalent to 200 kg/s of aquifer water. This has fallen by 30% since 1967.

A seasonal pattern is observed in the springs; in recent years there have been a number of temporary and permanent spring failures. These all occur over autumn-winter, i.e. the time of low aquifer pressure and high groundwater pressure. Unfortunately the instrumented springs show too much noise on their records to measure a seasonal flow change. Roto-A-Tamaheke, the largest spring, is now instrumented and appears to show a winter drop of 10-15% in flow, based on the part-year record available.

FIELD MODEL

Figure 5 shows a simple model of the field. The producing aquifer is idealised as a horizontal layer. Fluid enters it in the regions of upflow. Fluid leaves through wells, through springs and through discharge into the bed of Lake Rotorua. The flow of the wells is specified from measurement. The springs and the flow into the lake are both treated as flows through a constant resistance. Groundwater effects are ignored. Since the spring flows and geothermal pressures show changes opposed to groundwater changes the groundwater effects, while important to the spring behaviour, are not the dominant effect present. Regarding the springs as a constant resistance is also a considerable simplification, since they represent a nonlinear leak (see Appendix).

INFERENCES

Each of the monitor wells shows a seasonal cycle, varying with position in the field. this is created by the 6000 t/d reduction in flow of withdrawal in summer. If we assume that the aquifer is in a quasi-steady state (this assumption is valid provided the volume of two-phase fluid is small), and that the springs are a linear resistance then the pressure change created by a reduction of 31,000 t/d (i.e. return to an unexploited state) can be found by simple proportion -31/6) times the seasonal cycle. this produces Figure 6 showing the pressure distribution in the unexploited state of the field.

The unexploited pressure at Whakarewarewa is found to be 0.25 bar above the present. This depends on the amplitude of the seasonal cycle at M16, which has been recording less than a year. M7 is not yet working. the present aquifer pressure at Whaka is 11.6 bar. Overflow level at Roto-A-Tamaheke is RL+295 m, and other springs are at similar or slightly higher elevation. A column of boiling water beneath this will exert a pressure of 11.35 bar at RL+180 m, or say 11.4 bar on average so there is 0.2 bar of overpressure currently available to drive fluid to surface. Originally there was 0.4 bar. The overpressure has been reduced to half by exploitation. This implies a halving of the discharge (or reduction by more than half, on a nonlinear spring model).

Pressures have also fallen at the lake front and Ohinemutu. Associated with this has been the demise of much of the original surface activity in the northern part of the city.

MANAGEMENT POSSIBILITIES

The objective of the Monitoring Program has been to save the springs and geysers from failure, presuming that it would be concluded that they are in jeopardy. this could be achieved by reducing withdrawal, or by reinjection. At the same time it is presumably not desirable to restore spring flow in the northern area, now built on. So the objective of any field management must be to restore pressures at Whaka while keeping them depressed further north.

This selective pressure change requires selective changes in withdrawal. Wells near Whaka could be reduced in flow, or closed; perhaps the usage could be supplied by fluid piped south from production wells further north.

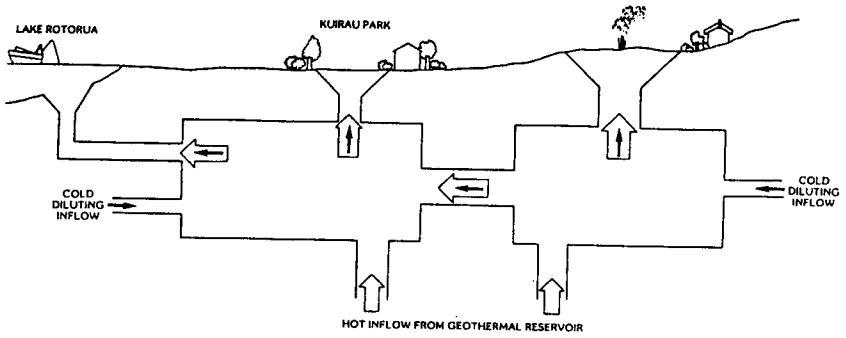

FIGURE 5

FIGURE 6

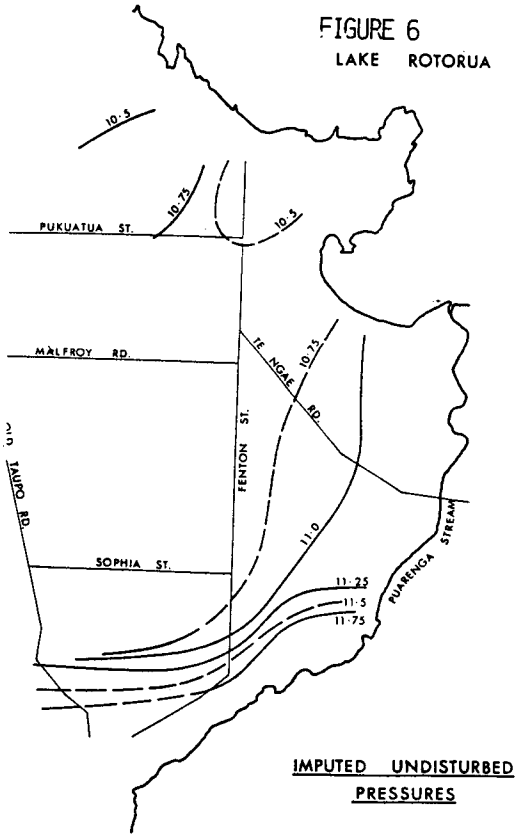

Reinjection is another possibility. At present about 5% of the waste is reinjected. The remaining 95% is disposed of to surface or to groundwater. Reinjection at aquifer depths would restore pressure, provided that it was not into two-phase fluid nor so close to springs that there is a danger of thermal returns. This excludes the eastern edge of the field and region south of ICBF. Downhole heat exchangers are equivalent to production/reinjection well combinations.

Different scenarious to restore pressure at Whaka, while maintaining supply to users, will be examined with the aid of the model.

CONCLUSION

The Monitoring Program database was defined and validated a model measuring the reduction in flow of the Whakarewarewa Springs as a result of exploitation.

ACKNOWLEDGEMENTS

I wish to thank all the Monitoring Program and Task Force teams for their efforts and helpfulness in providing data, interpretation and comment, and Ministry of Energy for their permission to publish. I thank Y. Hirako (Japan Metals and Chemicals) for providing much relevant material from Japanese sources.

REFERENCES

Benseman, R.F., 1959. "Subsurface discharge from thermal springs" Jl. Geoph. Res. v. 64 (8), pp 1063-1065.

Bradford, E., 1983. Personal communication.

Donaldson, I.G., 1980. "A preliminary appraisal of the hot water system underlying Rotorua City" Report 662, Physics and Engineering Laboratory, D.S.I.R.

Glover, R.B., 1974. "Geochemistry of the Rotorua geothermal district" in D.S.I.R. Geothermal Report 6 "Geothermal Resources Survey Rotorua Geothermal District".

Grant, M.A., McGuinness, M.J., Dalziel, S.B., O'Sullivan, M.J., and Razali, Y., 1985. "A model of Rotorua geothermal aquifer and springs" in Ministry of Energy, 1985a, Ch. 10.

Kanroji, Y., 1983. "Hot springs and geothermal resources" Jl. Japan Geothermal Energy Association, v. 10, No. 3. (In Japanese).

Ministry of Energy, 1985a. "Rotorua Monitoring Program Final Report".

Ministry of Energy, 1985b. "Rotorua Task Force Final Report".

Simpson, B.M., 1985a. "Structural controls on the shallow hydrology of Rotorua geothermal field" in Monitoring Program Progress Report, Jan-March 1985.

Simpson, B.M., 1985b. "An assessment of heat flow at Whakarewarewa" 7th N.Z. Geothermal Workshop, Auckland University.

Wood, C.P., 1985. "Geology of Rotorua" in Ministry of Energy, 1985a, Ch. 5.

APPENDIX

A spring can be idealised as a permeable feature striking upwards from an underlying aquifer, passing through groundwater and terminating at a pool. If the spring has an equivalent head above the overflow level of the pool, it flows at a rate proportional to this head. If the heat lies below overflow, there is no surface discharge. At all heads there is gain or loss of water through 'subsurface discharge' to groundwater (Benseman 1959). This produces a nonlinear relation between aquifer pressure for an individual spring (Figure A1) and a smoother but still nonlinear relation for a group of springs. This latter has been observed in the changes at exploited spa areas in Japan (Kanroji 1983).

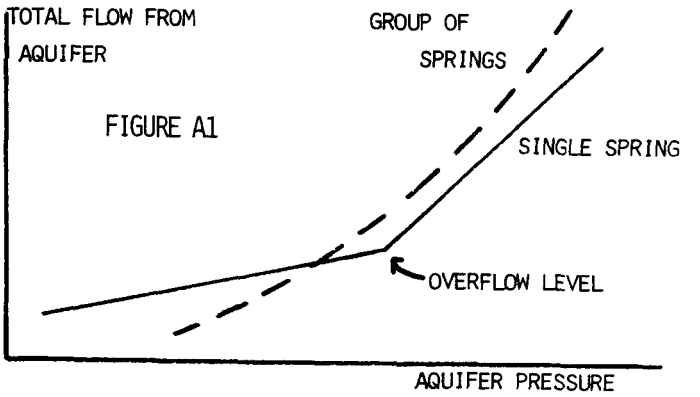

FIGURE A1

PROCEEDINGS, Eleventh Workshop on Geothermal Reservoir Engineering
Stanford University, Stanford, California, January 21-23, 1986
SGP-TR-93

GEOTHERMAL TWO-PHASE WELLBORE FLOW: PRESSURE DROP CORRELATIONS AND FLOW PATTERN TRANSITIONS

A.K. Ambastha and J.S. Gudmundsson

Petroleum Engineering Department, Stanford University

ABSTRACT

In this paper we present some basic concepts of two-phase flow and review the Orkiszewski (1967) correlations which have been suggested by various investigators to perform well for geothermal wellbore flow situations. We also present a flow regime map based on the transition criteria used by Orkiszewski (1967) and show that most geothermal wells flow under slug flow regime. We have rearranged bubble- to slug- flow transition criterion used by Orkiszewski (1967) to show that the transition depends on the dimensionless pipe diameter number in addition to dimensionless liquid and gas velocity numbers. Our aim is also to identify what research may lead to improvements in two-phase pressure drop calculations for geothermal wellbore flow.

INTRODUCTION

The Orkiszewski (1967) two-phase vertical upward flow correlations have been used by several investigators to model steam/water wellbore flow. In a companion paper we use a geothermal wellbore simulator based on the Orkiszewski (1967) correlations to calculate the flowing pressure and temperature profiles in several wells (Ambastha and Gudmundsson, 1986). There we study under what flowing conditions the measured and calculated profiles match. Our study differs from others because we use data sets from several geothermal wells, but only one set of two-phase flow correlations.

In addition to identifying the conditions when measured and calculated wellbore data match, we want to identify what research may lead to improvements of geothermal wellbore simulators. For this we need to know the details of the wellbore simulator used, flow regime transitions, and pressure drop calculations. We also need to know how the correlations relate to two-phase flow studies in general. The purpose of this paper is to present the details of the Orkiszewski (1967) two-phase vertical flow correlations used in a geothermal wellbore simulator, described by Ortiz-R. (1983). We also present a flow regime map based on the transition criteria used by Orkiszewski (1967) as applied to geothermal wells.

PREVIOUS WORK

Early studies of two-phase flow in geothermal wells are those of Gould (1974) and Nathenson (1974). The Gould (1974) study is based on flow pattern specific correlations; the applications considered were wellbore deposition and deliverability. The Nathenson (1974) study considered no-slip (homogeneous) wellbore flow, coupled to porous media flow in the reservoir. The problems considered by Nathenson (1974) were the same.

Geothermal wellbore flow simulators have been developed by universities, national laboratories, industry, and consultants. However, progress has been slow since the initial Gould (1974) and Nathenson (1974) studies. Upadhyay *et al.* (1977) compared calculated and observed pressure drops in geothermal wells producing steam/water mixtures. They compared flowing pressure profiles to several two-phase flow correlations and concluded that the Orkiszewski (1967) correlations are satisfactory - the Hagedorn and Brown (1965) correlations came second. Fandriana *et al.* (1981) developed the first version of the wellbore simulator used by Ortiz-R. (1983) and us. They compared four correlations and found that the Orkiszewski (1967) method was the best - the Hagedorn and Brown (1965) and Duns and Ros (1963) methods were found to give reasonable results also. Miller (1979) and Mitchell (1982) wrote geothermal wellbore simulators based on the Orkiszewski (1967) correlations. The above authors agreed on the general applicability of the Orkiszewski (1967) correlations to geothermal wellbore flow. Therefore, we think they form the best basis to compare predicted and measured pressure/temperature profiles in geothermal wells.

TWO-PHASE FLOW

The total pressure drop in wellbores consists of three components: frictional, accelerational, and gravitational. In typical two-phase wells the gravitational component dominates; the frictional component contributes only at high flow rates; and the accelerational component is usually insignificant. In *homogeneous* steady-state flow the total pressure drop in a constant cross-section duct is given by

$$-\frac{dp}{dz} = \frac{\tau S}{A} + \frac{d(G_M^2/\rho_M)}{dz} + g\,\rho_M \sin\theta \qquad (1)$$

In terms of pressure drop components the equation takes the form

$$\frac{dp}{dz} = \frac{dp_f}{dz} + \frac{dp_a}{dz} + \frac{dp_g}{dz} \qquad (2)$$

In *separated* steady-state flow the total pressure drop in a constant cross-section duct is given by

$$-\frac{dp}{dz} = \frac{\tau S}{A} + G_M \frac{d}{dz}\left[\frac{x^2}{\rho_G \alpha} + \frac{(1-x)^2}{\rho_L^*(1-\alpha)}\right] \quad (3)$$

where α is the void fraction given by

$$\alpha = \frac{A_G}{A} \quad (4)$$

An examination of Equations 1 and 3 shows that in homogeneous flow the wall shear stress τ is the unknown, while in separated flow both the wall shear stress and void fraction α are unknown. The wall shear stress is used to calculate the frictional component in both homogeneous and separated flow. The void fraction is used to calculate the gravitational component in both models, and the accelerational component in separated flow.

Two kinds of correlations have been developed for frictional pressure drop in two-phase flow; called generalized and specific correlations. The generalized correlations are empirical and make no reference to the flow pattern and physical nature of two-phase flow phenomena. Nevertheless, many engineering calculations are carried out using generalized methods; for example that of Hagedorn and Brown (1965). The specific correlations are specific to the flow pattern (bubbly, slug, churn, annular) and flow situation (vertical, inclined, horizontal).

The Orkiszewski (1967) correlations are the specific kind. They are specific to vertical upward flow in oil and gas wells and can also be used for geothermal wells. In addition to prescribing what correlation to use for pressure drop in different flow regimes, it is necessary to prescribe the criteria for transition between flow regimes. Small discontinuities in pressure drop can occur at transitions between flow patterns.

FLOW PATTERN TRANSITIONS

Our presentation follows that of Orkiszewski (1967), Brill and Beggs (1977), and Upadhyay *et al.* (1977). The flow regime transition criteria are essentially those of Ros (1961), and Duns and Ros (1963). They defined the following limits for the transition between flow regimes:

Bubble Flow $L_{b/s} > v_{SG}/v_{ST}$

Slug Flow $L_{b/s} < v_{SG}/v_{ST}$, $L_{s/t} > N_{GV}$

Transition Flow $L_{s/t} < N_{GV} < L_{t/m}$

Mist Flow $L_{t/m} < N_{GV}$

The definition of these terms are given in the nomenclature. The N's are dimensionless expressions of superficial velocities, the v's are superficial velocities, and the L's are flow regime boundary terms. They are given by the expressions:

$$L_{b/s} = 1.071 - 0.2218 \frac{v_{ST}^2}{d} \geq 0.13 \quad (5)$$

$$L_{s/t} = 50 + 36\, N_{LV} \quad (6)$$

$$L_{t/m} = 75 + 84\, (N_{LV})^{0.75} \quad (7)$$

$$N_{LV} = 1.938\, v_{SL}\left[\frac{\rho_L}{\sigma}\right]^{0.25} \quad (8)$$

$$N_{GV} = 1.938\, v_{SG}\left[\frac{\rho_L}{\sigma}\right]^{0.25} \quad (9)$$

$$v_{SL} = \frac{q_L}{A} \quad (10)$$

$$v_{SG} = \frac{q_G}{A} \quad (11)$$

$$v_{ST} = v_{SG} + v_{SL} \quad (12)$$

Note that the constant 1.938 in Equations 8 and 9 arises when engineering units are used. If we use the following definition of dimensionless pipe diameter number

$$N_D = 120.872\, d\sqrt{\frac{\rho_L}{\sigma}} \quad (13)$$

the criterion for bubble-to-slug flow can be rewritten as

$$\frac{N_{GV}}{N_{LV}+N_{GV}} < 1.071 - 13.8335 \frac{\left[N_{LV}+N_{GV}\right]^2}{N_D} \quad (14)$$

Thus, the transition from bubble to slug flow involves a nonlinear relationship between liquid and gas velocity numbers for a particular value of pipe diameter number. We prepared a flow pattern map using the above flow regime transition criteria. In our companion paper (Ambastha and Gudmundsson, 1986), the pipe diameter number varied in the range of 60 to 100. Therefore, the boundary between bubble and slug flow regime was evaluated for a representative pipe diameter number of 80. Figure 1 presents the flow pattern map on log-log coordinates. Figure 2 provides the same information on cartesian coordinates. Chierici *et al.* (1974) also present this flow pattern map on log-log coordinates. They note that the boundary between bubble and slug flow regimes results in a family of curves, corresponding to different sets of ρ_L, σ and d. We observe that the three parameters can be combined into a dimensionless pipe diameter number and that the boundary between bubble and slug flow regimes can be represented by Equation 14.

In a companion paper (Ambastha and Gudmundsson, 1986), we present flowing data for 10 two-phase geothermal wells. The flowrate ranges from 12.9 kg/s to 68.6 kg/s; the enthalpy from 965 kJ/kg to 1966 kJ/kg; wellhead pressure from 245 kPa to 6027 kPa; well depth from 913 m to 2600 m; wellbore diameter from about 7-5/8" to 9-5/8". We used our Orkiszewski-based geothermal wellbore simulator to calculate the flowing pressure and temperature profiles in the 10 wells. The two-phase flow patterns encountered in these calculations are shown in Figure 3. The

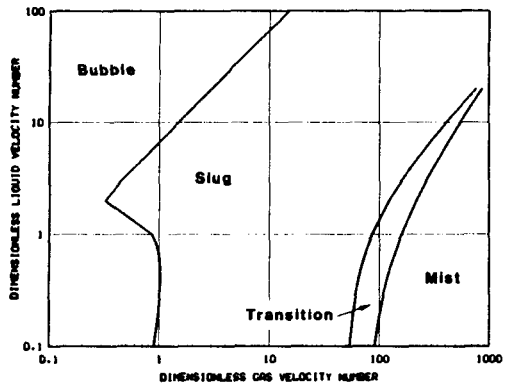

Figure 1. Orkiszewski flow pattern map (log-log coordinates).

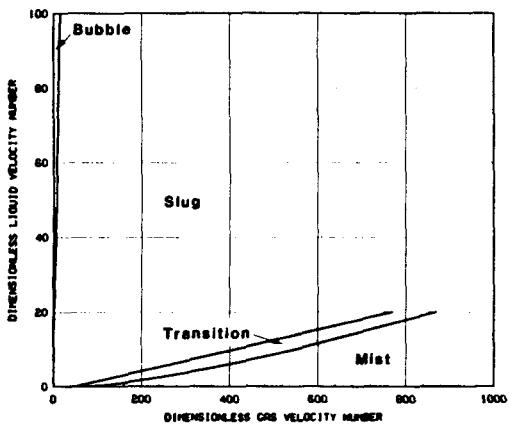

Figure 2. Orkiszewski flow pattern map (cartesian coordinates).

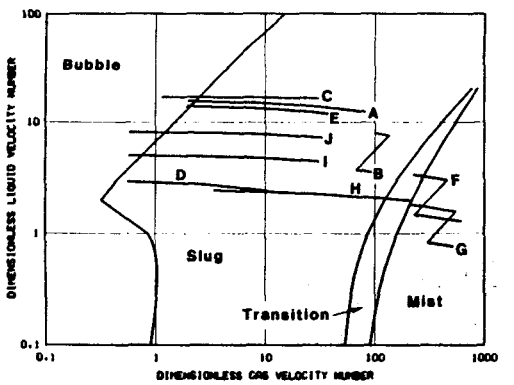

Figure 3. Flow regimes for geothermal wells.

figure gives the dimensionless superficial velocity of liquid water against steam vapor, so the flow lines for individual wells go from left to right. Low enthalpy wells tend to be in the upper left hand part of Figure 3, and high enthalpy wells in the lower right hand part. The steps in the lines result from wellbore diameter changes; increased flow area reduces the superficial velocity of both phases. Figure 3 shows that slug flow is the dominant flow regime in the 10 wells.

PRESSURE DROP CORRELATIONS

The Orkiszewski (1967) correlations for pressure drop calculations are based on several works: Griffith and Wallis (1961) for bubble flow regime, and Duns and Ros (1963) for transition and mist flow regimes. Orkiszewski (1967) developed a new correlation for slug flow based upon the experimental data of Hagedorn and Brown (1965). The pressure drop correlations for different flow regimes are presented below.

Bubble Flow (Griffith and Wallis, 1961)

Liquid holdup in this flow regime is given by the equation

$$H_L = 1 - 0.5 \left[1 + \frac{v_{ST}}{v_B} - \sqrt{(1+v_{ST}/v_B)^2 - 4v_{SG}/v_B} \right] \quad (15)$$

The bubble velocity, v_B (also called the slip velocity) is assumed to have a constant value of 0.8 ft/sec. Once the liquid holdup is obtained, the mixture density can be determined from

$$\rho_M = \rho_L H_L + \rho_G (1 - H_L) \quad (16)$$

The holdup is related to void fraction by

$$H_L = 1 - \alpha \quad (17)$$

The pressure drop due to friction is given by

$$\frac{dp_f}{dz} = \frac{f\rho_L \left[\frac{v_{SL}}{H_L}\right]^2}{2g_c d} \quad (18)$$

The friction factor f is obtained from the Moody diagram. The Reynolds number for this purpose is given by

$$N_{Re} = \frac{1488\ \rho_L\ v_{SL}\ d}{H_L\ \mu_L} \quad (19)$$

Note that the constant 1488 in Equations 19, 22 and 23, arises when engineering units are used. In this flow regime, pressure drop due to acceleration is considered negligible.

Slug Flow (Orkiszewski, 1967)

The mixture density in this flow regime is calculated by

$$\rho_M = \frac{\rho_L(v_{SL} + v_B) + \rho_G\ v_{SG}}{v_{ST} + v_B} + \rho_L \delta \quad (20)$$

where v_B is bubble rise velocity and is given by

$$v_B = C_1 C_2 \sqrt{gd} \tag{21}$$

C_1 is a function of N_{ReB} and C_2 is a function of both N_{ReB} and N_{ReL}, defined as

$$N_{ReB} = \frac{1488\ \rho_L\ v_B\ d}{\mu_L} \tag{22}$$

$$N_{ReL} = \frac{1488\ \rho_L\ v_{ST}\ d}{\mu_L} \tag{23}$$

The Griffith and Wallis (1961) coefficients, C_1 and C_2, were presented by Orkiszewski (1967) in the form of figures. Because of the interrelationship of v_B and N_{ReB}, the calculation of v_B requires an iterative procedure. v_B can also be calculated using Equations 24 through 27.

When $N_{ReB} \leq 3000$,

$$v_B = (0.546 + 8.74 \times 10^{-6} N_{ReL})\sqrt{gd} \tag{24}$$

When $N_{ReB} \geq 8000$,

$$v_B = (0.35 + 8.74 \times 10^{-6} N_{ReL})\sqrt{gd} \tag{25}$$

When $3000 < N_{ReB} < 8000$,

$$v_B = 0.5\left[\psi + \sqrt{\psi^2 + \frac{13.59\mu_L}{\rho_L\sqrt{d}}}\right] \tag{26}$$

$$\psi = (0.251 + 8.74 \times 10^{-6} N_{ReL})\sqrt{gd} \tag{27}$$

where ψ is an arbitrarily defined parameter.

The Orkiszewski (1967) liquid distribution coefficient δ, which is an empirical coefficient relating theory to reality, is given by the expressions:

For $v_{ST} < 10$,

$$\delta = (0.013 \log \mu_L)/d^{1.38} - 0.681 + 0.232 \log v_{ST} - 0.428 \log d \tag{28}$$

with the limit $\delta \geq -0.065\ v_{ST}$

For $v_{ST} > 10$,

$$\delta = (0.045 \log \mu_L)/d^{0.799} - 0.709 + 0.162 \log v_{ST} - 0.888 \log d \tag{29}$$

with the limit

$$\delta \geq -\frac{v_B}{v_{ST} + v_B}\left[1 - \frac{\rho_M}{\rho_L}\right]$$

Pressure drop due to friction is given by

$$\frac{dp_f}{dz} = \frac{f\rho_L v_{ST}^2}{2g_c d}\left[\left[\frac{v_{SL} + v_B}{v_{ST} + v_B}\right] + \delta\right] \tag{30}$$

The friction factor f is obtained from the Moody diagram using the Reynolds number given by Equation 23. The pressure drop due to acceleration in the slug flow regime is neglected.

Transition Flow (Duns and Ros, 1963)

In the transition flow regime, the total pressure gradient is obtained by linear interpolation between the slug and mist flow boundaries. The pressure gradient in the transition flow regime is then

$$\frac{dp}{dz} = M\left[\frac{dp}{dz}\right]_{slug} + (1-M)\left[\frac{dp}{dz}\right]_{mist} \tag{31}$$

where

$$M = \frac{L_{tm} - N_{GV}}{L_{tm} - L_{st}} \tag{32}$$

Mist Flow (Duns and Ros, 1963)

The gas phase is continuous in this flow regime. The slip velocity is assumed to be zero; that is, homogeneous flow. The mixture density is given by

$$\rho_M = \rho_L\ v_{SL}/v_{ST} + \rho_G\ v_{SG}/v_{ST} \tag{33}$$

The frictional pressure drop is calculated as:

$$\frac{dp_f}{dz} = \frac{f\rho_G\ v_{SG}^2}{2g_c d} \tag{34}$$

The friction factor f is obtained from the Moody diagram and the Reynolds number defined by

$$N_{Re} = \frac{1488\ \rho_G\ v_{SG}\ d}{\mu_G} \tag{35}$$

A modified relative roughness factor (e/d) is calculated to be used with the Moody diagram. This is done to take into account the effect of the liquid film on the pipe.

Pressure drop due to acceleration is given by

$$\frac{dp_a}{dz} = \frac{v_{ST}\ v_{SG}\ \rho_M}{g_c P}\left[\frac{dp}{dz}\right] \tag{36}$$

WELLBORE SIMULATOR

The wellbore simulator used in our work is that of Fandriana *et al.* (1981) and Ortiz-R. (1983). It is based on the Orkiszewski (1967) recommended flow regimes and pressure drop correlations. The computer code is written such that we can start the calculations from the wellhead or wellbottom. We divide the wellbore into segments and calculate the pressure drop due to friction, gravity, and acceleration. To calculate the frictional pressure drop, the casing roughness needs to be specified. The heat transfer to/from the wellbore can also be calculated. We specify the geothermal gradient and the overall heat transfer coefficient, which are then used to calculate the heat loss/gain between each wellbore segment and surrounding formation. Thermodynamic properties used in the computer code are from steam tables. However, when calculating the density of liquid water, its salinity is included. The effect of non-condensible gases is not included in our simulator.

SUMMARY

Most of the geothermal wells tested in our companion paper (Ambastha and Gudmundsson, 1986), flowed in the slug flow regime, as shown in Figure 3. As reported in the companion paper (Ambastha and Gudmundsson, 1986), we obtained not-so-good matches for some of the wells, and those wells also fall in the slug flow regime. Therefore, further research for geothermal two-phase flow applications should be directed towards the slug flow regime.

ACKNOWLEDGMENTS

This work was supported by the Stanford Geothermal Program, through contract DE-AT03-80SF11459 with the U.S. Department of Energy. This work was carried out in cooperation with CFE in Mexico, METU in Turkey, and MWD in New Zealand.

NOMENCLATURE

A	Pipe inside area, sq. ft.
A_G	Pipe area occupied by gas, sq. ft.
C_1–C_2	Parameters to calculate bubble rise velocity
d	Pipe inside diameter, ft
e	Absolute pipe roughness, ft
f	Moody friction factor
G_M	Total mass flux, lbm/sec- ft^2
g	Acceleration due to gravity, 32.2 ft/ sec^2
g_c	Conversion constant, 32.2 lbm-ft/lbf- sec^2
H_L	Liquid holdup, fraction
$L_{b/s}$	Bubble-slug boundary term
$L_{s/t}$	Slug-transition boundary term
$L_{t/m}$	Transition-mist boundary term
M	Parameter defined by Eq. 32
N_D	Pipe diameter number
N_{GV}	Gas velocity number
N_{LV}	Liquid velocity number
N_{Re}	Reynolds number
N_{ReB}	Bubble Reynolds number
N_{ReL}	Liquid Reynolds number
P	Pressure, psf
dp_a/dz	Acceleration pressure gradient, psf/ft
dp_f/dz	Frictional pressure gradient, psf/ft
dp_g/dz	Gravitational pressure gradient, psf/ft
S	Wetted Perimeter, ft
v_B	Bubble rise velocity, ft/sec
v_{ST}	Total superficial velocity, ft/sec
v_{SG}	Superficial gas velocity, ft/sec
v_{SL}	Superficial liquid velocity, ft/sec
z	Vertical length, ft

Greek symbols

α	Void fraction
δ	Liquid distribution coefficient
μ_G	Gas viscosity
μ_L	Liquid viscosity
μ_M	Mixture viscosity
ψ	Parameter defined by Eq. 27
ρ_G	Gas density, lbm/ ft^3
ρ_L	Liquid density, lbm/ ft^3
ρ_M	Mixture density, lbm/ ft^3
σ	Interfacial tension, dynes/cm
τ	Wall shear stress, dynes/ cm^2
θ	Inclination angle, radian

REFERENCES

Ambastha, A.K. and Gudmundsson, J.S.:"Pressure Profiles in Two-Phase Geothermal Wells: Comparison of Field Data and Model Calculations," Proc., 11th Workshop on Geothermal Reservoir Engineering, Stanford U., Stanford, CA (Jan. 21-23, 1986).

Brill, J.P. and Beggs, H.D.:"Two-Phase Flow in Pipes," Univ. of Tulsa (Dec. 1977).

Chierici, G.L., Ciucci, G.M. and Sclocchi, G.:"Two-Phase Vertical Flow in Oil Wells - Prediction of Pressure Drop," J. Pet. Tech. (Aug. 1974) 927-938.

Duns, H., Jr. and Ros, N.C.J.:"Vertical Flow of Gas and Liquid Mixtures in Wells," Proc., 6th World Pet. Congress (1963) 451-465.

Fandriana, L., Sanyal, S.K. and Ramey, H.J., Jr.:"A Numerical Simulator for Heat and Fluid Flow in a Geothermal Well," Pet. Eng. Dept., Stanford U., Stanford, CA (1981).

Gould, T.L.:"Vertical Two-Phase Steam-Water Flow in Geothermal Wells," J. Pet. Tech. (Aug. 1974) 833-842.

Griffith, P. and Wallis, G.B.:"Two-Phase Slug Flow," J. Heat Transfer; Trans. , ASME (Aug. 1961) 307-320.

Hagedorn, A.R. and Brown, K.E.:"Experimental Study of Pressure Gradients Occurring During Continuous Two-Phase Flow in Small-Diameter Vertical Conduits," J. Pet. Tech. (April 1965) 475-484.

Miller, C.W.:"Numerical Model of Transient Two-Phase Flow in a Wellbore," Lawrence Berkeley Laboratory, LBL-9056 (Oct. 1979) Berkeley, CA.

Mitchell, R.F.:"Advanced Wellbore Thermal Simulator GEOTEMP2" Sandia National Laboratory, Report SAND82-7003/1 (Feb. 1982).

Nathenson, M.:"Flashing Flow in Hot-Water Geothermal Wells," J. Research U.S. Geological Survey (Nov.- Dec. 1974) 743-751.

Orkiszewski, J.:"Predicting Two-Phase Pressure Drops in Vertical Pipe," J. Pet. Tech. (June 1967) 829-838.

Ortiz-R., J.: "Two-Phase Flow in Geothermal Wells: Development and Uses of a Computer Code," Stanford Geothermal Program, Report SGP-TR-66 (June 1983).

Ros, N.C.J.:"Simultaneous Flow of Gas and Liquid as Encountered in Well Tubing," J. Pet. Tech. (Oct. 1961) 1037-1049.

Upadhyay, R.N., Hartz, J.D., Tomokoria, B.N. and Gulati, M.S.:"Comparison of the Calculated and Observed Pressure Drops in Geothermal Wells Producing Steam-Water Mixtures," SPE of AIME, Paper SPE 6766, 52nd Annual Fall Tech. Conf. and Exhibition, Denver, CO., (Oct. 9-12, 1977).

PROCEEDINGS, Eleventh Workshop on Geothermal Reservoir Engineering
Stanford University, Stanford, California, January 21-23, 1986
SGP-TR-93

EVALUATION OF POROUS MEDIUM PERMEABILITY BY ACOUSTIC LOGGING FINDS GEOTHERMAL APPLICATIONS

B. CONCHE (1), F. LEBRETON (2), J. ROJAS (3)

(1) IPG - Institut de Physique du Globe de Strasbourg
(2) IFP - Institut Français du Pétrole, Rueil-Malmaison
(3) BRGM - Bureau de Recherches Géologiques et Minières, Orléans

ABSTRACT

In a well, after an acoustic waveform has circulated through the surrounding porous media, the study of its alteration can help in evaluating their permeability.

The treatment of the acoustic compressional wave's first three cycles yields a unique parameter called I-c.

The recording of this I-c log all along any open hole interval is now possible by respecting some practical rules known by logging companies.

Large flows of fluid found in geothermal low-enthalpy operations have provided an opportunity to check the validity of this method.

Cumulative I-c derived permeability with depth ("EXAFLO" log) correlates with the flowmeter log, as examples will show.

Some new aspects of the theory underlying the I-c/permeability relationship have been developed and are described here.

INTRODUCTION

Geothermal resources are now recovered by fluids circulating through wells drilled down to favourable porous permeable reservoirs. Whatever the exact process used for circulation on the site and for the engineering requirements, the permeability values of the rocks crossed through have to be known by direct or indirect measurements. A direct permeability measurement can be made in the lab on a core taken from the subsurface. Even in the oversimplified case of an infinite continuous homogeneous bed the core measurement value is not always equal to the corresponding in situ value because full downhole conditions are difficult to reproduce in the lab. On the contrary if determined by well logging the in situ rock permeability measurements will be representative since they are made on radially continuous media. Even borehole effects on permeability may be evaluated.

Since well logging is performed at regular depth intervals in vertically heterogeneous media, the corresponding volume of investigation is also heterogeneous. But a permeability log will integrate vertically overlapping values whose continuous variations will then reflect actual permeability variations better than a discrete core measurement profile. Of course the direction along which the logging measurement is made will have to be specified.

A logging method suited for a permeability measurement will surely have to put the various saturating fluids and the matrix into measurable relative motion. To date neither electric, nor radioactivity nor nuclear magnetic resonance logs can create a noteworthy relative fluids-matrix motion. Among all other available logging methods, acoustics seems to be the most apt for creating and detecting these relative motions.

Production logging tools, such as the spinner flowmeter (in the high permeability range) and shale indicators such as the natural gamma ray log (in the low permeability range) will be useful calibrators for checking any valid permeability log.

OJECTIVE

We propose to study acoustic logs derived from body waves having traveled into the rocks around the borehole. Surface waves have an undetermined (if any) volume of investigation in the rock around the borehole and are, for that reason, kept outside the scope of our paper.

CURRENT ACOUSTIC LOGGING TOOLS

A pressure wave is regularly emitted in the borehole liquid mud. It propagates by refraction in the surrounding media. Pressure signals are then reemitted into the mud and detected.

P-wave velocity logging has been practised since ca.1950. Starting in 1962 research has been performed on the wavetrains obtained

with a number of tools. S-wave velocity logs are now currently run with long-spacing tools.

The transducers are either magnetostrictive scrolls or ceramic cylinders (1" to 3" diameter). The waveforms are received at a few feet from the transmitter. In view of the well radius (a few inches) and of the spacing length (a few feet), transducers may be considered as pinpoint devices. According to the transducer type, the emitted signal modal frequency is comprised between 10 and 30 kHz. The signal is recorded at about every half-foot of depth and digitized at least every 4 microseconds.

METHOD

The successive steps of our study will comprise :

1. A mathematical modeling of the signal, showing the importance of certain parameters,
2. A physical theory attempting to describe the actual permeable medium behaviour when traversed by an acoustic vibration,
3. A number of examples where logging vs. direct permeability comparisons are shown.

1. MATHEMATICAL MODEL

Spot acoustic probes are placed on the axis of a liquid-filled cylinder surrounded by an infinite elastic solid. However to make the model more realistic, the receiver may be, in the following equations, eccentered on the borehole side. Permeability occurrence in the medium will be modeled by open fractures with given apertures.

For this model complete formalism was developed by B. Conche(1) who quotes earlier literature on the topic(2).

The wave induced displacement $\vec{U}$ obeys the Navier equations. When $\vec{U}$ is written in terms of potential the wave equations are :

$$\Delta\Phi = \frac{1}{V_p^2} \cdot \frac{\partial^2\Phi}{\partial t^2}$$

with Φ = compression potential
V_p = P-wave velocity

$$\Delta\Psi = \frac{1}{V_s^2} \cdot \frac{\partial^2\Psi}{\partial t^2}$$

with Ψ = shear potential
V_s = S-wave velocity

In the Fourier domain (frequency, wavenumber) the cylindrical symmetry provides a simplification of these equations. Bessel functions can supply the analytical solutions to these equations. The source term is introduced as the P-wave direct propagation in the fluid, i.e. a particular solution.

Boundary conditions expressed on the circular wellbore help fix the constants in the solutions :

- radial stress and strain continuity,
- zero shear stress on the surface of the wellbore.

The transfer function simulating the rock is thus obtained analytically. When convolved with the source signal it will yield the synthetic seismogram.

Study of the P-wave received for a given source

The concept of a single peak pressure pulse (Dirac) as a source, is first considered. After such a peak has traveled in an attenuating medium, its response will be a typical wavelet decreasing with time, fig. 1.

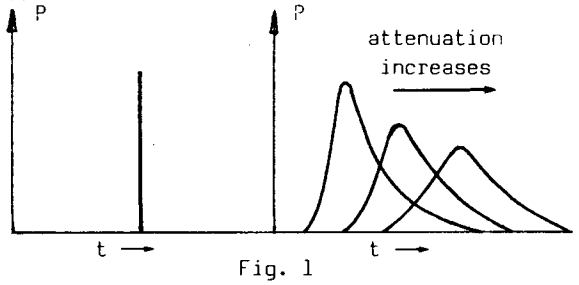

Fig. 1

Extension of this concept to any vibratory source signal focuses attention on the slope of the first amplitude. A plausible signature based on actual magnetostrictive scroll records will be found on fig. 2-26 and used in the rest of our model.

The effect of attenuation on the refracted P-wave is now the problem to be solved.

The parameter characterizing the P-wave signal must be chosen so that they are unaffected by the body wave interferences, i.e. picked up early enough in the first cycles of the P-wave.

We propose :

- the risetime (fig. 2-23), by definition it is the ratio of the first amplitude value over the slope at the inflexion point of the first rising branch of the signal,
- I-c index(3) (fig. 2-22), which is the ratio of the first two inflexion slopes with same polarity found on the P-wave.

These two parameters are apt to be altered by attenuation imposed on the signal, which in turn, is related, one way or another, to the permeability (if any) of the medium. The same parameters could be extracted from the S-wave, using special logging tools and processes (not treated here).

An attenuation-frequency relationship will now be imposed on the parameter calculation. The amplitude spectra will also be computed.

Results :

A Model with no intrinsic attenuation : see colunm 0 on the table I

B Model with attenuation. Here the attenuation is taken as an exponential function decreasing with the square of frequency.

The absorbed energy is modeled as a relative solid-fluid motion. The signal makes the solid drag the viscous fluid acting in VOIGT viscous-elastic model and governed by the DARCY's law.

For these signals the quality factor "Q" may be written as a function of the fracture equivalent aperture "l".

$$Q = 2\pi \frac{W}{\Delta W} = \frac{12\,\mu\,\rho_{solid}}{\rho^2_{liquid} \times l^2} \times \frac{1}{\omega}$$

For three different apertures of these fractures, the attenuated signals are represented on table I.

fracture aperture (in μ)	0	100	200	300
rise time (in μs)	6.6	7.4	11.2	16.3
I-c (dimensionless)	3.7	4.2	6.5	9.6
attenuation (fig)(2)		(40)	(43)	(46)
spectrum (fig)(2)	(27)	(41)	(44)	(47)
signal (fig)(2)	(26)	(42)	(45)	(48)

TABLE I

Both risetime and I-c increase with fracture apertures, i.e. with equivalent permeabilities.

A quite close model was used by Toksöz et al. (1984)(4) in which every factor, such as P-wave velocity and quality factors Q_p and Q_S were kept constant, but the S-wave velocity, i.e. the Poisson coefficient. For a Poisson coefficient varying from 0.22 to 0.37, I-c remains practically unchanged (6 to 7). This suggests that I-c for a given attenuation, (i.e. in the model for a given permeability) is largely independant of any lithology and porosity effects.

2. PHYSICAL THEORY

Porosity

A permeable medium always has a certain porosity though sometimes quite small ($\sim$ 0.001). If only made up of one-directional fractures the permeability will vary from very large in the fracture direction to almost nil in a perpendicular direction.

When the fractures have any direction or when the porosity is intergranular, the permeability value will be less affected by its direction.

A microscopic examination shows that even a so-called intergranular porosity is made up of voids of any shape. Their dimension ratios are rather high as in fractures. For the relative solid/fluids motion induced by acoustic signals, the intergranular porosity can thus be considered as an accumulation of random interconnected fractures.

Saturating fluids

Water is the basic fluid impregnating the whole porosity found in sediments. 95 % of this water is of meteoric origin. It is trapped in the sediments with a certain amount of atmospheric gases adsorbed on the matrix surface or dissolved in the water itself. This water reacts with the minerals making up the sediments. Depending on temperature, pressure and concentrations, the resulting connate water will reach an equilibrium. In some reservoirs oil and organic gases expelled from source rocks may displace the connate water but a fraction of it always remains in the porosity. For example a 4 to 17 % content of dissolved organic gases was found in the Paris basin geothermal reservoir porosity.

Among other gases found in the subsurface a special mention has to be made of argon and helium. For one thing Ar is trapped in connate water through atmospheric gases, but also because radiogenic processes continuously produce them from 40 K and U + Th. Now inert gases are less soluble in water than organic gases. H_2O-Ar concentration isotherms from 0 to 400 bars are represented in fig. 3. In the subsurface an additional solute content should lead us to estimate a still lower dissolved Ar fraction (see dotted curve 100°C). The cross-hatched region in fig. 3 is the one where liquid H_2O and gases coexist and where low-enthalpy geothermal reservoirs do occur.

Similar isotherms would be obtained for H_2O-He systems.

Experimental investigations of helium, argon and carbon in some natural gases

This study was performed on 39 samples of natural gases representing varying chemical composition and geological occurrences in the U.S.A. (1961)(5). Organic gases (CH^4, C^2H^6, CO^2) were found to represent from 50 to 98 % of the whole gas phases under surface conditions.

On figure 4 the volumetric concentrations of (He+Ar) are plotted vs. the concentration of total organic gases for the above-studied samples. Average result for about 20 geothermal Dogger reservoirs (France) obtained by Fouillac (1984)(6) was added. (He+Ar) content is found to increase regularly when organic gases content decreases.

Then in situ, at equilibrium, a free gas phase of 1 %, or more, in volume is to be expected in the connate water or in the mud-filtrate having invaded the drilled formations.

P-wave effect on the liquid-gas system in a porous medium

This free gas (bubbles or layers spread over the matrix surface) contributes to the attenuation of body waves traversing the formation. When a P-wave starting with a depression reaches a given depth in a porous formation, the gas-filled volume cannot increase if the surrounding uncompressible liquid cannot move, i.e. if there is no permeability at this depth.

On the contrary if there is a local permeability, the uncompressible liquid can move and the gas volume can increase. The greater the permeability, the more energy is absorbed from the P-wave for a given liquid of viscosity μ .

In view of the bubble or adsorbed layer size, the energy absorbed by the gas comes from the high frequency part of the signal spectrum. This intrinsic attenuation (A_i) adds up to the geometrical attenuation (A_g) :

$$\text{total attenuation} = (A_i).(A_g)$$

In the signal the positive pressure branch following immediately this first depression will tend to reduce the bubble, but the energy it has absorbed is not returned to the P-wave.

The second depression will now act from a somewhat different and weaker P-wave signal, cleared from a part of high-frequency, and the bubble size will not be so affected.

As the rock investigated volume and borehole section are the same in the two successive depressions, the geometrical attenuations (A_g) (independent of frequency) will be common for both cases.

This factor (A_g) covers the borehole effects (wellsize, mud-cake) and the solid-solid friction which varies with the lithology.

On the received signal the rates of depression are representative of the energy absorbed by attenuation. In forming the ratio I-c of both amplitude slopes, the effect of the geometrical attenuation is cancelled.

A single-valued relationship is linking I-c and permeability for a given liquid viscosity. We propose

$$\text{I-c} = \alpha \log \frac{Kv}{\mu} + \beta \qquad (1)$$

suggested, among others functions, by correlations with direct data.

Kv : being the permeability evaluated along the well bore axis direction,

α, β : constants attached to given tool and signal,

μ : the dynamic viscosity of the liquid phase.

As, in a well, the rock lithology and the borehole geometry are continuously varying with depth, the risetime parameter cannot be retained as a useful measurement of frequency dependent attenuation or permeability.

3. EXAMPLES

1. Two geothermal wells were drilled few miles apart by the B.R.G.M. (1982) through the Dogger formation in the Paris basin.

The reservoir was found in a limestone whose an interval of about 150 m thickness is represented on fig. 5.

Most of this interval is non-shaly and very porous ($20\ \% < \phi < 30\ \%$) as can be seen from the Neutron log. Core examination confirmed these properties. However only limited thickness intervals are actually water-producing as it can be inferred from the study of the spinner flowmeter log. The I-c log is showing some high values, i.e. some permeable intervals, but, at first glance, correlation with the flowmeter log is not evidently quantitative.

Cumulation of I-c derived permeability should yield a pseudo-flowmeter log, insofar as the reservoir pressure remains constant.

Here this cumulative permeability log (EXAFLO) is made from total depth up to casing shoe. For one of these wells, they will be found on fig. 5.

Correlation between both profiles is satisfactory. Permeability measurements derived from the flowmeter log may then confidently be used for calibrating the I-c log.

This calibration should prove valid for other I-c logs run with the same acoustic tool.

o
o o

The two following examples are relative to sand and shale formations.

Crouy 12 and Crouy 26 were drilled by Gaz de France (1982) through the aquifer sand of the Wealden formation (Paris basin) in view of extending an inderground gas storage. I-c log was run in both wells.

2. Crouy 26 (fig. 6). Over the 890-980 m interval I-c varies from 3 to 41. The histogram of I-c shows a number of modes which can be interpreted in the following way:

$3 < I\text{-}c < 10$ shale to shaly sands

$10 < I\text{-}c < 20$ clean sands

$22 < I\text{-}c < 41$ highly permeable coarse sands

Cumulative I-c (EXAFLO) singles out the upper part of the interval (890-923 m) as productive and/or injectable.

A similar interval is found from 942 to 950 m. These interpretations have been confirmed by tests. Flowmeter log was not run.

3. Crouy 12 (890-940 m). Direct permeability measurements are only known from plugs taken on recovered cores. Values spread from 1 to 10,000 millidarcy, fig. 7.

Apparently the upper part of this aquifer would be considered as highly favorable for gas injection. Now I-c log, run with the same tool as the one used for example (2) over the same formation, does not show values over 10, corresponding to a cut-off permeability in the example of Crouy 26.

Indeed CR-12 was eventually cased and the annulus was cemented, for further use as a surveillance well of the underground storage.

Starting in 1983, checks on gas content around CR-12 are regularly made by running of Gaz de France Neutron logs (fig. 7). To date no gas breakthrough was ever noticed within the investigated zone around CR-12. This fact does confirm that this sand-shale sequence is not permeable at CR-12 as I-c log had already shown it.

CONCLUSION

The first publication about I-c was made in 1978(3). As a permeability log derived from the computer treatment of acoustic waveforms, it was then used in geothermal wells in the Paris basin (1982). Its presentation is regularly improved and completed.

Mathematical models and physical theories are continuously adapted for better investigating the domain of this new logging method.

Large flows of fluid found in geothermal operations checked the validity of this method.

Low permeability shaly sands were correctly analysed.

For a given acoustic tool its calibration does not seem to vary with lithology or borehole variations.

REFERENCES

(1) CONCHE B., Apport des diagraphies dans l'identification de la fracturation, Mémoire IPG, Strasbourg, 1985.

(2) TSANG, RADER, Numerical evaluation of transient acoustic waveform due to a point source in a fluid-filled borehole, Geophysics, vol. 44, n° 10, october 1979.

(3) LEBRETON, SARDA, TROCQUEME, MORLIER, "Logging tests in porous media to evaluate the influence of their permeability on acoustic waveforms", SPWLA, El Paso, 1978.

(4) TOKSOZ, WILKENS, CHENG, Determination of shear wave velocity and attenuation from waveforms in low-velocity formation, M.I.T. (1984).

(5) ZARTMAN R.E., WASSERBURG G.J., REYNOLDS J.H., Journal of Geophysical Research vol. 66, n° 1, 1961.

(6) FOUILLAC C., GOYENECHE O., LOMBART R., SPITERI P., Hydrogéologie-Géologie de l'Ingénieur, n° 1, 1984.

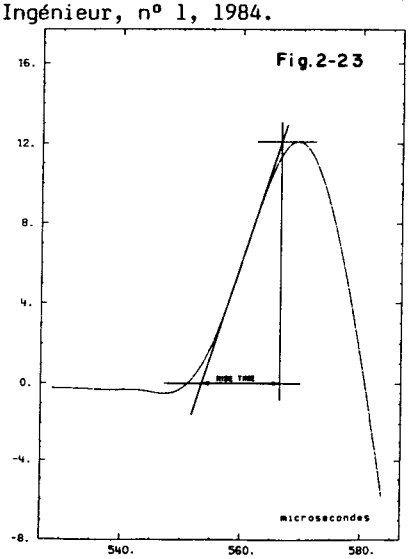

définition du " rise time " ou temps de montée : rapport de l'amplitude de la première crête sur la tangente au point d'inflexion de la première branche ascendante du signal

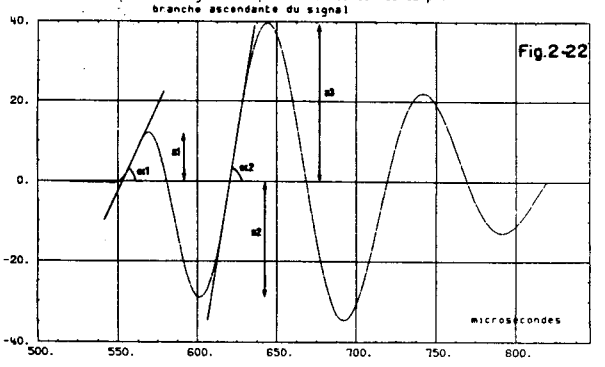

définition de l'indice ic :
- par les amplitudes (en valeurs absolues) : (a2+a3)/a1
- par les tangentes : Tang(alpha2)/Tang(alpha1)

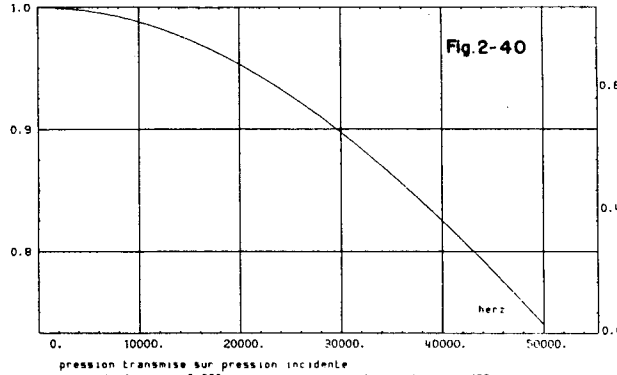

pression transmise sur pression incidente
rayon du forage = 0.080 m epaisseur de la fracture = 100. microns
d1=1050.kg/m3 vp1=1600.m/s d2=2600.kg/m3 vp2=5800.m/s vs2=3400.m/s

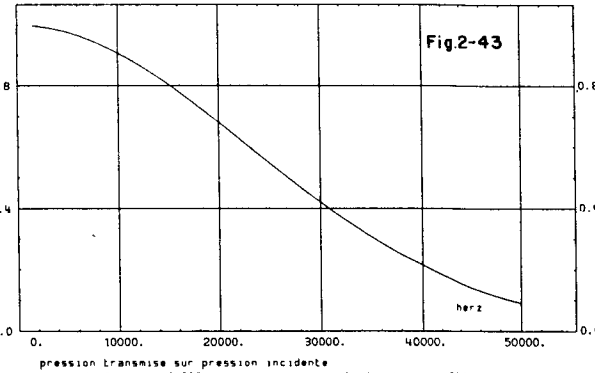

pression transmise sur pression incidente
rayon du forage = 0.080 m epaisseur de la fracture = 200. microns
d1=1050.kg/m3 vp1=1600.m/s d2=2600.kg/m3 vp2=5800.m/s vs2=3400.m/s

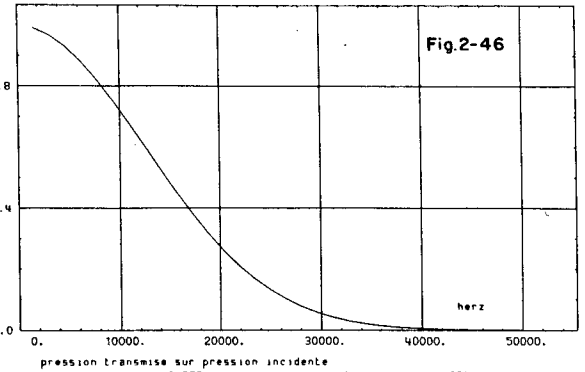

pression transmise sur pression incidente
rayon du forage = 0.080 m epaisseur de la fracture = 300. microns
d1=1050.kg/m3 vp1=1600.m/s d2=2600.kg/m3 vp2=5800.m/s vs2=3400.m/s

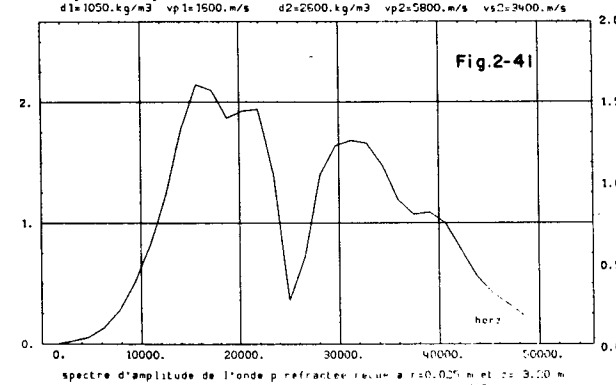

spectre d'amplitude de l'onde p refractee recue a r=0.025 m et z= 3.20 m
rayon du forage = 0.080 m epaisseur de la fracture = 100. microns
d1=1050.kg/m3 vp1=1600.m/s d2=2600.kg/m3 vp2=5800.m/s vs2=3400.m/s

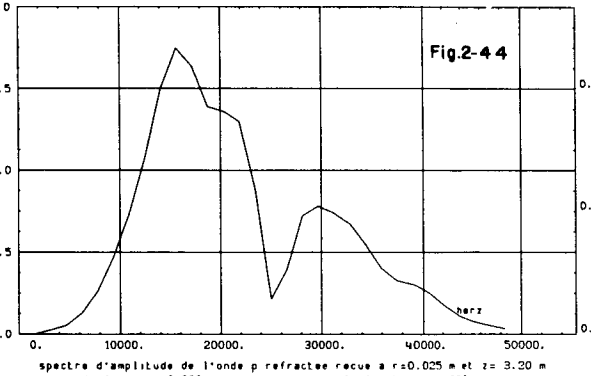

spectre d'amplitude de l'onde p refractee recue a r=0.025 m et z= 3.20 m
rayon du forage = 0.080 m epaisseur de la fracture = 200. microns
d1=1050.kg/m3 vp1=1600.m/s d2=2600.kg/m3 vp2=5800.m/s vs2=3400.m/s

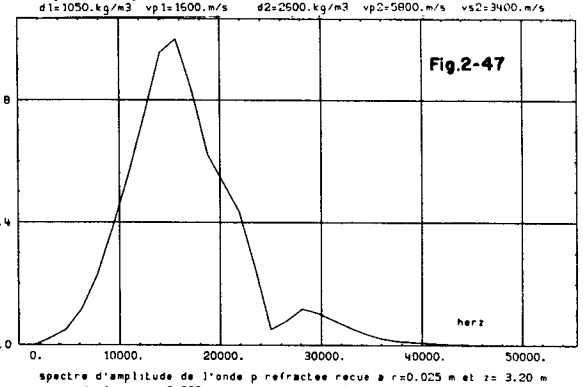

spectre d'amplitude de l'onde p refractee recue a r=0.025 m et z= 3.20 m
rayon du forage = 0.080 m epaisseur de la fracture = 300. microns
d1=1050.kg/m3 vp1=1600.m/s d2=2600.kg/m3 vp2=5800.m/s vs2=3400.m/s

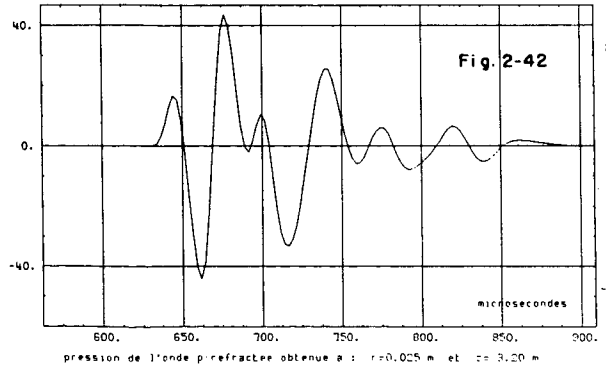

pression de l'onde p refractee obtenue a : r=0.025 m et z= 3.20 m
rayon du forage = 0.080 m epaisseur de la fracture = 100. microns
d1=1050.kg/m3 vp1=1600.m/s d2=2600.kg/m3 vp2=5800.m/s vs2=3400.m/s
ic(pics)= 5.3 ic(tangentes)= 4.2 rise time= 7.4 microsecondes

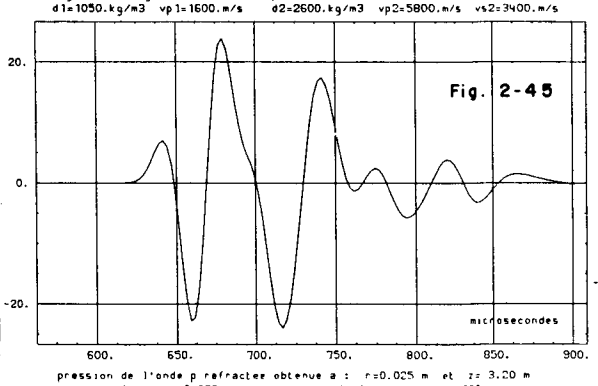

pression de l'onde p refractee obtenue a : r=0.025 m et z= 3.20 m
rayon du forage = 0.080 m epaisseur de la fracture = 200. microns
d1=1050.kg/m3 vp1=1600.m/s d2=2600.kg/m3 vp2=5800.m/s vs2=3400.m/s
ic(pics)= 6.7 ic(tangentes)= 6.5 rise time=11.2 microsecondes

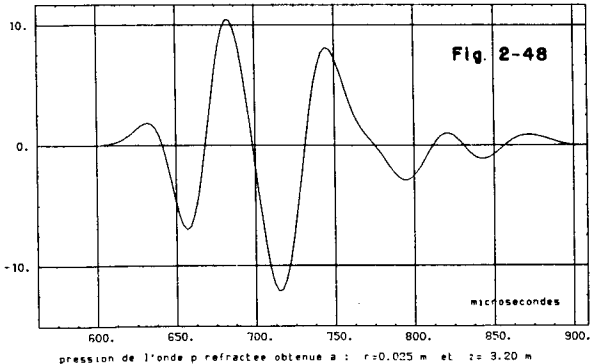

pression de l'onde p refractee obtenue a : r=0.025 m et z= 3.20 m
rayon du forage = 0.080 m epaisseur de la fracture = 300. microns
d1=1050.kg/m3 vp1=1600.m/s d2=2600.kg/m3 vp2=5800.m/s vs2=3400.m/s
ic(pics)= 9.4 ic(tangentes)= 9.6 rise time=16.3 microsecondes

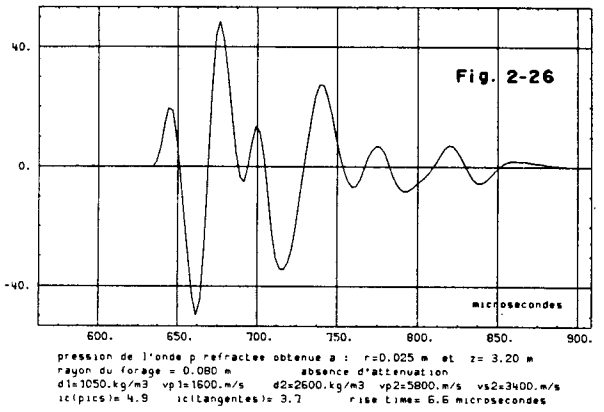

pression de l'onde p refractee obtenue a : r=0.025 m et z= 3.20 m
rayon du forage = 0.080 m absence d'attenuation
d1=1050.kg/m3 vp1=1600.m/s d2=2600.kg/m3 vp2=5800.m/s vs2=3400.m/s
ic(pics)= 4.9 ic(tangentes)= 3.7 rise time= 6.6 microsecondes

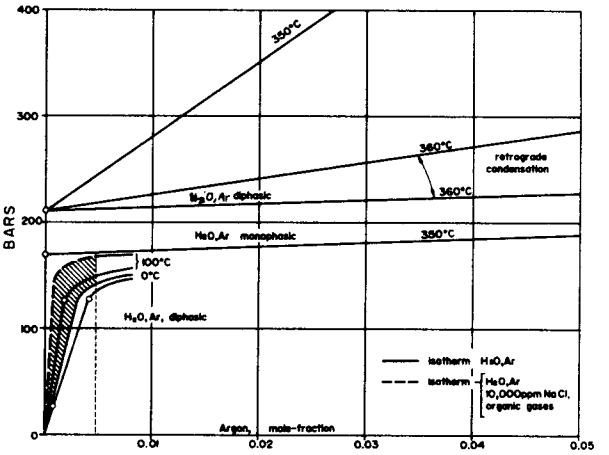

Fig:3- after International Union of Pure and Applied Chemistry Solubility data Series.

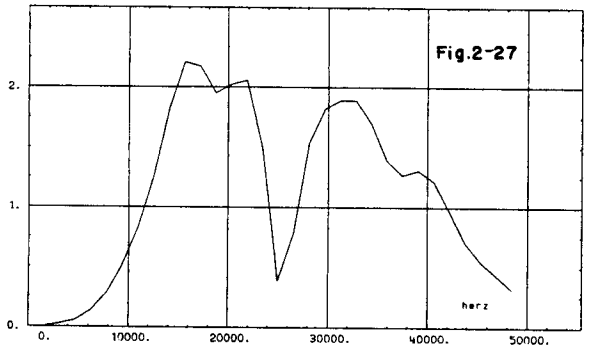

spectre d'amplitude de l'onde p refractee recue a r=0.025 m et z= 3.20 m
rayon du forage = 0.080 m absence d'attenuation
d1=1050.kg/m3 vp1=1600.m/s d2=2600.kg/m3 vp2=5800.m/s vs2=3400.m/s

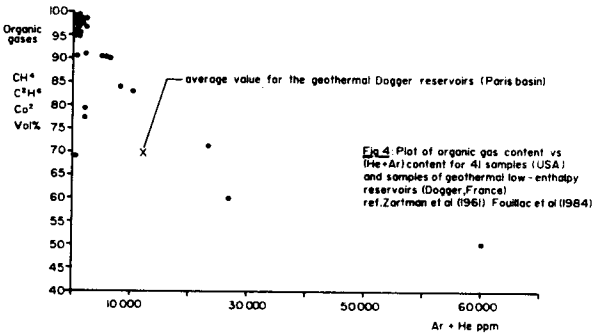

Fig.4 Plot of organic gas content vs (He+Ar) content for 41 samples (USA) and samples of geothermal low-enthalpy reservoirs (Dogger, France) ref. Zartman et al (1961) Fouillac et al (1984)

Fig5: AULNAY - SOUS - BOIS

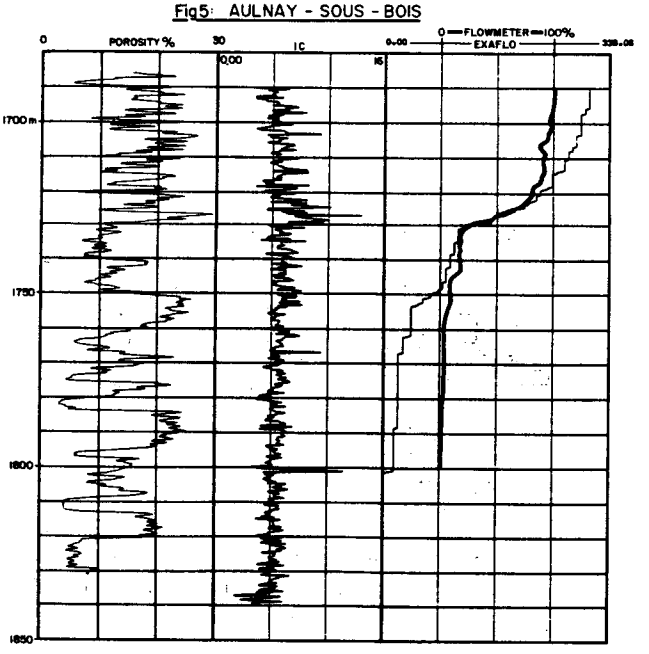

PUITS CR-26 (Gaz de France)

INDICE IC EXAFLO

Fig. 6

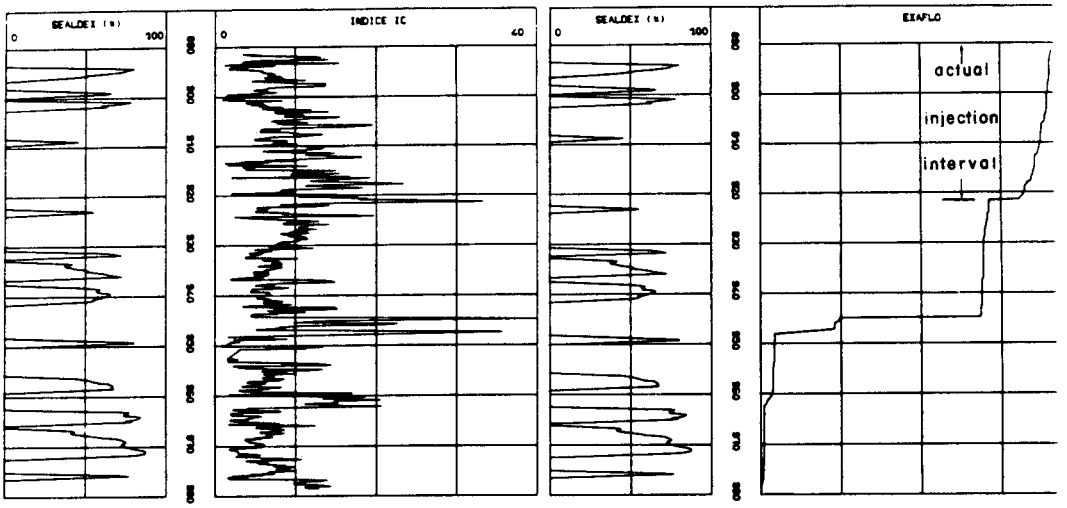

CROUY 12 (GAZ DE FRANCE)

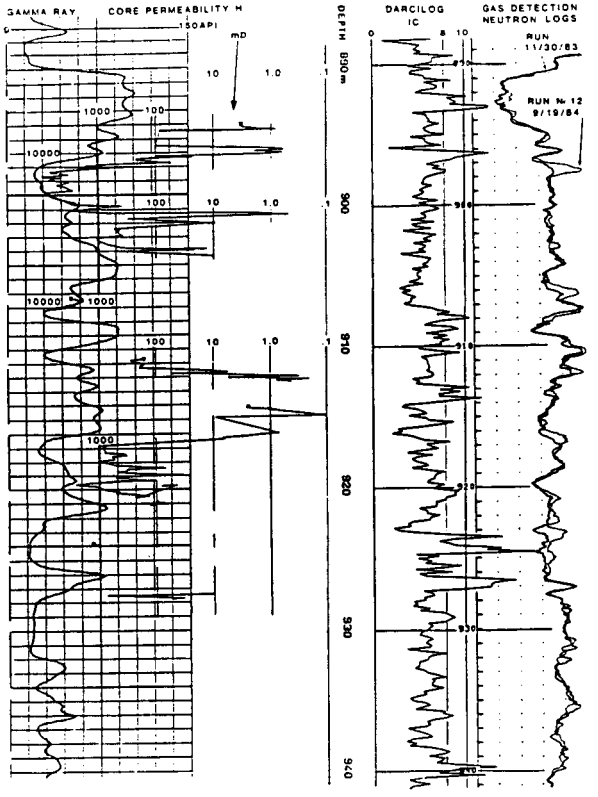

Fig. 7 - NO SIGNIFICANT GAS CONTENT IS DETECTED AROUND THIS SURVEILLANCE WELL DRILLED TROUGH AN UNDERGROUND GAS STORAGE

ELEVENTH WORKSHOP ON GEOTHERMAL RESERVOIR ENGINEERING

Participants' List

Michael C. Adams
ESL/UURI
391-A Chipeta Way
Salt Lake City, UT 84108

Jong-Heon Ahn
University of Utah Research Institute
1114 University Village
Salt Lake City, UT 84108

Greg Anderson
Unocal
Union Science and Technology
376 S. Valencia
Brea, CA 92621

Victor Arellano
IIE
APDO Postal #475
Cuernavaca, Mexico

Paul G. Atkinson
Unocal
2099 Range Avenue
Santa Rosa, CA 95401

Michael L. Barnes
District Engineer
Unocal Geothermal Division
81-711 Highway 111
Indio, CA 92201

Brian Barnett
Geothermal Energy N.Z. Ltd.
P.O. Box 37-231, Parnell
Auckland, New Zealand

A. S. Batchelor
Camborne School of Mines
Geothermal Energy Project
Rosemanowes Quarry, Herniss
Penryn, Cornwall, England

G. W. Beecroft
State Board of Equalization
2513 Corona Drive
Sacramento, CA 95814

Phil Beilin
U.S. Geological Survey
345 Middlefield Road, M/S 439
Menlo Park, CA

Sally Benson
Lawrence Berkeley Lab.
Building 50E
Berkeley, CA 94720

Dennis Bird
Geology Department
Stanford University

Bobbie Bishop
Geology Department
Stanford University

Paul Bixley
Ministry of Works
Wairakei, New Zealand

Bjornsson, G.
Lawrence Berkeley Laboratory
Earth Sciences Division, Bldg. 50E
One Cyclotron Road
Berkeley, CA 94720

Melissa Blanton, Editor
Geothermal Report
P.O. Box 1787
Alameda, CA 94501

A. R. Bobar
Calif. State Lands Commission
245 West Broadway, #425
Long Beach, CA 90802

Gudmunder Bodvarsson
Lawrence Berkeley Laboratory
Earth Sciences Division, Bldg. 50E
One Cyclotron Road
Berkeley, CA 94720

W. T. (Tom) Box, Jr.
Geysers Geothermal Co.
P.O. Box 11279
Santa Rosa, CA 95406

W. E. Brigham
Petroleum Engineering Department
Stanford University

Paul Brophy
California Energy Co., Inc.
3333 Mendocino Ave., Suite 100
Santa Rosa, CA 95406

Myron Burr
Union Oil Co. of California
2099 Range Avenue
Santa Rosa, CA 95406

Charles R. Carrigan
Geophysics Division 1541
Sandia National Laboratories
P.O. Box 5800
Albuquerque, New Mexico 87185

Louis Castanier
Petroleum Engineering Department
Stanford University

Kenneth Y. Chan
BLM - Sacramento
9 Mossbeach Ct.
Sacramento, CA 95831

Chieh Chu
Texaco, Inc.
Texaco Houston Research Center
3901 Briarpark
Houston, TX 77042

Tze Yao Chu
Division 6242
Sandia National Laboratories
P.O. Box 5800
Albuquerque, New Mexico 87185

Tom Clemo
Idaho National Engineering Lab.
P.O. Box 1625
Idaho Falls, ID 83415

Joseph G. Colosi
Harold W. Bertholf, Inc.
2775 Cottage Way, Suite 10
Sacramento, CA 95828

Jim Combs
Geothermal Resources Int'l, Inc.
1825 South Grant Street, Suite 900
San Mateo, CA 94402-2663

John Copp
Unocal
2099 Range Avenue
P.O. Box 6854
Santa Rosa, CA 95406

Richard E. Corbaley
California Division of Oil and Gas
485 Broadway, Suite B
El Centro, CA 92243

Herlander Correia
Manager of Geothermal Division
Compagnie Francaise de Geothermie
P.O. Box 6429
45064 Orleans
Cedex, France

John Counsil
Petroleum Engineering Department
Stanford University

B. Lea Cox
Lawrence Berkeley Lab.
One Cyclotron Road, Bldg. 50E
Berkeley, CA 94720

Harrison Crecraft
Unocal
2099 Range Avenue
Santa Rosa, CA 95401

Charles L. Crockett
Geysers Geothermal Company
P.O. Box 11279
Santa Rosa, CA 95406

Claudio Descalzi
AGIP S.p.A.
Via Bonarelli - S. Donato Milanese
P.O. Box 12069 - 20100 Milano

Richard F. Dondanville
Unocal
P.O. Box 6854
Santa Rosa, CA 95406

Andy Drenick
GEO Operator Corp.
1330 N. Dutton
Santa Rosa, CA 95401

Herman Dykstra
Petroleum Engineering Department
Stanford University

Kathleen L. Enedy
Geysers Geothermal Company
P.O. Box 11279
Santa Rosa, CA 95405

Steve Enedy
Unocal
2099 Range Avenue
Santa Rosa, CA 95406

Richard Estabrook
Bureau of Land Management
P.O. Box 940
Ukiah, CA 95482

David D. Faulder
Chevron Geothermal Co.
595 Market St., Room 2555
San Francisco, CA

James Ferguson
Massachusetts Institute of Technology
Department of Chemical Engineering, 66-418
Cambridge, MA 02139

Craig Forster
University of British Columbia
Dept. of Geological Science
University of British Columbia
Vancouver, B.C. Canada

Robert O. Fournier
U.S. Geological Survey
345 Middlefield Rd., M/S 910
Menlo Park, CA 94025

David T. Gambill
Unocal
2099 Range Ave
Santa Rosa, CA 95406

Scott Gaulke
Lawrence Berkeley Lab.
Earth Sciences Div., Bldg. 50E
One Cyclotron Road
Berkeley, CA 94720

Norman Goldstein
Lawrence Berkeley Lab., Bldg. 50E
One Cyclotron Road
Berkeley, CA 94720

J. S. Gudmundsson
National Energy Authority
Reykjavik, Iceland

Antonio Guidi
AGIP S.P.A.
20097 San Donato Milanese
Milan Italy

Mohinder Gulati
Union Oil Co. of California
2099 Range Avenue
Santa Rosa, CA 95406

Jill Haizlip
GEO Operator Corp.
2300 County Center Dr., Suite 250
Santa Rosa, CA 95401

Susan E. Halfman
Lawrence Berkeley Laboratory
Earth Science Division M/S 50E
One Cyclotron Road
Berkeley, CA 94720

Marjorie Hatter
Unocal
376 Valencia Avenue
Brea, CA 92621

Jeffrey Hebein
Thermal Power Company
3333 Mendocino Avenue, Suite 120
Santa Rosa, CA 95401

Viet T. Hoang
Chevron Resources
P.O. Box 7147
San Francisco, CA 94120-7147

Roland N. Horne
Petroleum Engineering Department
Stanford University

Atsushi Ibusuki
Japan Petroleum Exploration Co., Ltd.
Akasaka Twin Tower, East Wing
Akasaka 2-17-22, Minato-ku
Tokyo, 107, Japan

Eduardo R. Iglesias
IIE
Apartado Postal 475, Cuernavaca
Mor., Mexico

Steve Ingebritsen
U.S. Geological Survey
345 Middlefield Road
Menlo Park, CA 94025

Joe Iovenitti
Thermal Power Company
3333 Mendocino Avenue
Santa Rosa, CA 95401

Sharad Kelkar
Los Alamos National Lab
Los Alamos, NM 87545

Christopher W. Klein
GeothermEx, Inc.
5221 Central Avenue #201
Richmond, CA 94804

Paul Kruger
Civil Engineering Department
Stanford University

Mark Kumataka
Santa Fe Geothermal Inc.
3131 Turtle Creek Blvd., Suite 100
Dallas, Texas 75219

Erik B. Layman
AMOSEAS Indonesia, Inc.
Kotakpos No. 158
Jakarta, Indonesia

Jonathan Leaver
Petroleum Engineering Department
Stanford University

Steve Lipman
Unocal
2099 Range Avenue
Santa Rosa, CA 95401

Marcelo Lippmann
Lawrence Berkeley Lab.
Earth Sciences Division, Bldg. 50E
One Cyclotron Road
Berkeley, CA 94720

Carlos A. Lopez
California Energy Commission
1516 Ninth Street
Sacramento, CA 95814

Tom MacPhee
GEO Operator Corp.
2300 County Center Dr., Suite 250
Santa Rosa, CA 95401

Steven J. Maione
Unocal
2099 Range Avenue
Santa Rosa, CA 95406

Grasiano Manetti
ENEL-UNITA' Nazionale Geotermica
P.za.B. da Sassoferrato
n. 14-56100 Pisa, Italy

S. S. Marsden, Jr.
Petroleum Engineering Department
Stanford University

James R. McNitt
GeothermEx
5221 Central Avenue
Richmond, CA

M. G. Mefferd
Calif. Div. of Oil & Gas
1416 Ninth St., Room 1310
Sacramento, CA 95814

Will Menninger
Stanford University

Tony Menzies
GeothermEx
5221 Central Avenue, #201
Richmond, CA 94804

Cigni Michele
AGIP S.p.A.
C.P. 12069
20120 Milano

F. G. Miller
Petroleum Engineering Department
Stanford University

John Miller
INEL
Box 1625
Idaho Falls, ID 83415

Hideo Minowa
Japan Petroleum Exploration Co., Ltd.
Akasaka Twin Tower, East Wing
2-17-22, Minato-ku
Tokyo, 107, Japan

Richard A. Miram
PG&E
77 Beale Street, Room 1343
San Francisco, CA 94106

Ted Mock
U.S. Department of Energy
1000 Independence Ave., SW
Washington, D.C. 20585

Allen Moench
U.S. Geological Survey
345 Middlefield Road
Menlo Park, CA 94025

Phil Mogen
Unocal
2099 Range Avenue
Santa Rosa, CA 95406

Homayoun R. Moghaddam
Los Angeles Dept. of Water
and Power
111 N. Hope St., Room 1149
Los Angeles, CA 90012

Ing. Rafael Molinar-C.
Comision Federal de Electricidad
Morelia, Mich., C.P. 58270
Mexico

Martin W. Molloy
U.S. Department of Energy
San Francisco Operations Office
1333 Broadway
Oakland, CA 94612

Kent Murray
CSUS/CEC
1516 9th Street
Sacramento, CA 95814

Yoshihiko Nakai
Information and Math. Science Lab. Inc.
Daini Nishiwaki Bldg., 1558, Yoyog
Shibuyaku, Tokyo 151 Japan

Hamid V. Nejad
Los Angeles Department of Water and Power
111 No. Hope Street
Los Angeles, CA 90012

Gerald Niimi
Thermasource, Inc.
725 Farmers Lane
Santa Rosa, CA 95405

Ender Okandan
Middle East Technical University
Petroleum Engineering Dept.
Ankara, Turkey

Faruk Okandan
Homamciozlu TTAS
Ankara, Turkey

Kaneo Okazaki
Japan Petroleum Exploration Co., Ltd.
Akasaka Twin Tower, East Wing
Akasaka 2-17-22, Minato-ku
Tokyo, 107, Japan

Susan Petty
1563 Luneta Drive
Del Mar, CA 92014

Al S. Pingol
Unocal
2099 Range Avenue
Santa Rosa, CA 95401

Lynn Pittinger
Union Oil Co. of California
2099 Range Avenue
Santa Rosa, CA 95406

Susan M. Prestwich
U.S. Department of Energy
785 Doe Place
Idaho Falls, ID 83402

Charles P. Priddy
State Lands Commission
1807 13th Street
Sacramento, CA 95814

J. W. Pritchett
S-Cubed
P.O. Box 1620
La Jolla, CA 92038-1620

Alice Probst
Unocal
376 Valencia Avenue
Brea, CA 92621

Robert Prucha
Lawrence Berkeley Lab.
Bldg. 50E
Berkeley, CA 94720

Karsten Pruess
Lawrence Berkeley Lab.
One Cyclotron Road, Suite 50E
Berkeley, CA 94720

Peter M. Pyle
BGI
2000 Center St.
Berkeley, CA 94704

Greg Raasch
Union Oil Co. of Calif.
2099 Range Avenue
Santa Rosa, CA 95406

H. J. Ramey, Jr.
Petroleum Engineering Department
Stanford University

Marshall Reed
U.S. Department of Energy
CE-342
Washington, D.C. 20585

Joel L. Renner
EG&G Idaho, Inc.
WCB E-3, P.O. Box 1625
Idaho Falls, ID 83415

T. D. Riney
S-Cubed
P.O. Box 1620
La Jolla, CA 92038-1620

Bruce A. Robinson
Los Alamos National Lab., M/S J981
Los Alamos, NM 87545

Joel Robinson
Union Oil Co. of California
2099 Range Avenue
Santa Rosa, CA 95406

Ray Rotthermel
State Board of California
(State Board of Equalization)
P.O. Box 1799
Sacramento, CA 95808

Abraham Sageev
Petroleum Engineering Department
Stanford University

Subir K. Sanyal
GeothermEx, Inc.
5221 Central Avenue, #201
Richmond, CA 94804

Alex Schriener, Jr.
Unocal
2099 Range Avenue
Santa Rosa, CA 95406

Ron Schroeder
BGI
2000 Center, Suite 302
Berkeley, CA 94704

Hiroshi Shigeno
Geological Survey of Japan
345 Middlefield Road, M/S 910
Menlo Park, CA 94025

Mike Sorey
U.S. Geological Survey
345 Middlefield Road
Menlo Park, CA 94025

Amanda Spencer
Lawrence Berkeley Lab.
Earth Sciences Division, Bldg. 50E
One Cyclotron Road
Berkeley, CA 94720

Mitchell Alan Stark
Unocal
2099 Range Avenue
Santa Rosa, CA 95401

Valgardur Stefansson
United Nations
One United Nation Plaza, Room DC1-784
New York, NY 10017

Kenneth F. Stelling
State of California
50 "D" Street, Room 300
Santa Rosa, CA 95405

Susan G. Stiger
Idaho National Engineering Lab.
P.O. Box 1625
Idaho Falls, ID 83415

Douglas Stockton
Division Oil & Gas
1416 9th St., Room 1310
Sacramento, CA 95814

Stanley S. S. Sun
Bureau of Land Management
2800 Cottage Way
Sacramento, CA 95825

David Sussman
Unocal
2099 Range Avenue
Santa Rosa, CA 95401

Chandler A. Swanberg
GEO Operator Corporation
1825 South Grant St., Suite 900
San Mateo, CA 94402

Jefferson W. Tester
Massachusetts Institute of Technology
Department of Chemical Engineering, 66-309
Cambridge, MA 02139

Donald M. Thomas
Hawaii Institute of Geophysics
University of Hawaii
2525 Correa Road
Honolulu, HI 96822

Richard Thomas
California Division of Oil & Gas
1416 9th Street, Room 1310
Sacramento, CA 95820

Hiroyuki Tokita
West Japan Engring Consultants, Inc.
Denki Bldg., Sunselco
No. 1-1, 1-chome
Watanabe-Dori, Chuo-ku
Fukuoka, Japan

Ashok Verma
Lawrence Berkeley Laboratory
Earth Sciences Division, Bldg. 50E
One Cyclotron Road
Berkeley, CA 94720

Mark A. Walters
GEO Operator Corporation
2300 County Center Drive
Suite 250
Santa Rosa, CA 95401

Richard A. Whittle
Geoscience Limited
Pollen House, 10-12 Cork Street
London W1X 1PD, England

Ken Williamson
Union Oil Co. of Calif.
2099 Range Avenue
Santa Rosa, CA 95406

Ted Wilmsen
Thermal Power Company
3333 Mendocino Avenue
Santa Rosa, CA 95401

James L. Woodruff
Hawaii Natural Energy Institute
Holmes Hall, Room 246
University of Hawaii at Manoa
Honolulu, HI 96822

Phillip M. Wright
Highway 9 Utah Research Institute
391 Chipeta Way
Salt Lake City, UT

Tsukasa Yoshimura
New Energy Development Organization
Sunshine 60, 29F, 1-1, 3-Chome
Higashi-Ikebukuro
Toshima-Ku
Tokyo 170, Japan

SUBJECT INDEX VOLUMES 1-11

Acid stimulation: IX 421

Acoustic emission: IX 403

Acoustic logging: XI 283

Adsorption: X 247

Ahuachapan field: IX 97, XI 217

Air-steam-water systems: IX 351

Alaska: VI 66, VIII 25, VIII 31,
X 227

Albano field: IX 17

Alfina field: I 93

Amiata field: IX 17

Aquifer:
contamination: IX 351
Free surface: IX 351
geopressured-geothermal: VIII 261
linear: X 97

Aquitaine basin: IX 5

Autoclave test facilities: IX 415

Axial splitting: IX 381

Azores: VIII 73

Baca field: VI 28, VII 47, VII 53, VIII 91,
VIII 97, IX 145, XI 7

Back-pressure turbines: IX 275

Barometric pressure: XI 15

Basalt: VIII 189

Bejing field: IX 127

Beowaw field: IX 421

Berea sandstone: VIII 197, VIII 205

Boise KGRA: III 130

Boiling processes: IX 231

Borehole televiewer: X 13

Bottle Rock (The Geysers): IX 135

Bottom-hole pressure: IX 289, IX 291

Brady hot springs: IV 218

Breakthrough time: XI 93

Brines: II 176, VII 61, VIII 309, VIII 329,
reinjection: IV 42
scaling: IV 42
thermodynamic properties: II 247

Brittle-ductile transition: IX 381

Broadlands field: IV 139, IV 332, V 37,
V 313, VI 28, VI 238, VIII 127, VIII 183,
IX 107, X 189

Bubble flow: XI 277

Build-up tests: IX 403

Bulalo field: IV 228, V 255

Calcite: IX 317, X 247

Calcium: IX 317, X 37

California: I 52, I 74, I 84, I 89, I 135,
I 143, I 146, I 153, II 9, II 16, II 30,
II 39, II 61, II 75, II 116, II 126,
II 143, II 159, II 324, III 18, III 61,
III 107, III 116, III 145, III 178,
III 209, IV 96, IV 106, IV 118, IV 300,
V 83, V 131, V 139, V 189, V 211, VI 13,
VI 279, VI 303, VI 344, VI 351, VI 361,
VII 161, VIII 31, VIII 39, VIII 45,
VIII 177, VIII 295, IX 5, IX 157, IX 205,
IX 299, IX 311, IX 365, IX 409, X 89,
X 123, X 129, X 133, X 141, X 195, X 247,
X 297, XI 29, XI 43, XI 141, XI 197,
XI 251

Campi Flegrei Caldera: IX 17, IX 53

Canada: X 253

Capillary pressure effects: IX 351, IX 443

Carbon dioxide: X 233, X 273

Casa Diablo: X 297

Cascade volcanic belt: X 253

Castelnuovo: VIII 323, IX 17, IX 221

Casing corrosion: X 189

Cell boundaries: X 89

Cements:
testing: VI 126

Cerro Prieto: IV 5, V 44, V 55, V 228,
VI 121, VI 130, VI 258, VI 344, VII 23,

VII 29, VII 35, VIII 49, VIII 161, VIII 171, VIII 197, VIII 205, VIII 231, IX 81, IX 247, IX 291, IX 357, IX 427, X 73, X 301, XI 7, XI 51, XI 127

Chemical analysis:
standardization: V 139

Chemical tracers: VIII 289

China: IX 127

Chingshin field: V 64, V 96, V 277, IX 193

Chingshui field: IX 193

Choking: IX 279

Chloride concentration studies: IV 239

Chloride tracer: X 265

Circulation: X 195

Cold water injection: VII 175, VIII 279, IX 339, XI 161

Comision Federal de Electricidad (CFE)
research: VIII 49, IX 81

Composite reservoir: VIII 103

Compressibility: VIII 197, IX 279, IX 381

Computer codes: V 147, V 169, V 222, V 195
FRACSL: X 287, X 293
FRIP: IX 387
GEOCOM: IX 409
NSCGREATS: VIII 149
liquid-dominated systems: V 199

Computerized well test analysis: IX 199

Conceptual model: X 29, X 279, XI 65, XI 109, XI 197

Confining pressure: IX 427

Contamination of aquifers: IX 351

Continuum model: VII 157

Convection: VIII 5

Cool downflows: XI 169

Cooling effects: IX 351, X 73, X 195

Corrosion: X 189, XI 1

Coso field: VIII 45

Coso Hot Springs: IV 118

Costa Rica: VII 13, X 37

Costs: IX 409, X 31

Crack-like reservoirs: IX 403

Cracks: IX 415, IX 449

Critical flow slip model: VIII 143

Decline curve: X 105, X 163

Deliverability: X 31, X 97, X 105

Denmark: IX 5

Desert Peak: IX 151

Dilatancy: IX 381

Discrete fracture model: VII 157

Dispersion: VII 103, VIII 283, IX 253, IX 311, IX 373, X 259, X 287

Double porosity: VIII 115, VIII 219, IX 175, IX 181, X 163, X 293

Doublet systems: IX 331

Downhole instruments: XI 231

Downhole pressure transient data: IX 217

Drawdown: IX 261, X 45, XI 77, XI 149

Drift velocity: X 287

Drill cores:
data acquisition systems: II 46

Drilling mud: VIII 205

Dry steam: X 23, X 65, XI 225

Dual permeability: X 293, XI 71, XI 77

Ducts: IX 279

Earth tides: XI 15

East Africa: I 113

East Brawley: VIII 39

East Mesa: IX 299, IX 311, X 247, X 287

East Mesa field: I 23, I 52, I 146, II 9, II 39, II 75

Electrical potential: IX 421

Electric Power Research Institute (EPRI) VII 21

Ellidaar field: IX 37, X 279

El Salvador: VII 13, IX 97, XI 217

England: VIII 237, IX 387, XI 35

Enthalpy data: VII 143, VII 151, VIII 127, IX 253, IX 345, IX 357, X 133, X 241, X 273

Environmental effects: VIII 329

Epidote: IX 269

Europe: IX 5

Expansion: IX 427

Exploration: IX 167

Explosive fracturing: IX 409

Explosive stimulation: VIII 237

Falloff data: X 151

Fault-charged systems: VII 161

Fenton Hill: II 188, IV 244, IV 249, IV 256, VI 272, VI 367, VII 97, VIII 249, VIII 269, IX 397, XI 189

Ferrara: IX 17

Field studies: XI 175, XI 183, XI 189

Fissured reservoirs: IX 175

Flashing: VIII 143, IX 253, IX 279, IX 449, X 37

Flow and gas extraction model: VII 133

Flow data analysis: VII 47, VII 131, VIII 119, VIII 133, VIII 175, IX 199, IX 205, IX 345, IX 443, X 227

Flow, interporosity: X 163

Flowmeter: IX 205

Flow modeling: XI 77

Flowrate analysis: IX 345, IX 443

Flowrate prediction: IX 305, IX 365, IX 373

Flow velocity: XI 231

Fluid and heat model: VII 151, VIII 219

Fluid behavior: VIII 225

Fluid depletion: VIII 177, XI 161

Fluid flow: VII 151, VIII 211, VIII 219, X 37

Fluid flow:
- measuring methods: III 198, VI 126

Fluid migration: VIII 161, XI 71

Fluid reserves: X 113

Fossil-liquid-dominated system: XI 203

FRACSL code: X 287, X 293

Fracture:
- detection: X 13, XI 65, XI 207
- explosive: IX 409
- gas: XI 245
- ladders: VIII 139
- mechanics: IX 415
- modeling: XI 72
- networks: VIII 285, X 287, X 293
- skin: IX 175
- stimulation: VII 53, IX 409
- widths: IX 323

Fractured reservoirs: II 16, II 21, II 34, II 168, V 293, VII 151, VII 169, VIII 97,VIII 111, VIII 115, VIII 119, VIII 143,VIII 219, VIII 275, IX 135, IX 151,IX 299, IX 305, IX 311, IX 323, IX 331,IX 373, X 145, X 259, XI 35, XI 43, XI 51, XI 59, XI 65, XI 71, XI 77, XI 85, XI 149

- flow models: I 45, VI 178
- heat transfer: V 175
- permeability: V 103

Fractures:
- deformation: I 37

Fracturing pressure: IX 397, IX 409

France: IX 5

Fujian: IX 127

Fumarole steam: IX 231

Gabbro zone: X 97

Galzignano: IX 17

Garibaldi volcanic belt: X 253

Gas:
- composition: IX 221
- concentration: IX 247
- correction: VIII 133
- geothermometers: IX 231
- noncondensable: X 37

Gas-steam ratio: VIII 323

Gas-water ratio: VIII 261

Generating capacity: IX 157

GEOCOM model: IX 409

Geologic cross-sections: XI 251

Geological model: VIII 231

Geologic structures: I 37, III 209,
geothermal exploration: I 113
mathematical models: III 214

Geologic surveys:
Alaskan sites: VIII 31
Cerro Prieto: VIII 49
Imperial Valley: VIII 39
Los Humeros: VIII 19
Pilgrim Springs: VIII 25
Sarukawa: X 207

Geophysical surveys: I 52, III 18, III 36, III 61, III 70, VI 328, VI 338
evaluation: V 115

Geopressured-geothermal aquifer: VIII 261

Geopressured systems: I 130, I 146, VI 76, VI 84, VI 98, VI 105
geologic faults: III 209
geothermal wells: IV 280
ground subsidence: IV 280
mathematical models: II 299
sandstones: IV 280
simulation: II 299, V 159

Geosciences: XI 135, XI 141, XI 149

Geothermal energy:
research programs: I 23, I 198, I 199, I 219, III 192, IV 15, V 5, VI 150
resource assessment: VI 3
resource development: IV 5

Geothermal exploration: III 130, VI 338, VI 361

Geothermal fields:
geologic faults: II 46
geologic structure: II 46, VI 21
heat flow: II 30
mathematical models: IV 36
recharge: II 40, II 150, II 159, II 339, V 55, VI 21
reinjection: II 8, II 46, II 98, II 116, II 181, IV 322, V 26, V 37
rock-fluid interactions: II 34
tracer techniques: IV 249, VI 344
well temperature: II 290, VI 272, VI 279, VI 297, VI 316, VI 328

Geothermal fluids: V 278
chemical analysis: II 30, II 116, VI 21,
chemical composition: IV 96, V 262 VI 279
geochemistry: VI 84, VI 367
plugging: III 163, IV 275
reinjection: IV 294, V 355
scaling: I 185, IV 42
thermodynamic properties: I 247, II 247, IV 294
transport: V 329
water chemistry: VI 98

Geothermal power plants: I 117, I 153, II 9, II 116
economics: I 153
performance: I 135
steam separators: I 135

Geothermal reserves: IX 193

Geothermal resources:
brines: I 135
economic analysis: II 150, III 158, VI 3, VI 238
economics: I 161, I 167
geothermal fluids: I 113
management: II 181, V 5
remote sensing: II 30
reservoir engineering: IV 234
resource assessment: II 12, III 145, VI 238
resource development: VI 13, VI 34, VI 41, VI 374, VI 380
resource potential: III 3, III 9, III 70, III 96, III 107
risk assessment: VI 374, VI 380
temperature surveys: II 30, II 40, VI 28

Geothermal space heating: II 181

Geothermal systems:
convection: I 206, I 213, II 236, II 251, II 339, IV 300
flow models: I 26, I 42, I 45, I 52, I 62, I 201, I 213, I 267, II 193, II 200, II 229, III 188, III 209, IV 286, IV 300, IV 308, V 11, VI 194, VI 218, VI 322
fluid injection: VI 98, VI 204
heat extraction: II 46, II 181, II 188, II 200, VI 264, VI 272
homogeneous: XI 85
heat transfer: I 50, I 52, I 249, II 46, II 222, II 236, II 251, II 263, II 268, IV 112, IV 286, IV 300, IV 308, VI 243
hydrodynamics: IV 146, IV 160
mass transfer: II 268, IV 286, IV 300, IV 308
mathematical models: I 26, I 65, I 146, I 242, I 247, I 267, II 46, II 126, II 193, II 263, II 268, II 308, II 324, III 203, III 214, IV 36, IV 286, IV 300, IV 308, VI 194, VI 213, VI 264
natural convection: VI 194
reinjection: I 62
reservoir engineering: I 146, II 3, II 6, II 9, IV 36, V 5, VI 66, VI 253
rock-fluid interactions: I 240, IV 275, VI 322
simulation: I 130, I 198, I 201, I 225, I 232, I 247, II 116, II 159, II 222,

II 308, II 310, III 178, III 185, III 188, IV 308, IV 332, VI 188, VI 204, VI 213, VI 253
thermodynamic properties: VI 213
two-phase flow: I 42, III 185, III 192, IV 308, VI 28, VI 49, VI 170, VI 288
vapor pressure: IV 60
water chemistry: IV 42, IV 275, IV 294

Geothermal wells:
enthalpy: VI 224
explosive stimulation: I 192, II 213, II 219
field tests: II 109, II 176, IV 96
flow models: V 322, VI 130, VI 159, VI 188
flow rate: VI 139
fluid withdrawal: VI 139
hydraulic fracturing: I 174, I 178, I 180, II 188, II 198, II 200, III 36, VI 272, VI 303
mathematical models: VI 130, VI 159
measuring instruments: II 101, II 109, II 176, VI 126
performance: VI 218
plugging: III 163, IV 106
pressure measurement: IV 96
sampling: VI 84
scale control: I 185
sonic logging: IV 256
temperature measurement: II 136, IV 96
testing: I 69, I 74, I 77, I 93, I 101, I 117, I 124, II 21, II 75, II 85, II 98, II 116, II 143, II 168, III 64, III 96, III 116, III 125, III 130, III 138, III 145, III 172, IV 106, IV 112, IV 118, IV 133, IV 139, IV 146, IV 153, IV 160, IV 165, IV 176, IV 188, IV 201, IV 207, IV 213, IV 218, IV 322, V 11, V 44, V 55, V 64, V 77, V 83, V 90, V 115, VI 322, VI 76, VI 105, VI 145, VI 150, VI 159, VI 170, VI 288
transients: I 93, I 124, III 172, VI 159, VI 170
two-phase flow: I 77, II 21, III 198
well logging: I 74, II 21, II 66, III 36, III 70, III 81, V 282, V 316, VI 258, VI 279, VI 303, VI 310
well pressure: I 157, VI 28, VI 145, VI 150

Geothermometry: II 34, VI 367, VI 351, IX 231

Germany: IX 5

Geysers: I 84, I 89, I 153, II 16, II 30, II 61, II 143, III 18, III 61, IV 96, IV 106, IV 201, V 83, V 127, V 175, V 302, VI 13, VI 279, VI 344, VI 351, VI 361, VIII 177, VIII 295, IX 135, IX 409, X 89, X 105, X 123, X 129, X 133, X 141, XI 29, XI 43, XI 197, XI 251

Goddard Springs: VIII 31

Granite: VII 127, VII 133, IX 387

Gravity change/subsidence ratio: VIII 177

Greece: IX 73

Ground subsidence: I 65

Groundwater: XI 135

Guangdong: IX 127

Gulf coast, U.S.: VI 84

Hatchobaru, IX 115, X 79

Hawaii: I 219, II 109, III 138, IV 133, IV 201, VIII 155, VIII 309, X 65, X 201, XI 1

Heat:
conduction: X 195
extraction: VII 169, VIII 255, X 73
flow: VII 151, VIII 211, VIII 219, VIII 225
sweep model: X 73
transfer: VII 151, X 151
transmission model: VIII 269

Heat transfer: III 49, XI 175

Heber field: I 74, I 135, II 9, II 126 IX 157

Hengill geothermal area: X 23

High-energy gas fracturing: XI 245

High-temperature logging: VII 115

History matching: X 97

Hoki: X 79

Hot-dry-rock reservoirs: VII 97, VIII 237, VIII 249, VIII 269, IX 5, IX 387, IX 397, IX 403, XI 35, XI 59, XI 189

Hot-dry-rock systems: I 174, I 258, II 188, II 193, II 198, II 200, II 213, III 49, V 103, VI 272, VI 303, VI 367
fluid flow: IV 244, IV 249, IV 256, IV 264

Hot-dry-rock systems:
fracture properties: IV 244, IV 249, IV 256, IV 264, IV 270
growth: IV 270
heat extraction: IV 244
resource assessment: III 3

Hot springs: IX 365, X 123

Hot spring monitoring: XI 141

Hot-water reservoirs: IX 291

Hot-water systems: VI 351
economics: III 158
reservoir engineering: VI 3

Hydraulic conductivity: X 287, XI 71

Hydraulic fracturing: IX 397, IX 409, IX 415, XI 189

Hydraulic injections: IX 387

Hydraulic modeling: XI 35

Hydrogeologic model: VIII 171

Hydrogen sulfides:
renewal: I 153

Hydroisotopic studies: XI 175

Hydrologic flow: XI 231

Hydrology: VIII 67, VIII 275, VIII 285

Hydrothermal alteration: II 34, III 361, IX 145, IX 269, X 253

Hydrothermal convection systems: VIII 5

Hydrothermal systems: VIII 5, VIII 19, VIII 25, VIII 31, VIII 39, VIII 45, IX 135, IX 145, IX 151, IX 157, X 89

Hydrothermal systems:
ground subsidence: II 310
mathematical models: I 126, I 161, VI 21, VI 69
simulation: V 147, V 159, V 212

Iceland: IV 153, V 169, V 329, VI 49, VII 13, VII 61, VII 71, VII 139, VIII 111, VIII 189, VIII 211, IX 37, IX 345, X 23, X 45, X 177, X 279, XI 7, XI 109

Ihaho: I 117, I 124, II 75, II 168, III 125, III 130, V 26, V 120, V 183, VI 115, VIII 275, VIII 279, IX 299, IX 311, X 287, XI 71, XI 77

Imperial Valley: III 107, VIII 39, VIII 197, IX 5, IX 205, IX 409

Indium chelated tracers: XI 103

Industry advisory panel: X 5

Inhibitor degradation rate: IX 317

Injected fluid monitoring: X 297

Injection-backflow tracer tests: IX 299, IX 305, IX 311, X 247

Injection depth: IX 339

Injection intervals: XI 207

Injection studies: XI 167

Injection tests: VII 71, VII 77, VII 175, VIII 73, VIII 97, VIII 103, VIII 111, VIII 249, VIII 275, VIII 279, VIII 283, IX 299, IX 305, X 195

Injection wells:
performance: V 255
plugging: III 163
testing: V 26, V 37, VI 115

Injectivity-productivity estimation: XI 23

Interference testing: IX 151, IX 187, IX 193, XI 15

Isothermal flow systems: XI 135

Isotopic studies: VIII 45, VIII 309, VIII 323, IX 253, X 253

Italy: I 37, I 93, I 101, II 21, II 40, II 150, IV 201, IV 165, III 214, V 90, V 197, V 212, V 262, VI 21, VI 351, VII 13, VII 77, VII 85, VII 91, VIII 295, VIII 315, VIII 323, IX 5, IX 17, IX 53, IX 221, IX 247, XI 161

Ixtlan de los Hervores: IX 81

Japan: III 70, VII 13, VII 103, VII 115, VIII 149, VIII 155, IX 115, IX 403, X 79, X 207

Kakkonda: IX 115, IX 403

Kawerau field: VI 170, VIII 183

Kenya: IX 65

Kilauea volcano: VIII 309, X 65, X 201

Kirishima field: VIII 149

Kizildere field: X 53

Klamath Falls: IX 187, IX 331

Krafla field: V 169, VI 49, VII 71, VIII 211, IX 37, IX 211, IX 345, X 177, XI 7

Land leasing
legal aspects: I 153

La Primavera: IX 81, IX 87

Lardarello field: I 37, II 21, II 40, II 150, III 214, V 90, V 212, V 262, VI 21, VI 351, VII 77, VII 85, VII 91, VIII 295, VIII 315, VIII 323, IX 5, IX 17, IX 221, IX 247, X 113, X 273, XI 161

Lassen hydrothermal system: IX 365, XI 141

Latera field: IX 5, IX 17

Laugarnes field: IX 37

Lawrence Berkeley Laboratory: IX 205, IX 443, XI 65

Lawrence Berkeley Laboratory numerical simulator: VIII 255, IX 157

Leyte: IX 121

Linear acquifer: X 97

Linear boundary detection: XI 15

Linear elastic fracture mechanics: IX 415

Lip-pressure method: VIII 133

Liquid-dominated system: X 189, XI 197, XI 217

Liquid-phase heterogeneity: IX 253

Log-log type curve: X 163

Longevity: IX 157

Long Valley: II 324

Los Alamos: VIII 249, VIII 269, XI 59

Los Azufres field: IV 176, VII 41, VII 143, IX 81, IX 253, IX 269, IX 275, IX 285, X 213, X 219, X 233, X 241, X 265, XI 51, XI 237

Los Humeros field: VIII 19, IX 81

Los Negritos: IX 81

Louisiana: VI 76, VIII 261

Low-temperature reservoirs: VII 109

Lumped double porosity: VIII 189

Lumped parameter model: VII 23, X 45, X 97

Mak-Ban field: VI 34

Makushin volcano: VIII 31, IX 167, X 227

Mammoth-Pacific power plant: X 297

Maritaro: IX 269

Mathematical models
comparative evaluations: VI 121
wellbore: VI 130

Matrix diffusion: IX 323

Matrix-dominated reservoirs: IX 299

Matrix thermal expansion: IX 427

Matsukawa: IX 115

Maturing geothermal fields: XI 161, XI 169

Meager Creek: X 253

Methane: VII 133

Mexico: IV 5, IV 239, IV 176, V 44, V 55, V 228, VI 60, VI 130, VI 258, VI 328, VI 344, VII 13, VII 23, VII 29, VII 35, VII 41, VII 53, VIII 19, VIII 49, VIII 161, VIII 171, VIII 197, VIII 231, IX 81, IX 87, IX 253, IX 269, IX 275, IX 285, IX 357, IX 427, X 73, X 213, X 219, X 233, X 241, X 265, X 273, X 301, XI 7, XI 51, XI 127, XI 237

Microcracking: IX 381

Milos Island: IX 73

Mineral alteration zones: IX 269

Mineralogy: IX 269, X 89, X 253

Mineral precipitation: X 247

Miravalles field: X 37

Mist flow: XI 277

Modeling: XI 109, XI 117, XI 127, XI 283

Mofete: IX 5, IX 17, IX 53

Mokai field: IX 107, X 29

Momotombo: III 96

Monroe field: V 115

Monte Amiata: IX 5, IX 17

Mori: IX 115

Mountain Home field: V 183

Mountainous terrain: XI 135

Moving front: VIII 103

Mud contamination: VIII 205

Multi-component modeling: X 279

Multiple feed wells: XI 23

Multiple interacting continua
(MINC): VIII 219

Namafjall field: VI 49, IX 37

Natural gas wells: III 29

Nesjavellir field: IX 37, X 23, XI 109

Nevada: IV 218, V 329, IX 151, IX 421

New Mexico: II 88, V 103, V 238, VI 28,
VI 272, VI 367, VII 97, VIII 91, VIII 97,
VIII 249, IX 145, IX 397, XI 59, XI 189

New Zealand: I 126, II 40, II 308, II 310,
III 185, IV 36, IV 139, IV 217, IV 332,
V 37, V 199, V 205, V 302, V 309, VI 28,
VI 41, VI 126, VI 139, VI 145, VI 170,
VI 238, VII 13, VIII 67, VIII 111,
VIII 127, VIII 133, VIII 183, IX 107,
IX 323, X 31, X 189, XI 15, XI 169,
XI 217, XI 271

Nicaragua: III 96

Niland field: I 135, I 143, II 9

Ngawha field: V 309, VIII 133, IX 107

Nicaragua: VII 13

Nigorikawa: IX 403

Noncondensible gases: X 113, X 233

Nonisothermal injection: VIII 103, IX 211,
X 151, XI 59

NSCGREATS model: VIII 149

Ohaaki field: XI 15

Ohtake: X 79

Okoy field: VI 69

Olkaria: IX 65

One-dimensional sweep model: VIII 255

Onikobe: IX 115

Onuma: IX 115

Optimization: X 31

Oregon: IX 187, IX 331

Orthogonal fracture junctions: IX 373

Otake: IX 115

Output curve: X 37

Overexploitation: IX 97

Packer seats: XI 207

Paragenesis: IX 269

Paris basin: IX 5

Pauzhetka field: X 57, XI 175

Permeability: VII 121, VII 127, VIII 111,
VIII 127, VIII 205, VIII 211, VIII 261,
IX 145, IX 239, IX 299, IX 345, IX 387,
IX 443, X 301, XI 66, XI 223, XI 245,
XI 283

Permeability-thickness ratio: VIII 261

Petrochemistry: VIII 39

Petrophysical properties: XI 51

Petrothermal energy: IX 381, IX 387, IX 397,
IX 403, IX 409, IX 415

Phase separation: IX 253

Phase studies:
aqueous solutions: IV 66

Phase trapping: IX 443

Philippines: IV 228, V 255, VI 34, VI 69,
IX 121

Phlaegrean fields (Mofete): IX 5, IX 17

Pilgrim Springs field: VIII 25
flow models: II 229, VI 218
two-phase flow: IV 66

Plastic flow: IX 381

Porosity logging: VIII 189

Porosity prediction: IX 305

Porosity-thickness product: IX 193

Porous media: IX 443, X 287, X 293, XI 85,
XI 223, XI 283

Potassium concentration studies: IV 239

Power costs: XI 217

Power generation: VII 35, VII 21, IX 81,
IX 275, X 53, X 219, X 227, XI 169,
XI 215, XI 217

Pressure build-up tests: IX 193, X 177

Pressure drawdown: X 97, X 233

Pressure drop: XI 277

Pressure measurements: V 96, V 103, VIII 67, VIII 91,VIII 103, VIII 119, VIII 279, IX 199, X 241

Pressure prediction: IX 351

Pressure profiles: XI 187

Pressure-temperature-spinner tool: XI 198

Pressurized tests: X 169, XI 59

Pressure transient analysis: VII 161, IX 387, X 133, X 151, X 163, XI 7, XI 93

La Primavera field: VI 328

Production data: IX 345, X 57

Production engineering: X 183, X 189, X 195

Production/injection ratio: IX 339

Productivity index: IX 289, IX 291

Productivity (inferred): IX 211

Proximity functions: VIII 219

Pseudo-steady state flow: IX 175, IX 181

Puhagan field: IX 121

Puna: X 65, X 201, XI 1

Pyrite: IX 269

p/Z analysis: X 97

Quartz precipitation: IX 239

Quasi-three-dimensional model: VIII 225

Radial flow: IX 449

Radicondoli: IX 17

Radon: VII 133, VIII 315, IX 261
- simulation model: IX 261
- transport: IX 261

Radon 222:
- diffusion: V 302
- monitoring: II 61, V 309, VI 344
- tracer studies: IV 201

Raft River: VIII 275, VIII 279, IX 299, IX 311, XI 77

Raft River field: I 117, I 124, II 75, II 168, III 125, V 26, V 120, VI 115, VI 159

Rate testing: VIII 73, VIII 119, X 163

Reactive-solute transport: IX 239

Recharge (natural): IX 221, IX 351, IX 357, X 73

Redondo Creek: VIII 91, VIII 97, IX 145

Reinjection: VII 41, VII 77, VII 85, VIII 49, VIII 275, VIII 279, VIII 289, IX 17, IX 97, IX 121, IX 339, X 259, X 265, XI 85, XI 93, XI 97, XI 103, XI 267

Relative permeability: IX 443

Remote sensing: X 13

Research programs: DOE: VIII 1, VIII 49, IX 1; EPRI: VII 21
- International cooperation: VII 13, VII 29, VIII 49, IX 1
- University: VII 5, VIII 255
- U.S.: VII 7, VII 11

Reservoir:
- behavior: VII 143, XI 35
- boundaries: X 89
- decay: X 213
- evaluation: X 201, X 207, X 213, X 219, X 227
- longevity: VII 161
- performance study: X 207
- scale: IX 217
- simulation: VIII 137
- sizing: XI 149
- temperature: XI 267
- vapor-dominated: XI 161

Reservoir chemistry: VII 91, VII 127, VII 133, VII 143, VIII 45, VIII 295, VIII 309, VIII 315, VIII 323, VIII 329, IX 65, IX 221, IX 231, IX 239, IX 247, IX 253, IX 261, IX 269, X 113, X 133, X 233, X 241, X 247, X 253, X 259, X 265

Reservoir engineering: III 87, IV 36, VII 1, VII 5, VII 7, VII 11, VII 13, VII 21, VII 161, VIII 25, VIII 49, VIII 171, VIII 231, VIII 275, IX 17, IX 107, IX 121, IX 415, X 1, X 5, X 13, X 97, X 207, X 273, XI 1

Reservoir physics: VII 115, VII 121, VII 139, VII 143, VIII 19, VIII 49, VIII 161, VIII 171, VIII 177, VIII 183, VIII 189, VIII 197, VIII 205, IX 421, IX 427, IX 443, IX 449, X 293, X 297, X 301, X 307, XI 217, XI 223, XI 225, XI 231, XI 237, XI 245

Reservoir rock:
- permeability: I 26, I 192, II 16, II 34,

II 188, II 198, III 24, III 172, III 192, IV 50, VI 218, VI 224, VI 288, VI 297, VI 316, VI 361
plugging: II 34
rock mechanics: II 263

Resistivity monitoring: VIII 161, VIII 189, IX 421, X 45

Resistivity-porosity relationship: VIII 189

Resource assessment: VII 109, VIII 1, VIII 31

Resource development: VII 23, VII 29, VII 35, VII 41, VII 47, VII 53, VII 61, VII 71, VII 77, VII 85, VII 91, VIII 1, VIII 49, VIII 67, VIII 73, IX 5, IX 17, IX 37, IX 53, IX 65, IX 73, IX 81, IX 87, IX 97, IX 107, IX 115, IX 121, IX 127, X 23, X 31, X 37, X 45, X 53, X 57, X 65, X 73, X 79

Reykjanes field: VII 61, IX 37, X 45

Ribiera Grande field: VIII 73

Rift zone: X 65

Rock failure: IX 381

Roosevelt KGRA: I 77, III 89

Rotorua field: IX 107

Rotorua monitoring program: XI 271

Rotarua-Whakarewarewa Field: VI 41

Rotary drilling: II 3

Salton Sea area: X 195

Salton Sea field: III 145, III 178, V 120

San Donato: IX 17

Sandstone: VIII 197, VIII 205, IX 427, X 287

San Miguel Island: VIII 73

San Vito: IX 5

Sarukawa waterflood project: X 207

Scale inhibitor: IX 317

Scaling: VI 130, XI 207

Scaling effects: IX 217, IX 277, IX 449, X 37

Sedimentary rocks: IX 427

Seismicity: II 101

Seismic study: X 297

Seltjarnarnes field: IX 37

Serrazzano Field: IV 201, V 169

Shear failure: IX 383, IX 397

Silica: X 247, X 279, XI 1, XI 259

Simulation: VIII 115, VIII 149, VIII 211, VIII 219, VIII 225, VIII 231, VIII 255, VIII 261, IX 261, IX 351, IX 357, IX 365, IX 373, X 105, X 151, X 195, X 273, X 279, X 287, XI 117

Single borehole system: XI 215

Sitka: VIII 31

Skin: X 169

Slug flow: XI 277

Slug test: IX 181, X 169

Sodium concentration studies: IV 239

Solute breakthrough: VIII 285

Solute transport: IX 305, X 287

Southern Negros: IX 121

Soviet Union: XI 175

Spinner measurements: IX 199, IX 205

Stanford Geothermal Program: VIII 255, IX 199

Stanford hydrothermal model: VII 169

Steam:
condensation: IX 231
excess: X 233
flow model: VII 179
quality: IX 231
reservoirs: IX 285

Step-rate injection tests: VIII 103

Stimulation: VIII 237, XI 35

Stochastic fracture distributions: VIII 219, XI 71

Storage capacity: X 169

Stratigraphy: IX 145

Streaming potential: XI 225

Stress: IX 387, IX 397, IX 415, IX 427

Streamtube model: VIII 143

Subsidence: VIII 177, VIII 183

Suginoi: IX 115

Sulfate discharge: XI 143

Summer Bay: VIII 31

Surface electrical potential: IX 421

Surprise Valley: VI 303

Svartsengi field: IX 37

Sweet Lake aquifer: VIII 261

Tainjin field: IX 127

Taiwan: V 64, V 96, V 249, VII 13, IX 193

Tauhara field: VIII 67

Tectonics: VIII 39

Tejamaniles: IX 269

Temperature:
- cycling: IX 427
- distribution: IX 339
- drop model: X 183
- monitoring: X 265
- reversals: X 31

Temperature gradients:
- mathematical models: V 337, V 343

Temperature measurement: III 55, III 89, III 107

Tenakee Springs: VIII 31

Test well: IX 167

Texas: II 299, IV 280, VI 76, VI 105

Thermal conductivity: VIII 214

Thermal degradation: IX 351

Thermal expansion: VIII 197, IX 427

Thermal landslide: X 123

Thermal Shallow Reservoir: X 129, X 133, X 141

Thermal water discharge: XI 141

Thermodynamic behavior: X 213, X 241

Thermohydrodynamic model: X 57

Tibet: IX 127

Tiwi field: VI 34

Tongonan field: IX 121

Torre Alfina: IX 5, IX 17

Torvaliga: IX 17

Tracer:
- chelated indium: XI 103
- dispersivity: X 259
- fluorescein: XI 97
- hydrocarbon: XI 97
- inert and reacting: XI 149
- recovery: IX 299, IX 305, IX 311
- retention: VIII 289
- rhodamine: XI 97

Tracer tests: VII 41, VII 85, VII 103, VII 135, VIII 289, IX 261, IX 323, IX 331, X 133, X 247, X 265, XI 39, XI 77, XI 93, XI 97, XI 103, XI 189

Transient flow: IX 175, IX 181, XI 277

Transmissivity: VIII 279, IX 211, X 23

Travale: IX 5, IX 17

Travale KGRA: I 101, IV 165

Triangular probability: X 31

Tritium: VIII 323

Turbogenerators: IX 275

Two-phase flow: VII 175, VIII 91, VIII 127, VIII 133, VIII 137, VIII 143, VIII 149, VIII 155, IX 283, IX 443, X 23, X 65, X 183, X 227, X 241, XI 7, XI 183, XI 223, XI 277

Two-phase flow:
- monitoring: III 43

Unalaska Island: VIII 31, IX 167, X 227

United Kingdom: VIII 237, IX 5, IX 387

U.S. Department of Energy (DOE)
- research: VIII 1, VIII 9, IX 1, X 1

U.S. Geological Survey: VII 11

USSR: VIII 329, X 57

Utah: I 77, III 89, V 115, XI 97

Valles Caldera: V 238, VI 272, IX 145, IX 397

Valve closure: IX 403

Vapor-dominated system: VIII 295, VIII 315,

IX 247, IX 261, X 89, X 97, X 105, X 113, X 65, X 227, X 273, XI 117

Vapor-dominated systems: VI 194
bottom hole pressure: V 127
two-dimensional calculations: VI 194

Vapor separation: IX 253

Vertical flow model: VIII 155, XI 237

Vertical steam wells: IX 285

Vicenza: IX 17

Viscosity: IX 211, IX 443

Volcanic regions:
heat transfer: VI 243

Volcanoes:
Garibaldi belt: X 253
Kilauea: VIII 309, X 65, X 201
Makushin: VIII 31, IX 167, X 227

Vulcano: IX 17

Wairakei: II 40, II 308, II 310, III 185, IV 36, IV 217, V 199, V 205, V 302, V 309, VI 121, VI 126, VI 139, VI 145, VI 28, VI 41, VI 238, VI 253

Wairakei field: VIII 67, VIII 183, IX 107, IX 323, XI 169, XI 217

Water influx: X 45, X 97

Water-rock reaction: IX 317

Water reservoirs:
hydrodynamics: IV 146

Well:
completion: X 37
discharge: VII 61
drilling: VII 35, VIII 25, X 31
stimulation: VII 53, VIII 237, IX 17, IX 121

Wellbore:
heat transmission code: VIII 269
scale: IX 217, X 37
simulation: VIII 137

Wellbore simulator: XI 277

Wellhead power plant start-up: X 219

Wellhead pressure: IX 285, IX 291

Well logging: VII 29, VII 115, VIII 161, VIII 171, VIII 177, VIII 183, VIII 189, VIII 197, VIII 205, VIII 237, IX 205, X 13, X 189, XI 197, XI 207, XI 215, XI 207, XI 283

Well siting: VII 161

Well testing: VIII 73, VIII 91, VIII 97, VIII 103, VIII 111, VIII 115, VIII 119, VIII 137, VIII 261, IX 17, IX 53, IX 73, IX 167, IX 175, IX 181, IX 187, IX 193, IX 199, IX 205, IX 211, IX 217, X 145, X 151, X 163, X 169, X 177, XI 7, XI 15, XI 23, XI 29

Wet steam: XI 225

Whakarewarewa springs: XI 271

Wyoming: VI 28

X-ray diffraction: IX 269

Yangbajain field: IX 127

Yunnan: IX 127

Yellowstone: VI 28

AUTHOR INDEX VOLUMES 1-11

Aamont, R.L.: II 188

Abe, H.: I 180, II 200, IX 403, IX 415

Abou-Sayed, A.S.: V 26

Abriola, L.: V 175

Abril, A.: VII 29, VIII 231

Adams, M.C.: IX 299, X 247, X 253, XI 97

Adams, R.H.: III 96

Aguilar, R.G.,: VI 367

Ahmed, U.: V 26

Ahn, J.H.: XI 97

Albright, J.N.: IV 256

Allegrini, G.: VII 77, VIII 231

Allen, C.A.: III 125

Allis, R.G.: VIII 67, VIII 177, VIII 183

Allman, D.W.: XI 77

Alonso-E., H.A.: IV 5, V 228, IX 81

Ambastha, A.K.: XI 183, XI 227

Andrade, M.: VIII 261

Ansari, J.: VIII 31

Antonelli, G.: V 147

Aragon, A.: X 219, X 241

Archambeau, C.: II 263

Arce, G.N.: VIII 31

Arellano, V.: VII 29, IX 291, IX 357, X 241, X 301, XI 237

Arenas, A.: VIII 205

Arnorsson, S.: IX 65, IX 321

Asseus, G.E.: II 268

Atherton, R.W.: I 267

Atkinson, P.G.: II 46, III 29, III 64, V 257

Axelsson, G.: VIII 189

Ayatollahi, M.S.: IV 264

Banerdt, M.: VII 133

Barelli, A.: I 93, I 101, IV 165, V 11

Barkman, J.H.: II 116, III 116

Barnes, H.L.: I 185, II 176

Barr, H.: X 31

Barragan, R.M.: IX 253, X 219, X 265

Bartz, D.: IV 50

Batchelor, A.S.: VIII 237, XI 35

Bazant, Z.P.: I 232, IV 270

Bentley, H.: XI 97

Benoit, W.R.: IX 151

Benson, S.: VII 71, VII 161, VIII 103, IX 187, IX 205

Bermejo M., F.: VII 25, VIII 197, IX 427

Bertrami, R.: IX 221

Bickham, R.E.: V 316

Bixley, P.F.: V 37, VI 126, VI 238, VIII 133, IX 107, X 189, XI 169

Bjornsson, S.: IX 65, XI 109

Blair, C.K.: V 115, VI 98

Bloomster, C.H.: I 167

Bodvarsson, G.: I 45, II 52, III 203, IV 146, IV 153, IV 160, V 64, V 329, VI 338, VII 139

Bodvarsson, G.S.: VII 71, VII 161, VIII 161, VIII 211, IX 157, IX 211, IX 345, IX 351, IX 443, X 105, X 151, X 279, XI 7, XI 109, XI 127

Bories, S.: I 247, IV 66

Breitenbach, K.A.: VIII 289

Brigham, W.E.: I 26, IV 165, V 212, VI 297, VI 150, X 97

Brown, D.W.: II 188, VIII 249

Brown, G.L.: IX 409

Brown, L.S.: VI 279

Brown, S.: V 183, V 343

Brownell, D.H.: II 310, IV 280

Bunyak, M.J.: VII 53

Burns, K.L.: XI 207

Burr, M.: XI 29

Byerlee, J.D.: II 198, IV 50, VII 127

Cabrera, J.: X 265

Calamai, A.: IX 17

Calore, C.: VI 21, VII 85, VII 91, VIII 295, IX 221, IX 247, X 273, XI 161

Campbell, D.A.: II 116, III 116, IX 167, X 227

Cappetti, G.: VII 77

Capuano, R.M.: VIII 275, IX 299

Carella, R.: IX 53

Carrigan, C.R.: XI 231

Castaneda, M.: VII 29, VIII 231, IX 357

Castanier, L.M.: IV 66, VII 23

Cataldi, R.: IX 17

Cathelineau, M.: IX 269

Cederberg, G.: IV 201

Celati, R.: I 37, I 101, I 242, II 21, II 150, VI 21, VII 77, VII 91, VIII 295, IX 221, IX 247, X 273, XI 161

Chang, C.R.Y.: V 64, V 96, V 249, V 337

Chang, S.P.: II 193

Champman, D.S.: V 115

Chavez, P.: XI 207

Chen, B: II 109, III 138, IV 133, X 201, XI 1

Cheng, P.: I 219, II 236, V 192, V 322, VI 243

Chiang, C.Y.: V 337, IX 193

Chiang, S.C.: V 249

Chiu, T.L.: IX 193

Chrysikopoulos, C.: XI 103

Chu, T.Y.: XI 245

Cillerai, V: II 21

Cinco, H.: IV 165

Clemo, T.M.: X 287, XI 71

Cofo, J.: X 73

Conche, B.: XI 283

Contreras, E.: VIII 197, IX 427, X 307, XI 51

Corona, A.: X 265

Counce, D.A.: VI 367

Counsil, J.: III 192, IV 60

Cox, B.L.: X 151, XI 7

Crosby, G.: III 89

Cuderman, J.F.: XI 245

Cuella, G.: IX 97

Culver, G.C.: IX 331

D'Amore, F.: V 262, VI 21, VI 351, VII 91, VIII 295, VIII 315, IX 221, IX 247, X 113, X 273

Danesh, A.: IV 60

DaPrat, G.: VIII 119, X 163

Dash, Z.V.: VII 97, VIII 269, IX 397, XI 59, XI 207

Dee, J.F.: X 97

Delaney, P.T.: IX 239

de las Alas, V.F.: IV 228

Denlinger, R.: VI 178

DeVilgiss, J.: IV 84

Dibble, W.E.: VI 316

Dickinson, D.A.: IX 279

Dominguez A.,B.: IV 5, V 228, VII 35, IX 87

Donaldson, I.G.: IV 36, V 222, VI 41, VII 1

Dorfman, M.H.: I 130, II 299, VI 105, VIII 261

Dougherty, D.E.: VIII 115

Downs, W.F.: II 34, II 176, VIII 275, IX 311

Dreesen, D.S.: XI 207

Drenick, A.: XI 197

Duda, L.E.: X 195

Duffield, W.A.: VII 11

Dundurs, J.: I 178

Dunn, J.C.: XI 231

Dvorov, I.M.: VIII 329

Dvorov, V.I.: VIII 329

Dykstra, H.: III 96, VI 13

Eaton, R.R.: VI 218

Economides, M.: IV 165, V 83, V 127, VI 66, VIII 25, VIII 31, IX 73, IX 167, X 227

Ehlig-Economides, C.: IV 60, IV 188, VI 66, VIII 25, IX 73

Eliasson, E.T.: VIII 211

Eliasson, J.: VI 288

Engi, D.: IX 421

Ershaghi, I.: V 282, VI 258

Esquer, C.A.: IX 357, X 73

Fallon, J.B.: VIII 91

Fandriana, L.: V 183

Farrell, W.E.: X 79

Faust, C.R.: I 198, II 308, III 185, IV 275

Fehlberg, E.L.: I 84, II 16, V 83

Ferguson, J.H.: XI 149

Ferriz, H.: VIII 19

Fisher, H.N.: V 103

Forster, C.: XI 135

Fossum, M.P.: VIII 289

Fournier, R.O.: VIII 45

Fradkin, L.J.: V 199

Frimannsson, H.: IX 65

Frye, G.: I 89, II 30, IV 96

Fujinaga, Y.: VI 188, X 207

Gale, R.O.: IV 139

Garfias, A.: IX 253, IX 269, X 233, X 241, X 265

Garg, S.K.: I 65, II 310, III 178, IV 217, IV 280, V 195, VI 76, VII 47, VII 175, VIII 97, X 79

Ghaemian, S.: VI 258

Gilardi, J.: X 259

Giovannoni, A.: VII 77

Glover, R.B.: VIII 127

Gobran, B.D.: VI 279, VI 297, VII 121

Golabi, K.: II 181, III 158, VI 374, VI 380

Goldman, D.: II 168, III 130

Goldstein, N.E.: VIII 161, X 13, XI 65

Gonzalez, A.: VI 60

Gonzalez, J.: X 233

Goranson, C.: III 116, IV 118, IX 205

Gould, T.L.: I 146

Goyal, K.P.: III 209, IV 300, V 205, VI 130, IX 151

Graj, A.N.: IV 15

Granados, E.E.: X 37

Grant, M.A.: IV 78, IV 139, V 37, V 242, VI 170, VI 28, VIII 111, VIII 127, VIII 133, IX 107, X 31, XI 271

Gray, W.G.: II 222

Greenfield, R.J.: IV 275

Grisgsby, O.C.: IV 249, VI 367

Gringarten, A.C.: I 113

Gudmundsson, J.S.: VII 61, VIII 143, IX 331, X 45, XI 183, XI 217, XI 277

Guevara, M.: VIII 205

Guglielminetti, M.: IX 53

Guillot, A.: IX 199

Gulati, M.S.: I 69, V 238

Gunnarson, A.: XI 109

Gunnarsson, G.: VI 288

Gunnlaugsson, E.: IX 231, XI 109

Haas, J.L.: II 247

Halfman, S.E.: VIII 171, XI 127

Halldorsson, G.K.: VII 71

Hammond, D.E.: VII 133

Handy, L.L.: V 282

Haney, J.: IV 118

Hanson, J.M.: II 46, IV 160, V 120

Hanson, M.E.: I 192

Harban, D.C.: I 77

Hardee, H.C.: XI 231

Harrar, J.E. VI 98

Harrison, R.F.: IV 272, V 115

Hart, C.M.: IX 421

Hauksson, T.: VII 61

Hebein, J.J.: IX 135, X 89, XI 43, XI 251

Herkelrath, W.N.: III 43, IV 54, VI 322, VII 179

Hernandez, L.: X 73

Hinrichs, T.C.: I 143

Hirakawa, S.: III 70, IV 234, VI 188, VII 115, VIII 225, IX 115, X 207

Hiriart, G.: VII 41, IX 275, X 213

Hite, J.R.: II 16

Hoang, V.T.: VIII 137

Holcomb, D.: II 263

Horii, H.: IX 381

Horne, R.N.: III 192, IV 138, VI 150, VII 5, VII 103, VIII 143, VIII 289, IX 199, IX 323, IX 331, X 259

Hosca, H.: XI 85

Howard, J.H.: III 9, IV 15, V 5, VI 3

Hsieh, C.H.: III 192, IV 60

Hsieh, P.A.: X 169

Hulen, J.B.: IX 145

Hull, L.C.: VIII 285, IX 305, IX 311, X 293

Hunsbedt, A.: II 213, III 49, V 293, VI 264 VII 169, VIII 255, X 73

Ichikawa, M.: VIII 225

Iglesias, E.: XI 51, XI 237

Ingebritsen, S.E.: IX 365, XI 117

Inglesias, E.R.: VI 84, VII 41, VIII 197, VIII 205, IX 291, X 241, X 265, X 301

Iovenitti, J.L.: XI 65

Iregui, R.: II 213, III 49

Isherwood, W.: III 18

Ishido, T.: X 79

Isokrari, O.F.: I 130, II 299

Izaguirre, O.: IX 269

Izquierdo, G.: VIII 205

Jackson, P.B.: IX 331

Jacobson, R.D.: XI 245

James, R.: I 52, III 198, V 355, VI 139, VI 145, VIII 133, IX 449, XI 259, XI 267

Jamieson, I.: III 61

Jensen, C.L.: IX 323

Jig, H.: IV 84

Johnson, S.E.: IX 331

Jones, A.H.: V 26

Jones, T.: VI 328

Jung, J.: XI 245

Juprasest, S.: V 183

Karasaki, K.: VIII 219, X 145

Karmarkar, M.: IV 207, V 322

Kasameyer, P.W.: I 249, II 290, III 163, X 297

Kassoy, D.R.: I 23, II 263, III 209, IV 300

Keer, L.M.: I 180, II 200

Keith, L.A.: IX 239

Kelkar, S.: XI 59, XI 207

Kelsey, F.J.: II 251

Keskinen, M.: VIII 39

Keys, W.S.: II 66

Kihara, D.: II 109, III 138, IV 133

Killup, M.W.: VIII 127

King, M.S.: X 307

Kingston, R.: IX 121

Kiryukhin, A.V.: X 57, XI 175

Kjaran, S.P.: VI 288

Klein, C.W.: X 37

Knapp, R.M.: I 130, II 299

Kolar, J.: XI 207

Koslow, K.N.: VIII 285, IX 305

Kruger, P.: I 169, II 61, II 213, III 49, III 192, IV 201, V 327, VI 264, VI 344, VII 1, VIII 255, VIII 315, IX 261, X 73, X 219, XI 103

Kuide, X.: IX 127

Kunze, J.F.: I 117, II 168, III 125, III 130 VIII 25

Kuo, T.M.C.: V 139

Kuwada, J.T.: I 157

Lai, C.H.: X 279

Lam, S.T.: VIII 255, X 73

Laredo, F.: IX 253, IX 253

Lawton, R.G.: II 188

Leaver, J.D.: IX 107, XI 15, XI 23

Lebreton, F.: XI 283

Levy, S.S.: XI 207

Li, T.M.C.: II 34

Lin, J.J.: V 249

Lipman, S.C.: II 6

Lippmann, M.J.: IV 5, V 228, VI 130, VII 35, VIII 49, VIII 171, IX 87, IX 157, XI 127

Liguori, P.E.: V 147

Lockett, G.E.: XI 215

Lockner, D.: II 198, IV 50

Lofgren, B.: VIII 25

Lombard, G.L.: I 135

London, A.L.: II 213, III 49

Long, J.C.S.: X 145

Lowell, M.G.: I 117

Maas, J.P.: IX 151

MacDonald, R.C.: VI 105

Macias-Chapa, L.: V 302, IV 201

Maeder, P.F.: IX 279

Maes, M.E.: II 219

Maini, T.: I 258

Manetti, G.: I 93, I 101, I 242, II 150, IX 17

Maney, J.: X 141

Mangold, D.C.: VII 161

Mann, L.: I 74

Mannon, L.S.: III 29

Manon, A.: IV 5

Marconcini, R.: II 21, II 150

Marcou, J.A.: XI 217

Marquez, R.: VIII 231, IX 357, X 73

Marsden, S.S., Jr.: XI 225

Martin, J.C.: I 42, II 251, IV 42

Martinez, A.: X 265

Mateen, K.: IX 181

Mathews, M.: VI 303

Mathias, K.E.: II 39

Matthiasson, J.: IX 65

Mazor, E.: III 55

McAtee, R.E.: VIII 275

McCoy, R.L.: VII 29

McEdwards, D.G.: II 75, III 116

McKee, C.R.: I 192

McNitt, J.R.: X 37

Meidav, T.: I 52, II 126

Menninger, W.: XI 93

Menzies, A.J.: VIII 143

Mercado, S.: VI 60

Mercer, J.W.: I 198, II 308, III 185, IV 275

Messer, P.H.: II 136, IV 228, V 255

Mete, L.: VIII 73

Michels, D.E.: IX 317, X 183

Miller, C.W.: VI 130, VI 159

Miller, F.G.: II 3, IV 165, VI 150, VII 13

Miller, J.D.: IX 373, XI 77

Miller, L.G.: II 168

Miranda, C.: X 219, X 241, X 265

Miyoshi, M.: VI 188

Mlodinow, L.D.: III 172

Mock, J.E.: X 1

Moench, A.F.: II 229, III 64, IV 54, IV 112, V 90, VI 178, VI 322, VII 179, IX 175, X 169

Mogen, P.: X 141

Molinar, R.: V 228, IX 291, X 219, X 301

Moore, D.: VI 361

Moore, D.E.: VII 127, IX 239

Moore, J.N.: X 253, XI 97

Morris, C.W.: VII 53, X 227

Morris, H.E.: IX 421

Morrow, C.A.: VII 127

Morse, J.G.: III 145

Muffler, L.J.P.: III 3

Mura, T.: I 180, II 200

Murakami, K.: X 79

Murphy, H.D.: I 174, II 188, IV 244, VI 272, VII 97, IX 397

Murphy, W.: VI 328

Nair, K.: VI 380

Nakanishi, S.: X 79

Nakatsuka, K.: IX 403

Narasimhan, T.N.: I 124, II 75, III 116, V 205

Nathenson, M.: I 50, II 40, IV 96

Nelson, D.V.: V 293, VI 264

Nelson, L.B.: III 130

Nemet-Nasser, S.: I 232, IX 381

Neri, G.: I 37, I 101, I 242, II 21, II 150, V 90, V 229, IX 17, IX 97

Netherton, R.: III 163, VI 98

Nguyen, V.V.: VI 213

Nielson, D.: IX 145

Nieva, D.: IX 253, IX 269, X 233, X 265

Niitsuma, H.: IX 403

Nikitopoulos, D.E.: IX 279

Noble, J.E.: IV 15

Noto, P.: VII 85

Nugent, J.M.: I 135

Nur, A.: IV 84, VI 316, VI 328

Nuti, S.: VII 85

Ohkuma, H.: VIII 261

Ohtsubo, H.: I 232

Okandan, E.: IX 339, X 53, XI 85

Okazaki, J.: V 139

Oliver, R.: VIII 205, IX 269

Olhoeft, G.R.: V 282

Olsen, G.: X 45

O'Neill, K.: II 222

Ortiz, J.: X 219

Ortiz-Ramirez, J.: XI 237

O'Sullivan, M.J.: IV 332, VI 204, VI 224 IX 107

Owen, L.B.: III 163, VI 98

Palmason, G.: IX 37

Parlaktuna, M.: IX 339

Perusini, P.: I 37

Peters, E.: VIII 261

Petty, S.: VI 115, IX 217

Pinder, G.F.: I 199, II 222, III 188, IV 286, V 175, VI 213, VII 157, VIII 115

Pine, R.J.: IX 387

Piwinskii, A.J. & Netherton, R.: III 21

Pohoiki, H.I.: IV 201

Polat, T.: X 53

Potter, J.M.: VI 316

Potter, R.M.: II 188, III 36, VI 272

Potter, R.W.: II 247, III 55

Pritchett, J.W.: I 201, II 310, III 178, V 159, V 195, IV 217, VII 175, X 79

Pruess, K.: IV 308, V 169, VI 194, VI 204, VII 151, VIII 161, VIII 211, VIII 219, VIII 255, IX 345, IX 443, X 113, X 273, XI 109, XI 161, XI 223

Qilong, Y.: IX 127

Quijano, L.: IX 253

Raasch, G.D.: VI 34, X 129

Rago, F.: VIII 261

Ramey, H.J., Jr.: II 3, III 49, III 192, IV 1, IV 60, IV 165, V 64, V 175, VI 150, VI 297, VII 13, IX 181, X 163, XI 15

Randall, G.S.: IV 272

Razo, A. XI 51

Reda, D.C.: VI 218

Reed, M.: IV 3, VII 109, X 1

Reeder, J.W.: VIII 31

Rex, R.W.: II 116

Rice, L.F.: II 159, IV 217, V 195

Rigby, F.A.: VI 310

Rimstidt, J.D.: I 185, II 176

Rinehart, J.S.: II 263

Riney, T.D.: III 178, IV 280, V 195, VII 47, VIII 97

Ritz, C.L.: VII 19

Rivera-Rodriguez, J.: VIII 73, IX 97

Roberts, V.W.: II 9, VII 21

Robinson, B.A.: XI 149, XI 189

Rodriguez, F.: VII 103

Rodriguez, J.: IV 176

Rojas, J.: XI 283

Rosa, A.: IX 199

Rosser, J.R.: IX 151

Rothstein, S.: VI 380

Roux, B.: V 343

Rudisill, J.M.: IV 218

Russell, B.F.: IX 311

Safai, N.M.: III 188

Sageev, A.: VI 297, X 163, XI 15, XI 93

Saltuklaroglu, M.: IV 176, V 44, V 55, VII 143

Samaniego-V, F.: IX 97

Sammis, C.G.: I 240, II 34, VII 133

Samundsson, K.: IX 65

Sanchez, E.: X 213

Santoyo, S.: VIII 205

Sanyal, S.K.: I 52, II 126, III 81, V 183, V 316, V 343, VI 279, X 37

Scherer, C.R.: I 161, II 181, III 158

Schroeder, R.C.: I 249, II 85, II 290, III 116, IV 118, IV 308, V 169, IV 5, V 228

Schultz, A.: IV 165

Schwarz, W.J.: III 9, IV 15, V 5

Seki, A.: IV 133, X 201, XI 1

Semprini, L.: IV 201, V 302, VI 344, VIII 315, IX 261, X 219

Sengul, M.: II 126

Sepehrnoori, K.: VIII 261

Shapiro, A.: V 175, VII 157

Sharme, D.: I 258

Shen, H.W.: I 213

Shen, K.Y.: V 96

Sigurdsson, O.: VII 71, VIII 189, IX 211, X 177

Sill, W.: VIII 275

Sioshansi, F.: VI 380

Skiba, P.A.: VIII 279

Smith, A.T.: X 297

Smith, E.W.: VI 69

Smith, J.L.: II 116

Smith, L.: XI 135

Solbau, R.D.: IX 205

Sorey, M.L.: I 225, II 324, V 199, V 222, VI 253, VII 109, VIII 5, IX 365, XI 141

Speliotis, G.: IX 73

Spivak, A.: II 159

Squarci, P.: VI 21

Squerci, P.: I 37

Stauder, J.J. X 253

Stefansson, V.: VI 49, VII 71, VIII 189, VIII 211, IX 37, IX 65, IX 211, IX 345, X 23, X 177, XI 109

Steingrimsson, B.: VI 49, X 177

Sternfeld, J.: VIII 39

Stieltjes, L.: I 113

Stoker, R.C.: I 117, II 168, III 125, III 130

Strobel, C.J.: II 143, IV 106

Sugrobov, V.M.: X 57, XI 175

Summers, R.: II 198

Svanbjornsson, A.: IX 65

Swenson, L.W., Jr.: VII 169

Syms, M. C.: VI 126

Syms, P. H.: VI 126

Tachimori, M.: VIII 149, VIII 155

Takahashi, H.: IX 403, IX 415

Takahashi, P.: II 109, III 138, X 201, XI 1

Takanohashi, M.: IX 403

Tansev, E.: III 107, IV 213

Tester, J.W.: II 188, IV 249, V 103, VI 272, XI 149

Thomas, D.M.: VIII 309

Thompson, J.M.: VIII 45

Thorhallsson, S.: IX 37, X 45

Thorson, L.: III 163

Thorsteinsson, T.: IX 37

Todd, M.C.: IV 275

Tomasson, J.: VII 61

Toms, R.S.H.: VIII 1, IX 1

Truesdell, A.H.: III 55, IV 96, IV 239, V 262, VI 21, V 277, VI 194, VI 351

Trujillo, P.E.: VI 367

Tsang, C.F.: I 62, II 75, II 85, III 172, IV 322, VI 224, VII 7, IX 443

Tsang, Y.W.: IV 322

Tsao, L.: IV 294

Tyran, C.K.: XI 225

Ucok, H.: V 282

Ungemach, P.: IX 5

Veggeberg, S.: XI 97

Verma, A.K.: VI 243, IX 443, XI 223

Verma, S.: X 219, X 265

Vides-R., A.: IX 97

Voss, C.I.: IV 286

Vrouzi, F.: IX 73

Warren, G.: II 61

Wasserman, M.L.: III 107

Watson, A.: IX 121

Weertman, J.: II 193

Wegner, R.E.: II 251

Wells, L.E.: V 373

Weres, O.: III 214, IV 294

Wescott, E.: VI 60

Westwood, J.D.: VII 23

Whitehead, N.E.: V 309

Wilson, D.M.: X 189

Wilt, M.J.: VIII 161

Witherspoon, P.A.: I 62, I 124, IV 5, V 228, VII 7, IX 443, X 105, X 145, X 279

Woitke, L.J.: I 153

Wolgemuth, K.M.: V 26

Wooding, R.A.: I 126, I 206, II 339

Woodruff, J.: XI 1

Wright, P.M.: IX 299

Wu, T.M.: V 249

Wu, T.S.: IX 193

Yamaguchi, S.: VII 115, X 207

Yee, A.: IV 294

Yoshimura, T.: X 79

Yuen, P.: III 138, IV 133

Zais, E.: III 85, IV 153, V 190, VI 121

Zebib, A.: II 263

Zelwer, R.: VIII 171

Zerzan, J.: IV 308

Zyvoloski, G.A.: IV 332, VIII 269, XI 59